NASA Conference Publication 2338

Rotordynamic Instability Problems in High-Performance Turbomachinery 1984

Proceedings of a workshop
held at Texas A&M University
College Station, Texas
May 28–30, 1984

ERRATA

NASA Conference Publication 2338

ROTORDYNAMIC INSTABILITY PROBLEMS IN HIGH-PERFORMANCE TURBOMACHINERY -- 1984

December 1984

The attached paper entitled "A New Model of Labyrinth Seal for Prediction of the Dynamic Force" by Takuzo Iwatsubo, Kazuki Takahara, and Ryoji Kawai should be added to CP-2338.

Rotordynamic Instability Problems in High-Performance Turbomachinery - 1984.
Workshop Held at Texas A&M University, College Station Texas, 28-30 May 1984

A NEW MODEL OF LABYRINTH SEAL FOR PREDICTION OF THE DYNAMIC FORCE

Takuzo IWATSUBO, Kazuki TAKAHARA, and Ryoji KAWAI
Kobe University, Rokkodai Kobe, JAPAN

SUMMARY

In this paper, a new mathematical model of a labyrinth seal which represent the dynamic flow induced force is formulated, that is, the flow in each ground is divided into a throttle part and a chamber part and the flow is represented by using the conditions of continuity, momentum and energy in both parts. The derived equation is solved and the result is compared with the experimental one. Then it is found that the equation represents the flow better than the previously proposed one.

INTRODUCTION

As mentioned in the authors' previous paper, the prediction of labyrinth seal force has become important and the research on this problem is increasing. The authors' research group is investigating the instability mechanism and force of labyrinth seal since 1977 and some papers are published. However these results are not satisfactory good agreement with the experimental results from the qualitative point of view.

The first mathematical model is based on Kostyuk(refs. 1,2) and the effect of jet flow through the seal clearance and the deflection of cross area of seal chamber are added(refs. 4,5). The result is partly agreement with the experimental one qualitatively, but in this model the effect of energy loss due to vortex which exists in the seal chamber has not been considered. Then the model is improved by taken into account of the effect of the energy loss by the vortex (which model is called model II)(ref. 6). The result of this model is improved better than the first one, but still exists unsatisfactory points.

From the observation of flow pattern it is clear that the flow region should be divided into two parts(ref. 7), then this paper proposes a new mathematical model, which is divided the flow into two regions, one is throttle (nozzle) part in which the flow through the seal clearance and the other is the chamber part. Then assumptions are taken in each part and the equations are derived. The obtained equation is solved almost same way as the former report and the results are compared with the experimental one which is obtained by Wright(ref. 3).

DERIVATION OF EQUATIONS

2-1 Assumptions

In order to derive the equation, followings are assumed;

(1) The flow in the labyrinth seal is divided into two regions in each seal, i.e. flow on a current flow part(I) and a vortex flow part(II) as shown in figure 1.

(2) The current flow in the chamber diverges with constant angle and entrances into the next seal throttle nozzle.

(3) Vortex flow means the dead flow region and there exists only the energy exchange between the current flow on the wall and the vortex flow.
(4) It is assumed that the variation of the seal clearance due to whirl is effective to the current flow on the wall but not to the vortex flow. Thus the effect of the current flow on the wall is taken into account for evaluating the flow induced force in this analysis.
(5) It is assumed that the flow in the seal can be divided into the axial flow and the circumferential flow and these flows are independent.
(6) The deflection of rotor is assumed to be small, then each loss factor is evaluated by using the value of non-deflection of rotor.
(7) As the working fluid is gas, the equation of ideal gas can be used.
(8) In the labyrinth seal ground the constant entropy change (or polytrope change) is assumed in the throttle (nozzle) part and the constant temperature change is assumed in the chamber part.
(9) The variation of axial direction in the current flow on the wall in the ground should be continuous, but for the sake of simplicity, lumped system is used for each ground.
(10) The thickness of the current flow on the wall is small enough for the variation in the radial direction.

2-2 Derivation of equation

The flow in the seal is different between the throttle part and the chamber part, therefore the equations are formulated in each part of figure 2.

(1) Equations in the throttle part

Let us denote the throttle (nozzle) part n_i, where subscript i means the ith seal. The entrance conditions in ith nozzle is equal to the exit conditions of the (i-1)th chamber R_{i-1} and the exit conditions of the nozzle is noted L_i. Similar to the first and the second paper, inlet and outlet mass balance i.e. continuous equation, momentum in the circumferential direction and the energy in the axial direction are considered. Then the equations are obtained as follows;

(a) Continuous equation

$$\frac{\partial(f_{ni} \overline{\rho}_{ni})}{\partial t} + \frac{\partial(f_{ni} \overline{C}_{ni} \overline{\rho}_{ni})}{\partial \omega} + \alpha_i \delta_i V_{Li} \rho_{Li} - \beta_{i-1} \delta_i V_{Ri-1} \rho_{Ri-1} = 0 \qquad (1)$$

(b) Momentum equation in the circumferential direction

$$(\alpha_i \delta_i V_{Li} \rho_{Li}) C_{Li} - (\beta_{i-1} \delta_i V_{Ri-1} \rho_{Ri-1}) C_{Ri-1} + \frac{\partial(\overline{\rho}_{ni} f_{ni} \overline{C}_{ni}^2)}{\partial \omega}$$

$$+ \frac{\partial(f_{ni} \overline{\rho}_{ni} \overline{C}_{ni})}{\partial t} + f_{ni} \frac{\partial \overline{P}_{ni}}{\partial \omega} - \tau_{nri} U_{nri} + \tau_{nci} U_{nci} = 0 \qquad (2)$$

(c) Energy equation in the axial direction

The axial flow velocity through the seal throttle is determined by the nozzle flow with constant entropy when the gas is ideal, but if real gas is not ideal, then polytrope exchange may be used. Outlet jet velocity of the throttle becomes equal to the value of the ideal velocity multiplied by coefficient of velocity, but here the effect is neglected.

Using the relation of the constant entropy exchange, the flow equation of gas is represented as

$$V_2^2 - V_1^2 = 2 \frac{\kappa}{\kappa - 1} \frac{P_1}{\rho_1} \left\{ 1 - \left(\frac{P_2}{P_1} \right)^{\frac{\kappa-1}{\kappa}} \right\} \qquad (3)$$

If the polytrope exchange is applied instead of the entropy constant change, equation

(3) becomes

$$V_2^2 - V_1^2 = 2\frac{\kappa}{\kappa-1}\frac{P_1}{\rho_1}\left\{1 - \left(\frac{P_2}{P_1}\right)^{\frac{n-1}{n}}\right\} \tag{4}$$

Applying the above equation to the ith nozzle part, the energy equation of the axial direction is obtained as follows;

$$\begin{aligned} V_{Li}^2 - V_{Ri-1}^2 &= 2\frac{\kappa}{\kappa-1}\frac{P_{Ri-1}}{\rho_{Ri-1}}\left\{1 - \left(\frac{P_{Li}}{P_{Ri-1}}\right)^{\frac{n-1}{n}}\right\} \\ &= 2\frac{\kappa}{\kappa-1}RT_{i-1}\left\{1 - \left(\frac{P_{Li}}{P_{Ri-1}}\right)^{\frac{n-1}{n}}\right\} \end{aligned} \tag{5}$$

(2) Equations in chamber part

The equations in region C_i are considered in small element $d\omega$ in circumferential direction, then the mass balance of the inlet and the outlet flow (i.e. continuous equation), momentum equation in circumferential direction and energy equation in axial direction are formulated;

(a) Continuous equation

$$\frac{\partial(f_{ci}\overline{\rho}_{ci})}{\partial t} + \frac{\partial(f_{ci}\overline{C}_{ci}\overline{\rho}_{ci})}{\partial\omega} - \alpha_i\delta_i V_{Li}\rho_{Li} + \beta_i\delta_{i+1}V_{Ri}\rho_{Ri} = 0 \tag{6}$$

(b) Momentum equation in the circumferential direction

$$\begin{aligned} &-(\alpha_i\delta_i V_{Li}\rho_{Li})C_{Li} + (\beta_i\delta_{i+1}V_{Ri}\rho_{Ri})C_{Ri} + \frac{\partial(f_{ci}\overline{C}_{ci}^2\overline{\rho}_{ci})}{\partial\omega} \\ &+ \frac{\partial(f_{ci}\overline{C}_{ci}\overline{\rho}_{ci})}{\partial t} + f_{ci}\frac{\partial\overline{P_{ci}}}{\partial\omega} - \tau_{cri}U_{cri} + \tau_{cci}U_{cci} = 0 \end{aligned} \tag{7}$$

(c) Energy equation

Considering the energy equation for the compressible flow between location L_i and R_i in axial direction, the equation representing the flow is

$$\frac{V_{Li}^2}{2} - \frac{V_{Ri}^2}{2} + \int_{L_i}^{R_i}\frac{dP}{\rho} - \Delta h - \Delta h_f = 0 \tag{8}$$

where Δh is the energy loss due to the divergent flow and is represented $1/2(V_{Li}-V_{Ri})^2$, Δh_f is the energy loss due to both friction of wall and vortex and is represented $\lambda_f\Delta l/mV_i^2/2$, where λ_f is the coefficient of energy loss factor due to friction loss of wall and vortex, Δl is working length and m is the characteristic length of the channel flow.

From the assumption (8), applying the temperature constant change to the equation (8), then

$$\frac{V_{Li}^2}{2} - \frac{V_{Ri}^2}{2} + RT_i\ln\frac{P_{Li}}{P_{Ri}} - \frac{(V_{Li}-V_{Ri})^2}{2} - \lambda_f\frac{\Delta l}{m}\frac{\overline{V}_i^2}{2} = 0 \tag{9}$$

LINEARIZATION OF THE EQUATIONS

Representing the variables as the sum of steady state value and perturbation term,

$$P = P_*(1 + \S) \tag{10}$$

$$C = C_* (1 + \eta) \tag{11}$$

$$V = V_* (1 + \zeta) \tag{12}$$

$$\delta = \delta_* (1 + \psi) \tag{13}$$

and substituting these variables into the above equations, then the following linearized equations are obtained;

(1) Throttle part

$$\frac{P_{*Li} f_{*ni}}{2\kappa RT_i} (\dot{\xi}_{Li}) + \frac{P_{*Ri-1} f_{*ni}}{2\kappa RT_{i-1}} (\dot{\xi}_{Ri-1}) + \frac{P_{*Li} f_{*ni} \overline{C}_{*ni}}{2\kappa R_S RT_i} (\xi'_{Li})$$

$$+ \frac{P_{*Ri-1} f_{*ni} \overline{C}_{*ni}}{2\kappa R_S RT_{i-1}} (\xi'_{Ri-1}) + \frac{C_{*Li} f_{*ni} \overline{P}_{*ni}}{2R_S RT_{ni}} (\eta'_{Li}) + \frac{C_{*Ri-1} f_{*ni} \overline{P}_{*ni}}{2R_S RT_{ni}} (\eta'_{Ri-1})$$

$$+ \frac{\alpha_i \delta_{*i} V_{*Li} P_{*Li}}{RT_i} (\xi_{Li}) - \frac{\beta_{i-1} \delta_{*i} V_{*Ri-1} P_{*Ri-1}}{RT_{i-1}} (\xi_{Ri-1}) + \frac{\alpha_i \delta_{*i} V_{*Li} P_{*Li}}{RT_i} (\zeta_{Li})$$

$$- \frac{\beta_{i-1} \delta_{*i} V_{*Ri-1} P_{*Ri-1}}{RT_{i-1}} (\zeta_{Ri-1}) + \frac{f_{*ni} \overline{P}_{*ni}}{RT_{ni}} (\dot{\psi}_i) + \frac{f_{*ni} \overline{C}_{*ni} \overline{P}_{*ni}}{R_S RT_{ni}} (\psi'_i)$$

$$+ \left(\frac{\alpha_i \delta_{*i} V_{*Li} P_{*Li}}{RT_i} - \frac{\beta_{i-1} \delta_{*i} V_{*Ri-1} P_{*Ri-1}}{RT_{i-1}} \right) (\psi_i) + \frac{\alpha_i \delta_{*i} V_{*Li} P_{*Li}}{RT_i}$$

$$- \frac{\beta_{i-1} \delta_{*i} V_{*Ri-1} P_{*Ri-1}}{RT_{i-1}} = 0 \tag{14}$$

$$\frac{f_{*ni} \overline{C}_{*ni} P_{*Li}}{2\kappa RT_i} (\dot{\xi}_{Li}) + \frac{f_{*ni} C_{*ni} P_{*Ri-1}}{2\kappa RT_{i-1}} (\dot{\xi}_{Ri-1}) + \frac{f_{*ni} \overline{P}_{*ni} C_{*Li}}{2RT_{ni}} (\dot{\eta}_{Li})$$

$$+ \frac{f_{*ni} \overline{P}_{*ni} C_{*Ri-1}}{2RT_{ni}} (\dot{\eta}_{Ri-1}) + \left(\frac{f_{*ni} C^2_{*ni} P_{*Li}}{2\kappa RT_i} + \frac{f_{*ni} P_{*Li}}{2R_S} \right) (\xi'_{Li}) + \left(\frac{f_{*ni} C^2_{*ni} P_{*Ri-1}}{2\kappa R_S RT_{i-1}} \right.$$

$$\left. + \frac{f_{*ni} P_{*Ri-1}}{2R_S} \right) (\xi'_{Ri-1}) + \frac{f_{*ni} \overline{C}_{*ni} \overline{P}_{*ni} C_{*Li}}{R_S RT_{ni}} (\eta'_{Li}) + \frac{f_{*ni} \overline{C}_{*ni} \overline{P}_{*ni} C_{*Ri-1}}{R_S RT_{ni}} (\eta'_{Ri-1})$$

$$+ \left(\frac{\alpha_i \delta_{*i} V_{*Li} P_{*Li} C_{*Li}}{RT_i} - \frac{\lambda_{nri} U_{nri} (U - \overline{C}_{*ni})^2 P_{*Li}}{4RT_i} + \frac{\lambda_{nci} U_{nci} \overline{C}^2_{*ni} P_{*Li}}{4RT_i} \right) (\xi_{Li})$$

$$- \left(\frac{\beta_{i-1} \delta_{*i} V_{*Ri-1} P_{*Ri-1} C_{*Ri-1}}{RT_{i-1}} + \frac{\lambda_{nri} U_{nri} (U - \overline{C}_{*ni})^2 P_{*Ri-1}}{4RT_{i-1}} - \frac{\lambda_{nci} U_{nci} \overline{C}^2_{*ni} P_{*Ri-1}}{RT_{i-1}} \right) (\xi_{Ri-1})$$

$$+ \left(\frac{\alpha_i \delta_{*i} V_{*Li} P_{*Li} C_{*Li}}{RT_i} + \frac{\lambda_{nri} U_{nri} \overline{P}_{*ni} (U - \overline{C}_{*ni}) C_{*Li}}{2RT_{ni}} + \frac{\lambda_{nci} U_{nci} \overline{P}_{*ni} \overline{C}_{*ni} C_{*Li}}{2RT_{ni}} \right) (\eta_{Li})$$

$$-\left(\frac{\beta_{i-1}\delta_{*i}V_{*Ri-1}P_{*Ri-1}C_{*Ri-1}}{RT_{i-1}}+\frac{\lambda_{nri}U_{nri}\bar{P}_{*ni}(U-C_{*ni})\bar{C}_{*Ri-1}}{2RT_{ni}}-\frac{\lambda_{nci}U_{nci}\bar{P}_{*ni}\bar{C}_{*ni}C_{*Ri-1}}{2RT_{ni}}\right)(\eta_{Ri-1})$$

$$+\frac{\alpha_i\delta_{*i}V_{*Li}P_{*Li}C_{*Li}}{RT_i}(\zeta_{Li})-\frac{\beta_{i-1}\delta_{*i}V_{*Ri-1}P_{*Ri-1}C_{*Ri-1}}{RT_{i-1}}(\zeta_{Ri-1})+\frac{\bar{P}_{*ni}\bar{C}_{*ni}f_{*ni}}{RT_{ni}}(\dot{\psi}_i)$$

$$+\frac{\bar{C}_{*ni}^2\bar{P}_{*ni}f_{*ni}}{R_sRT_{ni}}(\psi_i')+\left(\frac{\alpha_i\delta_{*i}V_{*Ci}P_{*Li}C_{*Li}}{RT_i}-\frac{\beta_{i-1}\delta_{*i}V_{*Ri-1}P_{*Ri-1}C_{*Ri-1}}{RT_{i-1}}\right)(\psi_i)$$

$$+\frac{\alpha_i\delta_{*i}V_{*Li}P_{*Li}C_{*Li}}{RT_i}-\frac{\beta_{i-1}\delta_{*i}V_{*Ri-1}P_{*Ri-1}C_{*Ri-1}}{RT_{i-1}}$$

$$-\frac{\lambda_{nri}U_{nri}\bar{P}_{*ni}(U-\bar{C}_{*ni})^2}{2RT_{ni}}+\frac{\lambda_{nci}U_{nci}\bar{P}_{*ni}\bar{C}_{*ni}^2}{2RT_{ni}}=0 \qquad (15)$$

$$RT_{i-1}\left(\frac{P_{*Li}}{P_{*Ri-1}}\right)^{\frac{K-1}{K}}(\xi_{Li})-RT_{i-1}\left(\frac{P_{*Li}}{P_{*Ri-1}}\right)^{\frac{K-1}{K}}(\xi_{Ri-1})$$

$$+V_{*Li}^2(\zeta_{Li})-V_{*Ri-1}^2(\zeta_{Ri-1})+V_{*Li}^2-V_{*Ri-1}^2$$

$$+2\frac{K}{K-1}RT_{i-1}\left\{1-\left(\frac{P_{*Li}}{P_{*Ri-1}}\right)^{\frac{K-1}{K}}\right\}=0 \qquad (16)$$

(2) Chamber part

$$\frac{f_{*ci}P_{*Ri}}{2RT_i}(\dot{\xi}_{Ri})+\frac{f_{*ci}P_{*Li}}{2RT_i}(\dot{\xi}_{Li})+\frac{f_{*ci}\bar{C}_{*ci}P_{*Ri}}{2R_sRT_i}(\xi_{Ri}')$$

$$+\frac{f_{*ci}\bar{C}_{*ci}P_{*Li}}{2R_sRT_i}(\xi_{Li}')+\frac{f_{*ci}\bar{P}_{*ci}C_{*Ri}}{2R_sRT_i}(\eta_{Ri}')+\frac{f_{*ci}\bar{P}_{*ci}C_{*Li}}{2R_sRT_i}(\eta_{Li}')$$

$$-\frac{\alpha_i\delta_{*i}V_{*Li}P_{*Li}}{RT_i}(\xi_{Li})+\frac{\beta_i\delta_{*i+1}V_{*Ri}P_{*Ri}}{RT_i}(\xi_{Ri})-\frac{\alpha_i\delta_{*i}V_{*Li}P_{*Li}}{RT_i}(\zeta_{Li})$$

$$+\frac{\beta_i\delta_{*i+1}V_{*Ri}P_{*Ri}}{RT_i}(\zeta_{Ri})+\frac{\alpha_i\delta_{*i}\bar{P}_{*ci}P_{tc}}{2RT_i}(\dot{\psi}_i)+\frac{\beta_i\delta_{*i+1}\bar{P}_{*ci}P_{tc}}{2RT_i}(\dot{\psi}_{i+1})$$

$$+\frac{\alpha_i\delta_{*i}\bar{C}_{*ci}\bar{P}_{*ci}P_{tc}}{2R_sRT_i}(\psi_i')+\frac{\beta_i\delta_{*i+1}\bar{C}_{*ci}\bar{P}_{*ci}P_{tc}}{2R_sRT_i}(\psi_{i+1}')$$

$$-\frac{\alpha_i\delta_{*i}V_{*Li}P_{*Li}}{RT_i}(\psi_i)+\frac{\beta_i\delta_{*i+1}V_{*Ri}P_{*Ri}}{RT_i}(\psi_{i+1})$$

$$-\frac{\alpha_i\delta_{*i}V_{*Li}P_{*Li}}{RT_i}+\frac{\beta_i\delta_{*i+1}V_{*Ri}P_{*Ri}}{RT_i}=0 \qquad (17)$$

$$\frac{f_{*ci}\bar{C}_{*ci}P_{*Ri}}{2RT_i}(\dot{\xi}_{Ri})+\frac{f_{*ci}\bar{C}_{*ci}P_{*Li}}{2RT_i}(\dot{\xi}_{Li})+\frac{f_{*ci}\bar{P}_{*ci}C_{*Ri}}{2RT_i}(\dot{\eta}_{Ri})$$

$$+\frac{f_{*ci}\bar{P}_{*ci}C_{*Li}}{2RT_i}(\dot{\eta}_{Li})+\left(\frac{f_{*ci}\bar{C}_{*ci}^2P_{*Ri}}{2R_sRT_i}+\frac{f_{*ci}P_{*Ri}}{2R_s}\right)(\xi_{Ri}')$$

$$+\left(\frac{f_{*ci}\bar{C}_{*ci}^2P_{*Li}}{2R_sRT_i}+\frac{f_{*ci}P_{*Li}}{2R_s}\right)(\xi_{Li}')+\frac{f_{*ci}\bar{C}_{*ci}\bar{P}_{*ci}C_{*Ri}}{R_sRT_i}(\eta_{Ri}')$$

$$+\frac{f_{*Ci}\,\bar{C}_{*Ci}\,\bar{P}_{*Ci}\,C_{*Li}}{R_s\,RT_i}\left(\eta'_{Li}\right)+\left(\frac{\beta_i\,\delta_{*i+1}\,V_{*Ri}\,P_{*Ri}\,C_{*Ri}}{RT_i}\right.$$

$$-\frac{\lambda_{cri}\,V_{cri}\,P_{*Ri}\,(U-\bar{C}_{*Ci})^2}{4RT_i}+\left.\frac{\lambda_{cci}\,V_{cci}\,P_{*Ri}\,\bar{C}_{*Ci}^2}{4RT_i}\right)\left(\xi_{Ri}\right)$$

$$-\left(\frac{\alpha_i\,\delta_{*i}\,V_{*Li}\,P_{*Li}\,C_{*Li}}{RT_i}+\frac{\lambda_{cri}\,V_{cri}\,P_{*Li}\,(U-\bar{C}_{*Ci})^2}{4RT_i}-\frac{\lambda_{cci}\,V_{cci}\,P_{*Li}\,\bar{C}_{*Ci}^2}{4RT_i}\right)\left(\xi_{Li}\right)$$

$$+\left(\frac{\beta_i\,\delta_{*i+1}\,V_{*Ri}\,P_{*Ri}\,C_{*Ri}}{RT_i}+\frac{\lambda_{cri}\,V_{cri}\,\bar{P}_{*Ci}\,(U-\bar{C}_{*Ci})\,C_{*Ri}}{2RT_i}+\frac{\lambda_{cci}\,V_{cci}\,\bar{P}_{*Ci}\,\bar{C}_{*Ci}\,C_{*Ri}}{2RT_i}\right)\left(\eta_{Ri}\right)$$

$$-\left(\frac{\alpha_i\,\delta_{*i}\,V_{*Li}\,P_{*Li}\,C_{*Li}}{RT_i}-\frac{\lambda_{cri}\,V_{cri}\,\bar{P}_{*Ci}\,(U-\bar{C}_{*Ci})\,C_{*Li}}{2RT_i}-\frac{\lambda_{cci}\,V_{cci}\,\bar{P}_{*Ci}\,\bar{C}_{*Ci}\,C_{*Li}}{2RT_i}\right)\left(\eta_{Li}\right)$$

$$-\frac{\alpha_i\,\delta_{*i}\,V_{*Li}\,P_{*Li}\,C_{*Li}}{RT_i}\left(\zeta_{Li}\right)+\frac{\beta_i\,\delta_{*i+1}\,V_{*Ri}\,P_{*Ri}\,C_{*Ri}}{RT_i}\left(\zeta_{Ri}\right)+\frac{\alpha_i\,\delta_{*i}\,\bar{C}_{*Ci}\,\bar{P}_{*Ci}\,P_{tc}}{2RT_i}\left(\psi_i\right)$$

$$+\frac{\beta_i\,\delta_{*i+1}\,\bar{C}_{*Ci}\,\bar{P}_{*Ci}\,P_{tc}}{2RT_i}\left(\psi_{i+1}\right)+\frac{\alpha_i\,\delta_{*i}\,\bar{C}_{*Ci}^2\,\bar{P}_{*Ci}\,P_{tc}}{2R_s\,RT_i}\left(\psi'_i\right)$$

$$+\frac{\beta_i\,\delta_{*i+1}\,C_{*Ci}^2\,P_{*Ci}\,P_{tc}}{2R_s\,RT_i}\left(\psi'_{i+1}\right)-\frac{\alpha_i\,\delta_{*i}\,V_{*Li}\,P_{*Li}\,C_{*Li}}{RT_i}\left(\psi_i\right)$$

$$+\frac{\beta_i\,\delta_{*i+1}\,V_{*Ri}\,P_{*Ri}\,C_{*Ri}}{RT_i}\left(\psi_{i-1}\right)-\frac{\alpha_i\,\delta_{*i}\,V_{*Li}\,P_{*Li}\,C_{*Li}}{RT_i}+\frac{\beta_i\,\delta_{*i+1}\,V_{*Ri}\,P_{*Ri}\,C_{*Ri}}{RT_i}$$

$$-\frac{\lambda_{cri}\,V_{cri}\,\bar{P}_{*Ci}\,(U-\bar{C}_{*Ci})^2}{2RT_i}+\frac{\lambda_{cci}\,V_{cci}\,\bar{P}_{*Ci}\,\bar{C}_{*Ci}^2}{2RT_i}=0 \qquad (18)$$

$$-RT_i\left(\frac{P_{*Li}}{P_{*Ri}}\right)\left(\xi_{Ri}\right)+RT_i\left(\frac{P_{*Li}}{P_{*Ri}}\right)\left(\xi_{Li}\right)-\left(2V_{*Ri}^2-V_{*Li}\,V_{*Ri}\right.$$

$$\left.+\frac{\lambda_{fi}\,\Delta l\,\bar{V}_{*Ci}\,V_{*Li}}{2m}\right)\left(\zeta_{Ri}\right)+\left(V_{*Li}\,V_{*Ri}-\frac{\lambda_{fi}\,\Delta l\,\bar{V}_{*Ci}\,V_{*Ri}}{2m}\right)\left(\zeta_{Li}\right)$$

$$+\frac{V_{*Li}^2}{2}-\frac{V_{*Ri}^2}{2}+RT_i\,ln\left(\frac{P_{*Li}}{P_{*Ri}}\right)-\frac{(V_{*Li}-V_{*Ri})^2}{2}-\frac{\lambda_{fi}\,\Delta l\,V_{*Ci}}{2m}=0 \qquad (19)$$

CALCULATION OF STEADY STATE

In order to calculate the above first approximation, steady state values are necessary. So steady state values (0th order approximation) are obtained in this section, that is, the terms of time derivative put zero. Then the equation of the 0th order approximation is for the nozzle part

$$\frac{\alpha_i\,\delta_{*i}\,V_{*Li}\,P_{*Li}}{RT_i}-\frac{\beta_{i-1}\,\delta_{*i}\,V_{*Ri-1}\,P_{*Ri-1}}{RT_{i-1}}=0 \qquad (20)$$

$$\frac{\alpha_i\,\delta_{*i}\,V_{*Li}\,P_{*Li}\,C_{*Li}}{RT_i}-\frac{\beta_{i-1}\,\delta_{*i}\,V_{*Ri-1}\,P_{*Ri-1}\,C_{*Ri-1}}{RT_{i-1}}-\frac{\lambda_{nri}\,V_{nri}\,\bar{P}_{mi}\,(U-\bar{C}_{ni})^2}{2RT_{m_i}}$$

$$+\frac{\lambda_{nc_i} V_{nc_i} P_{*n_i} \bar{C}^2_{*n_i}}{2RT_{m_i}} = 0 \tag{21}$$

$$V^2_{*L_i} - V^2_{*R_{i-1}} + 2\frac{K}{K-1} RT_{i-1}\left\{1-\left(\frac{P_{*L_i}}{P_{*R_{i-1}}}\right)^{\frac{K-1}{K}}\right\} = 0 \tag{22}$$

for the chamber part

$$-\frac{\alpha_i \delta_{*i} V_{*L_i} P_{L_i}}{RT_i} + \frac{\beta_i \delta_{*i+1} V_{*R_i} P_{*R_i}}{R\bar{T}_i} = 0 \tag{23}$$

$$-\frac{\alpha_i \delta_{*i} V_{*L_i} P_{*L_i} C_{*L_i}}{RT_i} + \frac{\beta_i \delta_{*i+1} V_{*R_i} P_{*R_i} C_{*R_i}}{RT_i} - \frac{\lambda_{cr_i} U_{cr_i} \bar{P}_{*c_i}(U-\bar{C}_{*c_i})^2}{2RT_i}$$

$$+\frac{\lambda_{cc_i} U_{cc_i} \bar{P}_{*c_i} \bar{C}^2_{*c_i}}{2RT_i} = 0 \tag{24}$$

$$\frac{V^2_{*L_i}}{2} - \frac{V^2_{*R_i}}{2} + RT_i \ln\left(\frac{P_{*L_i}}{P_{*R_i}}\right) - \frac{(V_{*L_i}-V_{*R_i})^2}{2} - \frac{\lambda_{f_i}\Delta\ell\, \bar{V}^2_{*c_i}}{2m} = 0 \tag{25}$$

As the conditions of the inlet and the outlet are given, then the variables of each stage may be obtained by the iterative method. If the pressure drop is too large to occur the choke, the flow is choked at the last chamber. Then, the flow rate of the seal is determined by the flow rate at the last stage. The condition of the critical pressure ratio is represented by Komotori(ref. 8) as

$$\frac{P_{exit}}{P_{ent}} \geq 1\Big/\sqrt{\frac{K(K+1)}{2}n + \left(\frac{K+1}{2}\right)^{\frac{2K}{K-1}}} \tag{26}$$

As the flow rate is determined by the above condition at the critical condition, then the flow rate of each stage is known. From the flow rate, steady state values are determined.

MATRIX FORMULATION

The linearized equations (20)∿(25) are represented in the matrix form as

$$N1\theta_{L_i}\dot{u}_{L_i} + N1_{1_{L_i}} u'_{L_i} + N1_{2_{L_i}} u_{L_i}$$

$$= N1\theta_{R_{i-1}}\dot{u}_{R_{i-1}} + N1_{1_{R_{i-1}}} u'_{R_{i-1}} + N1_{2_{R_{i-1}}} u_{R_{i-1}}$$

$$+ \mathbb{D}\theta_{n_i}\dot{\Phi}_{n_i} + \mathbb{D}1_{n_i}\Phi'_{n_i} + \mathbb{D}2_{n_i}\Phi_{n_i} \tag{27}$$

$$\mathbb{C}\theta_{R_i}\dot{u}_{R_i} + \mathbb{C}1_{R_i} u'_{R_i} + \mathbb{C}2_{R_i} u_{R_i}$$

$$= \mathbb{C}\theta_{L_i}\dot{u}_{L_i} + \mathbb{C}1_{L_i} u'_{L_i} + \mathbb{C}2_{L_i} u_{L_i}$$

$$+ \mathbb{D}\theta_{c_i}\dot{\Phi}_{c_i} + \mathbb{D}1_{c_i}\Phi'_{c_i} + \mathbb{D}2_{c_i}\Phi_{c_i} \tag{28}$$

where

$$\mathbb{U}^T = [\xi,\ \eta,\ \zeta]$$

$$\mathbb{\Phi}_{n_i} = [\psi_i]$$

$$\mathbb{\Phi}_{c_i}^T = [\psi_i \quad \psi_{i+1}]$$

FIRST-ORDER SOLUTION

Assuming an eccentric motion (whirling motion) of the shaft, whose center follows an elliptic path, the motion of the nondimensional perturbation of seal clearance is represented as

$$\psi_i = -\frac{a_i}{\delta_{*i}} \cos\Omega t \cos\varphi - \frac{b_i}{\delta_{*i}} \sin\Omega t \sin\varphi \tag{29}$$

where

$$a_i = a_* + \{\beta_e + (i-1)P_t\}\theta_a$$
$$b_i = b_* + \{\beta_e + (i-1)P_t\}\theta_b$$

a_*, b_* : eccentricity in x and y direction, respectively
θ_a, θ_b : inclined angle of shaft in x and y directions, respectively
β_e : length from the cross section of shaft center line and casing center line shown in figure 3

Equation (29) is rewritten as

$$\psi_i = -\frac{1}{2\delta_{*i}}\left[a_* + \{\beta_e + (i-1)P_t\}\theta_a\right]\{\cos(\varphi+\Omega t) + \cos(\varphi-\Omega t)\}$$

$$+\frac{1}{2\delta_{*i}}\left[b_* + \{\beta_e + (i-1)P_t\}\theta_b\right]\{\cos(\varphi+\Omega t) - \cos(\varphi-\Omega t)\} \tag{30}$$

$\mathbb{\Phi}$, $\dot{\mathbb{\Phi}}$, $\mathbb{\Phi}'$ in equations (27)(28) are represented by using equation (30) as

$$\mathbb{\Phi} = \mathbb{P}1\cos(\varphi+\Omega t) + \$1\cos(\varphi-\Omega t) \tag{31}$$

$$\dot{\mathbb{\Phi}} = \mathbb{P}2\sin(\varphi+\Omega t) + \$2\sin(\varphi-\Omega t) \tag{32}$$

$$\mathbb{\Phi}' = \mathbb{P}3\sin(\varphi+\Omega t) + \$3\sin(\varphi-\Omega t) \tag{33}$$

where

$$\mathbb{P}1 = \mathbb{P}11\,a_* + \mathbb{P}12\,\theta_a + \mathbb{P}13\,b_* + \mathbb{P}14\,\theta_b$$
$$\$1 = \$11\,a_* + \$12\,\theta_a + \$13\,b_* + \$14\,\theta_b$$
$$\mathbb{P}2 = \mathbb{P}21\,a_* + \mathbb{P}22\,\theta_a + \mathbb{P}23\,b_* + \mathbb{P}24\,\theta_b$$
$$\$2 = \$21\,a_* + \$22\,\theta_a + \$23\,b_* + \$24\,\theta_b$$
$$\mathbb{P}3 = \mathbb{P}31\,a_* + \mathbb{P}32\,\theta_a + \mathbb{P}33\,b_* + \mathbb{P}34\,\theta_b$$
$$\$3 = \$31\,a_* + \$32\,\theta_a + \$33\,b_* + \$34\,\theta_b$$

Refering equations (31)∿(33), U can be set as follows;

$$U = \alpha_1 \sin(\varphi + \Omega t) + \beta_1 \cos(\varphi + \Omega t) + \alpha_2 \sin(\varphi - \Omega t) + \beta_2 \cos(\varphi - \Omega t) \tag{34}$$

where

$$\alpha_1 = K_1 a_* + K_2 \theta_a + K_3 b_* + K_4 \theta_b$$
$$\beta_1 = L_1 a_* + L_2 \theta_a + L_3 b_* + L_4 \theta_b$$
$$\alpha_2 = M_1 a_* + M_2 \theta_a + M_3 b_* + M_4 \theta_b$$
$$\beta_2 = N_1 a_* + N_2 \theta_a + N_3 b_* + N_4 \theta_b$$

Substituting equations (31)∿(34) into equations (27) and (28), and separating the equation to sinusoidal and cosinusoidal element,

$$(-\Omega) N_{1\theta_{Li}} \cdot \beta_{1_{Li}} - N_{1_{Li}} \cdot \beta_{1_{Li}} + N_{2_{Li}} \cdot \alpha_{1_{Li}} = (-\Omega) N_{1\theta_{Ri-1}} \cdot \beta_{1_{Ri-1}} - N_{1_{Ri-1}} \cdot \beta_{1_{Ri-1}} + N_{2_{Ri-1}} \cdot \alpha_{1_{Ri-1}} + D_{\theta_{ni}} P_{2_{ni}} + D_{1_{ni}} P_{3_{ni}} \tag{35}$$

$$(\Omega) N_{1\theta_{Li}} \cdot \alpha_{1_{Li}} + N_{1_{Li}} \cdot \alpha_{1_{Li}} + N_{2_{Li}} \cdot \beta_{1_{Li}} = (\Omega) N_{1\theta_{Ri-1}} \cdot \alpha_{1_{Ri-1}} + N_{1_{Ri-1}} \cdot \alpha_{1_{Ri-1}} + N_{2_{Ri-1}} \cdot \beta_{1_{Ri-1}} + D_{2_{mi}} \cdot P_{1_{ni}} \tag{36}$$

$$(\Omega) N_{1\theta_{Li}} \cdot \beta_{2_{Li}} - N_{1_{Li}} \cdot \beta_{2_{Li}} + N_{2_{Li}} \cdot \alpha_{2_{Li}} = (\Omega) N_{1\theta_{Ri-1}} \cdot \beta_{2_{Ri-1}} - N_{1_{Ri-1}} \cdot \beta_{2_{Ri-1}} + N_{2_{Ri-1}} \cdot \alpha_{2_{Ri-1}} + D_{\theta_{ni}} \cdot S_{2_{ni}} + D_{1_{ni}} \cdot S_{3_{ni}} \tag{37}$$

$$(-\Omega) N_{1\theta_{Li}} \cdot \alpha_{2_{Li}} + N_{1_{Li}} \cdot \alpha_{2_{Li}} + N_{2_{Li}} \cdot \beta_{2_{Li}} = (-\Omega) N_{1\theta_{Ri-1}} \cdot \alpha_{2_{Ri-1}} + N_{1_{Ri-1}} \cdot \alpha_{2_{Ri-1}} + N_{2_{Ri-1}} \cdot \beta_{2_{Ri-1}} + D_{2_{ni}} \cdot S_{1_{ni}} \tag{38}$$

$$(-\Omega) C_{\theta_{Ri}} \cdot \beta_{1_{Ri}} - C_{1_{Ri}} \cdot \beta_{1_{Ri}} + C_{2_{Ri}} \cdot \alpha_{1_{Ri}} = (-\Omega) C_{\theta_{Li}} \cdot \beta_{1_{Li}} - C_{1_{Li}} \cdot \beta_{1_{Li}} + C_{2_{Li}} \cdot \alpha_{1_{Li}} + D_{\theta_{ci}} \cdot P_{2_{ci}} + D_{1_{ci}} \cdot P_{3_{ci}} \tag{39}$$

$$(\Omega) C_{\theta_{Ri}} \cdot \alpha_{1_{Ri}} + C_{1_{Ri}} \cdot \alpha_{1_{Ri}} + C_{2_{Ri}} \cdot \beta_{1_{Ri}}$$

$$=(\Omega)\,\mathbb{C}\theta_{Li}\cdot\alpha 1_{Li}+\mathbb{C}1_{Li}\cdot\alpha 1_{Li}+\mathbb{C}2_{Li}\cdot\beta 1_{Li}$$
$$+\mathbb{D}2_{ci}\cdot\mathbb{P}1_{ci} \tag{40}$$

$$(\Omega)\,\mathbb{C}\theta_{Ri}\cdot\beta 2_{Ri}-\mathbb{C}1_{Ri}\cdot\beta 2_{Ri}+\mathbb{C}2_{Ri}\cdot\alpha 2_{Ri}$$
$$=(\Omega)\,\mathbb{C}\theta_{Li}\cdot\beta 2_{Li}-\mathbb{C}1_{Li}\cdot\beta 2_{Li}+\mathbb{C}2_{Li}\cdot\alpha 2_{Li}$$
$$+\mathbb{D}\theta_{ci}\cdot\$2_{ci}+\mathbb{D}1_{ci}\cdot\$3_{ci} \tag{41}$$

$$(-\Omega)\,\mathbb{C}\theta_{Ri}\cdot\alpha 2_{Ri}+\mathbb{C}1_{Ri}\cdot\alpha 2_{Ri}+\mathbb{C}2_{Ri}\cdot\beta 2_{Ri}$$
$$=(-\Omega)\,\mathbb{C}\theta_{Li}\cdot\alpha 2_{Li}+\mathbb{C}1_{Li}\cdot\alpha 2_{Li}+\mathbb{C}2_{Li}\cdot\beta 2_{Li}$$
$$+\mathbb{D}2_{ci}\cdot\$1_{ci} \tag{42}$$

These equations are solved simultaneously at each seal ground. Then the pressure distribution and other perturbations at each ground are known. From the results, the flow induced force due to the labyrinth seal can be calculated as similar as the previous paper(refs.4~6). The pressures at the nozzle part and the chamber part are used $\Delta P_{ni}=P^{*}_{Li}\xi_{Li}$ and $\Delta P_{Ci}=P^{*}_{Ri}\xi_{Ri}$, because the perturbations $\mathcal{U}_{Li}$ and $\mathcal{U}_{Ri}$ are suddenly satisfied after through the inlet of each chamber. Thus the fluid forces in x and y direction are obtained as

$$F_x=\sum_{i=1}^{n+1}\left\{\left(-\int_0^{2\pi}P_{ni}\cos\varphi\,d\varphi\right)R_s P_{tn}\right\}+\sum_{i=1}^{m}\left\{\left(-\int_0^{2\pi}P_{ci}\cos\varphi\,d\varphi\right)R_s P_{tc}\right\} \tag{43}$$

$$F_y=\sum_{i=1}^{n+1}\left\{\left(-\int_0^{2\pi}P_{ni}\sin\varphi\,d\varphi\right)R_s P_{tn}\right\}+\sum_{i=1}^{m}\left\{\left(-\int_0^{2\pi}P_{ci}\sin\varphi\,d\varphi\right)R_s P_{tc}\right\} \tag{44}$$

From the results, a common expression for the disturbance forces in terms of the x, y deviation of the shaft center

$$F_x=K_{xx}x+K_{xy}y+C_{xx}\dot{x}+C_{xy}\dot{y} \tag{45}$$

$$F_y=K_{yx}x+K_{yy}y+C_{yx}\dot{x}+C_{yy}\dot{y} \tag{46}$$

is obtained. This procedure is also written in the previous paper.

COMPARISON TO LITERATURE DATA

In this section a numerical example is calculated in order to compare the result of the presented model with the experimental result. Wright is experimented by the one chamber seal. His experimental model is shown in table 1, and the example data are shown in tables 2 and 3.

The results of the zero-th order equation (steady state) are shown for the straight type, the convergence type and the divergence type in tables 4~6, respectively, and the fluid force for the forward and the backward precession is shown in figures 4~6, in which the dotted line shows the result obtained by the present method and the full line shows Wright's result and also notations K and E

mean the radial and the tangential force, respectively. For the forward precession, signatures of the radial force K and the tangential force E coincide with the experimental ones and especially the amount of tangential force agree with the experimental one. From this result the presented mathematical model, that is, the flow is separated into the throttle part and the chamber part, is effective to represent the flow in the labyrinth seal and also to evaluate the radial and tangential fluid force. But for the backward precession, the value of the tangential force evaluates larger than the experimental one, so the effect of precession may not be perfectly represented in the derived equation. These results coincide with the convergence type seal, but for the divergence type seal, the result does not agree with the experimental one as shown in figure 6. This fact means that the flow patterns of the straight type and the convergent type labyrinth seal are similar but that of the divergence type is different.

CONCLUSION

In this paper, a new mathematical model, which is divided the flow of seal chamber into two regions, is presented, the derived equation is solved and the result is compared with the experimental one. As the result, it is found that the presented modeling can qualitatively and quantitatively represent the flow better than the previously presented one by authors. However the model should be improved more to represented the flow in the seal.

This study is supported by Scientific Research Fund of the Japan Ministry of Education No.5655018 (1981-1982) and No.58550172 (1983).

REFERENCES

(1) Kostyuk, A. G.: A Theoretical Analysis of the Aerodynamic Forces in the Labyrinth Grounds of Turbomachines. Teploenergetica, 1972, 19(11) pp.29-33.

(2) Kostyuk, A. G.: Circulation Forces over the Shrouding and Their Influence on the Threshold Capacity of Large Turbine Unit. Teploenergetica, 1975, 22(3) pp.41-46.

(3) Wright, D. V.: Labyrinth Seal Forces on a Whirling Rotor. ASME AMD,Vol.55, Rotor Dynamic Instability, 1983, pp.19.

(4) Iwatsubo, T.: Evaluation of Instability Forces of Labyrinth Seals in Turbines or Compressors. NASA CP 2133 Proceedings of a workshop at Texas A&M University 12-14 May 1980, Entitled Rotordynamic Instability Problems in High Performance Turbomachinery, pp.139-167.

(5) Iwatsubo, T.; Motooka, N.; and Kawai, R.: Flow Induced Force and Flow Pattern of Labyrinth Seal. NASA CP 2250 Proceeding of a workshop at Texas A&M University 10-12 May 1982, Entitled Rotordynamic Instability Problems in High Performance Turbomachinery, pp.205-222.

(6) Iwatsubo, T.; Takahara, K.; and Kawai, R.: Instability of Rotors due to Labyrinth Seal (part III, flow induced force considered the energy loss in the seal chamber)

(7) Iwatsubo, T.; Kawai, R.; Kagawa, N.; and Kakiuchi, T.: Analysis of the Dynamic Characteristics of the Fluid Force Induced by a Labyrinth Seal. 3rd workshop on Rotor Dynamic Instability Problems in High Performance Turbomachinery, 1984.

(8) Komotori, K.: Theory of Non-contact Seal (in Japanese). Corona Publishing Co.,LTD, 1973.

Table 1. - The experimental model.

Seal type		(a) Straight-through	(b) Convergence	(c) Divergence
Clearance (mm)	(ent)	0.1585	0.1915	0.1311
	(exit)	0.1585	0.1272	0.1963
Strip height (mm)	(ent)	5.0305	4.9975	5.0579
	(exit)	5.0305	5.0618	4.9927
Seal pitch (mm)		12.918		
Rotor radius (mm)		101.6		
Rotor rpm (rpm)		1800 rpm (30 Hz)		
Number of chamber		1		
Seal side		Casing side		

Table 2. - The example data of calculation.

ENTRANCE PRESSURE (kPa)	EXIT PRESSURE (kPa)	WHIRLING SPEED (rpm)		
		Straight-through	Convergence	Divergence
213.9	206.8	307.0(667.8)	325.0(693.0)	783.0(639.0)
220.8		833.4(693.0)	373.0(740.4)	798.0(646.2)
227.7		860.4(718.2)	900.0(771.0)	817.2(670.8)
234.6		886.8(743.4)	924.0(801.0)	832.8(688.8)
241.5		912.0(769.2)	948.0(828.6)	846.6(702.0)

( )---backward

Table 3. - Another example data of calculation.

Ratio of specific heat	K	1.4
Gas constant	R	0.287(kJ/kg K)
Coefficient of vena contracta	α	0.7
Divergent angle	θ	6

Table 4. - The results of steady state values for the straight type seal.

PRESSURE (kPa)				TEMPERATURE (K)			Q	SWIRL VELOCITY (m/s)			
P_{ent}	P_{Ll}	P_{Rl}	P_{exit}	T_{ent}	T_l	T_{exit}	(kg/s)	C_{ent}	C_{Ll}	C_{Rl}	C_{exit}
213.7	210.6	210.1			296.9	295.6	9.0×10^{-3} (8.5×10^{-3})		14.6	11.6	10.8
220.6	214.3	213.4			295.7	293.0	1.3×10^{-2} (1.4×10^{-2})		15.1	12.3	11.6
227.5	218.0	216.9	206.8	298.15	294.5	290.6	1.6×10^{-2} (1.7×10^{-2})	16.8	15.4	12.7	12.0
234.4	221.7	220.4			293.4	288.2	1.9×10^{-2} (1.9×10^{-2})		15.6	13.0	12.3
241.3	225.5	223.9			292.4	285.9	2.1×10^{-2} (2.2×10^{-2})		15.7	13.2	12.6

( )---backward

Table 5. - The results of steady state values for the convergence type seal.

PRESSURE (kPa)				TEMPERATURE (K)			Q	SWIRL VELOCITY (m/s)			
P_{ent}	P_{Ll}	P_{Rl}	P_{exit}	T_{ent}	T_l	T_{exit}	(kg/s)	C_{ent}	C_{Ll}	C_{Rl}	C_{exit}
213.7	211.8	211.5			297.4	295.5	8.7×10^{-3} (6.6×10^{-3})		14.6	11.6	10.7
220.6	216.7	216.2			296.6	292.9	1.2×10^{-2} (1.1×10^{-2})		15.1	12.2	11.5
227.5	221.7	221.0	206.8	298.15	295.9	290.4	1.5×10^{-2} (1.5×10^{-2})	16.8	15.4	12.6	11.9
234.4	226.8	226.0			295.3	287.9	1.8×10^{-2} (1.7×10^{-2})		15.5	12.9	12.2
241.3	231.9	231.1			294.8	285.6	2.0×10^{-2} (1.9×10^{-2})		15.6	13.0	12.4

( )---backward

Table 6. - The results of steady state values for the divergence type seal.

PRESSURE (kPa)				TEMPERATURE (K)			Q	SWIRL VELOCITY (m/s)			
P_{ent}	P_{L1}	P_{R1}	P_{exit}	T_{ent}	T_1	T_{exit}	(kg/s)	C_{ent}	C_{L1}	C_{R1}	C_{exit}
213.7	209.5	208.8			296.4	295.7	8.6×10^{-3}		14.5	11.5	10.8
							(7.8×10^{-3})				
220.6	212.0	210.7			294.8	293.2	1.2×10^{-2}		15.0	12.2	11.5
							(1.3×10^{-2})				
227.5	214.5	212.8	206.8	298.15	293.2	290.8	1.5×10^{-2}	16.8	15.3	12.6	11.9
							(1.6×10^{-2})				
234.4	216.9	214.8			291.6	288.5	1.8×10^{-2}		15.5	12.9	12.2
							(1.9×10^{-2})				
241.3	219.3	216.9			290.1	286.2	2.0×10^{-2}		15.6	13.1	12.5
							(2.1×10^{-2})				

( )---backward

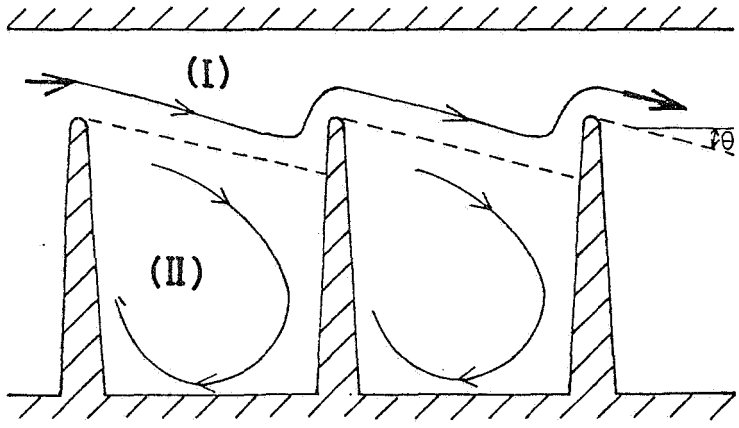

Figure 1. - The flow in the labyrinth seal.

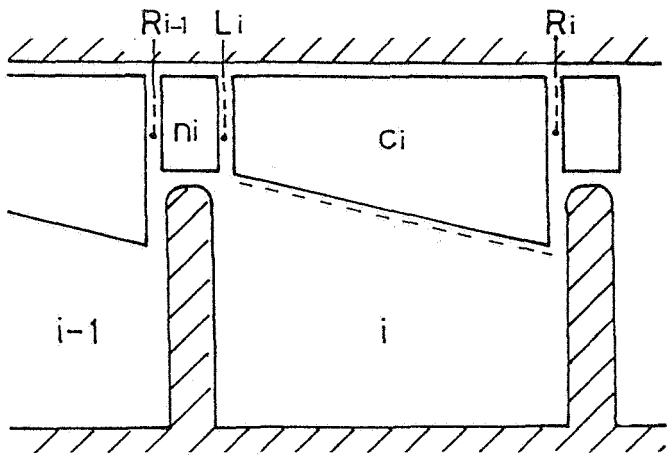

Figure 2. - Definitions of two regions and subscripts.

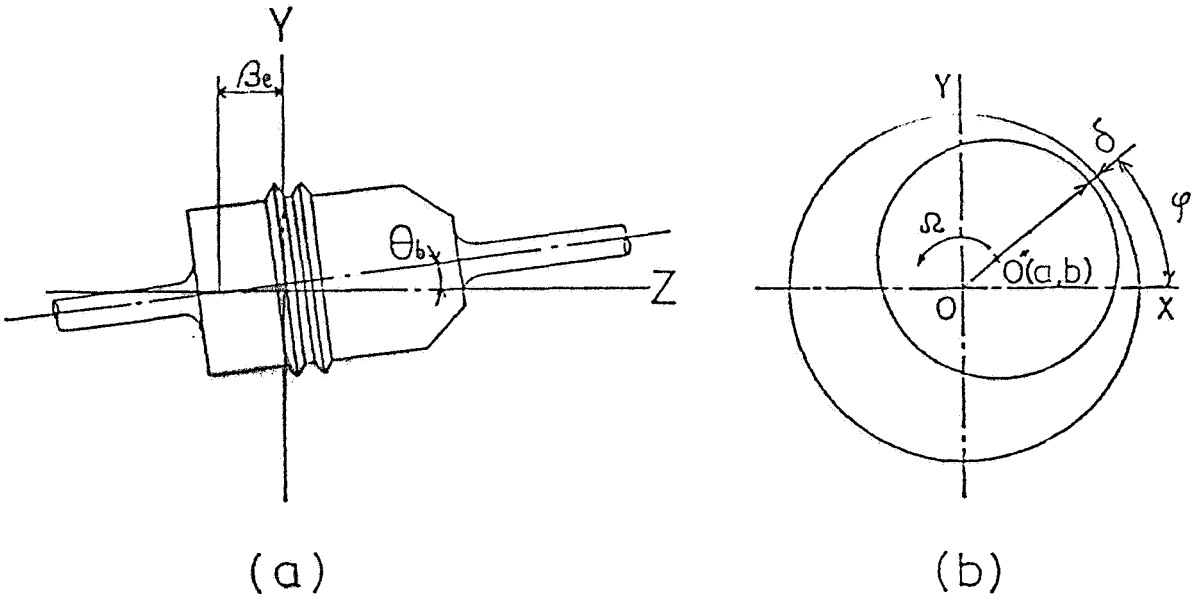

Figure 3. - The relation between casing and rotor.

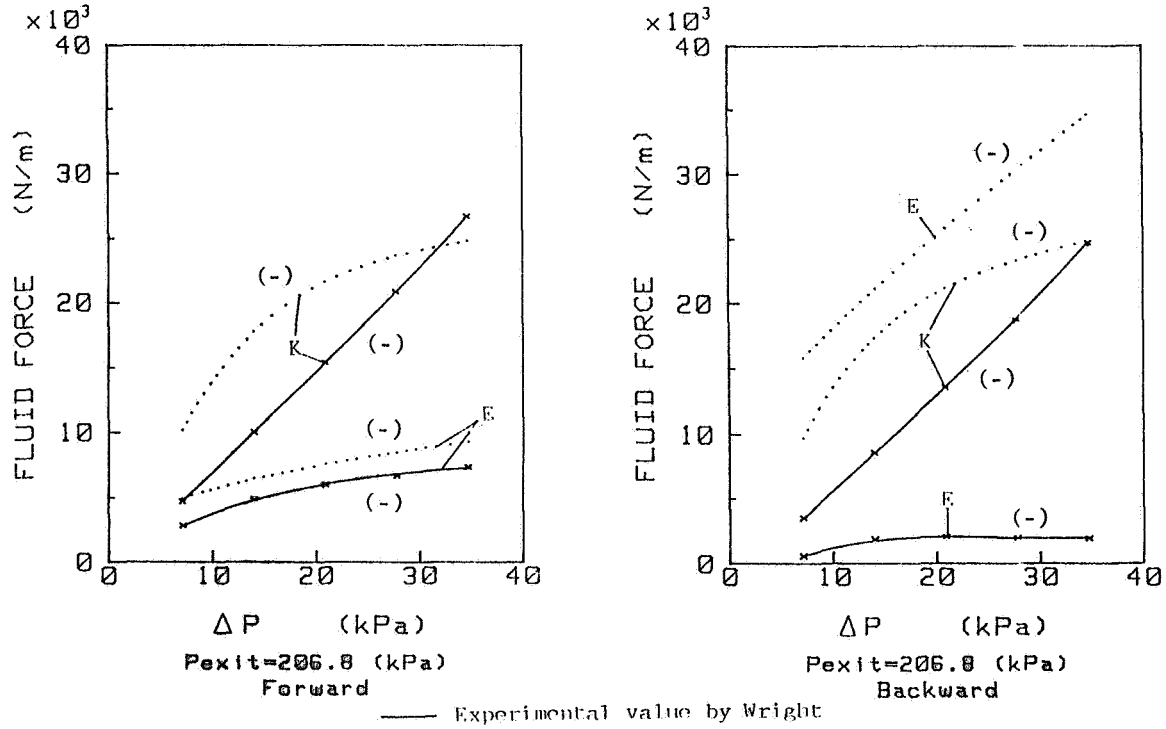

Figure 4. - The fluid force for the straight type seal.

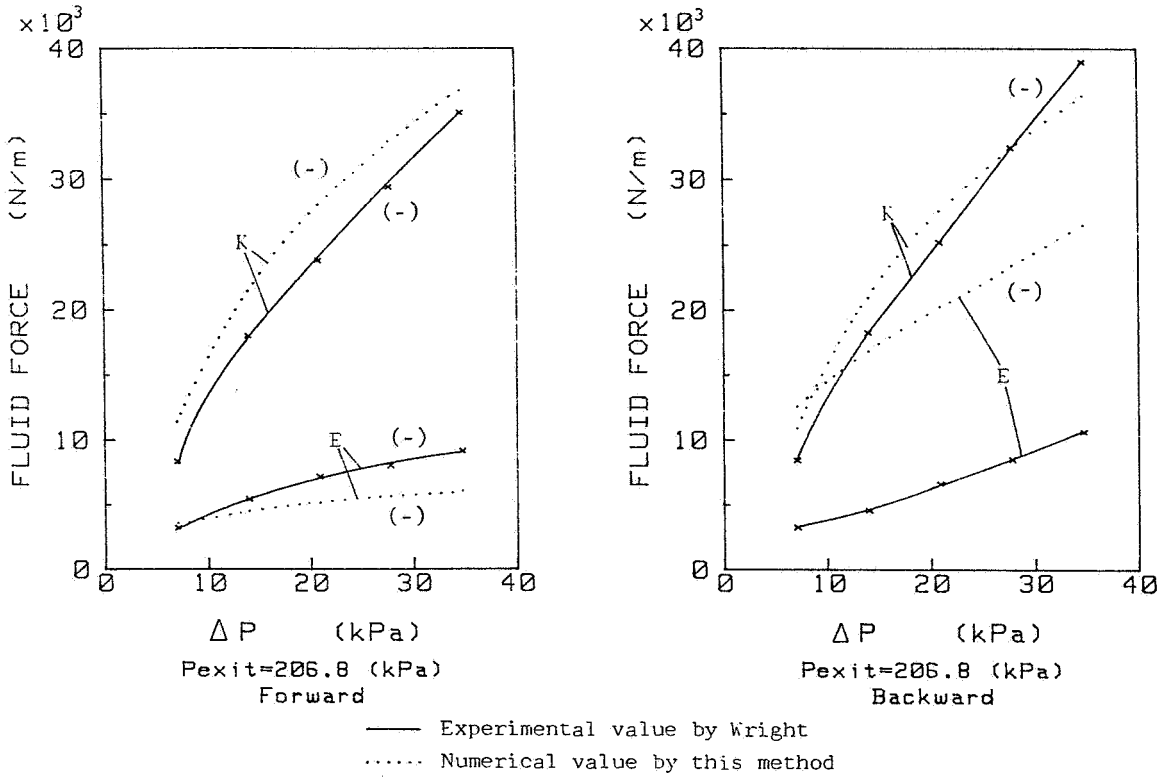

Figure 5. - The fluid force for the convergence type seal.

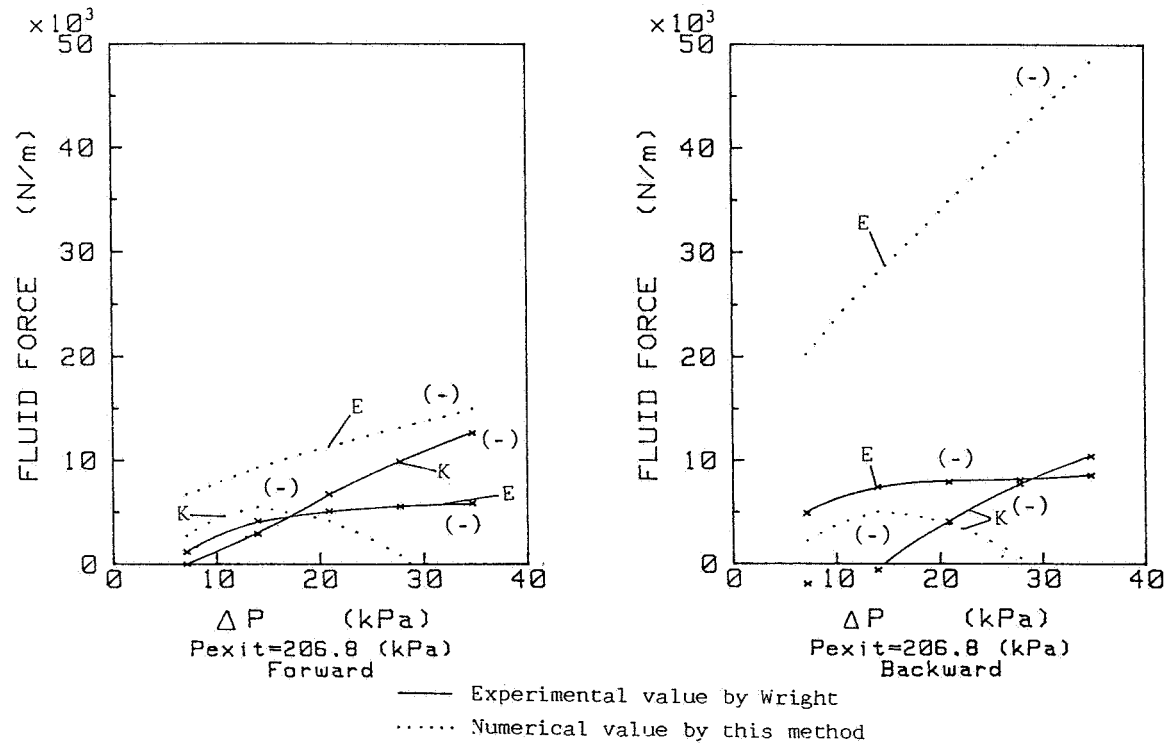

Figure 6. - The fluid force for the divergence type seal.

NASA Conference Publication 2338

Rotordynamic Instability Problems in High-Performance Turbomachinery 1984

Proceedings of a workshop sponsored by Texas A&M University, College Station, Texas, the U.S. Army Research Office, Durham, North Carolina, and the Aeropropulsion Laboratory, Wright Patterson Air Force Base, Ohio, and held at Texas A&M University, College Station, Texas, May 28–30, 1984

NASA

National Aeronautics
and Space Administration

**Scientific and Technical
Information Branch**

1984

PREFACE

A review of the proceedings from the past two workshops and the program of this workshop shows a continued trend toward a more quantified view of rotordynamic instability problems. Specifically, research programs that have been established to develop analysis techniques for predicting or measuring forces and force coefficients for seals, impellers, and other known force elements in high-performance turbomachinery are begining to yield results at an accelerated pace.

The test results that were presented at the third workshop provide, simultaneously, (1) new data to be used in designing machinery with more predictable stability characteristics and (2) continued humility for investigators who are trying either to explain discrepancies between theory and experiment or to develop entirely new theories to explain measured results. Despite our progress the problem of predicting rotordynamic forces does not seem to be in danger of imminent extinction.

This third workshop was organized to continue addressing the general problem of rotordynamic instability by gathering those persons with immediate interest, experience, and knowledge for a discussion and review of both past stability problems and present research and development efforts. The intent of the workshop organizers and sponsors is that the workshop and these proceedings provide a continuing impetus for an understanding and resolution of these problems.

Chairmen:

Dara W. Childs and
John M. Vance
Turbomachinery Laboratories
Texas A&M University

Robert C. Hendricks
NASA Lewis Research Center

CONTENTS

SESSION IV - LABYRINTH SEAL FORCES

SESSION V - ANNULAR SEAL FORCES

SESSION VI - CONTROL OF INSTABILITIES

SESSION VII - EXPERIMENTAL TECHNIQUES

FULL LOAD TESTING IN THE PLATFORM MODULE PRIOR TO TOW-OUT:

A CASE HISTORY OF SUBSYNCHRONOUS INSTABILITY

J. W. Fulton
Exxon Research and Engineering Company
Florham Park, New Jersey 07932

A recent project bought an electric motor driven centrifugal compressor to supply gas for further compression and reinjection on a petroleum production platform in the North Sea. Review of the compressor design, after manufacture was completed, raised concerns about susceptibility to subsynchronous instability. Consideration of log decrement, aerodynamic features, and the experience of other compressors with similar ratios of operating-to-critical speed ratio versus gas density led to the decision to full load test. Mixed hydrocarbon gas was chosen for the test to meet discharge temperature restrictions. This choice of gas led to the use of the module as the test site. On test, subsynchronous vibrations made the compressor inoperable above approximately one-half the rated discharge pressure of 14500 kPa (2100 psia).

Extensive modifications, including shortening the bearing span, changing leakage inlet flow direction on the back-to-back labyrinth, and removing the vaned diffusers on all stages were made simultaneously to meet project needs. Retest at 105 percent speed and overpressure proved the modifications successful, and established a margin of stability. The compressor was commissioned on schedule and is operating with satisfactory vibration levels.

The objectives of this paper are threefold:

- To provide the available case history for students of subsynchronous instability;
- To discuss empirical criteria for subsynchronous instability;
- To consider the benefits of pre-commissioning tests at rated speed and rated gas conditions.

The case history is a practical example to the petroleum industry. The case is also of theoretical interest because of two aerodynamic features of the initial test: the first feature was vaned diffusers on all stages, and the second was a blocked flow passage on one impeller. Both raise a speculative counterpoint to the current trend toward concentrating on labyrinth forces as the main cause of subsynchronous instability in centrifugal compressors. (For example, see Ref. 1.)

Empirical stability criteria compare such things as rotordynamic parameters and gas density for stable versus unstable compressors. In this case, several empirical criteria gave poor correlations. As a consequence, their utility is limited to serving as a rule of thumb before detailed design evaluations are possible.

The pre-commissioning test proved beneficial. The current state-of-the-art for rotor stability poses considerable risk of inoperable compressors to certain oil and gas projects, which can be addressed by such tests.

Equipment Description

The oil production platform is designed for crude oil production with reinjection of associated gas, which must be compressed from 19 psia to 6600 psia. Two compression systems, each handling half the total flow, are mounted in a single pre-assembled module, designed to be lifted onto the platform deck, complete with a local control room for each system. In each system, the gas first flows through a centrifugal compressor train and then into a reciprocating compressor. The centrifugal train has a motor and gear driving through the low pressure casing to the higher pressure casing. The higher pressure casing is a barrel type. Figure 1 is a photograph of the completed platform.

The subject of this paper is the high pressure casing of the centrifugal train. It is rated to compress 1650 m3/h (970 ACFM) of 27 molecular weight gas from 3030 to 14500 kPa (440 to 2100 psia) at 7732 RPM, absorbing 4200 kW (5600 HP). It has 10 impellers, in 2 groups of 5 each, arranged back-to-back. The flow from the first section to the second section is through an integral crossover pipe without an intercooler. A large labyrinth at the shaft midspan separates the fifth from the tenth stage, and contributes to thrust balance forces. In common with many compressors in similar duty, the aerodynamics are characterized by a low specific speed configuration, by relatively low (1520 m (5000 ft.)) head per stage, and by low Mach numbers. Figure 2 is the general cross-sectional arrangement of the compressor.

Vaned diffusers were used on all 10 stages. The vendor had not previously used vaned diffusers on every stage for compressors with gas densities as high as our rated gas densities. Also, they had not used this particular seal design, which uses face-contact inner seals, at such a high suction pressure. The compressor is equipped with 5-pad tilting pad bearings which have no cross-coupled spring coefficients to excite subsynchronous vibrations.

Background

Publication of other cases of subsynchronous vibration in the petroleum production industry provided the background for recognizing the risk of subsynchronous vibration occurring and potentially causing a major project delay. Accounts of Kabob (Ref. 2) and Ekofisk (Ref. 3, 4) demonstrated that the vibration would not be found until commissioning with rated density and pressure gas, and that the remedy, major mechanical redesign, could cause expensive project delay. Hawkins (Ref. 5), which was familiar, being an Exxon plant, pointed out the risk of subsynchronous vibration at more moderate gas pressures.

The phenomena of concern is self-excited vibration as defined in Ref. 6. That is, the force which causes the vibration depends on the motion of the rotor. This phenomena will be referred to as subsynchronous instability. As discussed in Ref. 6, subsynchronous instability is essentially independent of the frequency of any external stimulus. Instead, it occurs at the natural frequency of the rotor system.

It was recognized that aerodynamic instabilities could cause forced vibrations in a rotor system. Frequencies in the range of 5 to 15 percent of rotor

speed have been reported (Ref. 7) for that phenomena. Although a test conducted at full scale aerodynamic conditions would have the benefit of demonstrating aerodynamically forced vibrations, they were not the main concern. Neither were parametric instabilities, which typically occur at 1/3, 1/2, etc. of rotor speed.

Evaluating the Risk of Subsynchronous Instability

Due to the relatively low discharge pressure, no special concerns about subsynchronous vibration had been raised by the project team during the design phase. However, when an unrelated issue necessitated review of the design, concerns were raised because of design extrapolations. Further review concentrated on the following three areas:

(1) Low log decrement compared to conventional criteria;
(2) Empirical stability correlations;
(3) Vaned diffusers unproven in high density gas service.

The log decrement is a measure of the rate of decay of free vibration at the rotor natural frequency. Its calculation is covered in the classic paper by Lund (Ref. 8). Because we could not quantify the destabilizing aerodynamic forces acting on the rotor, we chose to compare the log decrements calculated for zero cross-coupled aerodynamic forces. Here we shall refer to the log decrement calculated for zero aerodynamic forces as the "basic" log decrement. The "basic" approach reduces the log decrement concept to an empirical criteria which requires a positive value of the log decrement as a design margin of safety against instability. A common recommendation for a safe "basic" log decrement is 0.3. Nowadays, we would attempt to quantify the destabilizing force at the labyrinths, but this technology was not available when the decision to test was made.

Figure 3 compares basic log decrement values for various compressors. The vendor calculated that the subject compressor had a basic log decrement of 0.16, which compared unfavorably to others, especially an inert gas compressor which was unstable at a lower gas density than the subject compressor's rated point. This implied a significant risk of subsynchronous instability. The vendor did not consider the risk to be high and cited a lower log decrement (approximately 0.14) for a very similar compressor at higher pressure, which they stated was marginally stable. The main features which were different from the similar compressor were vaned diffusers on every stage of our compressor, and oil-seals with a different atmospheric side sealing ring design.

The second empirical stability correlation used was proposed by Sood in Ref. 9. It plots stable and unstable compressors on two coordinates to define a threshold line for instability. The coordinates are "flexibility ratio" versus average gas density in the compressor. The flexibility ratio is defined as the "maximum continuous speed" divided by the "first critical speed on stiff supports." Although no numerical values are given in Ref. 9, several example points are available from the literature and from our experience. Some of these are shown on Figure 4.

We have drawn a line representing the approximate threshold where subsynchronous vibrations were believed to occur. Going above the line indicates an increasing tendency for subsynchronous vibration to occur, while staying below the line indicates that such vibration is less likely to occur. The line slopes down with increasing gas density because the higher gas forces on the rotor require a stiffer rotor to resist subsynchronous vibration. A stiffer rotor has a higher

first critical speed and thus a lower "flexibility ratio" for the same threshold speed. This line, labeled "Typical Threshold Line," is drawn through the scattered points labeled A, B and C which represent compressors at the threshold of subsynchronous vibration, as known at the time of the decision.

As indicated by point D in Figure 4, our intended operating conditions were marginally on the stable side of the typical threshold line. However, the inert gas compressor was also in the marginally safe zone (point B), when it first encountered subsynchronous vibrations. When the marginal position on this curve was considered simultaneously with the low log decrement, the risk of subsynchronous vibration became substantial. Note that the rotor flexibility ratio versus density curve does not consider the effect of bearing damping, being based only on shaft mass-elastic properties, as implied by the rigid bearing critical speed. Furthermore, no other compressor on Figure 4 had vaned diffusers.

Two separate effects may be produced by the vaned diffusers. Firstly, they might cause a forced vibration due to an aerodynamic instability, such as rotating stall in the diffuser, especially if the impeller and diffuser were mismatched. Secondly, the diffuser might interact with the impeller to produce aerodynamic cross-coupled forces on the impeller which could cause rotordynamic instability. We had practical interest in either case, even though rotordynamic instability was the main concern.

Vaned diffusers had not been used before by the vendor on all stages of a compressor for high density gas. The bulk of the vendor's experience with vaned diffusers on all stages was in hydrogen rich service, at much lower gas densities. Ref. 4 mentioned that vaned diffusers were tried at Ekofisk on the fourth and eighth stages with neutral results on that rotordynamic instability problem. Although the intent there was to cure the rotor instability, it was not clear that the vane's effect always had to be an improvement, especially if the aerodynamic design was off target. Our concerns on this point were raised due to the unexpectedly high head found on our ASME PTC-10 Class 3 performance test.

Based on the above risks of subsynchronous vibration and the large costs and delay if the problem remained undemonstrated until start-up in the field, a full-load test was recommended. By testing prior to tow-out of the module, any problems with the compressor or the module would be discovered a year in advance of commissioning, which allowed time for correction, before incurring start-up delays. Contingency modifications to reduce the risk were considered. However, attempts to plan reduced scale testing, or to make contingency modifications, were defeated by the lack of basic engineering knowledge or proven calculation techniques addressing the mechanism of subsynchronous instability.

Testing Requirements For Subsynchronous Instabilities

Testing for subsynchronous instability requires virtually full scale operating conditions. Full speed is required to obtain the same rotordynamic behavior during testing as during service conditions. The cross-coupled aerodynamic forces must also be reproduced at full scale to cause the instability. Using, as one example, labyrinth forces due to gas entry swirl, it can be shown that at least three variables, gas density, gas flow angles and differential pressure across the stage, must be the same for test as for service (see Ref. 10). Therefore, the compressor must be operated at full power and with aerodynamic simultude. Some deviation from rated suction and discharge pressures is permissible so long as the differential pressure for the test is the same as rated. The only significant

choice left after satisfying these three variables is whether a suitable non-flammable, non-toxic gas can be found to simulate the service gas within a reasonable tolerance.

For our test the additional constraint of a 204°C (400°F) casing design temperature limit defeated the search for a non-flammable gas. Meeting the suction and discharge densities for full speed and rated flow caused the discharge temperature to exceed the limit for all safe gas mixtures we tried.

The above considerations eliminated the possibility of testing with inert gas. The requirements of testing with hydrocarbon gas, plus the advantages of testing and precommissioning the other equipment in the module, led the project toward a test in the module.

The hydrocarbon gas used for the test was nominally 76 percent ethane and 24 percent methane. The intent was to be near ASME PTC-10, Class 1 conditions, with suction and discharge densities within 5 percent of rated, at close to the rated suction and discharge pressures. Literally blending the rated composition, shown on the compressor datasheet, was not practical because that gas is saturated and would condense if stored in a single vessel at high pressure and practical temperatures.

Test Conducted in Platform Module

The module is an enclosed structure designed to be lifted as a single unit when it is installed onto the oil production platform. Installation takes place by towing the module on a barge to the platform which has been previously erected in the North Sea. The module contains the two centrifugal compressor trains, the two reciprocating compressor trains, two local control rooms, the process piping, valves, and the compressor suction vessels.

The module formed a natural test site because the compressor trains and much of the equipment required to operate them were assembled in working order. Testing in the module had the additional advantage of pre-commissioning the ancilliary equipment in the module prior to its being installed in the North Sea, where the logistical burden of any corrections would be greater.

For the test, the module was placed on its tow-out barge, which was in the River Tyne, at Newcastle, U.K. A photo of two modules on the barge is shown in Figure 5. The module containing the compressor is on the left.

The following facilities were required in addition to the equipment permanently installed in the module:

- Nitrogen to inert and purge the hydrocarbon gas piping;
- Cooling water pumps;
- A hydrocarbon gas flare stack with associated liquid surge drums for safe release of the test gas;
- An electric power generator to supply power for driving the compressor motor. We used one of the gas turbine generators intended for permanent installation on the offshore platform. This stand-alone package is shown in Figure 6. Because our electric power system was independent of any other power system, we were able to vary the power supply frequency from the rated 60 Hertz to vary

compressor speed.

Results of the Testing

The testing for subsynchronous instability was conducted in four conceptual steps as follows:

A. A test of the compressor design configuration as purchased, at rated speed, by increasing suction and discharge pressure until the onset of subsynchronous instability;

B. As (A) except the journal bearing orientation was switched from having the rotor weight between 2 of the 5 tilting pad to having the weight on 1 of the 5;

C. After extensive design modifications and at rated speed and pressure;

D. At proof test conditions not obtainable in the actual duty, for the purpose of demonstrating a margin of safety against subsynchronous instability.

The highlights of the test results are shown in Figure 7. Step A of testing showed severe subsynchronous instability at suction and discharge pressures above approximately 1580 kPa (230 psig) and 6500 kPa (940 psig) respectively. The instability barrier limited further pressure increases by causing the subsynchronous shaft vibrations near the bearings to exceed the 100 micron (4 mils) peak-to-peak shutdown limit, stopping the compressor. The initial test point is shown as point E on the Sood coordinates, Figure 4.

Step B consisted of modifications that could be made to improve stability without removing the rotor and stator from the barrel casing. The contact face of the atmospheric side oil seal ring was improved in order to reduce the radial loads that could be transmitted to the shaft. Based on the wear pattern on the contact surface, it was theorized that the ring was not moving freely in the radial direction, as the designer intended, and therefore, the oil ring could act similarly to a cylindrical bearing and introduce cross-coupled forces onto the rotor.

The tilt pad bearings were modified as tabulated in Figure 8 (adapted from Ref. 12) to increase the effective damping and to introduce more asymetry between the vertical and horizontal spring coefficients. Asymetry is expected to increase stability according to Ref. 11.

The results from Step B were disappointing, with only a slight increase in discharge pressure, from 6500 kPa (940 psig) to 8200 kPa (1190 psig) before encountering instability again. The vendor's prediciton of a positive log decrement, as shown in Figure 8, was not born out in practice. We do not know whether the assumed cross-coupled stiffness of 810,000 N/M (4644 lb/in.) was too low, or whether the bearings were less effective than expected, or whether other unaccounted factors caused the analysis to fail.

Step C was made after extensive modifications described below. The compressor operated with only traces of subsynchronous vibration. Those traces, at 4575 CPM and 4800 CPM are of some theoretical interest compared to the calculated first natural frequency of 4400 CPM. The second frequency of 4800 CPM was not explained, but is clearly not due to some other harmonic or sub-harmonic frequency of the rotor, gear, or electrical system because the 4800 CPM remained unchanged

when the electrical supply frequency and motor speed was changed between steps C and D. Step C is shown as point F1 on the Sood coordinates, Figure 4.

Step D, the proof test, was entirely successful, with no significant subsynchronous components in the operating flow range. Step D was done by running at 105 percent rated RPM. 105 percent speed was achieved by increasing the power supply frequency from 60 Hertz to 63 Hertz to circumvent the limitation of having a constant speed motor drive. Step D is shown as point F2 on the Sood coordinates, Figure 4.

Possible Causes of the Subsynchronous Vibration

It is important to note that such a costly full scale test was necessary, because of the business risk created by engineering ignorance. No one knew for sure that the subsynchronous vibration would occur, but instead the risk was recognized and the options properly weighed. Typically, the business considerations which justified the test also required that all the changes, which might possibly help cure the problem, be made simultaneously. Therefore, the actual causes of the problem cannot be isolated or proven. We will give our opinion on the causes and try to rank their importance. The changes which are believed to have significant effect on subsynchronous vibration are as follows (in order of decreasing significance):

1. Bearing span was reduced by 6.5 inches.

   Reduced bearing span, which stiffens the fundamental bending mode, was estimated beforehand to have been sufficient to reach 1900 psi discharge versus the 2500 actually achieved during proof test at 105 percent speed. The estimate was based on a single mass (Jeffcott) rotor according to Figure 10 of Reference 11, by assuming the destabilizing out-of-phase coefficient is proportional to gas density.

2. Swirling flow entering into the central division-wall labyrinth was eliminated by introducing gas between the teeth at elevated pressure. (The higher pressure reverses the flow across the first two teeth so that gas that flows out of the high pressure side of the labyrinth instead of entering there.)

   Elimination of swirling flow into the most influential labyrinth is a common fix and is probably quite significant. The swirl in the labyrinth is not totally eliminated, because viscous forces reintroduce the swirl some number of teeth downstream. No estimate of labyringth cross-coupled forces could be made at the time.

3. All vaned diffusers were removed and narrower parallel wall vaneless diffusers were substituted.

   Removal of the vaned diffuser was prompted by the observation that the "similar compressor" operated without major subsynchronous instability at a less favorable point on the density speed-ratio plot. (See Figure 4, points A versus E.) The major difference between the designs was having vaned diffusers on all stages in our case. Excess head and efficiency were in hand at this time, so the loss in efficiency, caused by removing the vanes, could be tolerated.

   Removal of the vanes required reducing diffuser widths drastically to maintain

the meridional velocity of the flow and the incidence angle at the return vanes. For example, on the last stage the diffuser width was reduced from over one quarter inch to less than one tenth of an inch, which is even less than the normal width for this staging. The narrow width enhances aerodynamic stability at the expense of aerodynamic efficiency. Reduced widths were used for enhanced stability on another subsynchronous vibration problem as discussed in Reference 4.

4. Axial forces on the breakdown-side oil seal were reduced by an improved pressure balance configuration. The seal design used face contact inner seals. The particular seal design had a breakdown bushing which had limited experience at over 400 psi. The vendor chose to improve the axial balance, but no test was made to demonstrate how much influence on subsynchronous vibration the breakdown bush might have had by acting as a cylindrical bearing with oil whirl.

5. A foreign object was found blocking one vaned passage of the ninth impeller. It was removed for the retest.

   A consultant raised the point that the asymetric blockage might cause whirl. No practical evaluation of this point was possible. The blockage was removed simultaneously with the other changes and did not reoccur during the successful retest.

6. Division wall labyrinth and balance piston diameter were reduced in diameter from 9 1/4 inches to 8. Reduction of the balance piston diameter reduced area under influence of the destabilizing gas swirl pressures. The reduction also helped raise the first critical speed by removing mass from the center of the span. As an aside, the thrust balance was improved. We are aware of other load tests which have also revealed thrust problems, which cannot be assessed during API mechanical run tests at low pressure.

Evaluation of Empirical Stability Criteria

The test results provide additional comparisons for the empirical stability criteria. Here we will evaluate the "basic" log decrement, and the rotor stability plot on Sood's coordinates, plus a criteria which was published later, without reference to our test, by Kirk and Donald (Ref. 13). Generally speaking, all three empirical criteria show so much scatter that they are only useful as rules-of-thumb. The scatter is not surprising because these empirical citeria do not correlate a specific physical cause, but instead represent the results achieved by diverse design features.

The basic decrement of 0.3, often recommended for high gas density service, is reaffirmed by the test results. The log decrement before the major modifications, 0.16, was shown to be insufficient by the occurrence of subsynchronous instability, while the basic log decrement after major modifications, 0.32, was proven adequate. However, the 0.14 log decrement of the similar compressor from the same vendor, as shown in Figure 3, demonstrates that 0.3 is not always necessary.

When the initial test point is put onto Sood's coordinates for rotor stability, point E on Figure 4, that point represents a worst case. Compared to the "typical threshold line" in Figure 4, the compressor was much less stable than expected. We have drawn a line through the initial test point and parallel to

typical threshold line, and labeled it "worst case threshold line," because it represents the least stable case we know of using the Sood coordinates.

The scatter that can be introduced (into Figure 4) by special design features is demonstrated by point "G" which is for a compressor with "deswirl cascades" in front of the impeller eye labyrinths of each stage. The deswirl cascades reduce labyrinth cross-coupled forces and is similar to the devices covered by U.S. Patent 4,370,094, dated 1983. The point "G" compressor was demonstrated to European industry users as an example of high pressure centrifugal compressor technology.

Kirk and Donald proposed an empirical criteria using the product of the discharge pressure with the differential pressure of the compressor versus the critical speed ratio (operating speed divided by first rigid bearing critical speed, which is identical to the "flexibility ratio"). Because our initial and final test points, plus the Hawkins points, all have back-to-back staging, it is fair to plot them on Figure 9, which is adapted from Ref. 13. Our compressor is again a worst case, and we have drawn a "worst case" parallel line. The "Point G" compressor from Figure 4 is indicated as well to represent a best case.

The scatter found in these three empirical stability criteria reduce their utility where accuracy is required. However, these criteria do serve to indicate the general area of concern for subsynchronous instability for industrial centrifugal compressors. Purchasers of these compressors should find the worst case lines in Figures 4 and 9 a commercially useful criteria if they adopt the following strategy: we recommend that proposals for compressors on the unstable side of the worst case line be required to include prices for an optional full speed, full gas density test with rated differential pressure across the compressor. The final decision to test could then be made later when the information from complete analytic studies is available. For example, the decision to full-load test the compressor at point "H" in Figure 4 was influenced by similar criteria.

Conclusion

The cause of the subsynchronous instability was not determined. Perhaps the changes to the bearing span, the center labyrinth and the atmospheric-side oil seals would have been sufficient to eliminate the instability. With state-of-the-art analysis techniques for labyrinth forces, it may soon be possible to estimate whether those changes would have been sufficient, given enough detailed design data. However, compared to the very similar compressor from the same vendor, the instability threshold is inexplicably low. Therefore, the vaned diffusers and the non-axisymetric passage blockage of the ninth impeller cannot be dismissed out of hand.

Both empirical stability criteria, one using the Sood coordinates, and the other by Kirk and Donald, are shown to have an order of magnitude of scatter with respect to their aerodynamic force parameters. Therefore, the utility of these criteria for comparing different designs is reduced to applications which can tolerate the scatter, and/or the pessimism of using the "worst case" line. The "worst case" lines given should be a useful rule-of-thumb for indicating a threshold-of-concern for subsynchronous instability in similar industrial centrifugal compressors.

The test was a technical and commercial success. Subsynchronous instability was found and quickly remedied, preventing any delay in bringing a

valuable project onstream. Although the test was very expensive at approximately 3 million Pounds Sterling (see Ref. 12), the conservatively-estimated potential losses would have been substantially more than that amount, had subsynchronous instability delayed oil production.

References

(1) Wyssmann, H., "Rotor Dynamics of High Pressure Centrifugal Compressors: Critical Speed and Stability Considerations." I. Mech. E., Second European Congress, "Fluid Machinery for the Oil, Petrochemical and Related Industries," March 1984 - The Hague.

(2) Smith, K.J., "An Operational History of Fractional Frequency Whirl," 4th Turbomachinery Symposium, Texas A&M University, Oct. 1975, pp. 115-125.

(3) Cochrane, W.W., "New-generation Compressors Injecting Gas at Ekofisk," The Oil and Gas Journal, May 10, 1976, pp. 63-70.

(4) Geary, C.H. Jr., Damratowski, L.P., Sayer, C., "Design and Operation of the World's Highest Pressure Gas Injection Compressors," Paper No. OTC 2485, Offshore Technology Conference, Houston, Texas, May 1976.

(5) Kuehn, H.G., "Hawkins Inert Gas Plant: Design and Early Operation," 52nd Annual Fall Technical Conference and Exhibition of the Society of Petroleum Engineers of AIME, Denver, Colorado, October 1977, Paper No. SPE 6793.

(6) Ehrich, F. F., "Self-Excited Vibration," Shock and Vibration Handbook, 2nd Edition, edited by C. M. Harris and C. E. Crede, McGraw-Hill, 1976, pp 5-1 to 5-25.

(7) Bonciani, L., Ferrara, P.L., Timori, A., "Aero-Induced Vibrations in Centrifugal Compressors," Workshop on Rotordynamic Instability, Texas A&M University, May 1980. NASA CP-2133, 1980, pp. 85-94.

(8) Lund, J.W., "Stability and Damped Critical Speeds of a Flexible Rotor in Fluid-Film Bearings," Journal of Engineering for Industry, ASME Paper No. 73-DET-103.

(9) Sood, V.K., "Design and Full Load Testing of a High Pressure Centrifugal Natural Gas Injection Compressor," Proceedings of the Eighth Turbomachinery Symposium pp. 35-42.

(10) Benckert, H., Wachter, J., "Flow Induced Spring Constants of Labyrinth Seals," I. Mech E. 1980, Paper No. C258/80.

(11) Gunter, E. J., Dynamic Stability of Rotor Bearing Systems, NASA SP-113, Office of Technology Utilization, U.S. Government Printing Office, 1966. (See also NASA CP-2133, 1980, pp. 189-212).

(12) Desmond, A. D., "A Case Study and Rectification for Subsynchronous Instability in Turbocompressors," I. Mech. E, Second European Congress, "Fluid Machinery for the Oil Petrochemical and Related Industries," March 1984 - The Hague.

(13) Kirk, R. G. and Donald, G. H., "Design Criteria for Improved Stability of Centrifugal Compressors," Rotor Dynamical Instability, AMD Vol. 55, ASME, June 1983, pp 59-71.

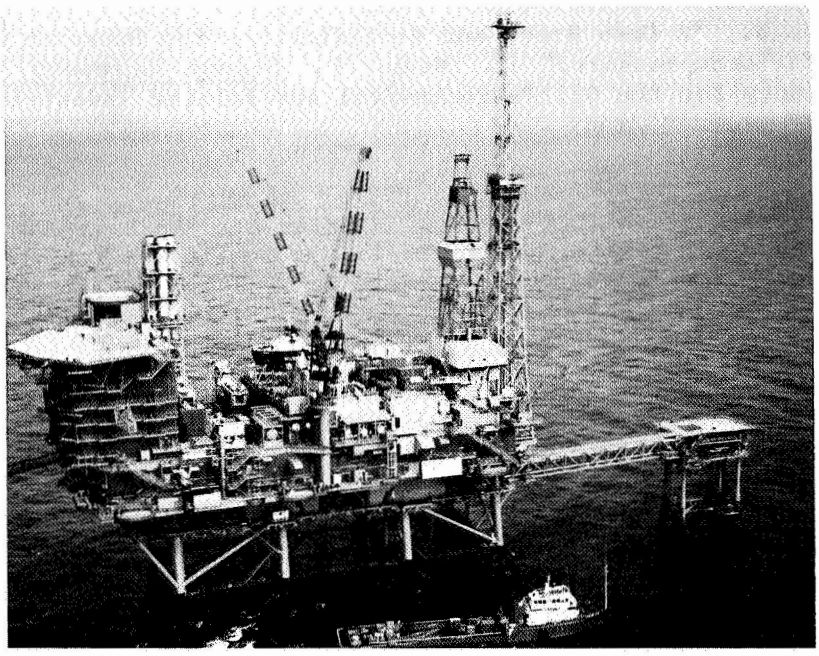

Figure 1. - North Sea petroleum production platform.

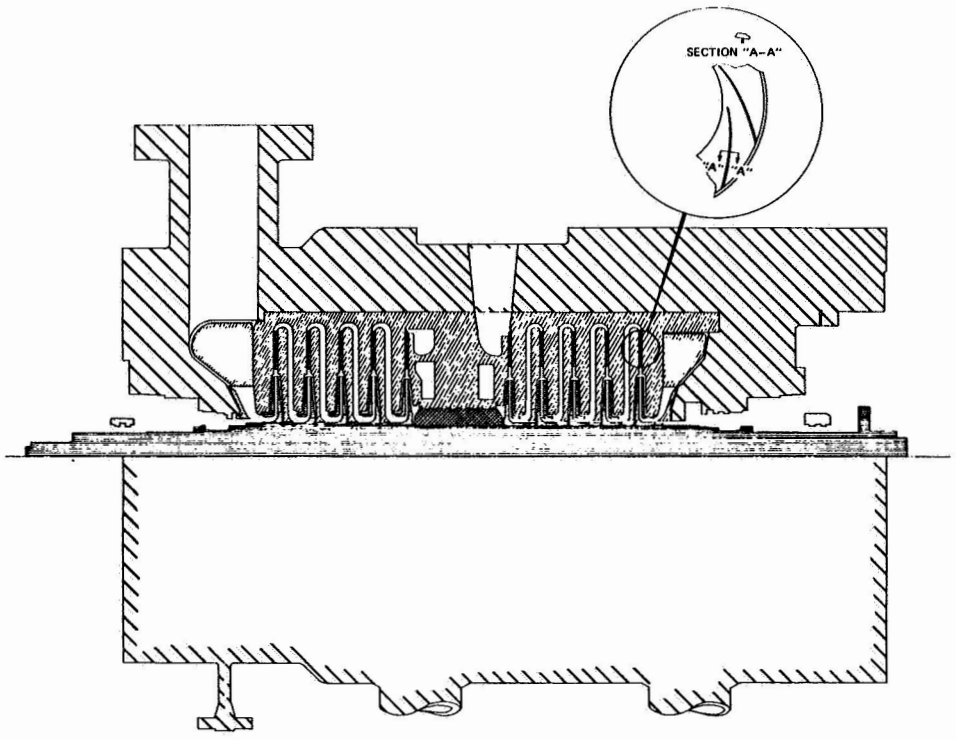

Figure 2. - Cross-sectional view of centrifugal compressor train.

	BASIC LOG DECREMENT	AVERAGE GAS DENSITY (KG/M^3)	(LBM/FT^3)
PRESENT CASE			
BEFORE MODIFICATION	0.16	32	(2)
AFTER MODIFICATION	0.32	30	(5)
SIMILAR COMPRESSOR (SAME VENDOR)	0.14	104	(6.5)
INERT GAS COMPRESSOR			
BEFORE MODIFICATION	0.23	43	(3)
AFTER MODIFICATION	0.43	82	(5)
REFERENCE 9 COMPRESSOR	0.443	208	(13)
RECOMMENDED LOG DECREMENT FOR HIGH DENSITY	0.3	-	-

Figure 3. - Log decrement values for various compressors.

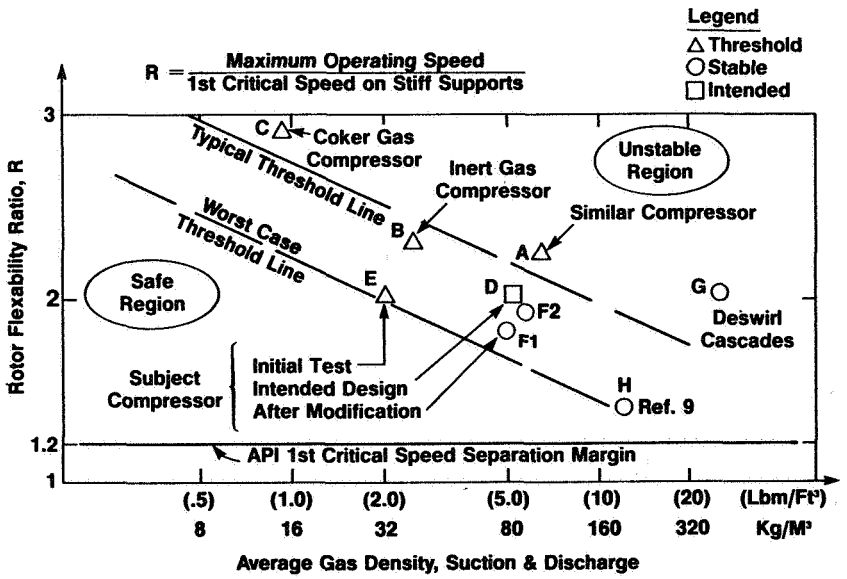

Figure 4. - Sood's model for instability thresholds applied to various compressors.

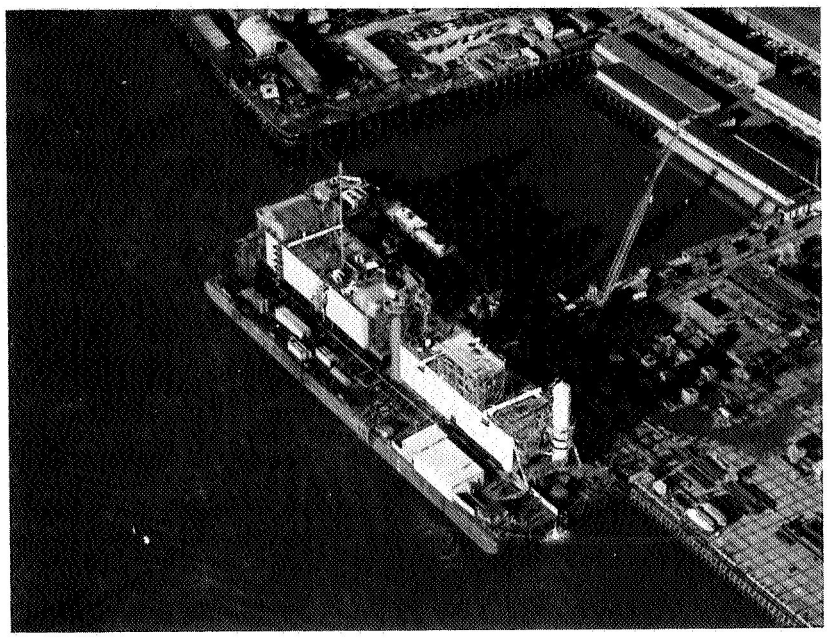

Figure 5. - Tow-out barge test platform.

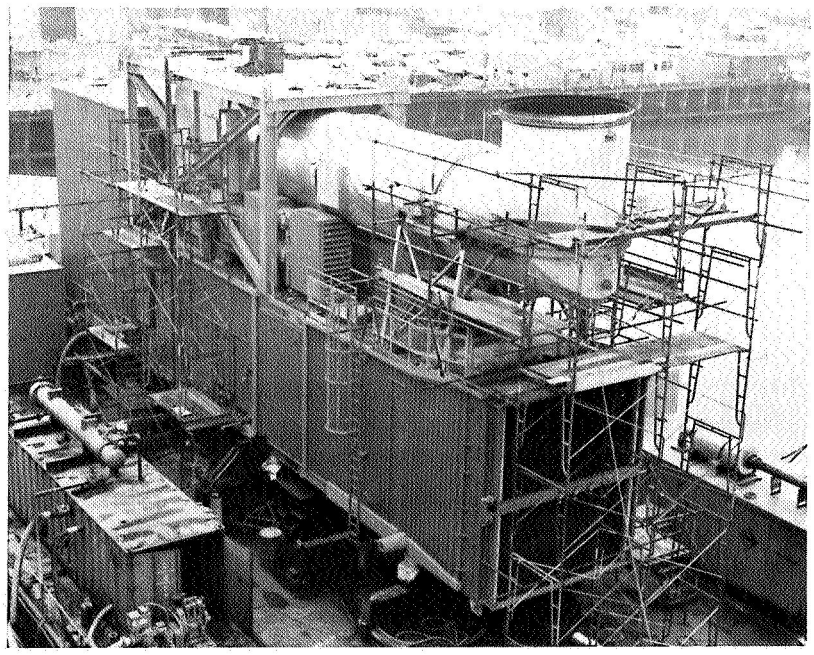

Figure 6. - Gas-turbine-driven electric generator for pump power.

TEST STEP	A	B	C	D
SUBSYNCHRONOUS FREQUENCIES (CPM)	4125	3825	4575 & 4800	4575 & 4800
SUBSYNCHRONOUS AMPLITUDES (MICRONS)	22	20	4 & 4	5 & 3
COMPRESSOR SPEED (RPM)	7800	7725	7742	8121
SUCTION PRESSURE (kPA GAUGE)	1580	1560	2280	2840
DISCHARGE PRESSURE (kPA GAUGE)	6500	8200	14400	17200
OBSERVED FIRST CRITICAL RANGE (RPM) (APPROXIMATE)	3800-3900	3900-4000	4100-4200	4100-4200

Figure 7. - Highlights of test results.

BEARING CONFIGURATION

TEST STEP	A	B
TYPE	TILTING PAD	TILTING PAD
ORIENTATION	LOAD BETWEEN PADS	LOAD ON PAD
LENGTH INS.	1.5	1.5
DIAMETER INS.	5.0	5.0
MACHINED DIAMETER CLEARANCE INS.	0.012	0.009
PRELOAD	0.489	0.0
ASSEMBLED CLEARANCE INS.	0.006	0.008
BASIC LOG DECREMENT	0.148	0.164
AERO CROSS-COUPLING STIFFNESS 'Q' LB/IN	4644	4644
LOG DECREMENT WITH 'Q' AERO CROSS-COUPLING	-0.284	0.122

Figure 8. - Tilt-pad-bearing modifications.

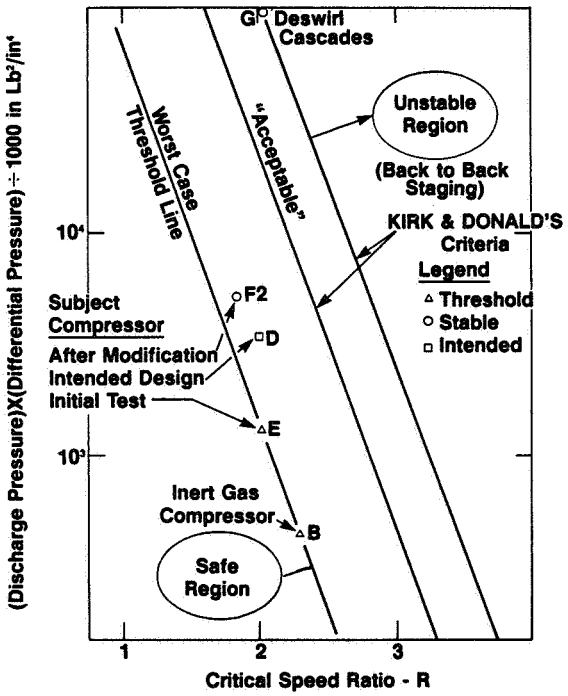

Figure 9. - Kirk and Donald's stability criteria applied to various compressors.

SUBSYNCHRONOUS VIBRATIONS IN A HIGH PRESSURE CENTRIFUGAL COMPRESSOR: A CASE HISTORY

B. F. Evans and A. J. Smalley
Southwest Research Institute
San Antonio, Texas 78284

This paper documents two distinct aerodynamically excited vibrations in a high pressure low flow centrifugal compressor. A measured vibration near 21 percent of running speed was identified as a non-resonant forced vibration resulting from rotating stall in the diffuser; a measured vibration near 50 percent of running speed was identified as a self-excited vibration sustained by cross-coupling forces acting at the compressor wheels. Measured data shows the dependence of these characteristics on speed, discharge pressure, and changes in bearing design. Analytical results are presented which provide strong evidence for the exciting mechanisms of diffuser stall and aerodynamic cross-coupling. Additional results show how the rotor characteristics would be expected to change as a result of proposed modifications. The satisfactory operation of the compressor after these modifications is described.

INTRODUCTION

Two distinct subsynchronous vibrations were encountered in commissioning an eight stage centrifugal compressor. The 3170 kW (4250 hp) compressor was specified to meet API 617 standards and is designed to run at 13,500 rpm with a design discharge pressure of 180 bar (2600 psi) and flow of 33,800 m^3/h (21,000 SCFM).

The compressor (Figure 1) is mounted in 5-shoe tilting-pad bearings with load on pad (5SLOP) and length to diameter ratio, L/D, of 1. Oil breakdown seals of the balanced floating type were initially located inboard of the bearings. Total rotor length is 1810 mm (71.3 inches) with a total mass of 245 Kg (total weight of 540 lb), and a bearing span of 1360 mm (53.7 inches).

Manufacturer's test stand data, from a run in a vacuum, showed a reasonably well damped first critical at about 5700 rpm, but there was a slight indication of subsynchronous response at the first critical frequency when the compressor was taken to overspeed (14,500 rpm).

After installation, the compressor ran satisfactorily on recycle up to the limiting horsepower capability of the gas turbine drive under recycle conditions--12,400 rpm. Closing the recycle valve would start to build discharge pressure, but at about 96.5 bar (1400 psi) a disturbing vibration started with a frequency of about 6000 cpm. This vibration would grow and decay but its maximum excursion would increase rapidly to above 50 μm (2 mils) as the recycle valve was further closed.

An initial change was made by cutting the bearing effective length by close to 50 percent without any change to clearance or preload. Because the bearing is lightly loaded, this change would tend to reduce stiffness, causing more amplitude and therefore more dissipation of vibration energy at the bearings. This change reduced the frequency of the unstable vibration to about 5700 cpm for a discharge

pressure of 121 bar (1750 psi). Before the unstable vibration peak amplitude became intolerable, maximum vibration amplitude at 5700 cpm and 121 bar was about 20 μm (0.8 mils), peak-to-peak. As discharge pressure was increased above 121 bar the unstable vibration amplitude increased exponentially. This modification allowed limited operation which had been impossible without the bearing change.

Along with improved control of the unstable vibration a new vibration at 21 percent of running speed with amplitudes of about 25 μm (1 mil) was observed. Thus, the bearing change allowed temporary operation but clearly showed that there were two subsynchronous vibration problems to be identified and corrected.

In response to this situation the manufacturer developed more substantial changes to the rotating and stationary elements of the compressor. This paper presents selected results from an independent study involving both measurement and analysis to identify the problems and to evaluate the proposed modifications to the rotor and its suspension. The objective of the paper is to contribute to the available body of data on subsynchronous vibration of turbomachinery and to show how existing state of the art criteria and analyses can be effectively applied in design and troubleshooting.

MEASURED DATA

The data presented was obtained using four installed 45° proximity probes. The two bearing locations are identified as drive end (DEX, DEY), and non-drive end (NDEX, NDEY).

Conditions are referred to as "original bearings" and "MOD 1 bearings;" the original bearings were 89 mm (3.5 inches) in diameter and 92 mm (3.625 inches) in total length with a groove 3.2 mm (0.125 inch) wide running circumferentially through the middle of each pad, creating two lands each 44.4 mm (1.75 inches) wide. The MOD 1 bearings were made from the original bearings by cutting the width of each land to 20.7 mm (0.813 inches). For both bearings the machined radial clearance, CP, was 117 μm (4.6 mils) (nominal) and the measured assembled clearance, CB, was 80 μm (3.13 mils) (average) giving a preload, m, of about 0.3.

Figure 2 shows the vibration spectrum at non-drive end with original bearings at 11,100 rpm and a discharge pressure of 117 bar (1700 psi); the 6000 cpm vibration is pronounced with an amplitude of 23 μm (0.9 mils). Running speed vibration amplitude is approximately 13 μm (0.5 mils).

Figure 3 shows vibration spectra at non-drive end for discharge pressures of 121 and 128 bar (1760 and 1850 psi) with the MOD 1 bearings. Speed is again 11,100 rpm. Note that the unstable vibration frequency dropped to 5700 cpm and is again pronounced, but there is now a vibration at 21 percent of running speed whose amplitude is comparable to the 5700 cpm vibration.

In Figure 4 the data has been organized to show how the unstable vibration varies as a function of discharge pressure for the original bearings. The 6000 cpm vibration shows an onset at 96.5 bar (1400 psi) and rapid growth with increasing pressure.

Figure 5 presents similar plots as a function of discharge pressure for the rotor with MOD 1 bearings installed. The 5700 cpm vibration appears at a similar pressure as did the 6000 cpm vibration for the original bearings, but grows more

gradually. The 21 percent vibration first appears noticeable at 96.5 bar (1400 psi) but is limited to about 25 μm (1 mil) as discharge pressure increases. Note also that the drive end amplitudes for the 21 percent (2323 cpm) vibration are much smaller than those at the non-drive end and that the non-drive end amplitudes do not show much variation with pressure. It was observed that the 21 percent vibration tracked running speed at a constant ratio and thus was referred to as such in some of the figures.

ANALYSIS

Subsynchronous vibrations can result from two distinct aerodynamic phenomena: in one the flow disturbances and resultant dynamic forces are directly influenced by the amplitude of mechanical vibration; in the other the flow disturbances and forces are a function of the flow itself and are not significantly influenced by the level of mechanical vibration. The latter are called rotating stall or surge; the former are referred to as self-excited vibrations, and the forces are commonly referred to as Alford forces (ref. 1).

Self-excited vibrations which are sustained by rotor motion generally occur on the order of 50 percent of operating speed. Excitations due to rotating stall fall into two categories which are distinguished by frequency. Impeller rotating stall is characterized by frequencies of approximately 70 percent of operating speed, while vibrations due to diffuser rotating stall generally occur in the 10 percent to 20 percent of operating speed range (ref. 2).

As mentioned above, two subsynchronous vibration problems existed. One subsynchronous vibration was at approximately half speed while the other was at approximately 21 percent of running speed and appeared to track speed. The calculations performed during this project indicated the first problem of half speed subsynchronous vibration was due to a rotor dynamic instability excited by aerodynamic cross-coupling forces. The second problem was believed to be a diffuser stall due to a very shallow flow angle from the wheel into the vaneless parallel wall diffuser.

The following analysis will deal first with the vibration at 50 percent of operating speed, and then vibrations at 21 percent.

Stability Analysis for Original Rotor

A mass-elastic model of the rotor was prepared and a critical speed map was generated as shown in Figure 6. Superimposed are plots of total impedance, Z, as a function of speed for the MOD 1 bearing (impedance = $\sqrt{K^2 + (\omega B)^2}$) where K and B refer to direct bearing stiffness and damping coefficients and ω is rotational speed. There are intersections between bearing lines and the first two rotor critical speed lines at:

- 2,800 rpm
- 4,800 rpm
- 7,300 rpm
- 11,000 rpm

The intersections at 2800 rpm and 7300 rpm are in the rigid body regime for first and second criticals and can be expected to be very highly damped. This is confirmed by unbalance response analysis as typified by Figure 7 which shows drive end bearing response as a function of speed for unbalance excitation at shaft center. Based on Figure 7, critical speeds occur only near the 6000 rpm and

10,800 rpm speeds. It was necessary to include stiffening effects of labyrinth and ring seals to match measured data.

The stability of the unit was calculated for the first forward mode and the results are presented in Figure 8. This plot illustrates the detrimental effect on stability of increasing aerodynamic cross-coupling. The estimated aerodynamic cross-coupling load was approximately 1230 N/mm/wheel (7000 lbs/in/wheel) for this compressor under design operating conditions (ref. 4). Based upon experience, a screening criteria was used, for this particular case, of 0.5 logarithmic decrement at low aerodynamic cross-coupling conditions and a 0.2 log decrement at design conditions with full aerodynamic cross-coupling. These criteria proved unattainable for a range of parameter variations and bearing changes evaluated for the existing rotor geometry. The calculated stability for the compressor's first damped natural frequency was marginal at low aerodynamic cross-coupling values and the log decrement tended to zero or below as design operating conditions were approached.

Figures 9 through 12 are a series of bar graphs which review stability comparisons for the original rotor. Two aero cross-coupling values 175 and 1230 N/mm/wheel (1000 and 7000 lbs/in/wheel) are illustrated. Also, shown in the figures is the desired log dec for reference purposes.

Figure 9 illustrates the difference due to original and modified bearings. The MOD 1 bearing shows a slight increase in log dec; however, calculations predict instability at design conditions which is consistent with the measured field data.

Calculations using synchronous bearing coefficients are compared to those with nonsynchronous bearing coefficients for a frequency ratio of 0.5 in Figure 10. Predicted system stability is altered greatly by the use of nonsynchronous bearing coefficients; at design operating conditions the calculated log dec drops from +0.1 to -0.25. In view of this significant difference, all other predictions account for frequency dependence of the tilting pad bearing characteristics.

The effect of preload on the MOD 1 bearing is shown in Figure 11. Increasing preload decreases stability slightly.

Figure 12 summarizes five other bearing modifications considered for this unit. These were:

(1)	MOD 1	L/D = 0.5	With Groove	5SLOP	m = 0.3
(2)	MOD 2	L/D = 0.5	Without Groove	5SLOP	m = 0.3
(3)	MOD 2A	L/D = 0.25	Without Groove	5SLOP	m = 0.3
(4)	MOD 3	L/D = 0.5	With Groove	5SLBP	m = 0.3
(5)	MOD 4	L/D = 0.5	With Groove	5SLOP	m = 0.0

None of the considered modifications increased the stability significantly above the MOD 1 bearing being used at the time this analysis was performed.

Other portions of the stability analysis addressed the following topics:

(1) Hysteretic Damping
(2) Seal Ring Lockup
(3) Labyrinth Effects
(4) Combination of (2) and (3)
(5) Squeeze Film Dampers

While these were not felt to be major factors contributing to the existing sta-

bility problems, some brief comments are worth including. Inclusion of hysteretic damping reduced calculated log dec values. Seal ring lockup, should it occur, significantly increased cross-coupled stiffness values at the seals which adversely affected stability; however, the pressure balancing features of the breakdown seals should preclude lockup. Analysis of the labyrinth seal at the balance drum can indicate either a positive or negative stiffness based upon geometry and certain assumptions (ref. 6). For this rotor, the main effect of ring and labyrinth seals was to act as a soft bearing, thus raising the lateral critical speed above rigid bearing calculations. Squeeze film dampers were investigated. The results were not promising and physical constraints prevented their addition.

Subsynchronous Response Analysis

Rotor system response to forced vibration at a subsynchronous frequency was investigated. This nonsynchronous excitation was imposed upon the shaft under conditions similar to those existing in the field.

The field measured vibrations in the vicinity of 2400 cpm with the MOD 1 bearings did not appear to be a resonant response of the rotor system, but rather the non-resonant response to a large rotating force. Figure 13 shows the predicted rotor response to forced excitation at 21 percent of operating speed. In the vicinity of the measured field vibrations, no resonant response is apparent. For these predictions the excitation force was varied with the square of speed and the magnitude of the force was adjusted to give response levels close to those observed as shown in Figure 13. This required a force of about 580 N (130 lbs) at an excitation frequency of 2400 cpm.

The location of the subsynchronous excitation along the length of the shaft was investigated and the results are shown in Figure 14. It can be seen that as the excitation location is moved toward the discharge end of the shaft, the ratio of amplitudes between non-drive end and drive end approaches that obtained from field data. This gives an indication that the forcing function is being applied near the discharge end of the rotor. The observed difference in measured amplitudes at the two ends is consistent with non-resonant response since at frequencies near resonance both ends are predicted to respond with similar amplitudes wherever the excitation is applied.

Figure 15 shows the effect of the same excitation on rotor response for the original bearing in the machine. The lower predicted amplitudes from the response curve could be attributed to stiffer bearings due to the longer length of the original bearings. This lower amplitude agrees with field data.

Figure 16 illustrates the effect of bearing modifications on the response amplitude in the vicinity of 2400 cpm. The old bearing refers to the original bearing in the machine, while the new bearing refers to the MOD 1 bearing operational at the time of this analysis. The minimum response amplitude was achieved with the old bearing which was an unacceptable alternative based upon the analysis of vibrations at 5700 cpm. The most beneficial alternatives were those that increased the bearing stiffness and thereby the impedance between excitation point and ground. However, bearing changes alone do not appear to eliminate the problem.

Since the vibrations in the vicinity of 2400 cpm appeared to track speed, were not related to a resonant rotor condition, and were at a frequency of approximately 21 percent of operating speed, an investigation was begun to determine if they could be attributed to rotating stall in the diffuser. Published data

concerning stall frequency ratio versus inlet flow angle is shown in Figure 17 for comparison with the observed vibration frequency. It is seen that diffuser rotating stall can occur in the 10 to 20 percent of operating speed range (ref. 2).

The angle at which flow enters the diffuser affects whether or not a stall condition might occur in a diffuser. Published criteria from two sources (refs. 2 and 3) for the critical inlet flow angle versus diffuser width to inlet radius ratio are shown in Figure 18. Based upon system geometry, the predicted flow angle at design conditions lies close to the criteria line. Flow angles below the curve shown in the figure predict rotating stall in the diffuser while angles above indicate diffuser stall should not occur. The width to radius ratio for the last stage of the subject machine was originally 0.029. Included in Figure 18 are predicted flow angles for a revised system which has a diffuser width to radius ratio of 0.021, and these will be discussed in more detail later in this paper.

Analysis of Revised Rotor Design

Since neither of the two subsynchronous vibrations appeared to be controlled at the same time by bearing changes alone, major shaft modifications were considered. The basis for the redesign of the shaft was that a stiffer shaft with a shorter bearing span and larger diameter shaft at the bearings should increase the first critical speed and thus alleviate the half speed vibration problem. At the same time the impedance between rotating stall excitation and ground would be increased, so reducing sensitivity to this excitation. To achieve this, the shaft was modified in the area outside of the balance drum and wheels; the diameter was increased at the bearings, the seals were moved outside the bearings (so that the bearings operate in a high pressure region) and both seal and bearing were redesigned. This also necessitated a change to the spacer in the drive coupling.

Total rotor length is 1700 mm (66.82 inches) and total rotor weight is 2450 N (550 lb). Bearing span was decreased by 186 mm (7.31 inches) to 1180 mm (46.4 inches). Diameter of the shaft at the bearings was increased to 102 mm (4 inches) with an L/D of approximately 1/2. No circumferential groove was included and a 0.2 nominal preload was called for. The seals were of a three lobe type and were located just outside of the bearings.

These modifications to the rotor required a new shaft to be built; however, to save as much time as possible, the area of the shaft which held the wheels and the labyrinth were not altered so that these parts could be reused. Also, the area of the shaft thrust collar was not significantly altered. A new bundle was to be supplied to facilitate the change of the rotor; modifications to the bundle included reductions in diffuser width for all stages and holes drilled in the last stage/labyrinth area to increase last stage flow.

For the revised rotor a critical speed map is shown in Figure 19. Note the higher rigid bearing first critical speed and the stiffer bearing characteristics. There are intersections of the first and second critical speed lines and the bearing total impedance lines at:

- 5,500 rpm
- 6,000 rpm
- 16,000 rpm
- 16,000 rpm

In the vicinity of the first critical speed intersection at approximately 70 to 88

kN/mm (4 to 5 x 10^5 lb/in) support stiffness, the corresponding undamped vibration mode shape shows more deflection at the bearings than the original rotor. This allows the bearing damping to be more effective in dissipating shaft vibrational energy.

Figure 20 shows calculated unbalance response for the drive end bearing as a function of speed for nominal 720 g-mm (1 oz-in) unbalance excitation at shaft center. The predicted first critical speed is now approximately 8200 rpm as opposed to 6000 rpm for the original rotor. As mentioned above, the bearings are in a different part of the vibration mode shape due to the shorter span. The labyrinth has not changed and should still contribute some stiffening effect, but the seals are now outboard of the bearings in an area less sensitive to their dynamic effects (if any).

Rotor stability is summarized in Figure 21 and Table 1 for the revised rotor. The general trend of decreasing log dec with increasing aerodynamic cross-coupling remains; however, the value with zero aero cross-coupling is over 0.7 and the cross-over point for zero log dec has been significantly shifted to the right. Also, the first forward mode's damped frequency predicted under design conditions has increased to above 6000 cpm. It should be pointed out that, for this rotor, a decrease in diffuser widths from the original system causes an increase in the predicted aerodynamic cross-coupling at design conditions. This increase to approximately 1750 N/mm/wheel (10,000 lbs/in/wheel) yields a calculated log dec of approximately 0.2 at design conditions. The increase in the damped natural frequency of the first forward mode is significant and coupled with the increased predicted log dec, the system appears satisfactory from the 50 percent speed self-excited vibration standpoint.

Hysteretic damping, seal and labyrinth effects on calculated stability were investigated. In essence, seal and labyrinth effects did not detrimentally alter the calculated log dec for the system. This was attributed to the fact that the seals were now outboard of the bearings which located them at a different part of the mode shape for vibration at this frequency. Also, the increase in frequency of the first damped critical speed helps increase the margin of stability for all cases investigated.

As with the original rotor the influence of accounting for nonsynchronous tilting pad coefficients was significant.

The predicted flow angles and their relationship to the predicted diffuser stall margin for the modified rotor and diffuser were previously included as part of Figure 18. The changes achieved a distinct increase in margin by over 2° relative to the original design. Coupled with the stiffer shaft, which reduced sensitivity to this excitation by a factor greater than 2, the new design was expected to see a substantial reduction if not total elimination of the 21 percent speed vibration.

The narrower diffuser passages increased the predicted aerodynamic cross-coupling as mentioned previously. The trade-off of higher aero loadings on the wheels versus eliminating diffuser stall is self-evident.

Running Experience with Revised Rotor

The rotor modifications described above have been installed. The compressor has been run to near design discharge pressure and speed with negligible self-

excited vibration. There is a slight hint of vibration at about 20 percent of running speed, but the levels are quite tolerable.

COMPARISON WITH AN ALTERNATIVE STABILITY CRITERIA

A comparison of past unstable compressors with a suggested stability screening criteria was recently presented (see Reference 7). Figure 22 is reproduced from this reference and plots the product of discharge pressure and pressure rise against the ratio of operating speed to first rigid bearing critical speed. The diagonal band is the suggested criteria of Reference 7, with rotors to the left of the leftmost line considered satisfactory.

To evaluate the applicability of the criterion to the compressor under consideration in this study, three points have been superimposed on Figure 22:

(1) The original design point.
(2) The design point with the revised rotor.
(3) The point at which vibration levels become intolerable with the MOD 1 bearing.

All these points lie to the left of the criteria band, indicating that this particular compressor requires a more conservative stability criterion than that of Reference 7.

The potential benefits of such a screening criterion as that proposed in Reference 7 are substantial. However, it appears that a more extensive data base is needed with some adjustment of the criterion band before universal application is contemplated.

CONCLUSIONS

1. This study adds to the data base of published information on subsynchronous vibration of centrifugal compressors.

2. The observed vibration near 50 percent of running speed appears to be a self-excited vibration due to self-sustaining aerodynamic cross-coupling effects.

3. Prediction of log decrement using published empirical data for aerodynamic cross-coupling (ref. 4) and nonsynchronous tilting pad bearing coefficients indicates that the rotor would have a damped critical speed with negative log decrement and frequency near (but below) that observed under design conditions; with zero aero cross-coupling the predicted log decrement is 0.35.

4. Using the same analysis for a design with revised rotor, bearings and seals, log decrement with full aero cross-coupling was predicted to be 0.2 and with zero aero cross-coupling to be 0.7.

5. With this redesigned rotor, subsynchronous vibrations were negligible.

6. There is strong evidence that vibration observed at about 21 percent of running speed was a non-resonant vibration excited by diffuser rotating stall.

7. Observations suggest that operation near to the diffuser rotating stall criteria of References 2 or 3 can result in this form of aerodynamic excitation.

8. If there is insufficient impedance between excitation point and ground, significant vibrations near 20 percent of running speed can result from diffuser rotating stall excitation.

REFERENCES

1. Alford, J. S., "Protecting Turbomachinery from Self-Excited Rotor Whirl", J. Eng. Power, Vol. 87A, 1965, pp. 333-344.

2. Frigne, P., Van Den Braembussche, R., "Comparative Study of Subsynchronous Rotating Flow Patterns in Centrifugal Compressors with Vaneless Diffusers", NASA Conference Publication 2250, Rotor Dynamic Instability Problems in High-Performance Turbomachinery-1982, Proceedings of a workshop at Texas A&M University, College Station, Texas, May 10-12, 1982, pp. 365-381.

3. Senoo, Y., Kinoshita, Y., "Influence of Inlet Flow Conditions and Geometries of Centrifugal Vaneless Diffusers on Critical Flow Angles for Reverse Flow", Journal of Fluids Engineering, March 1977, pp. 98-103.

4. Wachel, J. C., von Nimitz, W. W., "Ensuring the Reliability of Offshore Gas Compressor Systems", Society of Petroleum Engineering of AIME, Journal of Petroleum Technology, November 1981, pp. 2252-2260.

5. Benckert, H., Wachter, J., "Flow Induced Spring Coefficients of Labyrinth Seals for Application in Rotor Dynamics", NASA Conference Publication 2133, Rotordynamic Instability Problems in High-Performance Turbomachinery, Proceedings of a workshop held at Texas A&M University, College Station, Texas, May 12-14, 1980, pp. 189-212.

6. Wright, D. V., "Labyrinth Seal Forces on a Whirling Rotor", NASA Contractor Report 168016, January 1983, p. 32.

7. Kirk, R. G., Donald, G. H., "Design Criteria for Improved Stability of Centrifugal Compressors", ASME Publication "Rotor Dynamic Instability", AMD-Vol. 55, pp. 59-71.

8. American Petroleum Institute, "Centrifugal Compressors for General Refinery Service", API Standard 617, Fourth Edition, 1979.

TABLE 1
COMPARISON OF ROTORS

Rotor Model		Critical Speed Map Results, cpm	Unbalance Response Results, cpm	Stability Analysis Results, Frequency/Log Dec cpm
Original	1	4,800	6,000	4260/-0.24
	2	11,000	10,800	
	3	15,000	-	
Revised	1	6,000	8,200	6110/+0.2
	2	16,000	-	*
	3	20,000	-	

* Due to narrower diffuser passages, predicted aero cross-coupling forces at design conditions are greater for the revised rotor.

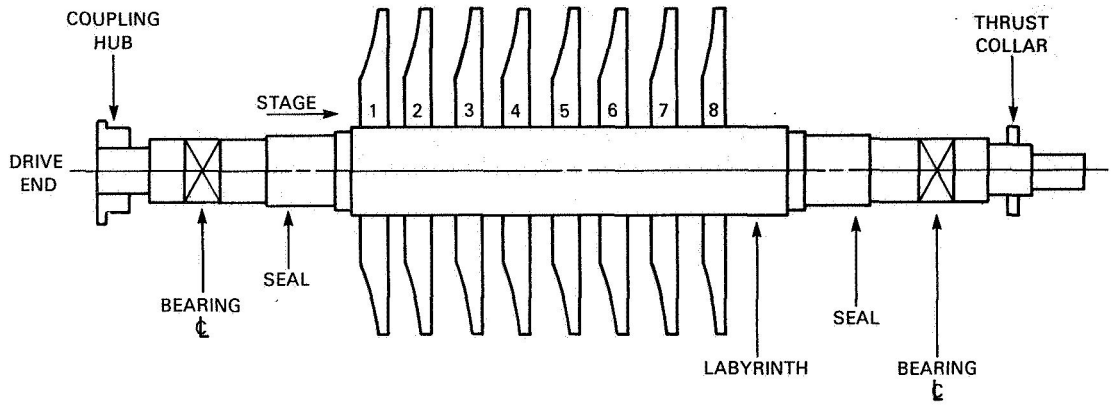

Figure 1. - Rotor sketch of high pressure, low flow centrifugal compressor.

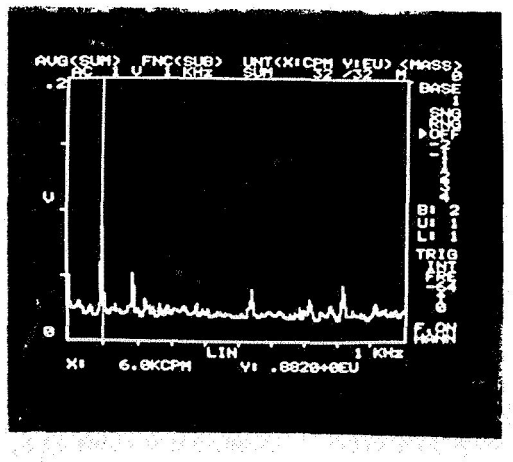

Figure 2. - Vibration spectrum for original rotor in original bearings. Speed, 11 100 rpm; discharge pressure, 1700 psi; non-drive-end X vibration (NDEX).

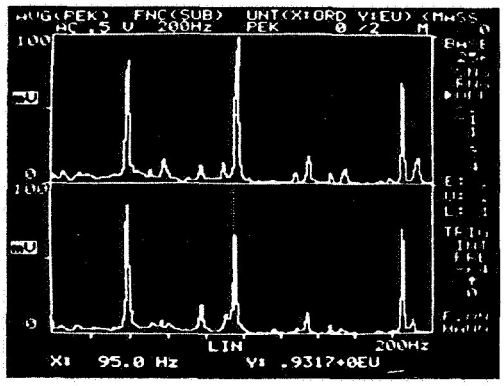

Figure 3. - Vibration spectrum for original rotor in mod 1 bearings. Speed, 11 100 rpm; discharge pressures, 1760 and 1850 psi; non-drive end X vibration (NDEX).

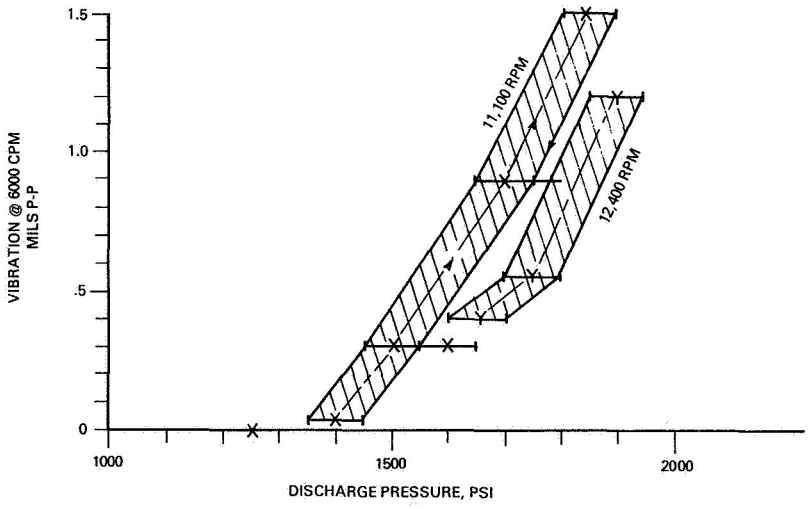

Figure 4. - Vibration as a function of discharge pressure for original rotor in original bearings.

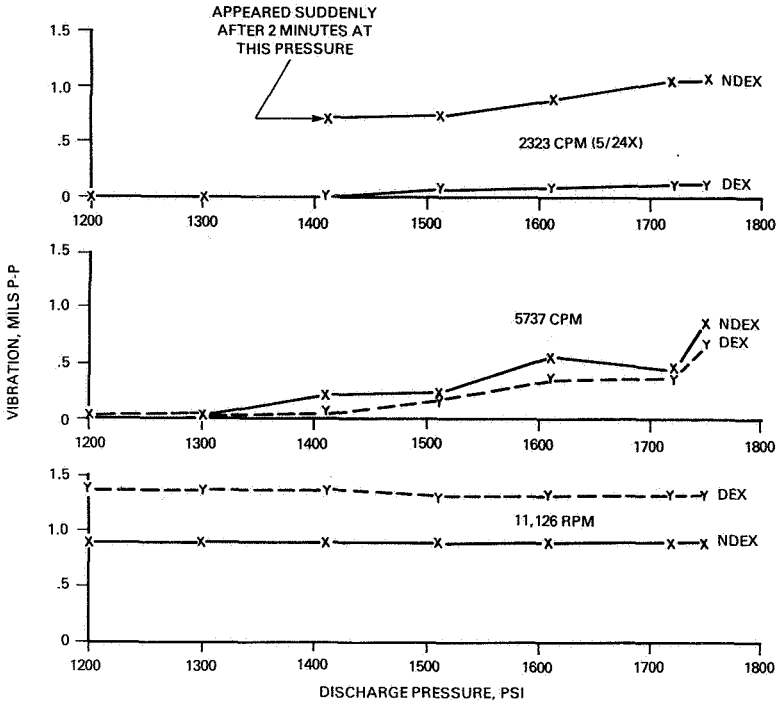

Figure 5. - Vibration as a function of discharge pressure for original rotor in mod 1 bearings. Vibration components at synchronous frequency, half speed, and 21 percent speed; drive-end and non-drive-end X vibration.

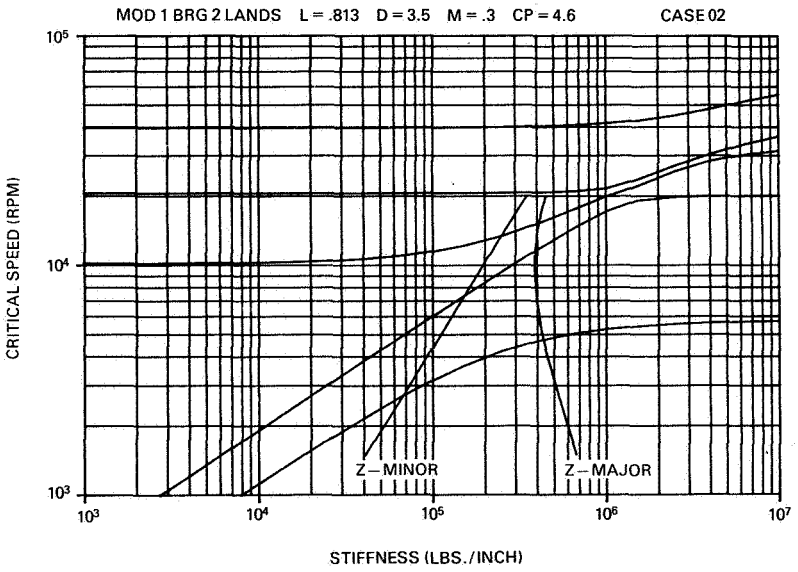

Figure 6. - Critical speed map for original rotor in mod 1 bearings.

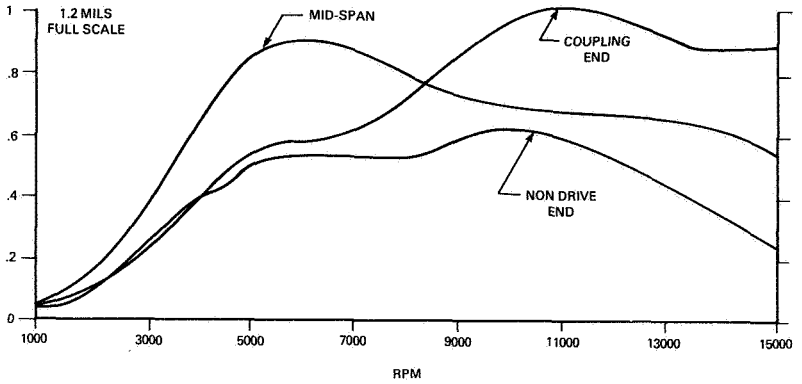

Figure 7. - Unbalanced response for original rotor in mod 1 bearings with 1 in-oz at midspan.

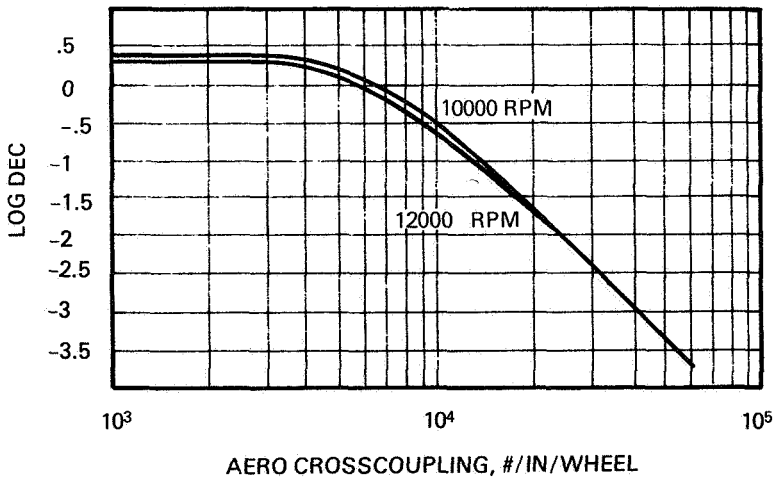

Figure 8. - Rotor stability analysis for original rotor in mod 1 bearings - log decrement as a function of aerodynamic cross-coupling.

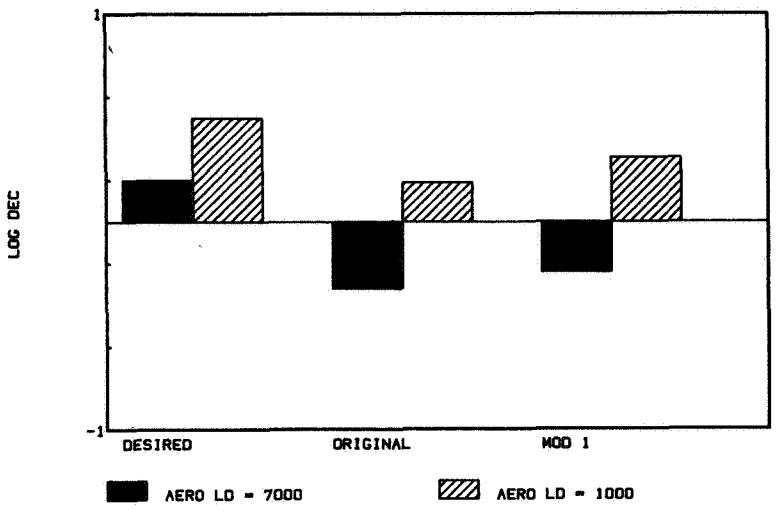

Figure 9. - Stability comparison of original rotor in original bearings versus original rotor in mod 1 bearings. Speed, 12 000 rpm.

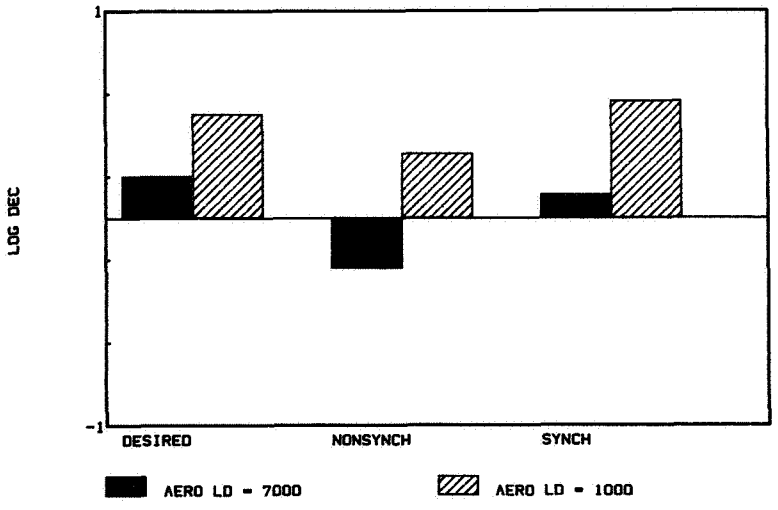

Figure 10. - Comparison of log decrement predicted using synchronous bearing coefficients versus log decrement predicted using nonsynchronous bearing coefficients - original rotor in mod 1 bearings. Speed, 12 000 rpm.

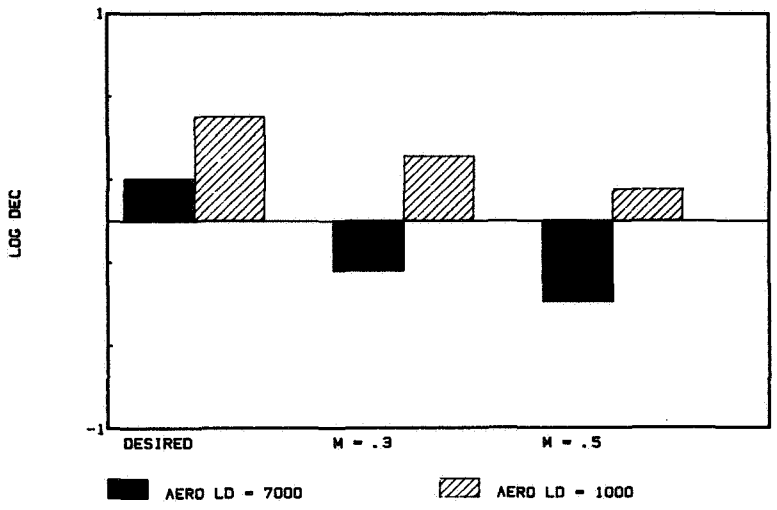

Figure 11. - Predicted stability as a function of preload for original rotor in mod 1 bearings. Speed. 12 000 rpm.

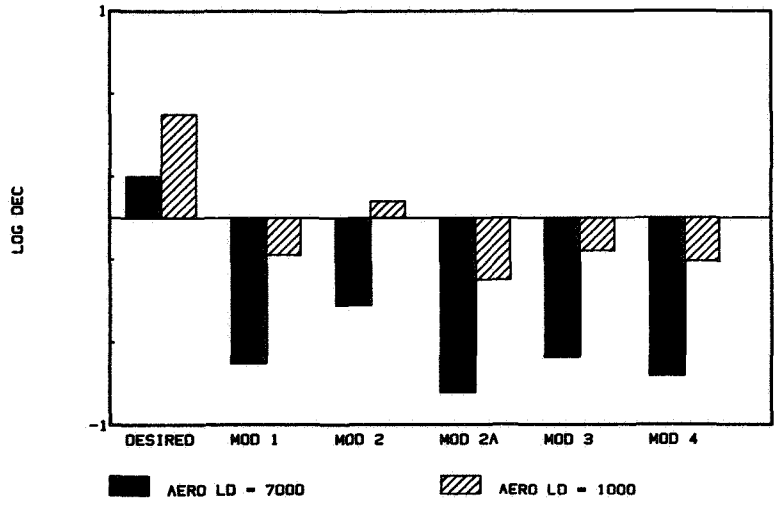

Figure 12. - Predicted log decrement as a function of various bearing modifications for original rotor. Speed, 12 000 rpm.

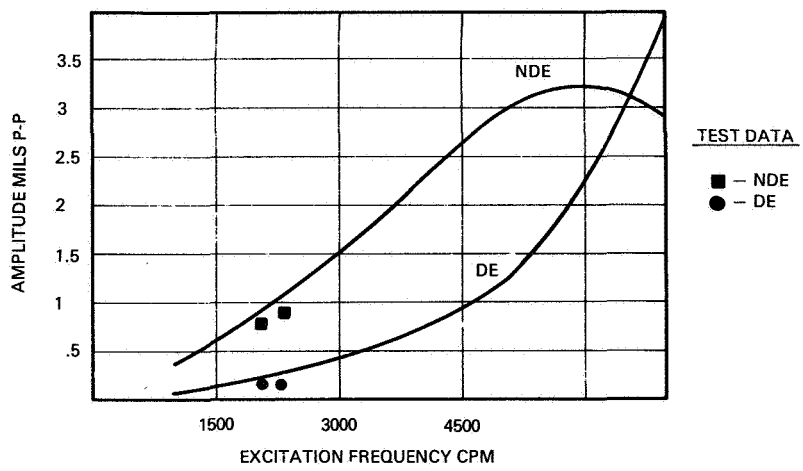

Figure 13. - Predicted response to rotating force applied near last stage at 21 percent speed - comparison of predictions with test data for original rotor in mod 1 bearings.

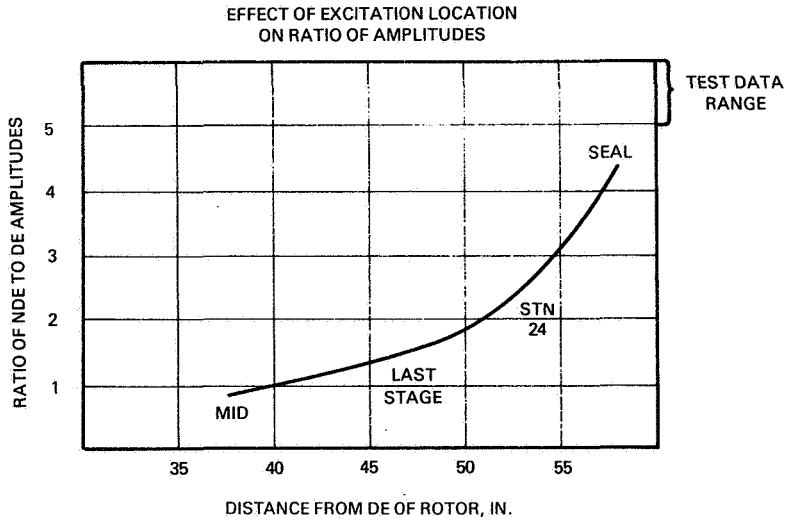

Figure 14. - Ratio of amplitudes for excitation at 21 percent of running speed as a function of excitation location for original rotor in mod 1 bearings.

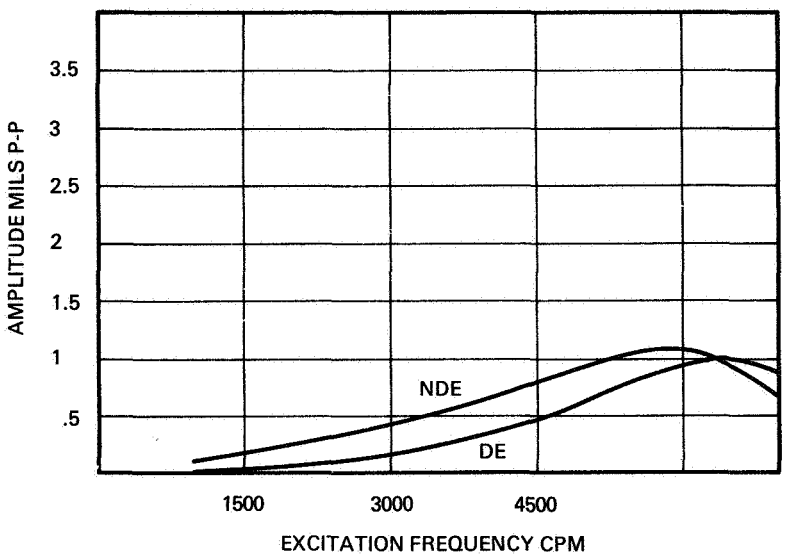

Figure 15. - Predicted response to rotating force excitation at last stage for original rotor in original bearings. Frequency of excitation, 21 percent of running speed.

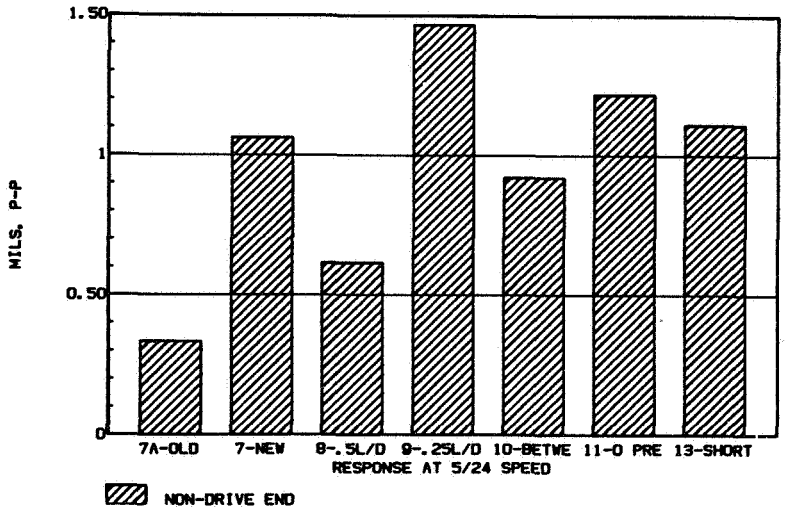

Figure 16. - Response at 21 percent of running speed as a function of bearing parameter changes.

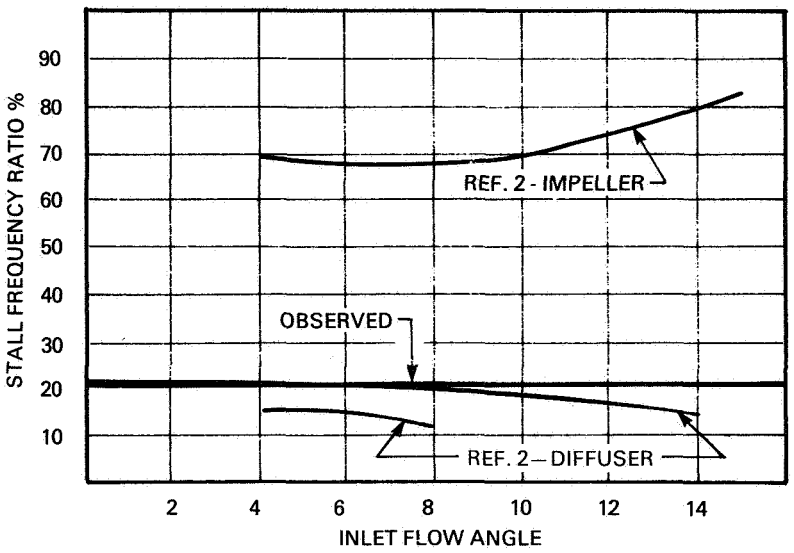

Figure 17. - Comparison of observed vibration frequency with data of reference 2.

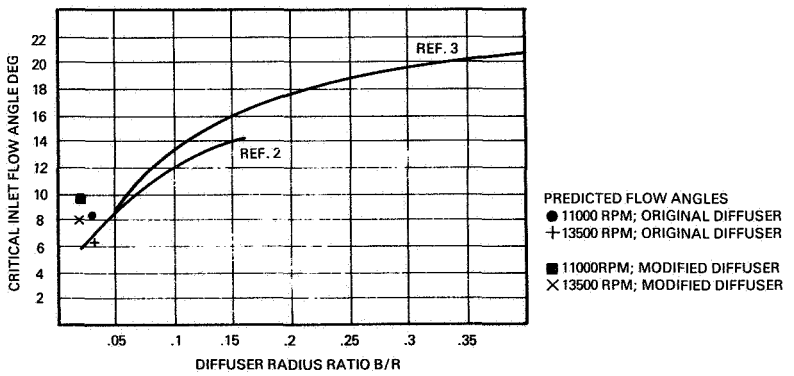

Figure 18. - Comparison of published data for diffuser rotating stall criteria.

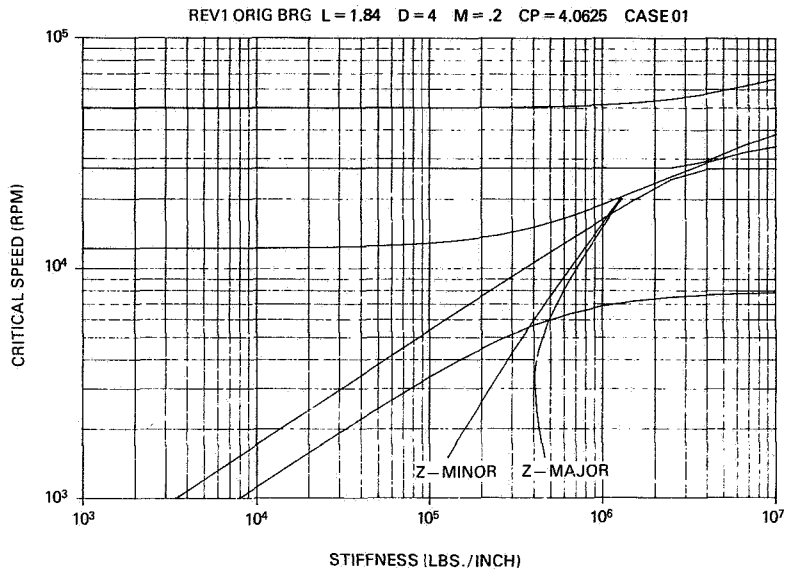

Figure 19. - Critical speed map for revised rotor.

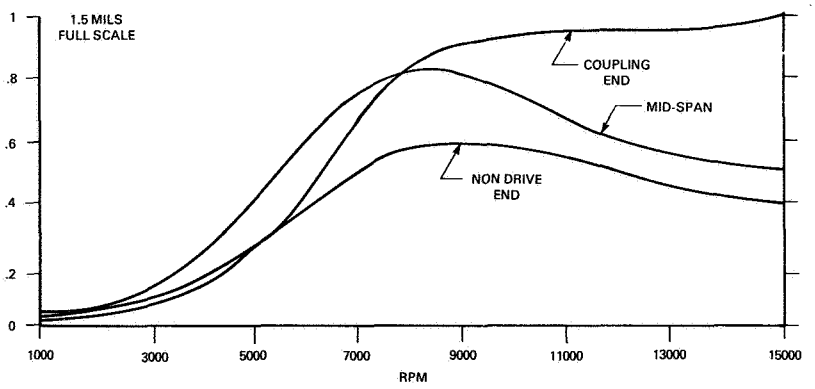

Figure 20. - Unbalanced response prediction for revised rotor in revised bearings with 1 in-oz at midspan.

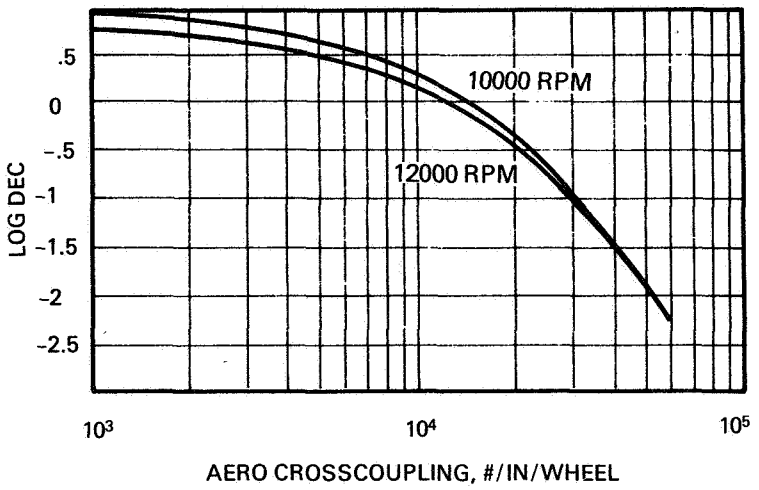

Figure 21. - Rotor stability analysis for revised rotor in revised bearings.

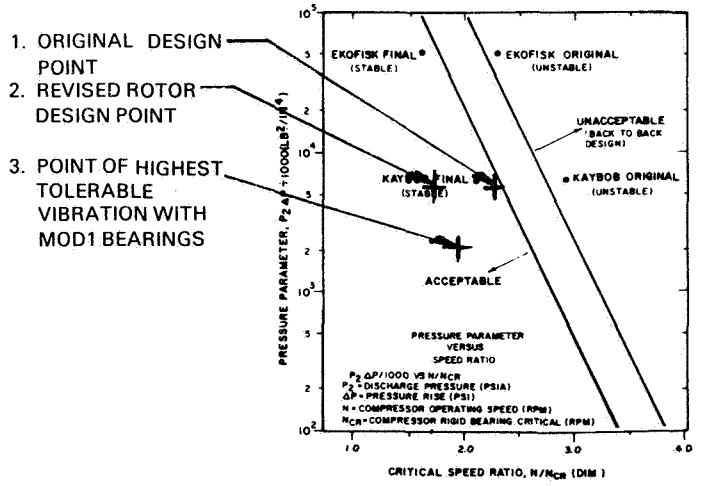

Figure 22. - Comparison of data from present study with suggested criteria of reference 6.

EXPERIENCES WITH NONSYNCHRONOUS FORCED VIBRATION IN CENTRIFUGAL COMPRESSORS

D. R. Smith and J. C. Wachel
Engineering Dynamics Incorporated
San Antonio, Texas 78232

When a compressor rotor experiences subsynchronous vibration, the problem is generally considered to be a shaft instability problem associated with the stability of the rotor on the bearing oil film. However, many times the high subsynchronous vibrations are forced vibrations caused by flow instabilities, such as stage stall. In these cases, modifications to improve the rotor stability by changing the bearings or seals will have little effect on the subsynchronous vibrations. It is therefore important to understand the differences between forced vibrations and self-excited vibrations so the problem can be properly diagnosed and corrected (References 1-4). The following is a list of characteristics of the two types of subsynchronous vibration.

Self-Excited

1. The vibrations generally occur near the first critical speed of the shaft.

2. The vibrations are controlled by the stability of the rotor and the oil film.

3. The vibration amplitudes can suddenly increase and become unbounded until the rotor contacts stationary parts, such as seals and labyrinths.

4. The rotor whirls at the subsynchronous frequency and the whirl direction can be in the direction of rotation (forward) or opposite the direction of rotation (backward).

Forced Vibration

1. The vibrations are caused by aerodynamic excitation (flow instabilites) and are influenced by the acoustical characteristics of the combined compressor and piping systems.

2. The subsynchronous vibrations occur at the lower flows near surge and are bounded in amplitude (as opposed to unstable shaft vibrations which can increase until the shaft contacts stationary parts).

3. The whirl direction is generally forward.

4. The subsynchronous vibration frequencies are usually 5 - 20% of the running speed frequency.

5. The subsynchronous amplitudes are a function of the impeller vane tip speed and gas density.

6. The subsynchronous shaft vibrations and pulsations are phase coherent.

7. The subsynchronous pulsations generally are higher amplitude on the discharge side and do not occur on the suction side unless there are inlet flow distortions.

8. In multi-stage compressors the subsynchronous pulsations are generally associated with the final stages.

9. The pulsation frequencies are determined by the acoustical responses of the entire system including the compressor internals and the piping. Many times there are multiple harmonics of some basic response frequency.

10. In centrifugal compressors, the excitations are often associated with stage stall in the diffuser or return channel.

SYMPTOMS OF FLOW INSTABILITIES

Subsynchronous forced vibrations are often an indication that the compressor is operating near a stage stall condition. Stage stall is a pre-surge condition which occurs when one of the final stages is unstable at reduced flow rates. If the unstable stage reacts with the rest of the system, then a surge condition may result. Therefore, the subsynchronous rotor vibrations can be an indication of incipient surge.

The stage stall or surge of one or more of the impellers can cause a loss of performance. Many times there will be a small drop in head as one particular frequency is excited. As the flow is further reduced, multiple frequency components are sometimes excited which can drastically reduce the performance.

Other indications of the flow instabilities, and often the most obvious, are low frequency vibrations of the attached piping. The piping vibration is due to low frequency pulsations at a fraction of the running speed frequency. This is in contrast to the normally occurring high frequency pulsations at multiples of running speed, such as blade and diffuser passing frequencies which do not normally excite the piping lateral mechanical natural frequencies.

The subsynchronous pulsations are generally less than 10 psi and seldom exceed 1% of line pressure on high pressure units. The pulsations couple at the piping elbows to produce shaking forces which can be significant in large diameter piping since the shaking force is approximately equal to the pipe cross sectional flow area multiplied by the pressure pulsations. For example, an 8 inch pipe with a pulsation of 4 psi could have a dynamic shaking force of approximately 200 lbs. Overhead piping can normally be clamped and restrained to withstand forces of 400-500 lbs; however, centrifugal piping systems typically have very few clamps due to the thermal flexibility requirements and thus the pulsation forces can produce high vibration amplitudes on the piping.

The following case histories were selected because they illustrate the effects and symptoms of subsynchronous pulsation and vibration in centrifugal equipment.

CASE A. TURBOEXPANDER/COMPRESSOR

A turboexpander/compressor unit installed in a gas processing plant experienced numerous mechanical failures, the performance was less than predicted, and the unit had high amplitude, low frequency piping vibrations. The unit operated from 11000 - 13500 rpm (183 - 225 Hz) and the piping and shaft vibrations were primarily near 12 Hz. As outlined above, these were all symptoms of forced vibrations.

Test Procedures

Field tests were made with special instrumentation to identify the source of the excitation. Dynamic pressure transducers were installed to measure the aerodynamic excitation in the turboexpander and compressor. Proximity probes were installed near the rotor bearings to confirm the existence and to assess the severity of the resulting shaft vibrations. Pressure pulsations were measured in the turboexpander inlet and discharge piping and in the compressor suction and discharge piping. Low frequency pulsations near 12 Hz were measured in the compressor suction and discharge piping. There was no indication of the low frequency pulsations in the turboexpander piping where the pulsations occurred primarily at multiples of running speed.

Vibrations of the turboexpander/compressor shaft relative to the bearing housing were measured with proximity probes. Two probes were installed near each bearing, 90 degrees apart, to obtain a shaft vibration orbit. The shaft vibration orbit showed total vibrations of approximately 4 mils peak-peak. The shaft vibration at the running speed frequency was only 1 mil peak-peak while the subsynchronous vibrations near 12 Hz were approximately 3 mils peak - peak. The shaft orbit was unsteady and similar to whirl phenomena experienced on shaft instability vibration problems (self-excited vibrations); however, the amplitude remained bounded. The shaft vibrations and suction pulsations near 12 Hz were phase coherent, which indicated that the shaft vibrations and the compressor pulsations were definitely related.

Although the data indicated that the shaft vibrations and compressor pulsations were related, it was not known which was the cause and which was the reaction. Experience has shown; however, that the shaft vibrations were probably due to the pulsations because it is difficult for the low amplitude subsynchronous shaft vibrations to produce high amplitude coherent pulsations in the gas stream. Therefore, it was felt that the shaft vibrations were forced vibrations and that modifications or balancing of the rotor would not reduce the vibrations.

While the unit was operating at a stable condition near 13000 rpm, speed modulations of 500 rpm near 12 Hz were measured. The speed modulation was obtained by analyzing the tachometer signal from a magnetic pickup with a frequency-to-voltage converter. The digital speed readout in the control room also indicated speed fluctuations, although to a lesser degree, because the signals were averaged for the readout. The speed modulation was another indication that the loading was not constant, which suggested a forced aerodynamic excitation on the system.

Solution

As shown in Figure 1, the suction piping was perpendicular to the compressor

shaft and the gas flow had to make a sharp 90 degree turn to enter the compressor impeller. There were no inlet guide vanes or turning vanes in the compressor inlet chamber. It was felt that the problems were caused by turbulence occurring at the inlet of the compressor impeller. In an effort to improve the flow into the compressor, a flow splitter was fabricated on-site and installed in the inlet chamber directly in line with the suction inlet. After the flow splitter was installed, the subsynchronous vibrations, pulsations and speed modulations were significantly reduced and the performance was improved (Figure 2). Similar flow splitters have been used on induced draft fans to prevent inlet vortices which create rotating stall conditions (Ref 5).

Based upon the data obtained with the flow splitter, a compressor inlet modification was designed to further improve the compressor inlet flow conditions. The modification used an elbow inside the compressor inlet chamber to direct the flow into the impeller. A vertical flow splitter was added to ensure that the flow was properly distributed over the flow area of the elbow. Tests showed that the inlet modification greatly improved the inlet flow conditions, reduced the subsynchronous shaft vibrations and pulsations, lowered the speed modulations, virtually eliminated the low frequency piping and case vibrations and improved the compressor performance (Table 1). It is interesting to note that the rotor vibration amplitudes at the running speed (13000 rpm) were not affected by the flow instabilities. This unit has operated successfully for several years since the inlet was modified.

CASE B. CENTRIFUGAL COMPRESSOR

This compressor system operated satisfactorily for several years until the aftercooler was replaced and the flow rate was reduced. The aftercooler was replaced with a larger unit designed to increase the cooling capacity with a lower pressure drop. The flow rates were down because of the reduced demand for the product. After these changes were made to the operating system, the unit experienced piping and aftercooler vibrations and subsynchronous shaft vibrations.

Test Procedures

A field study was performed to determine the causes of the vibrations. Pulsations were measured in the compressor discharge piping and at the inlet and outlet of the aftercooler. The discharge piping vibrations were measured with accelerometers at the points of maximum vibration. The rotor vibrations were obtained with proximity probes installed near the bearings.

Frequency analyses of the compressor discharge pulsations, aftercooler inlet pulsations, discharge piping vibrations and compressor shaft vibrations are plotted for comparisons in Figure 3. It was found that pulsation and vibration amplitudes could be significantly changed by running the compressor at different operating conditions (Figure 4). The operating condition with minimum pulsation and vibration amplitudes was the condition with maximum flow rate and minimum pressure ratio. The piping vibrations and pressure pulsations were primarily at subsynchronous frequencies near 25 Hz and 75 Hz. The amplitude of the frequency components were beating, as can be seen from the time cascade spectral plots given in Figures 5-6.

During the testing, the suction absolute pressure, the discharge gage pressure,

the compressor running speed and the total flow were logged every minute on the process computer in the control room. The test conditions were plotted on a performance map (Figure 7). As shown, the measured test conditions plotted on the performance map did not agree with the predicted curves displayed on the process computer. The source of the discrepancy was not known; however, it could have been caused by an instrumentation error or the actual performance curve was different from the curves stored in the computer.

Although the measured performance data was different than the predicted performance curve, the data did show that the subsynchronous vibration and pulsation amplitudes were greater at operating conditions closer to the calculated surge line shown on the performance map. The surge line shown on the performance map is the surge line for the combined low and high pressure compressors. Although the compressors did not appear to be operating near the system surge line, the high pressure compressor was probably operating near surge or stage stall conditions for one or more of the final stage impellers.

The problems observed on this compressor appeared to be due to stage stall in which the operation of a particular stage is unstable at reduced flow rates (Refs. 3-4). Similar unsteady flow phenomena have been documented on other centrifugal compressors (Ref. 4). It has been observed that the limit of stable operation is where the pressure ratio (PR) vs. mass flow characteristics (m) is horizontal. Therefore, the criterion for stage stall may be:

$\frac{\partial PR}{\partial m} < o$ stable

$\frac{\partial PR}{\partial m} = o$ metastable

$\frac{\partial PR}{\partial m} > o$ unstable

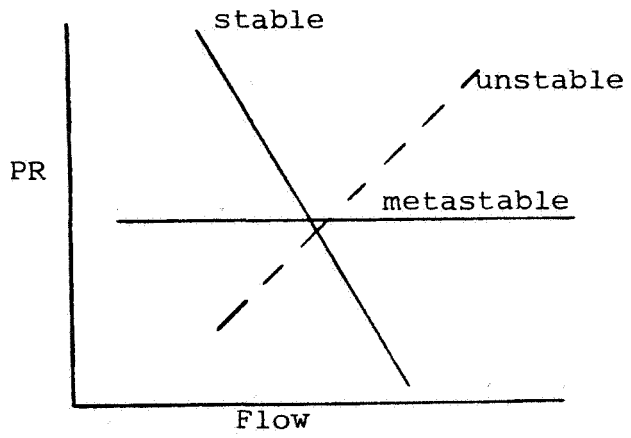

As shown on Figure 7, the plot of the measured pressure ratio versus flow was much flatter than the predicted curves. This would indicate that the compressor was operating near the metastable region.

A stage can operate in an unstable condition for extended time periods without any damage or significant pulsations or noise, if the stage does not react acoustically with the rest of the system. However, if the system, including the inlet elements and discharge elements (such as the aftercooler), interacts with the unstable stage to create high pulsations, then the entire system may become unstable and a surge condition can result.

It has been observed on other units that when a compressor is operating near surge, the frequencies of the nonsynchronous compressor shaft vibrations are generally at the acoustical natural frequencies of the piping system. This

helps to explain why changing the aftercooler changed the compressor discharge pulsations and increased the vibration amplitudes on the discharge piping. The discharge piping acoustical natural frequencies of the new aftercooler were considerably different from the original design. The new aftercooler had almost three times as many tubes in each section as the original design and the acoustic end conditions on either end of the U-bend pipe which connected both sections of the aftercooler were different. A comparison of the effective flow diameters for the original and new aftercoolers is shown in Figure 8. The flow area of the original aftercooler was approximately equal to the area of the discharge pipe. The flow area was much larger on the new aftercooler and appears acoustically as a volume-choke-volume which will respond as a Helmholtz resonator.

A Helmholtz resonator is a low pass filter which is typically used to filter or attenuate high frequency pulsations which are higher than the acoustical natural frequency of the Helmholtz resonator (referred to as the Helmholtz frequency). Pulsations at the Helmholtz frequency are amplified rather than attenuated. Using simplified equations, the Helmholtz frequency for the new aftercooler was calculated to be approximately 20 Hz which is near the measured fundamental pulsation frequency of 20-25 Hz.

The acoustical natural frequency of the choke tube (U bend between the aftercooler sections) was calculated to be approximately 72 Hz which was near the pulsation frequency of 62-75 Hz. This choke tube half-wave resonance is referred to as a pass band frequency and pulsations at this frequency can pass through the inlet and outlet of the filter. The pulsations near 75 Hz were undesirable because the first lateral critical speed of the high pressure compressor was also near 75 Hz. The pulsations from the aftercooler near 74 Hz increased the rotor subsynchronous vibrations because the rotor was sensitive to excitation at the first critical speed. The measured vibrations at 75 Hz were approximately 0.3 mils peak-peak at the bearings; however, the amplitudes could have been several times higher at the shaft midspan near the discharge flange. There was concern that the increased shaft vibrations could be damaging to the seals and bearings.

Solution

The measurements on the units illustrated several changes that could be implemented to reduce the subsynchronous vibrations.

1. The first step would be to operate the unit at high flow rates near the design point where the unit operated satisfactorily for several years. However, due to low product demand, the flow rates could not be increased.

2. The second modification was to operate the unit with more recycle flow which would allow the compressor to operate near the design point. The only disadvantage was that the unit was less efficient and required more horsepower for the same net flow. The recycle flow rate could easily be increased by redefining the surge control line on the process computer.

3. The third step would be to redesign the diffuser, impeller and return

channels on the last few stages to prevent the stage stall at reduced flow rates. This modification would be the most costly and may not be required if the second modification could be implemented.

4. A fourth possibility would be to change the acoustical response of the piping near the aftercooler. Orifices could be designed to reduce the pulsations without causing a significant pressure drop.

The stage stall phenomena exhibited on this compressor were similar to the symptoms shown on another centrifugal compressor which also experienced stage stall. Field data measured on the second compressor suggested that the problem could be corrected by increasing the recycle flow. Detailed tests were made to redefine the surge control valves.

The testing was begun with the compressor operating at high flow rates where the subsynchronous piping and shaft vibrations were not present. The data was continuously monitored as the flow rate was reduced while maintaining a constant speed. As the flow rate was reduced to a certain flow condition (Figure 9, Point A), subsynchronous discharge pulsations and shaft vibrations near 25 Hz would suddenly appear and the flow rate would simultaneously decrease. This flow condition was considerably to the right of the predicted surge line. This type of data was obtained at several different speed lines on the performance map (Figure 9, Point B). A line drawn through the points where the subsynchronous vibrations occurred paralleled the surge line. This line was considered to be due to stage stall or surge of one or more of the final stages.

The recycle control valve was adjusted to keep flow rates to the right of this new surge line and the compressor then operated satisfactorily without any subsynchronous pulsation or vibration. As shown, this line was considerably to the right of the manufacturer's surge line for the entire compressor. These stage-stall conditions are different from machine surge and should not be confused. The machine surge is usually much more violent compared to the surge for individual impellers.

CONCLUSIONS

These compressors exhibited subsynchronous vibrations which had characteristics similar to a shaft instability; however, these were forced nonsynchronous vibrations due to unstable flow conditions. These two compressor rotors were stable (vibrations were bounded) and modifications to the bearings and shafts would not have reduced the subsynchronous vibrations.

The stage stall and surge conditions are a function of the entire system which explains why a compressor can operate satisfactorily for several years and then become unstable after modifications are made to seemingly unrelated piping elements, such as heat exchangers or downstream receivers.

REFERENCES

1. D.R. Smith, J.C. Wachel, "Nonsynchronous Forced Vibration in Centrifugal Compressors", Turbomachinery International, January-February 1983.

2. J.C. Wachel, Nonsynchronous Instability of Centrifugal Compressors, ASME Paper No. 75-PET-22.

3. L. Bonciani, L. Terrinoni, A. Tesei, "Unsteady Flow Phenomena in Industrial Centrifugal Compressor Stage", Instability Workshop, Texas A&M University, NASA CP-2250, 1982, pp. 344-364.

4. David Japikse, "Stall, Stage Stall, and Surge", Proceedings of the Tenth Turbomachinery Symposium, Texas A&M University, December 1981.

5. D.R. Smith, J.C. Wachel, "Controlling Fan Vibration - Case Histories", EPRI Symposium on Power Plant Fans: The State of the Art, 1981.

TABLE I. - COMPARISON OF VIBRATIONS AND PULSATIONS WITH DIFFERENT INLET MODIFICATIONS

	Without Splitter	With Splitter	Modified Inlet
Shaft Vibration Mils peak-peak			
Compressor - Orbit	3.5-4	2.5	1.2
Running Speed @ 13000 rpm	1.1	0.9	1.1
Expander - Orbit	1.5	1.0	0.7
Running Speed @ 13000 rpm	0.5		0.5
Torsional speed modulation, rpm			
Peak-Peak Speed Modulation	500	400	40
Primary Frequencies, Hz	1,6,9,11	1,3,5,6,11	6,12
Pulsation psi peak-peak/Hz			
Compressor Suction	1.4/12	0.2/11	0.16, 0.2/12
Compressor Discharge	2.0/11	0.2/11	-
Piping Vibration mils peak-peak/Hz			
Compressor Suction at Elbow North-South @ 13000 rpm	5.0/11	2.6/12	-

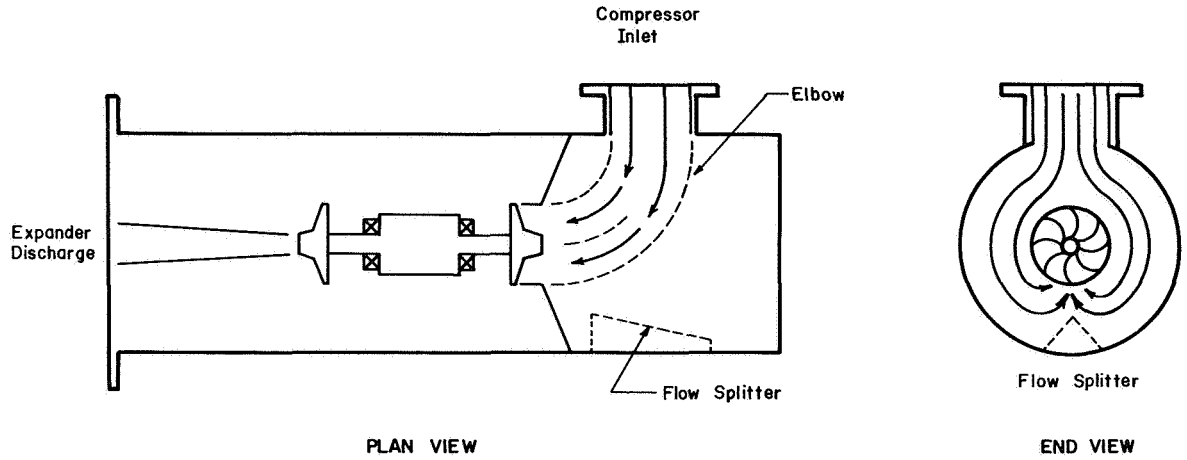

Figure 1. - Cutaway drawing of turboexpander/compressor, illustrating inlet modifications.

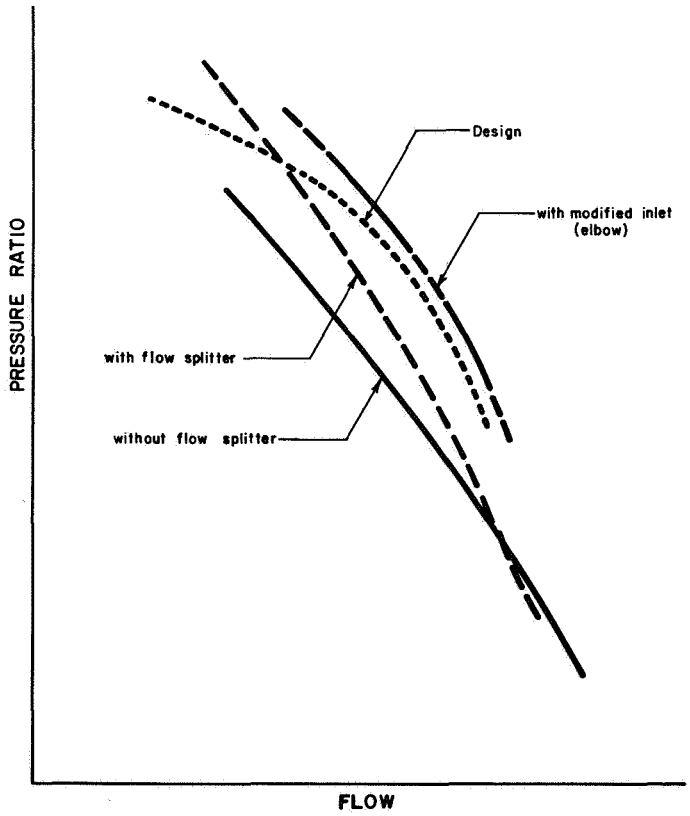

Figure 2. - Results of compressor performance test.

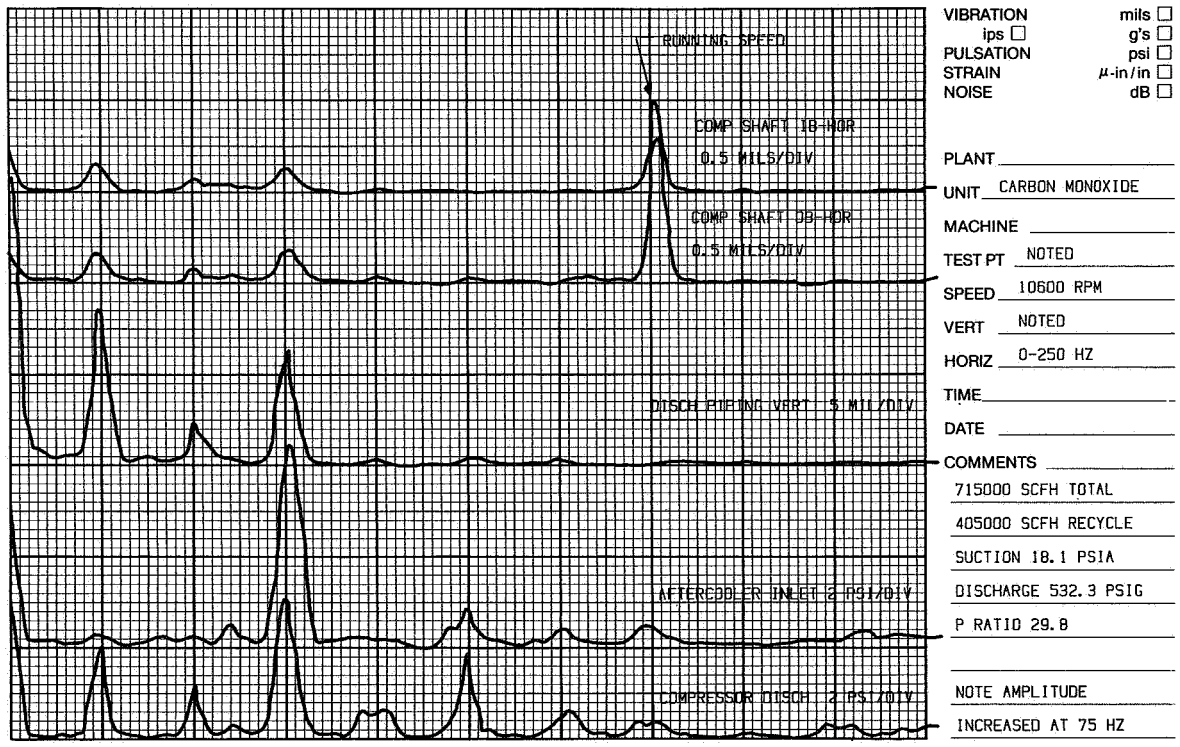

Figure 3. - Comparison of vibrations and pulsations with different inlet modifications.

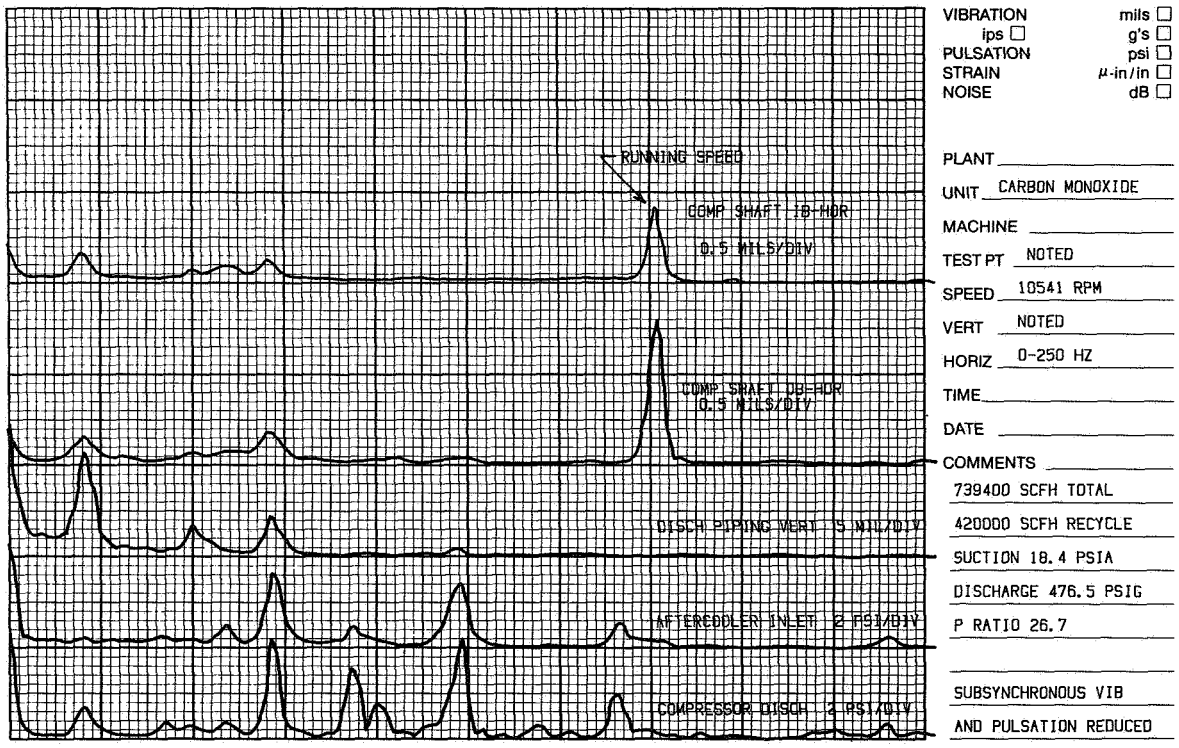

Figure 4. - Comparison of vibrations and pulsations at high flow rate and low pressure ratio.

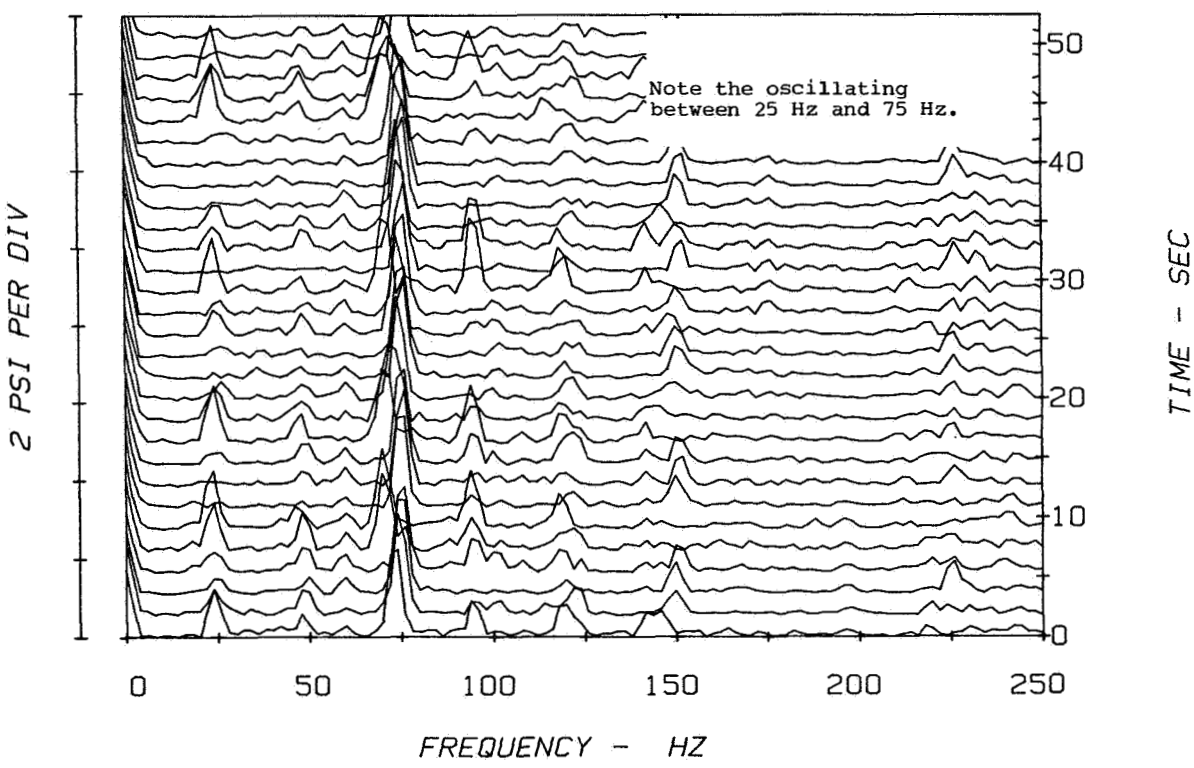

Figure 5. - Compressor discharge pulsations as a function of time.

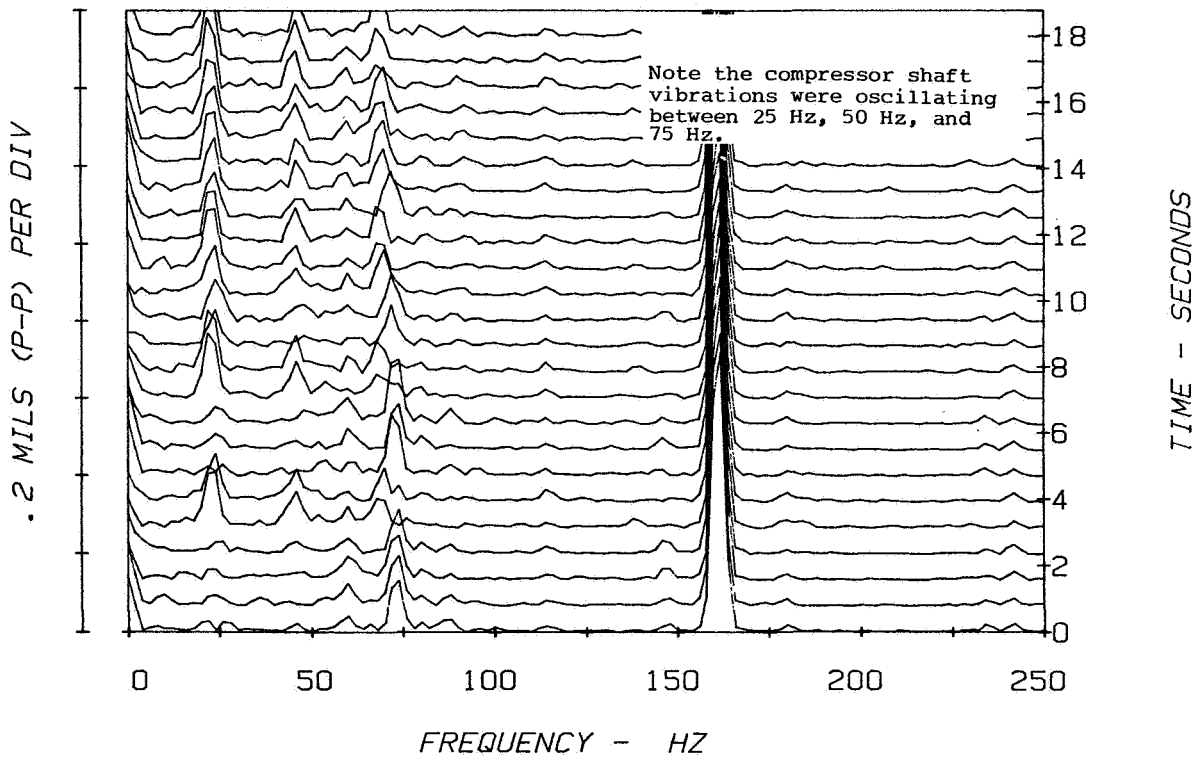

Figure 6. - Compressor shaft vibrations as a function of time.

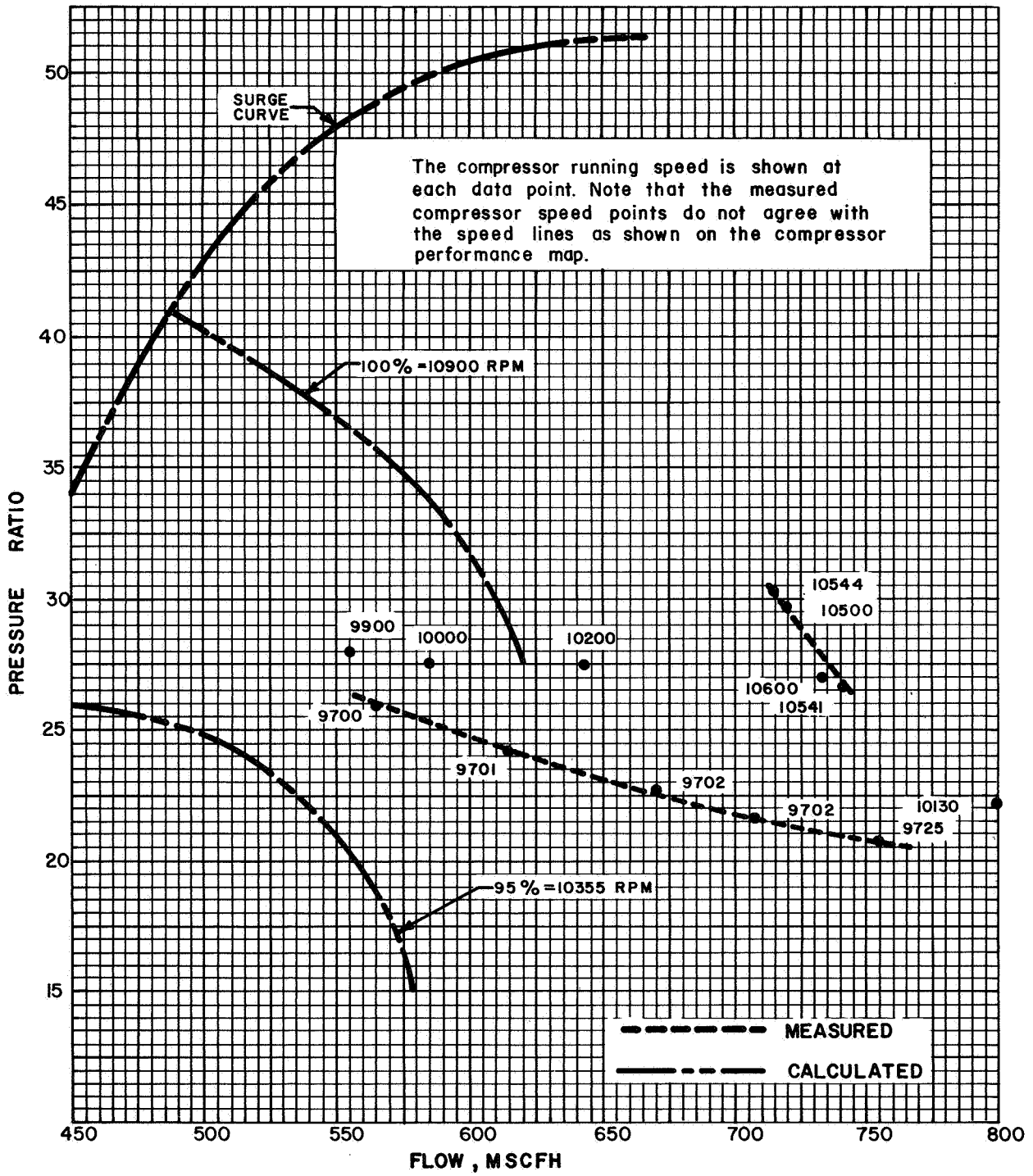

Figure 7. - Measured pressure ratio as a function of flow.

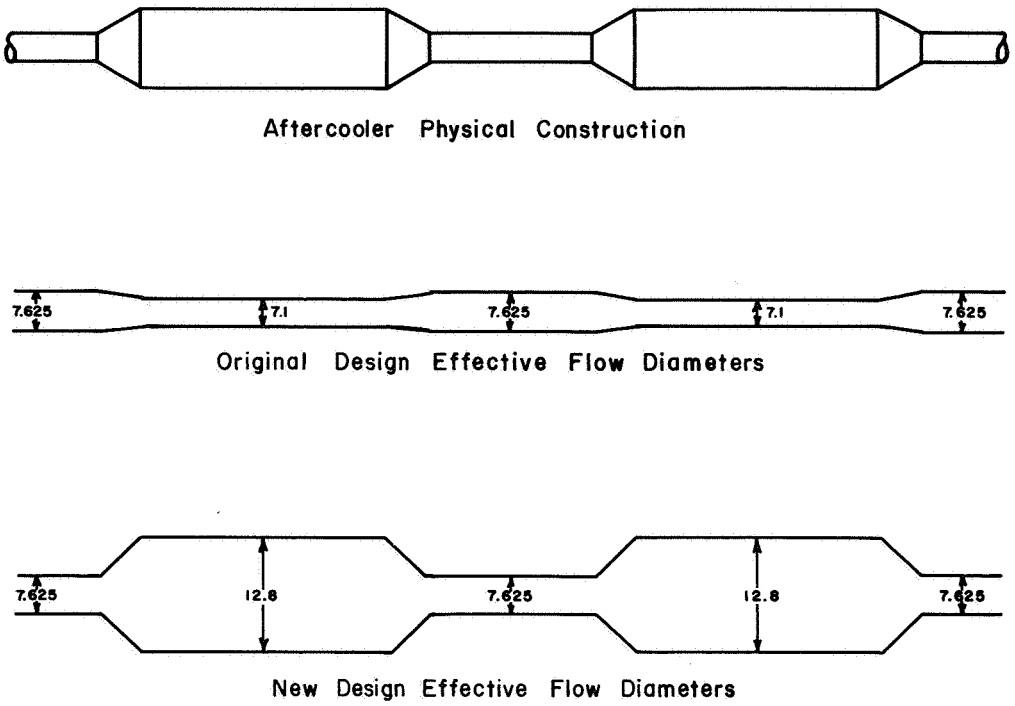

Figure 8. - Acoustical comparison of original and new aftercooler.

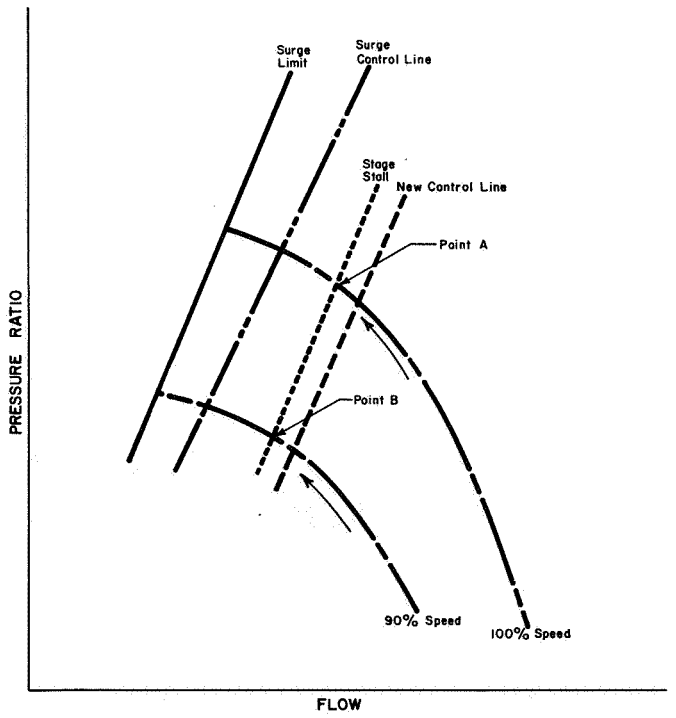

Figure 9. - Compressor performance surge curve.

CONTROL OF ROTORDYNAMIC INSTABILITY IN A TYPICAL GAS TURBINE'S POWER ROTOR SYSTEM

Nicholas M. Veikos, Richard H. Page, and Edward J. Tornillo
AVCO Lycoming Division
Stratford, Connecticut 06497

In the study of rotor systems operating above the first critical speed, it is important to include the effect of rotor internal friction on the system's stability. This internal friction is commonly caused by sliding press fits or sliding splines. Under conditions of high speed and low bearing damping, these systems will occasionally whirl at a frequency less than the shaft's rotational speed. This subsynchronous precession is a self-excited phenomenon, and unlike synchronous precession, stress reversals are created. Since the mid-sixties this phenomenon was observed during engine testing, and analysis has pointed the way for successful attenuation of the problem. The reduction of spline friction and/or the inclusion of squeeze film damping have controlled the instability. This case history along with the detail design of the squeeze film dampers will be discussed.

INTRODUCTION

It is not unusual for present day gas turbine rotor systems to operate above several rigid body critical speeds. These are critical speeds at which most of the deflection and strain energy is in the bearings and bearing supports while the shaft itself moves essentially as a rigid body. Modern balancing techniques and bearing designs permit the rotors to pass through these critical speeds during startup or shutdown, experiencing only a nominal increase in vibration levels at the resonance points. However, it cannot be assumed that the rotor design is satisfactory simply because it allows the system to run through critical speeds. When the rotor is operating in the supercritical regime, it is important to consider the possibility of rotor vibration caused by forces other than unbalance excitation.

One such type of vibration is nonsynchronous precession due to shaft internal friction caused by sliding splines or press fits. This is a self-induced vibration, not sensitive to imbalance, where the rotor will whirl at a frequency approximately equal to that of a critical speed even though the shaft rotational speed is supercritical. This behavior is unlike a critical speed resonance where the amplitude builds up to a maximum value and decreases as the rotor speed changes. At the onset of nonsynchronous whirl, the amplitude will continually increase with speed and time. As the speed increases, the vibration levels will grow. The exciting force is not imbalance but the frictional force due to the relative motion of the splines or press fits. It takes the form of $F = K(\omega - \omega_{cr})$, where K is a constant (>0) for a given rotational speed (ω), and ω_{cr} is the critical speed. When $\omega < \omega_{cr}$ the whirl motion is damped out and the system is stable. However, when $\omega > \omega_{cr}$ the rotating damping force becomes an excitation force, adding energy to the system and causing the whirl amplitude to increase. If unrestrained, this can lead to extensive damage or destructive failures.

The power rotor system of a typical gas turbine engine which has been experiencing some nonsynchronous vibration was analyzed to determine which parameters have the greatest effect on the system stability. It will be shown both analytically and by testing that external damping at a sensitive bearing location is an effective method for controlling nonsynchronous vibrations, and the squeeze film damper is a practical answer for achieving the required damping. The squeeze film damper's design philosophy, a description of its operation, and the avoidance of instability associated with the damper itself will be presented. It will also be shown that an alternative method for removing this instability is the complete elimination of spline friction by replacing the splined joints with flexible couplings.

ANALYSIS

The phenomenon of nonsynchronous vibration has been discussed extensively in the literature, beginning with A. L. Kimball, Jr. in 1923 (1). Crandall (2) published a physical explanation of the destabilizing mechanism using a planar model of a rotor with internal and external viscous damping. The internal damping is visualized as a drag force on the orbit. When the rotation is faster than the whirl, this drag force acts to excite the rotor. He shows that the stability of the system is dependent upon a balance between the power input into the system and the energy dissipated. If the power input is greater than the power dissipated, the energy of the orbit increases and the system becomes unstable.

Gunter (3) has conducted extensive mathematical analyses for a single mass rotor on an elastic foundation to determine what factors influence the rotor speed at which nonsynchronous vibration manifests itself. He calls this the stability threshold. Among his conclusions are that stability can be improved by reducing the internal friction and by introducing external damping. He also concludes that asymmetry of bearing supports, even without the benefit of external damping, can dramatically improve the system stability.

Figure 1 shows a model of the power rotor system whose vibration signature contains a nonsynchronous component at speeds higher than the first rigid body critical speed. The mechanism for the nonsynchronous excitation in this case is the friction force developed in the two splines. In order to analytically determine the factors that influence the stability of this rotor system, it was necessary to develop a "spline element" which accurately accounts for the destabilizing effects of rotating internal friction and incorporate this into a finite element rotor analysis program. Once this was accomplished, the stability of the system was studied by calculating the system complex eigenvalues. The imaginary part of the eigenvalue determines the frequency of oscillation and the real part determines stability. Negative (positive) values of the real part indicate that the system will be stable (unstable) for that mode of vibration.

Although the friction in the spline acts as coulomb friction, it can be adequately represented using an equivalent viscous damping coefficient (4). The equations relating force to displacement and velocity for a two degree of freedom spline element with rotating viscous damping have been derived. For simplicity, only the translational degrees of freedom have been considered. The equations for the rotational degrees of freedom follow in a similar manner. The governing equations for the translations become:

$$\begin{Bmatrix} F_X \\ F_y \end{Bmatrix} = \begin{bmatrix} b & 0 \\ 0 & b \end{bmatrix} \begin{Bmatrix} \dot{X} \\ \dot{Y} \end{Bmatrix} + \begin{bmatrix} k & 0 \\ 0 & k \end{bmatrix} \begin{Bmatrix} X \\ Y \end{Bmatrix} + \begin{bmatrix} 0 & b\omega \\ -b\omega & 0 \end{bmatrix} \begin{Bmatrix} X \\ Y \end{Bmatrix}$$

$$[B] \qquad [K] \qquad [K_r]$$

Where:

F_X, F_y	forces in the two mutually perpendicular directions, x and y respectively
X, Y	displacements of the two coupling parts relative to each other in the x and y directions
$\dot{X}, \dot{Y}$	relative velocities in these two directions
b	spline equivalent viscous damping coefficient
k	spline stiffness
ω	system rotational speed
B	spline damping matrix
K	spline stiffness matrix
K_r	spline rotating friction matrix

The skew - symmetric terms in the $[K_r]$ matrix are those which may cause the system to become unstable, depending on their magnitude. Thus, the system will tend to instability for high values of the damping coefficient and high rotor speeds, providing there is some relative motion in the spline.

The major difficulty in accurately modeling the system is that the spline stiffness and friction force vary with the transmitted torque. Because these values are difficult to predict, the analysis takes the form of a parametric study to determine the relative contribution of the variables to the system stability. This provides information as to the design changes which may be beneficial and the direction in which further testing should proceed. The variables to be investigated are spline friction, bearing damping, and support asymmetry.

The nominal values of the parameters are shown in Figure 1. Figure 2 shows the mode shape corresponding to the only critical speed in the rotor's running range of 0 - 22,000 rpm. The mode shape depicts the shafts moving as rigid bodies, essentially hinged at the two splines. Most of the strain energy is in the No. 2 bearing but there is substantial relative motion at the first spline and some relative motion at the second spline. The friction forces due to these motions will overcome the minimal damping at the bearing locations and induce a nonsynchronous vibration when the rotor speed is greater than the first critical speed for forward precession. The frequency of this vibration as a function of rotor speed is plotted in Figure 3. The speed dependence of the natural frequency is due to gyroscopic effects and the circled points denote the critical speeds for forward and reverse precession. In

this analysis, the mode for reverse precession was found to be stable for all cases. The result is in agreement with previous analytical work which has determined that internal damping will act to stabilize this mode (2, 5).

A stability map of the system (Figure 4) can be obtained by solving for the damped natural frequencies at various rotor speeds (ω) and plotting ω vs. the system logarithmic decrement. The logarithmic decrement is defined as δ = ln (X1/X2) where X1 and X2 are two successive peak amplitudes of deflection. It is a measure of the rate at which the vibration amplitude is decaying or growing with time and can be given by δ = -2 Re(λ)/Im(λ), where Re(λ) is the real part of the eigenvalue and Im(λ) is the imaginary part. The system is unstable for negative values of the logarithmic decrement. As is evident from Figure 4, the rotor system with minimal external damping becomes unstable at its critical speed for forward precession. (ω s= ω cr=9750 rpm). The rotor will continue to whirl at a frequency approximately equal to ω cr even though the rotor speed increases.

The behavior of the system at various rotor speeds is further explained by looking at the whirl orbits obtained from a transient analysis (Figure 5). The forcing function was taken as a small imbalance with a frequency equal to the rotor speed. For speeds below the critical speed, the imbalance causes the orbit to spiral out initially, but it recovers into a stable, synchronous motion. At the stability threshold, the motion is synchronous but unstable. For speeds above the critical speed, a component of nonsynchronous precession appears due to the friction in the splines. As time progresses the nonsynchronous component overpowers the synchronous motion and the orbit diverges.

It has been suggested in the literature that a reduction in spline friction can delay the onset of nonsynchronous vibration. This was analyzed by setting the friction in the second spline to zero and varying the friction in the first spline. Figure 6 plots the system logarithmic decrement against the spline angular damping coefficient for various rotor speeds. It is observed that reducing spline friction will improve the system stability but, in the absence of external damping, the friction must be all but eliminated to ensure stability throughout the operating range.

Anisotropic supports may also help stabilize a system. The stiffnesses of the No. 1 and No. 2 bearings were altered in one plane and left unchanged in the other orthogonal plane to determine the effect of support asymmetry on the stability of this system. Figure 7 shows the dependence of the stability threshold on the support flexibility ratio. Increasing the support stiffness in one direction will give a significant improvement in the stability threshold but will also introduce a system resonance in the range of steady operation. This is unacceptable and the only option is to reduce the support stiffness. The stability improvement for this condition is not dramatic, requiring supports which are very asymmetric to guarantee stability throughout the running range. This can cause large excursions due to imbalance.

A very effective way to increase the system stability threshold is to add external damping to the system. The easiest way to achieve this is to introduce damping at the bearing locations. For the mode shape of interest (Fig. 2) most of the motion is in the No. 2 bearing. This is a prime location to introduce damping, as the motion allows for greater energy dissipation. Figure 8 shows the improvement in the stability threshold due to external damping at this bearing.

CONCLUSIONS BASED ON ANALYSIS

The conclusions of the parametric analysis of spline - induced nonsynchronous vibration for this rotor system are as follows:

1. Asymmetric supports will help stabilize the system, but the asymmetry must be great to completely eliminate nonsynchronous precession. Therefore, the degree of asymmetry required to stabilize this system is impractical.

2. Reduction of spline friction will improve the stability, but without external damping, the spline friction must be all eliminated to ensure stability at all rotor speeds.

3. Introduction of external damping in the proper bearing location will dramatically improve the system stability characteristics and provide relief from nonsynchronous vibration.

TEST HISTORY

Instability Verification

A nonsynchronous excitation of the first whirl mode has frequently occurred during engine operation. The response, as measured by transducers on the engine casing, sometimes would be above the established acceptable limits. A Campbell diagram constructed from the response of a typical transduer from one of these engines is shown in Figure 9. The plot shows that the synchronous excitation of the whirl at the running speed of 9000 rpm was negligible, indicative of good balance. As the running speed increased the vibration remained low until approximately 11,000 rpm where a nonsynchronous excitation of the whirl was initiated. Once initiated the instability remained throughout the rest of the operating range up to 22,000 rpm. The precise frequency of this whirl varied from engine to engine between 150 hz and 195 hz. This difference may have been due to variation in geometry and load sharing of the number 1 and 2 bearings. The speed at which the instability was initiated also varied from engine to engine.

Instability Attenuation

During the initial development of this system the two splines were unlubricated. The introduction of lubrication into the splines substantially improved the system stability but, as indicated in the analysis, it did not eliminate thr problem for all engines. The mechanism of spline friction exciting this whirl was understood, however it was unclear why some engines were strongly excited while others ran smoothly. Balance and dimensional checks of the rotating hardware components did not reveal any consistent explanation for the variation in response.

A rig which closely simulates this system was used for some controlled studies. The rig allowed a parallel offset of the numbers 3 and 4 bearings with respect to numbers 1 and 2 bearings to be controlled, creating a misalignment angle in the two splines. A displacement probe transducer was used to measure the deflection of the center of the power shaft. The rig was run with different misalignment settings

from 0 degrees to 1 degree to determine the effect on the instability. Figure 10 shows Campbell diagrams generated by the response of this rig under three of the different misalignment conditions. The results indicated that the instability was effectively attenuated with misalignment angles greater than an eighth of a degree.

In the engine, the direct measurement of misalignment of the rotor system was not practical. In order to obtain some idea of the alignment condition of the rotor system in engines, a special tool was devised which quickly measured the radial and angular offsets due to the principal stackup items between the number 1 and 2 bearings and the number 3 bearing. These measurements were then used to calculate both the magnitude and orientation of misalignment angle in the two splines. This alignment check was conducted during the assembly of approximately sixty engines. Figure 11 shows polar charts of these results. The magnitude of the misalignment is represented radially outward while the orientation angle is represented circumferentially. The engines which produced a high nonsynchronous vibration are distinguished on the plot from the engines which ran smoothly.

The initial observation from these results was that there was no correlation between the magnitude of misalignment based on these measurements and the level of nonsynchronous vibration. However scrutiny of the discrepant engines' alignment data revealed them to be clustered between -30 degrees and +30 degrees orientation angle and a magnitude greater than 0.09 degrees misalignment angle.

This clustering of points is believed to be indicative of a shift in the alignment of this system between the measured state, before final assembly, and the assembled running state. This shift brings the points clustered in the critical zone down to near the perfect alignment area. While the bearing supports are essentially axi-symmetric, both the temperature distribution and the engine casing stiffness in this area are not uniform in the vertical plane. This may account for a static shift in the alignment condition of the splines.

The use of these measurements and the previously defined critical zone as a screening procedure for engines being assembled virtually eliminated the number of engines experiencing excessive nonsynchronous vibration levels at test. The residual misalignment left in the splines was always held to within one half degree to prevent spline wear or the introduction of high misalignment forces into the system.

The conclusion drawn from these results was that a small misalignment of a splined system significantly improved its stability. One explanation for this behavior is that the misalignment imposes a limit on the whirl orbit by creating an effective spline stiffness asymmetry.

The use of this controlled alignment procedure consistently reduced the amplitude of the instability to within acceptable limits however it did not eliminate it.

INSTABILITY ELIMINATION (FLEXIBLE COUPLINGS/SQUEEZE FILM DAMPERS)

Two possible approaches aimed at the complete elimination of the instability were indicated by the analysis. One is to replace the two splines with dry flexible couplings having no sliding friction surfaces to excite the instability. The second is to add external damping at the appropriate bearings in order to counteract the internal damping generated by the splines.

The first approach using a flexible coupling has been tested in the rig described earlier. The whirl mode of the system with the flexible couplings is essentially unchanged from the splined system. Figure 12 shows a Campbell diagram generated by the response from a displacement probe sensing the deflection of the shaft between the couplings. The synchronous response of the whirl mode is clearly seen to be excited but no nonsynchronous excitation is apparent. This result was repeatable for all misalignment settings. An additional benefit of this type of coupling is that no lubrication is required, since there is no sliding involved in the flexing joints. Due to other considerations some operating conditions may be too severe for this type of couplings use.

In order to address the second approach squeeze film dampers have been designed for the number 1 and 2 bearing locations. The analysis indicated that a damper located at only the number 2 bearing is sufficient. Dampers at both locations are being employed for nondynamic design considerations. A discussion of the design of squeeze film dampers follows.

SQUEEZE FILM DAMPER (ANALYSIS AND OPERATION)

The squeeze film damper is a practical answer to the external damping required by analysis. Its purpose is to reduce to acceptable limits the lateral amplitudes of shaft - rotor systems operating at or above a critical speed and/or to cushion the loads on rolling contact bearings when such loads are excessive. For rigid body whirl modes, with large excursions at one or more bearing locations, squeeze film dampers are placed at these bearings for effective vibration attenuation. The shaft's precessional motion associated with these whirl modes may be either synchronous or nonsynchronous. For shaft bending modes that possess little motion at a bearing location, a damper at that location is ineffective; therefore, a more strategic location must be determined or a rotor redesign considered.

A squeeze film damper consists of a cylindrical inner member and a hollowed outer member separated by a thin fluid film, usually oil. Figure 13 shows a typical squeeze film damper. During lateral motion of the inner member, which is the outer race of the bearing, oil is squeezed out from the cavity between the two members. This squeezing action produce fluid forces, which for a properly designed damper will dissipate energy and aid in the reduction of excessive amplitudes and/or bearing forces.

The squeeze film damper considered in this report is one whose inner member is prevented from rotating by an antirotation device and whose axial length, L, (or series of axial lengths) is sufficiently short, making the effect of circumferential flow negligible. The pressure generated by the squeezing action is assumed to be sufficiently high, allowing for the consideration of only the positive portion of the pressure wave, which is conservative for low values of the eccentricity, ϵ .

Reynold's equation for short damper analysis was simplified by assuming the following: the radial clearance, C, and displacements are small compared to the radius, R, of the damper; the viscosity, μ, is constant in the axial and circumferential directions; the film thickness is constant in the axial direction; and the pressure profile is parabolic in the axial direction. Integration of the simplified Reynold's equation was accomplished in closed form, yielding the pressure profile in the circumferential direction. Integration of the positive portion of the pressure

profile gave the load carrying capacity in the component directions, radial and tangential. The radial and tangential fluid forces on the inner member are given by:

$$\begin{bmatrix} W_R \\ W_T \end{bmatrix} = \mu R \left(\frac{L}{C}\right)^3 C \begin{bmatrix} J_{11} & J_{12} \\ J_{12} & J_{22} \end{bmatrix} \begin{Bmatrix} \dot{\varepsilon} \\ \varepsilon\dot{\phi} \end{Bmatrix}$$

WHERE $$J_{11} = \int_{\theta_1}^{\theta_2} \frac{\cos^2\theta \, d\theta}{(1+\varepsilon\cos\theta)^3}$$

$$J_{12} = \int_{\theta_1}^{\theta_2} \frac{\sin\theta\cos\theta \, d\theta}{(1+\varepsilon\cos\theta)^3}$$

$$J_{22} = \int_{\theta_1}^{\theta_2} \frac{\sin^2\theta \, d\theta}{(1+\varepsilon\cos\theta)^3}$$

AND $$\theta_1 = \tan^{-1}\left\{\frac{\dot{\varepsilon}}{\varepsilon\dot{\phi}}\right\}$$

$$\theta_2 = \theta_1 + \pi$$

The expressions $\dot{\varepsilon}$ and $\varepsilon\dot{\phi}$ are the dimensionless instantaneous velocities of the inner member's center in the radial and tangential directions, respectively.

If $\dot{\varepsilon}$ is set equal to zero, ε constant, and the precessional speed, $\dot{\phi}$, is set equal to the rotative speed ω, the special case of steady synchronous motion, commonly found in actual operation, is the result. The J factors are no longer time dependent, but reduce to simple, yet highly nonlinear algebraic expressions. The equation governing the dimensionless response for rigid body whirl for a rotor of effective mass, m, and unbalance distance, δ, is determined by vectorally equating the fluid forces to the rotor's inertia force. Figure 14 graphically depicts the response, ε, versus the dimensionless speed

$$\frac{m\omega}{\mu R}\left(\frac{C}{L}\right)^3 = \frac{\omega}{Q}$$

for various values of the dimensionless unbalance δ/C.

Squeeze film damper properties described above are also applicable to flexible rotor systems. Forced response computer programs based on both the transfer matrix approach and finite element approach have been developed for multidampers and multilevels. Before proceeding with specific applications, consider the general motion case.

For the general rigid body motion case, no assumptions concerning kinematics were made; rather, the radial and tangential components of the $m\bar{a}$ force in its full form were equated to the fluid forces, resulting in two time dependent equations, which were programmed with appropriate initial conditions and then solved. Polar

plots of ε versus the precessional angle were generated, representing the dimensionless motion of the center of the inner member during both steady-state and transient response. Plots were made for rotative speeds, ω, of 160, 400, 800, 1600 and 4000, while Q values of .4, 4, 40 and 400 were used. For each combination of ω and Q various values of the dimensionless unbalance δ/C were tried, which, during solutions were instantaneously increased to new values, yielding the ensuing transient response. Only a select few of these plots are shown in Figure 15, which is summarized as follows:

FIGURE	ω rad/sec	Q rad/sec	ω/Q	δ/C	COMMENT
15a	1600	400	4	.5 - 1.5	STABLE
15b	1600	40	40	.5 - .6	SOMEWHAT UNSTABLE
15c	1600	4	400	.5 - .55	UNSTABLE
15d	4000	.4	1000	.1 - .15	UNSTABLE

The ratio ω/Q is the main ingredient for determining damper stability. Low values of this ratio yielded stable and "safe" operation ($\varepsilon < .9$) for wide ranges of unbalance; high values of ω/Q produced unstable and often "critical" operation ($\varepsilon > .9$), even for small changes in unbalance; and intermediate values gave both stable and unstable results in the safe and critical ranges, depending on the magnitudes of the unbalances used and their increments.

Consideration of these computer solutions together with the plot, Figure 14, clarified the operational limits of the squeeze film damper described. These limits are summarized in Figure 16, which is a plot of dimensionless unbalance vs. dimensionless speed ω/Q. It defines those combinations of design parameters under which damper instability and/or critical operation is predicted.

Figure 17 shows a comparison of the predicted steady state synchronous response of the system with standard bearings versus squeeze film bearings at the numbers 1 and 2 locations. Based on the stability analysis described earlier the damping obtained from these squeeze films is well above the level found to be needed to suppress the nonsynchronous whirl. In order to prevent damper instability, the above damper analysis was used along with the steady state response analysis to size the damper dimensions. Testing of this rotor system with squeeze film dampers is pending. This analytical process has been used to design squeeze film dampers for another splined rotor system which experienced a similar subsynchronous excitation of a whirl mode. Subsequent testing of this rotor system confirmed the analytical results.

SQUEEZE FILM DAMPER DESIGN PHILOSOPHY

The design philosophy used at Lycoming for squeeze film dampers depends upon whether or not the bearing being damped carries a unidirectional thrust load. Figure 13 depicts a ball bearing/squeeze film damper configuration which carries a thrust directed to the left for all shaft speeds. For this condition the reaction takes place at the hard faced surface, which also acts as a seal against oil loss. Oil is introduced at the outer diameter of the bearing and flows through the annular

clearance provided between the bearing outer race and the liner inner diameter. An upstream orifice is sized to prevent pressurization of the damper while maintaining a copious supply of oil to replace that which is lost. The circumferential groove acts as an oil reservoir during the squeezing action; i.e., the rotating positive pressure profile generates flow into the reservoir while the virtual negative pressure profile, 180° away, causes the flow from the reservoir back into the annular clearance. Of course, there is still a net flow of oil out, as shown. For maximum load carrying capacity and minimum oil loss, the volume of the reservoir need not be greater than the flow into it, and it should be placed as close to the bearing's extremity as is practical.

If a squeeze film damper is required at a bearing that carries a bidirectional thrust load or none at all, sealing does not take place, rather oil flows out both ends of the damper (Figure 18). In this configuration, oil is introduced at the center of the damper into a circumferential groove and flows along the annular clearance and into the reservoirs, which serve the same purpose as the single reservoir in the previous configuration. Other parameters remaining unchanged, the flow requirement is doubled, and since the load carrying capacity varies as the cube of the length, the capacity for both "halves" is one-fourth. In order for the split configuration to carry the same load as the unsplit one, the length of each half must be made to 80% of the uninterrupted length. For certain applications the total length requirement may not be achievable by using a bearing of usual proportions, and in these cases bearing manufacturers can supply longer outer races.

CONCLUSIONS

Analysis and testing of the power rotor system of a typical gas turbine engine has resulted in certain conclusions regarding spline induced subsynchronous vibrations.

1. Asymmetric supports tend to stabilize the system, but the degree of asymmetry required is impractical, and other vibratory problems may be created.

2. Reduction of spline friction by lubrication did not consistently control the instability, but the use of flexible couplings, which eliminates the internal friction, is a viable solution.

3. Small spline misalignment in this system significantly improved the stability.

4. Introduction of external damping by employing a properly designed squeeze film damper at a sensitive bearing location eliminates the instability.

5. The dimensionless speed number (ω/Q), which reflects the squeeze film damper's geometry as well as speed, should be selected to avoid the damper's threshold of instability.

REFERENCES

1. Kimball, A. L., Jr.: Internal Friction Theory of Shaft Whirling. Phys. Rev. (2) 21, 703 (1923).

2. Crandall, S. H.: Physical Explanations of The Destabilizing Effect of Damping in Rotating Parts. NASA CP2133, May 1980, pp. 369-382

3. Gunter, E. J., Jr.: Dynamic Stability of Rotor - Bearing Systems. NASA SP-113, Office of Technology Utilization, U. S. Gov. Printing Office, 1966.

4. Marmol, R. A.; Smalley, A. J.; and Tecza, J. A.: Spline Coupling Induced Nonsynchronous Rotor Vibrations. ASME Paper No. 79 - DET - 60.

5. Bucciarelli, L. L.: On the Instability of Rotating Shafts Due to Internal Damping. Journal of Applied Mechanics, Trans ASME, vol. 49,1982, p. 425.

6. Foote, W. R.; Poritsky, H.; and Slade, J. J., Jr.: Critical Speeds of a Rotor With Unequal Shaft Flexibilities, Mounted in Bearings of Unequal Flexibility. Journal of Applied Mechanics, Trans ASME, vol. 65,1943, p. A77.

7. Crandall, S. H. and Brosens, P. J.: On the Stability of Rotation of a Rotor with Rotationally Unsymmetric Inertia and Stiffness Properties. Journal of Applied Mechanics, Trans ASME, vol. 83,1961, p. 567.

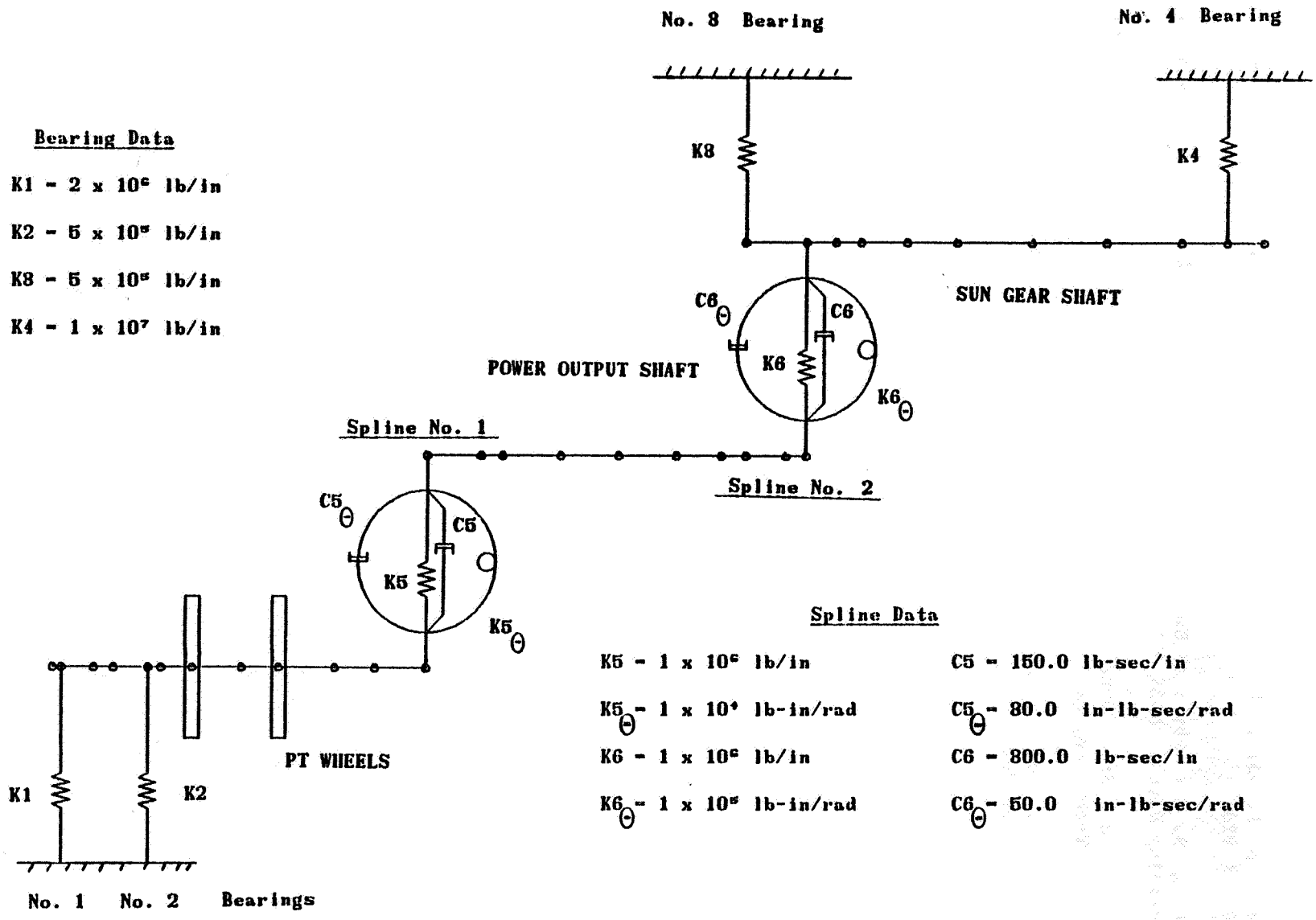

Figure 1. - Model of power turbine system with spline internal damping.

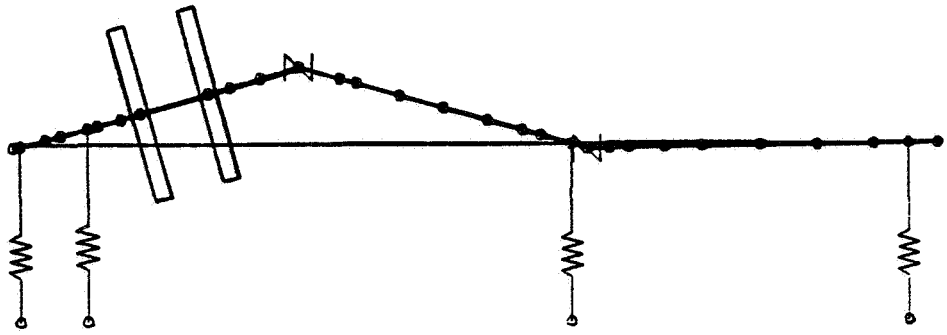

FREQUENCY - 162 Hz - 9750 CPM

Figure 2. - Power turbine whirl mode.

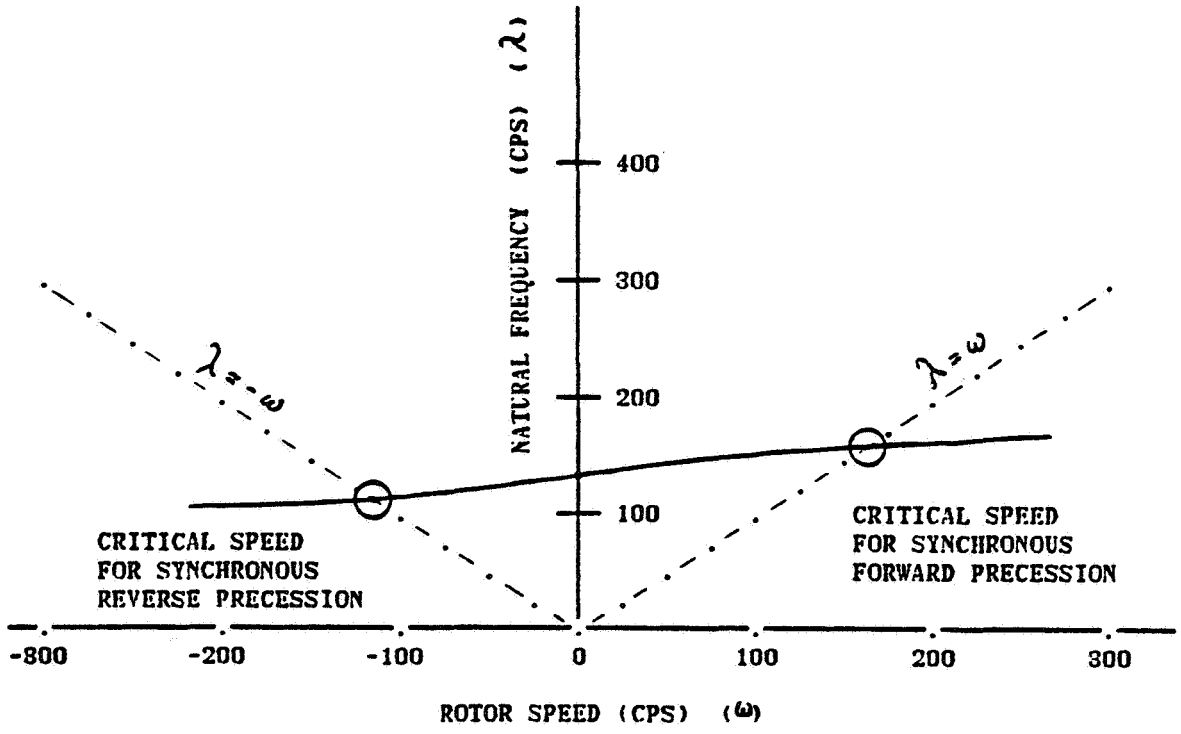

Figure 3. - Effect of rotor speed on natural frequency.

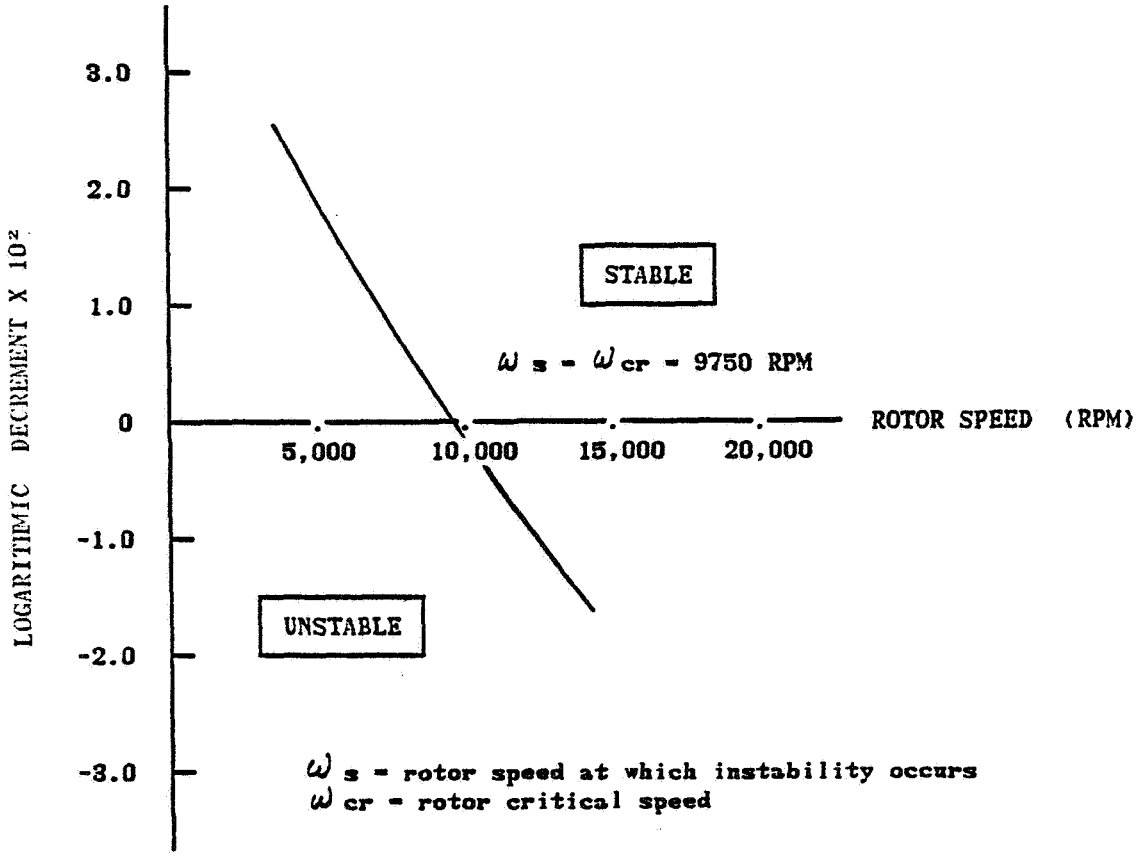

Figure 4. - Stability analysis for turbine system with no external damping (nominal case).

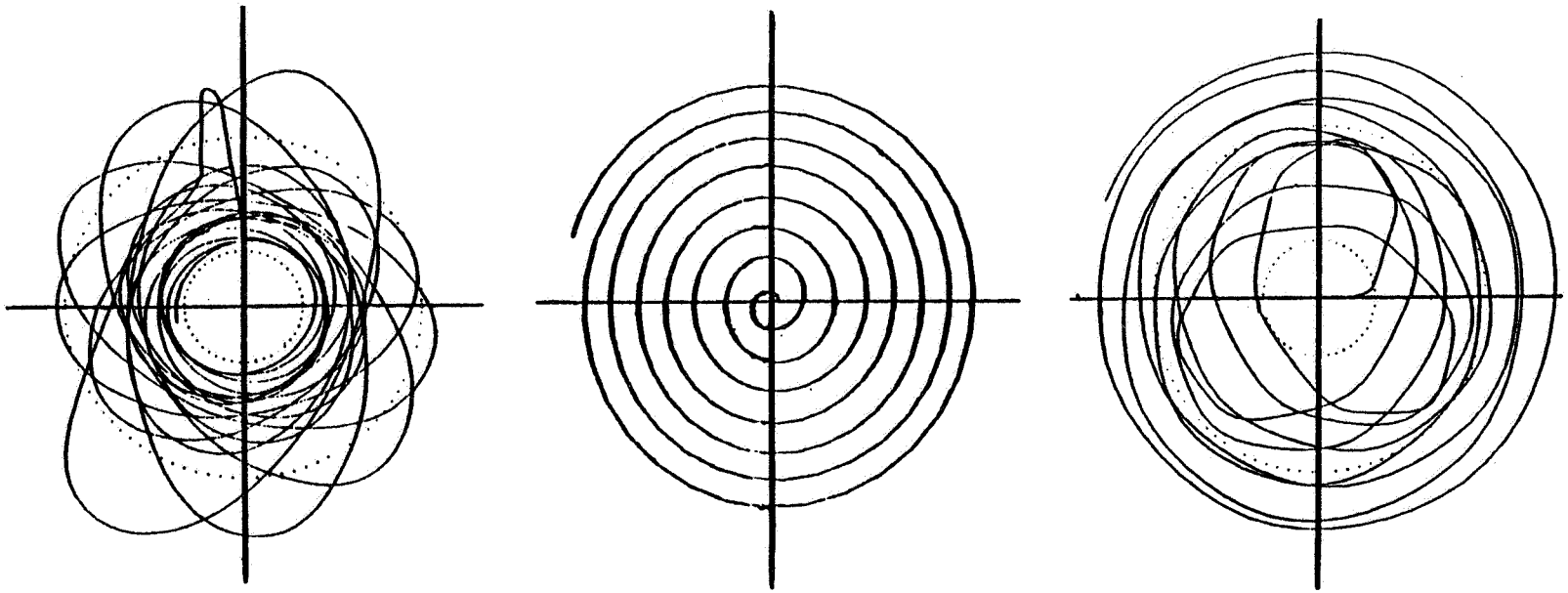

ROTOR SPEED - 5,000 RPM

$\omega < \omega_{cr}$

ROTOR SPEED - 9,750 RPM

$\omega = \omega_{cr}$

ROTOR SPEED - 20,000 RPM

$\omega > \omega_{cr}$

ω_{cr} - ROTOR FIRST CRITICAL SPEED - 9,750 RPM
ω - ROTOR SPEED (RPM)

Figure 5. - Whirl orbits for power turbine system at various rotor speeds (response to imbalance).

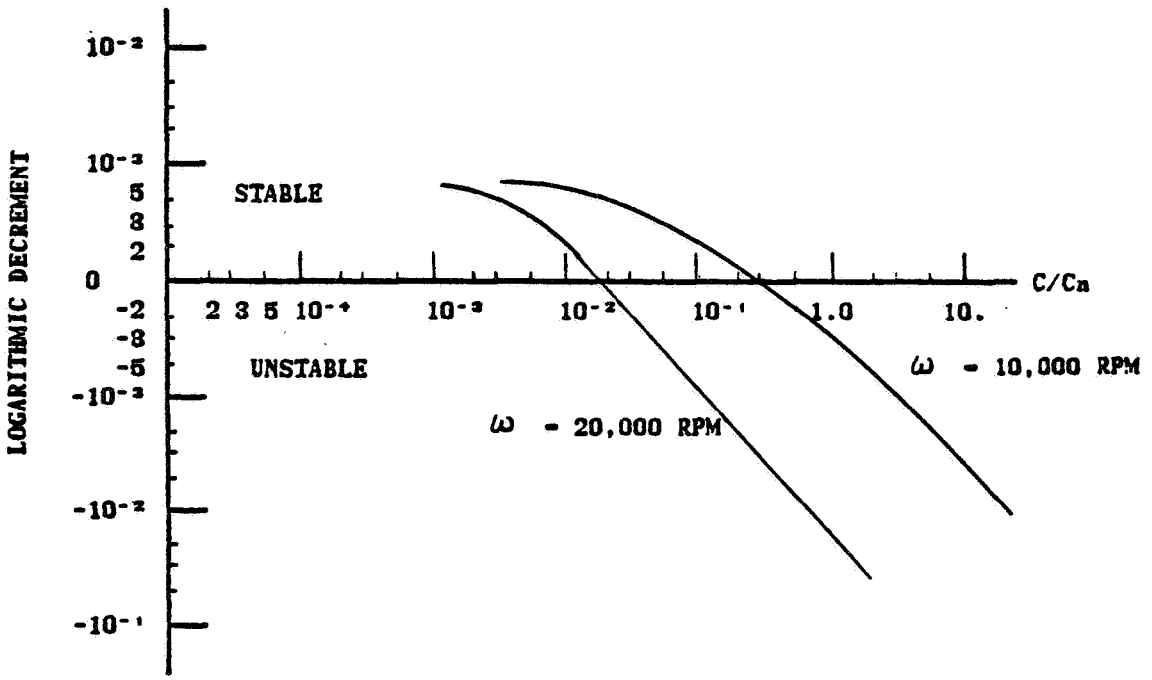

$$\frac{C}{Cn} = \frac{\text{Angular Damping Coefficient in Spline No. 1}}{\text{Nominal Value of Angular Damping Coefficient}}$$

ω - Rotor Speed

Lightly Damped Supports

Figure 6. - Effect of spline angular damping on system stability. Lightly damped supports.

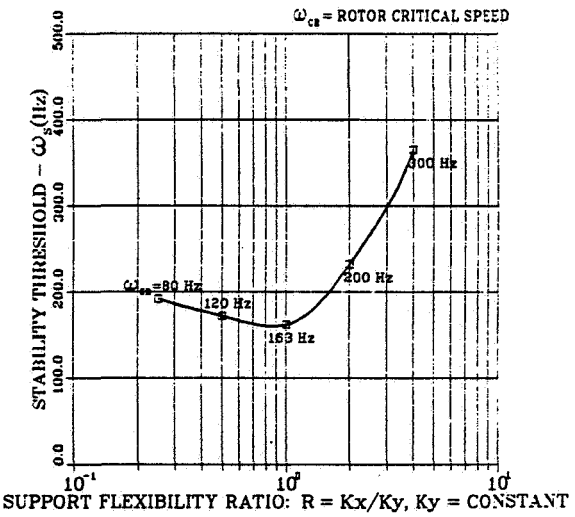

Figure 7. - Effect of foundation asymmetry on system stability threshold. Undamped supports.

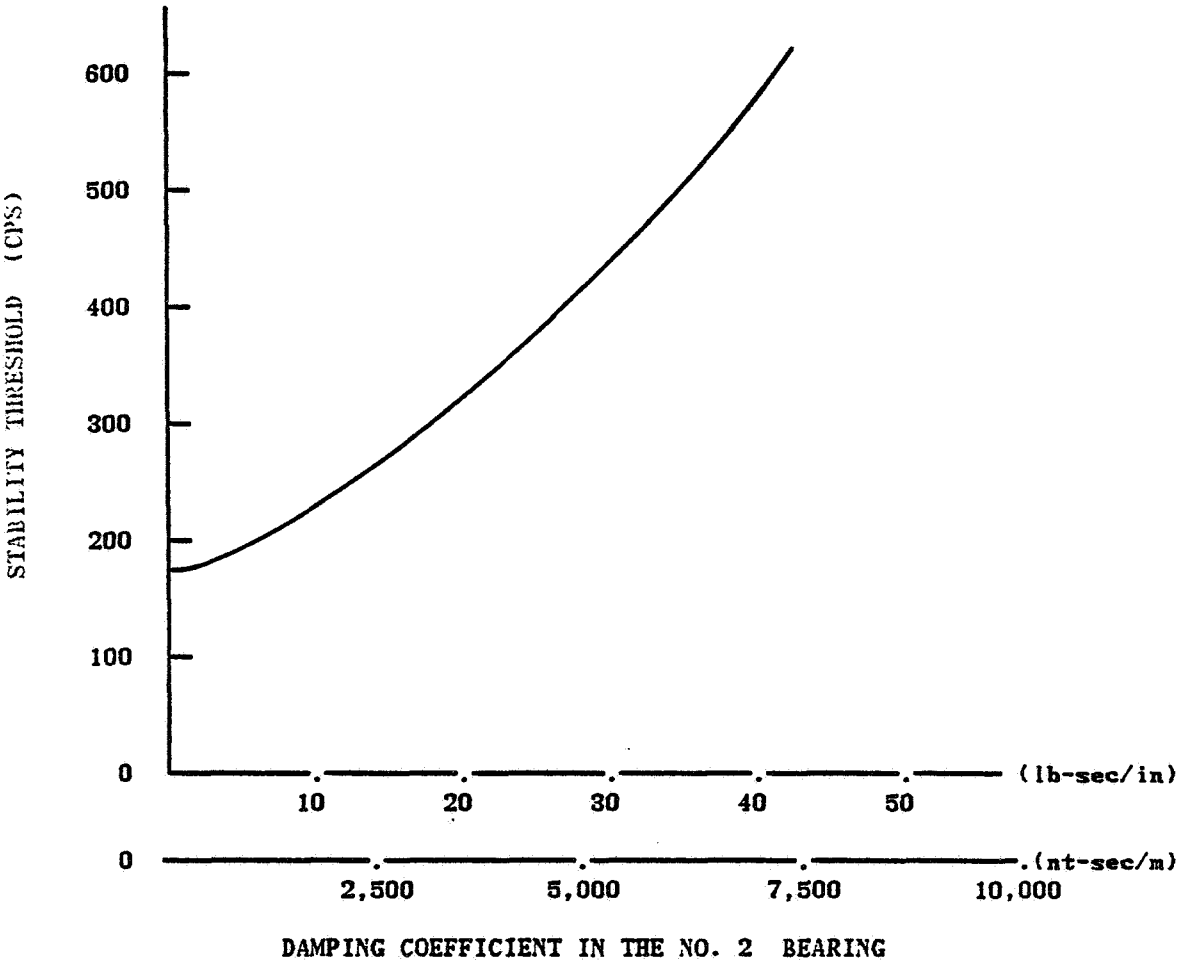

Figure 8. - Effect of damping in no. 2 bearing on system stability threshold.

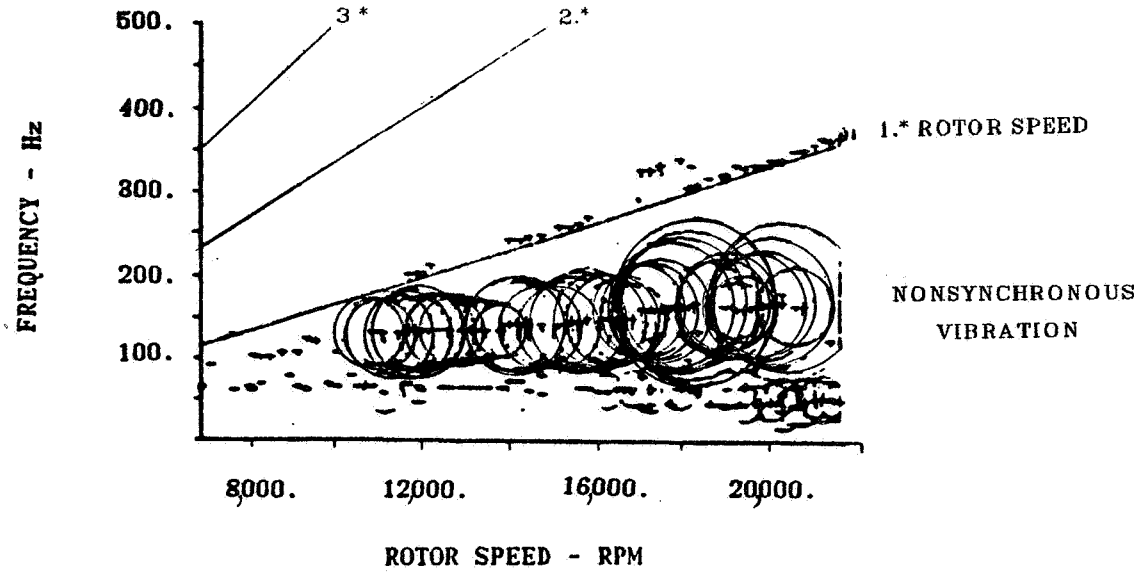

Figure 9. - Response from transducer mounted on engine casing.

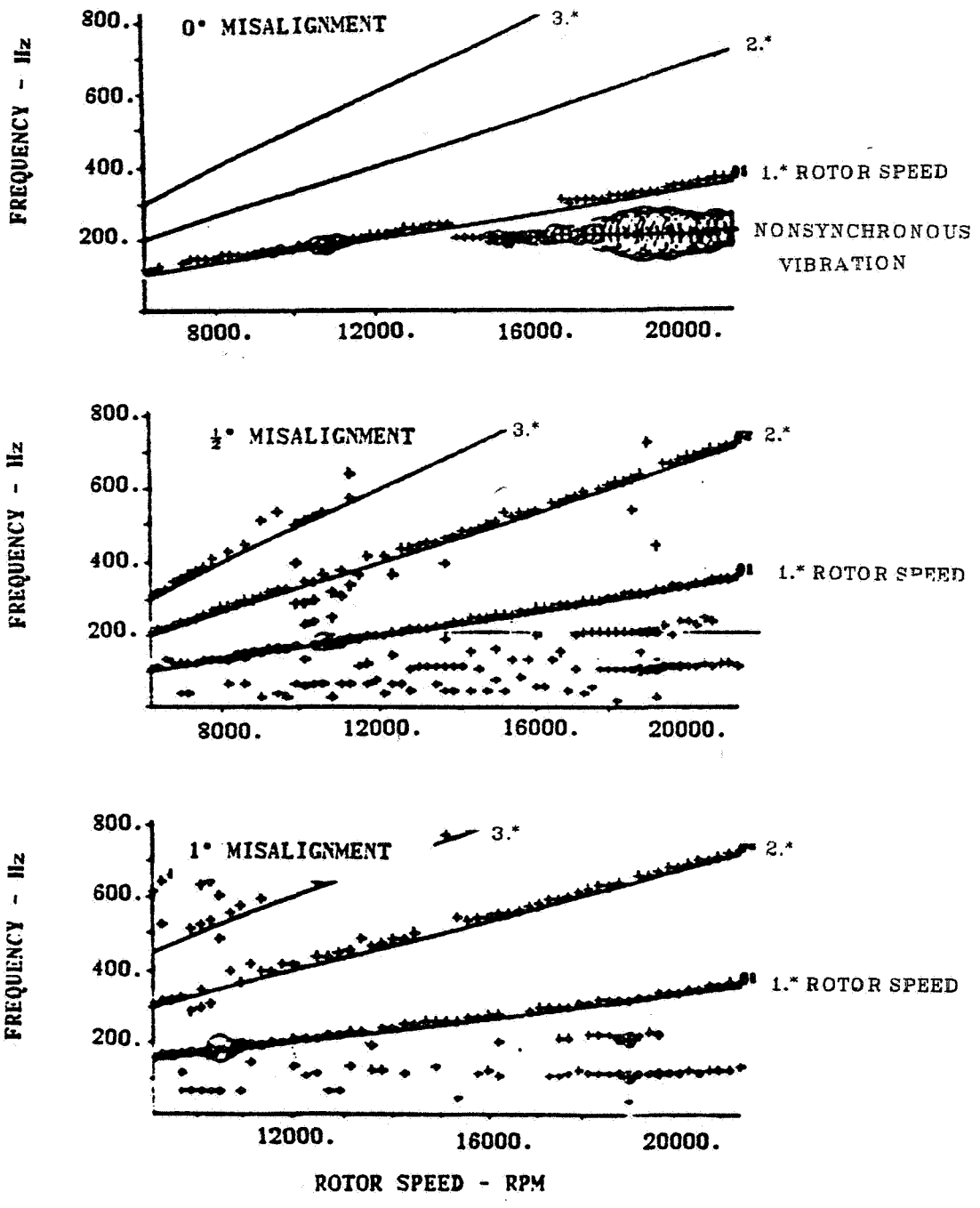

Figure 10. - Response of power shaft center from displacement probe rig with standard rotor system.

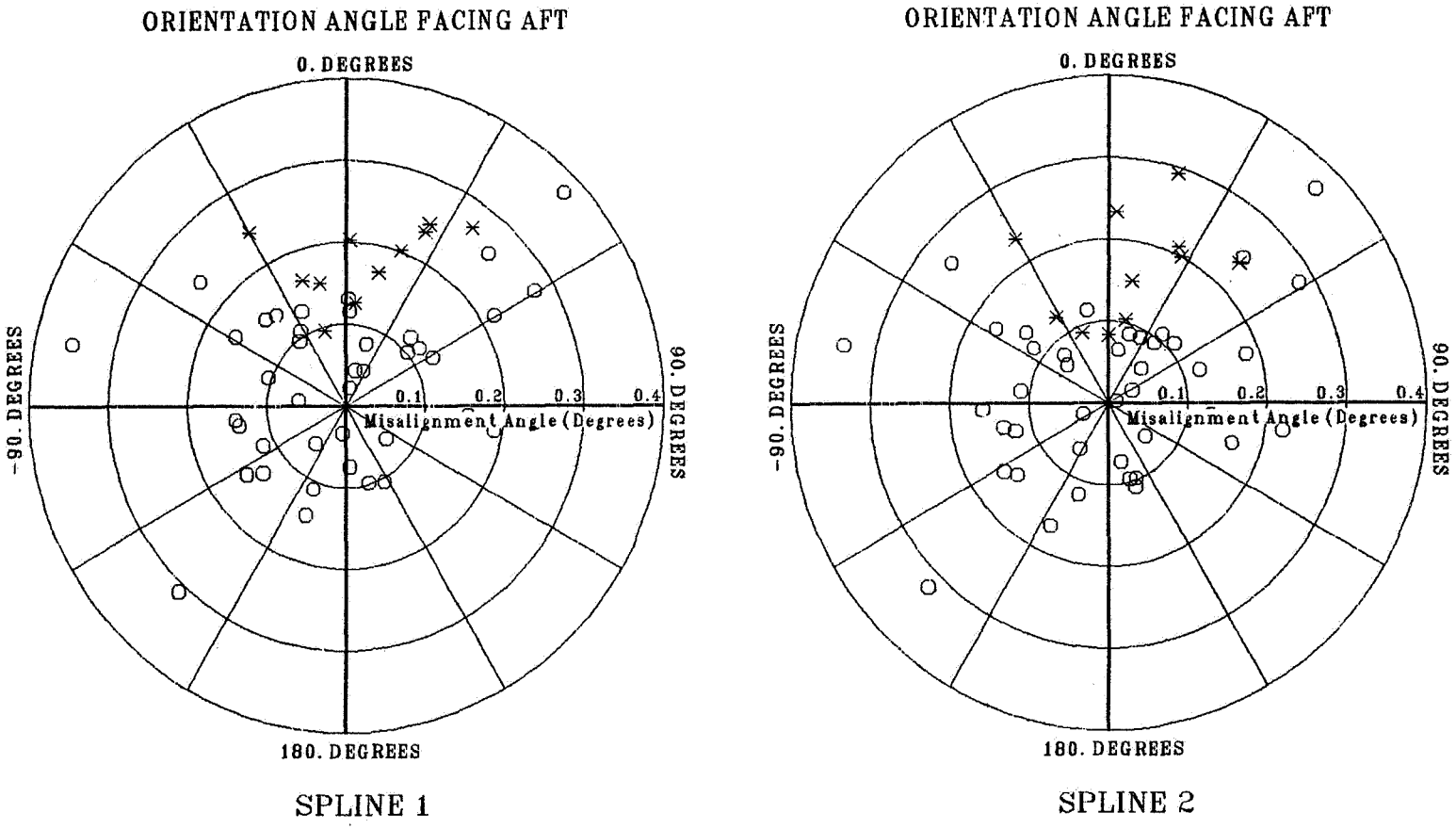

Figure 11. - Power rotor system spline alignment based on measurements of principal pilots.

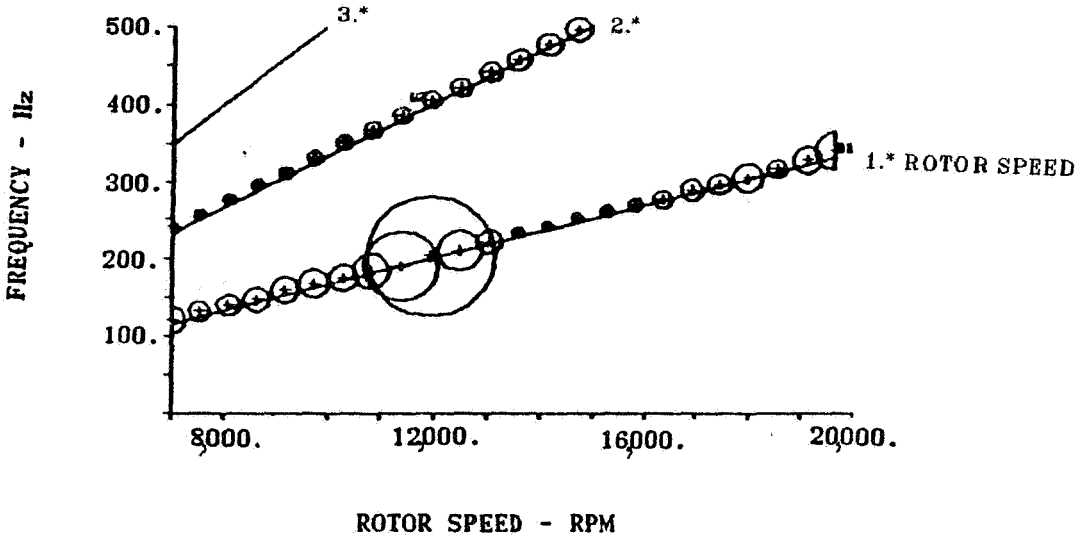

Figure 12. - Response of power shaft center from displacement probe. Rig with flexible coupling power shaft.

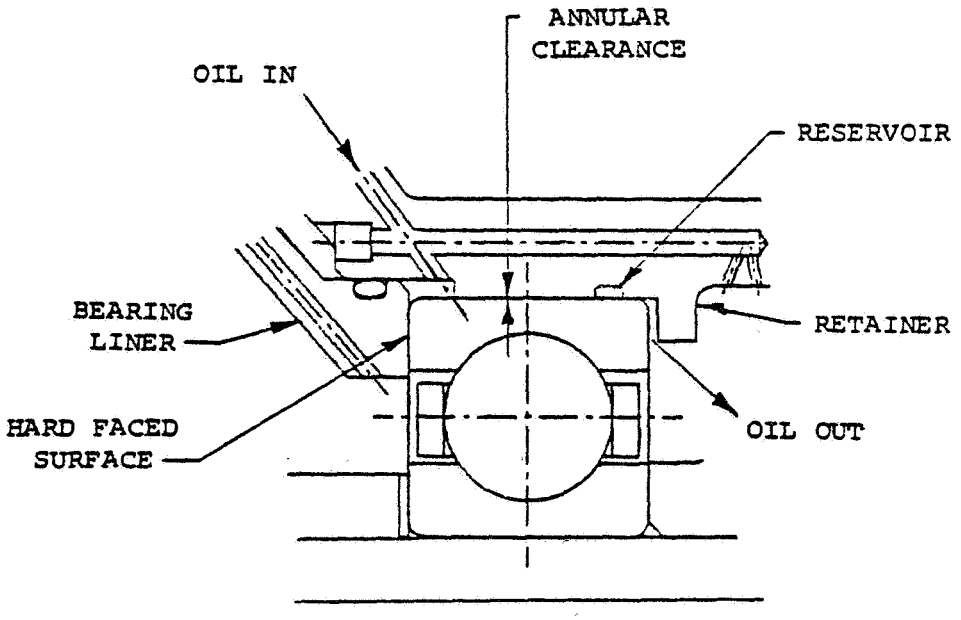

Figure 13. - Typical squeeze film damper.

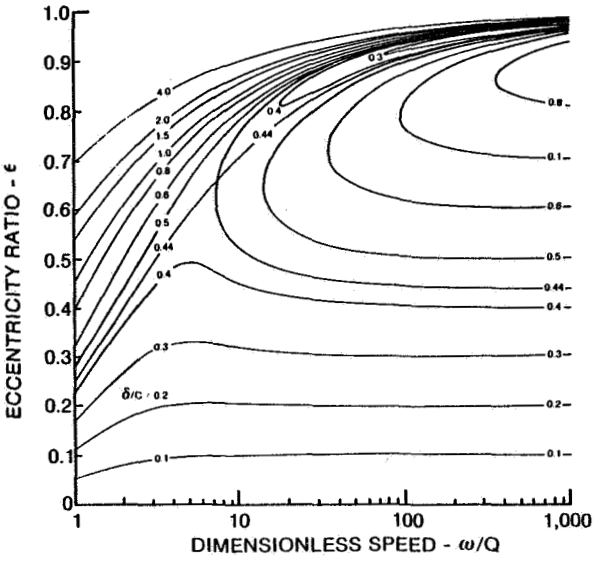

Figure 14. - Dimensionless steady state response of a squeeze film damper.

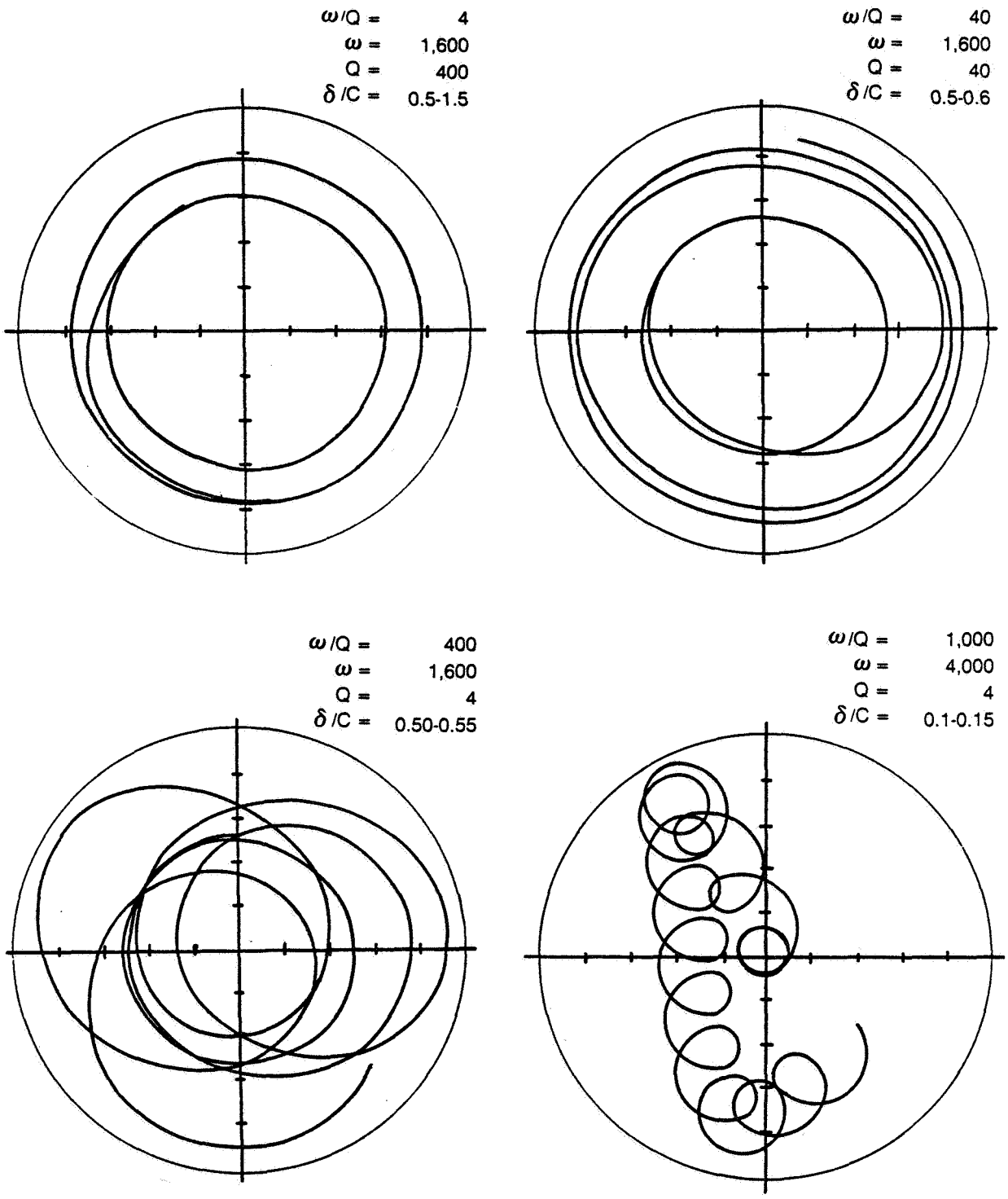

Figure 15. - Transient responses of a squeeze film damper.

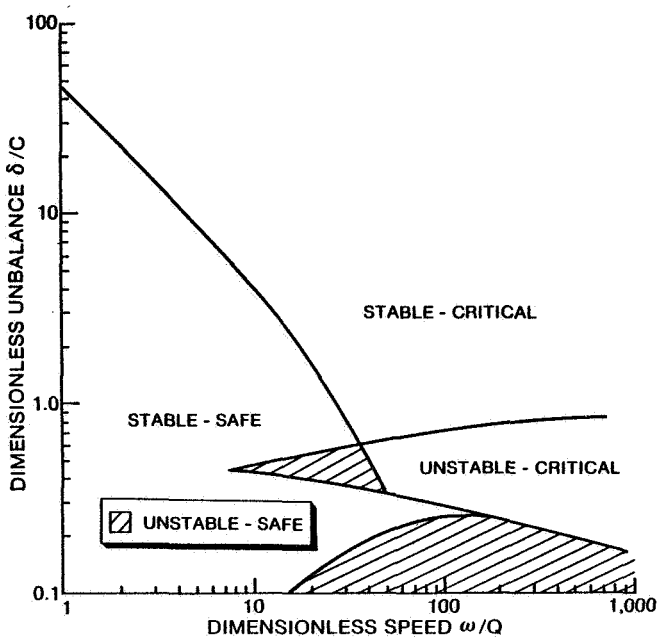

Figure 16. - Operational limits of a squeeze film damper.

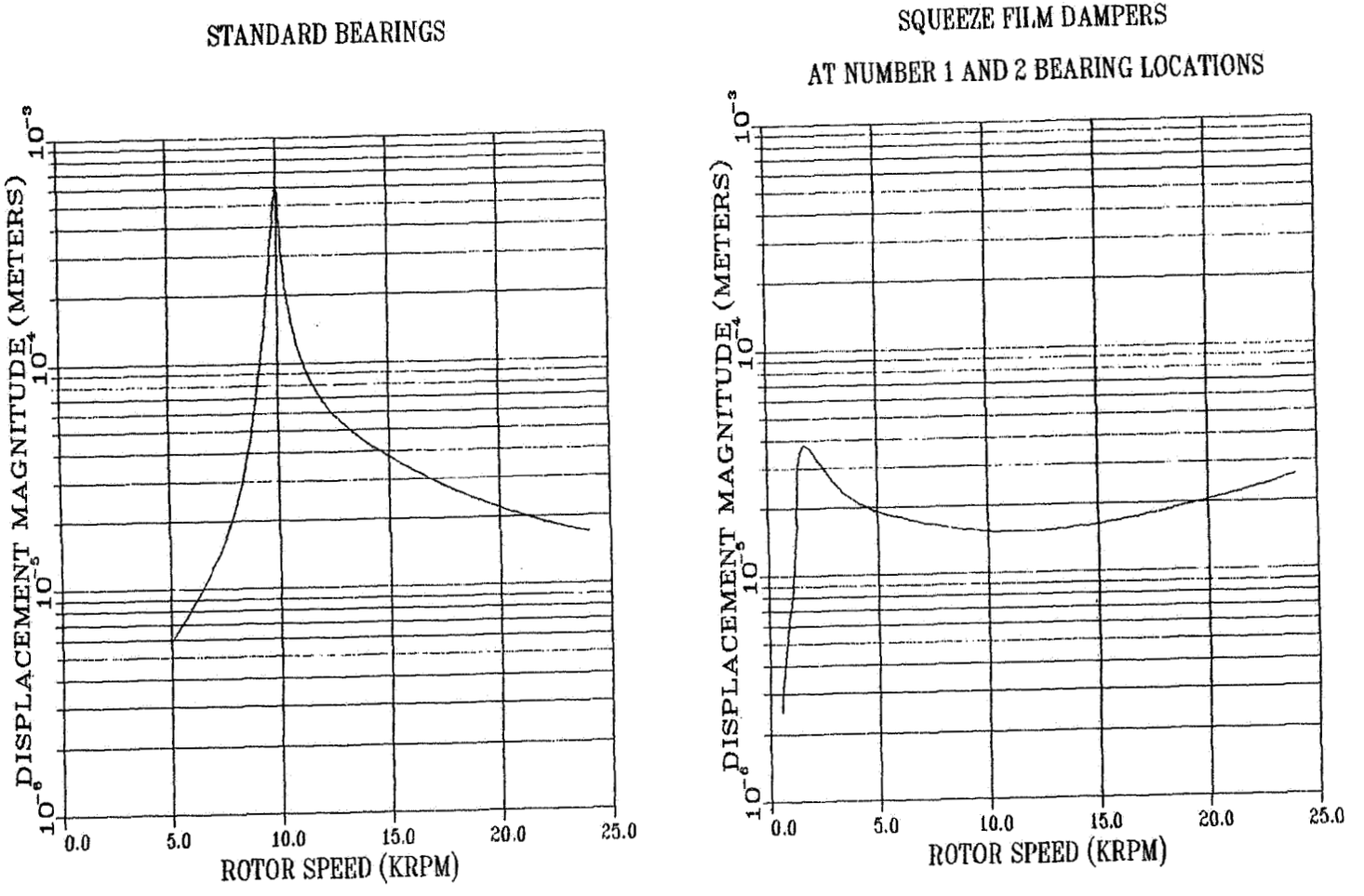

Figure 17. - Power rotor system response at spline 1 as predicted by steady state analysis.

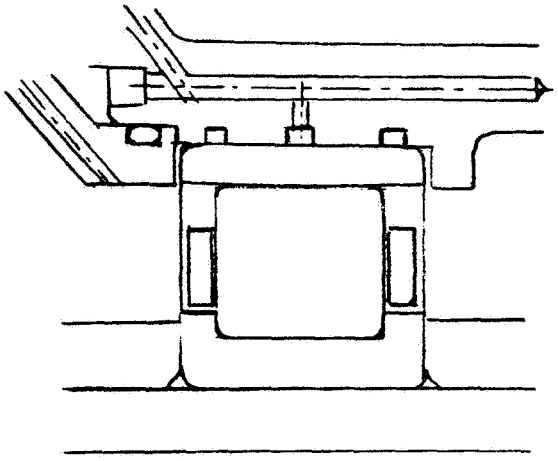

Figure 18. - Squeeze film damper applied to roller bearing.

EXPERIMENTAL ON-STREAM ELIMINATION OF RESONANT WHIRL IN A LARGE CENTRIFUGAL COMPRESSOR

G. I. Bhat and R. G. Eierman
Exxon Chemical Company
Baytown, Texas 77520

In October 1982, a severe resonant whirl condition was experienced when a multi-stage centrifugal compressor was first operated at higher than originally anticipated speeds and loads. Diagnosis of this condition was made easy by a large-scale computerized Machinery Condition Monitoring System ("MACMOS"). This computerized system was immediately able to verify that the predominant subsynchronous whirl frequency locked in on the first resonant frequency of the compressor rotor and did not vary with compressor speed.

Compressor stability calculations showed the rotor system had excessive bearing stiffness as well as inadequate effective damping. An optimum bearing design was developed to minimize the unbalance response and to maximize the stability threshold.

The above experience is not unusual and parallels that of many process plants using large centrifugal gas compression machinery. Of interest, however, is the approach taken by the plant to find a temporary remedy. The effective compressor bearing loading and effective clearance characteristics were modified with the machine continuing its process operation at normal load and speed. This approach involved the controlled application of heat to the compressor support legs while closely monitoring machine behavior. The experiment established the feasibility of extending the onset of rotor instability in the event that plant operations would call for higher speeds before the optimized bearings became available.

DISCUSSION OF PROBLEM UNIT

Description of Unit

The compressor is a two stage eight impeller horizontally split machine driven by a steam turbine. Oil seals are used at both ends and labyrinth seals are used at the center. The compresser runs at 175 psig inlet and 575 psig discharge. The rotor is supported by five shoe tilting pad load between pad bearings with 0.5 preload. The rotor has an unusually large ratio of bearing span to shaft diameter (99 in/5 in). The compressor train is safeguarded against high vibration with dual voting logic vibration trip circuits which shut the compressor down if vibration amplitude exceeds 4.5 mls at any time (Figure 1).

A Kingsbury thrust bearing is used to absorb the thrust. The compressor is driven through a Bendix type diaphragm coupling incorporating a torque meter and

hot alignment tubes. The compressor and the driver are supported on a solid concrete foundation.

Problem

Prior to the first half of 1982 the compressor was running with satisfactory performance at base capacity operating conditions of 6000 rpm as the maximum speed (Figure 2). The rotor was subsequently modified for a different mole weight gas with a revised maximum speed of 6500 rpm. The manufacturers' lateral critical speed and rotor sensitivity studies did not reveal any potential problems (Figure 3). The rotor was high speed balanced at 6700 rpm with an exceptional balance quality of 2 oz-in. residual unbalance (Figure 4).

However, when an attempt was made to increase the speed above 6000 rpm with an increase in load, a severe change in shaft vibration was noticed (amplitude increase from less than 1 mil to 3.6 mils). Below 6000 rpm the compressor was running at less than 1 mil vibration. Analysis of vibration spectra obtained from a computerized Machinery Condition Monitoring System ("MACMOS") revealed that the high vibration amplitudes occurred at a predominant frequency of 46.5 Hz (2760 cpm), which coincides with the first resonant frequency (critical speed) of the compressor rotor (Figure 5). Varying the rate of buffer gas injection to the seals produced significant changes in the vibration amplitude suggesting that this so called resonant whirl condition was aerodynamically induced. Aerodynamic impulses created by gas exiting impeller vanes (load dependent) provide excitation force which, for systems with inadequate damping, can amplify the vibration behavior at the first critical speed of the rotor. It is also believed that the low residual unbalance in this machine allowed a forcing impulse other than unbalance to predominate and thus excite the first resonant mode of the rotor.

A detailed analysis of the rotor-bearing system indicated excessive bearing stiffness as well as inadequate effective damping. A computerized study revealed that a four pad load between pad bearing is an optimum design for the machine which would maximize the stability threshold speed while yielding acceptable unbalance response (Table 1).

However, since the new four pad bearings were not readily available, the approach taken by the plant to find a temporary remedy with the machine continuing its process operation at normal load and speed, is innovative and worth sharing.

EXPERIMENTAL PROCEDURE

The goal was to establish the feasibility of increasing the rotor stability threshold, as plant operations would require increasing the rotor speed before the optimized bearings became available.

It was anticipated that the goal could be achieved by modifying effective compressor bearing loading and effective clearance characteristics without shutting the compressor down.

For the purpose of this experiment, the four compressor support legs were provided with induction heating elements which were wrapped with insulating material. In addition, dial indicators were set up to monitor vertical and horizontal movement of the compressor casing. Power supply and temperature control

responsibility were assigned to the truck-mounted laboratory, which was positioned near the compressor platform.

During the test relevant process parameters were held constant and were continuously monitored by MACMOS on a second-by-second basis and then converted to six-minute averages. The vibration behavior of the machine was, of course, also logged by an automated computer and a FM tape recorder during the entire test.

The actual test was conducted by step-wise heating of compressor legs in the following sequence: (1) inboard legs only, (2) outboard legs only, (3) all four legs, and (4) two diagonally opposite legs at a time. Temperatures started at 150°F and were raised at 50°F increments until final support leg temperatures of approximately 400°F were reached. The vibration amplitude behavior was continually monitored on platform-mounted vibration monitors and readings confirmed by simultaneously observing the computer-generated log. The taped vibration signals were subsequently analyzed and their spectra plotted as shown in Figure 6.

The onset of high vibration was noted on MACMOS printouts as typically shown in Figure 7. Whenever a preset limit is exceeded for a given parameter, an alarm occurs and data logging is initiated. Relevant data can then be retrieved and examined.

Figure 7 shows excessive average vibration of the compressor outboard bearing as monitored by an eddy current probe. Alarm-initiated data logging was actually triggered before 10:27:39 by vibration spikes which must have exceeded the preset limit of 3.2 mils. Note that outboard eddy current probe readings are represented by the numberal "8" whose second-by-second values are hand-connected for easier viewing in Figure 8.

The experiment demonstrated that low-vibration operation at train speeds of approximately 6,360 RPM was feasible with compressor outboard support legs heated to approximately 375°F. At these conditions, the compressor outboard end had grown 32 mils in the vertical, and 4 mils in the horizontal direction. The subsynchronous (2,760 cpm) vibration component was smaller than the once-per-revolution component at this speed. This is graphically illustrated in Figure 9, which shows compressor outboard spectra obtained under similar loads and speeds, with dissimilar support leg temperatures. At ambient temperatures, the subsynchronous frequency registers an uncomfortable 2.8 mils on the vertical eddy current probe. When the compressor outboard legs were heated to approximately 375°F, the once-per-revolution and subsynchronous vibration components dropped below 0.35 mils.

CONCLUSION

Severe aerodynamically induced subsynchronous vibration problems developed when the normal operating speed of a large centrifugal compressor was increased. An experiment was carried out to extend the onset of rotor instability to higher speeds on-line, without changing the basic rotor bearing system characteristics. The test results indicated that the effective compressor bearing support characteristics could be modified and the stability threshold be increased to an acceptable level.

This experiment has demonstrated that with proper instrumentation and monitoring, it is feasible to extend the stability threshold speed of centrifugal compressor, without requiring a shutdown of the equipment.

ACKNOWLEDGEMENT

The authors acknowledge Mr. H. P. Bloch, Mr. H. G. Elliott, Mr. D. G. Stroud, and Mr. R. H. Schmaus for their support during this test and subsequent data reduction.

REFERENCES

(1) "Four Pad Tilting Pad Bearing Design and Application for Multistage Axial Compressors", J. C. Nicholas and R. G. Kirk, ASME Paper, 81-LUB-12, 1981.

(2) "Selection and Design of Tilting Pad and Fixed Lobe Journal Bearings for Optimum Turborotor Dynamics", J. C. Nicholas and R. G. Kirk, Proceedings of the Eighth Turbomachinery Symposium, Texas A&M University, ed, P. E. Jenkins, November, 1979.

(3) "The Influence of Tilting Pad Bearing Characteristics on the Stability of High Speed Rotor Bearing Systems:, J. C. Nicholas, E. J. Gunter, and L. E. Barnett, Topics in Fluid Film Bearing and Rotor Bearing System Design and Optimization, an ASME special publication, 1978, pp. 55-78.

(4) "Optimum Bearing and Support Damping for Unbalance Response and Stability of Rotating Machinery", L. E. Barrett, E. J. Gunter, P. E. Allaire, ASME Paper No. 77-GT-27.

TABLE I. - SUMMARY OF POTENTIAL ALTERNATE BEARING PERFORMANCE

Bearing Case	$\bar{K}$ (1)	$\frac{C}{C_{OPT}}$ (1)	$AMP_{(2)}$	δ (2)	$\frac{\omega_D}{CPM}$ (2)
5 SLBP L/D = .3/PLF = .5	11.4	0.24	(-93.6)	-0.034	2,451
5 SLBP L/D = .43/PLF = .0	8.10	0.45	22.0	0.143	2,399
5 SLBP (55 percent offset)	8.97	0.40	53.7	0.058	2,431
3 SLOP	11.8	0.69	15.1	0.208	2,403
5 SLBP	10.96	0.70	25.7	0.122	2,415
5 SLOP	15.5	0.63	24.6	0.128	2,439
4 SLBP	6.11	1.12	8.7	0.362	2,421
7 SLOP TRESS-32	10.96	0.86	12.6	0.251	2,415
7 SLOP TRESS-68	17.24	0.59	31.5	0.100	2,446

Ref: (1) "Optimum Bearing and Support Damping for Unbalance Response and Stability of Rotating Machinery", L. E. Barrett, E. J. Gunter, P. E. Allaire, ASME Paper No. 77-GT-27.

(2) "Stability and Damped Critical Speeds of a Flexible Rotor in Fluid-Film Bearings", J. W. Lund, ASME Paper No. 73-DET-103.

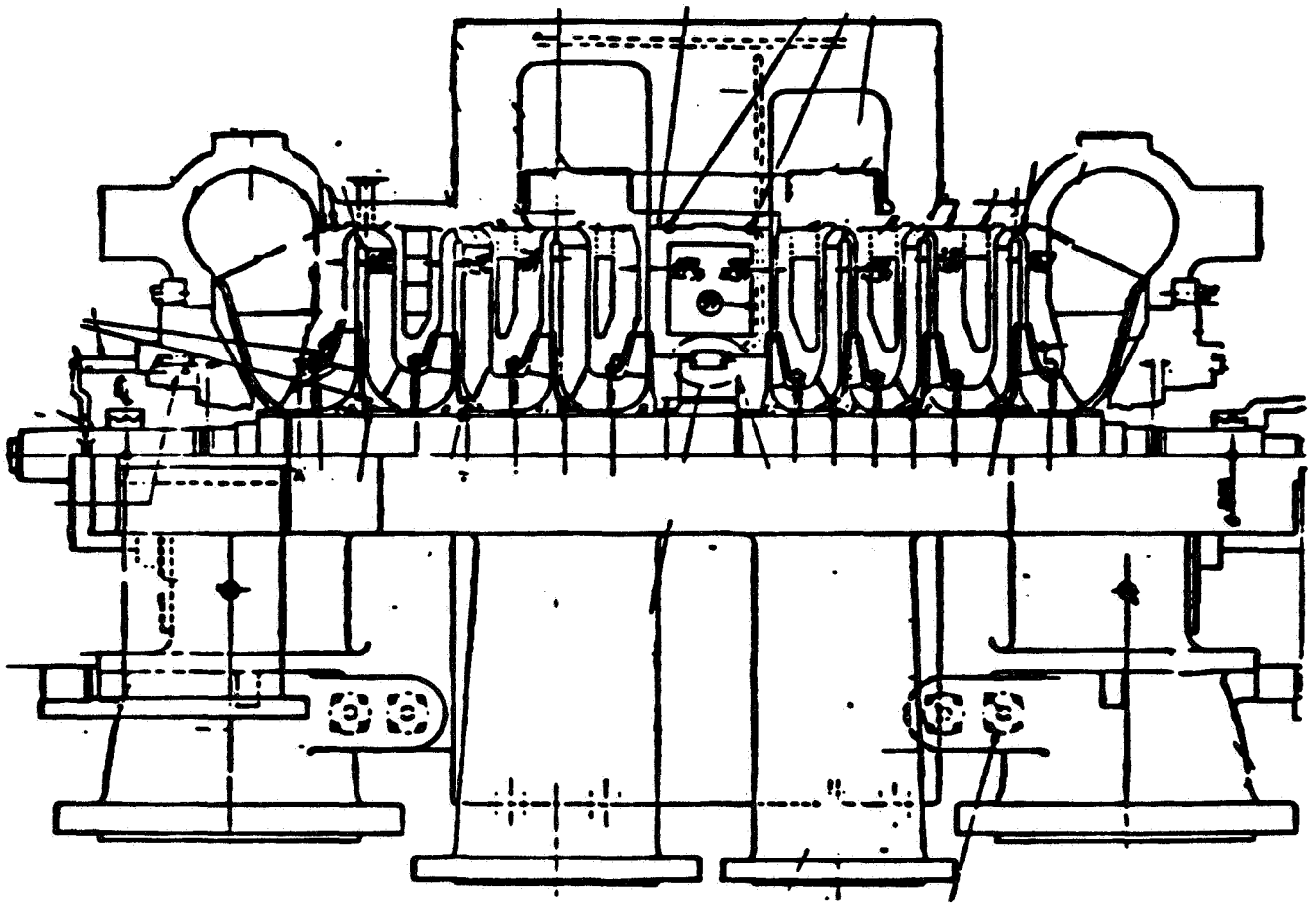

Figure 1. - Compressor X-section.

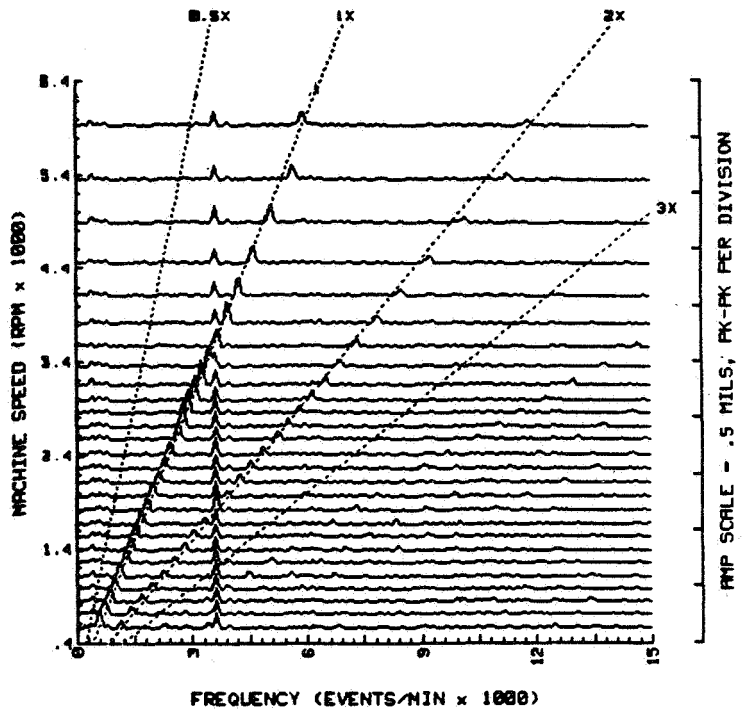

(a) Cascade plot.

Figure 2. - Base operating conditions.

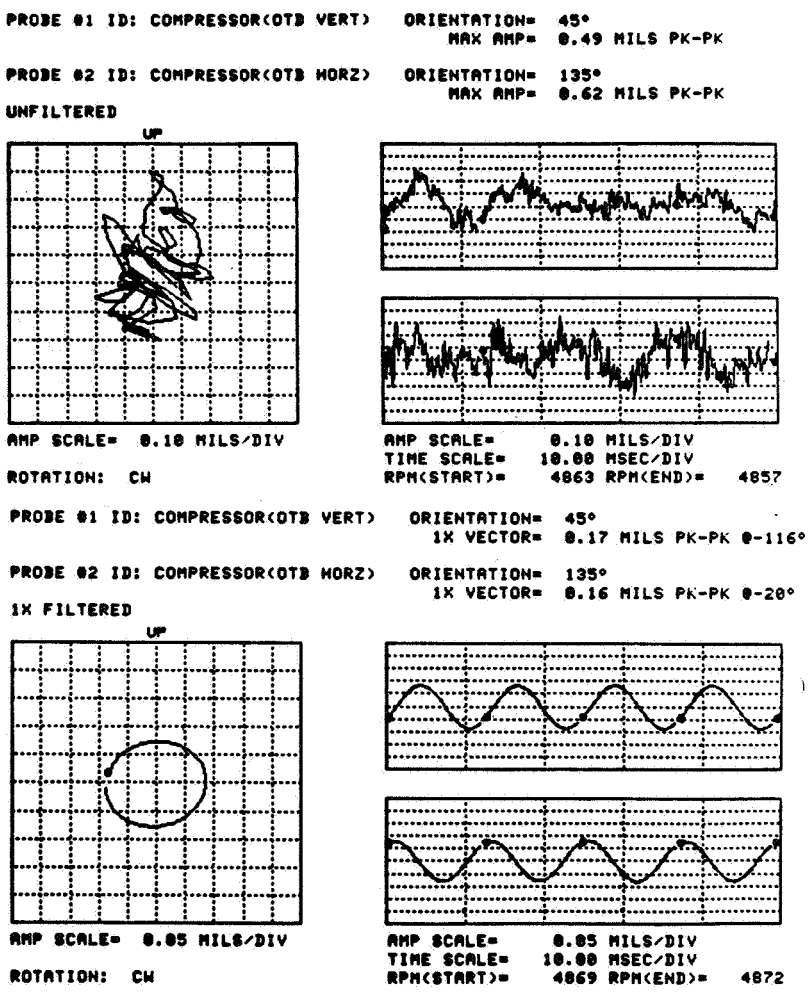

(b) Orbits.

Figure 2. - Concluded.

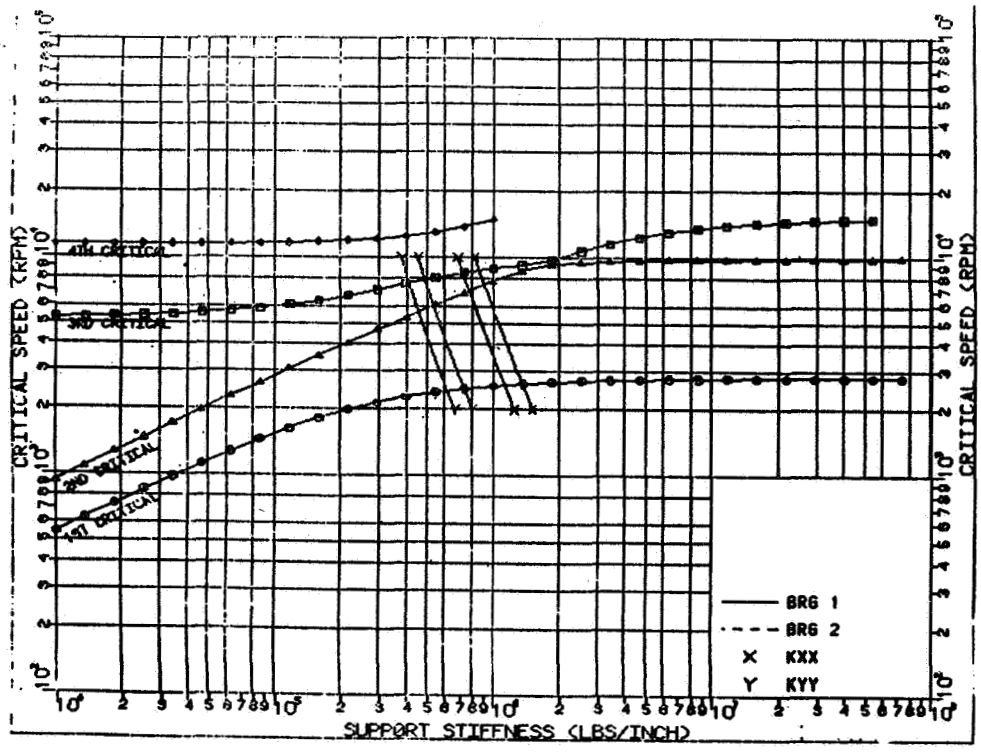

Figure 3. - Critical speed map.

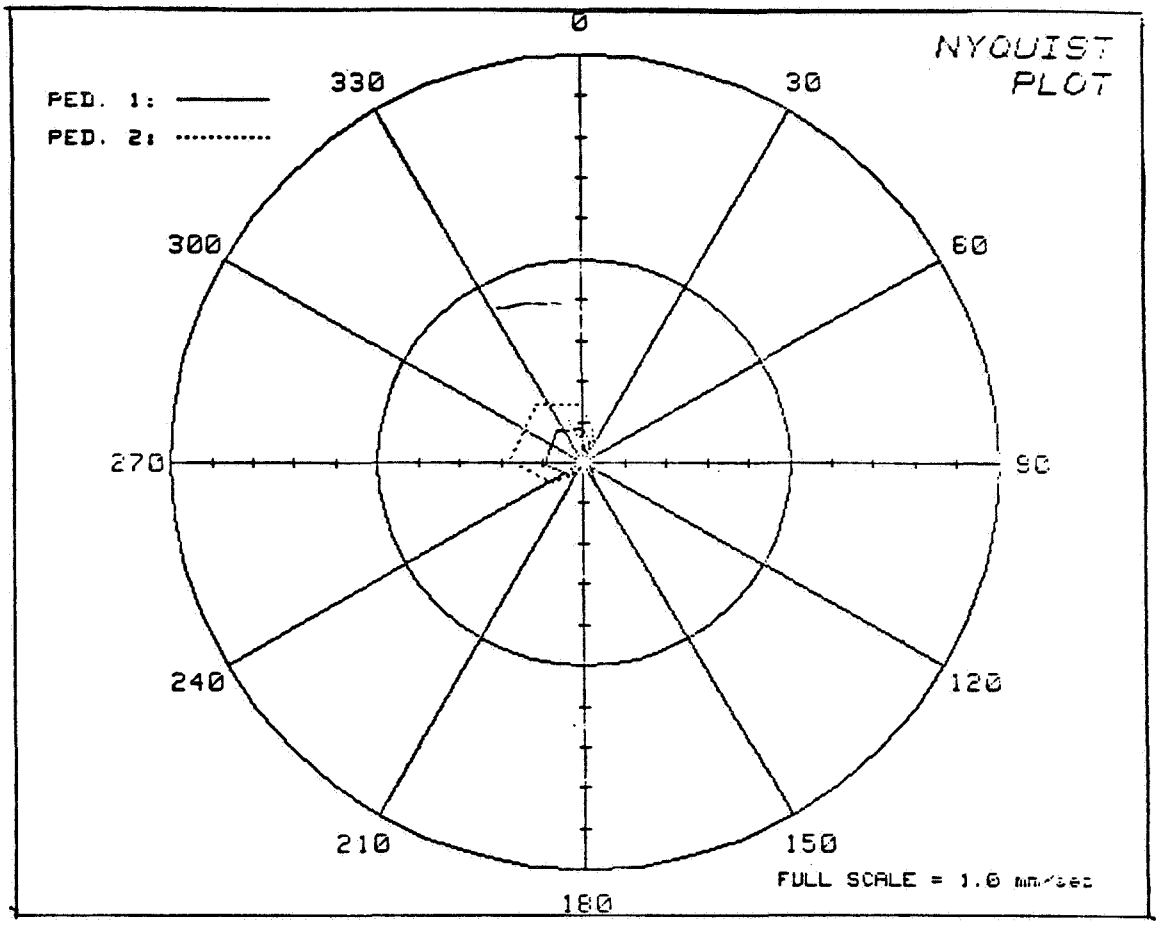

Figure 4. - High speed balance plot.

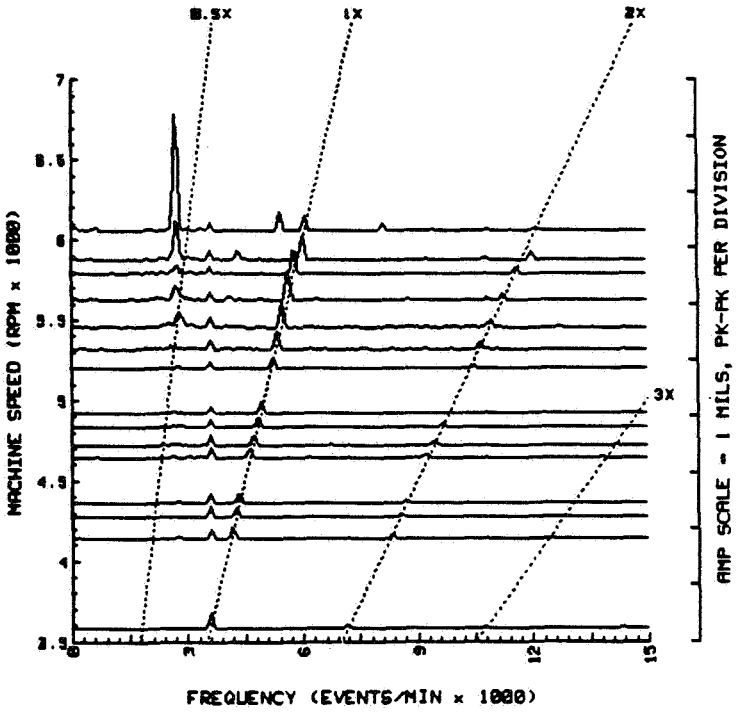

(a) Cascade plot.

Figure 5. - Uprated operating conditions.

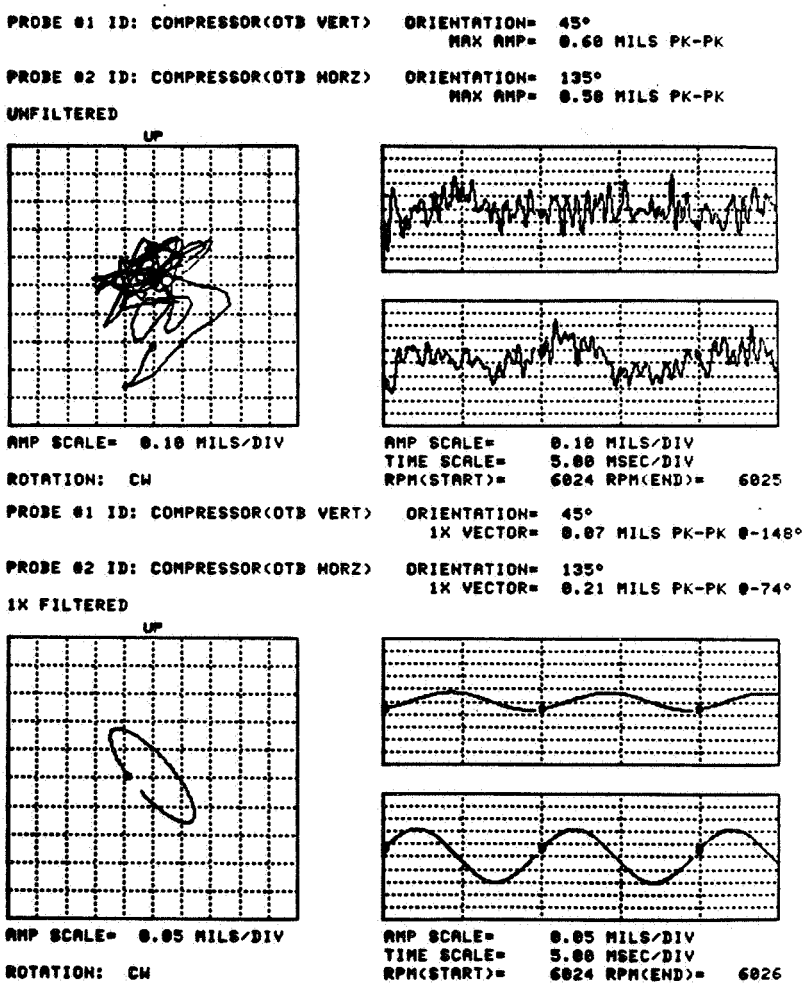

(b) Orbits.

Figure 5. - Concluded.

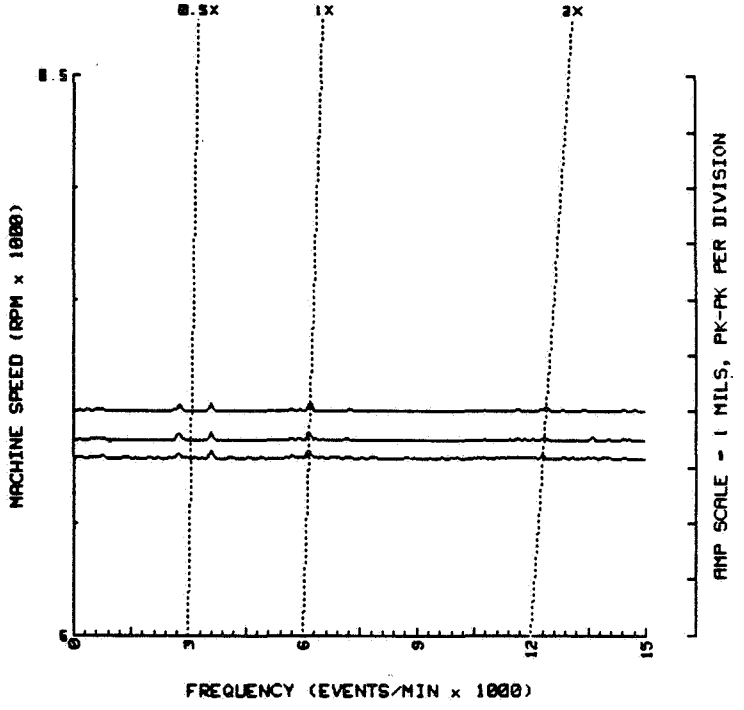

Figure 6. - Uprated operating conditions with heated legs: Cascade plot.

TIME	Machine Speed (RPM) 1	Machine Speed (RPM) 2	Inboard Bearing Vib., Mils	Inboard Bearing Vib., Mils	Accelero-meter (uncali-brated)	Inboard Bearing (Radial) T, °F	Inboard Bearing (Radial) T, °F	Outboard Bearing Vib., Mils	Outboard Bearing Vib., Mils	Outboard Bearing Vib., G	Rotor Thrust Posi-tion	Rotor Bearing Temp., °F
102829	6213.9	3967.8	1.3760	.72960	1.1424	188.06	180.58	1.8528	1.0752	.0	12.279	174.08
102824	6217.8	3973.7	1.4336	.75520	1.2288	188.45	180.96	1.9424	1.1968	.00960	12.326	174.43
102823	6213.9	3967.8	1.9440	.80	1.0944	188.26	180.67	2.1424	1.3152		12.301	174.24
102822	6209.9		1.6560	.83840	1.0752	188.35	180.58	2.3472	1.4816	.0	12.279	174.14
102821	6213.9	3971.8	1.7312	.86720	1.1136	188.26		2.4768	1.5856			174.05
102820		3967.8	1.6112	.81440	1.1328	188.35	180.48	2.3280	1.4608	-.0096	12.326	174.24
102819	6217.8	3971.8	1.5280	.77280	1.1424		180.67	2.1472	1.3008	.0	12.382	
102818	6209.9	3969.8	1.4560	.75840	1.1136		180.48	2.0144	1.1872	-.0288		174.14
102817	6213.9	3973.7	1.4096	.7360	1.1712	188.26	180.38	1.9120	1.1040		12.326	
102816		3971.8	1.3536	.71680	1.1136	188.35	180.48	1.7984	1.0160	-.0192	12.352	174.24
102815	6202.0	3969.8	1.3088	.69920	1.1040	188.26	180.58	1.7152	.95520	-.0288	12.301	
102814	6206.0	3971.8	1.3104	.69760	1.20	188.35	180.67	1.7168	.96320	-.0096	12.326	
102813	6209.9	3967.8	1.3136	.6960		188.45		1.7136	.97120			174.34
102812	6213.9	3971.8	1.3664	.73120	1.2384	188.54		1.8272	1.0624	.00960		
102811		3969.8	1.4320	.75360	1.0944	188.45	180.58	1.960	1.1664	.0		
102810	6206.0		1.5248	.79520	1.0752	188.26	180.48	2.1376	1.3168	-.0192	12.301	
102809	6213.9	3973.7	1.60	.8240	1.0176	188.45	180.29	2.2880	1.4352	.0	12.279	174.14
102808	6209.9	3967.8	1.5232	.78240			180.48	2.1328	1.3056	.00960	12.326	174.34
102807			1.3984	.72640	1.0272	188.54	180.38	1.8864	1.1056		12.398	
102806	6206.0	3971.8	1.2896	.68160	1.0560	188.45	180.48	1.6496	.91680	-.0096	12.301	
102805		3967.8	1.2672	.67680	1.1136		180.29	1.5968	.88480	.0	12.326	174.24
102804		3973.7	1.3008	.69120	1.20	188.74	180.38	1.6512	.9360		12.382	174.34
102803	6209.9	3967.8	1.3680	.71840	1.0848		180.48	1.8016	1.0320			
102802	6213.9	3971.8	1.3696	.7120	1.1712	188.64	180.29	1.8144	1.0416	-.0288		
102801	6206.0	3967.8	1.2912	.67840	1.2672	188.45		1.6656	.91840			
102800	6213.9		1.240	.66560	1.1520	188.64	180.48	1.5392	.83680	-.0192	12.378	
102799	6209.9	3973.7	1.2464	.67040	1.2096	188.45		1.5536	.85120	-.0288	12.326	174.24
102798		3969.8	1.2976	.67360	1.2576	188.54	180.38	1.5872	.87040	-.0096	12.382	174.43
102797	6213.9	3967.8	1.2752	.68320	1.1424	188.64	180.29	1.6224	.89920	.00960	12.326	174.34
102796	6209.9		1.3152	.69760	1.1136		180.38	1.7056	.9440	.0	12.301	
102795	6217.8		1.2832	.68480	1.1232			1.6432	.89760	.00960	12.326	174.43
102794	6209.9	3975.7	1.2384	.66560	1.1808	188.54	180.29	1.5472	.8320	0	12.301	174.34
102793	6221.7	3967.8	1.2336	.66720	1.2096	188.83	180.38	1.5248		.00960	12.352	174.43
102792	6209.9		1.2576	.6720	1.2288	188.54	180.19	1.5680	.86880	-.0192	12.301	174.24
102791	6217.8	3969.8	1.3248	.69760	1.2384	188.64	180.29	1.7184	.95840	.00960	12.326	174.43
102790	6209.9		1.3040	.68480	1.2288			1.6864	.9360	-.0096		
102789	6217.8	3971.8	1.2896	.68320			180.58	1.6496	.91040	.00960	12.378	174.62
102788	6213.9	3969.8	1.240	.66080	1.1904	188.54	180.38	1.5296	.83040	-.0096	12.352	174.53
102787		3971.8	1.1984	.64160	1.1424	188.64	180.19	1.4416	.77120	0		174.43
102786	6209.9	3969.8	1.1920	.64320	1.1232		180.38	1.4224	.7680	-.0096		
102785		3969.8	1.2160	.64480		188.54	180.29	1.4752	.79680		12.326	
102784	6213.9	3973.7	1.1808	.64320	1.20	188.64		1.4112	760			174.34
102783		3971.8	1.2064	.64960		188.54		1.4624	.79840			
102782	6209.9	3969.8	1.2640	.67360	1.2096	188.64		1.5984	.87520	-.0192		174.43
102781		3973.7	1.2720	.67520	1.20			1.6160	880	-.0096		
102780	6217.8	3971.8	1.240	.66560	1.1424			1.5472	.83520	0	12.352	
102779	6209.9	3973.7	1.20	.64480	1.1520	188.54	180.38	1.4624	.78240	-.0096	12.301	

Figure 7. - "Alarm-initiated data log" in 10:28:08 to 10:28:10, and 10:28:18 to 10:28:23 time frame. Vibration exceeded 2 mils.

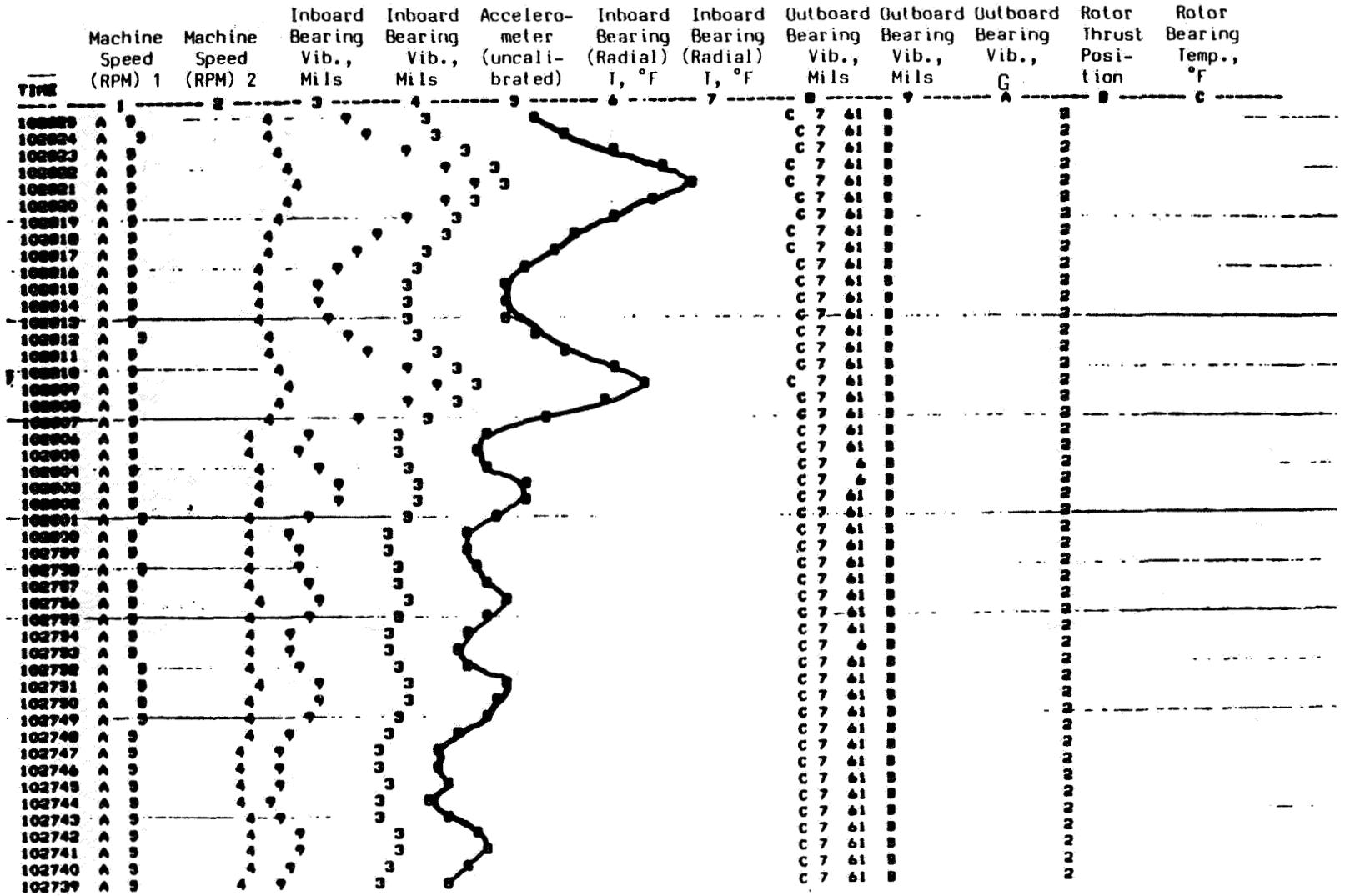

Figure 8. - Outboard bearing vibration in X-direction for 10:27:39 to 10:28:25 time frame.

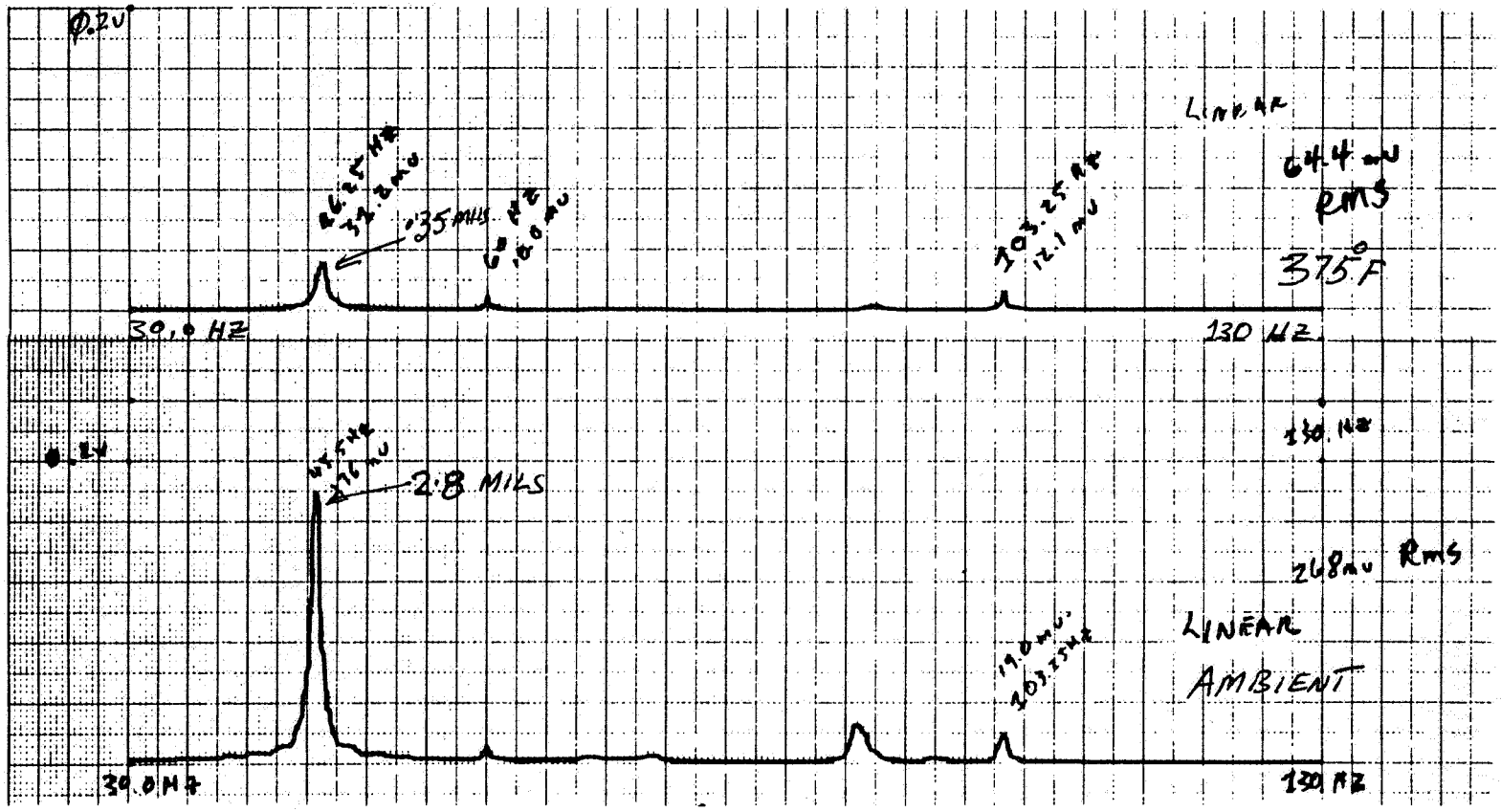

Figure 9. - Compressor outboard vertical vibration at near identical load with outboard support legs at ambient versus approx. 375° temperature.

INTERNAL HYSTERESIS EXPERIENCED ON A HIGH PRESSURE SYN GAS COMPRESSOR

F. Y. Zeidan
Qatar Fertiliser Company
Umm Said, Qatar

This paper describes a vibration instability phenomenon experienced in operating high pressure syn gas centrifugal compressors in two Ammonia plants at Qatar Fertiliser Company. The compressors were closely monitored using orbit and spectrum analysis to follow up changes from baseline readings. Tape recordings of run up and run down data presented a clue to the cause of the instability, which was later confirmed through physical examination of the rotor assembly. Internal hysteresis was the major destabilizing force. However, the problem was further complicated by seal lock-up at the suction end of the compressor. Also, a coupling lock-up problem and a coupling fit problem, which caused frettage of the shaft, should not be counted out as contributors to the self-excited vibrations.

INTRODUCTION

Instabilities in high-speed, high-pressure centrifugal compressors are quite common today. These compressors are usually running above two times their first critical speed, are quite light, and have high horsepower and pressure ratings. A recent survey (ref. 1) on causes of Ammonia plant shutdowns reported that syn gas compressor failures caused more downtime than any other major equipment, accounting for 23 to 31% of the major equipment downtime. The average Ammonia plant has a syn gas compressor failure every 7 to 9 months, and of the 88 world-wide plants surveyed in reference 1, 89% suffered a syn gas compressor failure during the survey period. The results of this survey are not surprising to those familiar with the operation of Ammonia plants. The syn gas compressor is subjected to a severe operating environment which is much tougher than that demanded of other compression units in the plant.

GENERAL CONFIGURATION

A schematic of the high pressure compressor train is shown in fig. 1. An aircraft derivative gas turbine (gas generator) powers a free power turbine which then drives the high pressure compressor through a speed increasing gear. The normal start-up sequence is to start the gas turbine and hold it at warm-up speed of 1500 rpm, which corresponds to 4500 rpm on the compressor. Upon completion of the warm-up time, the unit is then quickly accelerated to the minimum governed speed, which is equivalent to 11,000 rpm for the compressor. A sketch of the high pressure rotor is shown in figure 2, outlining the major components. The

rotor consists of two stages: the high pressure stage consisting of 7 impellers, and the circulator stage with one impeller. The two stages are separated by a long interstage labyrinth seal, and are housed in a common barrel casing. The rotor is supported on tilt pad bearings with 5 pads in a load on pad configuration. The oil seals are of the floating ring type, where the sealing is applied through lapping of the housing lip with the mating face of the outer seal ring. An "O" ring seal is used on the housing face of the inner seal ring.

HISTORY

The syn gas high pressure compressor has always been the bottle neck in the operation of the Ammonia plants at Qatar Fertiliser Company. It has been plagued by several design problems that were detrimental to the safe operation of the unit, and consequently it had to be run below its rated speed and horsepower. The unit was running at too high an axial thrust during the first two years of operation. This required the resizing of the balance piston twice before we were able to run it at full load. Another design deficiency which also caused interrupted operation and damage to the rotor, was the improperly heat treated tie rods which hold the aerodynamic assembly together. These would often break during start-up at the threaded section of the rod and fall through the thrust balance line opening into the suction of the compressor damaging labyrinth seals and shifting impellers on the rotor shaft.

Recognizing the problems caused by this compressor and others in the plant, attention was directed towards acquiring more sophisticated diagnostic instrumentation to enable plant personnel to follow up developments on the machines.

INTERNAL HYSTERESIS

The normal vibration spectrum for the rotor obtained after an overhaul always contained a subsynchronous component approximately equal to 50% of the running speed frequency. As seen in figure 3 it was bounded, and the synchronous component due to residual unbalance was the dominant component in the baseline spectrum. Figure 4 shows the unfiltered orbit which agrees with the information designated by spectrum analysis, where the subsynchronous component forms an internal loop and is smaller in magnitude compared to the synchronous component. However, after being in service for some time, we always noted an increase in vibration. Figure 5 shows a spectrum of the same rotor taken 7 months later where the subsynchronous component became the dominant frequency. The orbit analysis also confirmed this fact. As noted in figures 4 and 6, the subsynchronous component has increased and predominates the total motion masking the effect of unbalance. Gunter (ref. 2) describes investigations which produced results similar to what we have experienced.

Our suspicion of internal friction damping to be the driving force of this instability was later verified during the annual shutdown when the rotor was pulled out and inspected. All 7 impellers of the high pressure stage, including the sleeves, had travelled along the shaft in a direction towards the suction end of the compressor. It was later hypothesized that the shrink fit was not adequate to start with , which explains why we had subsynchronous vibrations right after

starting up with a newly overhauled rotor. After running for some time, the impellers apparently start to travel towards the suction end of the compressor. As they begin to make contact with the sleeves, this gives rise to more friction and subsequently increases the contribution of the internal friction forces acting on the rotor. This causes the subsynchronous precession to predominate over the unbalance response.

TRANSIENT DATA

Through the use of a tape recorder, transient data were obtained and further confirmed our previous findings. Figure 7 shows the run-up data of a newly overhauled rotor that was installed during an annual turnaround. At a speed of 5700 rpm (95 HZ), we noted a peak in amplitude of the synchronous component indicating the critical speed of the rotor. The synchronous component continued to be the only apparent signature until the rotor crossed the threshold speed and a subsynchronous component appeared at exactly 50% of running speed frequency. The subsynchronous component traced the running speed frequency until it reached the critical speed frequency and locked on it. At this point, changes in the running speed did not affect the instability which remained locked on to the rotor's first critical speed.

This verification eliminated the possibility of oil whirl in the seals as being the exciting force, since the seals were also replaced during the annual turnaround and could not have been locked-up at this stage. We have had the seals lock-up after several months of operation, and noticed that the vibration characteristics in such a case are quite distinct from what we witnessed here. Fig. 8 shows a frequency spectrum display of the rotor with a subharmonic component at 72 HZ which amounts to about 40% of running speed frequency. This was the result of the seals locking-up and acting as a sleeve bearing.

MAJOR RECONFIGURATION

The information from our findings was reported to the manufacturer of the compressor, who quickly confirmed that the rotor design was marginal and very susceptible to the form of instability just described. They claimed that knowledge to predict such a phenomenon was not available at the time this compressor was designed, and proposed a major redesign (3) to solve the problem. This involved a change in rotor stiffness by increasing the shaft diameter and reducing the bearing span. This would eventually mean scrapping all of the five existing rotor shafts, and the replacement and/or reworking of existing bearing and seal assemblies to reduce the bearing span. All spacers would have to be replaced by new ones to accommodate the larger diameter rotor shaft, in addition to reworking all the impellers and balance piston bores. The proposed arrangement also included putting the journal bearings between the oil film bushing seals on each end of the compressor.

This extensive modification was rejected for several reasons. First, it was very expensive; over half a million dollars, not including the cost of scrapped parts and the additionally required spares. Second, it would require a rather long

downtime in order to carry out the proposed rework. Third, it was based completely on a computer program simulation, and as stated in Reference 4, this is questionable for the case of rotordynamic simulation since machine parameters such as damping, internal friction, bearing support stiffness, etc., usually cannot be calculated accurately. These parameters must be adjusted in the computer simulation until the behaviour of the machine in the field can be reproduced faithfully. No such attempt to take field measurements was made by the manufacturer. Finally, a single minor modification which we proposed showed good promise of reducing or eliminating the major driving force of the instability.

CORRECTIVE ACTION

The objective here was to determine the most economical way to make the machine run smoothly and reliably. It was apparent that increasing the shrink fit by plating the shaft about one mil oversize should be the first step in such a solution, since it requires a minimum of expenditure. This solution was sound since it does not have an adverse effect on material strength, cause stress concentrations or stress corrosion, and will not exceed the yield strength of the material.

Figure 9 shows a cascade spectrum of a rotor that had the shrink fit improved by plating the shaft 1 mil oversize. No appreciable subsynchronous vibrations were observed throughout the speed range of the compressor. What is also apparent in Figure 9, and of interest to note, is that the rotor's first critical speed was still around 95 HZ. The unit was operating at a very low vibration level allowing the plant to run at loads as high as 125%, a level never before achieved.

It is important to note here that problems arising from loose fits have been known to the manufacturer and in a particular case (5) caused them to thoroughly scrutinize and modify their methods for assembly of spacers and impellers. The fractional frequency problem they experienced was similar in nature to the one described here, and also involved a rotor with a back-to-back impeller arrangement. The sleeve at the center, required to separate the two sections was modified and made integral with the shaft with shoulders at each end to provide impeller stops. This particular rotor was also fitted with a squeeze film damper bearing to enable it to operate through the full speed/pressure range.

SUMMARY AND CONCLUSION

- Instabilities in high speed compressors are numerous; to tackle these problems we must be able to first identify them. This requires both an increased understanding of the causes of instabilities, in addition to the availability of modern sophisticated diagnostic instrumentation.

- Hysteretic whirl is not a rare source of instability (6). It can come from loose impeller and spacer fits, can be caused by poor coupling hub fit, or can result from tooth friction in a poorly misaligned gear coupling. It can also be provoked by a sudden impact or shock and cause an otherwise stable rotor to whirl.

We were the victims of such an occurrence, where one of the tie rods on the aerodynamic assembly broke off and caused impact damage. The rotor was balanced and restarted, but experienced severe subsynchronous vibration diagnosed as hysteretic whirl. The damage caused shifting of the impellers on the shaft and started relative internal slippage in the fit.

- It has apparently been assumed by many turbomachinery users that tilt pad bearings are the solution to all rotordynamic problems. While this might hold true in many cases involving oil whirl excited instabilities, it is certainly not a solution to all problems. The case just presented is a good example of this since the rotor was supported by tilt pad bearings.

- A large percentage of centrifugal compressors in the process industry today are operating at speeds higher than two times their first critical speed, and a significant portion of these are susceptible to instability. The instability can be the result of several exciting forces (4), which makes it difficult to pinpoint the fault. The solution of increasing shaft stiffness by increasing shaft diameter is not a favorable one, since this will increase the peripheral speed of the shaft's journal, restrict gas flow, and increase horsepower consumption.

- Instabilities like the one described here have been around for some time and still exist in many plants. Many machinery operators, however, still accept these problems as a fact of life, partly because they are not aware of recent advances in this field as well as the availability of easy to use diagnostic instrumentation. As such, the failures are accepted as something normal and they continue to regularly change and replace failed components.

ACKNOWLEDGEMENTS

The author wishes to thank Dr. John Vance of Texas A&M University for his valuable suggestions, which proved very helpful in diagnosing the instability problem described in this paper.

REFERENCES

1. Williams, G.P. and Hoehing, W.W., "Causes of Ammonia plant shutdowns, Survey IV", Ammonia plant and related facilities safety symposium, Los Angeles, California, AICHE paper No. 124g.

2. Gunter, E.J., "Dynamic Stability of Rotor-Bearing Systems", NASA SP-113, 1969.

3. Shade, W.N., "RB10-8B HPC Rotor Stability Problems", Cooper Energy Services, Rotating Machinery Engineering Dept., Centrifugal Compressor Design Report No. CCD-108, Oct. 21, 1982.

4. Vance, J.M., "Instabilities in Turbomachinery", Proceedings of Machinery Vibration Monitoring and Analysis Seminar, New Orleans, Louisiana, April 7-9, 1981, pps. 107-113, Sponsored by The Vibration Institute, Clarendon Hills, Illinois.

5. Smith, K.J., "An Operation History of Fractional Frequency Whirl", Proceedings of the Fourth Turbomachinery Symposium, Texas A&M University, College Station, Texas, 1975, pp. 115-125.

6. John Sohre, "Operating Problems With High-Speed Turbomachinery Causes and Correction", Part II, Case Histories, 1976.

7. Vance, J.M. and Lee, J., "Stability Of High Speed Rotors With Internal Friction", ASME Journal of Engineering for Industry.

8. Childs, D.W., "Fractional Frequency Rotor Motion Due To Non-Symmetric Clearance Effects", ASME paper No. 81-GT-145, Gas Turbine Conference, Houston, Texas, March 9-12, 1981.

9. Murphy, B.T., and Vance, J.M., "Labyrinth Seal Effects on Rotor Whirl Instability", Proceedings of The Second International Conference on Vibrations in Rotating Machinery, Churchill College, Cambridge, September 1-4, 1980.

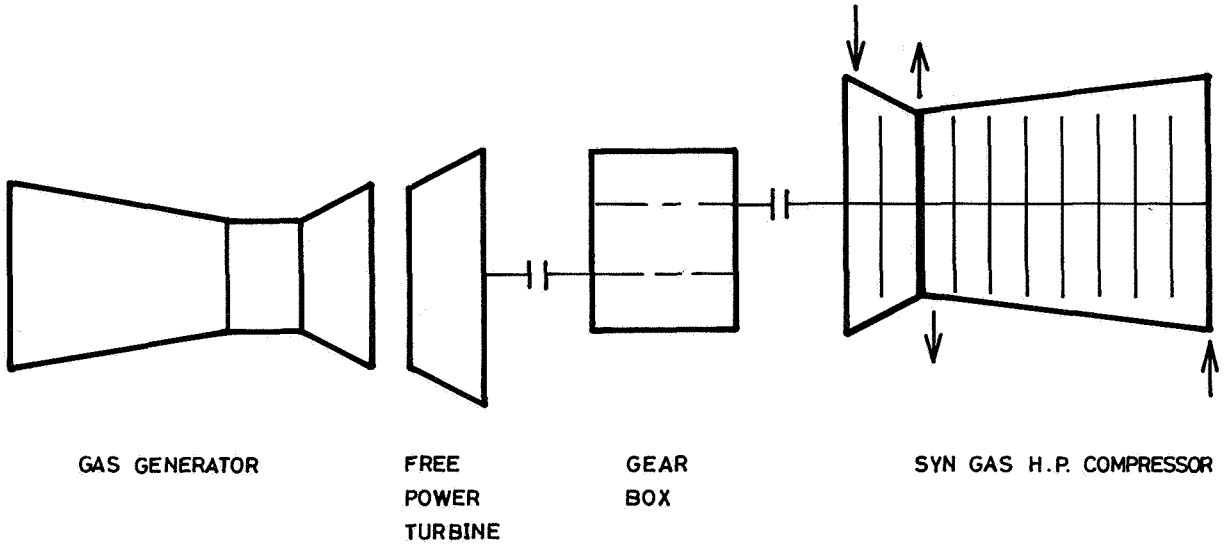

Figure 1. - Schematic of compressor train.

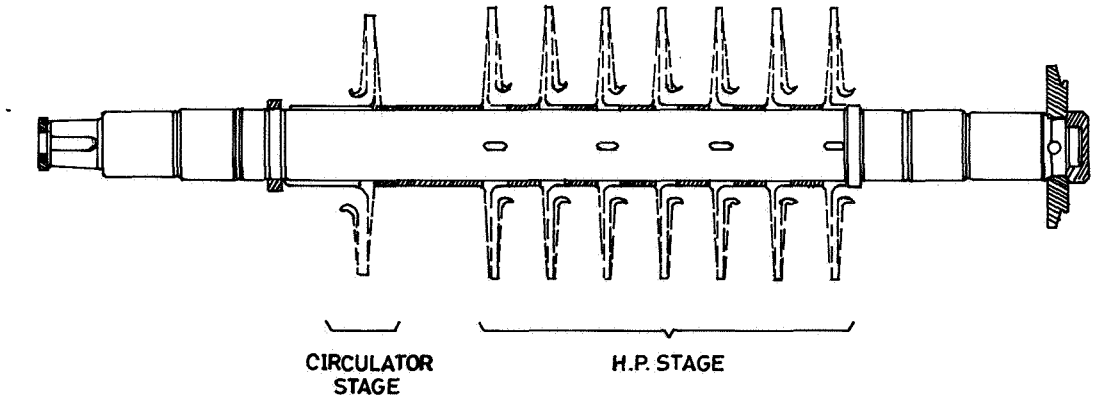

Figure 2. - Syn. gas compressor rotor.

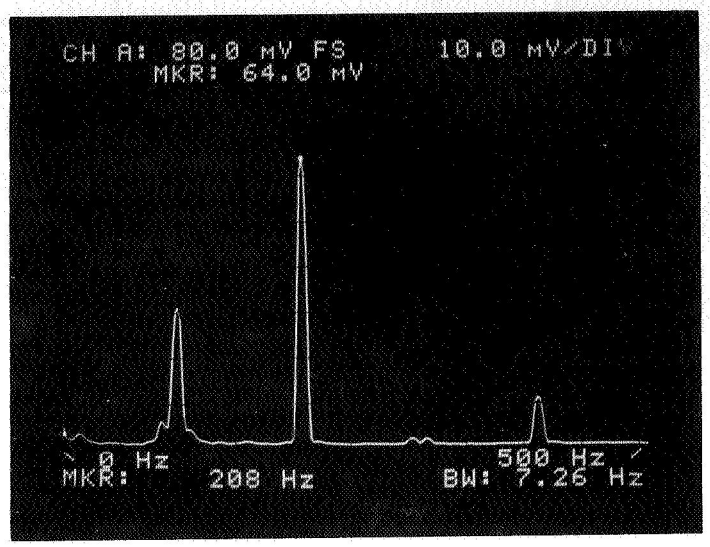

Figure 3. - High-pressure compressor 3101; location, A-II compressor house; date, 28/4/1981; 8 V; 50 mV rms/div.; 200 mV/mil; frequency range, 0-500 Hz.

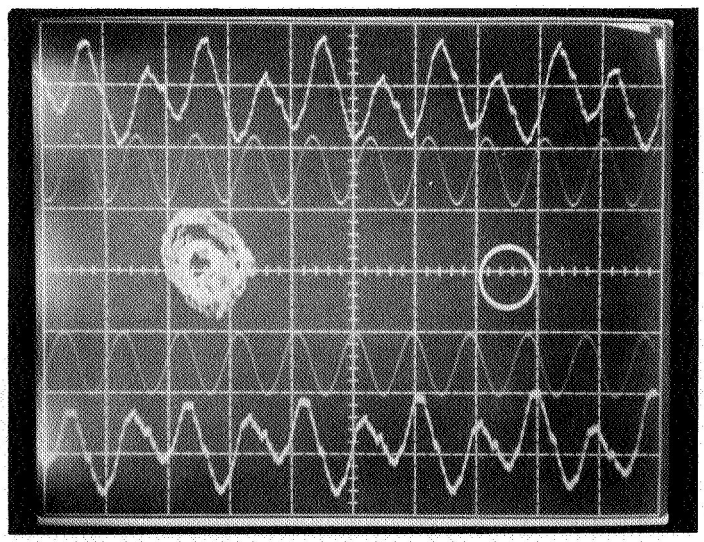

Figure 4. - High-pressure compressor 3101; location, A-II compressor house; date, 28/4/1981; 8 V/8 H; 0.2 V/div.; 1 mil/div.; sweep rate, 5 ms/div.; rotational speed, 12 471 rpm.

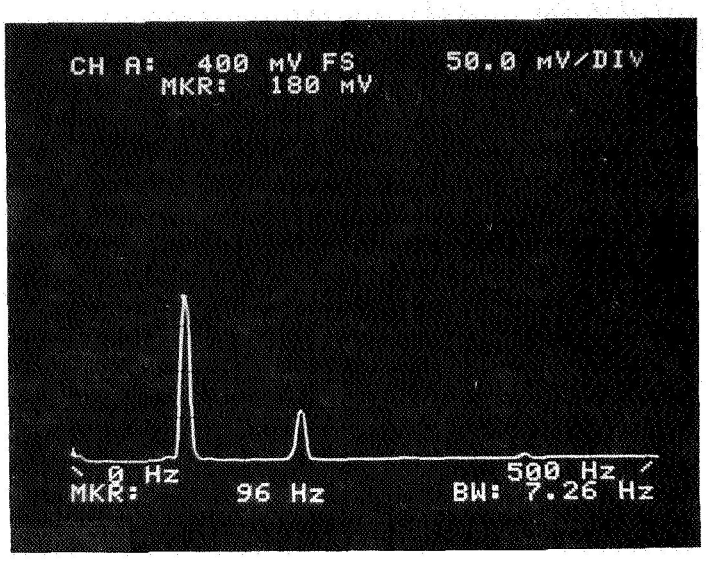

Figure 5. - High-pressure compressor 3101; location, A-II compressor house; date, 31/12/1981; 8 V; 10 mV rms/div.; 200 mV/mil; frequency range, 0-500 Hz.

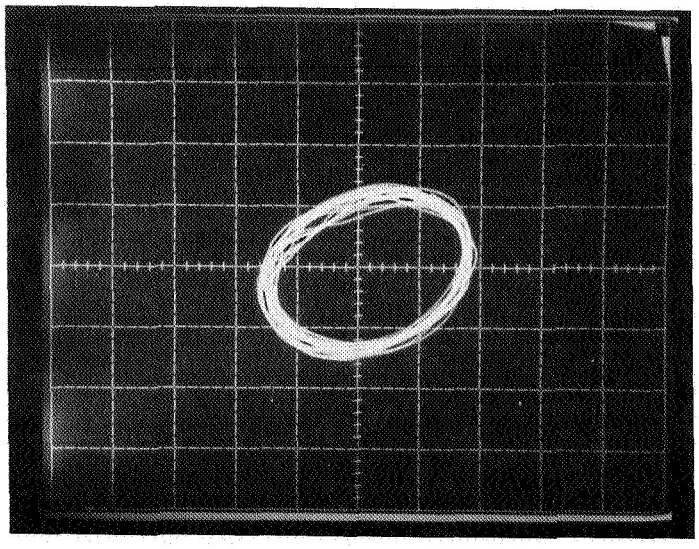

Figure 6. - High-pressure compressor 3101; Location, A-II compressor house; date, 31/12/1981; 8 V/7 H; 0.2 V/div.; 1 mil/div.; sweep rate, 5 ms/div.; rotational speed, 11 500 rpm.

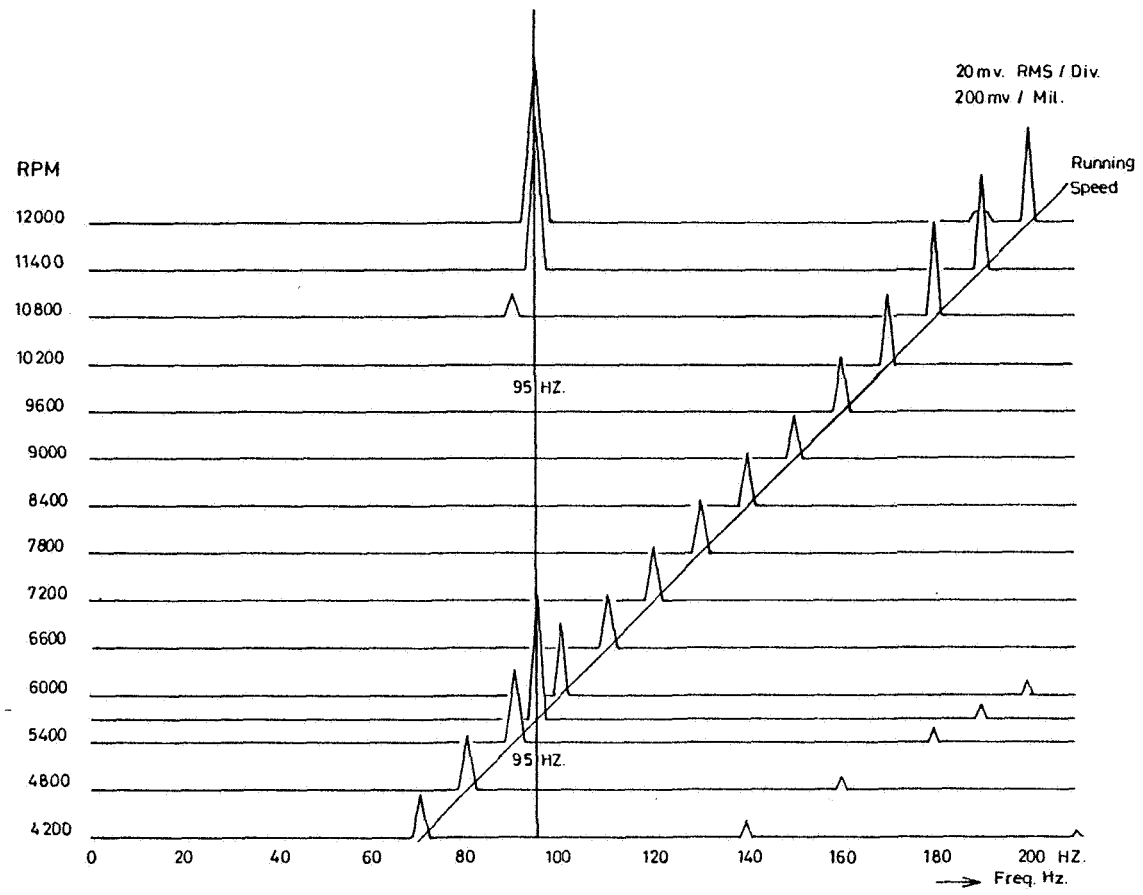

Figure 7. - High-pressure compressor runup.

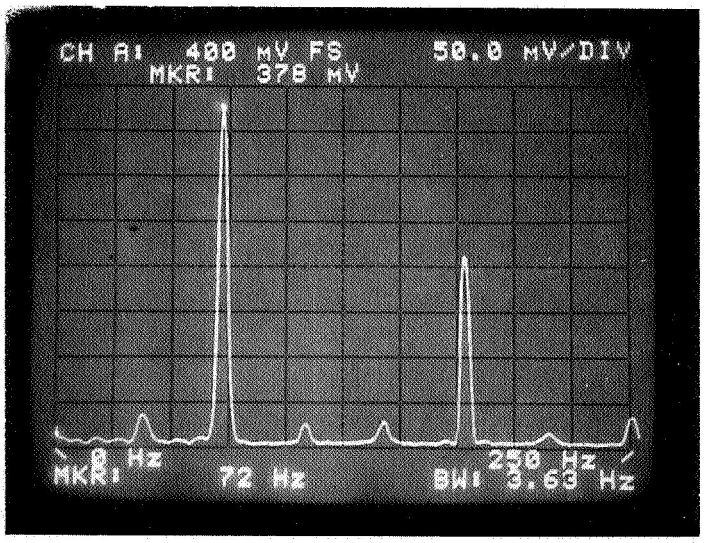

Figure 8. - High-pressure compressor 3101; location, A-II compressor house; date, 8/8/1983; 8 V; 20 mV rms/div.; 200 mV/mil; frequency range; 0-250 Hz.

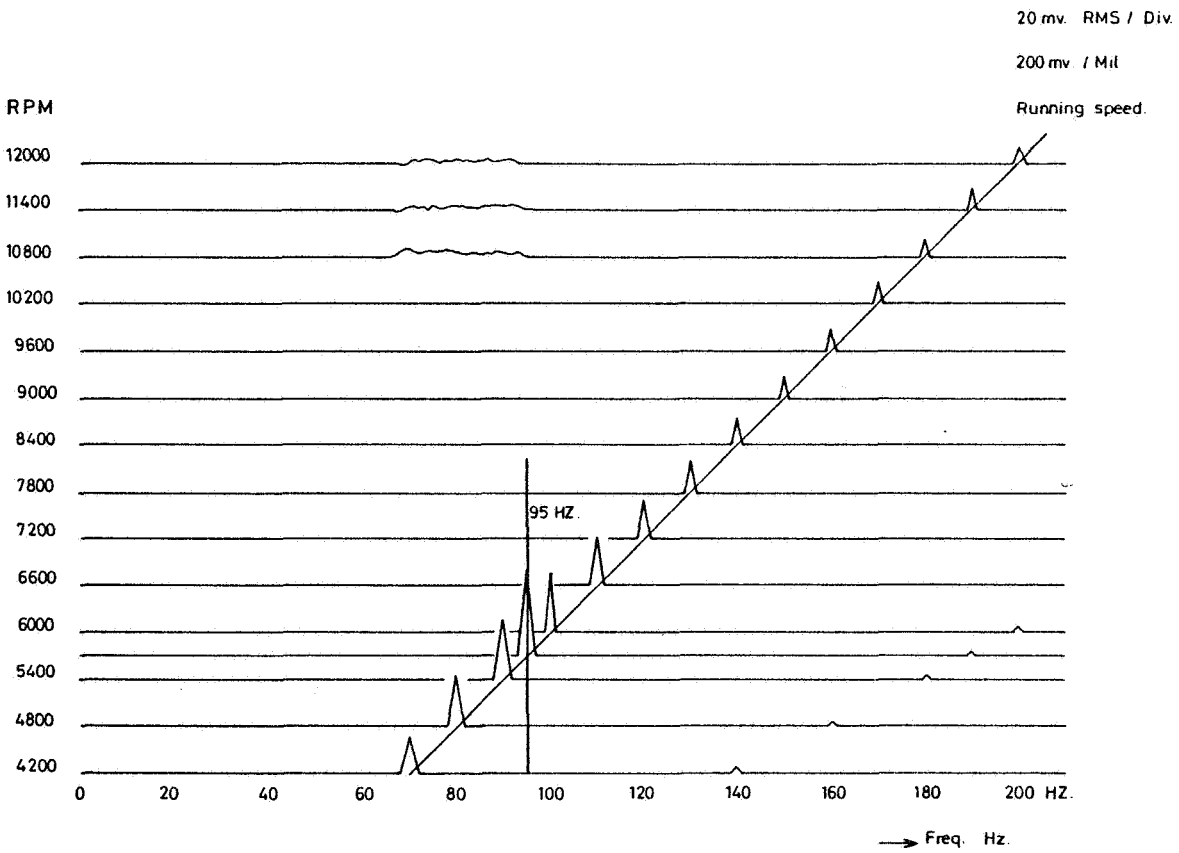

Figure 9. - High-pressure compressor runup with shrink fit improved.

LATERAL FLUID FORCES ACTING ON A WHIRLING CENTRIFUGAL IMPELLER IN VANELESS AND VANED DIFFUSER*

Hideo Ohashi
University of Tokyo
Tokyo 113, Japan

Hidenobu Shoji
Tsukuba University
Ibaragi-ken 305, Japan

Fluid forces on a rotating centrifugal impeller in whirling motion were studied experimentally. A two-dimensional impeller installed in a parallel-walled vaneless and vaned diffuser whirled on a circular orbit with various positive and negative angular velocities. The results showed that the fluid forces exert a damping effect on the rotor in most operating conditions, but become excitatory when the impeller operates at very low partial discharge while rotating far faster than the whirl speed.

The fluid forces were also expressed in terms of mass, damping and stiffness matrices. Calculations were conducted for impellers with the same geometry and whirl condition as those in the experiment. Quantitative agreement was obtained especially in positive whirl.

INTRODUCTION

As to fluid forces acting on a centrifugal impeller of pumps and compressors, many studies have been done on the steady lateral forces (radial thrust), which occur either by azimuthally asymmetric configuration of volute casing or by misalignment of impeller and casing center. To the contrary, limited contributions have been made to the unsteady part of lateral forces, which is induced by the whirling motion of rotating impellers. This is the very information sought for the precise analysis of rotor stability and seismic response.

Experimental study on this subject is quite few. Two projects are presently under way as far as known to the authors, one at California Institute of Technology and the other at University of Tokyo.

The latter, i.e. the present experimental study is the direct counterpart to the theoretical calculation reported at the 1st Workshop [ref. 1]. Therefore the geometries of the test impeller and casing were determined to be similar to those of sample calculations. This is the reason why this experiment adopted deliberately much simpler configurations than those of actual pumps and compressors. The project at CIT seems to lay more stress on the practical side than we intend, because the adopted impeller/casing configuration is similar to those of pumps for industrial application. The progress of CIT project was reported twice at the 1st and 2nd Workshop by Acosta et al. [ref. 2, 3].

---

* This study was supported by Grant in Aid for Scientific Research by the Ministry of Education, Technical Research Institute for Integrity of Structures at Elevated Service Temperatures and Hitachi, Ltd. Messrs. S. Yanagisawa, K. Tomita, J. Hanawa, K. Kawakami and C. Kato contributed to this study as their Master theses.

TEST FACILITY

The test pump is a single-stage, vertical shaft, centrifugal type. The mechanism of the forced whirling motion is illustrated schematically in fig. 1. The impeller is supported overhung by two self-alignment roller bearings, which are mounted separately on the upper and lower whirl plates. Fluid forces acting on the impeller are evaluated from the reaction force to the lower bearing. As seen from fig. 1, the outer race of the lower bearing is attached to the lower whirl plate by four load cells arranged with 90 degree angle difference (x- and y-direction).

Fig. 2 shows the relative arrangement of impeller and diffuser. In order to avoid the generation of steady lateral forces, the flow passage was designed to ensure axisymmetric flow by means of resistance screen at the diffuser exit and two symmetrically arranged discharge pipes for instance. Test was conducted mainly for vaneless diffuser. Additional test was also done for vaned diffuser with 2, 4 and 8 guide vanes, though the corresponding theory had not been established for comparison. Two impellers, A and B, with different vane angle were tested. The rotational speed of the impeller shaft was kept constant (8.8 Hz), while the whirl speed was varied widely from negative to positive whirl. Both pump and eccentric drive shafts were equipped with rotary encoders to detect phase angle. Principal specifications of test pump are listed in table 1.

DATA EVALUATION

Calibration

The load cells were calibrated dynamically by a rotating disc with known unbalance mass. The conversion factors (a = impeller force (N)/load cell output (V)) were determined for the x- and y-direction separately. The linearity of the cells was satisfactory and all cross terms, output of y-cells to x-directed force for instance, remained less than two percent of their principal terms.

Data Aquisition

Outputs of load cells were A/D converted and stored by sampling signals generated at every 10 degree on whirling orbit. For experiment to check the statistical character of the data, ensemble average and rms were evaluated from 512 sampled data at the same condition. In other cases 200 to 300 data were collected to give an ensemble average with intended confidence interval. In the experiment with vaned diffuser, samplings were made when the phase angle of whirl and impeller shaft, θ_1 and θ_2 (cf. fig. 4(a)), coincided simultaneously with the preset values.

Evaluation of Fluid Forces on Impeller Vanes

Since the theoretical results which are to be compared with the experiment, consider only fluid forces acting on the impeller vanes, and exclude all other forces on shroud, shaft, seal etc, it is necessary also in the experiment to extract pure vane force from the resultant reaction force measured at the lower bearing. For this purpose, four experiments were carried as shown in fig. 3, that is, experiments with whirling impeller in water and in air, and with whirling dummy rotor in water and in air.

The fluid force on the impeller vanes, $F(F_x, F_y)$, can be evaluated by the relation,

$$F = a\ (\ E_1 - E_2 - E_3 + E_4\ ) \qquad \text{.....(1)}$$

where $E_i(E_x, E_y)$ denotes load cell outputs in the above mentioned four sub-

experiments. The following interpretation will also help understand the meaning of eq. (1):

$a(E_1-E_2)$; fluid forces on whirling components submarged in water.

$a(E_3-E_4)$; fluid forces on whirling components submarged in water except vanes, i.e. those on shrouds, shaft and seal (see fig. 1).

The reaction of driving shaft torque on the lower bearing was calculated and the influence was compensated in the final evaluation of impeller force.

As seen from fig. 4 (a), fluid forces on whirling impeller are dependent of rotational speed ω, whirl speed Ω, eccentricity ε, phase angle of whirl θ_1 and rotation θ_2 and flow rate Q. The dependence on θ_2 disappers in vaneless diffuser.

Test Condition

The eccentricity was kept constant (ε = 1.5 mm), since linearity could be expected for such small displacement. From the rotordynamic consideration the whirl speed Ω corresponds to the first damped natural frequency in bending mode of the rotor (critical speed). Although most troubles associated with non-synchronous rotor vibration occur at supercritical rotational speed, $\Omega/\omega<1$, the test was done at whirl speed ratio Ω/ω up to 1.3 both for positive and negative whirl. Because impeller forces are sensitive to the operating condition of the impeller, discharge rate was varied from shutoff to maximum.

Presentation of Fluid Forces

Fluid forces F acting on the impeller vanes are divided into two components as illustrated in fig. 4 (b). The component normal to the orbit and directed outward is called radial force F_r, while the component parallel and opposite to the clockwise (positive) whirl is called tangential force F_θ. A negative sign means the direction is opposite to the above definition.

TEST RESULTS AND DISCUSSION

Pump Characteristics

The hydraulic performance of the test pump (impeller A and B) at steady operation is plotted in fig. 5 in non-dimensional form, in which flow coefficient ϕ and head coefficient ψ are defined by (see notation in table 1)

$$\phi = Q / 2\pi r_2 b u_2 , \quad u_2 = \omega r_2 \qquad \psi = H / (u_2^2/2g) \qquad \text{.....(2)}$$

Since impeller B has smaller exit vane angle than that of A, it has larger work input and hence higher head. Guide vanes have logarithmic spiral form and the vane angle is set to have no loading at design (shock-free) discharge of the impeller. Because of this design principle, the influence of guide vanes on the steady performance is not remarkable. Design flow coefficient, at which the relative inlet flow to the impeller vanes becomes shock-free, is denoted by ϕ_{sf}.

The machine Reynolds number of the test pump, $Re = u_2 d_2/\nu$, was about 3.4×10^6 in all test cases.

Character of Unsteady Fluid Forces

Fluid forces acting on whirling vanes, F, are evaluated from four forces obtained by four sub-experiments (see eq. (1)). The relative magnitude and direction of these four forces are illustrated in fig. 6 for a typical test condition (impeller A, $\phi=\phi_{sf}$, ε=2 mm, Ω/ω=0.83 and θ_1=0). F_2 and F_4 measured in air are caused by inertial centrifugal force and thus have only radial component.

The effort to reduce the mass of whirling components by using aluminum helped keep the level of fluid force substantially larger than that of inertia force.

Outputs of load cells oscillate primarily with the whirl speed Ω, but contain also fluctuations caused by mass unbalance of impeller, rolling noise of bearings, noise of measuring system, turbulence of flow and so on. From the preliminary studies, it became clear that the largest and predominant source of data scattering resulted from the fluctuation of flow field in impeller and diffuser. Fig. 7 illustrates Lissajous figures of overall impeller force, when impeller A rotates in water without whirling motion. As seen from fig. 7 (a), fluctuation of measured force is rather trivial at design, i.e. shock-free discharge condition. As the discharge decreases, the fluctuation gets larger and at shutoff the fluctuation becomes quite violent as seen from fig. 7 (b). The reason is obviously the separation and large scale turbulence of the flow in impeller. The fluctuation of measured force can therefore be attributed mostly to the inherent flow turbulence.

Fig. 8 shows fluid forces on whirling impeller vanes at 9 locations of the orbit (impeller A, ε=1.5 mm , vaneless dif.) for the combination of two flow rates (design and shutoff) and two whirl speed ratios (positive and negative). Each vector indicates ensemble average of 512 sampled data, while the magnitude of fluctuation is indicated by a circle with rms as its radius. Fluid forces are nearly axisymmetric and uniform on the orbit as they should be. It is worth to note, that especially near shutoff the fluctuation in rms can be severalfold as high as its average.

Fluid Forces on Whirling Impeller in Vaneless Diffuser

In spite of precautions to establish azimuthally symmetric flow, the ensemble averaged force vectors on the orbit were not completely uniform as seen from fig. 8. Since the influence of fluid forces on the dynamics of rotor is accumulative, the force components, F_r and F_θ, are hereafter averaged over one cycle of whirl angle θ_1 and shaft angle θ_2, and are denoted by $\overline{F}_r$ and $\overline{F}_\theta$. These forces are further normalized by the following definitions;

$$f_r = \overline{F}_r / M\varepsilon\omega^2, \qquad f_\theta = \overline{F}_\theta / M\varepsilon\omega^2 \qquad \text{.....(3)}$$

$$M = \rho\pi r_2^2 b$$

where ρ is the density of the working fluid and M is the mass of fluid displaced by the silhouette volume of impeller vanes.

Fig. 9 shows the dependence of f_r and f_θ on the whirl speed ratio Ω/ω from -1.3 to +1.3, when impeller A (β=68°) whirls with eccentricity ε=1.5 mm in vaneless diffuser and operates at five different flow rates from shutoff to maximum. The broken line in the figure indicates calculated result for shock-free entry condition ($\phi=\phi_{sf}$). Fig. 10 shows the corresponding result of impeller B (β=60°).

As to radial component followings can be observed: 1) The apparent mass of impellers A and B is about 0.9 and 0.7 times displaced fluid mass M, respectively, when it merely oscillates without rotation. Therefore, if there is no influence of pumping action on the fluid forces, f_r must be equal to $0.9\times(\Omega/\omega)^2$ for impeller A and $0.7\times(\Omega/\omega)^2$ for impeller B. The calculated f_r at shock-free entry agrees with this simple prediction quantitatively in positive whirl, but becomes almost twice as large as the prediction in negative whirl. It suggests that the pumping impeller in negative whirl has a certain flow mechanism to generate large radial force even in potential theory. 2) At design discharge, that is, shock-free entry condition, the measured radial forces agree with the theory well in tendency. In positive whirl quantitative agreement is fairly good, while in negative whirl the measurement is remarkably larger than the theory. 3) Radial force decreases as discharge decreases in positive whirl.

In negative whirl the tendency is quite opposite. 4) At and near $\Omega/\omega=1.0$, where the relative flow in impeller becomes stationary, radial force becomes negative at very low discharge. 5) At $\Omega/\omega=0$ (stationary displacement), rotating impeller produces positive radial force, that is, force to the direction of impeller displacement. This means that radial fluid force has negative-spring characteristics. 6) Impeller A has slightly larger radial force than that of impeller B.

As to tangential component: 1) Except a few test conditions, tangential forces are positive in positive whirl and negative in negative whirl. This indicates that fluid forces exert a damping effect on whirling impeller in most cases. 2) Negative tangential force emerges in positive whirl when the pump operates at very low discharge while rotating more than twice as fast as whirl speed ($\Omega/\omega<0.5$). In this condition the fluid force feeds energy to the whirling system and can cause a self-excited oscillation, a sort of impeller whip. 3) The agreement with theory is good in positive whirl. In negative whirl the measurement is again remarkably higher than the theory predicts. 4) In negative whirl larger damping can be expected than in positive whirl. 5) The influence of discharge rate on tangential component is generally small.

Influence of Guide Vanes on Rotor Stability

Since the radial clearance between impeller and guide vanes was chosen relatively large (11% of radius), the hydrodynamic interference of guide vanes to impeller vanes was so limited that the dependence of impeller force on the phase angle of impeller shaft, θ_2, was undetectably small. Consequently the installation of guide vanes resulted in little difference of the mean components of fluid forces from those given in fig. 9 and 10.

Guide vanes augmented the damping effect on the rotor stability to some extent. For the convenience of stability judgement, a new normalized parameter of tangential force is introduced as

$$f_\theta' = \overline{F}_\theta / M \varepsilon \Omega \omega \qquad \text{.....(4)}$$

According to this definition small f_θ at small whirl speed ratio Ω/ω can be enlarged by dividing by Ω. f_θ' has also the feature that it keeps positive throughout positive and negative whirl range, as far as the fluid force exerts damping effect. Fig. 11 shows f_θ' of impeller A at various flow rates, when it whirls in vaneless (no GV) and vaned diffuser with 2 and 8 guide vanes. In the case of vaneless diffuser, theoretical prediction for shock-free entry condition is also plotted by broken lines. From these figures it is evident that guide vanes reduce the range of whirl speed ratio with negative f_θ', thus resulting in increased damping on the whirling rotor.

Comparison with Theory by Vector Diagram

Fluid forces at shock-free entry condition are compared with the theoretical result [ref. 1] using vector diagrams as shown in fig. 12. Normalized force vectors are plotted with whirl speed ratio Ω/ω as their parameter on the curves. Theoretical and experimental curves coincide fairly well as a shape of curves but there is a considerable difference of the location of parameters. This difference could be caused either by the viscous effect neglected in this theory or by unaware factors hidden in the test setup and instrumentation.

CONVERSION TO MATRIX ELEMENTS

In the analysis of rotor dynamics it is convenient to express fluid forces in terms which are proportional to the displacement, velocity and acceleration of impeller center. As illustrated in fig. 4 (a), the location of impeller

center O(x, y) is expressed by the absolute coordinate system with its origin at the whirl center O'. Denoting x- and y-components of fluid forces by F_x and F_y, they are expressed in the following linear form;

$$\begin{bmatrix} F_x \\ F_y \end{bmatrix} = -\underset{\text{mass}}{\begin{bmatrix} m_{xx} & m_{xy} \\ m_{yx} & m_{yy} \end{bmatrix}} \begin{bmatrix} \ddot{x} \\ \ddot{y} \end{bmatrix} - \underset{\text{damping}}{\begin{bmatrix} b_{xx} & b_{xy} \\ b_{yx} & b_{yy} \end{bmatrix}} \begin{bmatrix} \dot{x} \\ \dot{y} \end{bmatrix} - \underset{\text{stiffness}}{\begin{bmatrix} k_{xx} & k_{xy} \\ k_{yx} & k_{yy} \end{bmatrix}} \begin{bmatrix} x \\ y \end{bmatrix} \quad \text{.....(5)}$$

where $x = \varepsilon \cos\theta_1$, $y = \varepsilon \sin\theta_1$ and $\theta_1 = -\Omega t$.

Because the measured fluid forces are non-linear with respect to location, velocity and acceleration of impeller center, it is impossible to determine the above matrix elements in an exact meaning. However, if the fluid forces are axisymmetric on the whirling orbit (independent of θ_1), and can be approximated by the equations

$$F_r(\varepsilon, \Omega) = \varepsilon (F_{r0} + F_{r1}\Omega + F_{r2}\Omega^2) \quad \text{.....(6)}$$

$$F_\theta(\varepsilon, \Omega) = \varepsilon (F_{\theta 0} + F_{\theta 1}\Omega + F_{\theta 2}\Omega^2)$$

the matrix elements can be related to the above terms as;

$$\begin{aligned} m_{xx} &= m_{yy} = F_{r2}, \quad m_{xy} = -m_{yx} = -F_{\theta 2} \\ b_{xx} &= b_{yy} = F_{\theta 1}, \quad b_{xy} = -b_{yx} = F_{r1} \\ k_{xx} &= k_{yy} = -F_{r0}, \quad k_{xy} = -k_{yx} = F_{\theta 0} \end{aligned} \quad \text{.....(7)}$$

The fitting of measured data to eq. (6) can be performed by applying the method of least squares.

Fig. 13 shows the fitted curve of impeller A at shock-free condition. The fitting was made for all data in positive and negative whirl, $-1.3<\Omega/\omega<+1.3$. Since the real fluid forces are non-linear, the fitted curve cannot represent the measured data satisfactorily in the whole whirl speed ratio. Especially the delicate change of fluid forces near $\Omega/\omega = 1$ is neglected in the fitting completely. The quality of fitting deteriorates gradually as flow rate decreases and the flow in impeller deviates from shock-free condition.

Fig. 14 illustrates the fitted curves of impeller A in vaneless diffuser at various flow rates. As seen from the figure tangential force f_θ changes almost linearly with whirl speed ratio. This indicates that cross mass term $m_{xy}=-m_{yx}$ is insignificant. The feature of radial force f_r consists in the fact that it is parabolic in general but the minimum takes place around $\Omega/\omega=0.4$. This result infers that cross damping term $b_{xy}=-b_{yx}$ plays an important role.

In table 2 and 3 matrix elements of impeller A and B in vaneless diffuser are listed for various flow rates. All values are normalized by the quantities given in the tables.

CONCLUSION

Fluid forces acting on two-dimensional centrifugal impeller whirling in vaneless and vaned diffuser were measured and compared with the corresponding theoretical results. Principal findings from two tested impellers are:

1) Fluid forces have tangential components to damp whirling motion of the rotating shaft in most operating condition.

2) At low flow rate near shutoff and low whirl speed ratio, i.e. at high supercritical rotational speed, there are possibilities that the fluid forces do exert negative damping to the rotor in positive whirl, a sort of impeller whip.
3) Theoretical calculation can predict fluid forces qualitatively. Quantitative agreement can be obtained in positive whirl.
4) Fluid forces are expressed as elements of mass, damping and stiffness matrices by assuming linear relation.

This study will be extended further to the cases in which impeller whirls in a volute casing. The 2nd generation test rig with improved whirling mechanism, instrumentation and versatile applicability is under construction.

LITERATURES

1. Shoji, H. and Ohashi, H., "Fluid Forces on Rotating Centrifugal Impeller with Whirling Motion," NASA Conference Publication 2133, 1980, p. 317-328.
2. Brennen, C.E., Acosta, A.J. and Caughey, T.K., "A Test Program to Measure Fluid Mechanical Whirl-Excitation Forces in Centrifugal Pumps," NASA CP 2133, 1980, p. 229-235.
3. Chamieh, D.S. et al, "Experimental Measurements of Hydrodynamic Stiffness Matrices for a Centrifugal Pump Impeller," NASA CP 2250, 1982, p. 382-398.

Table 1 Principal specifications

Impeller	Two-dimensional, closed type
outer diameter $d_2=2r_2$	350 mm
inner diameter	175 mm
vane width b	35 mm
suction diameter	160 mm
number of vanes	6
vane angle to radius β	68° for impeller A
(logarithmic spiral)	60° for impeller B
mass	4.1 kg
Vaneless diffuser	Parallel walled
exit diameter	700 mm
screen	40 mesh per inch, 51% opening
width	70 mm
Vaned diffuser	Logarithmic spiral, 5 mm thickness
inner diameter	390 mm
	(20 mm radial clearance)
outer diameter	600 mm
width	60 mm
number of vanes	2, 4 and 8
vane angle to radius	75.5°
Test condition	
rotational speed ω	525 rpm
whirl speed Ω	-683 to +683 rpm
eccentricity ε	variable, mainly 1.5 mm
shock-free flow rate	2.25 m^3/min for impeller A
	3.21 m^3/min for impeller B

Table 2 Matrix elements of impeller A

matrix element	m_{xx}, m_{yy}	m_{xy},$-m_{yx}$	b_{xx}, b_{yy}	b_{xy},$-b_{yx}$	k_{xx}, k_{yy}	k_{xy},$-k_{yx}$
normalized by	$\pi\rho r_2^2 b$		$\pi\rho r_2^2 b\omega$		$\pi\rho r_2^2 b\omega^2$	
ϕ = 0	1.64	0.27	1.14	-2.02	-0.55	-0.13
0.2 ϕ_{sf}	1.72	0.35	1.10	-2.01	-0.55	-0.17
0.6 ϕ_{sf}	1.87	0.32	1.08	-1.88	-0.56	-0.10
ϕ_{sf}	1.86	0.27	0.98	-1.33	-0.42	0.09
1.3 ϕ_{sf}	1.82	0.23	1.09	-1.01	-0.43	0.08

Table 3 Matrix elements of impeller B

matrix element	m_{xx}, m_{yy}	m_{xy},$-m_{yx}$	b_{xx}, b_{yy}	b_{xy},$-b_{yx}$	k_{xx}, k_{yy}	k_{xy},$-k_{yx}$
normalized by	$\pi\rho r_2^2 b$		$\pi\rho r_2^2 b\omega$		$\pi\rho r_2^2 b\omega^2$	
ϕ = 0	1.30	0.21	0.98	-1.98	-0.58	-0.12
0.2 ϕ_{sf}	1.32	0.33	0.94	-1.96	-0.57	-0.17
0.6 ϕ_{sf}	1.26	0.20	1.06	-1.80	-0.43	-0.13
ϕ_{sf}	1.34	0.19	1.01	-1.62	-0.39	-0.05
1.3 ϕ_{sf}	1.32	0.05	1.00	-1.35	-0.35	0.01

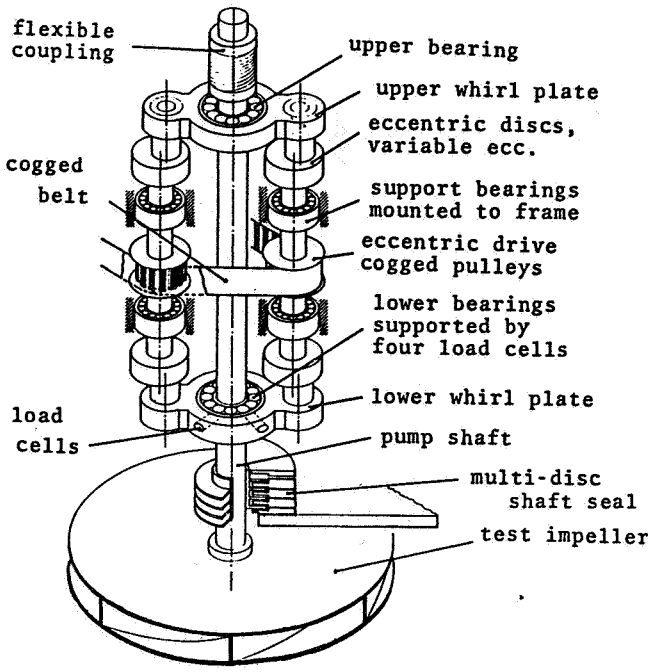

Fig. 1 Whirling mechanism

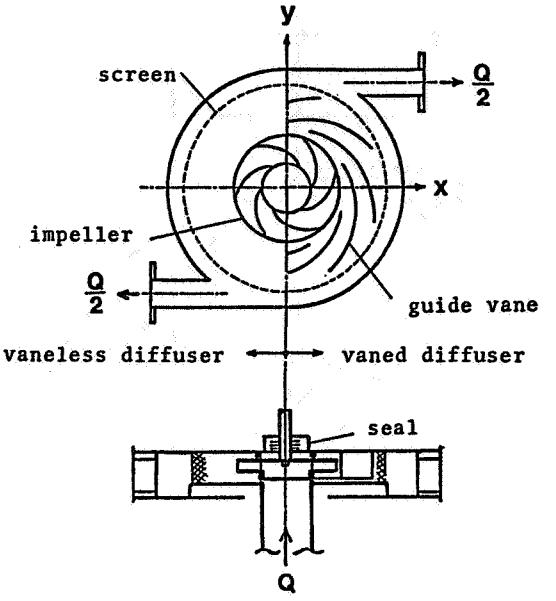

Fig. 2 Configuration of impeller and diffuser

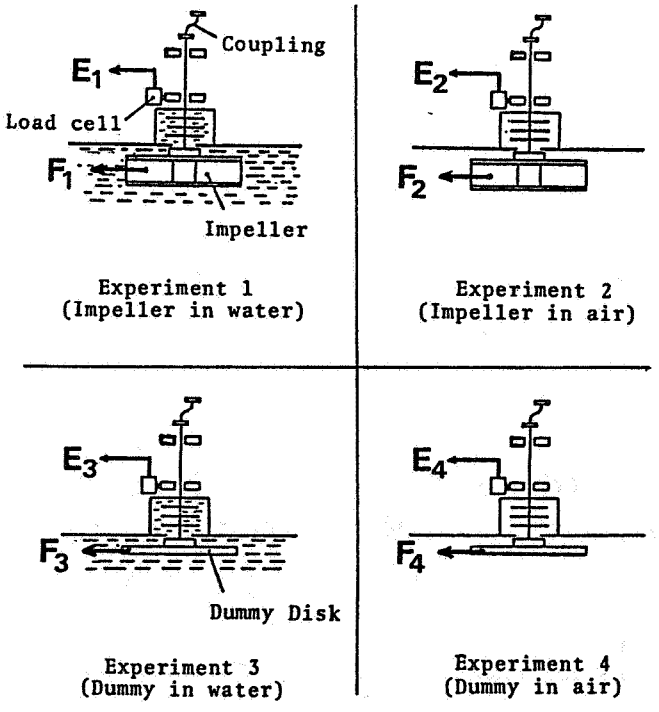

Fig. 3 Four sub-experiments

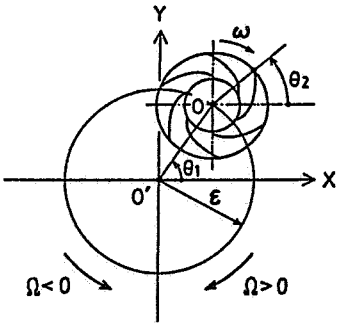

(a) Coordinates

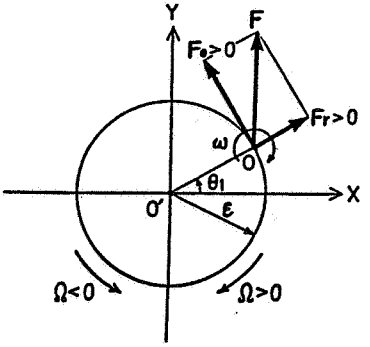

(b) Force vector

Fig. 4 Notations

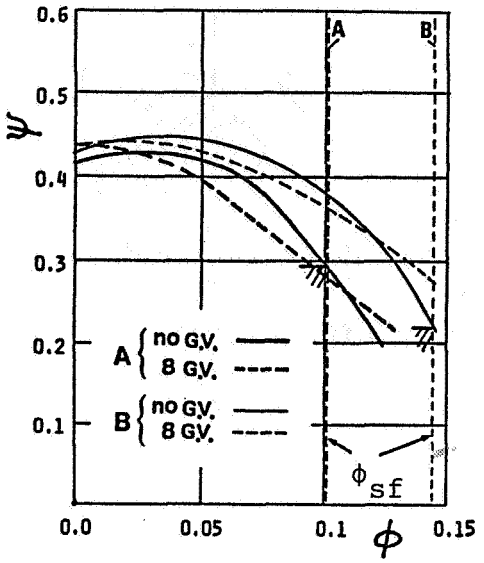

Fig. 5 Characteristics of test pumps

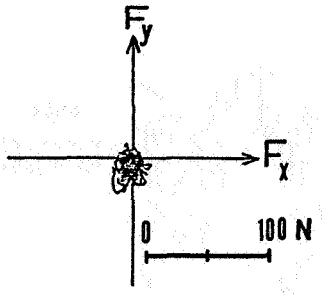

(a) $\phi = \phi_{sf}$

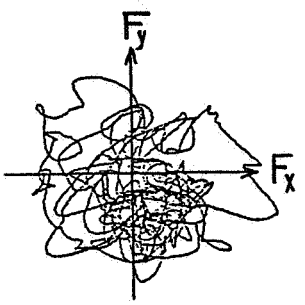

(b) $\phi = 0$

Fig. 7 Time histories of fluid force vector

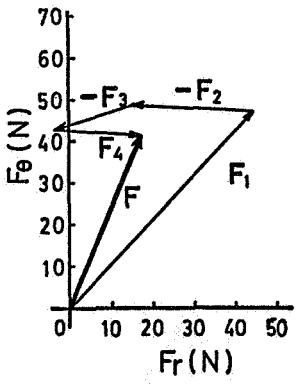

Fig. 6 Relative disposition of force vectors

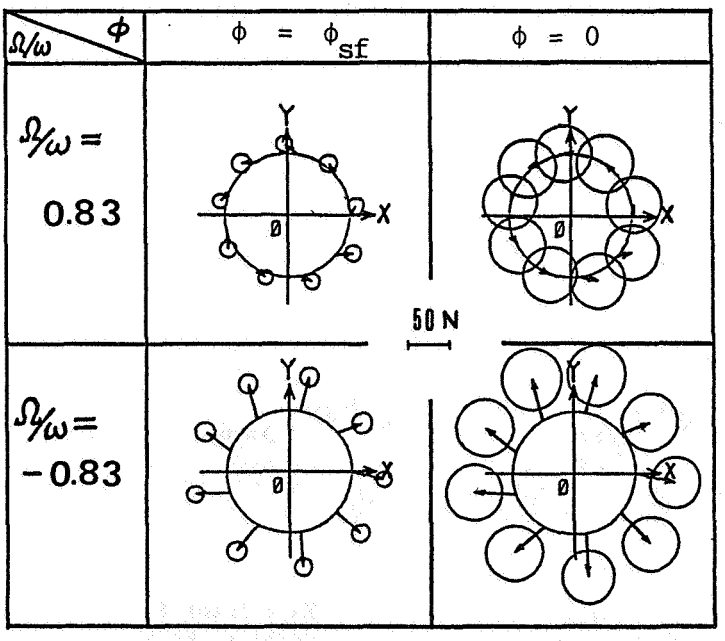

Fig. 8 Ensemble averaged fluid forces and their fluctuation

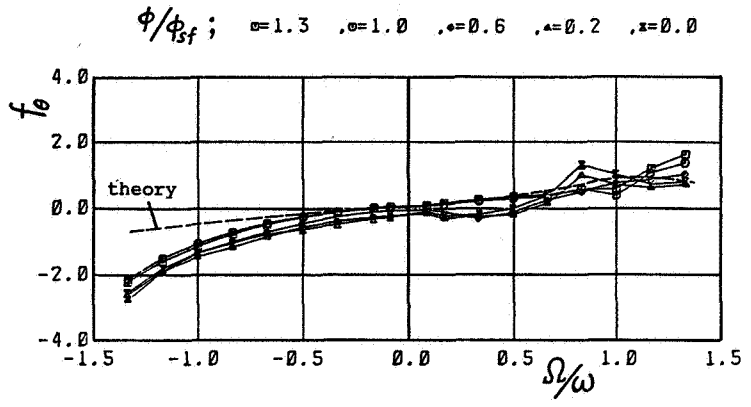

(a) Tangential component

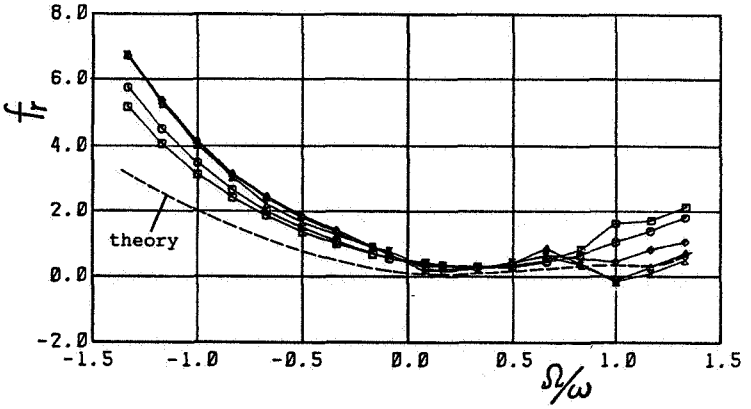

(b) Radial component

Fig. 9 Normalized fluid forces of impeller A in vaneless diffuser.

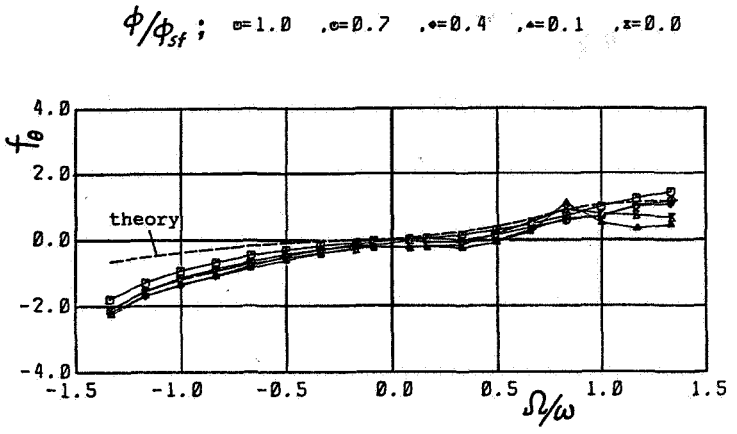

(a) Tangential component

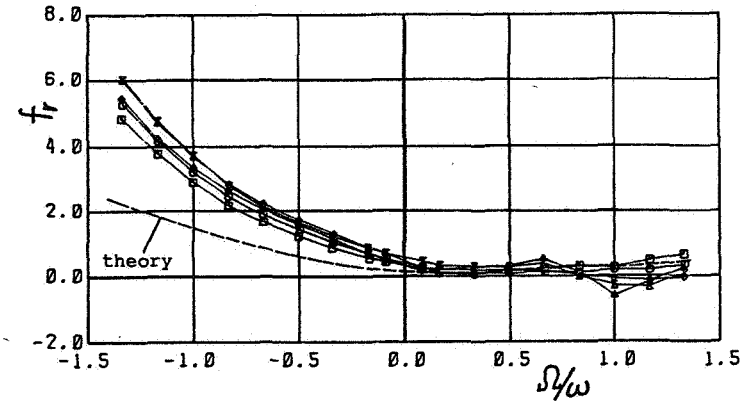

(b) Radial component

Fig. 10 Normalized fluid forces of impeller B in vaneless diffuser.

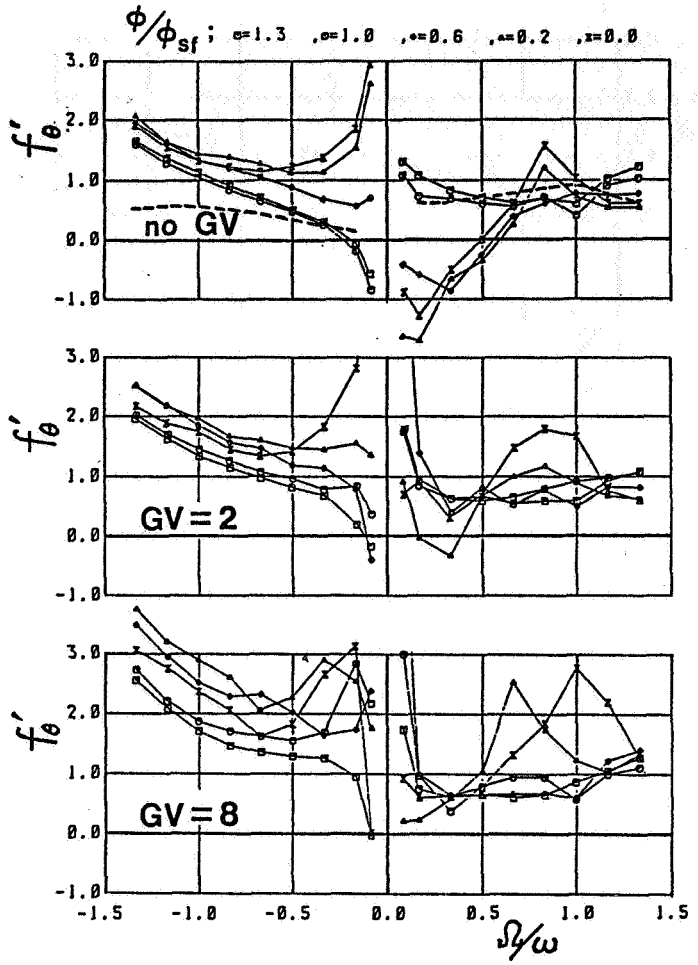

Fig.11 Effect of guide vanes on rotor stability, impeller A

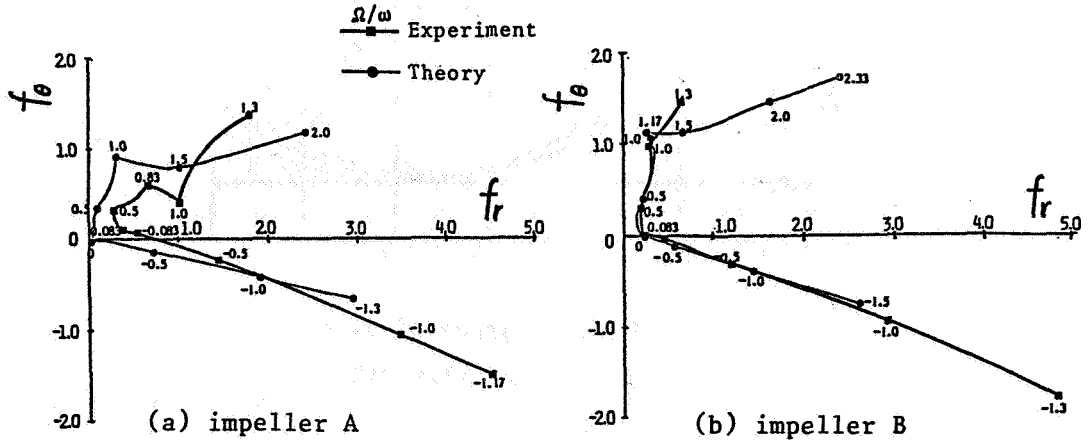

Fig. 12 Comparison between theory and experiment at shock-free entry

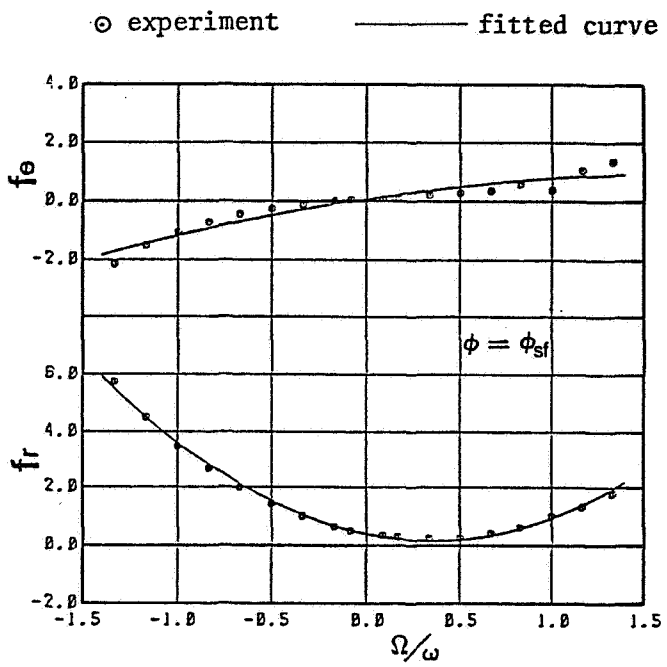

Fig. 13 Measured data and fitted curves of impeller A at shock-free entry

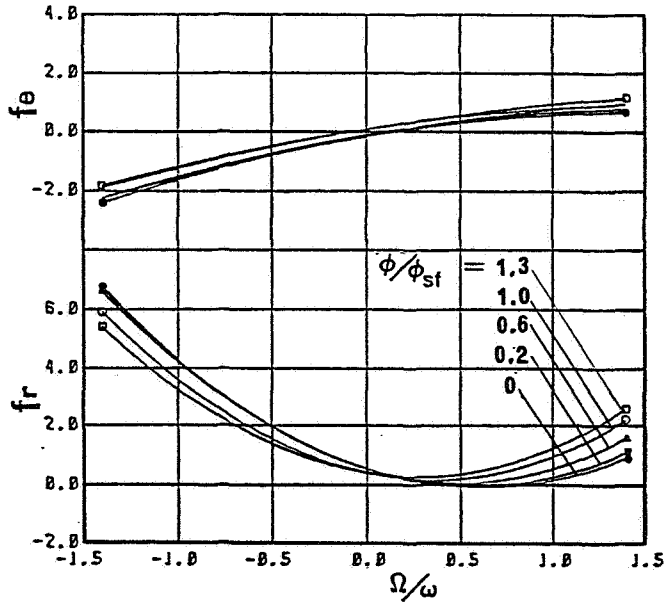

Fig. 14 Fitted curves of impeller A at various flow rate

HYDRAULIC FORCES ON A CENTRIFUGAL IMPELLER

UNDERGOING SYNCHRONOUS WHIRL*

Paul E. Allaire
University of Virginia
Charlottesville, Virginia 22901

Cheryl J. Sato
BE&K Engineering Company
Birmingham, Alabama 35243

Lyle A. Branagan
Pacific Gas and Electric Company
San Ramon, California 94583

High speed centrifugal rotating machinery can have large vibrations caused by aerodynamic forces on impellers. This work develops a method of calculating forces in a two dimensional orbitting impeller in an unbounded fluid with non-uniform entering flow. A finite element model of the full impeller is employed to solve the inviscid flow equations. Five forces acting on the impeller are included: Coriolis forces, centripetal forces, changes in linear momentum, changes in pressure due to rotation and pressure changes due to linear momentum. Both principal and cross-coupled stiffness coefficients are calculated for the impeller. Agreement with experimental results is fair.

NOMENCLATURE

A_3	Impeller discharge area, $A_3 = 2\pi R_{3b}$
b	Impeller thickness
F	Force
F_{xx}	Principal force
F_{yx}	Cross-coupling force
K	Stiffness
K_{xx}	Principal stiffness
K_{yx}	Cross-coupled stiffness
$\overline{K_{xx}}$	Dimensionless principal stiffness
$\overline{K_{yx}}$	Dimensionless cross-coupled stiffness
P	Pressure
Q	Flow rate
r	radius
R_1	Inner radius of inner flow region
R_2	Inner radius of impeller
R_3	Outer radius of impeller
R_4	Outer radius of outer flow region
U_3	Impeller tip speed, $U_3 = \Omega R_3$
$\vec{V}$	Particle velocity in reference frame
Δx	Displacement in positive x-direction
Δy	Displacement in positive y-direction

*This work was funded in part by NASA Contract NAG 3-180.

β	Blade angle
Γ	Circulation
ε	Eccentricity
θ	Angle with respect to the x-axis
θ_c	Unknown angle approximated by the blade sweep angle
θ_s	Blade sweep angle
ρ	Density of fluid
ϕ	Velocity potential
ψ	Stream function
$\overline{\psi}$	Dimensionless stream function
Ω	Rotor rotation speed

INTRODUCTION

Vibration problems in turbomachinery such as the U.S. Space Shuttle turbopumps (ref. 1) are an important issue in industry. Considerable efforts have been made to understand their causes and prevent catastrophic failure. Modifications in the bearings, dampers and seals (ref. 1,2) in a given machine can often alleviate such problems, but are not always effective. Because relatively little is known about the influence of an impeller on vibrations, it is of interest to investigate impeller force levels in attempts to further understand and reduce vibration problems.

It is known that fluid forces act on an impeller during operation and often initiate serious vibration problems, but they are not easy to calculate. Initially, the impeller may be displaced due to residual unbalances or other causes. Impeller forces then arise both parallel to and perpendicular to the direction of displacement. They are known as hydraulic or aerodynamic forces. This phenomenon can be additive, such that a small perturbation can eventually result in large vibrations and possible shaft failure. Several works concerning rotor dynamics and flow in impellers have been published, but relatively few papers have dealt with the calculation of aerodynamic forces on impellers.

A study of aerodynamic forces on centrifugal impellers, published by Colding-Jorgensen (ref. 3), involved calculating the impeller force caused by rotor eccentricity along with the associated stiffness and damping coefficients. The final objective was to determine the effect of this force on rotor stability. Two-dimensional potential flow was used, representing the impeller by a source-vortex point. The diffuser was modelled by a distribution of vortices and the flow field was solved by the singularity method. The velocity induced by the singularity distribution on the diffuser was considered to be a parallel stream; thus, the impeller force was obtained by relating the impeller to a body with circulation, influenced by a source, and in a parallel stream, and using the theorems of Joukowski and Lagally.

Shoji and Ohashi (ref. 4) calculated fluid forces on a centrifugal impeller using unsteady potential theory. Incompressible, two-dimensional flow was assumed and the rotating axis whirled at constant speed. Other assumptions included shockless entry at the leading edges of the blades and the Kutta condition at the trailing edges. Free vortices were assumed to be shed from the trailing edges and carried downstream with steady velocities along steady streamlines, and blade thickness was neglected. The forces acting on the impeller were calculated by integrating the pressure distribution on the blades.

Recently, Imaichi, Tsujimoto and Yoshida (ref. 5) analyzed unsteady torque on a two-dimensional radial impeller using singularity methods. They recognized that studies of unsteady flow were necessary for prediction of unsteady forces on an impeller but unsteady torque was examined because it was one of the most typical unsteady characteristics of impellers. It was shown that unsteady torque could be divided into three components: quasisteady, apparent mass, and wake. The wake component was usually found to be the smallest quantity. Approximations of fluctuating torque were made using apparent mass coefficients for various blade angles, blade numbers and diameter ratios of logarithmic impellers.

Iino's work (ref. 6) dealt with potential interaction between a centrifugal impeller and a vaned diffuser. The dynamic load on the impeller blades due to this interaction was examined. Unsteady flow was analyzed using the method of singularities assuming two-dimensional, potential flow and infinitely thin blades. The unsteady Bernoulli equation for a rotating coordinate system was used to solve for the unsteady pressures. Pressure distributions were examined for various impeller configurations. Load distribution on diffuser blades was related to pressure fluctuations; the dynamic load on impeller blades was affected by consideration of this load distribution.

An unbounded eccentric centrifugal impeller with an infinite number of logarithmic spiral blades was considered by Allaire et al. (ref. 7). A simple kinematic analysis of flow in the impeller was carried out and impeller stiffnesses calculated. Fire forces acting on the eccentric impeller were identified: Coriolis forces, centripetal forces, changes in linear momentum, changes in pressure due to rotation and pressure changes due to linear momentum.

In addition to theoretical studies of forces on impellers, some work has been done experimentally. A paper on experimental measurement was presented by Uchida, Imaichi and Shirai (ref. 8). They measured radial forces on a centrifugal pump with a volute and examined the effect of the cross-sectional area and shape of the volute tongue on the force. The dynamic component of force and the effect of cavitation on the force were also investigated.

Research by Kanki, Kawata and Kawatani (ref. 9) also involved experimentally measuring forces on a centrifugal pump impeller. They specifically measured hydraulic radial forces on impellers with double volutes or vaned diffusers. Both static and dynamic loads were measured with varying flow rates.

Chamieh et al. (ref. 10) measured hydrodynamic stiffnesses experimentally for a centrifugal pump impeller with a volute. Forces on the impeller were measured as the center of rotation was orbited for low frequencies. Pressure distributions around the volute were obtained and static pressure forces were measured, providing a more complete force analysis.

This paper examines centrifugal impellers and develops a method of calculating the forces induced by eccentric operation. The analysis is done in a rotating reference frame and considers a two-dimensional, unbounded impeller with synchronous motion. Incompressible, potential flow is assumed. The analysis utilizes the finite element method to solve for the flow field. A control volume formulation is used to calculate the forces acting on the shaft of an eccentric impeller. Stiffnesses are computed for different impeller designs. Plots of the finite element meshes as well as corresponding streamline plots are included, along with velocity profiles and graphs of stiffnesses versus blade number and blade angle.

METHOD OF ANALYSIS

The two dimensional impeller region is divided into three regions: inlet region, blade region, and outlet region. Figure 1 shows the three regions with one blade for illustration purposes. Potential flow is assumed in the analysis with the radial flow calculated using a velocity potential and the tangential flow calculated using a stream function (ref. 11,12). Both ϕ and ψ satisfy Laplace's equation

$$\nabla^2\phi = 0 \tag{1}$$

$$\nabla^2\psi = 0 \tag{2}$$

in the region between R_1 and R_4.

Two cases are considered - impeller centered and impeller eccentric. In the first case, the impeller blades are centered in the coordinate system. The flow through each blade passage is the same. For the second case, the inlet flow is assumed centered at the origin while the impeller is physically moved the distance ε along the x axis (in the relative coordinate system). Thus the flow through the passages on the positive x axis side is smaller than the flow through those on the negative x axis side. A typical value of $\varepsilon_1/R_2 = 0.0025$ was used. It was found that varying ε_1/R_2 from 0.01 to 0.00125 changed the calculated stiffness by less than 10%.

For the radial flow, the boundary condition at the inlet is that due to a source at the origin

$$\left.\frac{\partial\phi}{\partial n}\right|_{r=R_1} = \frac{Q}{2\pi R_1 b} \tag{3}$$

and no flow is allowed through the blades

$$\left.\frac{\partial\phi}{\partial n}\right|_{\text{Blade}} = 0 \tag{4}$$

If the shaft is centered, the outlet boundary condition is

$$\left.\frac{\partial\phi}{\partial n}\right|_{r=R_4} = \frac{Q}{2\pi R_4 b} \tag{5}$$

In the case of an eccentric shaft, the exit flow cannot be uniform around the impeller. It is assumed to depend upon the angle θ with the form (ref. 13)

$$\left.\frac{\partial\phi}{\partial n}\right|_{r=R_4} = \frac{Q}{2\rho R_4 b}\left[1 - \frac{\varepsilon_4}{R_4}\right]\cos(\theta-\theta_c) \tag{6}$$

where θ_c is the approximate sweep angle. It was found that varying the sweep angle by $\pm$ 10 degrees changed the stiffnesses by approximately 1% or less.

With tangential flow, the boundary conditions at the inner and outer radii are

$$\psi|_{r=R_1} = -\frac{\Gamma}{2\pi}\ln R_1$$

$$\psi|_{r=R_4} = -\frac{\Gamma}{2\pi}\ln R_4$$

However, for vortex flow representing an impeller with angular velocity Ω, the value for Γ is

$$\Gamma = -2\pi\Omega R_2^2$$

The boundary conditions become

$$\psi|_{r=R_1} = \Omega R_2^2 \ln R_1 \tag{7}$$

$$\psi|_{r=R_4} = \Omega R_2^2 \ln R_4 \tag{8}$$

Along the blade, the stream function is an unknown constant.

$$\psi|_{\text{Blade}} = \text{Constant} \tag{9}$$

The constant is evaluated when the total flow, due to the superposition of radial and tangential flow, satisfies the Kutta condition at the trailing edge of all blades. A Newton-Raphson iteration process is used to obtain values of stream function on the blades. In the centered case, the stream function over all of the blades is the same while it varies for the eccentric case.

Finite elements (ref. 14,15) were used to solve Laplace's equation for both the radial and tangential flow. A typical mesh is shown in Figure 2. Because of the large number of nodes, a profile solver (ref. 14) was required. Finite width blades were included in the analysis.

FORCES AND STIFFNESS

The net surface force on the control volume (analysis region) is (ref. 16)

$$\vec{F}_s = \int_{CV} \left[2\vec{\Omega} \times \vec{V} + \vec{\Omega} \times (\vec{\Omega} \times \vec{r}) \right] \rho \, d\forall + \int_{CS} \vec{V} \; \rho \vec{V} \cdot d\vec{A} \tag{10}$$

The surface forces are composed of the pressure forces on the control volume ($\vec{F}_p$) and the forces of the shaft on the control volume ($\vec{F}_{SHAFT}$). Thus,

$$\vec{F}_s = \vec{F}_{SHAFT} + \vec{F}_p$$

From the Bernoulli equation for a rotating reference frame:

$$\frac{P}{\rho} - \frac{1}{2} |\vec{\Omega} \times \vec{r}|^2 + \frac{1}{2} |\vec{V}|^2 = \text{constant} \tag{11}$$

This can be solved for pressure and integrated over the control surface:

$$\int_{CS} P \, dA = \int_{CS} \left\{ \frac{\rho}{2} \left[|\vec{\Omega} \times \vec{r}|^2 - |\vec{V}|^2 \right] + \text{constant} \right\} d\vec{A} \tag{12}$$

The forces due to pressure are expressed as:

$$\vec{F}_p = -\int P \, d\vec{A} \tag{13}$$

since the force vector is opposite the area vector.

The force on the shaft due to control volume is

$$\begin{aligned}
\vec{F}_{\substack{ON \\ SHAFT}} &= -\vec{F}_{SHAFT} = \vec{F}_p - \vec{F}_s \\
\vec{F}_{\substack{ON \\ SHAFT}} &= -\int_{cs} \frac{\rho}{2} \left[|\vec{\Omega} \times \vec{r}|^2 - |\vec{V}|^2 \right] d\vec{A} \\
&\quad - \int_{cv} \left[2\vec{\Omega} \times \vec{V} + \vec{\Omega} \times (\vec{\Omega} \times \vec{r}) \right] \rho d\forall \\
&\quad - \int_{cs} \vec{V} \; \rho \vec{V} \cdot d\vec{A}
\end{aligned} \tag{14}$$

The five components of this force are:

1. $-\int_{cv} \rho (2 \vec{\Omega} \times \vec{V}) \, d\forall$ — Coriolis force

2. $-\int_{cv} \rho \, \vec{\Omega} \times (\vec{\Omega} \times \vec{r}) \, d\forall$ — Centripetal force

3. $-\int_{cs} \vec{V} \; \rho \vec{V} \cdot d\vec{A}$ — Force due to change in linear momentum

4. $-\int_{cs} \frac{\rho}{2} |\vec{\Omega} \times \vec{r}|^2 \, d\vec{A}$ — Force due to change in pressure due to rotation

5. $\int_{cs} \frac{\rho}{2} |\vec{V}|^2 \, d\vec{A}$ — Force due to change in pressure due to change in linear momentum

For the finite element analysis, the integral expressions are used in summation form.

Stiffness is defined as the negative of the change in force divided by the change in displacement, or:

$$K = -\frac{\Delta F}{\Delta x}$$

In this analysis, principal (K_{xx}) and cross-coupled (K_{yx}) stiffnesses are calculated, where:

$$K_{xx} = -\frac{\Delta F_x}{\Delta x} \qquad K_{yx} = -\frac{\Delta F_y}{\Delta x} \tag{15}$$

Also it is assumed here due to symmetry that the other two stiffness coefficients are given by

$$K_{xy} = -\frac{\Delta F_x}{\Delta y} = -K_{yx} \qquad K_{yy} = -\frac{\Delta F_y}{\Delta y} = K_{xx} \tag{16}$$

The impeller is displaced in the positive x-direction and the rotation is positive in the counterclockwise direction. A positive force F_x aggravates x displacements whereas a negative force resists x displacements. Thus, positive principal stiffness K_{xx}, which indicates a restoring force, is desirable. The cross-coupled force should oppose motion (for a shaft forward whirl mode) to promote rotor stability. Thus F_y should be negative and the cross-coupled stiffness K_{yx} should be positive for stabilizing effects in forward whirl.

Generally it is desired to use the calculations discussed here for rotor dynamics analysis. The stiffness is more useful than the force so stiffnesses are presented in the results section. Dimensionless stiffnesses have the form

$$\overline{K}_{ij} = \frac{K_{ij} R_3}{\frac{1}{2}\rho A_3 U_3}$$

in the next section.

RESULTS

Twelve different cases typical of pump impeller geometries were run. Table 1 gives the geometric properties. Quantities varied were number of blades, blade angle, radius ratios, and blade thickness. In each case, the following rotor parameters were held constant

ω = 600 rpm
b = 0.5 inches
ρ = 0.0361 lbm/in^3

A finite element mesh was generated for each case.

Once velocities were determined at all of the finite element node points, Eq. (14) was used to evaluate the forces acting on the impeller control volume. It should be noted that these forces calculated for the centered impeller were not zero due to the numerical averaging. However, the change in force calculated for the eccentric impeller is two to four orders of magnitude larger than the centered force. The five components of force for each case are not given here due to lack of space. They are presented in ref. (12).

The analysis described in Section 2 was carried out for the twelve cases. Table 2 presents the calculated values of dimensionless blade stream function for each blade. Here the stream function is made dimensionless via

$$\bar{\psi} = \frac{\psi}{R_3 U_3}$$

It can be seen that an eccentricity of the order of 0.001 produces changes in the blade stream function of the order of 0.001 as well.

A comparison between the theory and two experimental results can be presented. Case 4 is chosen as the closest to the test impellers of Uchida (8) and Kanki (9). Uchida employed a single volute while Kanki used a double volute. The dimensionless forces are

F_{radial}	
0.00187	Uchida, et. al. (8)
0.00122	Kanki, et. al. (9)
0.001023	Theory, Case 4

The agreement with Kanki's results is within 20%.

Table 3 gives the dimensionless principal and cross-coupled stiffnesses as determined by the finite element analysis. In all cases, the principal stiffness is negative while the cross-coupled stiffness is positive. Several patterns emerge from the series of cases run.

Cases 1 and 7-11 indicate the effect of varying blade angle β. Figure 3 indicates the stiffness variation with blade angle. The magnitude of the principal stiffness decreases strongly with increasing blade angle. However, the magnitude of the cross-coupled stiffness does not seem to be a strong function of blade angle.

The effect of number of blades can be seen in cases 1, 4, 5. Figure 4 plots the results. The magnitude of the principal coefficient increases somewhat with number of blades but, again, the magnitude of the cross-coupled stiffness does not seem to be a strong function of the number of blades.

Cases 1 and 12 indicated the effect of impeller inner to outer radius (R_3/R_2). This produced the largest change in the cross coupling stiffness. The values are

Case	R_3/R_2	$\bar{K}_{xx}$	$\bar{K}_{yx}$
1	2.0	- 0.3529	0.6057
12	3.0	- 0.1047	0.0728

Also, the effect of the other radius ratios R_1/R_2 and R_4/R_2 can be seen from cases 2,5 and 5,3 respectively. Blade thickness (cases 1,6) did not have a strong effect.

The calculated dimensionless stiffnesses can be compared to the measured values by Chamieh et. al. (10). The results are (using the sign convention for stiffness normal to rotor dynamics as defined in Section 3)

$\bar{K}_{xx}$	$\bar{K}_{yx}$	
- 2.0	- 0.9	Chamieh et. al. (10)
- 0.2987	0.6922	Case 3

The principal terms have the same sign but differ by an order of magnitude. The cross-coupled terms have the same order of magnitude but different sign.

CONCLUSIONS

This study investigates the effect of non-uniform inlet flow in two dimensional eccentric unbounded impellers. A comparison of the calculated radial force to available experimental results indicates reasonably good agreement. It seems safe to conclude that non-uniform inlet flow is an important factor in hydraulic force calculations with applications to rotor dynamics.

Comparisons of the theoretical stiffnesses to measured values are less good. Perhaps this indicates that other effects not modeled here are equally important. These are likely to include three dimensional effects, viscous effects, and volute (or diffuser) effects.

REFERENCES

1. Ek, M. C.: Solution of the Subsynchronous Whirl Problem in the High Pressure Hydrogen Turbomachinery of the Space Shuttle Main Engine. AIAA/SAE 14th Joint Propulsion Conference, Paper 78-1002, July 1978.

2. Allaire, P. E., Lee, C. C. and Gunter, E. J.: Dynamics of Short Eccentric Plain Seals with High Axial Reynolds Number. Journal of Spacecraft and Rockets, Vol. 15, No. 10, November 1978.

3. Colding-Jorgensen, J.: Effect of Fluid Forces on Rotor Stability of Centrifugal Compressors and Pumps. Proceedings of NASA/ARO Workshop on Rotordynamic Instability Problems in High-Performance Turbomachinery, NASA CP-2133, 1980, pp. 249-265.

4. Shoji, H. and Ohashi, H.: Fluid Forces on Rotating Centrifugal Impeller with Whirling Motion. Proceedings of NASA/ARO Workshop on Rotordynamic Instability Problems in High-Performance Turbomachinery, NASA CP-2133, 1980, pp. 317-328.

5. Imaichi, K., Tsujimoto, Y., and Yoshida, Y.: An Analysis of Unsteady Torque on a Two-Dimensional Radial Impeller. ASME Winter Annual Meeting, Washington, D.C., November 1981.

6. Iino, T.: Potential Interaction Between a Centrifugal Impeller and a Vaned Diffuser. ASME Winter Annual Meeting, Fluid-Structure Interactions in Turbomachinery, November 1981, pp. 63-69.

7. Allaire, P. E., Branagan, L. A., and Kocur, J. A.: Aerodynamic Stiffness of an Unbounded Eccentric Whirling Centrifugal Impeller with an Infinite Number of Blades. Proceedings of NASA/ARO Workshop on Rotordynamic Instability Problems in High Performance Turbomachinery, NASA CP-2250, 1982, pp. 323-343.

8. Uchida, N., Imaichi, K., and Shirai, T.: Radial Force on the Impeller of a Centrifugal Pump. Bulletin of the JSME, Vol. 14, No. 76, 1971, pp. 1106-1117.

9. Kanki, H., Kawata, Y., and Kawatani, T.: Experimental Research on the Hydraulic Excitation Force on the Pump Shaft. ASME paper no. B1-DET-71.

10. Chamieh, D. S., Acosta, A. J., Brennen, C. E., Caughey, T. K., and Franz, R.: Experimental Measurements of Hydrodynamic Stiffness Matrices for a Centrifugal Pump Impeller. Proceedings of NASA/ARO Workshop on Rotordynamic Instability Problems in High-Performance Turbomachinery, NASA CP-2250, 1982, pp. 382-398.

11. Busemann, A.: The Delivery Head Ratio for Radial Centrifugal Pumps with Logarithmic Blades. Zeitschrift fur Angewandte Mathematik und Mechanik, Vol. 8, No. 5, 1928, pp. 372-384.

12. Sato, C. J.: Aerodynamic Forces On An Unbounded Centrifugal Impeller Undergoing Synchronous Whirl. M.S. Thesis, University of Virginia, August 1982.

13. Stanitz, J.: Personal Communication, 1981.

14. Zienkiewicz, O. C.: The Finite Element Method. McGraw-Hill Book Company, New York, 1977, pp. 677-757.

15. Bathe, K. and Wilson, E. L.: Numerical Methods in Finite Element Analysis. Prentice-Hall, Inc., New Jersey, 1976, pp. 203-213.

16. Fox, R. W. and McDonald, A. T.: Introduction to Fluid Mechanics, John Wiley & Sons, New York, 1978, p. 166.

TABLE 1 - IMPELLER GEOMETRIES FOR TWELVE CASES

Case No.	No. of Blades	Blade Angle	R_1/R_2	R_4/R_2	Thickness (inches)	R_3/R_2	θ_s
1	4	30	0.5	2.5	1/8	2.0	-140
2	3	30	0.25	2.5	1/8	2.0	-140
3	3	30	0.5	2.75	1/8	2.0	-140
4	7	30	0.5	2.5	1/8	2.0	-140
5	3	30	0.5	2.5	1/8	2.0	-140
6	4	30	0.5	2.5	3/16	2.0	-140
7	4	16	0.5	2.5	1/8	2.5	-152
8	4	22	0.5	2.5	1/8	2.5	-143
9	4	26	0.5	2.5	1/8	2.5	-140
10	4	37	0.5	2.5	1/8	2.5	-107
11	4	45	0.5	2.5	1/8	2.5	- 95
12	4	30	0.5	2.5	1/8	2.5	-178

TABLE 2. DIMENSIONLESS VALUES OF BLADE STREAM FUNCTION FOR IMPELLER SHAPES

Case	No. of Blades		Centered Impeller	Blade Stream Functions: Eccentric Impeller (ε/R_2 = 0.0025) (1)	(2)	(3)	(4)	(5)	(6)	(7)
1	4	30	.2062	.2056	.2058	.2068	.2065			
2	3	30	.1941	.1934	.1942	.1949				
3	3	30	.1505	.1499	.1507	.1511				
4	7	30	.2440	.2435	.2434	.2437	.2442	.2445	.2444	.2439
5	3	30	.1941	.1933	.1941	.1948				
6	4	30	.2123	.2117	.2120	.2129	.2126			
7	4	16	.3115	.3112	.3114	.3118	.3116			
8	4	22	.2697	.2693	.2695	.2701	.2700			
9	4	26	.2365	.2360	.2362	.2370	.2368			
10	4	37	.2276	.2275	.2268	.2277	.2284			
11	4	45	.2253	.2254	.2244	.2252	.2262			
12	4	30	.1588	.1586	.1588	.1590	.1588			

TABLE 3. PRINCIPAL AND CROSS COUPLED STIFFNESS OF TWELVE IMPELLER CASES

Case Number	Principal Stiffness K_{xx}	Cross Coupled Stiffness K_{yx}
1	-0.3529	0.6057
2	-0.2145	0.6523
3	-0.2052	0.5197
4	-0.5571	0.6025
5	-0.2988	0.6922
6	-0.4446	0.6055
7	-0.8532	0.2525
8	-0.5807	0.4345
9	-0.3968	0.5011
10	-0.1423	0.4506
11	-0.1203	0.3940
12	-0.1047	0.0728

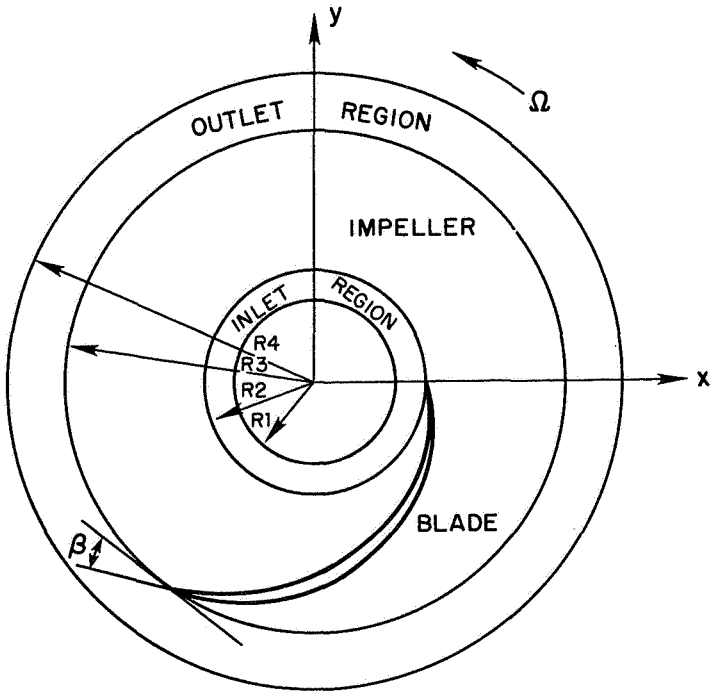

Figure 1. Impeller Geometry

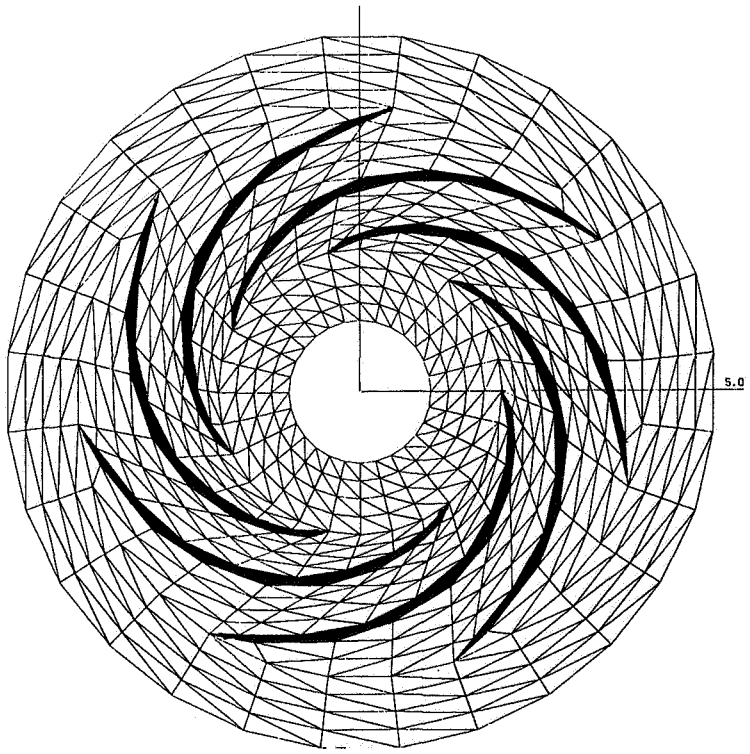

Figure 2. Finite Element Model for Case 4 - Seven Bladed Impeller (560 Nodes and 952 Elements)

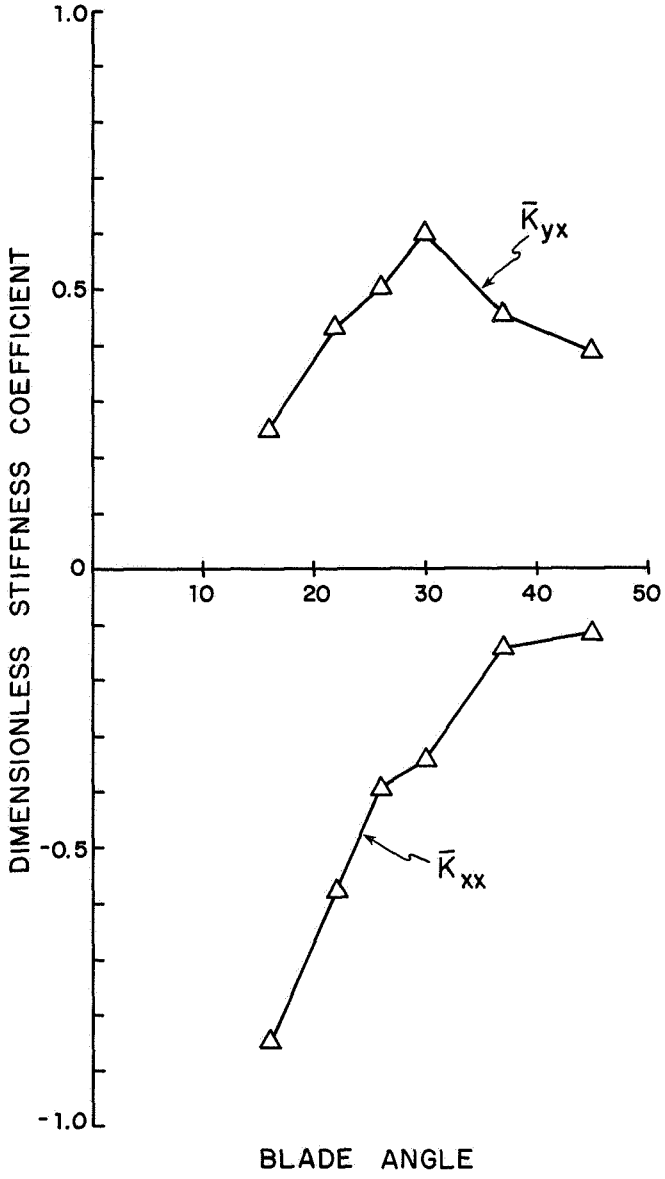

Figure 3. Stiffness vs. Blade Angle (Cases 1 and 7-11)

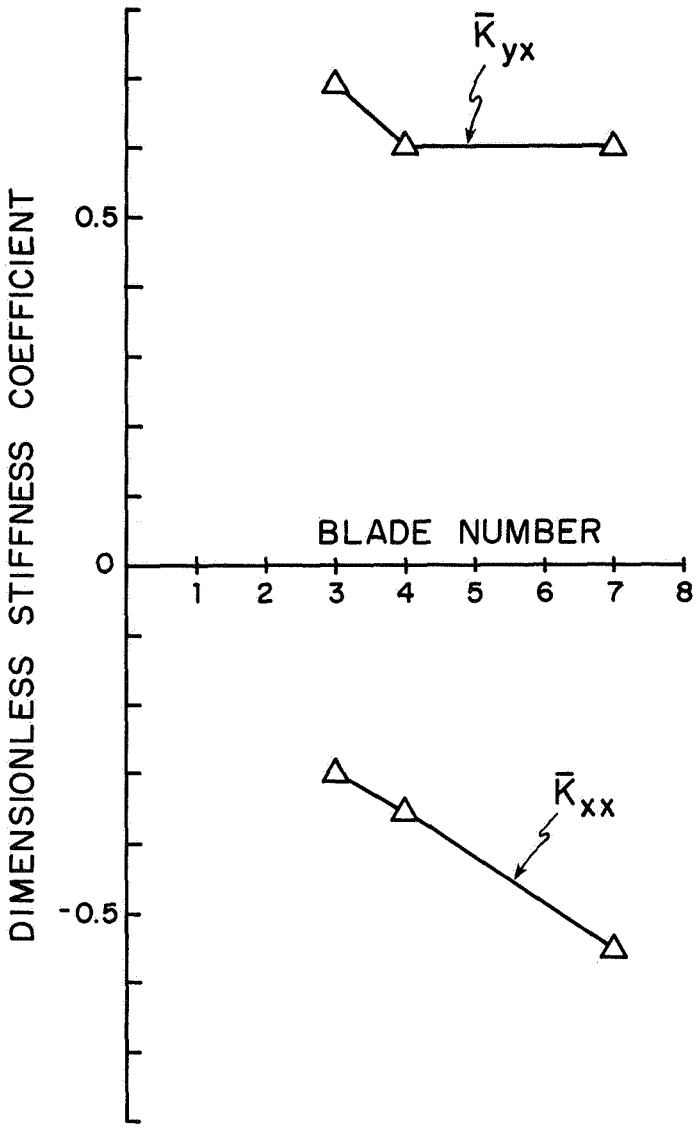

Figure 4. Stiffness vs. Blade Number (Cases 1, 4, 5)

HYDRODYNAMIC IMPELLER STIFFNESS, DAMPING, AND INERTIA IN THE ROTORDYNAMICS OF CENTRIFUGAL FLOW PUMPS

B. Jery, A. J. Acosta, C. E. Brennen, and T. K. Caughey
California Institute of Technology
Pasadena, California 91125

Measurements were made of the lateral hydrodynamic forces experienced by a centrifugal pump impeller performing circular whirl motions within several volute geometries. Experiments were conducted for various flow coefficients, ϕ, impeller rotating speeds or angular frequencies, ω, and the angular frequency of the whirl motion, Ω, was varied from zero to nearly synchronous ($\Omega=\omega$) and to nearly anti-synchronous ($\Omega=-\omega$). The lateral forces were decomposed into (i) time averaged lateral forces and (ii) hydrodynamic force matrices representing the variation of the lateral forces with position of the impeller center. No assumptions concerning the form of these matrices need to be made. The latter can be further decomposed according to the variation with whirl frequency, the result being "stiffness", "damping", and "fluid inertial" rotordynamic force matrices. It was found that these force matrices essentially consist of equal diagonal terms and skew-symmetric off-diagonal terms. One consequence of this is that during its whirl motion the impeller experiences forces acting normal and tangential to the locus of whirl. Data on these normal and tangential forces are presented; in particular it is shown that there exists a region of positive reduced whirl frequencies, Ω/ω, within which the hydrodynamic forces can be destabilizing with respect to whirl.

NOMENCLATURE

[A]	=	dimensionless hydrodynamic force matrix
[B]	=	the 6X6 internal balance calibration matrix
[C]	=	hydrodynamic damping matrix as defined by Eq.(3).
b_2	=	impeller discharge width

* The authors are indebted to the NASA George Marshall Space Flight Center, Huntsville, Alabama for their continued sponsorship of this research under contract NAS8-33108. We are also most grateful for the help given by graduate students D. Adkins and R. Franz and undergraduates W. Goda and S. Moriarty. One of the authors (B.J.) would also like to thank Byron-Jackson Pump Division, Borg-Warner Industrial Products, Inc. for financial support.

$\{F\}$ = 6-component generalized force vector

F_1, F_2 = components of instantaneous lateral force on impeller in the rotating internal balance reference frame

F_x, F_y = components of instantaneous lateral force on impeller in fixed laboratory reference frame (X,Y) non-dimensionalized by $\frac{1}{2}\rho\pi r_2^3\omega^2 b_2$

F_{ox}, F_{oy} = values of F_x and F_y when impeller axis remains coincident with the origin of the (X,Y) coordinate system

F_N, F_T = Components of instantaneous lateral force on impeller normal to and tangential to the whirl orbit, non-dimensionalized by $\frac{1}{2}\rho\pi r_2^2\omega^2 b_2\varepsilon$

I,J = integers such that $\Omega = I\omega/J$

[K] = hydrodynamic stiffness matrix as defined by Eq. (3)

[M] = hydrodynamic inertial matrix as defined by Eq. (3)

N = pump rpm = $60\omega/2\pi$

r_2 = impeller discharge radius

t = time

$\{V\}$ = 6-component vector of internal balance bridge output voltages

(X,Y) = fixed laboratory reference frame

x,y = instantaneous coordinates of impeller center in fixed laboratory reference frame (X,Y), non-dimensionalized by r_2

$\dot{x},\dot{y},\ddot{x},\ddot{y}$ = first and second time derivatives of impeller position non-dimensionalized using the distance r_2 and the time ω^{-1}

ε = radius of circular whirl orbit

ρ = density of water

ϕ = pump flow coefficient based on impeller discharge area and tip speed

Ψ = pump total head coefficient = total head rise divided by $\rho r_2^2\omega^2$

ω = radian frequency of pump shaft rotation

Ω = radian frequency of whirl motion = $I\omega/J$

Additional subscripts P and Q and superscript k refer to the Fourier decomposition of F_1 and F_2 defined in Eq. (7).

INTRODUCTION

In recent years it has been increasingly recognized that hydrodynamic cross-coupling forces can cause serious rotor dynamic problems in high speed turbomachines. Such problems have been experienced not only in steam turbines (Refs.1,2), but also in large compressors (Refs.3,4), in turbines (Ref.5) and in high speed pumps (Ref.6). Though other instability mechanisms such as internal damping or non-isotropic shaft stiffness or rotor inertia can be fairly readily characterized the same cannot be said of the hydrodynamic cross-coupling forces. Various hydrodynamic flows have been identified as possible contributors to these destabilizing forces. Bearings and particularly seals can clearly play such a role as the papers in this workshop (and previous workshops in the same series) attest. But much less is known about the potential for destabilizing forces arising from the flows associated with the impeller and diffuser of a compressor or pump; this paper will be confined to this issue.

Consider the hydrodynamic forces acting on a pump impeller in the plane perpendicular to the axis of rotation, the so-called lateral hydrodynamic forces. For present purposes a set of axes, X,Y in this plane are defined as fixed in the laboratory or "volute" frame. The origin of these axes corresponds to the design position for the axis of rotation of the impeller (impeller center) for that impeller/volute combination, also called the "volute center". Because of the asymmetry of most volute designs an impeller rotating with its center fixed in this coordinate frame will normally experience a steady force whose magnitude and direction will differ according to the position of the impeller center, denoted by O in Figure 1. Whether or not this force is zero when the impeller center, O, coincides with the volute center obviously depends upon the wisdom of the designer. In any case the lateral forces on the impeller for any position of the impeller can be represented by

$$\begin{Bmatrix} F_x \\ F_y \end{Bmatrix} = \begin{Bmatrix} F_{ox} \\ F_{oy} \end{Bmatrix} + [A] \begin{Bmatrix} x \\ y \end{Bmatrix} \tag{1}$$

In both this equation and all the equations and results which follow dimensionless forces and deflections are used (see Nomenclature for definitions). Equation (1) implicitly assumes small offsets x,y in the impeller center so that the force variations can be represented by such a linear equation (at the present time little is known of possible non-linear effects). It follows that the steady lateral forces F_x, F_y due to a fixed offset of the impeller center can be represented by the forces F_{ox}, F_{oy} generated when the impeller center coincides with the volute center (or at least some fixed laboratory position) plus a "stiffness" matrix [A]. Both will be functions of the flow conditions as represented by the flow coefficient ϕ.

A substantial body of data now exists on the lateral forces F_{ox},F_{oy} thanks to the work of Domm and Hergt (Ref.7), Agostonelli et al (Ref.8) and Iverson et al (Ref.9) among others. The present program of research at Caltech began with measurements of both the lateral forces F_{ox},F_{oy} and the hydrodynamic "stiffness" matrices [A]. This information, some of which was presented at the last workshop has been reported in Refs.10-13 and will not be repeated here. It was obtained by very slowly moving the impeller center around a circular orbit (as shown in Figure 1) and measuring the lateral forces at each location. One of the most significant features of the results is best illustrated by evaluating the forces components F_N, F_T normal and tangential to the orbit of this very slow whirl motion. It transpired that the hydrodynamic forces give rise to a positive tangential force in

the same direction as the direction of impeller rotation which would be rotordynamically destabilizing.

The present paper extends these results to the case of non-negligible velocity of the orbiting motion. Specifically a whirl motion with a circular orbit and an angular frequency, Ω, is imposed on the impeller and resulting unsteady forces are measured. Denoting the orbit radius by ε this implies that $x = \varepsilon \cos \Omega t/r_2$; $y = \varepsilon \sin \Omega t/r_2$ and that Equation (1) needs to be generalized to the form:

$$\begin{Bmatrix} F_x(t) \\ F_y(t) \end{Bmatrix} = \begin{Bmatrix} F_{ox} \\ F_{oy} \end{Bmatrix} + \frac{\varepsilon}{r_2} \left[A(\Omega/\omega)\right] \begin{Bmatrix} \cos \Omega t \\ \sin \Omega t \end{Bmatrix} \tag{2}$$

where the rotordynamic force matrix $[A(\Omega/\omega)]$ is now a function of the ratio of whirl frequency to impeller rotating frequency Ω/ω as well as the flow coefficient. On the other hand the matrices required for input into most rotordynamic analysis are the stiffness, [K], damping, [C], and inertial, [M], matrices defined by the dimensionless matrix equation

$$\begin{Bmatrix} F_x \\ F_y \end{Bmatrix} = - [M] \begin{Bmatrix} \ddot{x} \\ \ddot{y} \end{Bmatrix} - [C] \begin{Bmatrix} \dot{x} \\ \dot{y} \end{Bmatrix} - [K] \begin{Bmatrix} x \\ y \end{Bmatrix} \tag{3}$$

It follows by comparing the definitions (2) and (3) that

$$\begin{aligned} A_{xx} &= M_{xx} \frac{\Omega^2}{\omega^2} - C_{xy} \frac{\Omega}{\omega} - K_{xx} \\ A_{xy} &= M_{xy} \frac{\Omega^2}{\omega^2} + C_{xx} \frac{\Omega}{\omega} - K_{xy} \\ A_{yx} &= M_{yx} \frac{\Omega^2}{\omega^2} - C_{yy} \frac{\Omega}{\omega} - K_{yx} \\ A_{yy} &= M_{yy} \frac{\Omega^2}{\omega^2} + C_{yx} \frac{\Omega}{\omega} - K_{yy} \end{aligned} \tag{4}$$

It should be observed that Equation (3) makes the a priori assumption that the matrix [A] varies quadratically with Ω/ω. There is no fundamental reason why the hydrodynamic forces should follow such a simple behavior. Nevertheless the results of the present study do seem to be well represented by quadratics and values of [M], [C] and [K] evaluated from least squares fits to the $[A(\Omega/\omega)]$ data are presented later. Finally we note that the imposition of a circular orbit motion is analogous to performing a forced vibration experiment in a mechanical system; data are thereby extracted which have use in a more general dynamic analysis of the system.

EXPERIMENTAL FACILITY

The facility used to conduct the present experiments has been described in detail elsewhere (Refs.10,11,12,14). Only a brief description will be given here; modifications made for the purpose of the present experiments will be given more

attention. The site of the experiments is a pump loop (Figure 2) containing flow control and measuring systems. Installed in the lower left hand corner of this loop is the test pump and drive system known as the Rotor Force Test Facility (RFTF) shown schematically in Figure 3. The flow enters the centrifugal impeller (5) from the inlet connection (3) and inlet bell (4). Volutes (2) of various geometries are contained in the pump housing (1) so that the volutes can be of lightweight construction (most are made of fiberglass). The impeller (5) is mounted directly on the internal force balance (6) which is new to the present experiments and is discussed more fully below. Face seals on both the inlet and discharge side of the impeller are backed-off to prescribed clearances in order to minimize their contribution to the force on the impeller. The main pump shaft (10) rotates in a double bearing system (7,8,11) designed so that rotation of the sprocket (9) attached to the intermediate bearing cartridge causes the orbiting motion. The radius of the orbiting motion is set at 0.126cm for all of the present experiments. This motion is driven by the eccentric drive motor (2 H.P.) The main shaft is driven by the main drive motor (20 H.P.) through a gear box and a flexible shaft system designed to accommodate the whirl motion. The maximum speed of the main shaft is about 3600 rpm (Ω = 60Hz) though the current experiments have been performed at 1000 and 2000 rpm (ω = 16.7 and 33.3Hz). For reasons discussed below the whirl speed is presently limited to 1000 rpm.

Previous measurements of the steady forces at zero whirl frequency (Ref.10,11,12,13) were made using an external force balance whose operation required floating the entire bearing system and measuring the forces on this floating mass. Though simpler to implement, this external balance system was severely limited in its dynamic capability. The internal balance was designed to measure the unsteady forces implicit in the case of non-zero whirl frequencies (as well as other unsteady forces such as caused by rotor/stator blade interactions though these are not addressed in the present paper). It is also designed to measure all 6 components of force and moment experienced by the impeller. The design of the internal balance is shown in the schematic of Figure 4. Essentially, it consists of four equally spaced "posts" parallel to the axis which connect two substantial end plates one of which is rigidly connected to the drive shaft and the other is used as a mounting base for the impeller. The four "posts" which are 2.54 cm long and have a square cross-section of 0.51cm on a side are placed at a radius of 4.76 cm. The posts and rigid end plates were machined monolithically from stainless steel. Semi-conductor strain gauges were bonded to all four faces of each post at locations indicated in Figure 4 (1/4, 1/2 and 3/4 span points). Different combinations of strain gauges were wired into bridges, designed so as to be sensitive to each of the six components of force (or force and moment components) experienced by the balance. This balance was designed to have high natural frequencies both for torsional and lateral deflections and yet be sufficiently sensitive to the forces it is intended to measure. Both the torsional and lateral natural frequencies with the impeller attached to the "free" end plate were estimated to be about 480 Hz. However Fourier analysis of the spectrum of natural frequencies when the balance was installed indicated a considerably lower natural frequency of about 160 Hz (see Figure 5). The additional flexibility is attributed to the shaft and the bearing system. Structurally the balance was completed by a waterproof shield enveloping the two end plates. The internal air pressure was maintained at a constant, regulated value using the hole through the center of the shaft and a pneumatic collar connecting this with an exterior air supply. The wires from the strain gauges were led through the same hollow shaft and connected to a set of 52 slip rings. For the purpose of the analysis discussed below it should be noted that the lateral forces F_1, F_2 registered by the impeller

are in a frame of reference rotating and whirling with the impeller.

Unsteady fluid flow measurements such as those attempted here require sufficient control to permit data to be taken over many cycles of both the whirl and main shaft frequencies. This demands close control of both motions which was achieved by means of the control system shown diagrammatically in Figure 6. A single frequency generator feeds a frequency multiplier/divider utilizing the input of two integers I,J chosen by the operator. One output signal at a frequency ω drives the main shaft motor, a feedback control system ensuring close adherence to that driving signal. Another output at a frequency $\Omega = I\omega/J$ controls the eccentric drive motor which is also provided with a feedback control system. Three other outputs from the frequency multiplier/divider at frequencies of $\omega \pm \Omega$ or $(J \pm I)\omega/J$ and ω/J are used in the data acquisition and processing systems. The flow fluctuator control system which is also shown in Figure 6 has not as yet been used in the research program.

The central component of the signal processing system is a 16-channel digital signal processor which utilizes a reference frequency (ω, $\Omega = I\omega/J$, ω/J or $\omega \pm \Omega$) and accumulates an "average cycle" of data for each of the 16 data input channels, described by 64 digital values per cycle per channel. This data is accumulated for up to 4096 reference cycles. Subsequent Fourier analysis of this digital data evaluates not only the magnitude and phase of the fundamental present in each data channel but also the same information for many higher harmonics. In the present experiments the lowest common frequency ω/J, was used as the reference frequency; thus the Jth harmonic yields the magnitude and phase (or in-phase and quadrature components) of the component of the measurement at the main shaft frequency and the Ith harmonic does likewise for the component at the whirl frequency. (The importance of the control system described earlier in which integer values for I and J are chosen by the operator should now be apparent.) The present paper concentrates on the results obtained for the impeller forces as measured by the internal balance. Since this is <u>rotating</u> with the impeller it follows that the primary results of interest follow from the Jth, $|J-I|$th and $|J+I|$th harmonics (see below). Auxiliary information on flow rates, pressures, etc was obtained in the same way as reported in Ref.10,11,12 and 13.

INTERNAL BALANCE CALIBRATION

As discussed above the internal balance includes nine full Wheatstone bridges each of which is primarily sensitive to one or two of the force and moment components. Six of these nine bridges were selected to sense the six components, the other three being monitored as a back-up check on the main measurements. The purpose of the calibration procedure was to produce a 6X6 calibration matrix, [B], which would include all of the possible balance interactions so that the six component vector of forces {F} could be subsequently calculated from the six component vector of output voltages {V} by

$$\{F\} = [B]\ \{V\} \tag{5}$$

A number of different calibrations, hysteresis tests and dynamic response tests were performed on the balance in situ. The basic calibration matrix was obtained by in situ static loading of the balance using wires, pulleys and weights. The resulting 36 graphs displayed satisfactory linearity in both the principal and interaction

matrix elements. One of the principal element calibrations is shown in Figure 7. The largest interactions occurred in the thrust measuring bridge and these were less than 5% of the principal element outputs. The interactions in the lateral force bridges was of the order of 1%. Hysteresis tests performed by fairly rapid manual operation of the static calibration system revealed virtually no significant hysteretic effects.

Further static and dynamic calibration tests were carried out under rotating and whirling conditions. First a smooth flywheel with hidden and known off-balance weights was used to check the earlier static calibration by rotating in air without any whirl motion. This corresponds to a static loading in the rotating frame of the balance. Secondly the balanced impeller was rotated in air without whirl motion in order to detect the lateral force resulting from the weight of the impeller. This is seen by the balance as a dynamic load and allowed evaluation of the dynamic response of the balance up to about 50Hz. The magnitude and phase of the balance element response remained unchanged up to this frequency; phase angles for example were constant within $\pm 3^{o}$. Further dynamic checks were conducted using whirl motion in air.

LATERAL FORCE MEASUREMENT TECHNIQUE

Though the design and location of the internal balance was chosen to minimize parasitic forces, nevertheless it was necessary to subtract some inevitable tare forces from the raw data in order to extract the essential hydrodynamic forces imparted to the impeller. This was accomplished by performing four different sets of measurements for each eventual data point:

(i) The forces for the impeller run at the required speed and flow coefficient

(ii) The forces when the impeller is run in air at the same speed

(iii) The forces when experiment (i) is performed in water with the impeller removed

(iv) Experiment (iii) performed in air.

Subtracting (ii) from (i) and (iv) from (iii) removes the parasitic forces due to the impeller and shaft weight and small mass imbalances. Subtraction of these two results yields the force on the impeller and eliminates parasitic hydrodynamic forces on the exterior surface of the internal balance. Indeed it transpired that the annular gap between the exterior of the internal balance and the surrounding casing was sufficiently small ($\sim$ 0.5cm) to cause measurable hydrodynamic tare forces and matrices to be present in the data of (iii) minus (iv). Some of these data are given later.

The lateral forces detected by the internal balance are in a rotating reference frame. Denoting the lateral force components in the balance frame by F_1, F_2 (see Figure 8) it is necessary to describe how the average forces F_{ox}, F_{oy} and the elements of the hydrodynamic matrix [A] were obtained. First it is clear that F_x, F_y are related to F_1, F_2 by

$$F_x(t) = F_1(t) \cos \omega t - F_2(t) \sin \omega t$$
$$F_y(t) = F_1(t) \sin \omega t + F_2(t) \cos \omega t \tag{6}$$

As described earlier $F_1(t)$, $F_2(t)$ are Fourier analyzed using the reference frequency ω/J so that

$$F_1(t) = F_1^o + \sum_{k=1}^{\infty} \left(F_{1P}^k \sin \frac{k\omega t}{J} + F_{1Q}^k \cos \frac{k\omega t}{J} \right)$$
$$F_2(t) = F_2^o + \sum_{k=1}^{\infty} \left(F_{2P}^k \sin \frac{k\omega t}{J} + F_{2Q} \cos \frac{k\omega t}{J} \right) \tag{7}$$

and F_1^o, F_2^o, F_{1P}^k, F_{1Q}^k and F_{2Q}^k are available up to some limiting value of k from the digital data acquisition system and software. Eliminating F_1, F_2 from (6) and (7), substituting the resulting expressions for F_x, F_y into (2) and then integrating over one cycle of frequency ω/J results in the following relations

$$F_{ox} = -\tfrac{1}{2} \left(F_{2P}^J - F_{1Q}^J \right)$$

$$F_{oy} = \tfrac{1}{2} \left(F_{1P}^J + F_{2Q}^J \right)$$

$$A_{xx} = \frac{1}{2\varepsilon} \left(-F_{2P}^{J-I} + F_{1Q}^{J-I} - F_{2P}^{J+I} + F_{1Q}^{J+I} \right)$$

$$A_{xy} = \frac{1}{2\varepsilon} \left(-F_{1P}^{J-I} - F_{2Q}^{J-I} + F_{1P}^{J+I} + F_{2Q}^{J+I} \right)$$

$$A_{yx} = \frac{1}{2\varepsilon} \left(F_{1P}^{J-I} + F_{2Q}^{J-I} + F_{1P}^{J+I} + F_{2Q}^{J+I} \right)$$

$$A_{yy} = \frac{1}{2\varepsilon} \left(-F_{2P}^{J-I} + F_{1Q}^{J-I} + F_{2P}^{J+I} - F_{1Q}^{J+I} \right)$$

Thus evaluation of the Jth, (J-I)th and (J+I)th harmonics are required. The usual value chosen for J was 10 though the data points at the lowest whirl frequency used J=20,18,16,14 and 12; I ranged from -9 to +9.

Experimental Test Matrix

Altogether seven sets of measurements have been made to date. In each of these sets the whirl motion radian frequency Ω (as given by the choice of integers I and J) was varied while holding the pump speed ω, flow coefficient ϕ and the face seal clearances fixed.

All seven sets of measurements used the same five-bladed centrifugal impeller (Impeller X) which has an outer radius r_2=16.2cm and discharge angle of 25 degrees. This impeller was cast out of bronze and has a specific speed of 0.57. In five out of the seven sets a logarithmic spiral volute (Volute A) was used. This is a well-matched trapezoidal cross-section fiberglass volute that was designed to be used

with Impeller X. The ratio of the base circle diameter to impeller diameter is 1.13, and the area at the cutwater was 20.75cm^2. One set of measurements was conducted using a circular volute (Volute B), deliberately mismatched with its 5.42cm constant diameter circular cross-section. Finally, a set of measurements was made with Impeller X rotating and whirling inside the pump outer casing, in the absence of any volute.

A face-seal clearance 0.13mm was maintained throughout all the experiments. However, in one particular set of measurements two circular rings were attached to the interior of the volute on either side of the impeller discharge in order to reduce the leakage flow.

Six of the sets were conducted at 1000 rpm impeller speed, while the whirl speed was varied from 0 to 900 rpm in both directions ($-0.9 \leq \Omega/\omega \leq 0.9$). The remaining set was made at 2000 rpm to study the influence of pump speed on the hydrodynamic forces; in this case the whirl speed was varied from 0 to 1000 rpm in both directions ($-0.5 \leq \Omega/\omega \leq 0.5$). The restriction on the highest whirl speed is merely a precautionary measure to limit the inertial loads and mechanical vibrations on the eccentric drive assembly and dynamometer. The combination of Volute A and Impeller X was tested at 3 values of ϕ (.06, .092 and 0.131) and 1000 rpm pump speed. All other experiments mentioned earlier were conducted at "design" condition of $\phi = .092$.

RESULTS

The results presented in this paper will be confined to the data obtained for the hydrodynamic force matrix $[A(\Omega/\omega)]$, the associated average normal and tangential forces F_N, F_T given by

$$F_N = \frac{1}{2}(A_{xx} + A_{yy})$$

$$F_T = \frac{1}{2}(-A_{xy} + A_{yx})$$

and the stiffness, damping and inertia matrices [K], [C] and [M] as defined by Eq. (3). Other data such as the hydrodynamic performance ($\Psi(\phi)$) and the average lateral forces F_{ox}, F_{oy} will be presented in later reports. It should however be noted that the F_{ox}, F_{oy} values obtained were essentially independent of the whirl speed and agreed with those measured by Chamieh et al (Refs. 10,11,12). Thus we concentrate here on one of the results of primary importance in the rotordynamic analysis of centrifugal pumps.

The various experimental measurements are compared with a base case, namely the results for the Volute A/Impeller X combination run at 1000 rpm and the design flow coefficient ϕ of 0.092 with face seal clearances set at 0.13mm. The $[A(\Omega/\omega)]$ matrix for this case is shown in Figure 9 plotted against Ω/ω. In common with all the other cases tested this matrix has almost equal diagonal terms and off-diagonal terms which are almost equal but of opposite sign. This skew-symmetric form for the hydrodynamic matrix is remarkable since there is no fundamental reason why it should take this form. This form is often <u>assumed</u> but this is the first confirmation that we are aware of.

Because of this skew-symmetric form of the hydrodynamic force matrix it is convenient to present only the arithmetic mean of the diagonal terms which, in fact, corresponds to the dimensionless normal force, F_N, averaged over the whirl orbit and half the difference of the off-diagonal terms which in fact corresponds to the dimensionless tangential force, F_T, similarly averaged. The values of F_N, F_T corresponding to Figure 9 are shown in Figure 10. The variation in these quantities with flow coefficient and with speed are shown in Figures 11 and 12. The effect of two rings that were attached to the volute on either side of the impeller discharge in order to reduce the seal leakage is shown in Figure 13. Finally a comparison of the results for Volutes A and B is included in Figure 14.

Several general features of these results should be emphasized. Considering first F_N note that the hydrodynamic force is almost always in the radially outward direction. At zero whirl frequency it has a positive value which is in close agreement with the results of Chamieh et al (Refs. 10,11,12); this corresponds to a negative stiffness at zero whirl speed. The sign of the tangential force, F_T is such as to produce a rotordynamically stabilizing effect at negative whirl speeds and for the larger positive whirl speed. However it is important to note that there is a region of positive whirl speeds between zero and $\Omega/\omega = 0.25 \rightarrow 0.5$ in which the tangential force is destabilizing rotordynamically. It would appear from Figure 11 that this destabilizing interval increases somewhat as the flow coefficient decreases.

Conventional scaling of forces with speed in pumps would imply that the data for 1000 rpm and 2000 rpm should be identical when plotted in the chosen dimensionless form. Figure 12 demonstrates that this is the case for the normal force F_N. but the tangential force, F_T, at negative whirl speeds appears to be significantly different for these two pump speeds. This could be due to viscous, frictional forces which do not scale with the square of the velocity.

The addition of the leakage reducing rings shown in Figure 13 had little effect on the results except for F_T at negative whirl speeds.

Note that all of the F_N data in Figures 10 to 13 is essentially the same. Only when the volute is changed (Figure 14) is the normal force altered. The lower values of F_N for Volute B would be expected since it has a larger cross-sectional area. However the tangential forces were similar for the two volutes.

As an aside we included here the hydrodynamic tares caused by the flow exterior to the balance and shaft. These were earlier described as the difference in the results of experiments (iii) and (iv). Note from Figure 15 that these tares amount to about 5-10% of the measured impeller effects. However it is interesting to note that the functional form of these tare forces is similar to that for the impeller forces.

The conventional stiffness, damping and inertia matrices used by rotordynamicists were defined in Eq. (3) and (4). It is clear from Figures 9 through 14 that the data can be fairly well represented by the quadratics given in Eq. (4). Dimensionless values of [K], [C] and [M] for the various experiments are presented in Table II. The values without parentheses are the result of quadratic least squares fits to the data for both positive and negative whirl speeds. The data in parentheses are the result of quadratic least squares fits to the data for positive whirl speeds only. Discrepancies between these values are therefore a

result of a combination of deviation from the quadratic behavior and uncertainty in the matrix element values. For example it is clear that the curvature of the F_T is small and somewhat uncertain; this results in substantial discrepancies in the off-diagonal terms of the inertia matrix, [M]. On the other hand all the elements of the stiffness matrix, [K], are well defined. The latter are quite consistent with the quasi-statically measured stiffness matrices of Chamieh et al (Ref.10,11,12). The damping and inertia matrices represent new data. They can be directly compared with the matrices presented by Ohashi at this workshop. In doing so one notes that the values for all matrices are substantially larger than those of Ohashi's. Though the reasons for this are not clear at this time, it should be pointed out that the volute boundaries are much closer to the impeller in the present experiments and this should result in higher values of the damping and added mass (or inertial effects). Note for example the last line of Table II which represents values obtained in the absence of a volute (though the pressure casing is still close enough to produce a significant effect).

CONCLUSIONS

In conclusion we note that the data presented in this paper represents the first experimental measurements of the complete hydrodynamic force matrix for a whirling centrifugal pump impeller. The common assumption of skew-symmetry for these matrices is justified by the experiments and the results come close to the commonly used quadratic variation with whirl frequency. The steady forces and stiffness matrices agree with those measured by Chamieh et al (Refs.10,11,12). The damping and inertial matrices are new and the effects of these on the rotordynamics of a typical pump should be tested. Many more tests are planned with the present experimental facility including tests with other impellers, volutes (with and without diffuser vanes) under a wide variety of flow conditions. The effects of cavitation will also be examined soon.

Postscript

Some preliminary data was released in June 1983. This should now be disregarded; it is superseded by the data of the present paper.

REFERENCES

1. Alford, J. S., "Protecting Turbomachinery from Self-Excited Rotor Whirl", J. of Eng. for Power, Vol. 87, pp. 333-344, Oct. 1965.

2. Pollman, E., Schwerdtfeger, H., and Termuehlen, H., "Flow Excited Vibrations in High Pressure Turbines (Steam Whirl)", J. of Eng. for Power, Vol. 100, pp. 219-228, April 1978.

3. Thompson, W. E., "Fluid Dynamic Excitation of Centrifugal Compressor Rotor Vibrations", J. Fluid Engineering, Vol. 100, pp. 73-78, March 1978.

4. Doyle, H. E., "Field Experiences with Rotodynamic Instability in High-Performance Turbomachinery", First Workshop on Rotordynamic Instability Problems in High-Performance Turbomachinery, Texas A&M University, NASA Conf. Pub. 2133, pp. 3-13, 1980.

5. Rossi, G. and Zanetti, V. 1982. "Attempt of synthesis of radial thrust measures". Symp. on Operating Problems of Pump Stations and Power Plants, (Proc. 11th IAHR Symp. on Hydraulic Machinery, Equipment and Cavitation), Amsterdam, Netherlands, Sept. 1982, Vol.2, Paper 52.

6. Ek, M. C., "Solution of the Subsynchronous Whirl Problem in the High Pressure Hydrogen Turbomachinery of the Space Shuttle Main Engine", Paper No. 78-1002, AIAA/SAE 14th Joint Propulsion Conf., Las Vegas, Nevada, July 25-28 1978.

7. Domm, H., and Hergt, P., "Radial Forces on Impeller of Volute Casing Pumps", Flow Research on Blading (L. S. Dzung, ed.), Elsevier Pub. Co., The Netherlands, pp. 305-321, 1970.

8. Agostinelli, A., Nobles, D., and Mockridge, C. R., "An Experimental Investigation of Radial Thrust in Centrifugal Pumps", Trans. ASME, J. of Eng. for Power, Vol. 82, pp. 120-126, April 1960.

9. Iversen, H. W., Rolling, R. E., and Carlson, J. J., "Volute Pressure Distribution, Radial Force on the Impeller and Volute Mixing Losses of a Radial Flow Centrifugal Pump", Trans. ASME, J. of Eng. for Power, Vol. 82, pp. 136-144, April 1960.

10. Chamieh, D. S. "Forces on a Whirling Centrifugal Pump - Theory and Experiments", Ph. D. Thesis, Division of Engineering and Applied Science, California Institute of Technology, February 1983.

11. Chamieh, D. S., Acosta, A. J., Brennen, C. E. and Caughey, T. K. "Experimental Measurements of Hydrodynamic Radial Forces and Stiffness Matrices for a Whirling Centrifugal Pump Impeller" (Submitted to J. Fl. Eng.)

12. Chamieh, D. S., Acosta, A. J., Brennen, C. E., Caughey, T. K. and Franz, R., "Experimental Measurements of Hydrodynamic Stiffness Matrices for a Centrifugal Pump Impeller", Proceedings of NASA/ARO Workshop on Rotordynamic Instability Problems in High Performance Turbomachinery, NASA CP-2250, 1982, pp. 382-398.

13. Jery, B. and Franz, R., "Stiffness Matrices for the Rocketdyne Diffuser Volute", California Institute of Technology, Div. of Eng. and Appl. Sci., Report No. E249.1, October, 1982.

14. Brennen, C. E., Acosta, A. J. and Caughey, T. K., "A Test Program to Measure Cross-Coupling Forces in Centrifugal Pumps and Compressors", Proc. Workshop on Rotordynamic Instability Problems in High Performance Turbomachinery, Texas A&M Univ., May 1980.

TABLE I

Rotordynamic stiffness, damping and inertia matrices. Values shown without parenthesis represent quadratic fits for both positive and negative whirl speeds. Values shown in parenthesis are the corresponding fits for positive whirl speeds only.

Volute Type	Speed, N and Flow, ϕ	K_{xx} K_{yx}	K_{xy} K_{yy}	C_{xx} C_{xy}	C_{xy} C_{yy}	M_{xx} M_{yx}	M_{xy} M_{yy}
A Spiral	1000 rpm ϕ=0.06	-1.60 (-1.59) -1.03 (-1.04)	0.80 (0.85) -1.46 (-1.18)	2.13 (1.64) -7.13 (-5.05)	7.08 (6.48) 2.59 (1.63)	6.72 (5.91) 0.52 (-0.84)	0.12 (0.91) 6.61 (4.37)
A	1000 rpm ϕ=0.092	-1.43 (-1.11) -0.84 (-0.72)	0.77 (0.72) -1.42 (-1.19)	2.67 (1.87) -7.06 (-5.58)	6.88 (4.95) 2.74 (1.52)	6.76 (4.77) -0.04 (-1.45)	-0.10 (0.90) 6.57 (5.02)
A	1000 rpm ϕ=0.131	-1.48 (-1.50) -0.78 (-0.46)	0.82 (0.36) -1.60 (-1.57)	4.01 (0.62) -6.46 (-5.54)	6.35 (6.34) 3.77 (2.16)	6.00 (5.91) 1.89 (0.41)	-2.67 (1.00) 5.91 (4.69)
A	2000 rpm ϕ=0.092	-1.88 (-2.07) -1.45 (-1.39)	1.31 (1.20) -1.80 (-2.03)	4.11 (2.99) -6.53 (-7.41)	6.63 (6.82) 4.17 (3.23)	6.10 (4.97) 1.19 (-0.65)	-1.04 (0.89) 6.30 (6.60)
A with rings	1000 rpm ϕ=0.092	-1.48 (-1.63) -0.97 (-0.74)	0.94 (0.86) -1.48 (-1.47)	3.92 (2.69) -6.87 (-6.33)	6.92 (6.87) 3.98 (1.80)	6.71 (6.30) 2.25 (-0.29)	-1.98 (-0.44) 6.12 (5.39)
B circular	1000 rpm ϕ=0.092	-1.24 (-1.40) -0.81 (-0.79)	0.83 (0.77) -1.39 (-1.33)	3.4 (2.18) -5.28 (-4.23)	5.5 (5.55) 3.12 (2.39)	5.11 (4.80) 1.34 (0.35)	-1.74 (-0.15) 4.56 (3.25)
No volute	1000 rpm ϕ=0.092	-0.32 (-0.37) -0.39 (-0.73)	0.44 (0.75) -0.22 (-0.06)	2.1 (2.34) -3.03 (-0.23)	2.9 (2.04) 1.9 (2.18)	4.41 (3.08) 0.54 (0.15)	-0.31 (0.08) 4.21 (0.64)

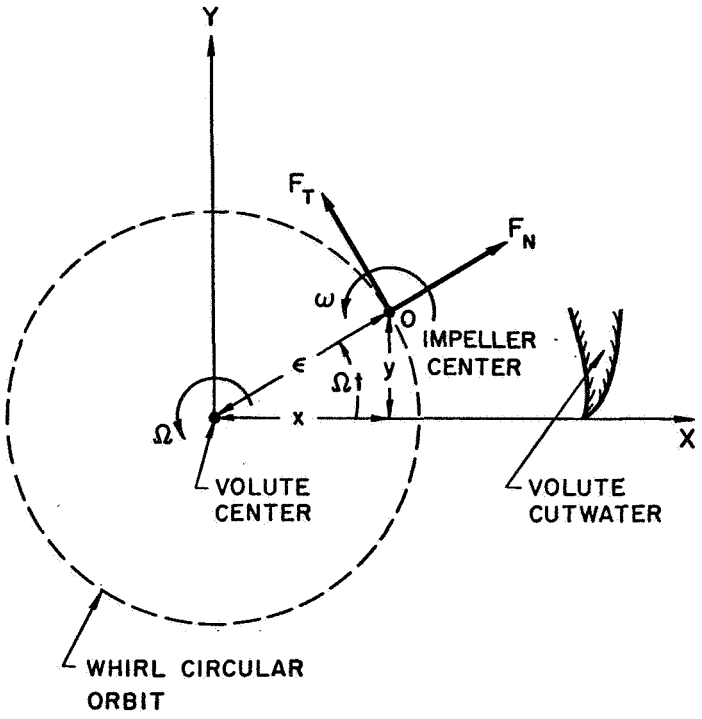

Figure 1. Coordinate system and force notation in a plane perpendicular to the axis of rotation of the impeller.

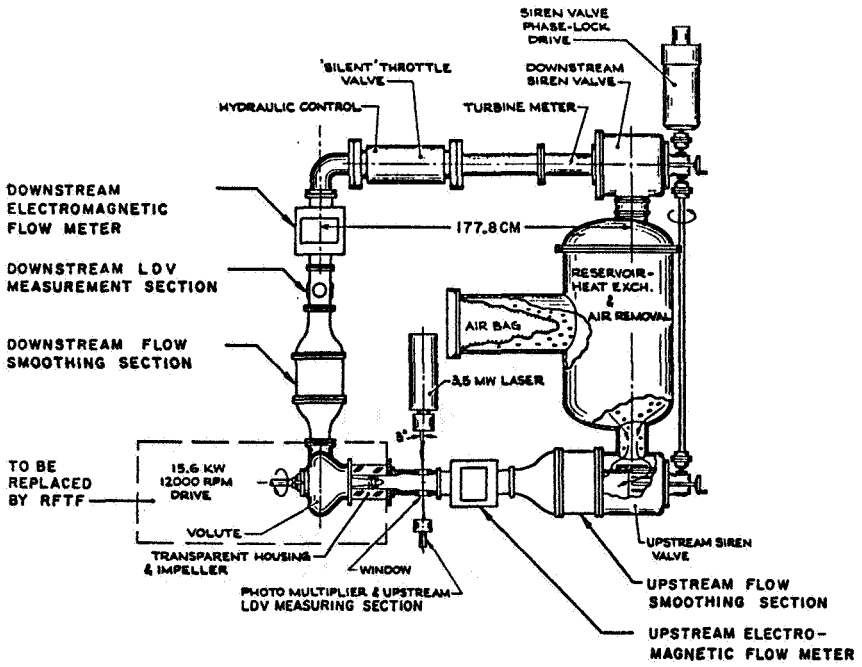

Figure 2. Schematic plan view of the pump loop prior to installation of the Rotor Force Test Facility (RFTF).

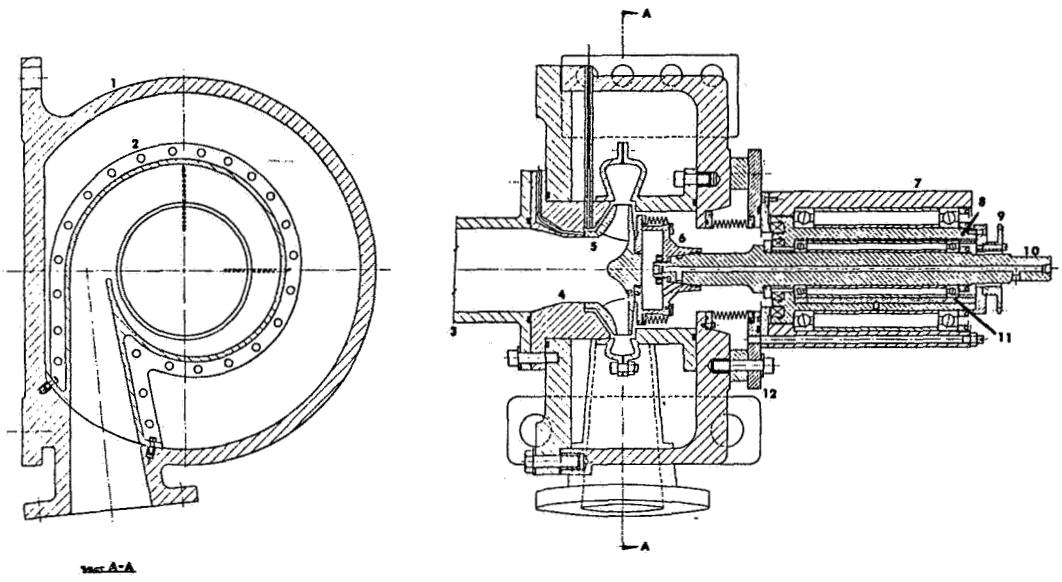

Figure 3. Cross-section of the main structure of the Rotor Force Test Facility (see text for numbered components).

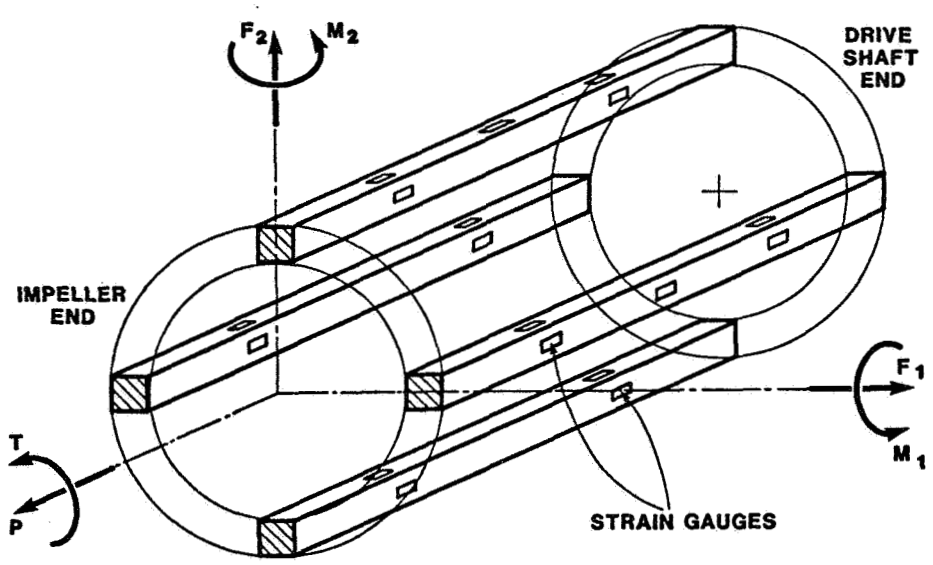

Figure 4. Schematic of the internal force balance.

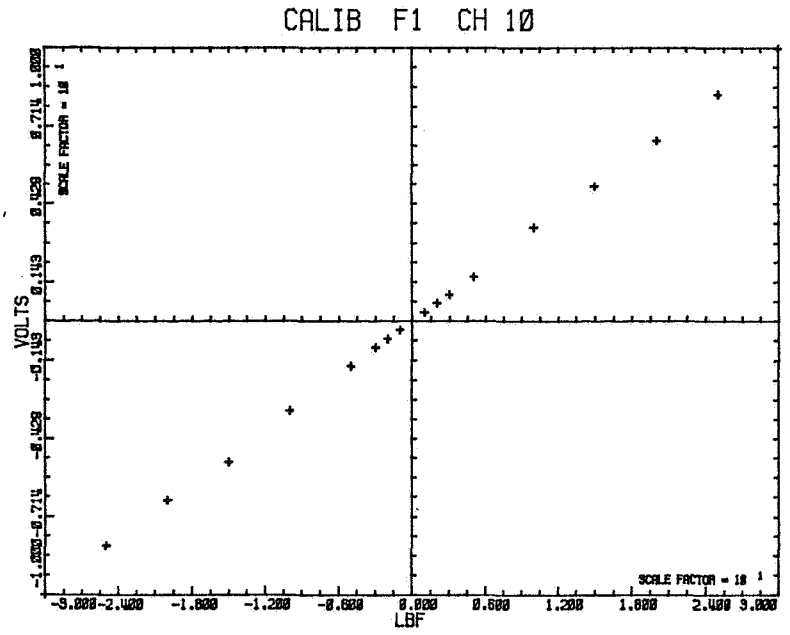

Figure 7. Typical in situ static calibration curve showing the voltage output of a principal bridge for various F_1 lateral loadings. Typical interaction outputs were also linear but only 1→2 percent of the principal outputs.

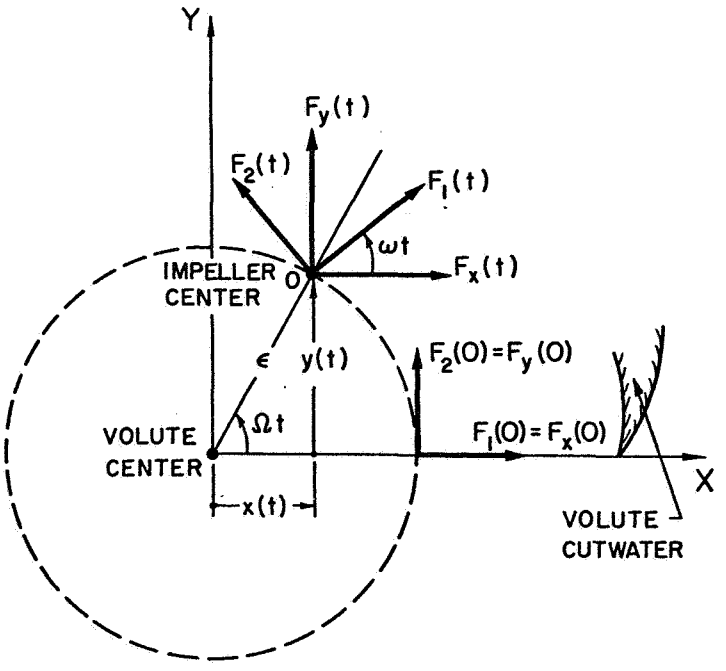

Figure 8. Schematic showing the relation between the lateral forces in the stationary X,Y frame and the rotating frame of the balance.

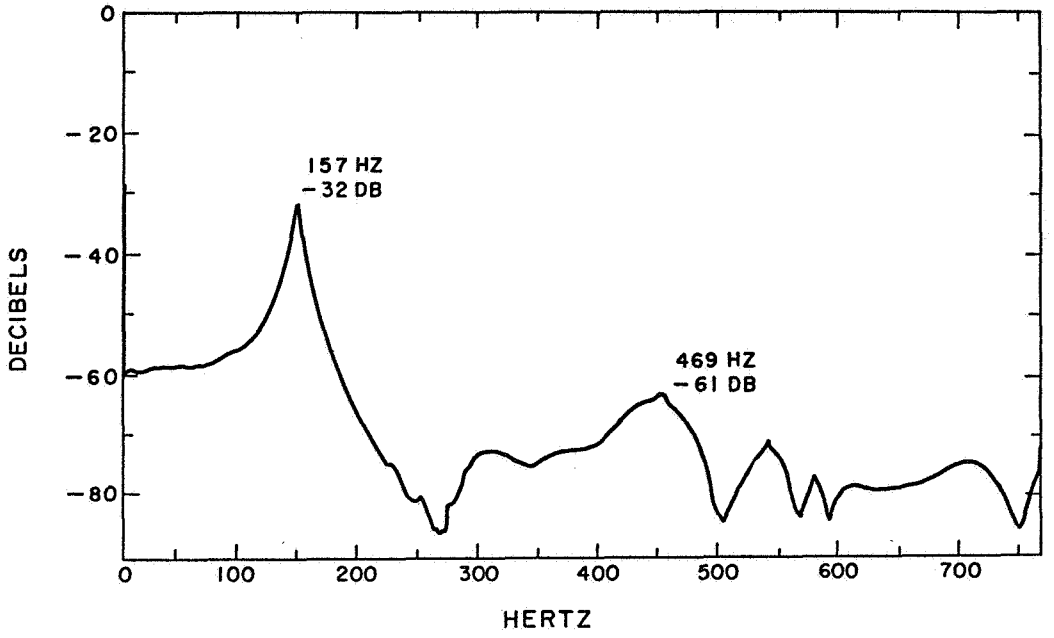

Figure 5. Frequency analysis of the installed impeller/internal balance/shaft/eccentric drive system when a lateral impulse is applied to the impeller.

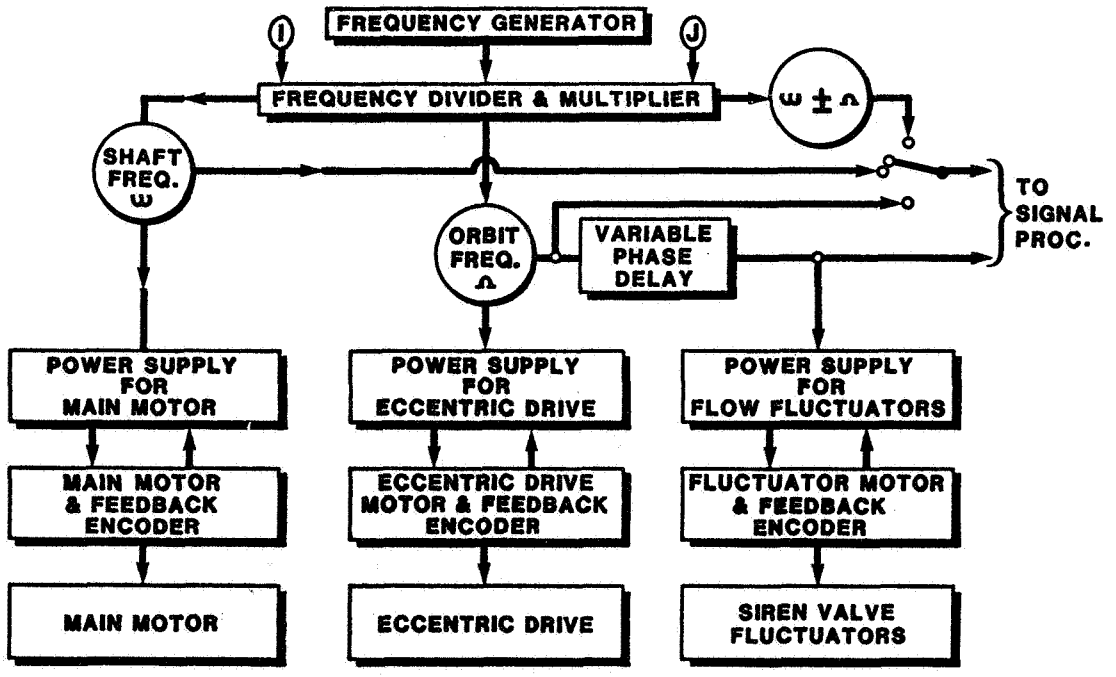

Figure 6. Schematic of the control system for the Rotor Force Test Facility.

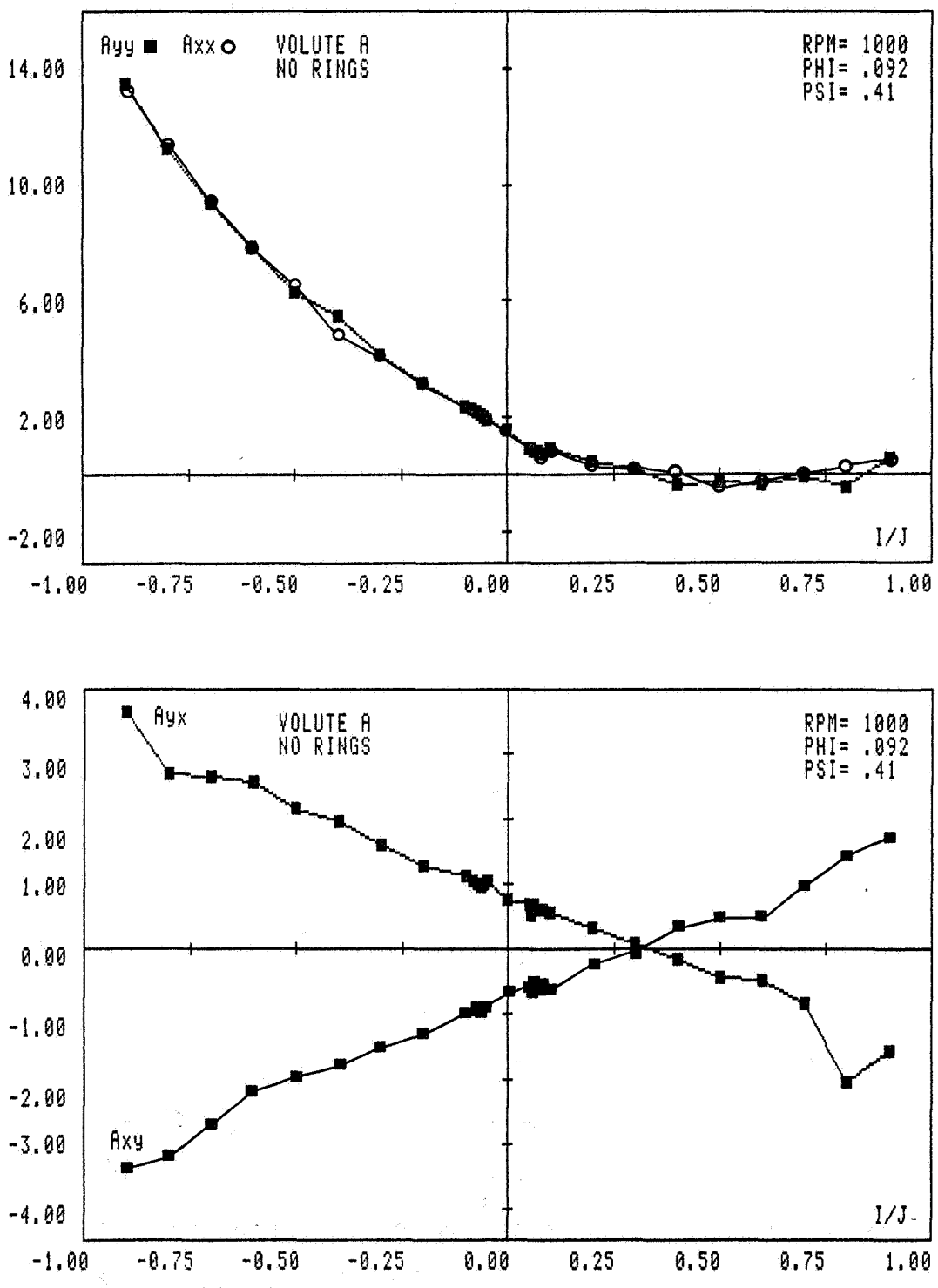

Figure 9. The hydrodynamic force matrix, [A] as a function of Ω/ω for the Volute A/Impeller X combination at 1000 rpm and ϕ = 0.092.

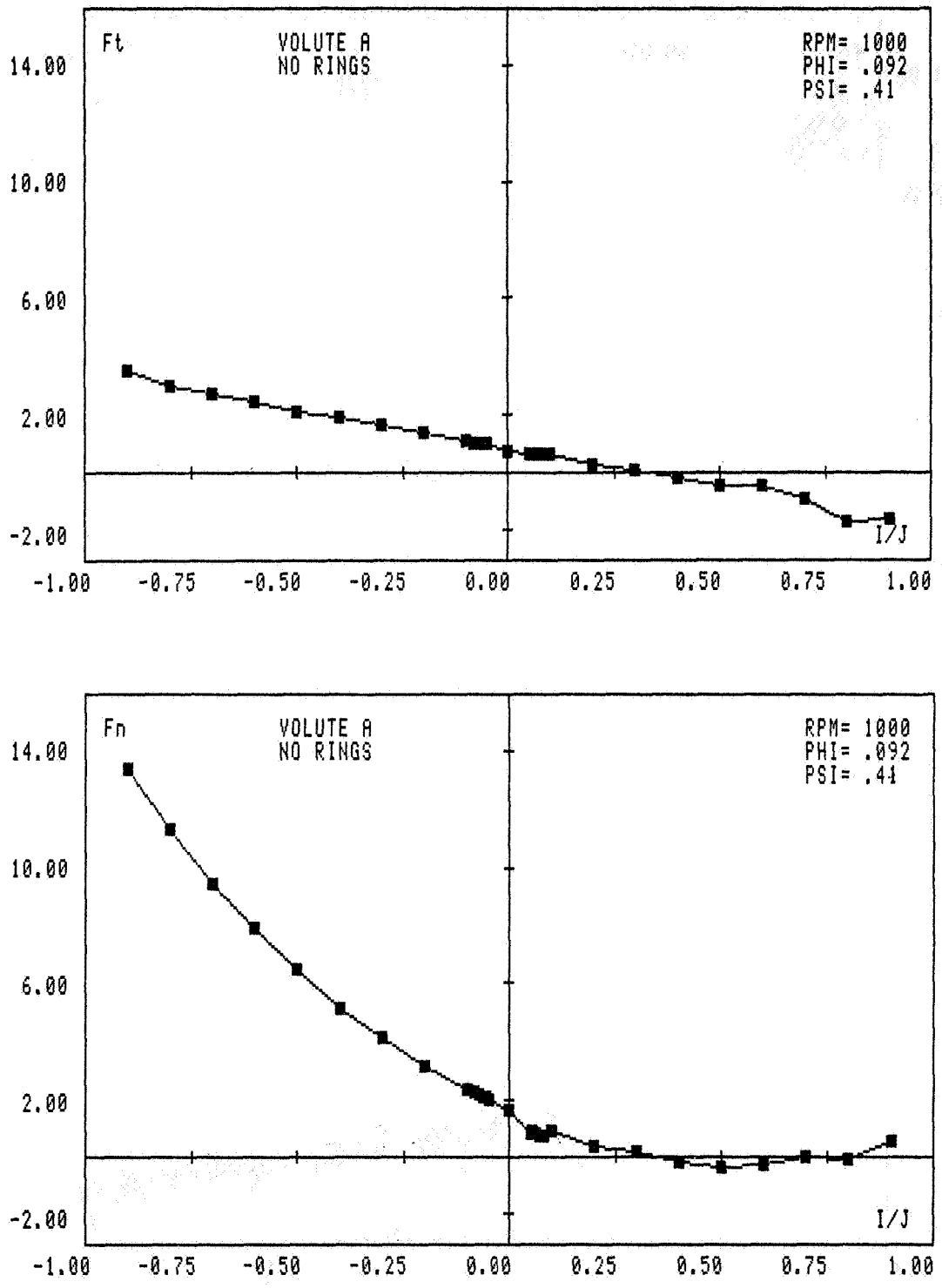

Figure 10. The dimensionless normal and tangential forces, F_N, F_T corresponding to Figure 9.

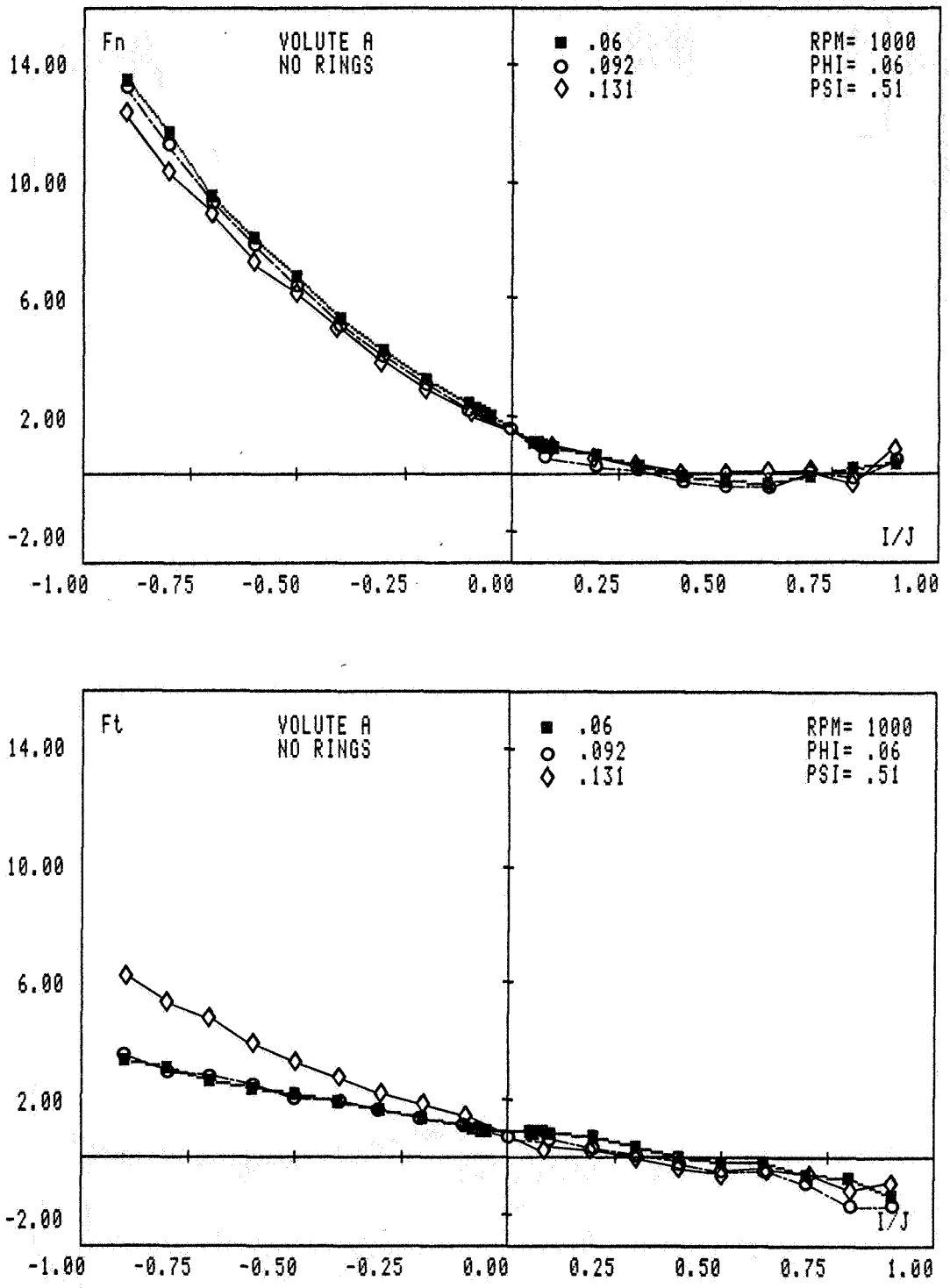

Figure 11. The normal and tangential forces for Volute A/Impeller X at 1000 rpm for three flow coefficients ϕ = 0.06, 0.092, 0.131.

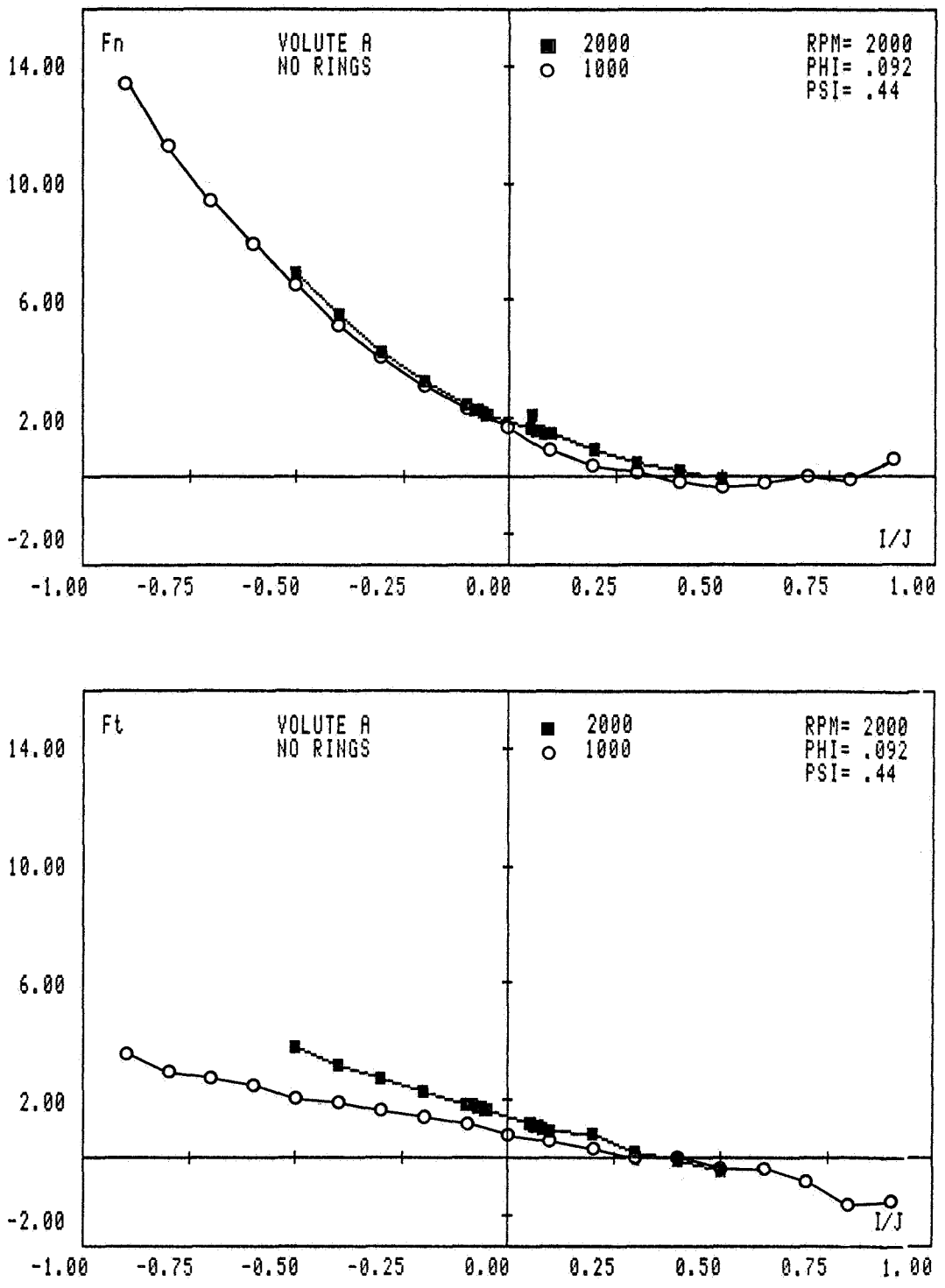

Figure 12. The normal and tangential forces, for Volute A/Impeller X at the design flow coefficient ϕ = 0.092 and two different pump speeds, 1000 rpm and 2000 rpm.

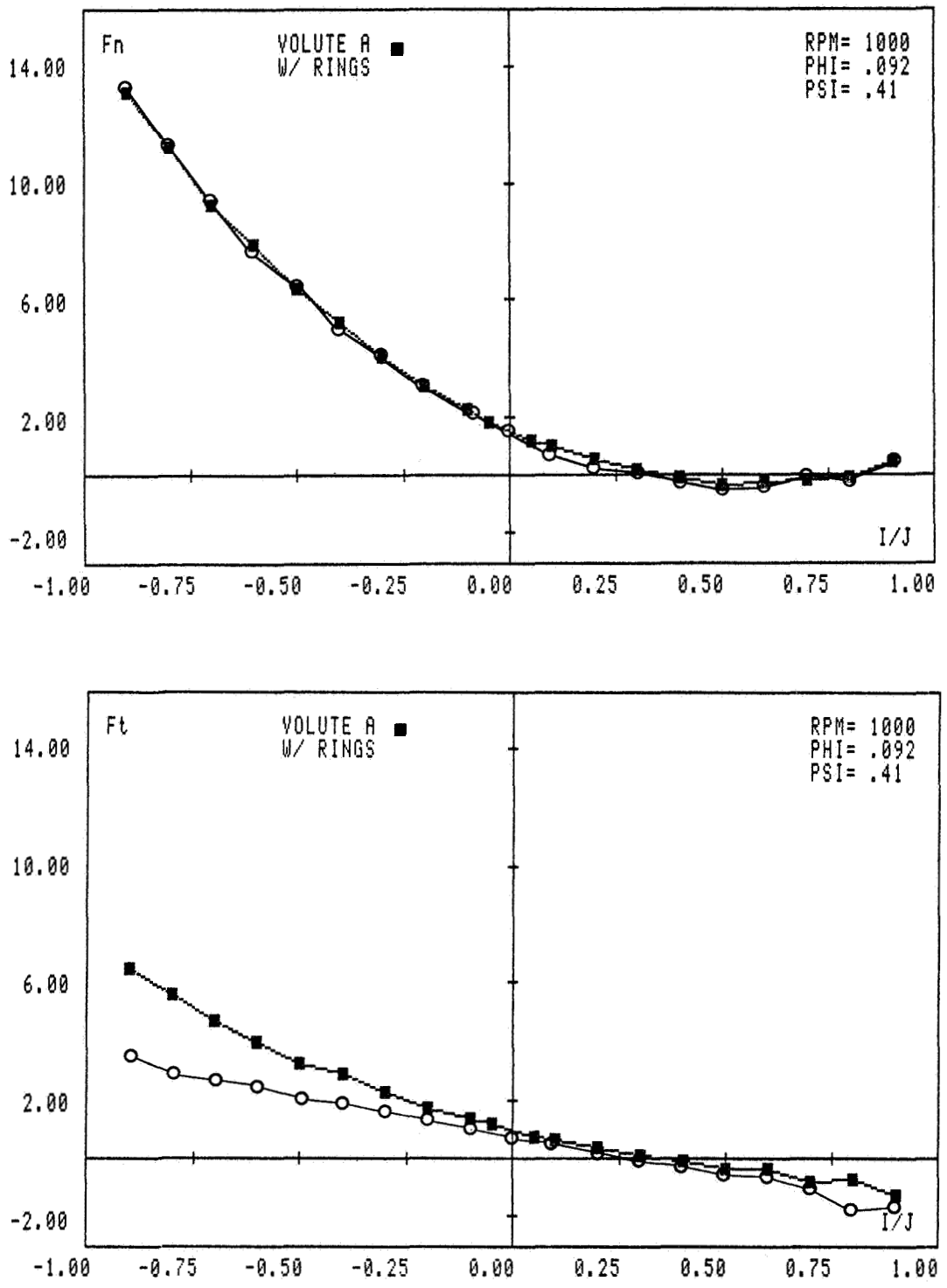

Figure 13. The normal and tangential forces F_N, F_T for Volute A/Impeller X at 1000 rpm and the design flow coefficient, $\phi = 0.092$ showing the effect of the leakage limiting rings.

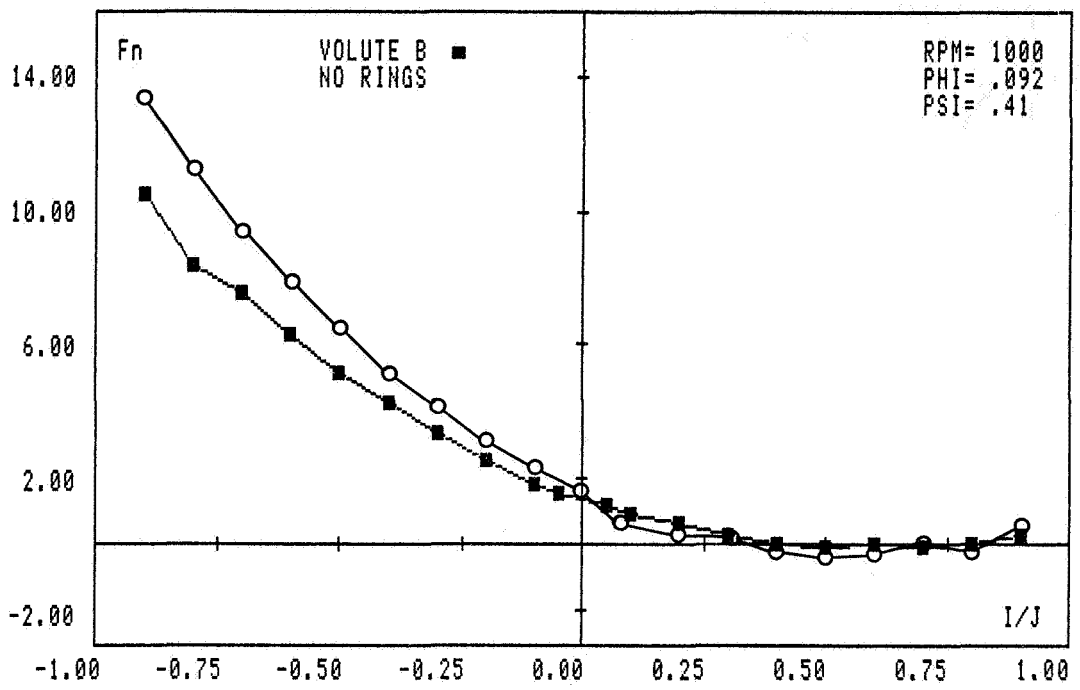

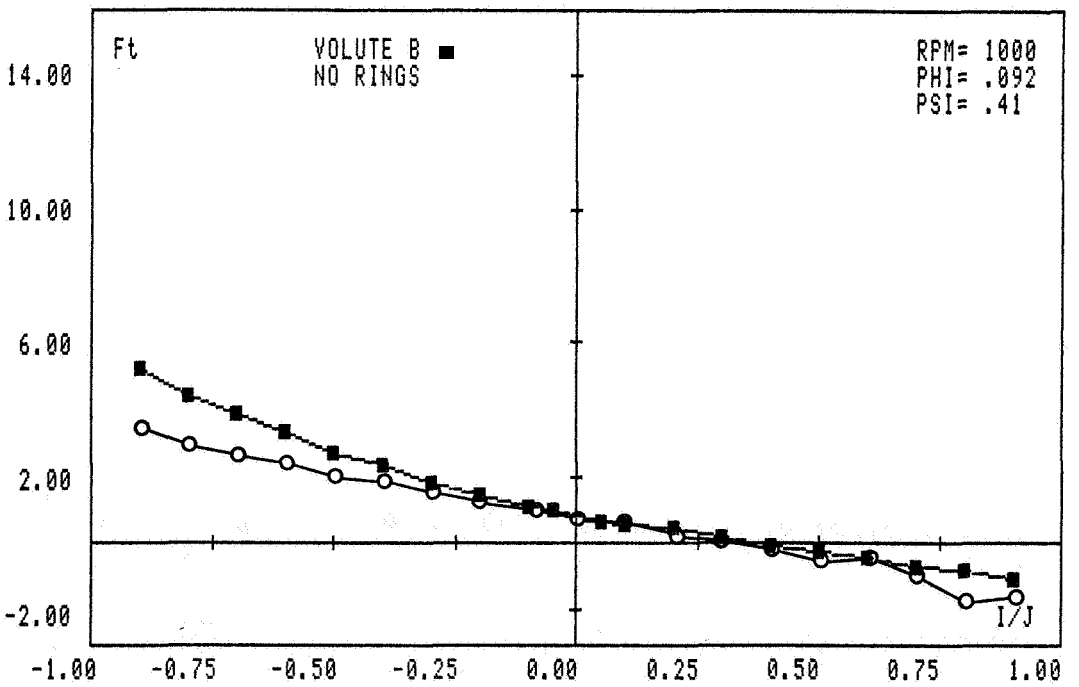

Figure 14. Comparison of F_N, F_T for Volutes A and B at 1000 rpm and ϕ = 0.092.

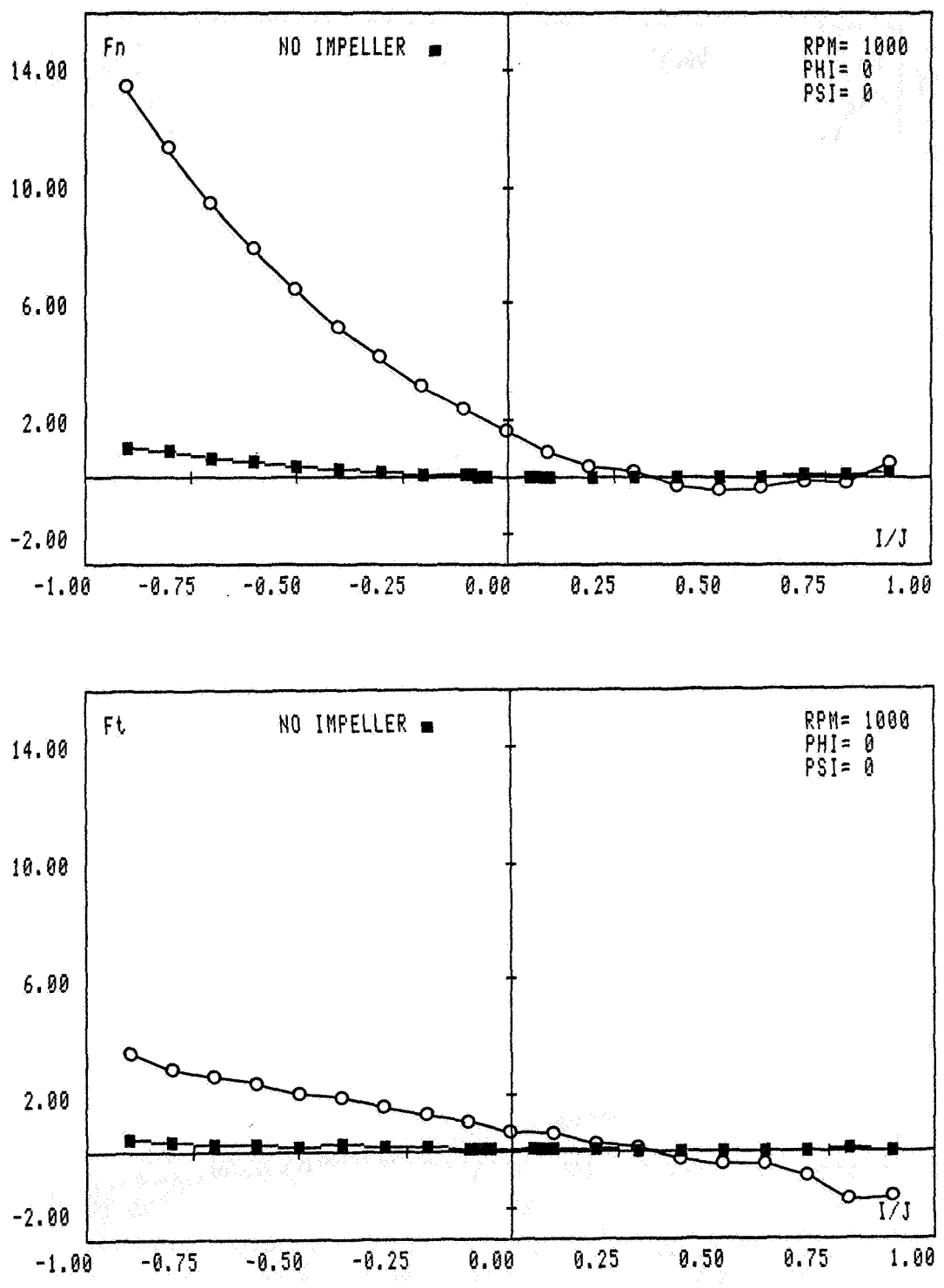

Figure 15. **The hydrodynamic tare effect of the internal balance when tested without an impeller at 1000 rpm.**

TWO-DIMENSIONAL UNSTEADY ANALYSIS OF FLUID FORCES ON A WHIRLING CENTRIFUGAL IMPELLER IN A VOLUTE*

Y. Tsujimoto+
Osaka University
560 Toyonaka, Osaka, Japan

A. J. Acosta and C. E. Brennen
California Institute of Technology
Pasadena, California 91125

Destabilizing fluid forces on a whirling centrifugal impeller rotating in a volute have been observed (Ref.1). A quasisteady analysis neglecting shed vorticity (Ref.2) or an unsteady analysis without a volute (Ref.3) does not predict the existence of such destabilizing fluid forces on a whirling impeller.

The present report is intended to take into account the effects of a volute and the shed vorticity. We treat cases when an impeller with an infinite number of vanes rotates with a constant velocity Ω and its center whirls with a constant eccentric radius ε and a constant whirling velocity ω.

Major assumptions are as follows:

(1) The number of the vanes is so large that the impeller can be treated as an actuator impeller in which the flow is perfectly guided.

(2) Flow is inviscid, incompressible and two-dimensional.

(3) The eccentricity ε is so small that unsteady components can be linearized.

(4) Vorticity is transported on a prescribed mean flow, i.e., the operating point is near design flow rate.

(5) The volute can be represented by a curved plate (see Fig.1).

* Partial support by the Yamada Science Foundation, Japan and the National Aeronautics and Space Administration under Contract NAS8-33108.

+ Visiting Associate, California Institute of Technology (1983-84).

SYMBOLS

$Z = X + iY$: stationary frame with its origin 0 fixed to the center of the whirling motion

$Z' = X' + iY' = Z - \varepsilon e^{i\omega t}$: translating frame with its origin 0' fixed to the center of the impeller and its axes parallel to those of Z.

r_1 , r_2 : inner and outer radius of the impeller

$\beta(r)$: vane angle measured from circumferential direction

ε : eccentricity

ω : angular velocity of whirling motion

Ω : angular velocity of the impeller

Γ_i : prerotation, Q: flow rate

$\underset{(v_r, v_\theta)}{\underset{\sim}{V}} = u + iv$: absolute velocity

$\underset{(v_r', v_\theta')}{\underset{\sim}{V}'} = u' + iv'$: velocity relative to x'y' frame

$\underset{(w_r, w_\theta)}{\underset{\sim}{W}}$: velocity relative to the impeller

t : time, t=0 when 00' is in the direction of x

n : circumferential mode number

Subscripts

$1, 2$: quantities at the inner and outer radius respectively

Superscripts

$\bar{}$: steady component ~ ; unsteady component

BASIC EQUATIONS

Euler's equation in the rotating and translating frame fixed to the rotor is,

$$\frac{\partial \underset{\sim}{V}}{\partial t^*} + \nabla\left(\frac{\underset{\sim}{W}^2}{2} - \frac{(\underset{\sim}{V} + \underset{\sim}{\Omega} \times \underset{\sim}{Z}')^2}{2} + \frac{p}{\rho}\right) - \underset{\sim}{W} \times (\nabla \times \underset{\sim}{V}) = \underset{\sim}{f} \qquad (1)$$

where $\partial/\partial t^*_{i\theta}$ is the time derivative in the rotating frame and $\underset{\sim}{U} = i\omega\varepsilon e^{i\omega t}$ and $\underset{\sim}{\Omega} \times \underset{\sim}{x}' = ir\Omega e^{i\theta}$ are the translational velocity due to whirling and the rotational velocity of the impeller. In an actuator impeller with an infinite number of vanes,

the effects of the vorticity distribution on the vanes and the forces exerted by the vanes are represented by the vorticity $\nabla \times \underset{\sim}{y}$ and the external force $\underset{\sim}{f}$ respectively in the above equation. For inviscid flow through actuator impellers, $\underset{\sim}{f}$ and $\underset{\sim}{w} \times (\nabla \times \underset{\sim}{y})$ are normal to the vane surface and the component of Equation (1) parallel to the vane surface is

$$\frac{\partial v_s}{\partial t^*} + \frac{\partial}{\partial s}\left(\frac{w^2}{2} - \frac{v_t^2}{2} + \frac{p}{\rho}\right) = 0 \qquad (2)$$

where

$$v_s = w - r\Omega\cos\beta - \omega\varepsilon\cos(\theta+\beta-\omega t)$$

$$w(r,\theta) = w_r(r_2, \theta-\vartheta(r))\, r_2 / (r(s)\sin\beta(r))$$

$$v_t^2 = r^2\Omega^2 + \varepsilon^2\omega^2 + 2r\omega\varepsilon\Omega\cos(\theta-\omega t)$$

$$\partial/\partial t^* = \partial/\partial t + \Omega\,\partial/\partial\theta$$

Integrating Equation (2) along the vane surface we get the following total pressure increase.

$$\frac{p_{t2}-p_{t1}}{\rho} = [r\Omega v_\theta']_1^2 - M\left(\frac{\partial}{\partial t}+\Omega\frac{\partial}{\partial\theta}\right)v_{r2}' - \varepsilon\omega(\Omega-\omega)\int_1^2 \sin(\theta+\beta-\omega t)\,ds$$
$$+ \varepsilon\omega\left[(r\Omega + v_\theta')\cos(\theta-\omega t) + v_r'\sin(\theta-\omega t)\right]_1^2 \qquad (3)$$

where

$$M = \int_1^2 \frac{r_2}{r\sin\beta(r)}\,dr$$

Downstream of the impeller, where $\underset{\sim}{f}=0$, Equation (1) can be expressed as

$$\underset{\sim}{w} \times (\nabla \times \underset{\sim}{v}) = \frac{\partial \underset{\sim}{v}}{\partial t^*} + \frac{1}{2}\nabla H', \quad H' = \frac{p}{\rho} + \frac{w^2}{2} - \frac{v_t^2}{2} \qquad (4)$$

By multiplying $\underset{\sim}{e}_x dx + \underset{\sim}{e}_y dy = r_2(\underset{\sim}{e}_y\cos\theta - \underset{\sim}{e}_z\sin\theta)d\theta$ on both sides of the above equation we get the following vorticity distribution at the outer radius of the impeller;

$$\zeta_2(r_2,\theta) = -\frac{1}{r_2 w_{r2}}\frac{\partial H_2'}{\partial\theta} - \frac{1}{w_{r2}}\left(\frac{\partial}{\partial t}+\Omega\frac{\partial}{\partial\theta}\right)v_{\theta 2}'$$
$$= \frac{1}{r_2 w_{r2}}\Big[r_1\Omega\frac{\partial v_{\theta 1}'}{\partial\theta} + \omega\varepsilon\Big\{v_{r1}'\cos(\theta_1-\omega t) - v_{\theta 1}'\sin(\theta_1-\omega t)$$
$$+ \frac{\partial v_{\theta 1}'}{\partial\theta}\cos(\theta_1-\omega t) + \frac{\partial v_{r1}'}{\partial\theta}\sin(\theta_1-\omega t) - r_1\Omega\sin(\theta_1-\omega t)\Big\}$$
$$+ \left(\frac{\partial}{\partial t}+\Omega\frac{\partial}{\partial\theta}\right)\frac{\partial v_{r2}'}{\partial\theta}\cdot M + \varepsilon\omega(\Omega-\omega)\int_1^2\cos(\theta+\beta-\omega t)\,ds$$
$$- \frac{1}{w_r}\left(\frac{\partial}{\partial t}+\Omega\frac{\partial}{\partial\theta}\right)v_{\theta 2}' + \frac{1}{w_r}\varepsilon\omega(\Omega-\omega)\sin(\theta-\omega t) \qquad (5)$$

ELEMENTARY FLOW COMPONENTS

The flow tangency condition at the impeller outlet is,

$$v_{\theta 2}' = r_2\Omega - v_{r2}' \cot\beta_2 \tag{6}$$

The first term on the right hand side of the above equation is cancelled by the flow component

$$v_r' - i\, v_\theta' = \frac{1}{2\pi r}\left\{ Q - 2\pi i r_2 \left(r_2\Omega - \frac{Q}{2\pi r_2}\cot\beta_2 \right) \right\} \tag{7}$$

and other disturbance components should satisfy the following equation

$$v_{\theta 2}' = - v_{r2}' \cot\beta_2 \ . \tag{8}$$

For the region outside the impeller we consider two types of elementary velocity disturbances satisfying Equation (8):

First, consider the following velocity field:

$$u' - i v' = \frac{i\Gamma}{2\pi}\left\{ \frac{1}{z' - z_0'} + e^{-2i\beta_2}\left(\frac{1}{z'} - \frac{1}{z' - r_2^2/\bar{z}_0'} \right) \right\} \tag{9}$$

This velocity field has a vortex Γ at $z'=z'_0$ and satisfies Equation (8) with no circulation/net flow around/from the impeller. Consider a vortex distribution $\Gamma(s) = \Gamma_s(s) + \varepsilon\Gamma_d^s(s)\sin\omega t + \varepsilon\Gamma_d^c(s)\cos\omega t$ on the volute surface $z_o(s)=z'_o+\varepsilon e^{i\omega t}$. Assuming $\varepsilon \ll r_2$, we get the following steady and unsteady velocity components

$$\bar{u}' - i\bar{v}'|_{z'} = \frac{i}{2\pi}\int_0^{S_2} \Gamma_s(s)\left[\frac{1}{\bar{z}' - \bar{z}_0(s)} - \frac{e^{-2i\beta_2}}{z'}\frac{r_2^2}{(z'\bar{z}_0(s) - r_2^2)} \right] ds \tag{10}$$

$$\begin{aligned} \tilde{u}' - i\tilde{v}'|_{z'} = &-\frac{i\varepsilon}{2\pi}\int_0^{S_2} \Gamma_s(s)\left[\frac{e^{i\omega t}}{(\bar{z}' - \bar{z}_0(s))^2} + e^{-2i\beta_2}\frac{r_2^2 e^{-i\omega t}}{(z'\bar{z}_0(s) - r_2^2)^2} \right] ds \\ &+ \frac{i\varepsilon}{2\pi}\int_0^{S_2} (\Gamma_d^s(s)\sin\omega t + \Gamma_d^c(s)\cos\omega t)\left[\frac{1}{\bar{z}' - \bar{z}_0(s)} - \frac{r_2^2 e^{-2i\beta_2}}{z'(z'\bar{z}_0(s) - r_2^2)} \right] ds \end{aligned} \tag{11}$$

where z' is fixed to $x'y'$-plane. At $z=z_s=z'+\varepsilon e^{i\omega t}$, which is fixed to the volute, we get the following expressions:

$$\bar{u}' - i\bar{v}'|_{z_s} = \frac{i}{2\pi}\int_0^{S_2} \Gamma_s(s)\left[\frac{1}{\bar{z}_s - \bar{z}_0(s)} - \frac{r_2^2 e^{-2i\beta_2}}{z_s(z_s\bar{z}_0(s) - r_2^2)} \right] ds \tag{12}$$

$$\tilde{u}' - i\tilde{v}'|_{z_s} = -\frac{i\varepsilon}{2\pi}\int_0^{s_e}\Gamma_s(s)\frac{r_2^2 e^{-2i\beta_2}}{z_s(z_s\bar{z}_o(s)-r_2^2)}\left(\frac{e^{i\omega t}}{z_s}+\frac{\bar{z}_o(s)e^{i\omega t}+z_s e^{-i\omega t}}{z_s\bar{z}_o(s)+r_2^2}\right)ds$$

$$+\frac{i\varepsilon}{2\pi}\int_0^{s_e}(\Gamma_d^c(s)\cos\omega t+\Gamma_d^s(s)\sin\omega t)\left[\frac{1}{z_s-z_o(s)}-\frac{r_2^2 e^{-2i\beta_2}}{z_s(z_s\bar{z}_o(s)-r_2^2)}\right]ds \qquad (13)$$

In the same way the velocity component (7) has the following steady and unsteady components at the volute surface $z_s=r_s e^{i\theta_s}=z'+\varepsilon e^{i\omega t}$.

$$\bar{v}_r' - i\bar{v}_\theta'|_{z_s} = \frac{1}{2\pi r_s}\left\{Q - 2\pi i r_2\left(r_2\Omega - \frac{Q}{2\pi r_2}\cot\beta_2\right)\right\} \qquad (14)$$

$$\tilde{v}_r' - i\tilde{v}_\theta'|_{z_s} = \frac{1}{2\pi r_s}\left\{Q - 2\pi i r_2\left(r_2\Omega - \frac{Q}{2\pi r_2}\cot\beta_2\right)\right\}\frac{\varepsilon}{r_s}e^{i(\omega t-\theta_s)} \qquad (15)$$

Next consider the velocity field due to shed vorticity. If we assume that the vorticity is transported on a streamline

$$v_r' - i v_\theta' = (Q - i\Gamma)/(2\pi r)$$

we have the following elementary vorticity field

$$\zeta_n = \zeta_{cn}\cos\left\{\mp\omega\left(t-\frac{\pi}{Q}(r^2-r_2^2)\right)+n\left(\theta-\frac{\Gamma}{Q}\log(r/r_2)\right)\right\}$$
$$+\zeta_{sn}\sin\left\{\mp\omega\left(t-\frac{\pi}{Q}(r^2-r_2^2)\right)+n\left(\theta-\frac{\Gamma}{Q}\log(r/r_2)\right)\right\} \qquad (16)$$

and the corresponding velocity field

$$v_{rn}^{\zeta} - i v_{\theta n}^{\zeta} = (\zeta_{cn}Z_{Rn}+\zeta_{sn}Z_{In})\cos(n\theta\mp\omega t)+(\zeta_{sn}Z_{Rn}-\zeta_{cn}Z_{In})\sin(n\theta\mp\omega t) \qquad (17)$$

where

$$Z_{Rn} = R_{Rn} - i\Theta_{Rn}, \qquad Z_{In} = R_{In} - i\Theta_{In}$$

$$R_{Rn} + j R_{In} = -j[F(r)+G(r)], \qquad \Theta_{Rn} + j\Theta_{In} = -F(r)+G(r)$$

$$F(r) = \frac{1}{2}\int_{r_2}^{r}\exp\left\{j\left(\mp\omega\frac{\pi}{Q}(r_0^2-r_2^2)-n\frac{\Gamma}{Q}\log(r_0/r_2)\right)\right\}(r_0/r)^{n+1}dr_0$$

$$G(r) = \frac{1}{2}\int_{r_2}^{r}\exp\left\{j\left(\mp\omega\frac{\pi}{Q}(r_0^2-r_2^2)-n\frac{\Gamma}{Q}\log(r_0/r_2)\right)\right\}(r/r_0)^{n-1}dr_0$$

Equation (17) includes the effects of the vorticity in $r_2<r<R$. Since G(r) is convergent only for $n\geq 3$ as $R\to\infty$, we should artificially prescribe some appropriate finite value for R. Equation (17) does not satisfy Equation (8) and we should add a potential component

$$v_{rn}^{P} - i v_{\theta n}^{P} = -e^{-i\beta_2}(\zeta_{cn}+i\zeta_{sn})\left[(\Theta_R - i\Theta_I)\sin\beta_2+(R_R-iR_I)\cos\beta_2\right]_{r=r_2}\frac{e^{i\theta\mp i\omega t}}{z^{n+1}} \qquad (18)$$

such that

$$v_{rn}' - i\, v_{\theta n}' = \left(v_{rn}^{S} - i\, v_{\theta n}^{S} \right) + \left(v_{rn}^{P} - i\, v_{\theta n}^{P} \right) \tag{19}$$

satisfies the boundary condition of Equation (8). We may now note that there are steady and unsteady components as follows:

(i) Steady component; in Equations (16)-(19) we put $\omega=0$ and represent the related quantities with superscript $\bar{}$ and suffix n (n=1,2...) for each mode, $\bar{\zeta}_{cn}$ etc.

(ii) Unsteady component; correspondingly to the sign on ω and the mode n, we represent the related quantities such that $\hat{\zeta}_{cn}^{\pm}$ etc.

On the volute $z=z_s=z'+\varepsilon e^{i\omega t}$, the steady and unsteady velocity fields are expressed as follows:

$$\begin{aligned}
\bar{u}' - i\,\bar{v}'|_{z_s} = \sum_{n=1}^{\infty} \Big[& \Big[(\bar{\zeta}_{cn}\bar{z}_{Rn} + \bar{\zeta}_{sn}\bar{z}_{In}) \cos n\theta_s + (\bar{\zeta}_{sn}\bar{z}_{Rn} - \bar{\zeta}_{cn}\bar{z}_{In}) \sin n\theta_s \Big] e^{-i\theta_s} \\
& - e^{-i\beta_2} (\bar{\zeta}_{cn} + i\,\bar{\zeta}_{sn}) \Big[(\bar{\Theta}_{Rn} - i\bar{\Theta}_{In}) \sin\beta_2 + (\bar{R}_{Rn} - i\,\bar{R}_{In}) \cos\beta_2 \Big]_{r=r_2} / z_s^{n+1} \Big]
\end{aligned} \tag{20}$$

$$\begin{aligned}
\hat{u}' - i\,\hat{v}'|_{z_s}/\varepsilon = \sum_{n=1}^{\infty} \Big[& \Big[(\bar{\zeta}_{cn}\bar{z}_{Rn} + \bar{\zeta}_{sn}\bar{z}_{In})(-n\sin n\theta_s - i\cos n\theta_s) \\
& + (\bar{\zeta}_{sn}\bar{z}_{Rn} - \bar{\zeta}_{cn}\bar{z}_{In})(n\cos n\theta_s - i\sin n\theta_s) \Big] \frac{1}{r_s} \sin(\theta_s - \omega t)\, e^{-i\theta_s} \\
& - \Big[(\bar{\zeta}_{cn}\bar{z}_{Rn}' + \bar{\zeta}_{sn}\bar{z}_{In}') \cos n\theta_s + (\bar{\zeta}_{sn}\bar{z}_{Rn}' - \bar{\zeta}_{cn}\bar{z}_{In}') \sin n\theta_s \Big] \cos(\theta_s - \omega t)\, e^{-i\theta_s} \\
& - (n+1) e^{-i\beta_2} (\bar{\zeta}_{cn} + i\,\bar{\zeta}_{sn}) \Big[(\bar{\Theta}_{Rn} - i\bar{\Theta}_{In}) \sin\beta_2 + (\bar{R}_{Rn} - i\,\bar{R}_{In}) \cos\beta_2 \Big]_{r=r_2} \frac{e^{i\omega t}}{z_s^{n+2}} \Big] \\
& + \sum_{n=1}^{\infty} \sum^{\pm} \Big[\Big[(\hat{\zeta}_{cn}^{\pm} \hat{z}_{Rn}^{I} + \hat{\zeta}_{sn}^{I} \hat{z}_{In}^{\pm}) \cos(n\theta_s \pm \omega t) + (\hat{\zeta}_{sn}^{I} \hat{z}_{Rn}^{I} - \hat{\zeta}_{cn}^{I} \hat{z}_{In}^{\pm}) \sin(n\theta_s \pm \omega t) \Big] e^{-i\theta_s} \\
& - e^{i\beta_2} (\hat{\zeta}_{cn}^{I} + i\,\hat{\zeta}_{sn}^{I}) \Big[(\hat{\Theta}_{Rn}^{I} - i\hat{\Theta}_{In}^{\pm}) \sin\beta_2 + (\hat{R}_{Rn}^{I} - i\,\hat{R}_{In}^{\pm}) \cos\beta_2 \Big]_{r=r_2} \frac{e^{\mp i\omega t}}{z_s^{n+1}} \Big]
\end{aligned} \tag{21}$$

In the region upstream of the impeller ($r \le r_1$), we consider a source Q and prerotation of strength Γ_i at the center of the volute. Then the velocity can be expressed in the series

$$v_r' - i\, v_\theta' = \Big[\frac{Q + i\Gamma_i}{2\pi} \frac{1}{z' + \varepsilon e^{i\omega t}} + \sum_{n=1}^{\infty} \left\{ \bar{A}_n + \varepsilon (A_n^s \sin\omega t + A_n^c \cos\omega t) \right\} z'^{n-1} \Big] e^{i\theta} \tag{22}$$

where $\bar{A}_n = \bar{A}_{Rn} + i\bar{A}_{In}$, $A_n^s = A_{Rn}^s + iA_{In}^s$, $A_n^c = A_{Rn}^c + iA_{In}^c$ are complex constants.

Now we have given all of the elementary flow components necessary for the construction of the entire flow field. Each of them contains several unknowns that are determined in the following sections.

BOUNDARY CONDITIONS ON THE VOLUTE

The flow tangency condition on the volute surface is,

$$\varepsilon\omega\cos(\alpha-\omega t) + v'\cos\alpha - u'\sin\alpha = v_n = 0 \tag{23}$$

where α is the angle between volute and x-axis. If we put

$$u' = \bar{u}' + \hat{u}'_c\cos\omega t + \hat{u}'_s\sin\omega t$$

$$v' = \bar{v}' + \hat{v}'_c\cos\omega t + \hat{v}'_s\sin\omega t$$

we get the following conditions,

$$\bar{v}'\cos\alpha - \bar{u}'\sin\alpha = 0, \tag{24}$$

$$\hat{v}'_c\cos\alpha - \hat{u}'_c\sin\alpha = -\varepsilon\omega\cos\alpha, \tag{25}$$

$$\hat{v}'_s\cos\alpha - \hat{u}'_s\sin\alpha = -\varepsilon\omega\sin\alpha. \tag{26}$$

The steady velocity $\bar{u}', \bar{v}'$ is given as a sum of the velocity components in Equations (12), (14) and (20). The unsteady components $\tilde{u}'_c$, $\tilde{v}'_c$ and $\tilde{u}'_s$, $\tilde{u}'_s$ are the cosine and sine components of the velocity of Equations (13), (15) and (21). Equations (24)-(26) constitute integral equations for $\Gamma_s(s)$, $\Gamma_d^s(s)$ and $\Gamma_d^c(s)$.

CONTINUITY EQUATION

The continuity equation across the impeller is

$$v_r'(r_1, \theta_1 = \theta + \vartheta_0) = \frac{r_2}{r_1} v_r'(r_2, \theta) \tag{27}$$

where ϑ_0 is the angle between corresponding leading and trailing edges of a vane. At the outer radius the total of the steady velocity components given by Equations (7), (10) and (19) can be expressed as a Fourier series; namely,

$$\left.\begin{aligned} \bar{v}_r'(r_2,\theta) &= \frac{Q}{2\pi r_2} + \sum_{n=1}^{\infty}\left(\bar{v}_{rn}^s\sin n\theta + \bar{v}_{rn}^c\cos n\theta\right) \\ \bar{v}_\theta'(r_2,\theta) &= r_2\Omega - \frac{Q}{2\pi r_2}\cot\beta_2 + \sum_{n=1}^{\infty}\left(\bar{v}_{\theta n}^s\sin n\theta + \bar{v}_{\theta n}^c\cos n\theta\right) \end{aligned}\right\} \tag{28}$$

In the same way, the unsteady components of Equations (11), and (19) can be expressed as

$$\left.\begin{aligned}\tilde{v}_r'(r_2,\theta) &= \varepsilon\sum_{n=1}^{\infty}\left[\left(\tilde{v}_{rn}^{cc}\cos n\theta+\tilde{v}_{rn}^{cs}\sin n\theta\right)\cos\omega t+\left(\tilde{v}_{rn}^{sc}\cos n\theta+\tilde{v}_{rn}^{ss}\sin n\theta\right)\sin\omega t\right]\\ \tilde{v}_\theta'(r_2,\theta) &= \varepsilon\sum_{n=1}^{\infty}\left[\left(\tilde{v}_{\theta n}^{cc}\cos n\theta+\tilde{v}_{\theta n}^{cs}\sin n\theta\right)\cos\omega t+\left(\tilde{v}_{\theta n}^{sc}\cos n\theta+\tilde{v}_{\theta n}^{ss}\sin n\theta\right)\sin\omega t\right]\end{aligned}\right\} \quad (29)$$

At the inner radius $r=r_1$ we expand Equation (22) in $\theta=\theta_1-\vartheta_o$ rather than in θ_1; then,

$$\left.\begin{aligned}\bar{v}_r'(r_1,\theta_1=\theta+\vartheta_o) &= \frac{Q}{2\pi r_1}+\sum_{n=1}^{\infty}\left\{\bar{\bar{v}}_{rn}^{s}\sin n\theta+\bar{\bar{v}}_{rn}^{c}\cos n\theta\right\}\\ \bar{v}_\theta'(r_1,\theta_1=\theta+\vartheta_o) &= -\frac{\Gamma_2}{2\pi r_1}+\sum_{n=1}^{\infty}\left\{\bar{\bar{v}}_{\theta n}^{s}\sin n\theta+\bar{\bar{v}}_{\theta n}^{c}\cos n\theta\right\}\end{aligned}\right\} \quad (30)$$

$$\left.\begin{aligned}\tilde{v}_r'(r_1,\theta_1=\theta+\vartheta_o) &= \varepsilon\sum_{n=1}^{\infty}\left[\left(\tilde{\bar{v}}_{rn}^{cc}\cos n\theta+\tilde{\bar{v}}_{rn}^{cs}\sin n\theta\right)\cos\omega t+\left(\tilde{\bar{v}}_{rn}^{sc}\cos n\theta+\tilde{\bar{v}}_{rn}^{ss}\sin n\theta\right)\sin\omega t\right]\\ \tilde{v}_\theta'(r_1,\theta_1=\theta+\vartheta_o) &= \varepsilon\sum_{n=1}^{\infty}\left[\left(\tilde{\bar{v}}_{\theta n}^{cc}\cos n\theta+\tilde{\bar{v}}_{\theta n}^{cs}\sin n\theta\right)\cos\omega t+\left(\tilde{\bar{v}}_{\theta n}^{sc}\cos n\theta+\tilde{\bar{v}}_{\theta n}^{ss}\sin n\theta\right)\sin\omega t\right]\end{aligned}\right\} \quad (31)$$

From Equation (27) we get the following relations

$$\bar{\bar{v}}_{rn}^{s}=(r_2/r_1)\,\bar{v}_{rn}^{s} \quad (32) \qquad \bar{\bar{v}}_{rn}^{c}=(r_2/r_1)\,\bar{v}_{rn}^{c} \quad (33)$$

$$\tilde{\bar{v}}_{rn}^{cc}=(r_2/r_1)\,\tilde{v}_{rn}^{cc} \quad (34) \qquad \tilde{\bar{v}}_{rn}^{cs}=(r_2/r_1)\,\tilde{v}_{rn}^{cs} \quad (35)$$

$$\tilde{\bar{v}}_{rn}^{sc}=(r_2/r_1)\,\tilde{v}_{rn}^{sc} \quad (36) \qquad \tilde{\bar{v}}_{rn}^{ss}=(r_2/r_1)\,\tilde{v}_{rn}^{ss} \quad (37)$$

Equations (32) and (33) give the relations to determine $\bar{A}_{Rn}$ and $\bar{A}_{In}$, and Equations (34)-(37) determine A_{Rn}^{c}, A_{Rn}^{s}, A_{In}^{c} and A_{In}^{s}.

STRENGTH OF SHED VORTICITY

If we use the expressions (28-31) in Equation (5), the steady vorticity components can be expressed as

$$\bar{\zeta}_{cn}=-\frac{2\pi r_2}{Q}\Omega n\left(\frac{Mn}{r_2}\,\bar{v}_{rn}^{c}+\bar{v}_{\theta n}^{s}-\frac{r_1}{r_2}\,\bar{\bar{v}}_{\theta n}^{s}\right) \quad (38)$$

$$\bar{\zeta}_{sn}=-\frac{2\pi r_2}{Q}\Omega n\left(\frac{Mn}{r_2}\,\bar{v}_{rn}^{s}-\bar{v}_{\theta n}^{c}+\frac{r_1}{r_2}\,\bar{\bar{v}}_{\theta n}^{c}\right) \quad (39)$$

where we have used $w_r=\frac{Q}{2\pi r_2}$ because of the assumption on the transport of the vorticity. In the same way, if we express the vorticity by

$$\tilde{\zeta}(r_2,\theta)=\frac{2\pi r_2}{Q}\,\varepsilon\sum_{n=1}^{\infty}\left[\left(\tilde{\zeta}_{sn}^{sc}\cos n\theta+\tilde{\zeta}_{sn}^{ss}\sin n\theta\right)\sin\omega t+\left(\tilde{\zeta}_{sn}^{cc}\cos n\theta+\tilde{\zeta}_{sn}^{cs}\sin n\theta\right)\cos\omega t\right] \quad (40)$$

and use the expressions (28-31) in Equation (5), we can express $\tilde{\zeta}$ in terms of the Fourier coefficients in Equations (28)-(31). Comparing Equation (40) and Equation (16), we get the following relations,

$$\tilde{\zeta}^{+}_{sm} = \frac{\pi r_2}{Q}\left(\tilde{\zeta}^{cs}_{m} + \tilde{\zeta}^{sc}_{m}\right) \qquad (41)$$

$$\tilde{\zeta}^{-}_{sm} = \frac{\pi r_2}{Q}\left(\tilde{\zeta}^{cs}_{m} - \tilde{\zeta}^{sc}_{m}\right) \qquad (42)$$

$$\tilde{\zeta}^{+}_{cm} = \frac{\pi r_2}{Q}\left(\tilde{\zeta}^{cc}_{m} - \tilde{\zeta}^{ss}_{m}\right) \qquad (43)$$

$$\tilde{\zeta}^{-}_{cm} = \frac{\pi r_2}{Q}\left(\tilde{\zeta}^{cc}_{m} + \tilde{\zeta}^{ss}_{m}\right) \qquad (44)$$

METHOD OF SOLUTION

We have used the following unknowns for the expression of the flow field

	steady component	unsteady component
$r \geq r_2$	$\Gamma_s(s)$	$\Gamma_d^c(s)$, $\Gamma_d^s(s)$
	$\bar{\zeta}_{cm}$, $\bar{\zeta}_{sm}$	$\tilde{\zeta}^{+}_{cm}$, $\tilde{\zeta}^{+}_{sm}$, $\tilde{\zeta}^{-}_{cm}$, $\tilde{\zeta}^{-}_{sm}$
$r \leq r_2$	$\bar{A}_{Rm}$, $\bar{A}_{Im}$	A^s_{Rm} , A^s_{Im} , A^c_{Rm} , A^c_{Im}

These unknowns are determined by the following relations:

	Steady Component	Unsteady Component
B.C. on the volute:	Eq.(24)	Eqs.(25),(26)
Continuity:	Eqs.(32),(33)	Eqs.(34),(35),(36),(37)
Vorticity:	Eqs.(38),(39)	Eqs.(41),(42),(43),(44)

These equations include integrals related to the vortex distribution on the volute surface, which should be evaluated by some appropriate method. Equations (24)-(26) are integral equations for the vortex distributions on the volute surface and could be reduced to simultaneous linear equations by a singularity method. In the solution of the vortex distributions the "Kutta condition" at the trailing edge should be applied. Strictly speaking the circulation around the volute fluctuates and a free vortex sheet is shed from the trailing edge of the volute. Since we are mainly interested in the forces on the impeller, we will neglect the effect of the free vortex sheet but apply the following conditions at the trailing edge.

Steady part:

$$\Gamma_s(S_\ell) = 0 \qquad (45)$$

Unsteady parts:

$$\omega \int_0^{S_\ell} \Gamma_d^c(s)\, ds = \Gamma_d^s(S_\ell)\, \bar{w}(S_\ell) \qquad (46)$$

$$-\omega \int_0^{S_\ell} \Gamma_d^s(s)\, ds = \Gamma_d^c(S_\ell)\, \bar{w}(S_\ell) \qquad (47)$$

Now we can express all the relations as a set of simultaneous linear equations which can be solved numerically. The steady component may be solved independently of

unsteady component, and the result used in the analysis of the unsteady components.

UNSTEADY FORCES ON THE IMPELLER

By considering the balance of the momentum of the fluid in the impeller, we can express the forces on the impeller as follows;

Steady component

$$\bar{X} - i\bar{Y} = -i\left[\oint_{C_2} \bar{p}_t\, d\bar{z}' - \oint_{C_1} \bar{p}_t\, d\bar{z}'\right] + \frac{i\rho}{2}\left[\oint_{C_2} (\bar{u}' - i\bar{v}')^2 d\bar{z}' - \oint_{C_1} (\bar{u}' - i\bar{v}')^2 d\bar{z}'\right] \tag{48}$$

and unsteady component

$$\begin{aligned}
&(\tilde{X}_c - i\tilde{Y}_c)\cos\omega t + (\tilde{X}_s - i\tilde{Y}_s)\sin\omega t \\
&= -i\left[\oint_{C_2} \tilde{p}_t\, d\bar{z}' - \oint_{C_1} \tilde{p}_t\, d\bar{z}'\right] + \rho\omega^2\varepsilon\pi(r_2^2 - r_1^2)e^{-i\omega t} \\
&\quad + i\rho\left[\oint_{C_2} (\bar{u}' - i\bar{v}')(\tilde{u}' - i\tilde{v}')\, d\bar{z}' - \oint_{C_1} (\bar{u}' - i\bar{v}')(\tilde{u}' - i\tilde{v}')\, d\bar{z}'\right] \\
&\quad + i\rho\omega\varepsilon\left[\oint_{C_2} (\bar{u}' - i\bar{v}')\cos(\theta - \omega t)\, r_2\, d\theta - \oint_{C_1} (\bar{u}' - i\bar{v}')\cos(\theta - \omega t)\, r_1\, d\theta\right] \\
&\quad - \rho\frac{d}{dt}\iint v_r'\left(r_2, \theta - \vartheta(r_2)\right)\frac{r_2}{r\sin\beta(r)}\, e^{-i(\theta - \frac{\pi}{2} + \beta)}\, r\, dr\, d\theta
\end{aligned} \tag{49}$$

The total pressure is given by Equation (3) and the integrals can be evaluated analytically by using the expressions (28–31).

CONCLUDING REMARKS

The unsteady forces can eventually be expressed in the form of stiffness matrix,

$$\begin{pmatrix} \tilde{X} \\ \tilde{Y} \end{pmatrix} = \begin{pmatrix} \tilde{X}_c/\varepsilon & , & \tilde{X}_s/\varepsilon \\ \tilde{Y}_c/\varepsilon & , & \tilde{Y}_s/\varepsilon \end{pmatrix} \begin{pmatrix} x = \varepsilon\cos\omega t \\ y = \varepsilon\sin\omega t \end{pmatrix} \tag{50}$$

The time average of the force component in the direction of whirling motion is given by $\frac{1}{2}(\tilde{Y}_c - \tilde{X}_s)$ and the sign of this quantity determines whether or not the fluid forces have destabilizing effects on the whirling motion. The sum $\frac{1}{2}(\tilde{X}_c + \tilde{Y}_s)$ gives the time average of the force component in the radial direction and thus the hydrodynamic stiffness. The ultimate goal of the present study is to examine these factors for realistic impeller–volute combinations.

REFERENCES

1. Chamieh, D. S., Acosta, A. J., Brennen, C. E., Caughey, T. K. and Franz, R., "Experimental Measurements of Hydrodynamic Stiffness Matrices for a Centrifugal Pump Impeller", Proceedings of NASA/ARO Workshop on Rotordynamic Instability Problems in High Performance Turbomachinery, NASA CP-2250, pp. 382-398.

2. Chamieh, D. S. "Forces on a Whirling Centrifugal Pump Impeller", Report E249.2, Div. of Eng. & Appl. Sci., Calif. Inst. of Tech., 1983: see also

   Chamieh, D., Acosta, A. J., Brennen, C. E. and Caughey, T. K. 1980. "A Brief Note on the Interaction of an Actuator Cascade with a Singularity. Proceedings of NASA/ARO Workshop on Rotordynamic Instability Problems in High Performance Turbomachinery", NASA CP-2133, 1980, pp. 237-248. Which formed the stimulus for the present work.

3. Shoji, H. and Ohashi, H. "Fluid forces on rotating centrifugal impeller with whirling motion", 1st Workshop on Rotordynamic Instability Problems in High Performance Turbomachinery, Texas A&M Univ., NASA Conf. Pub. 2133, (1980).

   Shoji, H. and Ohashi, H. "Fluid forces on rotating centrifugal impeller with whirling motion", Japan Soc. Mech. Engrs. (in Japanese), Vol.47, No.1, B(1981-7), p. 1187.

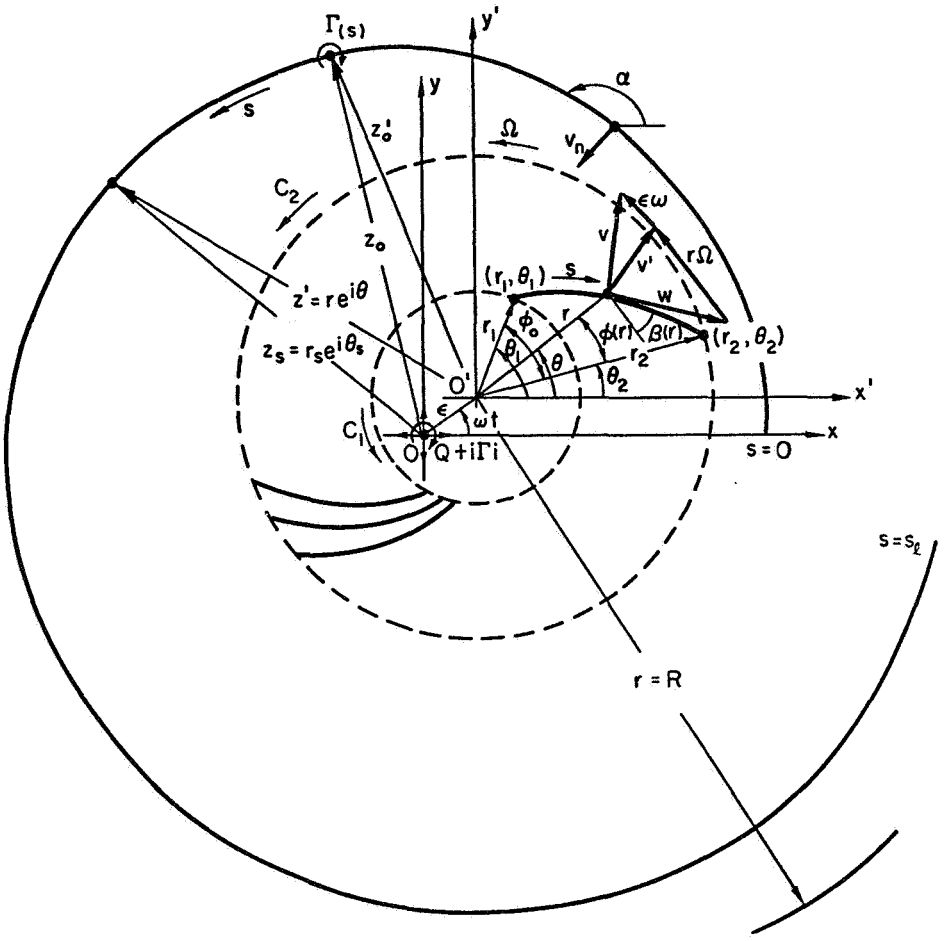

Figure 1. - Impeller and volute configuration.

THEORETICAL APPROACH TO LABYRINTH SEAL FORCES -

CROSS-COUPLED STIFFNESS OF A STRAIGHT-THROUGH LABYRINTH SEAL

Toshio Kameoka, Toru Abe, and Takeshi Fujikawa
Kobe Steel Ltd.
Kobe, Japan

Considering that there are two kinds of three dimensional flows in a labyrinth seal, a jet flow and a core flow, theoretical equations are set up concerning the motion of each flow. The pressure distribution within the labirinth is calculated, when the rotor shaft makes a small displacement from the center line of the casing, keeping parallel with it.

The theoretical values of cross coupled stiffness obtained by integrating the pressure under different labyrinth geometries and operating conditions through these formulas are compared with the experimental data presented by other researchers. The theoretical and experimental results show a satisfactory agreement.

1. INTRODUCTION

A self-excited rotor whirl sometimes occurs in high speed, high pressure turbo-machinery, and it is argued that one of the causes of the vibration is due to the labyrinth seal force. Recently, carefully prepared and precisely measured experiments have been carried out, which make possible a fairly exact prediction of the labyrinth seal forces. However, the scope of validation of the prediction should be within the range of reference of the experiments, because of the complexity of the phenomena, unless theoretical formulas verified with experimental data are available. In reality, commercial turbo--machines are normally furnished with labyrinth seals having a number of mixing chambers and are operated under much higher pressure than in experiments.

This paper proposes a method of calculating the asymmetrical pressure distribution in a labyrinth seal caused by the parallel displacement of the shaft, introducing a new mathematical model suggesting that there exist two kinds of independent three dimensional flows, interacting with each other, and that the circumferential variation of static pressure in the mixing chamber comes from the lack of uniformity of the circumferential velocity of the core flow, which is partly originated from the spiral flow effect of the jet flow.

2. NOTATION

$a_o, b_o, c_o, d_1, d_2, d_3, e_o$ = factors relating to fluid friction

c, [m/s] = circumferential velocity of core flow
f, f_m, [m^2] = cross sectional area of mixing chamber and that of core flow, respectively
f_s, [m^2] = cross sectional area of jet flow on the meridian plane between successive seal strips
N, [−] = number of mixing chamber
n, [m^{-1}] = convergency of seal clearance
p, [P_a] = pressure
p_o, [P_a] = inlet pressure
q, [kg/m-s] = mass flow of leakage per unit time per unit circumferential length
q_o, [kg/m-s] = ditto, under concentric position of rotor
R, [J/kg-K] = gas constant
R_o, [m] = inner radius of casing
r, [m] = radius of rotor
s, [m] = pitch of seal strips
s_o, [m] = wetted perimeter of core flow
T, [K] = gas temperature
u, [m/s] = circumferential velocity of jet flow
u_o, [m/s] = tangential velocity of entry swirl
u_r, [m/s] = circumferential velocity of rotor
α, [−] = factor of contraction of flow
β, [−] = pressure ratio, exit to inlet
δ, [m] = tip clearance of seal strips
δ_o, [m] = ditto, in the middle of labyrinth
θ, [rad] = helical angle of jet flow
θ_o, [rad] = angle of expansion of jet flow in meridian plane
$\lambda_1, \lambda_2, \lambda_{12}, \lambda_3$, [−] = coeficients of fluid friction in circumferential direction for $\tau_1, \tau_2, \tau_{12}, \tau_3$, respectively
μ, [P_a-s] = viscosity of gas
$\nu_{i-1,i}$, [−] = coeficient of carry over from (i-1)-th to i-th chamber
ρ, [kg/m^3] = density of gas
$\tau_1, \tau_2, \tau_{12}, \tau_3$ [P_a] = circumferential component of shear stress due to fluid friction between jet flow and casing wall, between the core flow and the rotor, between the jet flow and the core flow, and between the jet flow and the seal strip, respectively

Subscript, Superscript

i = quantity at the i-th chamber in the direction φ
$i-1,i$ = quantity at the boundary between (i-1)-th and i-th chamber in the direction φ
$\wedge$ = quantity under concentric position of rotor

3. FLOW OF GAS IN A LABYLINTH

3.1 Jet flow and core flow

It has been known for many years that the meridian flow in a labyrinth is somewhat similar to the flow ilustrated in Fig. 1. The flow of gas which has passed through the tip clearance of the seal strip, here called a jet flow, expands and increases its width when it goes through the mixing chamber. This flow also has a circumferential velocity due to the entry swirl and the peripheral velocity of the rotor. Thus, gas particles in this flow move

downwards along a helical stream line,illustrated in Fig.2. On the other hand, the gas flow in the mixing chamber, here called a core flow, forms a vortex within the surrounding walls on a meridian plane. This core flow also moves in a circumferencial direction induced by the tangential speed of the rotor,and consequently the particles in this flow move along a helical stream line in the mixing chamber, as illustrated in Fig. 2.

3.2 Assumptions on the flow

The following assumptions are used to analyze the three dimensional flows:

(a) Fluid which flows in the labyrinth is an ideal gas.
(b) Since the change in temperature caused by a change of pressure is neutralized immediately, the temperature in the labyrinth is constant.
(c) The static pressure is constant on a meridian plane in a mixing chamber.
(d) The coefficient of "carry over", the coefficient of fluid friction and the wetted perimeter of the channel when the rotor is in a eccentric position, are to be the same value as those under the concentric position of the rotor.
(e) Pressure difference between two adjoining points partitioned with a seal strip is small.
(f) The boundary of the jet flow in a chamber on a meridian plane is a tangent to the outer edge of the throat.
(g) Interchanging of fluid mass takes place between the jet flow and the core flow.
(h) The circumferential component of the core flow velocity is constant on a meridian plane in a chamber.
(i) Even in the eccentric position of the rotor, the influence of the eccentricity on the jet flow velocity is small enough for its variation to be neglected.

3.3 Fluid friction acting at the boundary of the flow

The shearing stress τ, due to fluid friction, acting at the boundary of a turbulent flow which flows in a narrow gap between two parallel planes can be expressed by the formula,

$$\tau = \frac{1}{4}\lambda\rho V^2 \ , \quad \lambda = 0.133\,Re^{-1/4}$$

Where V is the mean velocity of the flow, and Re is Reynold's number relating to the distance of the planes.

In order to estimate the force acting between the flows in a labyrinth the above relationship is applied to the flows. Here, since, the movement of fluid particles in both the jet and the core flow in a circumferential direction is mainly discussed, it becomes necessary to know the relationship between the shearing stress and the velocity, both in a circumferential direction. This relationship can be obtained by considering the relation between the circumferential flow velocity and the circumferential component of shearing stress acting in the direction of absolute velocity. Thus,in case of a labyrinth with rotating seal strips and of the conditions, $u < c < u_r$ the shearing stress τ_1, τ_2 and τ_3 acting between the jet flow and the casing wall, between the core flow and the channel wall,and between the jet flow and the seal strip, respectively relating to the circumferential direction, can be expressed as follows:

$$\tau_1 = \frac{1}{4}\rho\lambda_1 u^2,\quad \lambda_1 = 0.133\left[1+(v/u)^2\right]^{\frac{3}{8}}\left[a_0 q_0 u/(\mu v)\right]^{-\frac{1}{4}} \tag{1}$$

$$\tau_2 = \frac{1}{4}\rho\lambda_2 (u_r - c)^2,\quad \lambda_2 = 0.133\left[1+(b_0 v)^2/(u_r-c)^2\right]^{\frac{2}{8}}\left[(u_r-c)c_0 f_m \rho/(s_0\mu)\right]^{-\frac{1}{4}} \tag{2}$$

$$\tau_3 = \frac{1}{4}\rho\lambda_3 (u_r - u)^2,\quad \lambda_3 = d_3\lambda_1 \tag{2}'$$

By a similar principle, the shearing stress acting at the boundary between the jet flow and the core flow in a circumferential direction leadsto the following equation.

$$\tau_{12} = \frac{1}{4}\rho\lambda_{12}(c-u)^2,\quad \lambda_{12} = d_1 d_2 \lambda_1\lambda_2\left(\sqrt{\lambda_1 d_1}+\sqrt{\lambda_2 d_2}\right)^{-2}\sqrt{1+(1-e_0)^2 v^2/(u-c)^2} \tag{3}$$

4. FUNDAMENTAL EQUATIONS OF THE FLOW IN A LABYRINTH

4.1 Equations at the eccentric position of the rotor

By the small displacement x, y of the rotating shaft , as shown in Fig. 3, a small variation in static pressure will be added to the pressure distribution of the concentric labyrinth. When the seal strips are mounted on the rotor and the circumferential velocity of the jet flow is smaller than the peripheral velocity of the rotor, the fundamental equations dominating the flows are derived in the following way in order to calculate such a variation in pressure.

(1) Seal clearance

From the geometrical configuration, comes the equation,

$$\delta_{i-1,i} = \delta_0\left[1 - ns(2i-N-2)/2\right] - x\cos\varphi - y\sin\varphi \tag{4}$$

(2) Mass flow of gas leaking through the seal clearance

Instead of neglecting the approaching speed of gas to the throat, the effects of "carry over" of the labyrinth seal is introduced. Thermodynamic relations provide:

$$q_{i-1,i}^2 = \delta_{i-1,i}^2 \alpha_{i-1,i}^2 (p_{i-1}^2 - p_i^2)/(RT) \tag{5}$$

(3) The equation of continuity

The stream lines of the jet flow in a mixing chamber are approximately represented by straight lines having gradient of $\hat{\theta}_1$, as shown in Fig. 4(a). A and B is the inlet and the outlet of a stream tube having a small circumferential length $rd\varphi$ at the center of the mixing chamber, and q_A and q_B represent the mass flow rate at A and B, respectively. Due to the difference in the mass flow rate $q_A - q_B$ the mass in the stream tube segment AB is increased by $(q_A - q_B)\cdot rd\varphi dt$ in the duration of time dt. A part of the above increase in gas increases its own density and the rest of the quantity, q_{si} moves to the core flow just beneath the stream tube, so that

$$q_{si} = (q_{i-1,i} - q_{i,i+1}) - \frac{s}{2r}\tan\hat{\theta}_i \frac{\partial}{\partial\varphi}(q_{i-1,i} + q_{i,i+1}) - \frac{\partial(\rho_1 f_{si})}{\partial t}$$

On the other hand, as illustrated in Fig. 4 (b), the core flow segment which exists between D and E at the time t is to be shifted circumferentially to the position between D' and E' at the time $t+dt$.

Since the increase of mass in the volume element D'E' against that in the volume element DE is equal to the quantity of gas having come from the jet flow, the equation for the conservation of mass in a circumferential direction

provides the following equation of continuity.

$$r\frac{\partial(p_i f_i)}{\partial t}+\frac{\partial(f_{mi}p_i c_i)}{\partial\varphi}+RT\left\{r(q_{i,i+1}-q_{i-1,i})+\frac{s}{2}\tan\hat{\theta}_i\frac{\partial}{\partial\varphi}(q_{i-1,i}+q_{i,i+1})\right\}=0 \qquad (6)$$

(4) The equation for the conservation of momentum of the core flow in a circumferential direction

As the increase of momentum in a circumferential direction in the volume element D'E' against that in the volume element DE, shown in Fig. 4 (b), consists of the increase in the circumferential momentum of the gas coming from the jet flow, of that due to the pressure gradient and the increase of the cross-sectional area of the core flow, and of that due to the fluid friction, the following equation can be obtained.

$$\left[\frac{c-u}{pf_m}\right]_i\frac{\partial(pf_m)_i}{\partial t}+\frac{\partial c_i}{\partial t}+\left[\frac{(c-u)c}{pf_m r}\right]_i\frac{\partial(pf_m)_i}{\partial\varphi}+\frac{(2c-u)_i}{r}\frac{\partial c_i}{\partial\varphi}+\frac{RT}{p_{ir}}\frac{\partial p_i}{\partial\varphi}+\left[\kappa'(c-u)^2-\kappa''(u_r-c)^2\right]_i=0 \qquad (7)$$

where $\kappa'=\lambda_{12}s/4f_m$, $\kappa''=\lambda_2 s_o/4f_m$

4.2 Relationships when the shaft is at the center line of the casing

(1) Coefficient of "carry over" in a straight-through labyrinth

The following equation, which is a slightly modified version of Komotori's equation(ref.1) is used.

$$\hat{\nu}_{i-1,i}=\left[1-\left(\frac{\hat{\delta}_{i-1,i}}{\hat{\delta}_{i-2,i-1}}\right)^2\frac{\hat{\rho}_i}{\hat{\rho}_{i-1}}\hat{A}_{i-1}(2-\hat{A}_{i-1})\right]^{-\frac{1}{2}},\quad \hat{A}_{i-1}=\frac{\hat{\delta}_{i-2,i-1}\cdot\alpha}{\hat{\delta}_{i-2,i-1}\cdot\alpha+s\tan\theta_o} \qquad (8)$$

(2) Equation of conservation of momentum for the jet flow

As already mentioned, it is assumed in this case that, so that the positive direction of $\tau_1,\tau_2,\tau_{12},\tau_3$ should be determined, $\hat{u}_i<c_i<u_r$

τ_1 :in such a direction that the jet flow is decelerated
τ_2 : " " " the core flow is accelerated
τ_{12}: " " " the jet flow is accelerated by the core flow
τ_3 : " " " the jet flow is accelerated.

In the stream tube segment AB, illustrated in Fig. 5, the increase in the momentum of the gas in a circumferential direction in the volume element A'B' against AB in a small duration of time dt should be equal to the sum of the momentum added to this stream tube segment by the (i-1)-th and i-th and core flow in a circumferential direction. Thus, the following equation is obtained.

$$(\hat{u}_i-\hat{u}_{i-1})q_o dt=\frac{1}{2}\left(-\hat{\tau}_{1,i-1}+\hat{\tau}_{12,i-1}+\hat{\tau}_{3,i-1}\tan\theta_o\right)sdt+\frac{1}{2}\left(-\hat{\tau}_{1,i}+\hat{\tau}_{12,i}+\hat{\tau}_{3,i}\tan\theta_o\right)sdt \qquad (9)$$

(3) Fundamental equations when the rotor is in a concentric position

Substituting x=y=0 and $\partial/\partial t=\partial/\partial\varphi=0$ for the fundamental equations, give

$$\hat{\delta}_{i-1,i}=\delta_o\left[1-\frac{ns}{2}(2i-N-2)\right] \qquad (10)$$

$$q_o^2=(\alpha\cdot\hat{\delta}_{i-1,i}\cdot\hat{\nu}_{i-1,i})^2(\hat{p}_{i-1}^2-\hat{p}_i^2)/RT \qquad (11)$$

$$\hat{\kappa}_i'(\hat{c}_i-\hat{u}_i)-\hat{\kappa}_i''(u_r-\hat{c}_i)^2=0 \qquad (12)$$

5. SOLUTION OF THE EQUATIONS

5.1 Mass flow rate, pressure, and circumferential velocity of flow at the concentric position of the rotor

These parameters can be calculated in the following way.

(a) Values of $\hat{p}_i$ and $\hat{q}_o$

From eqs. (8), (10) and (11), qo can be written as follows:

$$q_o^2 = \frac{\hat{p}_o^2 - \hat{p}_{N+1}^2}{\sum_{i=1}^{N+1} \hat{B}_i}$$

$$\hat{B}_i = \frac{RT}{(a\delta_o)^2}\left[\left\{1-\frac{sn}{2}(2i-N-2)\right\}^{-2} - \frac{\hat{\rho}_i}{\hat{\rho}_{i-1}}\left\{1-\frac{sn}{2}(2i-N-4)\right\}^{-2}\hat{A}_{i-1}(2-\hat{A}_{i-1})\right] \quad (13)$$

Using the pressure at the inlet $\hat{p}_o = \hat{p}_o$, and at the outlet $\hat{p}_{N+1} = \beta p_o$, values of qo and $\hat{p}_1 \sim \hat{p}_N$ can be obtained with the necessary accuracy from the above equation through iterative calculation.

(b) Values of $\hat{u}_i$ and $\hat{c}_i$

From eq. (12)

$$\hat{c}_i = \hat{A}_{2,i}\, u_r + \hat{A}_{1,i}\,\hat{u}_i \quad (14)$$

and, from eq. (14) and eq. (9) substituted by eqs. (1)-(3)

$$\left[\frac{s\hat{p}_i(\hat{\lambda}_{1,i}-\hat{E}_i)}{8RT}\right]\hat{u}_i^2 + \left[q_o + \frac{s\hat{p}_i\hat{E}_i\, u_r}{4RT}\right]\hat{u}_i + \left[\frac{s\hat{p}_{i-1}(\hat{\lambda}_{1,i-1}-\hat{E}_{i-1})\hat{u}_{i-1}^2}{8RT}\right.$$

$$\left. + \left(-q_o + \frac{s\hat{p}_{i-1}\hat{E}_{i-1}\cdot u_r}{4RT}\right)\hat{u}_{i-1} - \frac{su_r^2(\hat{p}_i\hat{E}_i + \hat{p}_{i-1}\cdot\hat{E}_{i-1})}{8RT}\right] = 0 \quad (15)$$

are derived, where

$$\hat{E}_i = \hat{\lambda}_{i2,i}(\hat{A}_{2,i})^2 + d_3\,\hat{\lambda}_{1,i}\tan\theta_o \qquad , \quad \hat{A}_{2,i} = 1-\hat{A}_{1,i}$$

$$\hat{A}_{1,i} = \frac{K\sqrt{s/s_o}}{1+\sqrt{\hat{\lambda}_{2,i}/\hat{\lambda}_{1,i}}+K\sqrt{s/s_o}} \qquad K = \left[1+\left\{\frac{(1-e_o)\hat{v}_i}{\hat{u}_i-\hat{c}_i}\right\}^2\right]^{\frac{1}{4}}$$

For the given value of parameters at the (i-1)-th chamber, $\hat{u}_i$ can be obtained by solving the quadratic equation (15) for $\hat{u}_i$. However, the values $\hat{\lambda}_{i1}$ and $\hat{\lambda}_{i21}$ which appear in the coefficient of that equation, are unfortunately a complicated function of $\hat{u}_i$, so that $\hat{u}_i$ can be obtained from that equation by applying an iterative calculation for each chamber.

5.2 Pressure distribution when the rotor is located in the eccentric position

The variation of p, c and q due to a small amount of displacement of the rotating shaft, must be small compared with those values at the concentric position of the rotor. Further, each increment of p, c and q must be a periodic function of φ , so that the increment can be expanded by Fourier series. Taking the terms of lowest order of the series, the solution of the fundamental equations (5), (6), (7) can be simply put as follows.

$$p_i=\hat{p}_i+p_o\{a_i\cos\varphi+b_i\sin\varphi\}$$
$$c_i=\hat{c}_i+u_r\{d_i\cos\varphi+e_i\sin\varphi\} \tag{16}$$
$$q_{i-1,i}=q_o+q_o\{k_{i-1,i}\cos\varphi+l_{i-1,i}\sin\varphi\}$$

where unknown parameters a_i, b_i...are the linear function of x,y ,and

$$|a_i\cos\varphi+b_i\sin\varphi|\ll\hat{p}_i/p_o$$
$$|d_i\cos\varphi+e_i\sin\varphi|\ll\hat{c}_i/u_r \tag{17}$$
$$|k_{i-1,i}\cos\varphi+l_{i-1,i}\sin\varphi|\ll 1 .$$

Since the equation obtained by substituting eq.(16) into eq.(5) must hold true for any value of φ , the following equations can be obtained.

$$q_o^2 k_{i-1,i}=p_o\hat{D}_{1,i}(\hat{p}_{i-1}a_{i-1}-\hat{p}_i a_i)-(\hat{p}_{i-1}^2-\hat{p}_i^2)\hat{D}_{2,i}\,x$$
$$q_o^2 l_{i-1,i}=p_o\hat{D}_{1,i}(\hat{p}_{i-1}b_{i-1}-\hat{p}_i b_i)-(\hat{p}_{i-1}^2-\hat{p}_i^2)\hat{D}_{2,i}\,y \tag{18}$$

As similar equations can be also obtained from eqs.(6) and (7) both substituted by $\partial/\partial t=0$, by eliminating k,l,d,e from these six equations obtained, the following equations result eventually.

$$A_{i,i-1}a_{i-1}+B_{i,i-1}b_{i-1}+A_{i,i}a_i+B_{i,i}b_i+A_{i,i+1}a_{i+1}+B_{i,i+1}b_{i+1}=X_i\cdot x+Y_i\cdot y$$
$$-B_{i,i-1}a_{i-1}+A_{i,i-1}b_{i-1}-B_{i,i}a_i+A_{i,i}b_i-B_{i,i+1}a_{i+1}+A_{i,i+1}b_{i+1}=-Y_i\cdot x+X_i\cdot y \tag{19}$$

where

$$A_{i,i-1}=-(1/q_o)RTr\,p_o\hat{D}_{1,i}\hat{p}_{i-1}$$
$$A_{i,i}=2p_o r\hat{m}_i\hat{f}_{m,i}\{(\hat{c}_i-\hat{u}_i)\hat{c}_i+RT\}(u_r-\hat{u}_i)/\hat{M}_i+(1/q_o)RTr\,p_o(\hat{D}_{1,i+1}+\hat{D}_{1,i})\hat{p}_i$$
$$A_{i,i+1}=-(1/q_o)RTr\,p_o\hat{D}_{1,i+1}\hat{p}_{i+1}$$
$$B_{i,i-1}=RTs\,p_o\hat{J}_i\hat{D}_{1,i}\hat{p}_{i-1}/(2q_o)$$
$$B_{i,i}=-p_o\hat{f}_{m,i}\{(\hat{c}_i-\hat{u}_i)\hat{c}_i+RT\}(2\hat{c}_i-\hat{u}_i)/\hat{M}_i+RTs\,p_o\hat{J}_i(\hat{D}_{1,i+1}-\hat{D}_{1,i})\hat{p}_i/(2q_o)$$
$$B_{i,i+1}=-RTs\,p_o\hat{J}_i\hat{D}_{1,i+1}\hat{p}_{i+1}/(2q_o)$$
$$X_i=2(1-\alpha)s\,r\hat{m}_i\hat{p}_i\hat{c}_i(\hat{c}_i-\hat{u}_i)(u_r-\hat{u}_i)/\hat{M}_i$$
$$-(1/q_o)RTr\{\hat{D}_{2,i}\hat{p}_{i-1}^2-(\hat{D}_{2,i}+\hat{D}_{2,i+1})\hat{p}_i^2+\hat{D}_{2,i+1}\hat{p}_{i+1}^2\}$$
$$Y_i=(1-\alpha)s\,\hat{p}_i\hat{c}_i\{1-(\hat{c}_i-\hat{u}_i)(2\hat{c}_i-\hat{u}_i)/\hat{M}_i\}$$
$$+RTs\,\hat{J}_i\{\hat{D}_{2,i}\hat{p}_{i-1}^2+(\hat{D}_{2,i+1}-\hat{D}_{2,i})\hat{p}_i^2-\hat{D}_{2,i+1}\hat{p}_{i+1}^2\}/(2q_o)$$
$$\hat{M}_i=\{2r\hat{m}_i(u_r-\hat{u}_i)\}^2+(2\hat{c}_i-\hat{u}_i)^2$$
$$\hat{D}_{1,i}=\alpha^2\delta_o^2\hat{\nu}_{i-1,i}^2\left\{1-\frac{sn}{2}(2i-N-2)\right\}^2/(RT)$$
$$\hat{D}_{2,i}=\alpha^2\delta_o\hat{\nu}_{i-1,i}^2\left\{1-\frac{sn}{2}(2i-N-2)\right\}/(RT)$$
$$\hat{f}_{m,i}=s\left[R_o-r-\frac{s}{2}\cdot\tan\theta_o-\alpha\delta_o\left\{1-\frac{sn}{2}(2i-N-2)\right\}\right]$$

$$\hat{J}_i=\hat{u}_i/\hat{v}_i \qquad \hat{m}_i=\kappa'\hat{A}_{2,i}+\kappa''\hat{A}_{1,i}$$

Equations (19) can be written for i=1 upto i=N, so that the total number of the equation is 2N. Since $(a_{i-1})_{i=1}=(b_{i-1})_{i=1}=(a_{i+1})_{i=N}=(b_{i+1})_{i=N}=0$ is evident, the unknown quantities are $a_1 \sim a_N$ and $b_1 \sim b_N$. And the total number is also 2N. The solution, a_i and b_i, therefore, can be obtained by solving the simultaneons linear equation(19) considering the following relationship.

$$a_1=\bar{\alpha}_1 x-\bar{\beta}_1 y \quad , \quad b_1=\bar{\beta}_1 x+\bar{\alpha}_1 y$$

The static pressure distribution in a labyrinth can be calculated from the eq.(16).

5.3 Cross coupled stiffness

The pressure in the labyrinth, expressed by eq.(16), provides the force F_x and F_y, acting in the negative direction of x and y axis respectively so that

$$F_x=\sum_{i=1}^{N} s\cdot r\int_0^{2\pi} p_1\cos\varphi d\varphi=\pi s r p_o\sum_{i=1}^{N} a_1 \qquad (20)$$

$$F_y=\sum_{i=1}^{N} s\cdot r\int_0^{2\pi} p_1\sin\varphi d\varphi=\pi s r p_o\sum_{i=1}^{N} b_1$$

The forward tangential force divided by the displacement of the rotating shaft, so called the coefficient of the cross coupled spring constant K_{xy}, can be represented as follows.

$$K_{xy}=-\pi s r p_o\sum_{i=1}^{N}\beta_1 \qquad (21)$$

6. THE FUNDAMENTAL EQUATIONS FOR THE LABYRINTH HAVING DIFFERENT GEOMETRIES OR OPERATING CONDITIONS

The preceding theory refers to the case when the seal strips are mounted on the rotor and when the peripheral velocity of the rotor is larger than the circumferencial velocity of the jet flow. If, on the same geometry of the labyrinth, the peripheral velocity of the rotor is smaller than the circumferential velocity of the jet flow, the positive direction of τ_1 and τ_{12} should be determined to be in such a direction that the jet flow is decelerated. Similarly, the positive direction of τ_2 should be the direction in which the core flow is decelerated. The equations can be obtained, in this case, by the same procedure as explained in the previous section. Among these equations thus obtained, the following equations are the essentially different as compared with those of the preceding section.

$$\lambda_2=0.133\left[1+(b_o v)^2/(c-u_r)^2\right]^{\frac{3}{8}}\left[(c-u_r)\,c_o f_m\rho/(s_o\mu)\right]^{-\frac{1}{4}} \qquad (2a)$$

$$\left[\frac{s\hat{p}_1(\hat{\lambda}_{1,1}+\hat{E}_1)}{8RT}\right]\hat{u}_1^2+\left[q_o\frac{s\hat{p}_1\hat{E}_1 u_r}{4RT}\right]\hat{u}_1+\left[\frac{s\hat{p}_{1-1}(\hat{\lambda}_{1,1-1}+\hat{E}_{1-1})\hat{u}_{1-1}^2}{8RT}\right.$$

$$-\left(q_0+\frac{s\hat{p}_{1-1}\hat{E}_{1-1}\cdot u_r}{4RT}\right)\hat{u}_{1-1}+\frac{su_r^2(\hat{p}_1\hat{E}_1+\hat{p}_{1-1}\cdot\hat{E}_{1-1})}{8RT}\Big]=0 \qquad (14a)$$

$$\left[\frac{c-u}{pf_m}\right]_1\frac{\partial(pf_m)_1}{\partial t}+\frac{\partial c_1}{\partial t}+\left[\frac{(c-u)c}{pf_m r}\right]_1\frac{\partial(pf_m)_1}{\partial\varphi}+\frac{(2c-u)_1}{r}\frac{\partial c_1}{\partial\varphi}$$

$$+\frac{RT}{p_1 r}\frac{\partial p_1}{\partial\varphi}-\left[\kappa'(u-c)^2-\kappa'(c-u_r)^2\right]_1=0 \qquad (7a)$$

For the straight-through labyrinth, in which the seal strips are mounted inside the casing, the equations can also be obtained by modifying the original equations with the same principle.

7. RESULTS OF NUMERICAL CALCULATION AND THE COMPARISON WITH THE EXPERIMENTAL DATA PRESENTED BY OTHER RESEARCHERS

Factors, $a_o, b_o, c_o, d_1, d_2, d_3, e_o$ which are included in eqs.(1)-(3), as well as α and θ_o included in eq.(8), are to be decided by the observation of the flow in a labgrinth. However, as some of this data was not available, these factors have been tentatively estimabed as follows throughont the calculation based on the procedure here explained.

$a_o=1.5 \quad b_o=0.5 \quad c_o=1.0 \quad d_1=1.0 \quad d_2=1.0 \quad d_3=1.0 \quad e_o=0.5$

Wachter and Benckert(ref.2) have done an experiment of the static characteristics of a labyrinth having different geometries under different operating conditions. Results of numerical calculation in accordance with the procedure explained in this paper have been compared with the results of the above experiments. The results of their experiments shown in Fig.6 and in Fig.7(a) are obtained using a land-and-groove labyrinth, whereas numerical calculation is on a labyrinth which is deemed to be equivalent to this kind of labyrinth and assumed complete mixing of gas in the mixing chamber on making calculation. As to the effect of the peripheral velocity of the rotor on the lateral force excitation constants, as well as the effect of entry swirl on the constants, calculations not only agree with experiments qualitatively, but also fairly good quantitive agreement is seen between the two. The dimensionless lateral force excitation constants $\bar{K}_Q^*$ taken on the ordinate of these diagrams, and the relative admission energy E_o^* taken on the abcissa in Fig.7 are the following values respectively.

$$\bar{K}_Q^*=\frac{\delta_o K_{XY}}{r\,sN\bar{P}_o(1-\beta)}\ ,\quad E_o^*=\frac{u_o^2}{2(1-\beta)RT+(2R_o q_o RT/\bar{P}_o(R_o^2-r^2))^2}$$

Wachter and Benckert have done a further experiment using a straight-through labyrinth with seal strips morticed inside the casing,and examined the effect of entry swirl on the lateral force excitation constants. Comparison of experiments and calculations have also been made in this case, and shown in Fig.7(b). A qualitative agreement of the two values is obtained. However, from a view-point of quantity, the calculated values are much smaller in this case.

Also,Jenny(ref.3) has presented his theoretical formulas, which are composed partly by adopting the empirical relation of parameters. Results of calculation on one example of a labyrinth with axial admission using his formula and those by the procedure in this paper are compared and shown in Fig.8. These two calculated values agree very well.

It is said that, when swirl is applied to a rotating labyrinth in an eccentric position, an additional exciting force is generated in it whose intensity depends on the intensity of the swirl. Calculation has been made to see the influence of the swirl on the rotating labyrinth. The results agree with the tendency, as shown in Fig.9.

Kurohashi et al.(ref.4) have done experiment to examine the influence of the divergency of the seal clearance on the exciting force of a straight through labyrinth. The comparison of calculated values with their experimental data is illustrated in Fig.10. With regard to the statical characteristics it is seen in both values that the diverging clearance provides a stabilizing tendency against the foreward whirl of the shaft, and the calculated value agrees qualitatively with the experimental value.

9. CONCLUSION

On the assumption that there exist two kinds of three dimensional flow in a labyrinth, a jet and a core flow, an analysis of the behavior of the flow was made, and a method to calculate the statical behavior of a labyrinth seal was shown. The results of calculation on some examples of labyrinths showed a fairly good agreement with results of experiments, and it can be said that this method is useful to predict the destabilizing force,which originates from a labyrinth seal, and acts on the rotating shaft.

REFERENCES

(1) Komotori,K.:A Consideration on the Labylinth Paking of Straight Through Type. Trans.Jpn.Soc.Mech.Eng. 23-133(1957),617

(2) Wachter,J.and Benckert,H.:Querkräfte aus Spaltdichtungen-Eine mögliche Ursache für die Laufunruhe von Tourbomaschinen. Atomkernenergie Bd.32 (1978),239 (See also NASA CP-2133, 1980, pp. 189-212.)

(3) Jenny,R.: Labylinth as a Cause of Self excited Roter Ocillations in Centrifugal Compressors. Sulzer Tech.Rev. 4(1980),149

(4) Kurohashi,M. et al:Spring and Damping Coefficients of the Labylinth Seals. Int.Conf.on Vibrations in Rotating Machinery, Cambridge,(1980)

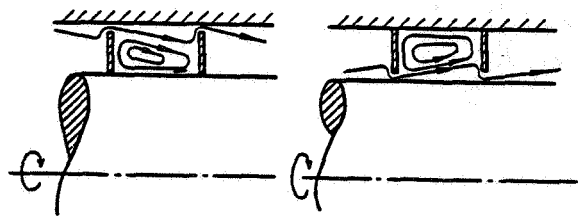

Fig.1 Meridian flow in a straight-through labyrinth seal

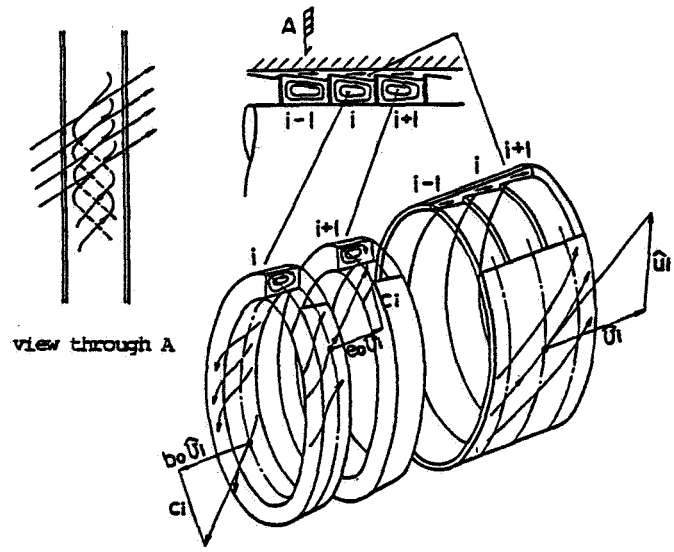

Fig.2 Three dimensional flow in a labyrinth

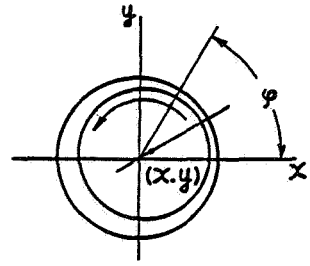

Fig.3 Displacement of rotating shaft

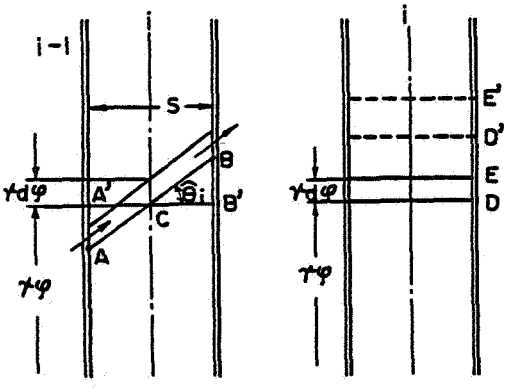

(a) Jet flow (b) Core flow

Fig.4 Flow on the development surface

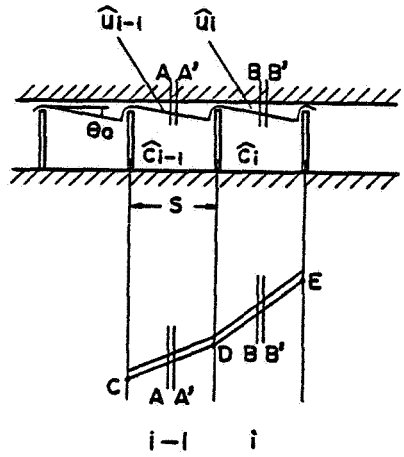

Fig.5 Stream line of jet flow

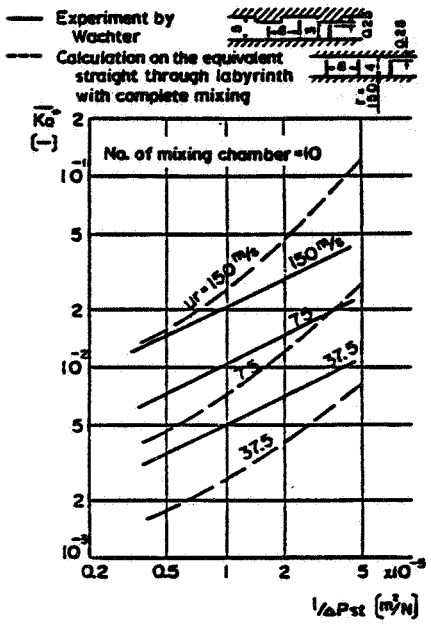

Fig.6 Lateral force spring coefficient

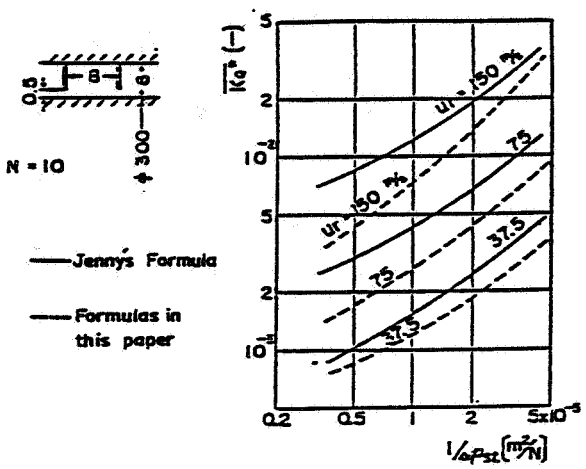

Fig.8 Comparison of lateral force spring coefficient with Jenny's formula

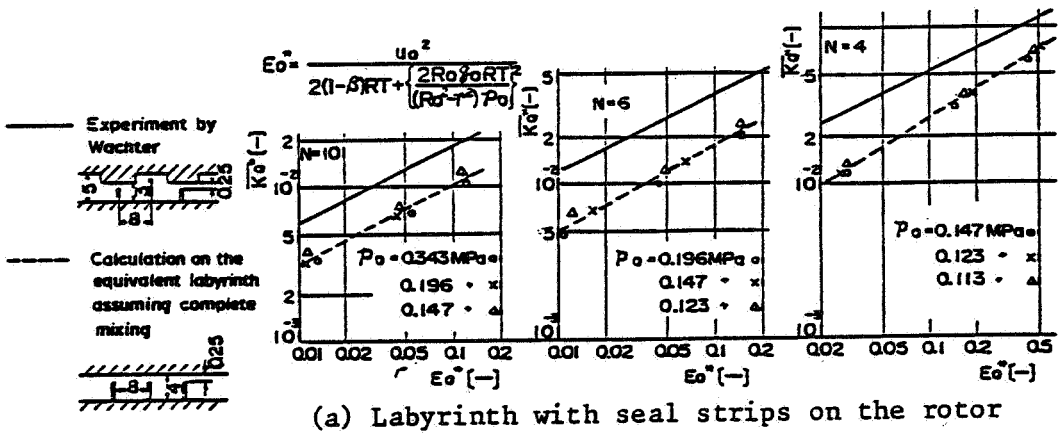

(a) Labyrinth with seal strips on the rotor

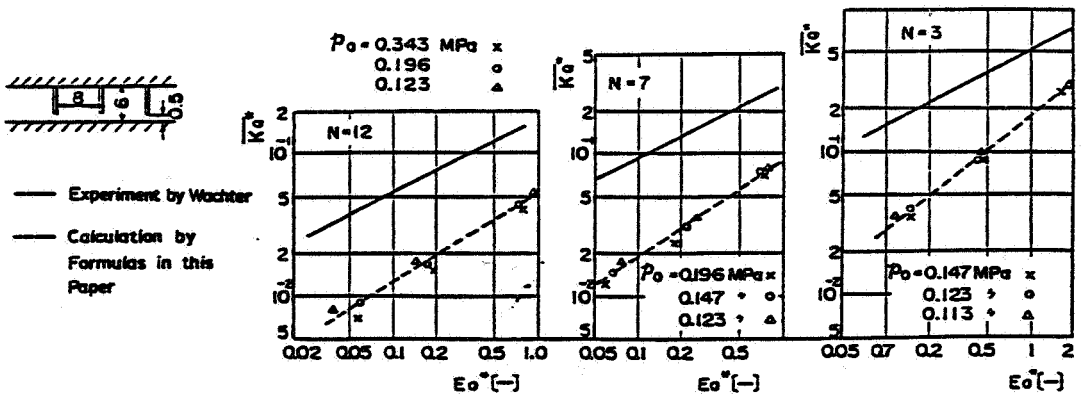

(b) Labyrinth with seal strips inside the casing

Fig.7 Lateral force spring coefficient vs relative admission-energy of the flow (U_r=0)

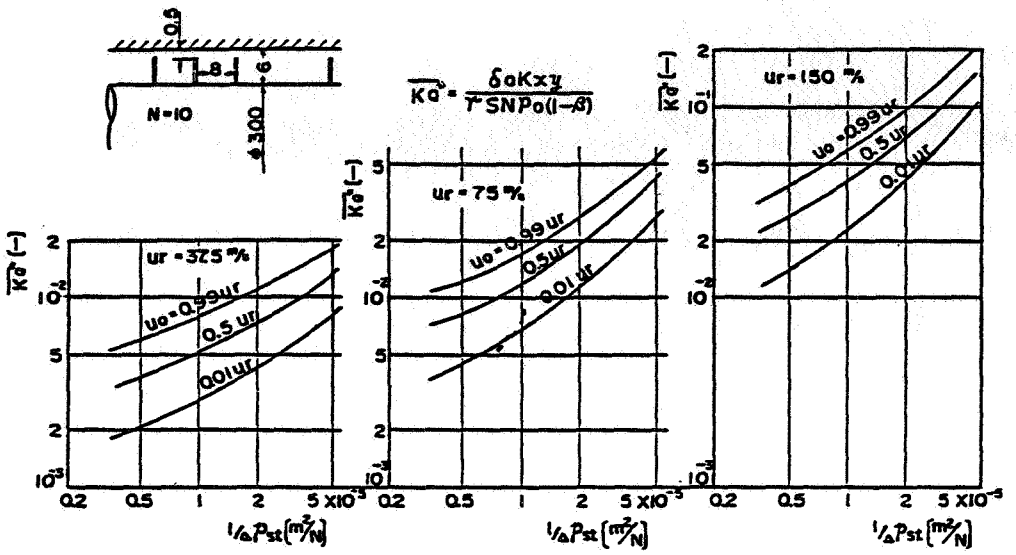

Fig.9 Lateral force spring coefficient of a rotating labyrinth affected by the imposing of entry swirl

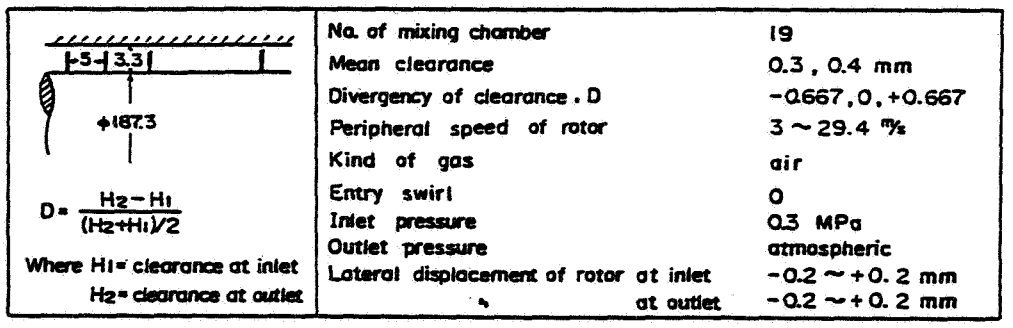

No. of mixing chamber	19
Mean clearance	0.3 , 0.4 mm
Divergency of clearance . D	−0.667, 0, +0.667
Peripheral speed of rotor	3 ~ 29.4 m/s
Kind of gas	air
Entry swirl	0
Inlet pressure	0.3 MPa
Outlet pressure	atmospheric
Lateral displacement of rotor at inlet	−0.2 ~ +0.2 mm
at outlet	−0.2 ~ +0.2 mm

(a) Parameters of experiment

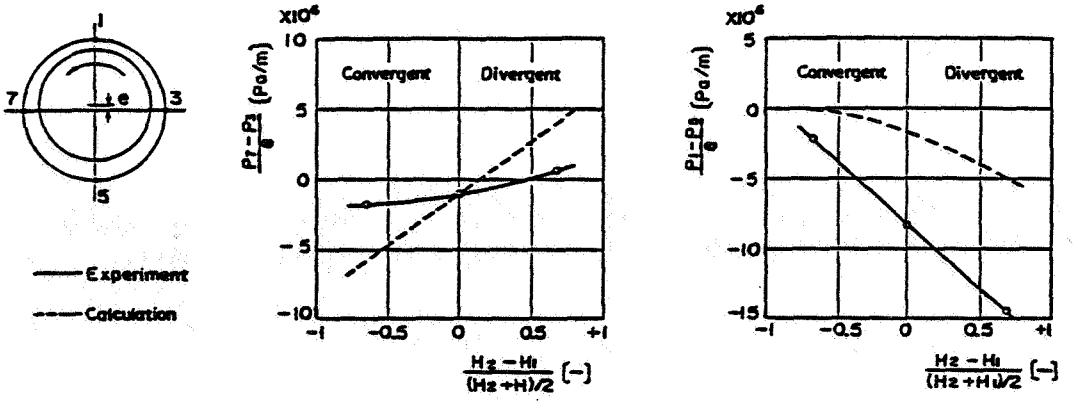

(b) Comparison of experiments and calculations

Fig.10 Effect of divergency of seal clearance on the pressure distribution in a labyrinth

EXPERIMENTAL INVESTIGATIONS OF LATERAL FORCES INDUCED BY FLOW THROUGH MODEL LABYRINTH GLANDS

Y. M. M. Salman Leong
Universiti Teknologi Malaysia
Jalan Gurney, Kuala Lumpur
Malaysia

R. David Brown
Heriot-Watt University
Riccarton, Edinburgh EH14 4AS
Scotland

A research programme has been undertaken to investigate the lateral forces induced by flow through model labyrinth glands. Circumferential pressure distributions, lateral forces and stiffness coefficients data obtained experimentally are presented and discussed. The force system can be represented as a negative spring and a tagential force orthogonal to eccentricity. The magnitude of these forces were dependent on eccentricity, entry swirl, rotor peripheral velocity and seal size. Tests with a pressure equalisation chamber at mid-gland resulted in significantly reduced forces and stiffness coefficients.

INTRODUCTION

The increase in power density of turbomachinery has highlighted the need to consider more carefully the various excitation mechanisms that may result in high level subsynchronous vibrations. Labyrinth seals are a possible cause of self-excited vibration. The reduction of leakage in turbomachinery has often been sought after for efficiency improvements. Seal clearances and its overall dimensions have been made smaller to achieve this improvement. However undue attention to low leakage may result in unacceptably high forces acting on the rotor. Rotors on the other hand have become relatively more flexible and consequently more susceptible to excitations. Thus a potentially highly efficient machine may prove unreliable in service.

Examples of instabilities thought to be caused by labyrinth seals have been reported in the literature (ref. 1,2). The subsynchronous vibrations observed on operational machines were highly load dependent and the instability frequency greater than half speed. Evidently the destabilising force re-excites the lower criticals.

The possibility of lateral vibrations from labyrinth seal leakage flow dates back to the pioneering work of ALFORD (ref. 3). Efforts had been made to quantify the instability in the literature (ref. 4,5,6,7). However most of this work lacks experimental verification. There is a definite need for more experimental data to assess the nature and significance of these labyrinth leakage flow induced instabilities. Experimental tests on single stage labyrinth gland have been reported by WRIGHT (ref. 8). However extrapolation of single stage labyrinth results to the more practical multistage labyrinths would not be conclusive due to

V_s m/s	Big seals (Set A)				Small seals (Set C & D)			
	U = 0		U = 94 m/s		U = 0		U = 94 m/s	
	K_{xx}^*	K_{xy}^*	K_{xx}^*	K_{xy}^*	K_{xx}^*	K_{xy}^*	K_{xx}^*	K_{xy}^*
0	-0.188	0.000	-0.188	-0.017	-0.081	-0.038	-0.113	-0.109
6	-0.225	0.023	-0.233	0.000	-0.105	0.013	-0.135	-0.113
23	-	-	-	-	-0.075	0.041	-0.124	-0.105

Table 1. Typical dimensionless stiffness coefficients

	BENCKERT et al			GREATHEAD et al		CURRENT WORK	
Labyrinths & Number of Stages	Stepped m = 11	Stepped m = 11	Plain m = 18	Combination m = 24	Combination m = 12	Plain m = 12	Set D
U at which K^* evaluated	0	0	0	N/A	N/A	0	94.3 m/s
$\tilde{E}_{swirl}^*$	0.011	0.072	0.004 ~0.100	N/A	N/A	0.005	0.005
K_{xx}^*	-0.100	-0.067	N/A	-0.010	-0.009	-0.075	-0.124
K_{xy}^*	0.067	0.133	0.090 ~0.720	0.040	0.012	0.041	-0.105

N/A : *Details not available from the text*

Table 2. Comparison of dimensionless stiffness coefficients with other works (ref. 10 and 12)

the interaction in behaviour of the various chambers within in the gland. As this current work and work elsewhere (ref. 9) has shown, the first chamber in a multi-stage gland has a unique behaviour. The work of BENCKERT et al (ref. 9,10) represents the first comprehensive work on multistage labyrinths. The tests and results reported here complement the work of Benckert et al.

NOTATION

e	eccentricity	r	rotor radius
Ecc, ε	eccentricity ratio (e/δ)	U	rotor peripheral velocity
E_{swirl}	swirl energy index	V_s	entry swirl velocity
F	force	θ	peripheral angle, measured from maximum gap
K	stiffness coefficient	ρ	density
L	pitch of labyrinth fins	δ	radial clearance
m	number of stages	Δ	difference
p	absolute pressure	ω	angular velocity
p_o	absolute pressure at inlet		
p_m	absolute pressure at exit		

Subscripts		Superscripts	
i	counter	*	dimensionless
max	maximum	-	mean
r	radial		
t	transverse		
x,y	cartesian coordinates		

EXPERIMENTAL PROGRAMME

An experimental programme to investigate lateral forces resulting from flow through model labyrinth glands has been undertaken. The objectives and philosophy of the programme had been discussed in the previous workshop, NASA CP 2250 (ref. 11). A test rig was designed and manufactured for these investigations. A rigid rotor with rigid bearings was used: this eliminated shaft flexibility and hydodynamic effects. The fundamental mode of measurement was pressure rather than force as it is the unequal pressure field that is responsible for the instability. Static circumferential pressures were measured at 30° intervals at every sealing stage; these measurements were taken off the stator. Figure 1 gives the schematic diagram

of the test bed, and figure 2 the assembly drawing of the test rig. For scaling and cross comparison of various seal geometry, experimental and operational, a seal length parameter was used; defined as

$$\text{seal length parameter} = \frac{\text{cross sectional area of labyrinth chamber}}{\text{rotor radius}}$$

The geometry used was verified to have a length parameter value within those found in operational steam turbines, with the exception of a particular geometry that was made larger to determine the effect of size variation. The various geometry and sealing arrangement used is given in figure 3. Set A and B are those with a big seal dimension. Although the number of stages used could be varied to any combination sealing stages of 12 and 6 were used for the tests. The small seals, set C and D, are as shown; set D being the same as C except with a much higher entry swirl velocity. A series of tests were done with a pressure equalisation chamber in the form of a mid-gland plenum to investigate the effect of such an arrangement. The previous seal set was used and the mid-gland plenum as shown, set E. A short gland arrangement was also used for the smaller seals, set F; and finally a combination seal arrangement, set G. Tests were done with low and moderate entry swirl ($V_s < U_{max}/3$). To obtain a swirl greater than this would necessitate the use of nozzles; this was not used as to avoid a possible pressure bias at entry to the gland.

The experimental parameters were hence

(i) seal geometry

(ii) number of stages

(iii) inlet flow conditions (swirl)

(iv) eccentricity

(v) rotor peripheral velocity.

Figure 4 gives the sign convention adopted for peripheral angle, eccentricity and forces. The circumferential pressure distributions were numerically integrated to obtain forces. A dimensionless force was defined, where

$$F_{r_i}^* = \int_0^{2\pi} \frac{(p \cos\theta \, d\theta)_i}{(p_o - p_m)} \qquad (1.a)$$

$$F_{t_i}^* = \int_0^{2\pi} \frac{(p \sin\theta \, d\theta)_i}{(p_o - p_m)} \qquad (1.b)$$

$$\text{Hence } F_{r,t_i} = F_{r,t_i}^* \times r_i L (p_o - p_m) \qquad (2)$$

and

$$\text{Resultant force } F = \sum_{i=0}^{m} F_i \qquad (3)$$

Note that no extraneous sign was introduced in the relations. A positive radial force is a decentreing force (negative spring force) and a negative radial force a restoring force. A positive transverse force is a forward whirl force.

The stiffness coefficients are as conventionally defined;

Direct stiffness coefficient i.e. restoring force coefficient

$$K_{xx}^* = \frac{-\Delta F_r^*}{\Delta \varepsilon} \qquad (4.a)$$

and Cross-coupled stiffness coefficient

$$K_{xy}^* = \frac{F_t^*}{\Delta \varepsilon} \qquad (4.b)$$

Assuming linearity,

$$| K_{yy}^* | = | K_{xx}^* |$$

$$| K_{yx}^* | = -| K_{xy}^* | \qquad (5)$$

Also

$$K = K^* \, r \, L \, (\bar{p}_o - \bar{p}_m) / e \qquad (6)$$

EXPERIMENTAL RESULTS

Circumferential Pressure Distributions

Examples of the circumferential pressure distributions, normalised against the pressure drop across the gland, are given in figures 5 - 8. The pressure distribution for the large seals (set A) is as shown, figure 5. Moderate asymmetric pressure field does exist, with consistently regular semi-symmetric suction pressure in all the chambers beyond the first chamber; the first chamber having a positive pressure field. The smaller seals (set D) had a very much more significant asymmetric pressure field, figure 6. The positive pressure in the first chamber was still observed. Beyond the chambers at the entry end unsymmetric suction pressure fields were obtained, with chambers towards the exit end developing a larger sinusoidal component. The introduction of a plenum chamber in the mid-gland of the same seal set (set E) shows a significant alteration to the pressure field, figure 7. The circumferential pressure variation in the chambers prior to the plenum was reduced. The chamber immediately after the plenum (i.e. chamber number 7) now behaved as a "first chamber" in a normal gland assembly, thereby breaking down the build up of the pressure field in the stages along the gland. In the sealing arrangement with a lesser number of stages, set F, the pressure variation was greater than the long glands, figure 8. This was obvious as the axial pressure drop per stage was larger.

In the larger seal geometry, set A and B, there was no appreciable circumferential pressure variation for zero eccentricity, as should be the case. However in the

smaller seals, significant residual asymmetric field did exist at zero eccentricity. It was not thought to be due to pecularities in the individual seal unit or alignment and concentricity as these were thoroughly checked and verified. These residual pressure fields were thought to be caused by flow dissymmetry resulting from a random build effect and random variations in the actual fin clearances; the chambers were sufficiently small as not to allow pressure equalisation. Such an occurrence had also been noted by Greathead et al on a scaled model rig of an operational machine (ref. 12).

Lateral Force Distributions

The graph of dimensionless force (pressure coefficient) plotted against seal chamber number for the large seals, set A, is given in figure 9. An immediate observation was that variation did exist in the force levels with respect to chambers. The radial force in the first chamber was a restoring force and beyond this chamber decentreing forces existed. The transverse forces were significantly smaller than the radial forces. Variation due to eccentricity is also indicated. The relatively larger pressure variation of the smaller seals not unnaturally gave higher force levels than the large seals, figure 10. Variation in force levels with chamber number was also observed. In contrast with results from the big seals, the transverse forces were now considerably larger in magnitude, having the same order in magnitude as the radial forces. It does suggest that small seals are potentially more destablising than large seals. What was further obvious was the significant force that existed even at zero eccentricity. Significant variation in the force levels was observed as a result of variation in the rotor velocity, figure 11. The resultant decentreing force increased significantly with rotor velocity, and the resultant transverse force from being a forward whirl force at U = 0 changed to a backward whirl force at high rotor velocity ($U > V_s$). Swirl slightly increased the decentreing force as well as the forward transverse force at U = 0, figure 12.

The comparison of forces for the sealing arrangment with and without the plenum chamber, figure 13, strengthens the observation already seen in the circumferential pressure distributions. The radial force level in the chambers were generally very much reduced, and hence the resultant decentreing force more than halved its previous value. The transverse force was similarly reduced.

Stiffness Coefficients

Negative radial stiffness was generally obtained for most of the seal arrangements; with either forward or backward cross-coupled stiffness: this being dependent on several parameters. Table 1 gives a selection of the dimensionless stiffness coefficients obtained from graphs of dimensionless force plotted against eccentricity ratio.

For the big seals, set A, a relatively large negative radial stiffness coefficient was obtained. The cross-coupled stiffness coefficient was significantly smaller, figure 14. This observation was also true for the short gland seals (set B) of the same geometry, figure 15. High rotor velocity tended to give a backward cross-coupled stiffness coefficient; however at U = 0 ($V_s > U$) increasing swirl resulted in increasing forward cross-coupled stiffness coefficient (positive K_{xy}*). The effect of rotor peripheral velocity on the coefficients is even more evident in the small seals (set C and D), where increasing rotor velocity increases the

negative direct stiffness coefficients, as well as greatly altering the characteristics of K_{xy}*. The transverse force from being a positive (forward whirl) force changed to a negative (backward whirl) force, figure 16. At low or no rotor velocity, increasing swirl rate resulted in increasing forward cross-coupled stiffness coefficient, figures 16 and 17.

The introduction of a mid-gland plenum was seen to have a significant moderating effect on the force levels and the stiffness coefficients, figure 18. Force levels and coefficients were greatly reduced. The previous observation of the effect of swirl and rotor velocity was still true although of lesser influence. The short gland small seals (set F) had positive direct stiffness in contrast with the other seals, figure 19. The cross-coupled stiffness behaved in the same manner as previously observed, i.e. effects due to swirl and rotor peripheral velocity on K_{xy}*. The combination seals (set G) due to its design of small and large chambers showed the influence of size variation on the pressure distributions; and the resulting stiffness coefficients reflected this, figure 20. Variation due to rotor velocity and swirl were again consistent in behaviour.

DISCUSSIONS

Lateral forces do exist as a result of flow through labyrinth glands. These forces generally increased with eccentricity. Significant decentreing radial forces were obtained in all the seal configurations, except for the small short gland with restoring forces. The decentreing forces generally increased with seal size. Transverse forces orthogonal to displacement however are of most interest. Both forward and backward transverse forces were obtained; very much dependent on rotor peripheral velocity, swirl and seal size. The experimental observations suggest that small seals are potentially more destablising than big seals; with the smaller seals yielding a larger cross-coupled stiffness coefficient. This would be consistent with an experience of KIRK (ref. 13) where a rotor instability in a compressor was eliminated by replacing the labyringth seals with seals twice the original dimensions.

The experimental results also suggest the important influence of rotor peripheral velocity on the resultant forces. This effect of rotor velocity was more prominent in the small seals. Increasing rotor velocity generally increased the decentreing force in the glands, and thus gave a negative direct stiffness coefficient. All tests further indicated that increasing rotor velocity resulted in negative cross-coupled stiffness coefficient. If a nett positive transverse force F_t* already exists in the gland (by virtue of swirl for example) then rotor velocity reduces this nett force and could give a negative F_t* (backward whirl force). A strong self-excited backward whirl has been reported by WRIGHT (ref. 8) on a whirling rotor model.

The moderate swirl that was obtained on the current rig indicated an increased positive transverse force (forward whirl) with increased swirl, and yielded a forward cross-coupled stiffness coefficient. This observation was prominent in zero or low rotor velocity tests. However as rotor velocity increases the nett backward transverse force resulting from inertia effects was seen to dominate the forward transverse force originating from entry swirl. Figure 21 gives a plot of dimensionless cross-coupled stiffness coefficient against swirl energy for the small seals (sets C and D). A distinct increase in K_{xy}* with entry swirl energy was observed and indicates the strong dependence of K_{xy} on entry swirl. It is reasonable to suppose that if a higher swirl velocity was used higher values of cross-coupled stiffness coefficient would be obtained. This conclusion on the

influence of entry swirl on the cross-coupled stiffness is in agreement with results obtained by BENCKERT et al with high entry swirl energy (ref. 9, 10). The effect of swirl on the direct stiffness coefficient K_{xx} is not as significant. Table 2 gives a comparison of stiffness coefficients with works elsewhere (ref. 9, 10, 12). Results from this work compares well, recognising in particular that the work done by Benckert et al at extremely high entry swirl was not obtained on the current rig.

In order to appreciate the full significance of the dimensionless parameters seen so far, a K* value of 0.050 on a 83 bar pressure drop, rotor radius 254 mm, labyrinth pitch 8 mm and eccentricity 0.50 mm would give a stiffness coefficient of 1.8×10^6 N/m. Hence if the results from Table 2, $K_{xy}^* = 0.04$ and $K_{xx}^* = -0.004$ and $K_{xx}^* = -0.075$, were to be applied to this typical steam turbine, then the respective coefficients are: $K_{xy} = 1.5 \times 10^6$ N/m and $K_{xx} = -2.7 \times 10^6$ N/m. Values of similar order in magnitude for a steam turbine had been quoted by Benckert et al (ref. 10).

The current work further suggests the importance of the relationship between the rotor peripheral velocity U and the swirl velocity V_s. Apparently when $V_s > U$ a forward cross-coupled stiffness coefficient was obtained and when $V_s < U$ a backward cross-coupled stiffness was obtained instead. This draws parallel to the proposals of ROSENBERG et al (ref. 14) and also as noted by GREATHEAD et al (ref. 15), that a positive transverse force would be obtained when the swirl velocity was greater than the rotor precession, and vice versa.

Results and implications from the tests involving a mid-gland plenum were very interesting. The direct stiffness coefficient was a mere 10% to 15% of previous values without the plenum, and the cross-coupled stiffness coefficients 25% to 45%. Inevitably questions would be asked on the penalty of increased leakage flow resulting from the use of this gland with the plenum. Flowrate measurements monitored on this gland arrangement showed no increase in mass flow for the same pressure head. Such a pressure equalisation chamber is also relatively simple to incorporate in existing operational machines. Suggestions had been made by KOSTYUK et al (ref. 16) on a pressure equalisation stability unit at the entry to the gland in an operational machine; reported of improvement to its instability threshold. The results of this work and by Benckert et al also confirm the wisdom in recent attempts to reduce swirl by the use of vortex brakes (ref. 17).

Shortcomings in existing theories particularly those not predicting forces or instability with parallel rotor displacement were certainly highlighted. Tapered seal clearances (either converging or diverging) are not necessarily a prerequisite for instability. New theoretical attempts to formulate labyrinth forces are required and should accommodate the fact that forces do exist for parallel rotor displacements.

CONCLUSIONS

This current work shows that an assymmetric pressure field does exist in all chambers within a gland assembly, even for parallel eccentricity displacements contrary to what is predicted by existing theories. The lateral forces were dependent on eccentricity, swirl, rotor peripheral velocity and seal size. The force system could normally be represented as a negative spring and a tangential force orthogonal to eccentricity. Both forward and backward cross-coupled stiffness coefficients were obtained, the direction being dependent on the ratio between swirl and rotor peripheral velocity. Small seals were also shown to be

potentially more destabilising. The use of a mid-gland plenum chamber showed marked reduction in forces and stiffness coefficients, without any increase in leakage flow.

REFERENCES

1. Greathead, S.H. and Bastow, P.: Investigations into Load Dependent Vibrations of the High Pressure Rotor on Large Turbo-Generators. I.Mech.E. Conference on Vibrations in Rotating Machinery, September 1976, pp. 279-285.

2. Jenny, R.: Labyrinths as a Cause of Self-Excited Rotor Oscillations in Centrifugal Compressors. Sulzer Technical Review 4/1980, pp. 149-156.

3. Alford, J.S.: Protecting Turbomachinery from Self-Excited Rotor Whirl. Trans. ASME, J.Engng. Power, October 1965, pp. 333-344.

4. Spurk, J.H. and Keiper, R.: Self-Excited Vibration in Turbomachines resulting from Flow through Labyrinth Glands. C.E. Trans. 6785. Translated from Ingenieur Archiv. Vol. 43 (1974), pp. 127-135.

5. Kostyuk, A.G.: A Theoretical Analysis of the Aerodynamic Forces in the Labyrinth Glands of Turbomachines. Thermal Engineering Vol. 19 (11) 1972, pp. 39-44. (Teploenergetika 1972. 19 (11), pp. 29-33).

6. Iwatsubo, T.: Evaluation of the Instability Forces of Labyrinth Seals in Turbines or Compressors. Workshop on Rotordynamic Instability Problems in High-Performance Turbomachinery. Texas A & M Univ., May 1980. NASA Conference Publication 2133, pp. 139-167.

7. Kurohashi, M., Inoue, Y., Abe. T. and Fujikawa, T. : Spring and Damping Coefficients of the Labyrinth Seals. I.Mech.E. Conference on Vibrations in Rotating Machinery, September 1980, pp. 215-222.

8. Wright, D.V.: Air Model Tests of Labyrinth Seal Forces on a Whirling Rotor. Trans. ASME, J.Engng. Power, October 1978, pp. 533-543.

9. Benckert, H. and Wachter, J.: Flow Induced Coefficients of Labyrinth Seals for Application in Rotordynamics. Workshop on Rotordynamic Instability Problems in High-Performance Turbomachinery. Texas A & M Univ., May 1980. NASA Conference Publication 2133, pp. 189-212.

10. Benckert, H. and Wachter, J.: Flow Induced Constants of Labyrinth Seals. I.Mech.E. Conference on Vibrations in Rotating Machinery, September 1980, pp. 53-63.

11. Leong, Y.M.M.S. and Brown, R.D.: Circumferential Pressure Distributions in a Model Labyrinth Seal. Workshop on Rotordynamic Instability Problems in High-Performance Turbomachinery, Texas A & M Univ., May 1982, NASA Conference Publication 2250, pp. 223-241.

12. Greathead, S.H. and Slocombe, M.D.: Further Investigations into Load Dependent Low Frequency Vibration of the High Pressure Rotor on Large Turbo-Generators. I.Mech.E. Conference on Vibrations in Rotating Machinery, September 1980, pp. 401-413.

13. Kirk, R.G.: Private communication, Texas A & M Univ., May 1982.

14. Rosenberg, C.S., Orlik, W.G. and Marshenko, U.A.: Investigating Aerodynamic Transverse Forces in Labyrinth Seals in Cases Involving Rotor Eccentricy. C.E. Trans. 7083. Translated from Energomashinostrojenie Vol. 8, 1974, pp. 15-17.

15. Greathead, S.H. and Slocombe, M.D.: Investigations into Output Dependent Rotordynamic Instability of the High Pressure Rotor on a Large Turbogenerator. IFTOMM Conference on Rotorydynamic Problems in Power Plants, Italy, September 1982, pp. 27-35.

16. Kostyuk, A.G., Pis'min, I.N., Serkov, S.A., ,Shoshin, V.G. and Shatin, S.A.: Raising the Threshold Capacity and Efficiency of Turbine Plants when Using Stabilising Units. Thermal Engineering Vol. 28 (5) 1981, pp. 311. (Teploenergetika 1981 28 (5) pp. 50-53).

17. Jenny, R. and Wyssmann, H.: Lateral Vibration Reduction in High Pressure Centrifugal Compressors. Proceedings 9th Turbomachinery Symposium, Houston, December 1980, pp. 45-56.

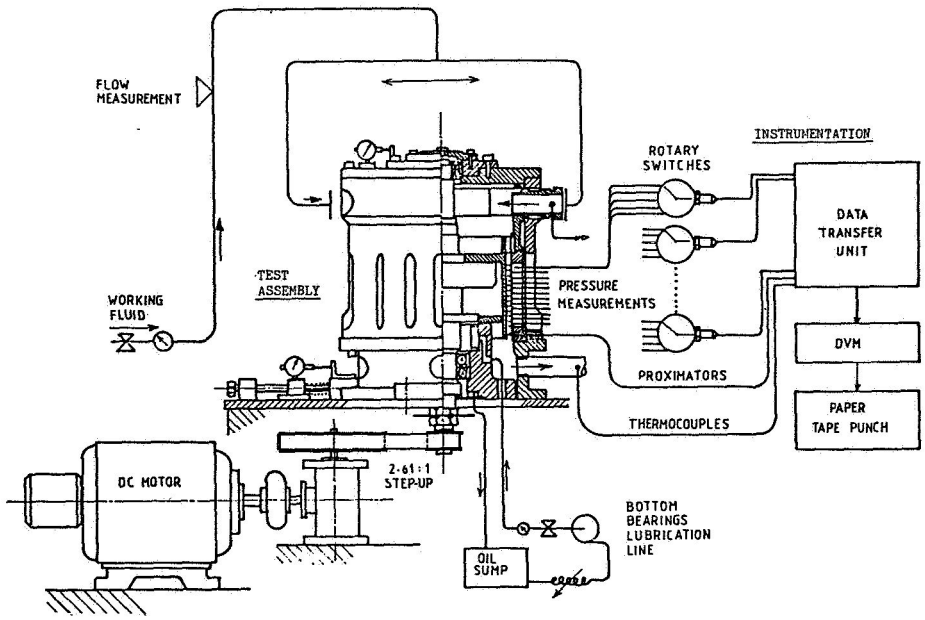

Figure 1. Schematic layout of test bed and instrumentations

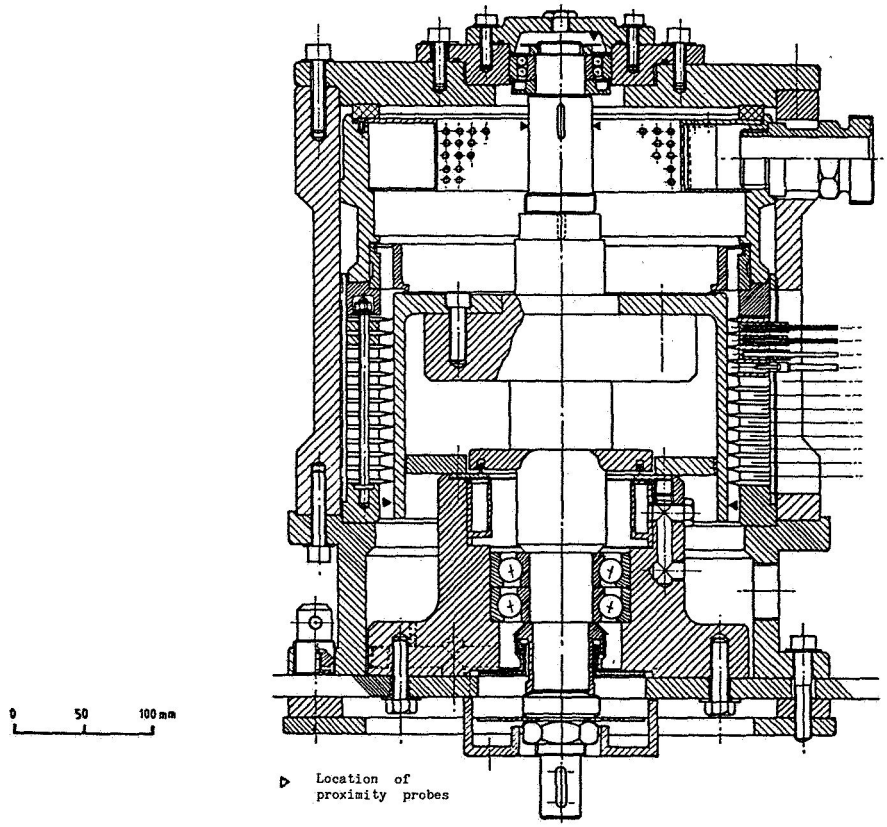

Figure 2. Sectioned assembly drawing of test rig (main assembly)

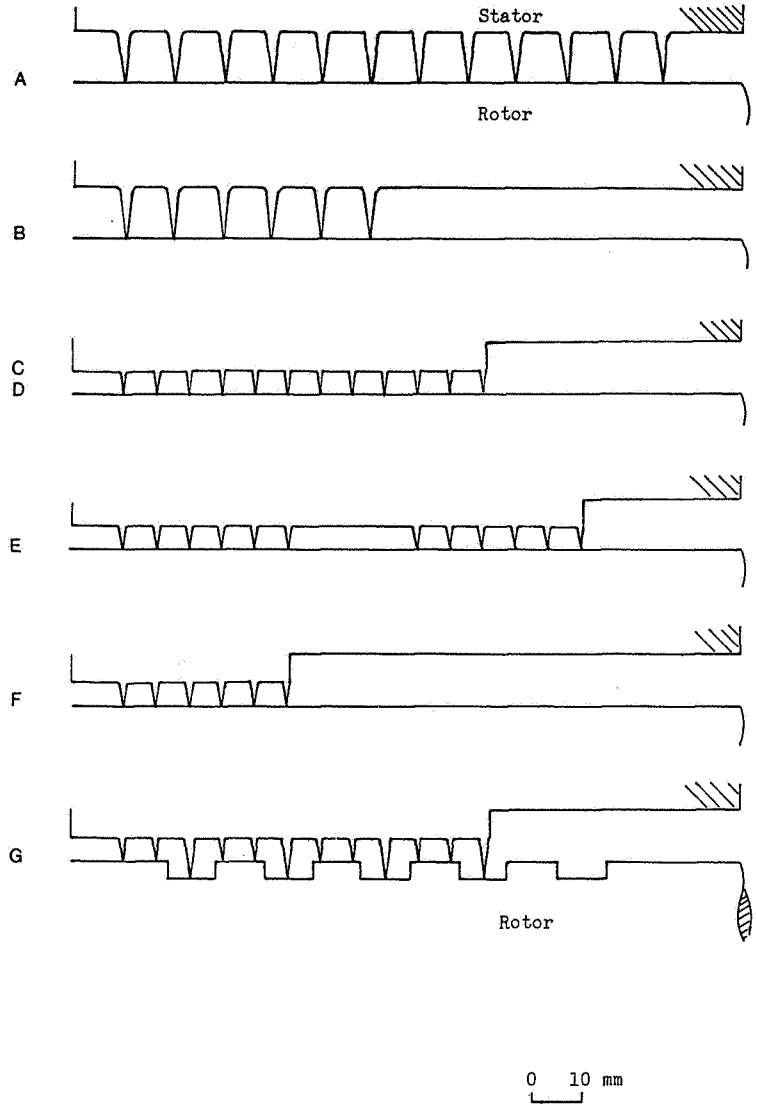

Figure 3. Experimental seal geometry and number of stages of stages combination used

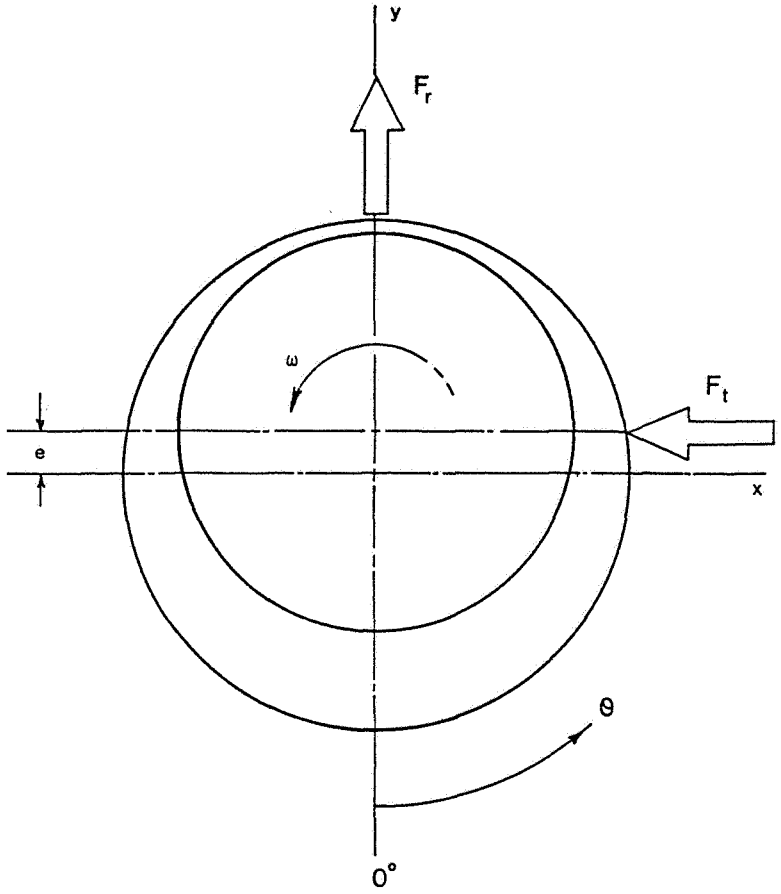

Figure 4. Sign convention of peripheral angle, eccentricity and forces

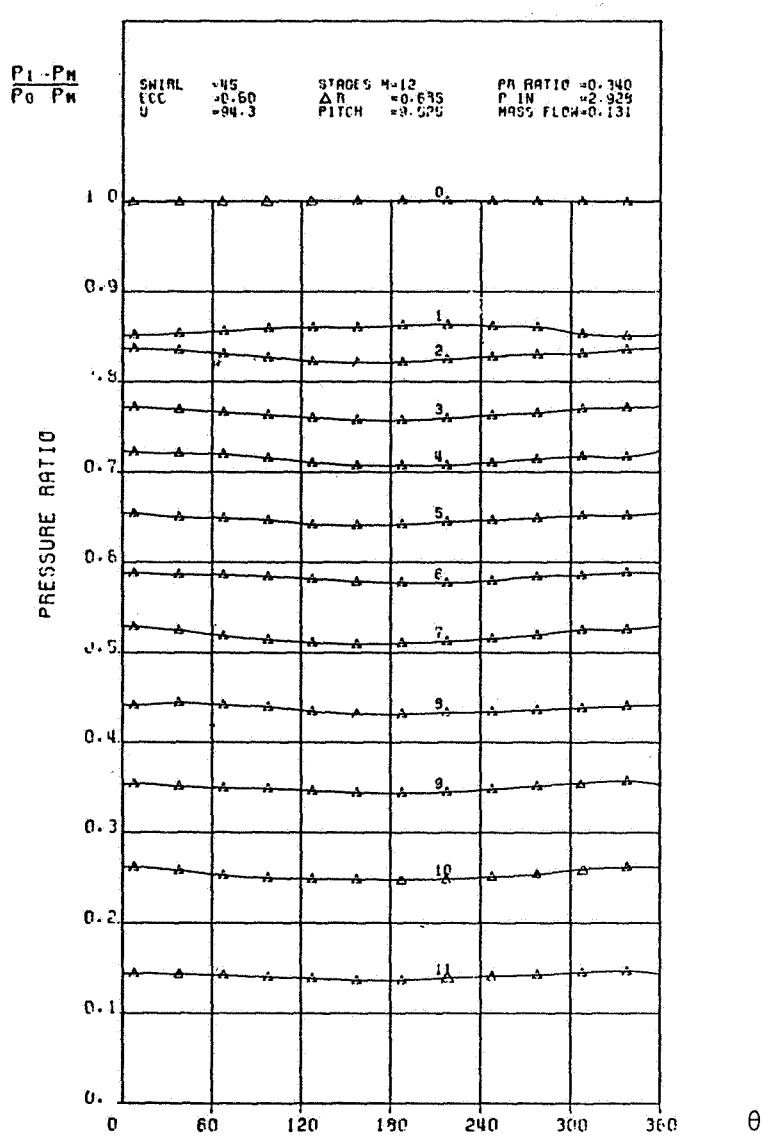

Figure 5. Pressure ratio; set A, $\varepsilon = 0.6$, $U = 94$ m/s, $V_s = 6$ m/s

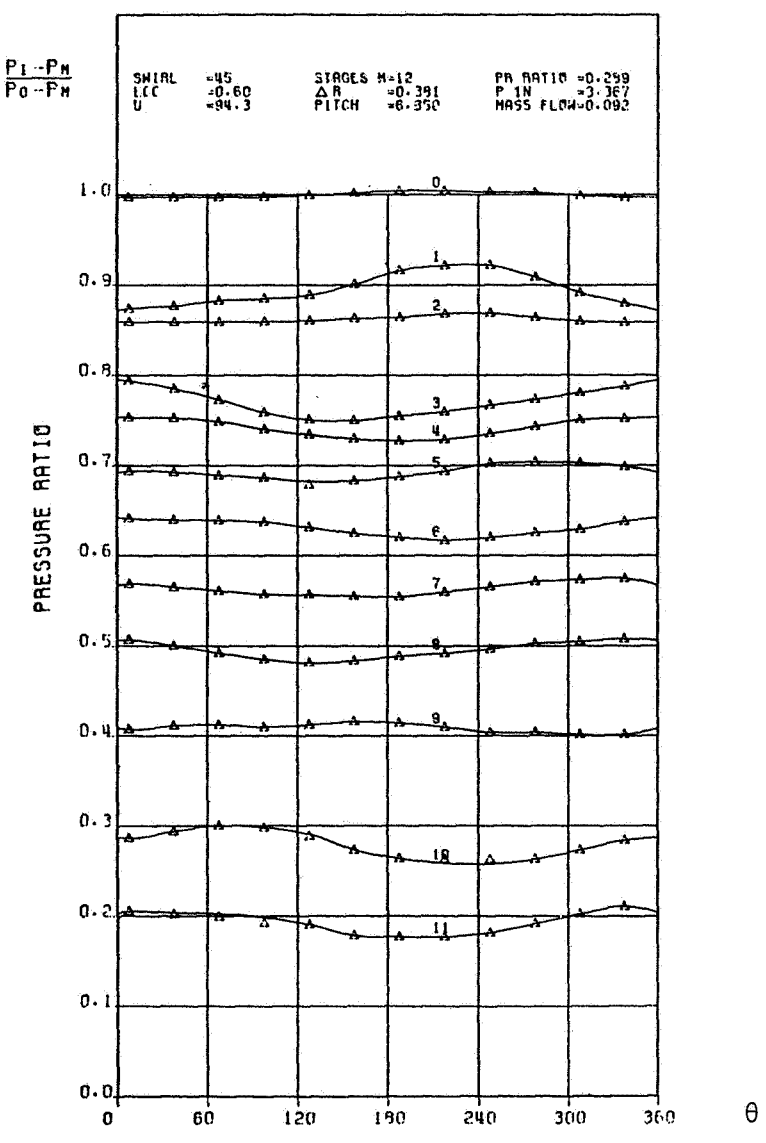

Figure 6. Pressure ratio; set D, $\varepsilon = 0.6$, $U = 94$ m/s, $V_s = 23$ m/s

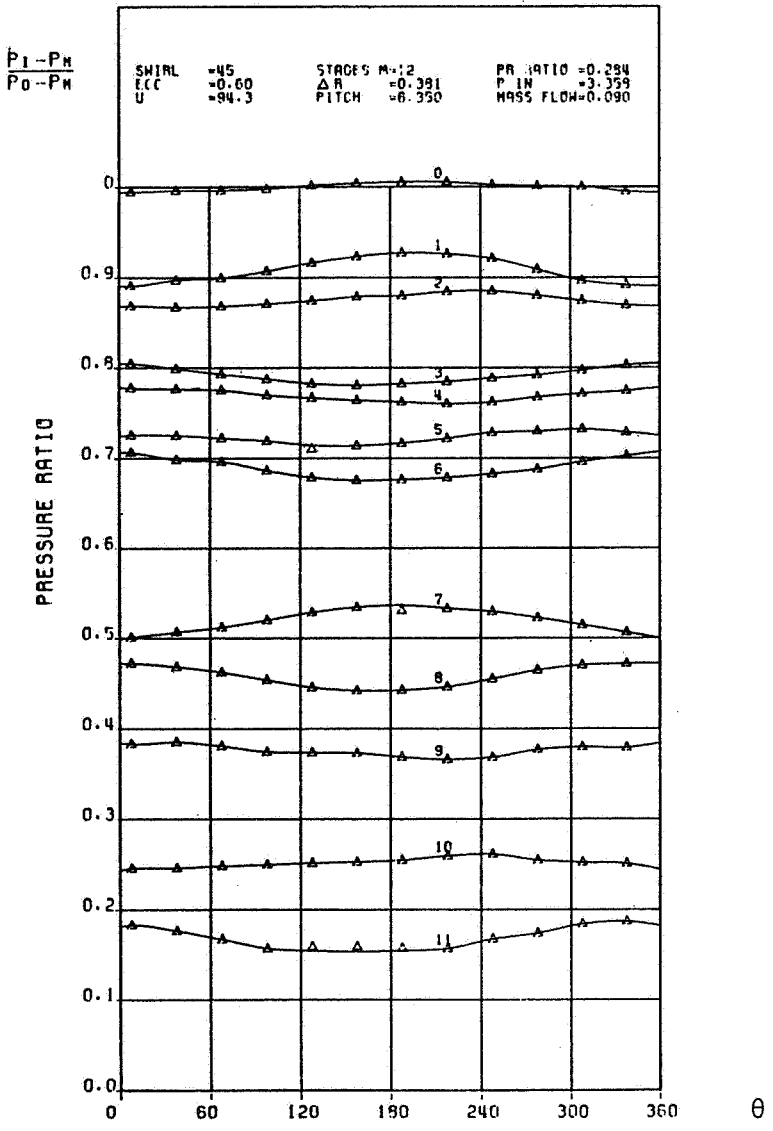

Figure 7. Pressure ratio; set E, $\varepsilon = 0.6$
$U = 94$ m/s, $V_s = 23$ m/s

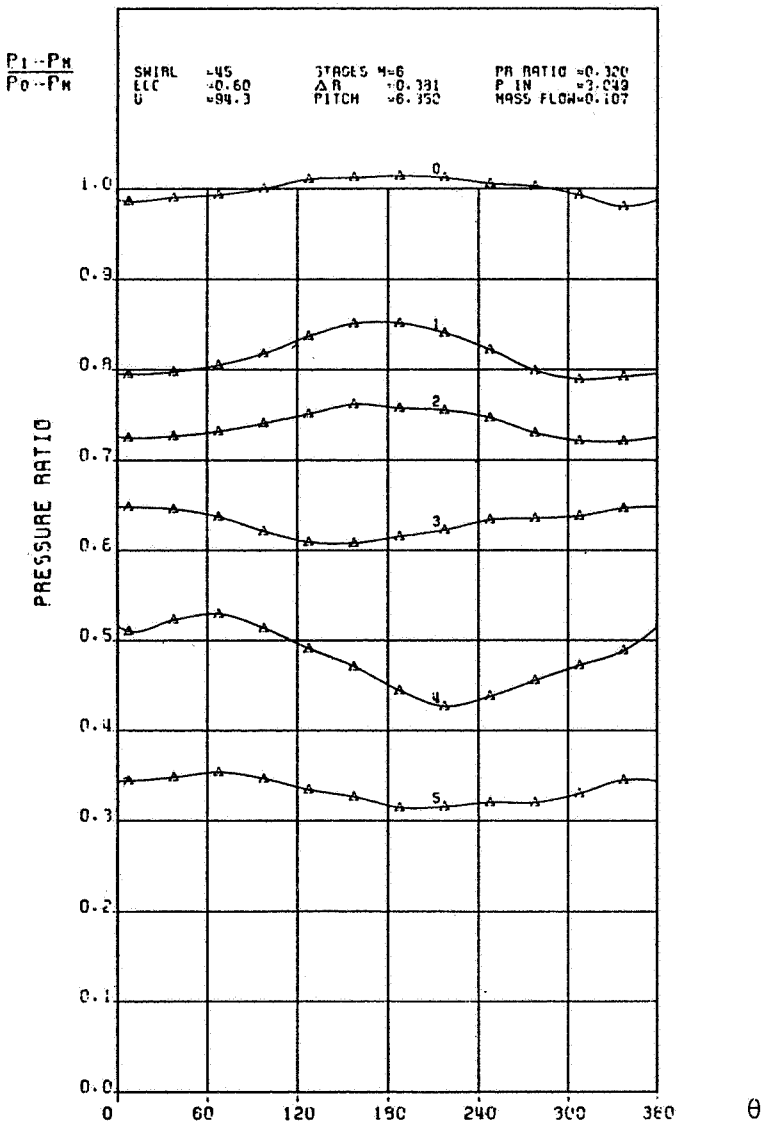

Figure 8. Pressure ratio; set F, $\varepsilon = 0.6$
$U = 94$ m/s, $V_s = 30$ m/s

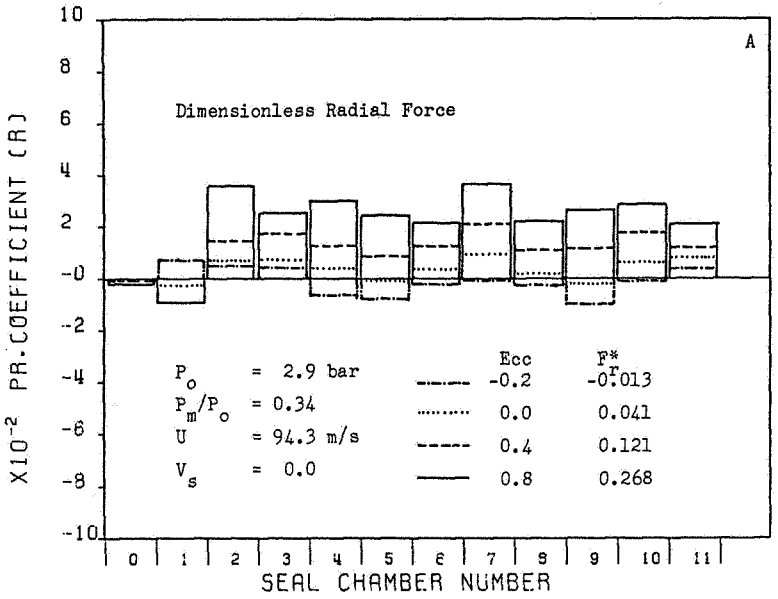

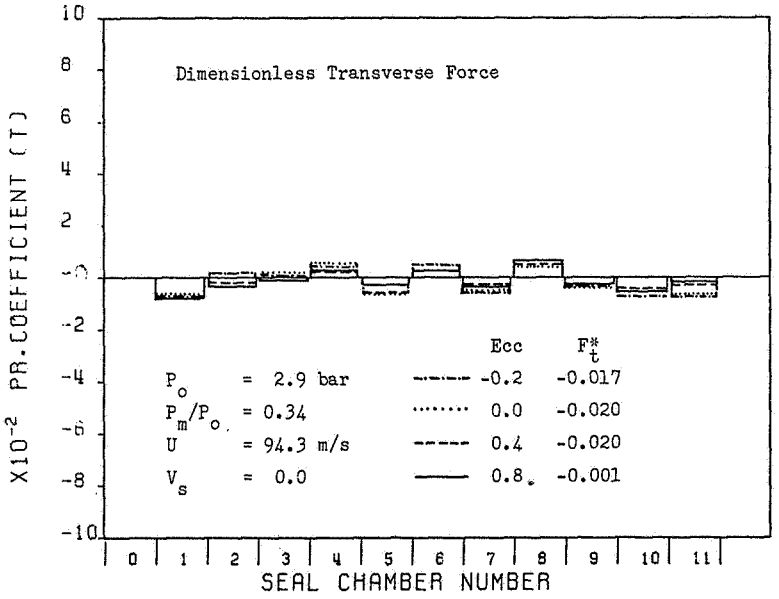

Figure 9. Dimensionless force in individual seal chamber : Effect of eccentricity; set A

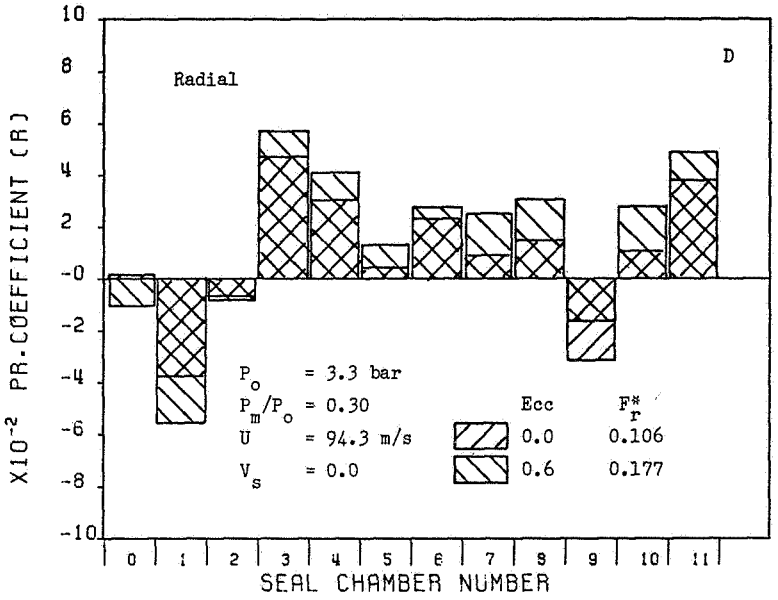

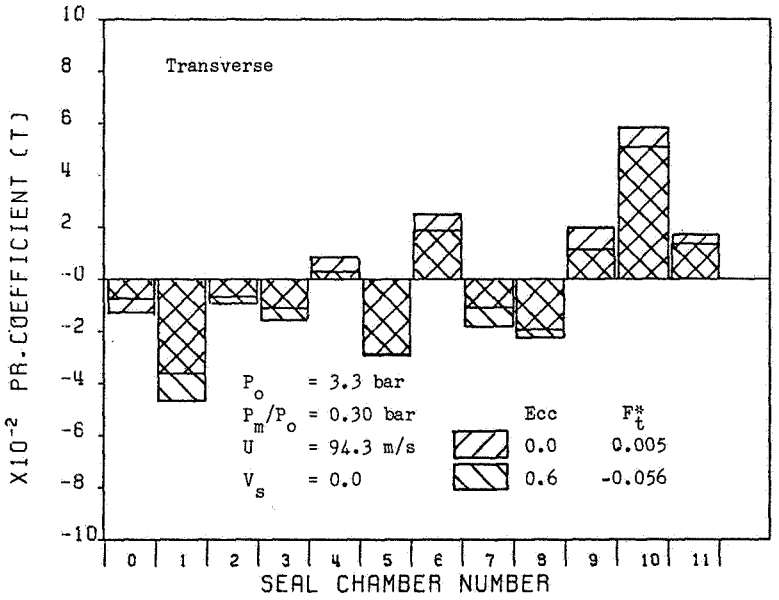

Figure 10. Effect of eccentricity on the dimensionless force; set D

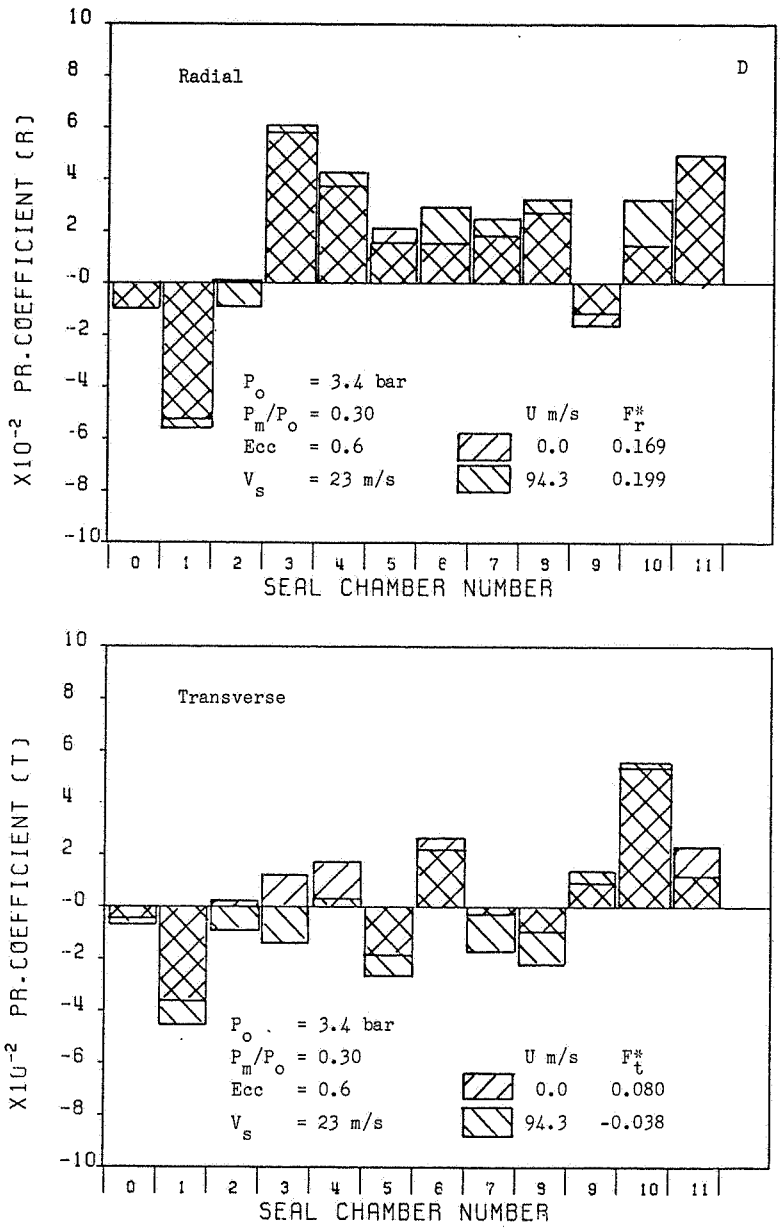

Figure 11. Effect of rotor peripheral velocity on the dimensionless force; set D

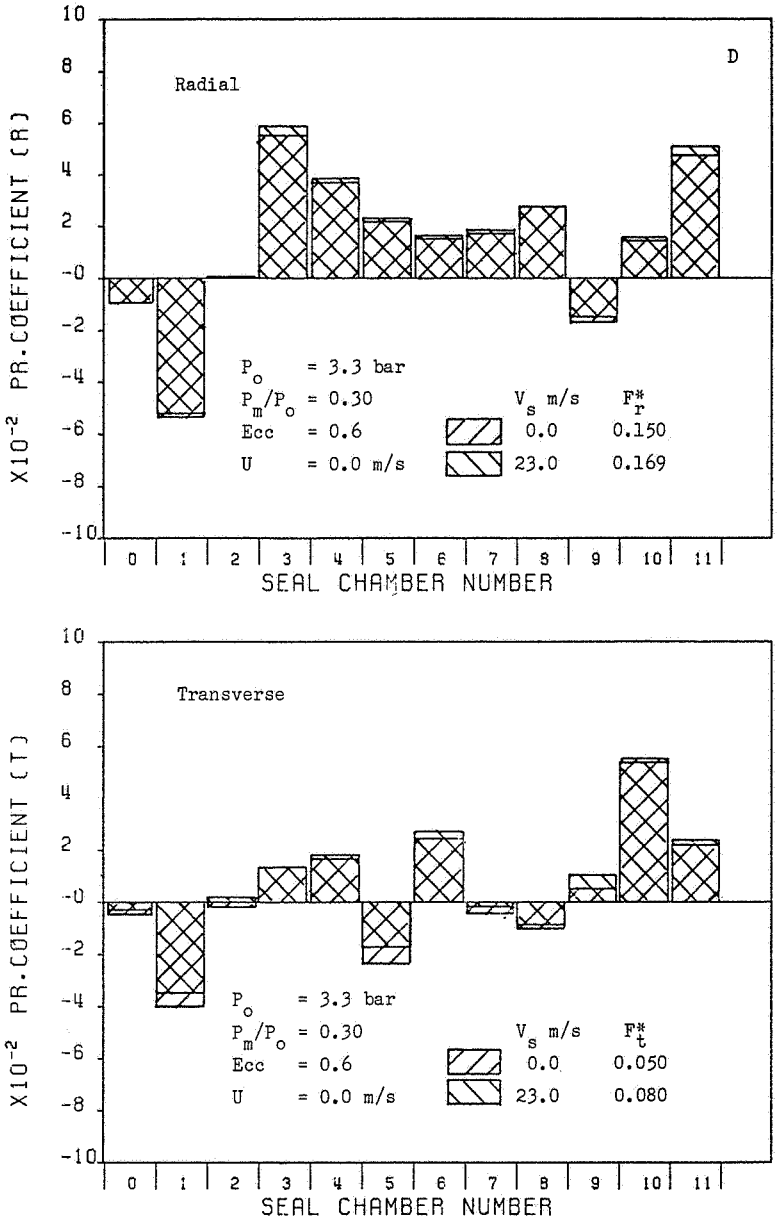

Figure 12. Effect of moderate swirl on the dimensionless force, U = 0; set D

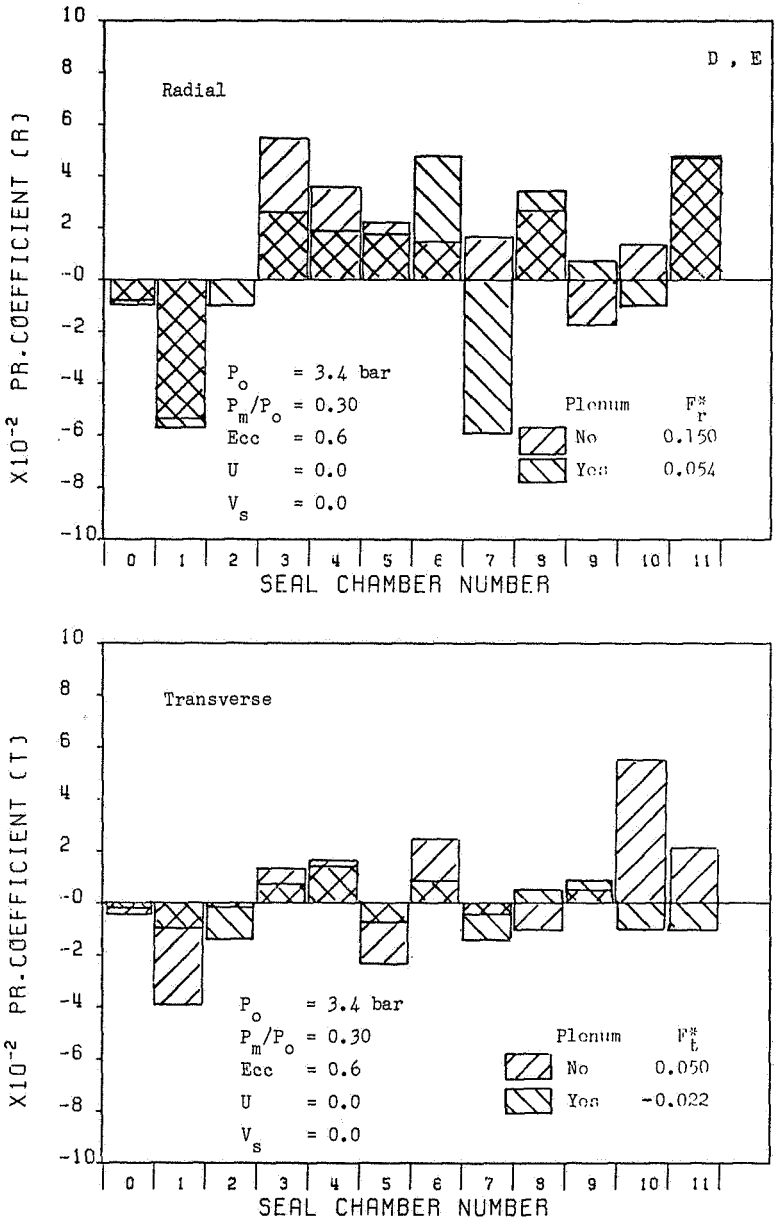

Figure 13. Comparison of dimensionless force with and without mid-gland plenum

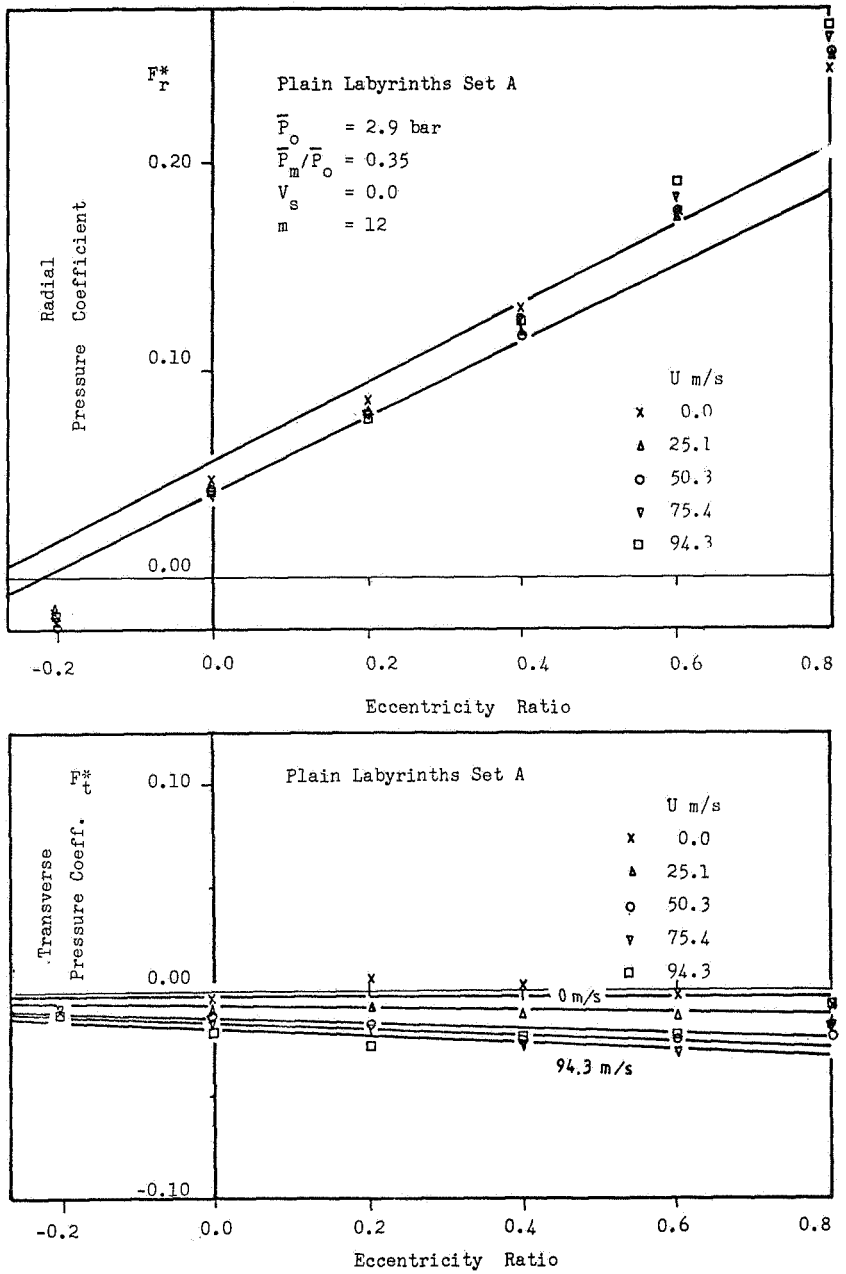

Figure 14. Graphs of dimensionless force against eccentricity ratio; set A, $V_s = 0$

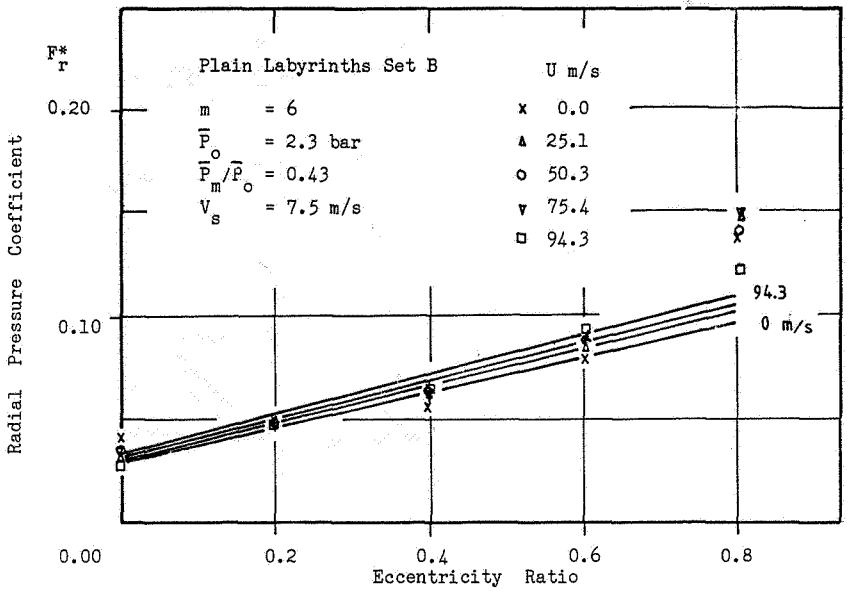

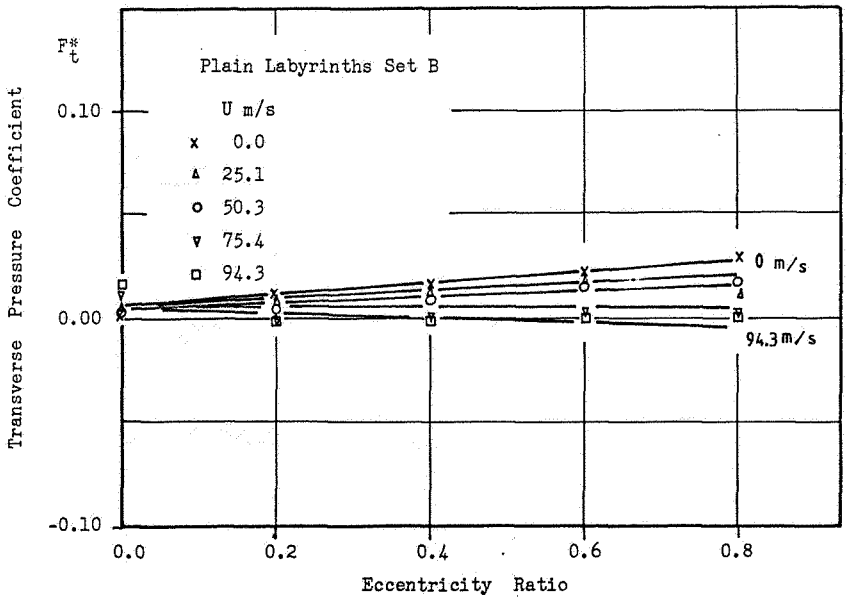

Figure 15. Graphs of dimensionless force against eccentricity ratio; set B, V_s = 7.5 m/s

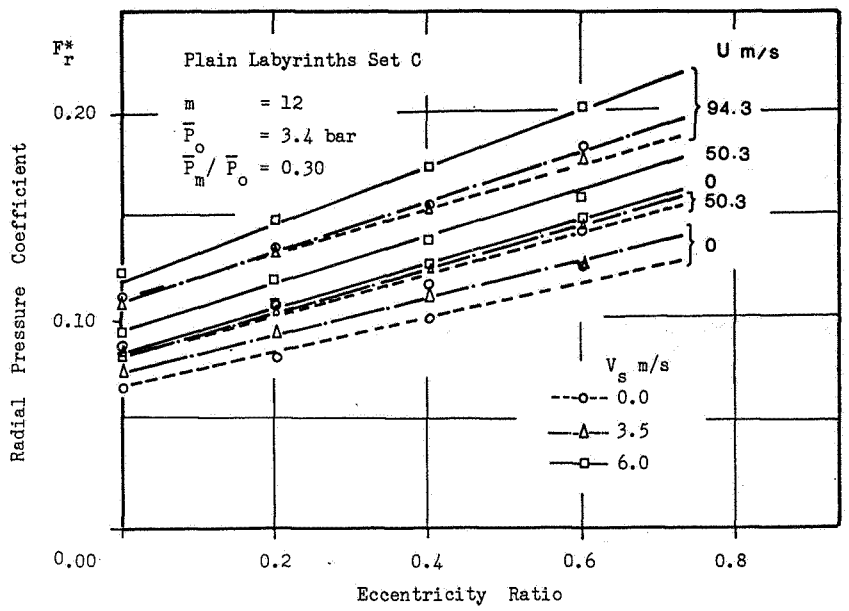

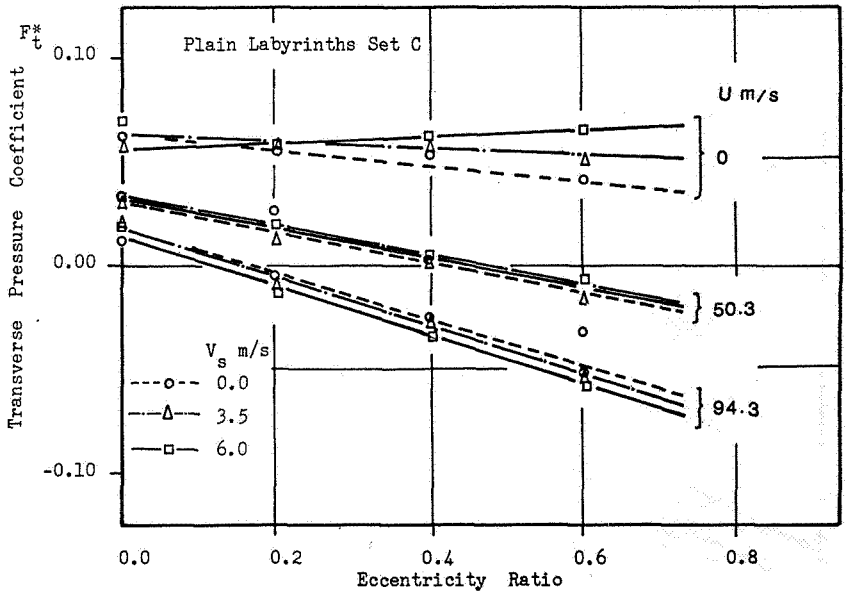

Figure 16. Graphs of dimensionless force against eccentricity ratio; set C

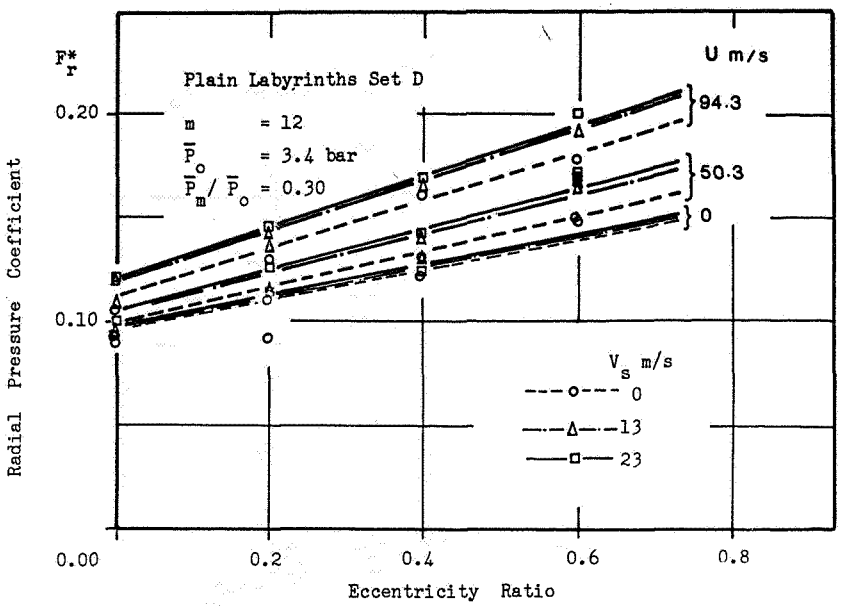

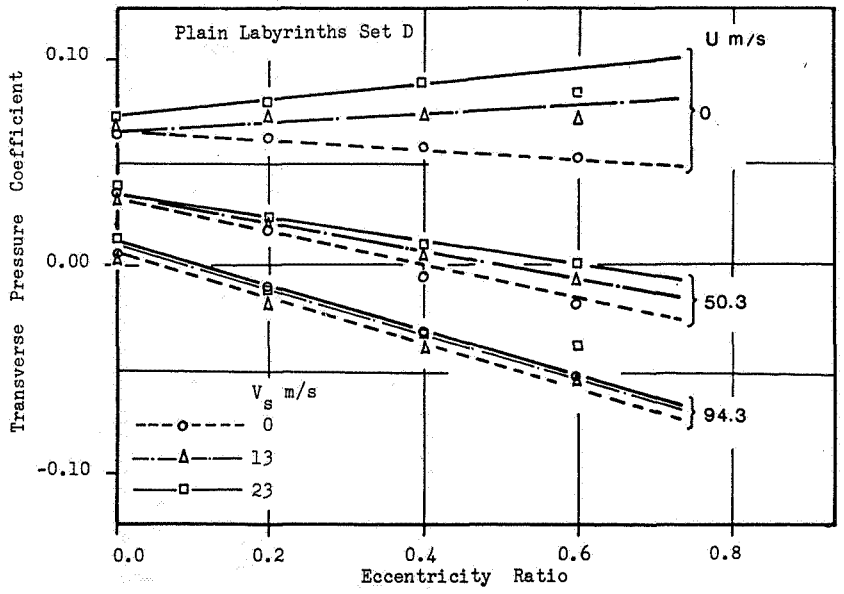

Figure 17. Graphs of dimensionless ratio against eccentricity ratio; set D

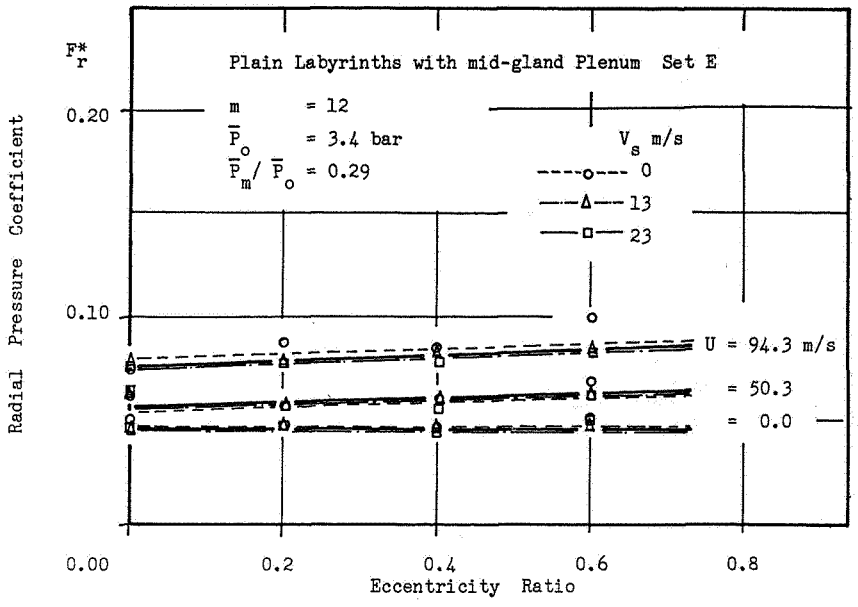

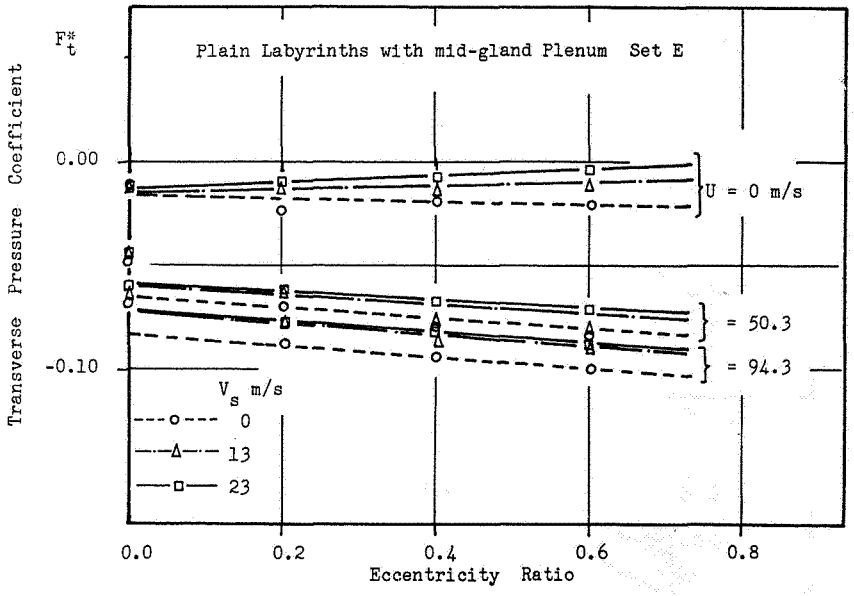

Figure 18. Graphs of dimensionless ratio against eccentricity ratio; set E

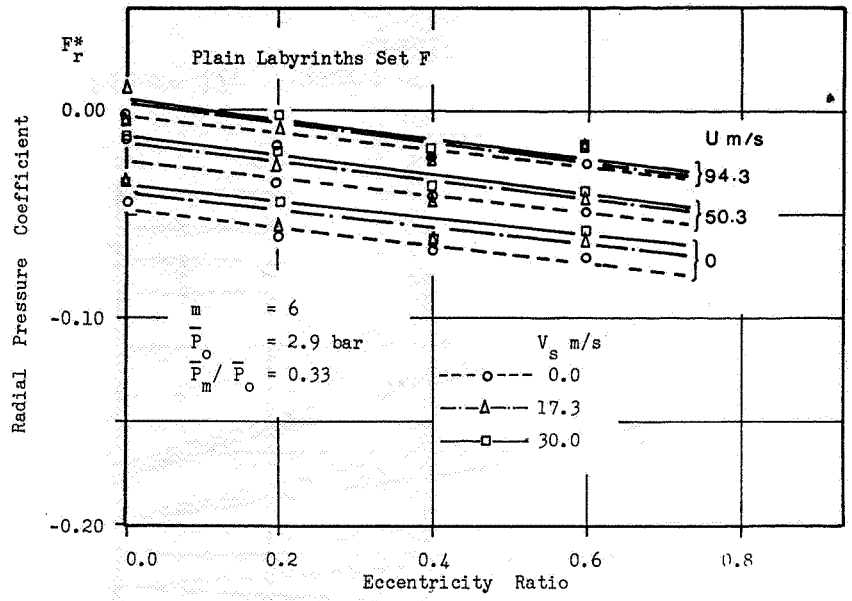

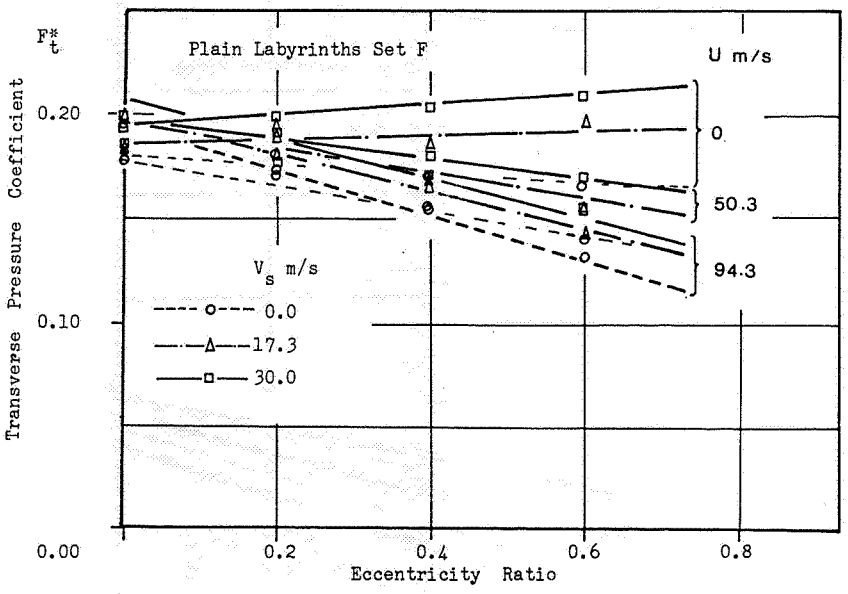

Figure 19. Graphs of dimensionless ratio against eccentricity ratio; set F

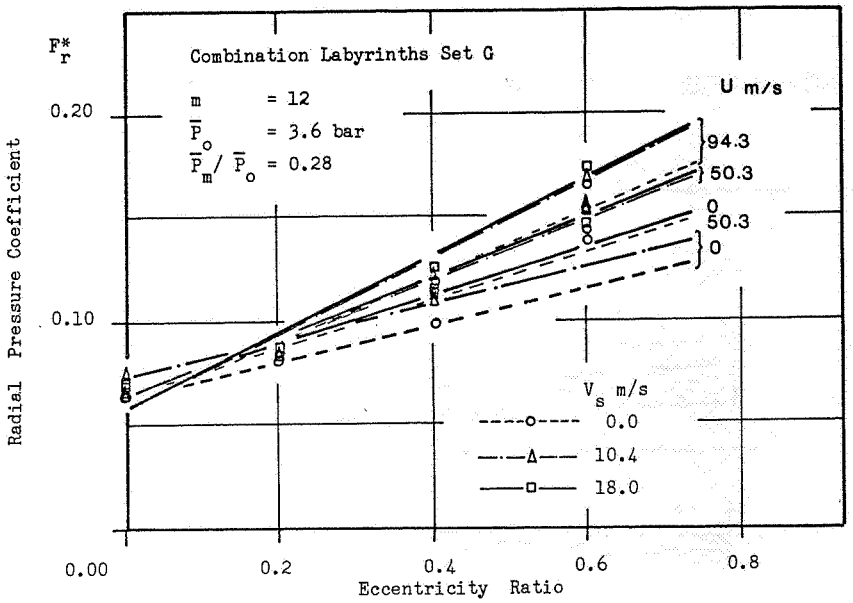

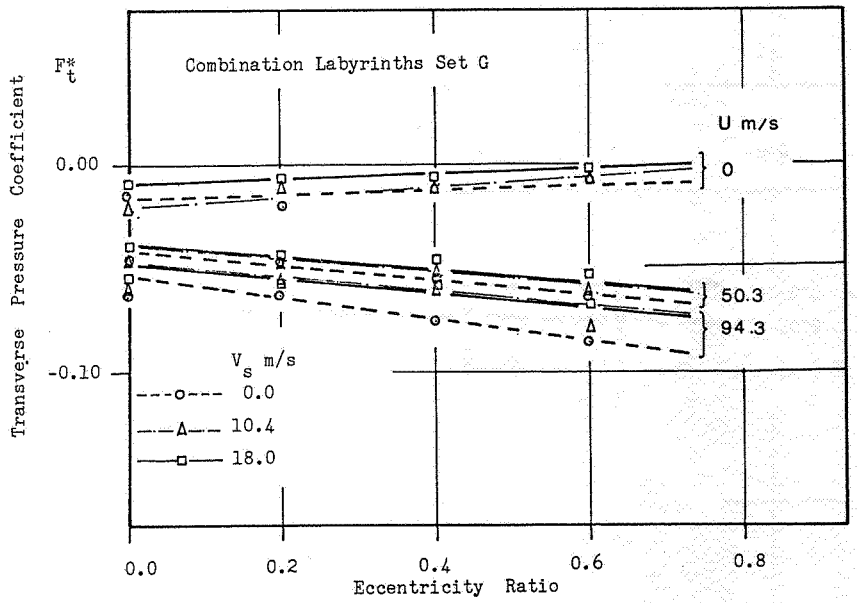

Figure 20. Graphs of dimensionless ratio against eccentricity ratio; set G

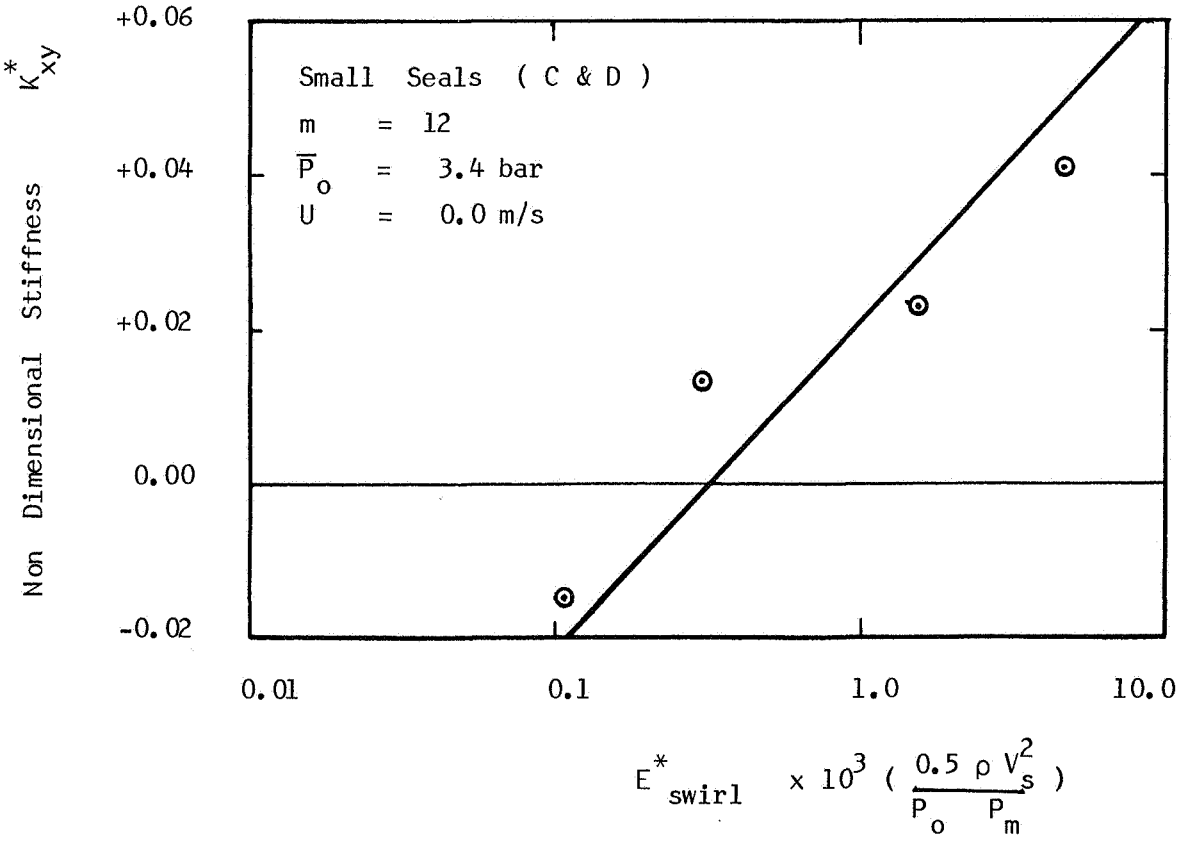

Figure 21. - Variation of cross-coupling with swirl.

ADDITIONAL MATERIAL PRESENT AT WORKSHOP

R.D. Brown J.A. Hart B.E. Falconer

One of the major results from the experimental work was a confirmation that swirl energy was a significant factor in promoting cross-coupling. A rotor kit was adapted as part of an undergraduate project. A plenum chamber was designed around the central mass on a flexible rotor. Four jets in the plenum discharged high velocity air in a tangential direction on the periphery of the central mass. The synchronous critical speed of the rotor was about 3200 r.p.m.

typical results are shown in figures 22 and 23. A gauge pressure of 6 - 8 p.s.i. was maintained in the plenum. Clearly the jet velocity was considerably less than sonic although much greater than the peripheral speed of the rotor.

In both forward and backward flow situations a resonant whip is initiated at a rotor speed between 4500 and 5000 rpm. Thus whirl ratio is between 0.64 and 0.70 considerably greater than 0.5. Typical orbit pattern are shown for 4 revolutions of the rotor. It should be noted that the orbit pattern is not stationary but rotates (as might be expected from the whirl ratio).

These experiments on a small scale rotor provide a laboratory demonstration of high sub-synchronous whirl. The measurements presented here are purely fluid driven, i.e. no physical contact between rotor and stator.

A more sophisticated rig is currently being assembled and experimental results will be reported later.

APPENDIX : Test Seals Data

Set A, B	8.890mm (height) x 9.525 mm (pitch) Fin edge thickness 0.508 mm + 0.050 mm Bore 241.300 mm $\pm$ 0.010 mm Nominal radial clearance 0.635 mm
Set C,D,E,F	4.064 mm x 6.350 mm Fin edge thickness 0.305 mm + 0.050 mm Bore 240.665 mm $\pm$ 0.010 mm Nominal radial clearance 0.381 mm
Set G	4.064 mm, 7.620 mm x 6.350 mm Fin edge thickness 0.305 mm + 0.050 mm Bore (plain seal) 240.665 mm $\pm$ 0.010 mm Bore (split seal) 233.553 mm $\pm$ 0.010 mm Nominal radial clearance 0.381 mm

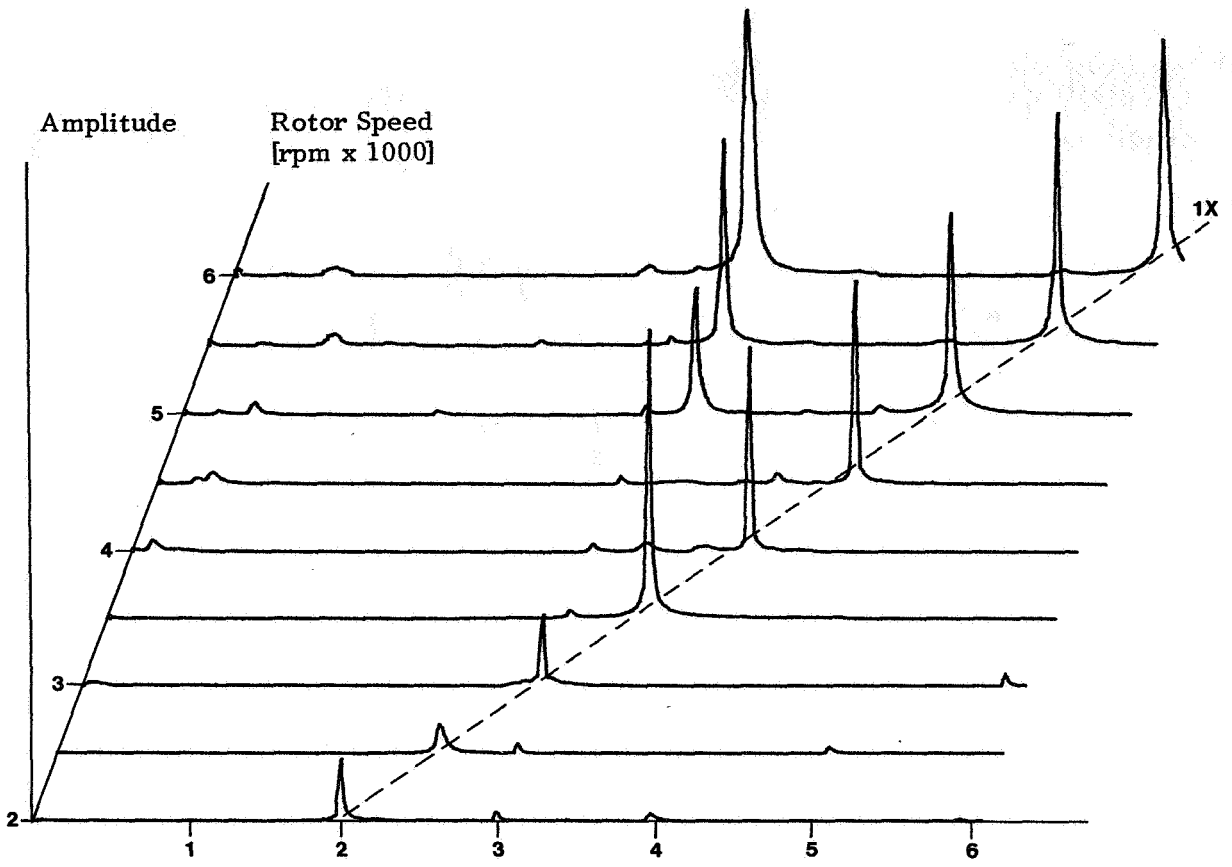

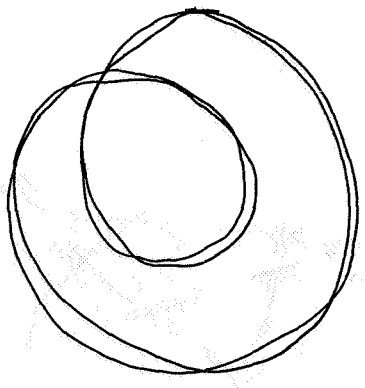

Typical Orbit at 5000 rpm.

Figure 22. - Forward flow.

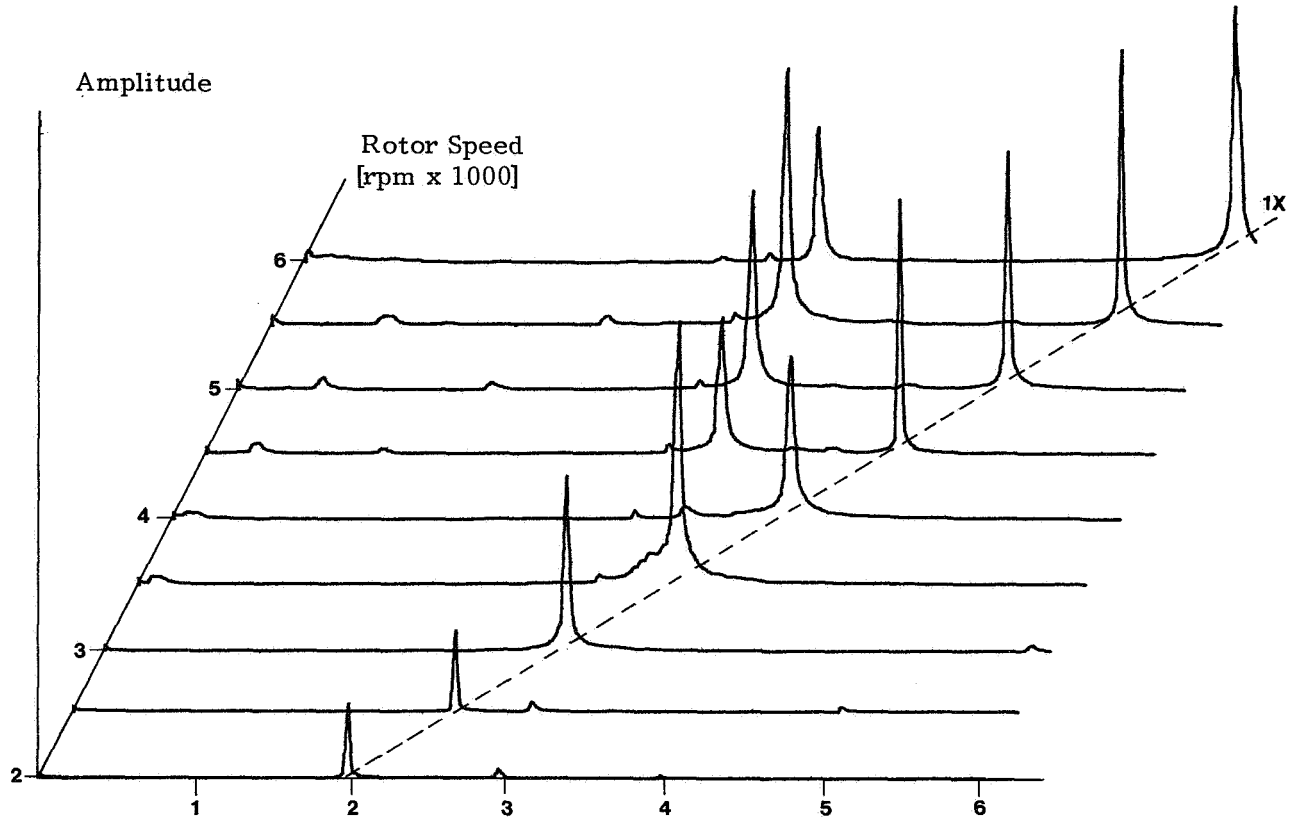

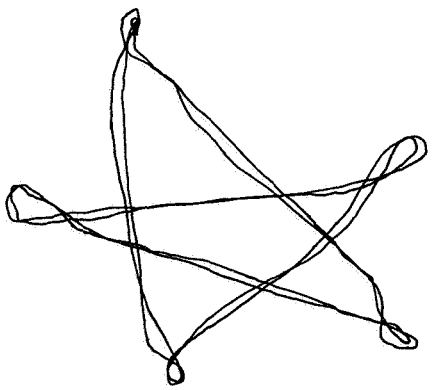

Typical Orbit at 5000 rpm.

Figure 23. - Reverse flow.

ANALYSIS OF DYNAMIC CHARACTERISTICS OF FLUID FORCE INDUCED BY LABYRINTH SEAL

Takuzo Iwatsubo, Ryoji Kawai,
Naoya Kagawa, Tetsuya Kakiuchi, and Kazuki Takahara
Kobe University, Rokkodai Kobe
Japan

In this paper flow patterns of the labyrinth seal are experimentally investigated for making a mathematical model of labyrinth seal and to obtain the flow induced force of the seal.

First, the flow patterns in the labyrinth chamber are studied on the circumferential flow using bubble and on the cross section of the seal chamber using aluminum powder as tracers. And next, the fluid force and its phase angle are obtained from the measured pressure distribution in the chamber and the fluid force coefficients are derived from the fluid force and the phase angle. Those are similar to the expression of oil film coefficients.

As the results it is found that the vortexes exist in the labyrinth chambers and its center moves up and down periodically. The pressure drop is biggest in the first stage of chambers and next in the last stage of chambers.

INTRODUCTION

Labyrinth seal are used as the non-contact type seals between rotor and stator of fluid machineries, such as, steam turbines, gas turbines, compressors and so on. To improve the efficiency of these fluid machineries, pressure of the working fluid and rotating speed of rotor tend to become high while the clearance of labyrinth seal is designed narrow to prevent for the leakage flow. As a risk of seeking such a high performance machinery, unstable vibrations of rotor occur and they draw an industrial important problem. The labyrinth seal is considered as one of these vibrations. Unstable vibration induced by the labyrinth seal was first pointed out by Alford(ref. 1), and after that it has been studied by many investigators. Among them, Boyman & Suter(ref. 2) made experimental studies and sketched the flow patterns. In this study, they had interested in the static characteristics of the labyrinth seal, but not in the dynamic characteristic, so, they did not concern with the flow induced force of labyrinth seal. On the other hand, Benckert & Wachter(ref. 3) had interested in the dynamic characteristic and they measured the hydraulic spring coefficients by using the static method. That is, rotor was fixed eccentrically toward casing and the hydraulic spring coefficient was measured by static way. The weak point of this study is not to be able to consider the effect of damping and its effect can not be neglected. On the contrary, Wright(ref. 4) investigated the instability condition of rotors induced by the labyrinth seal force for two seal strips model under many test conditions and also measured the destabilizing fluid force which included the damping coefficient. This study is valuable because it considers the hydraulic spring and damping coefficients, however it lacks generality because the rotor has only two seal strips.

The purpose of this paper is to study the flow patterns, which is needed mathematically to model the flow in the labyrinth seal. Namely, the flow pattern of the cross section and the circumference of the labyrinth chamber are observed. Bubble is used as a tracer for the visualization of the circumference and aluminum powder is also used in that of the cross section, and the photographs of them are taken. Moreover, the flow induced force is measured under the condition of both spinning and whirling motions of the rotor and measuring the change of pressure and of the phase angle in the labyrinth chamber. The eight coefficients, which represent the flow induced force of labyrinth seal by the function of velocity and displacement, i.e. they are correspond to the coefficients of the journal bearing, are obtained.

TEST APPARATUS

The test apparatus to observe the flow patterns and to measure the fluid force is shown in figure 1. In this figure the rotor ① is driven by the three-phase motor ⑩ through the variable-speed drive for spinning motion of ⑨ . The rotor is supported at the upper and the lower part by the eccentric bearings ④ . The dimensions and directions of both eccentricities are set to be equal. Therefore, the rotor is whirled by rotation of the eccentric bearing. The eccentric bearings are driven by the three-phase motor ⑫ through the variable-speed drive ⑪ for whirling motion. Since the rotor and the eccentric bearing are driven by different motors, the rotor can be spun in the same direction as whirl direction (forward) and in the opposite direction (backward), and these spin and whirl speeds are continuously changed from 1.6(Hz) to 5.2(Hz).

The schematic piping of the hydraulic circulating system is shown in figure 2. The working fluid is compressed and transported from the tank 1 to the tank 2. The tank 2 acts as an accumulator, and is installed to lower the pulsation of pressure by the pump using the air which is in the upper part of the tank 2. The working fluid is transported from the tank 2 into the test casing through four pipes, and is transported to the measuring part through the rectifier. The test seals have two or six strips and are the straight-through type seals. After that, the working fluid is returned to the tank 1 by natural draining. Two test casings are prepared, i.e. one is made of acrylic resin for the observation of streamline and the other is made of stainless steel for the measurement of the flow induced force.

The rotating speed of the rotor is measured by the pulse of the notched disk which is installed on the upper end of the rotor. The whirl frequency of the rotor is measured by the measurement of the whirl amplitude of the rotor. The change of pressure by the whirl of rotor is measured through the needle of injector, which is fixed in the measuring point of the test casing where the middle point between two confronted strips corresponds, by the semiconductive pressure transducer. The measured signal current is sent to the signal analyser through the D.C. amplifire and is analyzed.

EXPERIMENT I (Observation of flow patterns)

Two kinds of experiment, that is, experiment I-1 and experiment I-2 , are done using the acrylic resin test casing in experiment I. And two kinds of test seal are prepared, i.e. one has two seal strips and the other has six seal strips. The flow pattern of the cross section of the labyrinth chamber is observed in experiment I-1 and the circumferential flow pattern is observed in experiment I-2 . From the limit of stress of the test casing, two kinds of entrance pressure, i.e. 122.5(kPa) and

147.0(kPa), and three kinds of spinning speed 0(Hz), 2(Hz), and 3(Hz), are tested.

Test procedure of experiment I-1 (Cross section)

To observe the cross section of the labyrinth chamber, the stroboscopic light is thrown through the slit whose clearance is 1.5(mm) as shown in figure 3, and the reflected light of the tracer of aluminum powder is photographed.

Test procedure of experiment I-2 (Circumference)

To observe the circumferential flow of the labyrinth chamber, the light of reflector lamp is used and the motion of vortex in the labyrinth chamber is photographed using bubble tracer.

EXPERIMENTAL RESULTS AND CONSIDERATION

Figures 4 and 5 show the flow patterns of one chamber seal, in which the flow in cross section is shown in figure 4 and the circumferential flow is shown in figure 5. The flow which through the first seal forms the vortex row in the labyrinth chamber. The center of vortex row does not stay and moves sinusoidally as shown in figure 5, and the sinusoidal wave moves in the same direction as spin direction at a lower speed than rotating speed of rotor as shown in figure 6(a). This phenomenon is clear from three photographs of figure 4 that the cross sections of labyrinth chamber are taken. It is found from these photographs that the vortex moves up and down against flow as shown in figure 6(b).

Figures 7 and 8 show the flow pattern of 5 chambers seal. The flow in cross section is shown in figure 7 and the circumferential flow is shown in figure 8. As the case of one chamber seal, the flow in each chamber also forms sinusoidal vortex row. The periods of vortex rows in 5 chambers are almost the same, but there is no particular regularity between the phase angles of the vortex rows. Bubble which through the first seal is big. It means that the pressure drop in the first chamber is high. This result corresponds to the measurement results of the pressure drop in each chamber. As the case of one chamber seal, it is found from figure 7 of the cross sectional photograph that there are vortexes.

EXPERIMENT II (Measurement of fluid force)

Two kinds of experiment, that is, experiment II-1 and experiment II-2, are performed using one chamber seal and 5 chambers seal in experiment II. The fluid force F which acts on the rotor, and the phase angle ϕ between whirl and fluid force, are measured in experiment II-1. The spring coefficients and the damping coefficients of the working fluid are measured in experiment II-2.

Experiment II-1 (Fluid force and phase angle)

The rotating speed is set to the whirl speed, and the change of pressure and its phase angle to the whirling motion are measured in each chamber. In case of one chamber seal, three points of figure 9(b), that is, ①, ②, and ③, are used and in

case of 5 chambers seal, seven points of figure 9(c), that is, ① to ⑦ are used. And the position of these measuring points is (III) of figure 9(a). The changes of pressure in each chamber are measured from ② to ⑥ of figure 9(c) in order. In the analysis by the signal analyser, the 10 Hz-low pass filter is used to protect the noise of high frequency. Parameters are set to be entrance pressure, eccentricity, rotating speed, and direction of rotation. Conditions of experiment II-1 are shown in table 1.

Experiment II-2 (Spring and damping coefficients)

The rotor is spun at the fixed eccentricity without whirling motion, and the circumferential pressure distribution is measured. As in the case of experiment II-1, the measuring points are ① to ⑦ in the position of (III) in figure 9. So, the directions of static eccentricity are changed one after another, its procedure is (III)→(IV)→(I)→(II) in figure 9(a), and the pressure of each eccentric state is measured at the measuring points. Consequently, the circumferential pressure distribution of the statically eccentric rotor is measured. The procedure of measurement is that, first, the pressure in each chamber is measured one by one when the rotor's eccentric direction is one of four directions ((I) to (IV) in figure 9(a)) and next the direction of eccentricity is changed and the pressure is measured. Conditions of the experiment II-2 are shown in table 2.

ANALYSIS OF MEASURED DATA

The data obtained in experiment II are the maximum change of pressure ΔP_{max}, the phase angle of pressure to the whirl motion $\angle\phi$ and the change of the circumferential pressure distribution $\Delta P'$ when the rotor is spun without whirl. So, first, the x and the y directional force F_{xo} and F_{yo} are obtained from ΔP_{max} and $\angle\phi$ when the rotor is whirling. Next, the principal spring coefficient K_{xx} and the cross coupled spring coefficient K_{yx} are obtained from $\Delta P'$. And last, the principal damping coefficient C_{yy} and the cross coupled damping coefficient C_{xy} are calculated using the equation of fluid force and the expression is similar to that of the journal bearing.

It is assumed that the circumferential pressure distribution in the whirling motion is circular and the center of it is O_p as shown in figure 10. Thus, the change of the circumferential pressure distribution in the chamber ΔP is given as;

$$\Delta P = \Delta P_{max} \cos(\varphi + \phi - \pi) \tag{1}$$

The x and y direction components F_{xo} and F_{yo} of the fluid force are obtained by using equation (1).

$$F_{xo} = -\int_0^{2\pi} (\Delta P \cos\varphi)\, \ell R_s\, d\varphi$$

$$= -\ell R_s \pi \Delta P_{max} \cos(\pi - \phi) \tag{2}$$

$$F_{yo} = -\int_0^{2\pi} (\Delta P \sin\varphi)\, \ell R_s\, d\varphi$$

$$= -\ell R_s \pi \Delta P_{max} \sin(\pi - \phi) \tag{3}$$

Then the fluid force and its phase angle acting on the rotor are as follows;

$$|F_o| = \sqrt{F_{xo}^2 + F_{yo}^2} \tag{4}$$

$$\phi = \cos^{-1} \frac{F_{xo}}{F_o} \tag{5}$$

where R_s is radius of rotor and ℓ is strip pitch.

On the other hand, K_{xx} and K_{yx} are obtained from the change of the circumferential pressure distribution $\Delta P'$ when the rotor is spun and no whirl with the fixed eccentricity,

$$K_{xx} = \frac{1}{e} \int_0^{2\pi} (\Delta P' \cos\varphi)\, \ell R_s d\varphi \tag{6}$$

$$K_{yx} = \frac{1}{e} \int_0^{2\pi} (\Delta P' \sin\varphi)\, \ell R_s d\varphi \tag{7}$$

where e is eccentricity of rotor. $\Delta P'$ are measured for four cases, that is, $\varphi=0$, $\varphi=\pi/2$, $\varphi=\pi$, and $\varphi=3\pi/2$, and are approximated to a circular distribution, as the case of ΔP, as follows;

$$\Delta P' = \Delta P'_{max} \cos(\varphi + \phi' - \pi) \tag{8}$$

where $\Delta P'_{max}$ is the maximum change of pressure and ϕ' is the phase angle between the position of $\Delta P'_{max}$ and the maximum clearance.

So, the principal spring coefficient K_{xx} and the cross coupled spring coefficient K_{yx} are obtained as follows;

$$K_{xx} = \frac{1}{e} \ell R_s \pi \Delta P'_{max} \cos(\pi - \phi) \tag{9}$$

$$K_{yx} = \frac{1}{e} \ell R_s \pi \Delta P'_{max} \sin(\pi - \phi) \tag{10}$$

Last, the expressions of fluid force induced by labyrinth seal are obtained as follows;

$$F_x = -(K_{xx} + \omega_n C_{xy})x - (K_{xy} - \omega_n C_{xx})y \tag{11}$$

$$F_y = -(K_{yx} + \omega_n C_{yy})x - (K_{yy} - \omega_n C_{yx})y \tag{12}$$

where F_x and F_y are the function of time and ω_n is critical speed of rotor system. Then equations (11) and (12) are considered at the same time as equations (2) to (5) as follows;

$$F_{xo} = -K_{xx} e - \omega_n C_{xy} e \tag{13}$$

$$F_{yo} = -K_{yx} e - \omega_n C_{yy} e \tag{14}$$

Substituting equations (2), (3), (9) and (10) into equations (13) and (14), the cross coupled damping coefficient C_{xy} and the principal damping coefficient C_{yy} are obtained.

EXPERIMENTAL RESULTS AND DISCUSSION

Experiment II-1 (Fluid force and phase angle)

Figure 11 shows an example of wave mode of the signal analyser. The upper part is the wave of the rotor's whirl, and the lower part is that of the pressure change in the chamber. The noise of this wave is pressure disturbance induced by turbulent flow. It is found from figure 11 that there is phase lag between whirl and fluid force.

Experimental results of one chamber seal are shown in figures 12 and 13. In the case of one chamber seal, the fluid force increases with the increase of eccentricity in every condition of both entrance pressures and whirl directions. In many cases, the fluid force increases with the increase of rotating speed. But in the cases of the high entrance pressure and forward precession the fluid force tends to decrease with more than a certain rotating speed. The phase angle ϕ is constant, of which value is about $3\pi/2$(rad) in all cases.

Experimental results of 5 chambers seal are shown in figures 14 to 19. First, the discussions about the forward precession are as follows. The fluid force in each chamber increases with the increase of the entrance pressure. The fluid force in the 1st chamber is more remarkably affected than the others by the rotating speed. The fluid force in the other chambers varies hardly or increases slightly with the increase of the rotating speed. And the fluid force increases with the increase of the eccentricity. The change of fluid force is shown in figure 16. This is the case that the rotating speed is 3.1(Hz) and the tendencies of the fluid force do not change in the other cases. The fluid force in the 2nd chamber decreases, and in the other chambers after the 3rd chamber it gradually increases. The fluid force of the whole labyrinth seal F increases with the increase of rotating speed, entrance pressure or eccentricity (fig. 15). The phase angle ϕ is constant at about $3\pi/2$(rad) and has no relations to entrance pressure, rotating speed, and eccentricity, except for the case in the 2nd chamber. The phase angle in the 2nd chamber is changed by conditions. The reason of this phenomenon is considered as follows. Since the fluid force in the 2nd chamber is small, there is no remarkable difference between the pressure disturbance induced by turbulent flow and the change of pressure induced by whirl. Then, to obtain the accurate phase angle is difficult. In the case that eccentricity is large i.e. 1.0(mm) and the fluid force is greater than the other cases, the phase angle ϕ is constant by about $3\pi/2$(rad). Thus, it is considered that the phase angles ϕ in all chambers are constant by about $3\pi/2$(rad) and have no relation to parameters. In case of backward precession, the tendency of the fluid force is almost same as the case of forward precession. And the fluid force of backward precession is more remarkably affected than that of forward precession by the rotating speed.

Experiment II-2 (Spring and damping coefficients)

Part of experimental results of the spring and damping coefficients are shown in figures 20 to 31. Variation in each figure may depend on the accuracy of instrument and measurement. K_{xx} and K_{yx} have no relation to the rotating speed of rotor. K_{xx} increases with the increase of entrance pressure, but K_{yx} has no relation to entrance pressure. K_{xx} and K_{yx} decrease during the working fluid flows from the 1st chamber to the 5th chamber. C_{yy} and C_{xy} have no relation to entrance pressure and rotating speed. And C_{xy} increases during the working fluid flows from the 1st chamber to the 5th chamber.

CONCLUSIONS

In this paper, the flow patterns of one chamber and 5 chambers seals are investigated, and the fluid force and its phase angle, and the coefficients of fluid force are experimentally obtained. The conclusions are as follows:

(1) In the chamber, the vortex forms the sinusoidal wave and its wave moves in the same direction of rotation in the circumferential direction. Observing a certain cross section of seal chamber, the center of vortex moves up and down periodically.

(2) The fluid force and its phase angle of one chamber seal are qualitatively agree with 5 chambers seal.

(3) The fluid force increases with the increase of entrance pressure, rotating speed or eccentricity.

(4) The fluid force in the 1st chamber and the 5th chamber of the 5 chambers seal, that is, the fluid force of entrance and exit part of labyrinth seal, is great, and the fluid force in the middle region of labyrinth seal is small.

(5) The phase angle of fluid force is constant and has no relation to all parameters.

(6) The principal spring coefficient increases with the increase of entrance pressure, and it decreases from the 1st chamber to the 5th chamber. The damping coefficients have no relation between entrance pressure and rotating speed.

This study is supported by Scientific Research Fund of the Ministry of Education No.56550180 (1981-1982) and No.58550172 (1983).

REFERENCES

(1) Alford, J. S.: Protecting Turbomachinery From Self-Excited Rotor Whirl. Trans. ASME, J. Engng. Power, Oct. 1965, pp. 333-344.

(2) Boyman, T.; and Suter, P.: Transport Phenomena in Labyrinth-Seals of Turbomachines. Institut de Thermique Appliquée CH-1015 Lausanne, Switzerland, pp. 8.1-8.10.

(3) Benckert, H.; and Wachter, J.: Flow Induced Spring Coefficients of Labyrinth Seals for Application in Rotor Dynamics. NASA Lewis, Conference Publication 2133, Rotordynamic Instability Problems in High-Performance Turbomachinery, 1980, pp. 189-212.

(4) Wright, D. V.: Rotor Dynamic Instability. ASME AMD, Vol. 55, 1983, pp. 19.

TABLE 1. - EXPERIMENT Ⅱ-1
EXPERIMENTAL CONDITION

ENTRANCE PRESSURE (kPa)		122.5 147.0 171.5 196.0
ECCENTRICITY (mm)		0.5 0.75 1.0
ω_n/ω		1.0
ω	FORWARD (Hz)	1.9 - 5.2 STEP 0.3
	BACKWARD (Hz)	1.9 - 4.3 STEP 0.3
NUMBER OF CHAMBER		1 5

TABLE 2. - EXPERIMENT Ⅱ-2
EXPERIMENTAL CONDITION

ENTRANCE PRESSURE (kPa)	122.5 147.0 171.5 196.0
ECCENTRICITY (mm)	1.0
WHIRLING SPEED (Hz)	0.0
ROTATING SPEED (Hz)	1.9 - 5.2 STEP 0.3
NUMBER OF CHAMBER	1 5

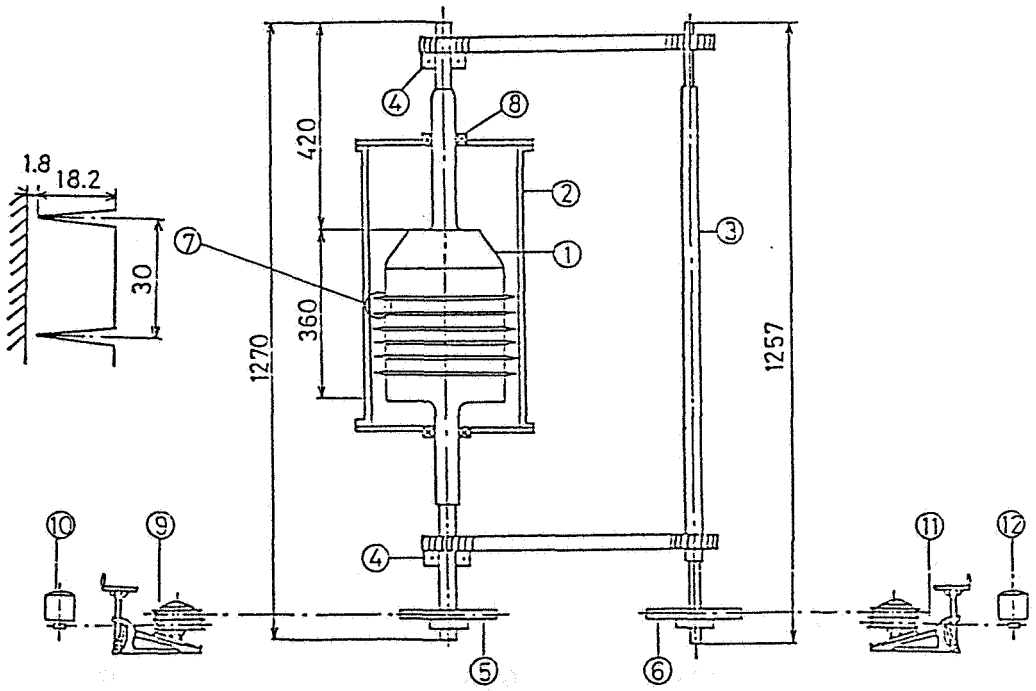

①. ROTOR ②. TEST CASING ③. SHAFT
④. ECCENTRIC BEARING ⑤. PULLEY ⑥. PULLEY
⑦ TEST SEAL ⑧. DIAPHRAGM SEAL
⑨,⑪. VARIABLE-SPEED DRIVE ⑩,⑫. THREE-PHASE MOTOR

Figure 1. - The schematic layout of the test apparatus.

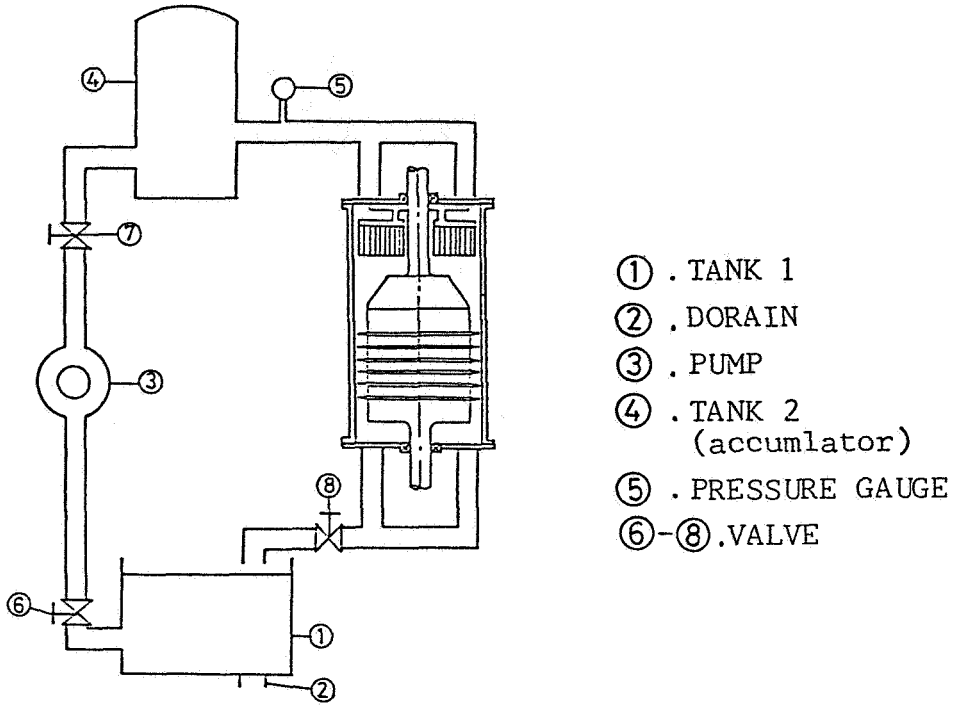

Figure 2. - The schematic piping of the circulating system

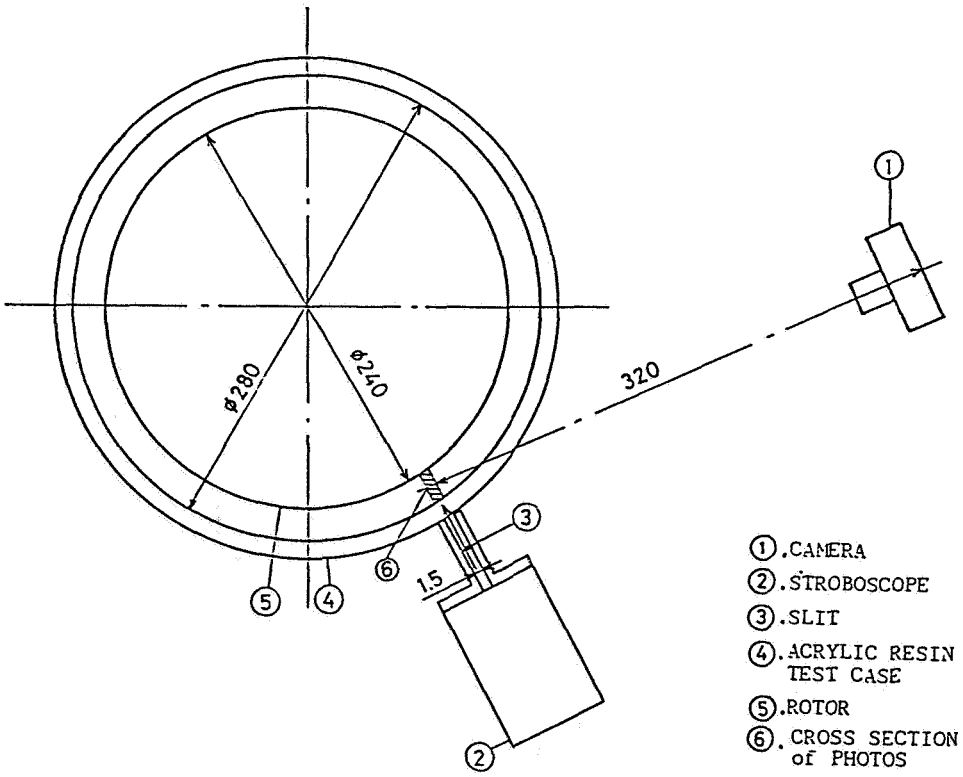

Figure 3. - The schematic layout of the visualizational apparatus.

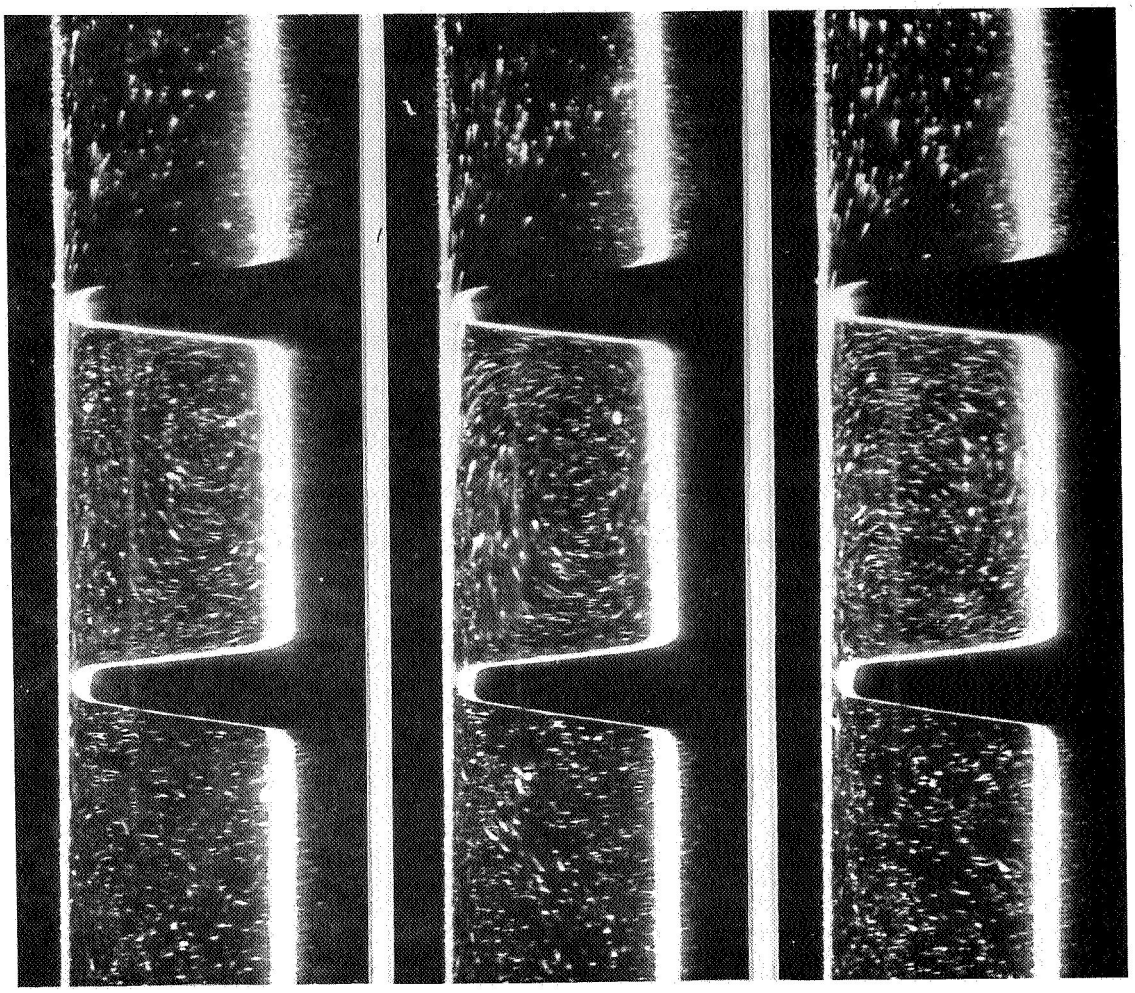

Figure 4. - Cross section of one chamber seal.

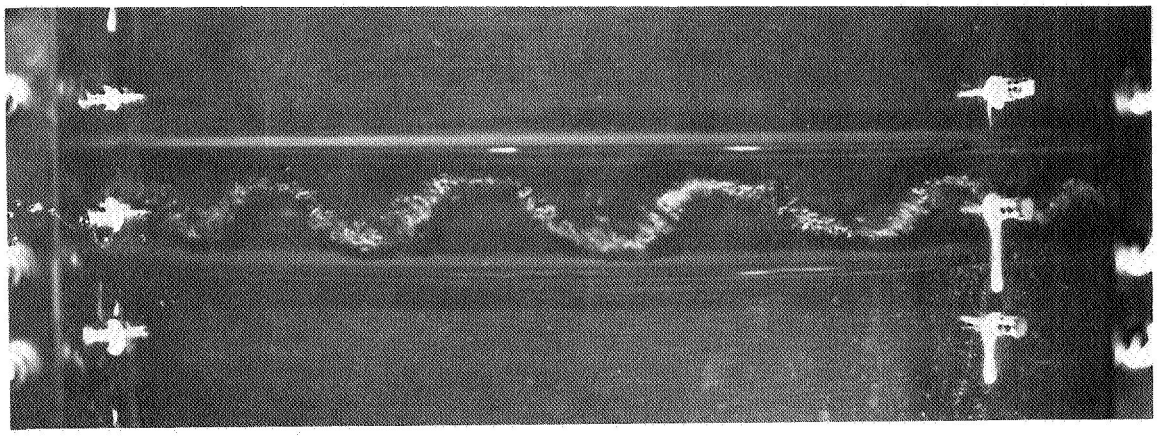

Figure 5. - The movement of vortex row in one chamber seal.

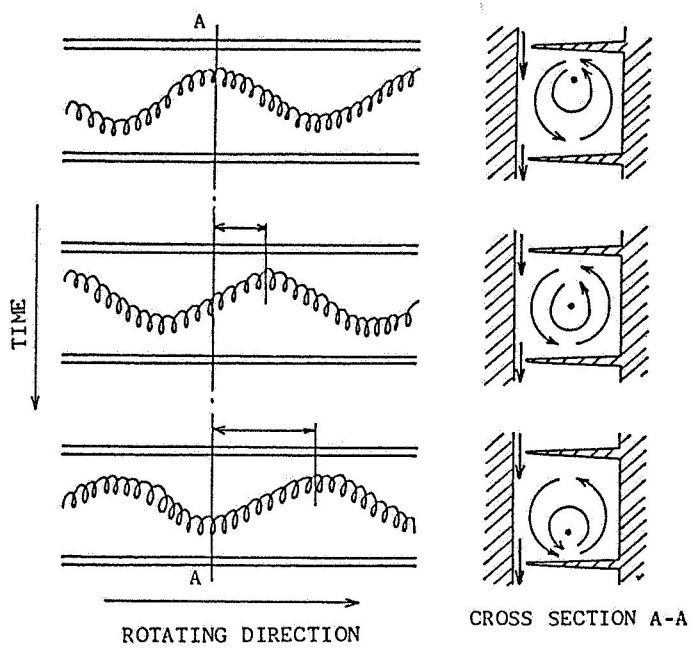

(a) (b)

Figure 6. - The movement of vortex row.

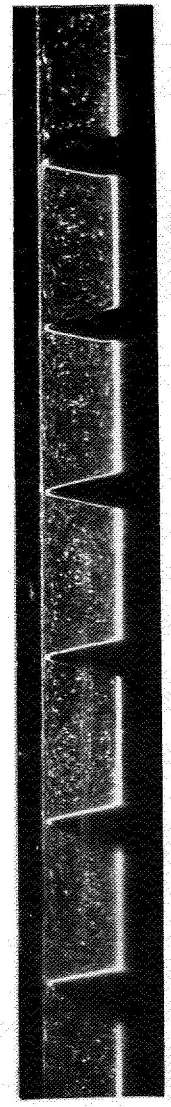

Figure 7. - Cross section of 5 chambers seal.

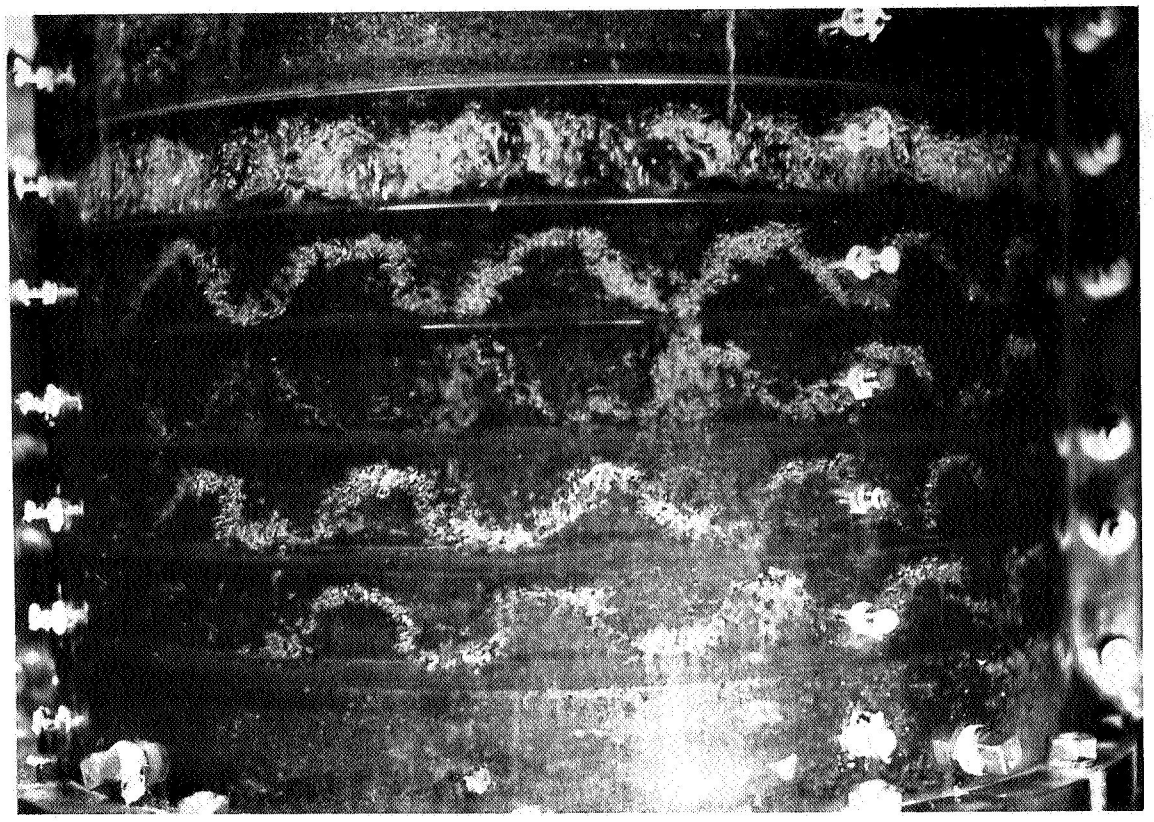

Figure 8. - The movement of vortex row in 5 chambers seal.

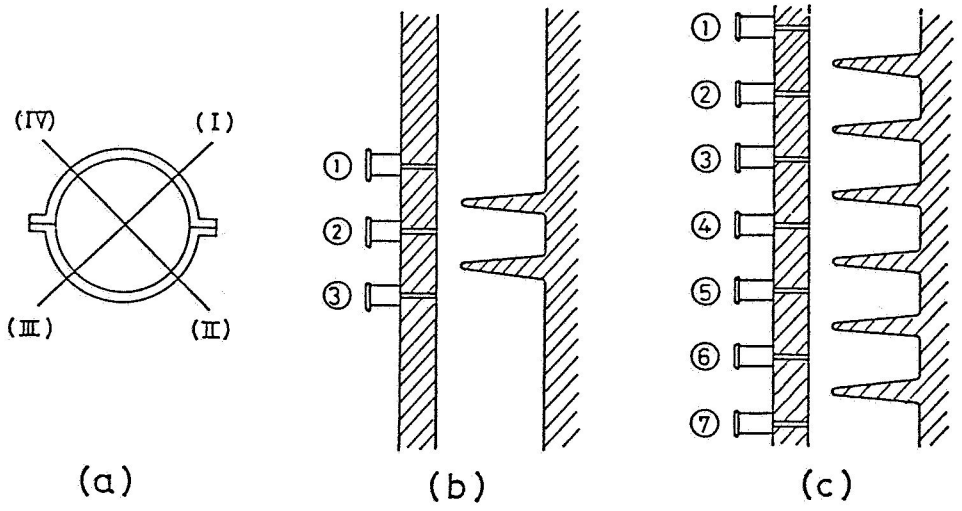

Figure 9. - The measuring points of pressure installed on the test casing.

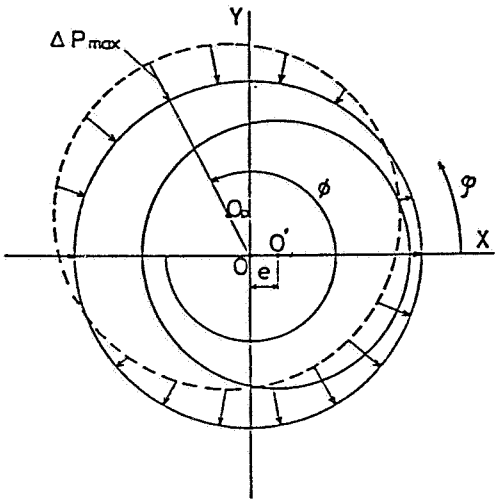

O :CENTER of CASE
O':CENTER of ROTOR
Op:CENTER of PRESSURE DISTRIBUTION
φ :PHASE ANGLE of PRESSURE
e :ECCENTRICITY of SEAL
ΔPmax:MAXIMUM PRESSURE CHANGE

Figure 10. - The assumption of the circumferential pressure distribution.

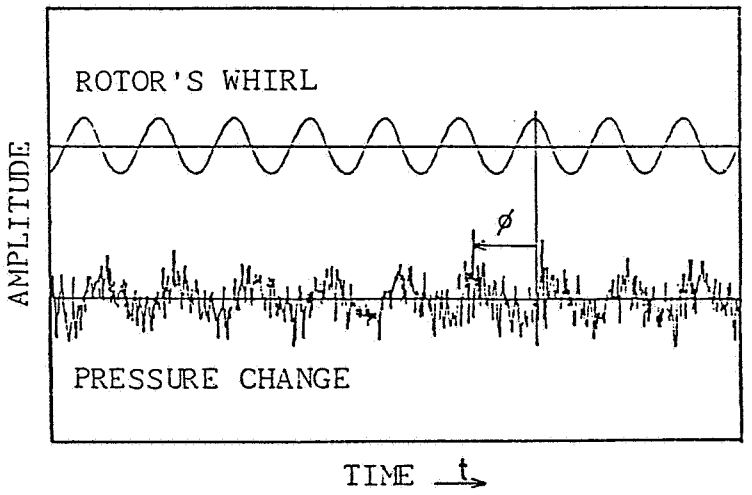

FORWARD
P=147.0(kPa)
e=0.75 (mm)
ω=3.7 (Hz)

Figure 11. - An example of the analytic wave.

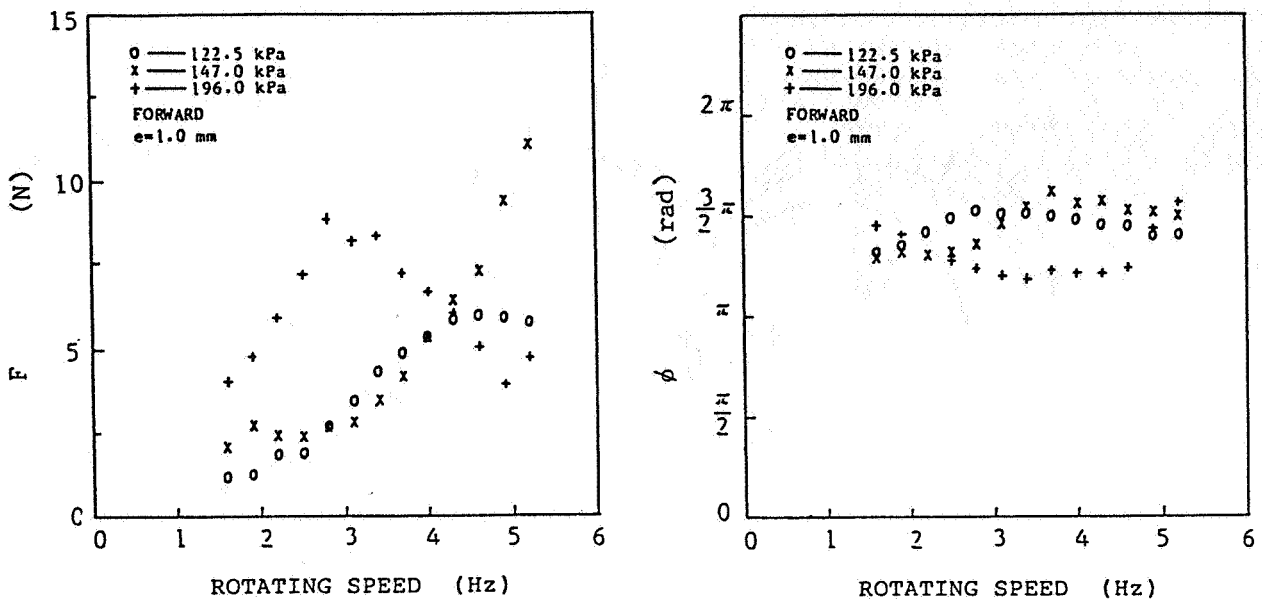

Figure 12. - Fluid force and phase angle of one chamber seal.

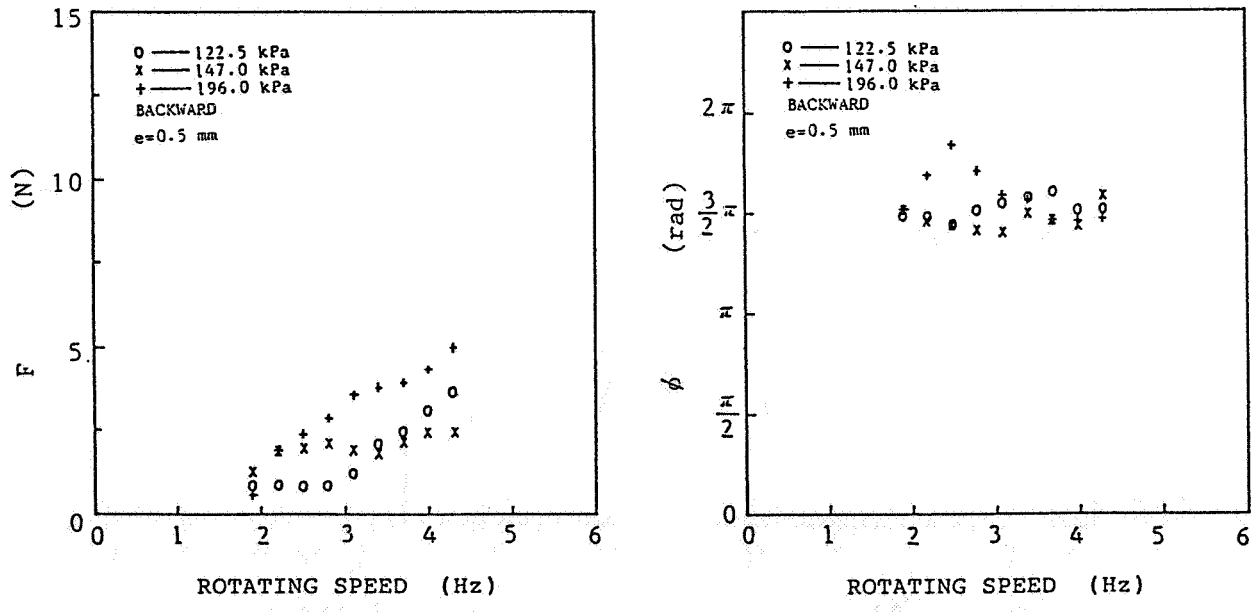

Figure 13.- Fluid force and phase angle of one chamber seal.

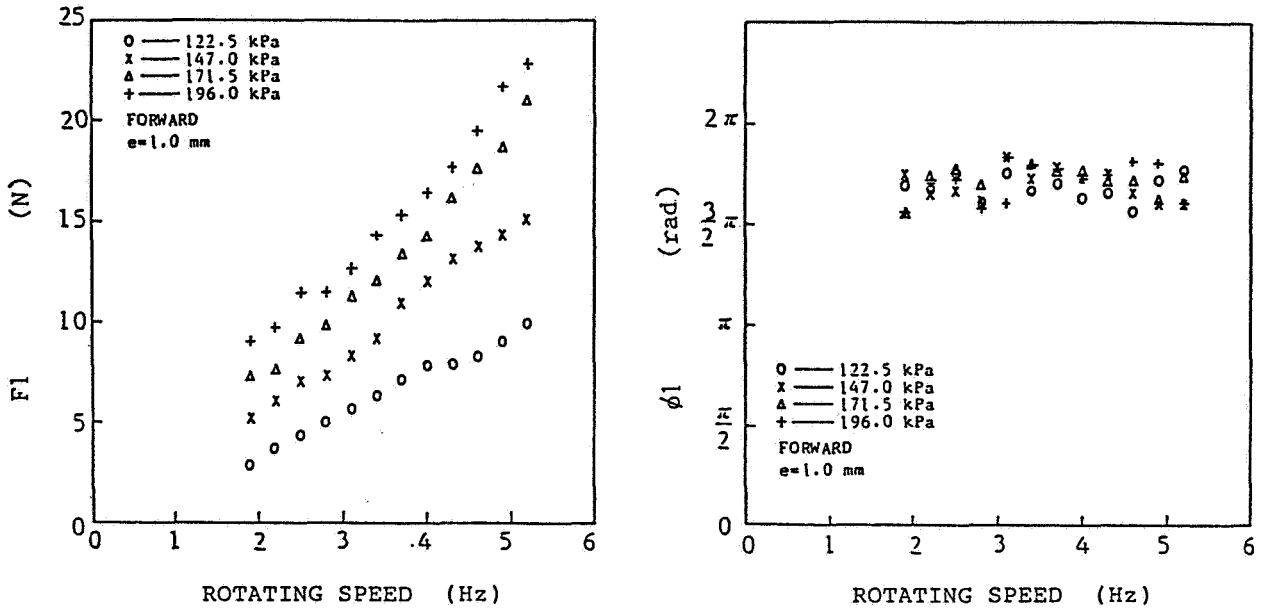

(a)

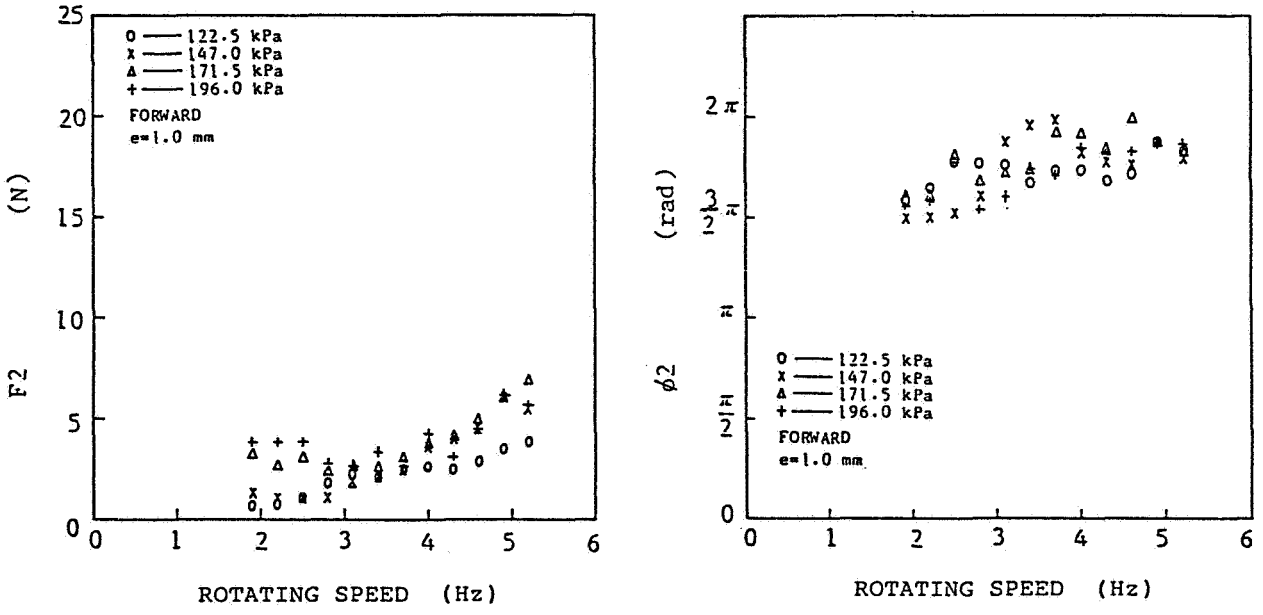

(b)

Figure 14.- Fluid force and phase angle of 5 chambers seal.

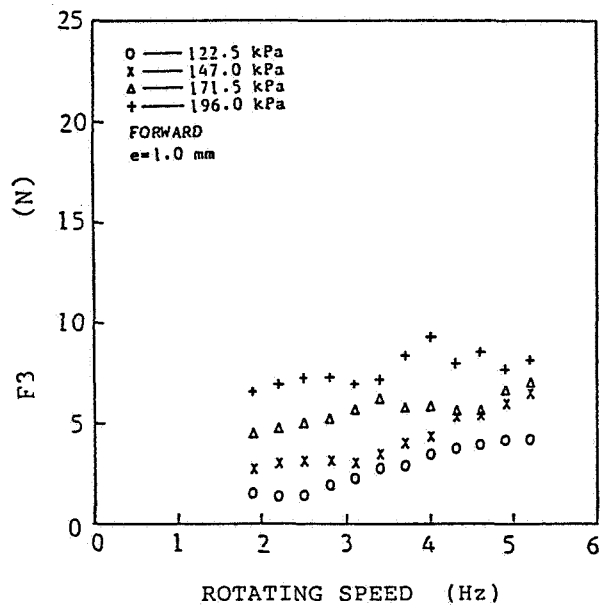
o —— 122.5 kPa
x —— 147.0 kPa
Δ —— 171.5 kPa
+ —— 196.0 kPa
FORWARD
e=1.0 mm
F3
(N)
ROTATING SPEED (Hz)

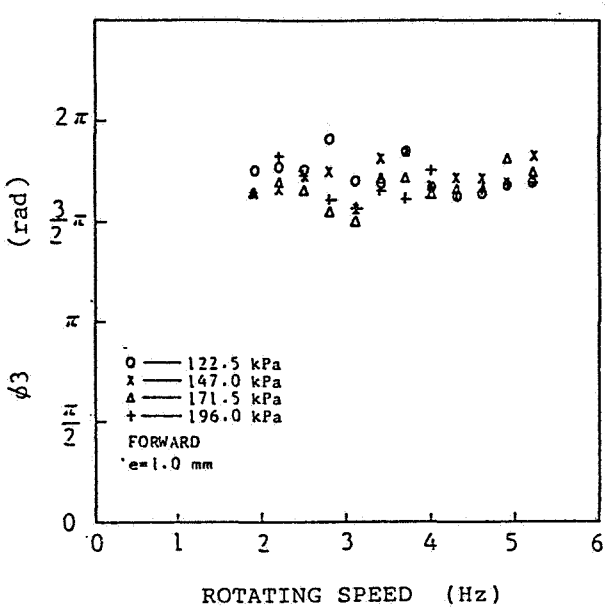
o —— 122.5 kPa
x —— 147.0 kPa
Δ —— 171.5 kPa
+ —— 196.0 kPa
FORWARD
e=1.0 mm
φ3
(rad)
ROTATING SPEED (Hz)

(c)

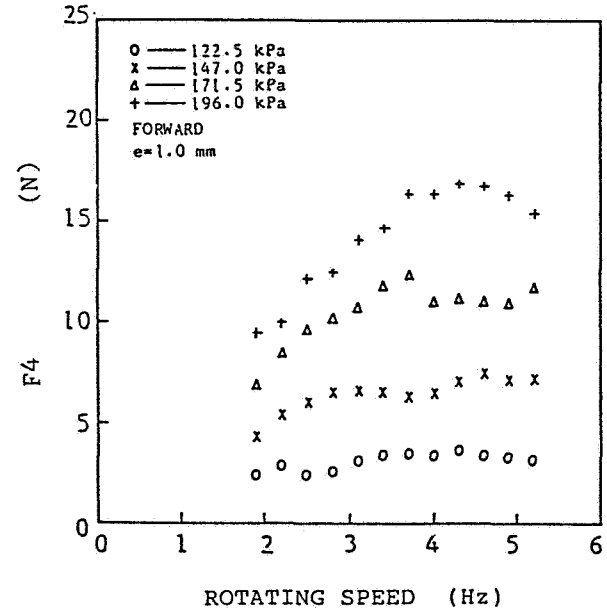
o —— 122.5 kPa
x —— 147.0 kPa
Δ —— 171.5 kPa
+ —— 196.0 kPa
FORWARD
e=1.0 mm
F4
(N)
ROTATING SPEED (Hz)

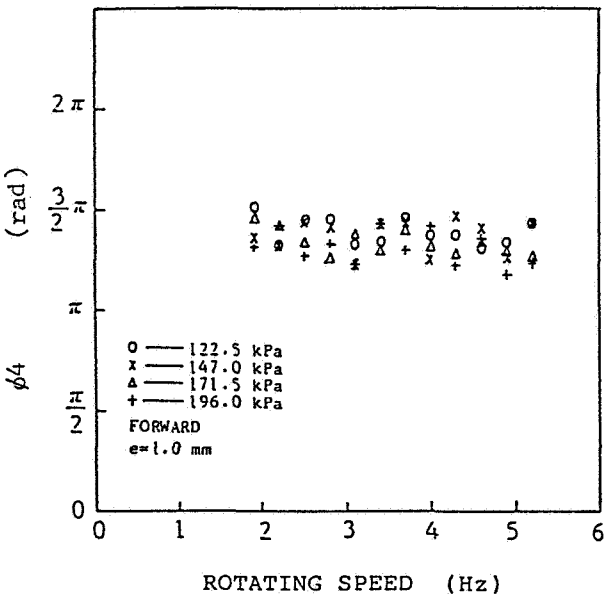
o —— 122.5 kPa
x —— 147.0 kPa
Δ —— 171.5 kPa
+ —— 196.0 kPa
FORWARD
e=1.0 mm
φ4
(rad)
ROTATING SPEED (Hz)

(d)

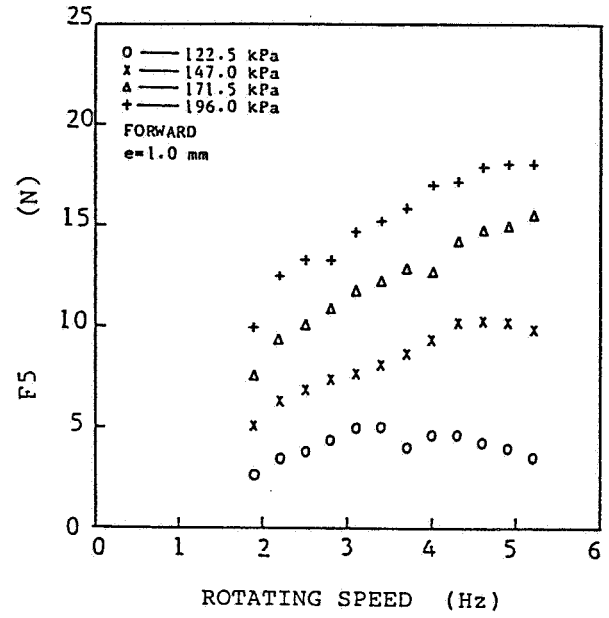

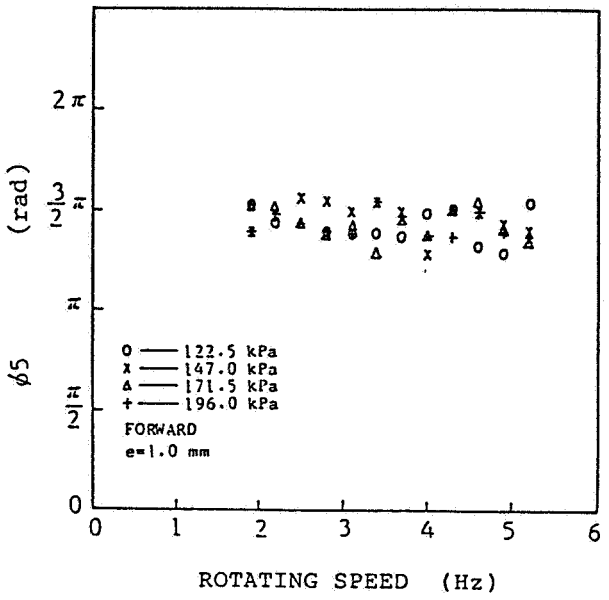

(e)

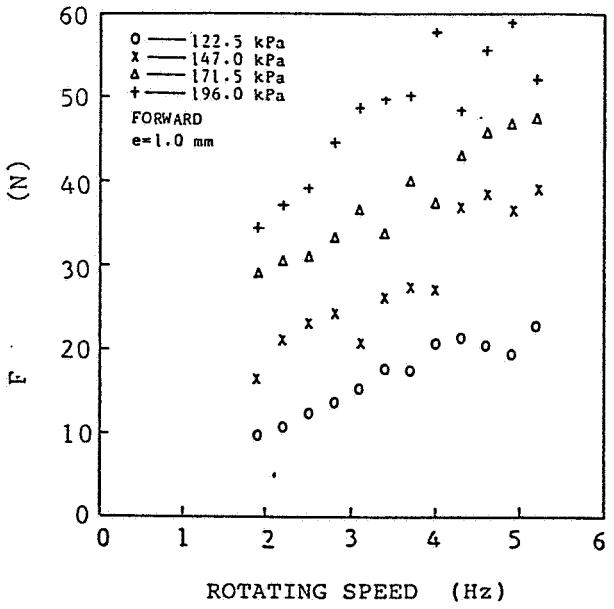

Figure 15. - Fluid force of the whole labyrinth seal.

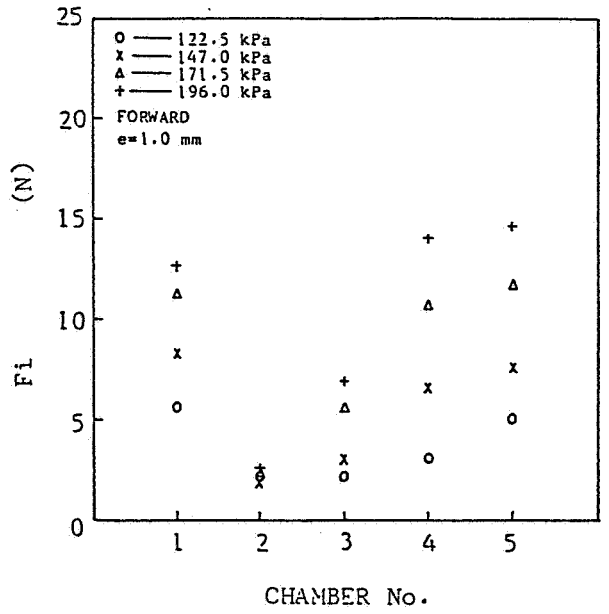

Figure 16. - Fluid force in each chamber.

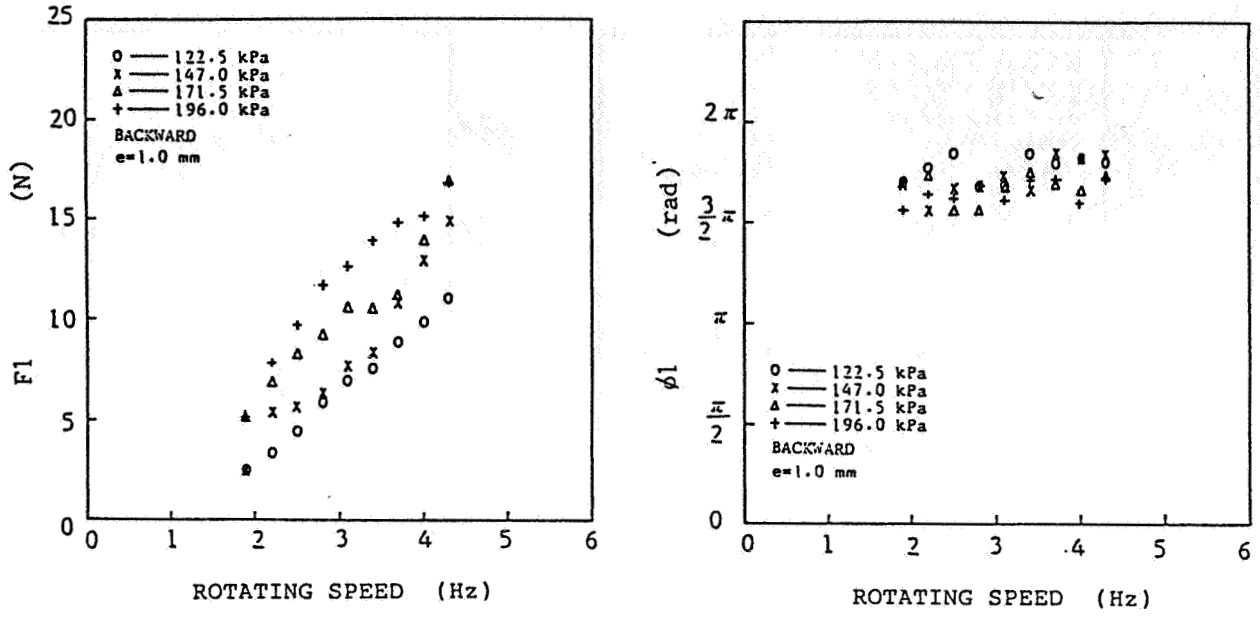

Figure 17. - Fluid force and phase angle of 5 chambers seal.

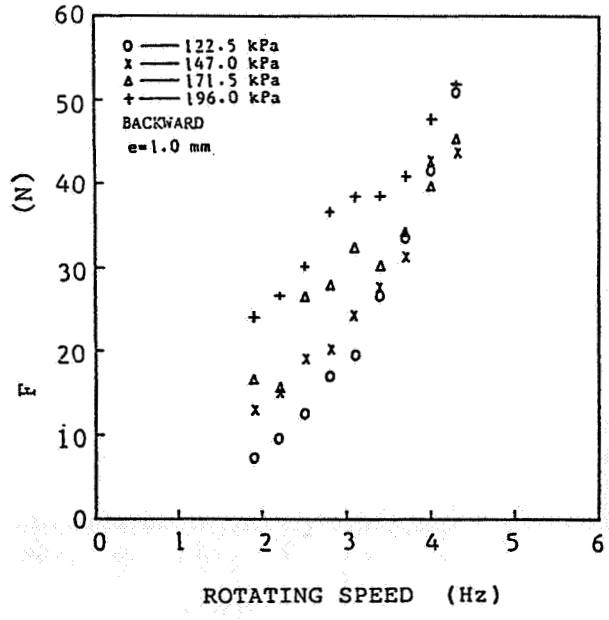

Figure 18. - Fluid force of the whole labyrinth seal.

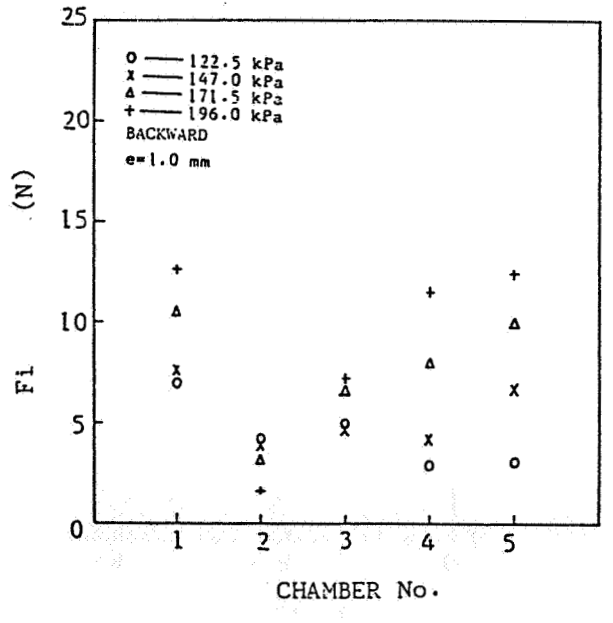

Figure 19. - Fluid force in each chamber.

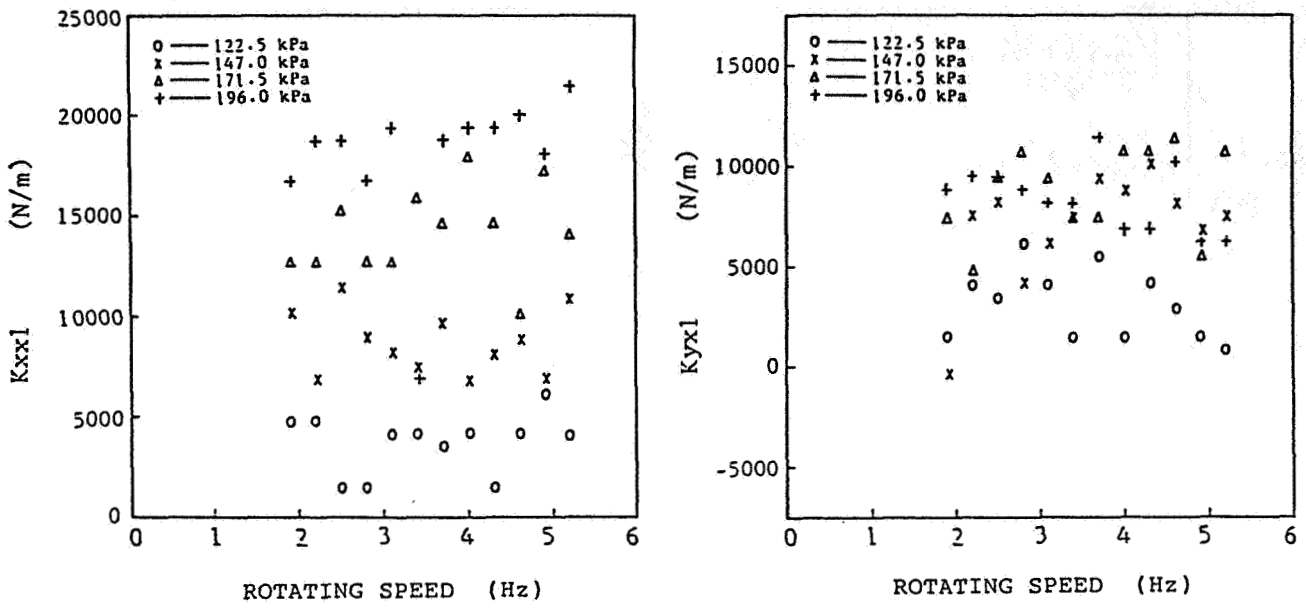

Figure 20. - Spring coefficients in the 1st chamber

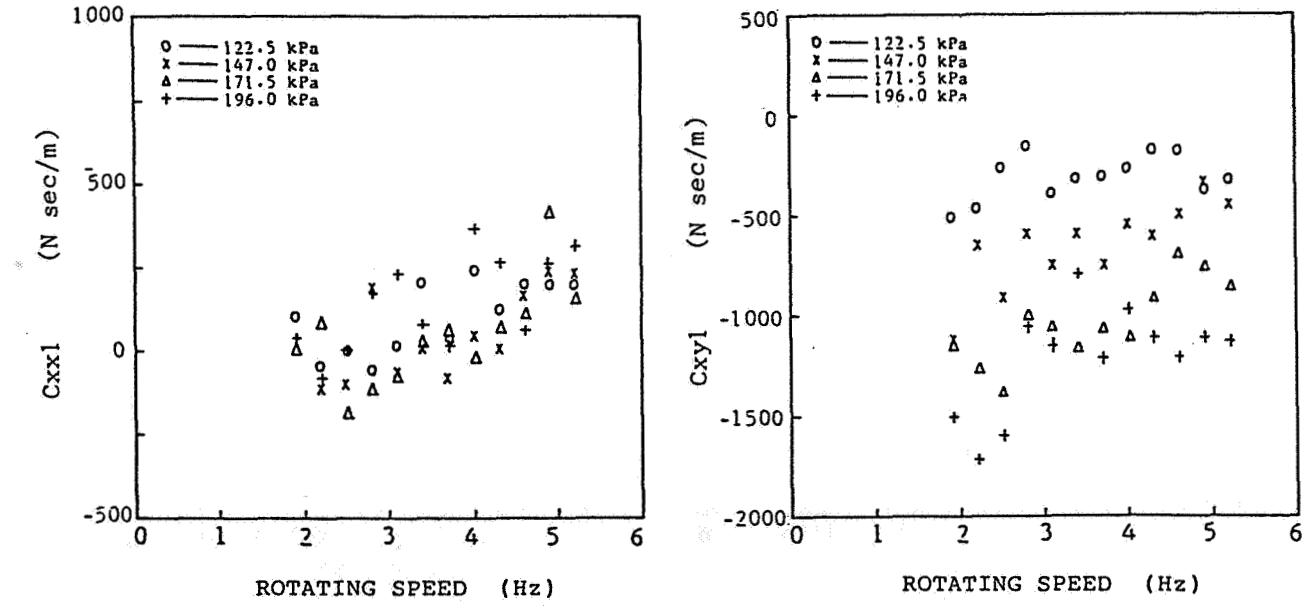

Figure 21. - Damping coefficients in the 1st chamber

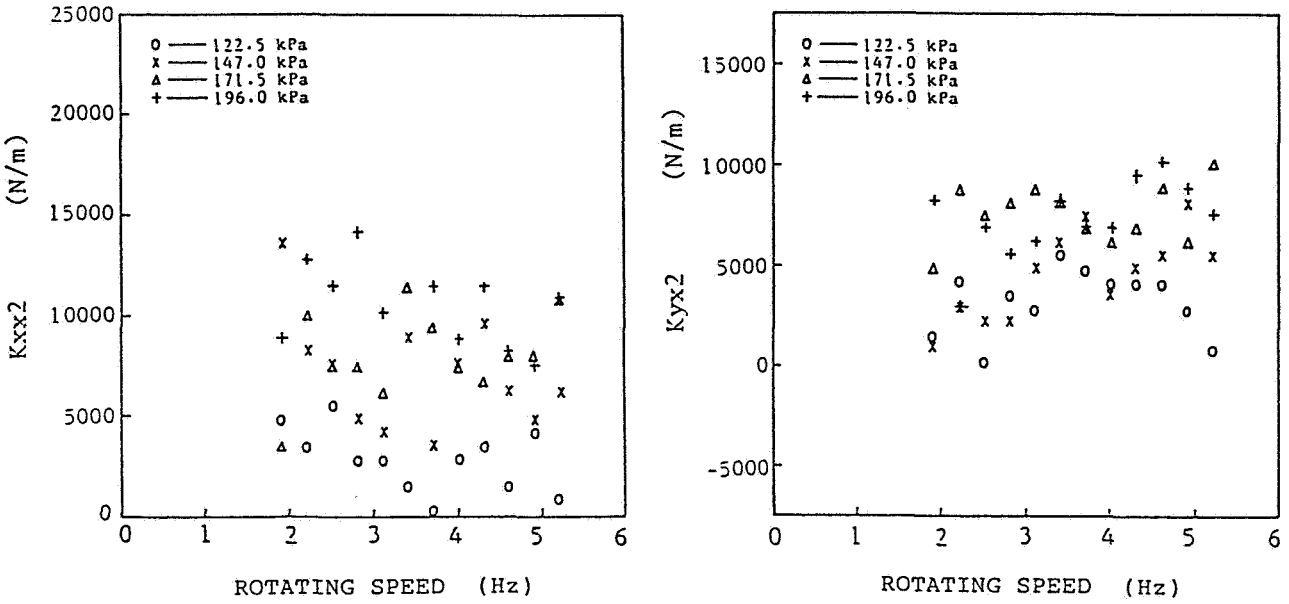

Figure 22. - Spring coefficients in the 2nd chamber

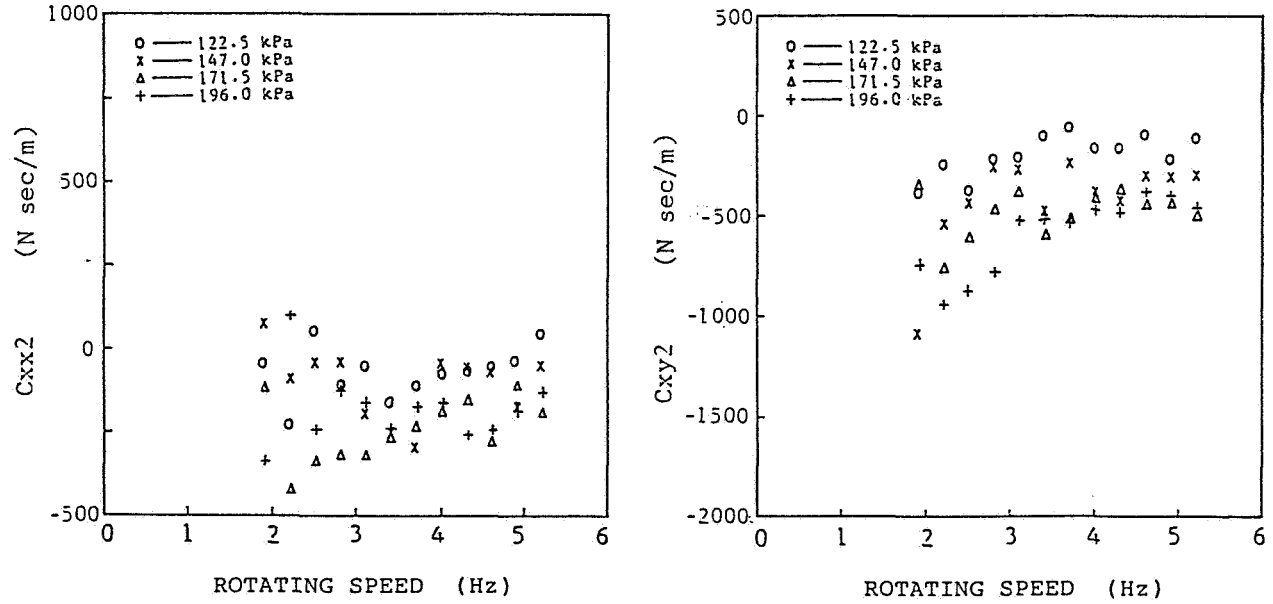

Figure 23. - Damping coefficients in the 2nd chamber

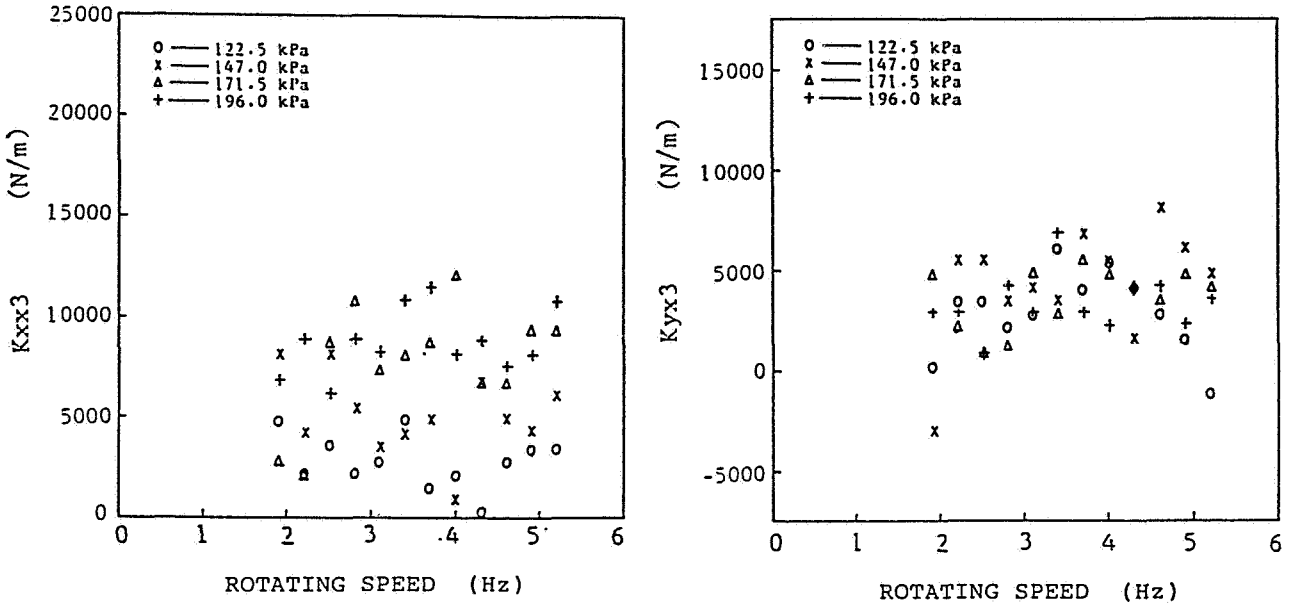

Figure 24. - Spring coefficients in the 3rd chamber

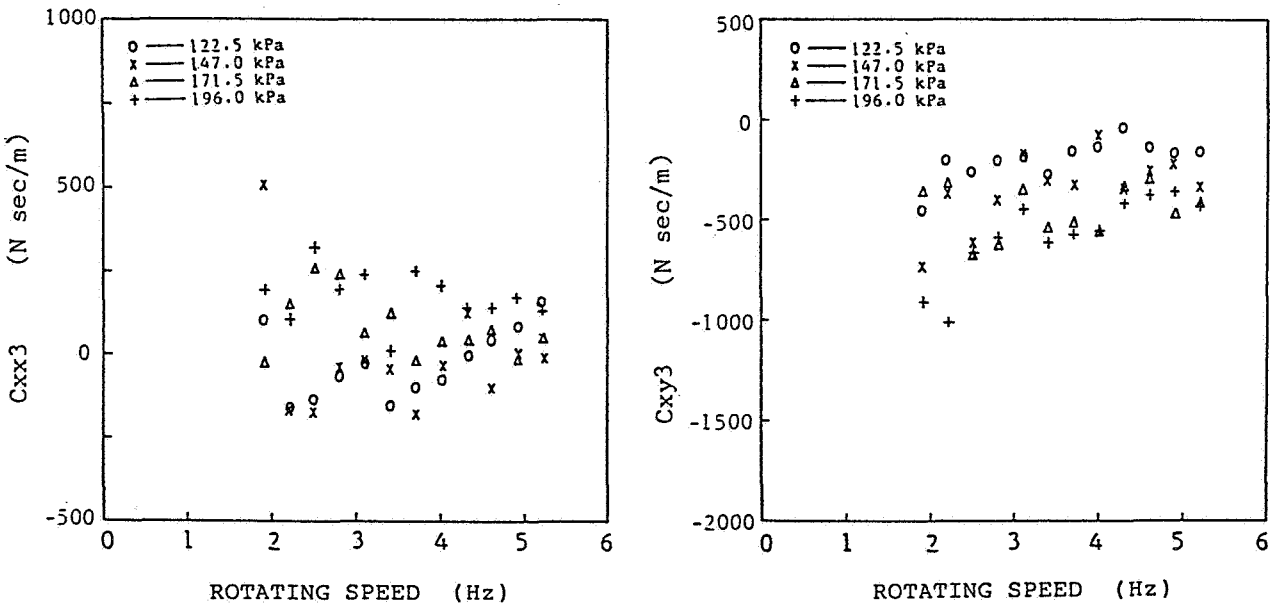

Figure 25. - Damping coefficients in the 3rd chamber

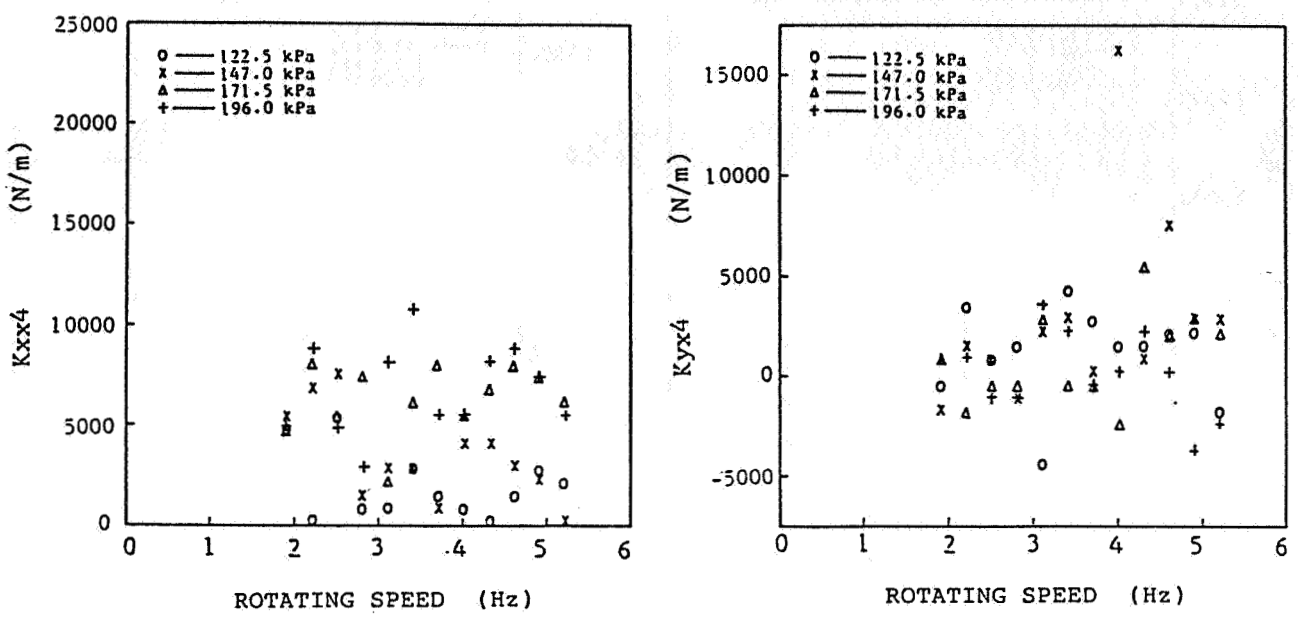

Figure 26.- Spring coefficients in the 4th chamber

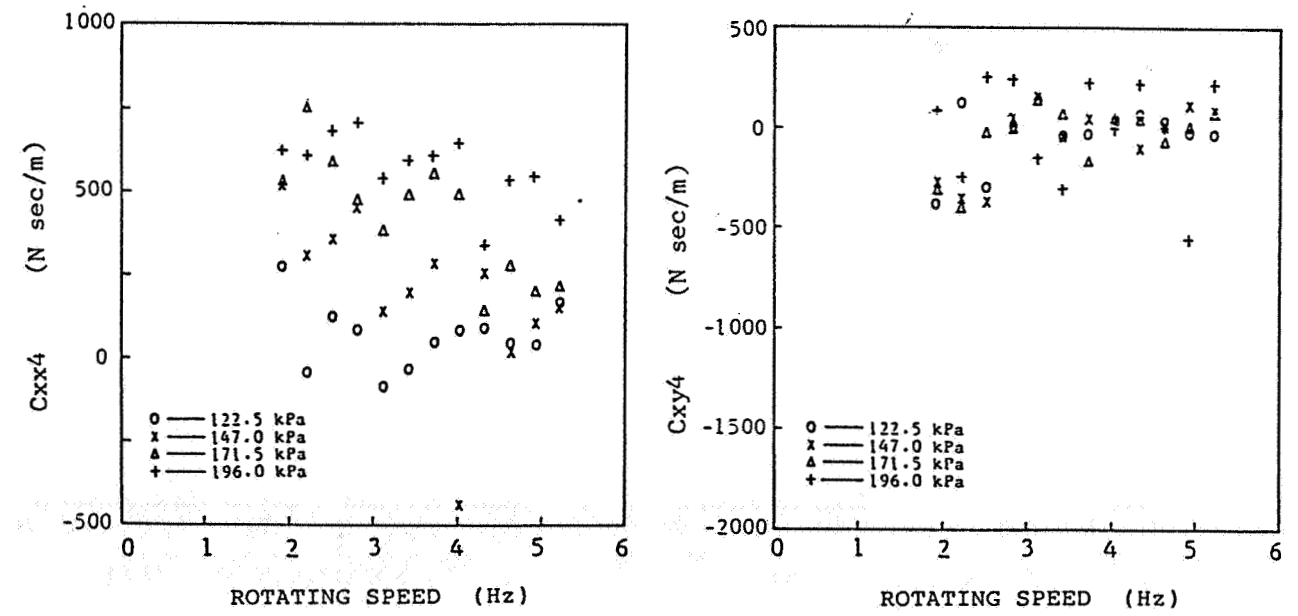

Figure 27. - Damping coefficients in the 4th chamber

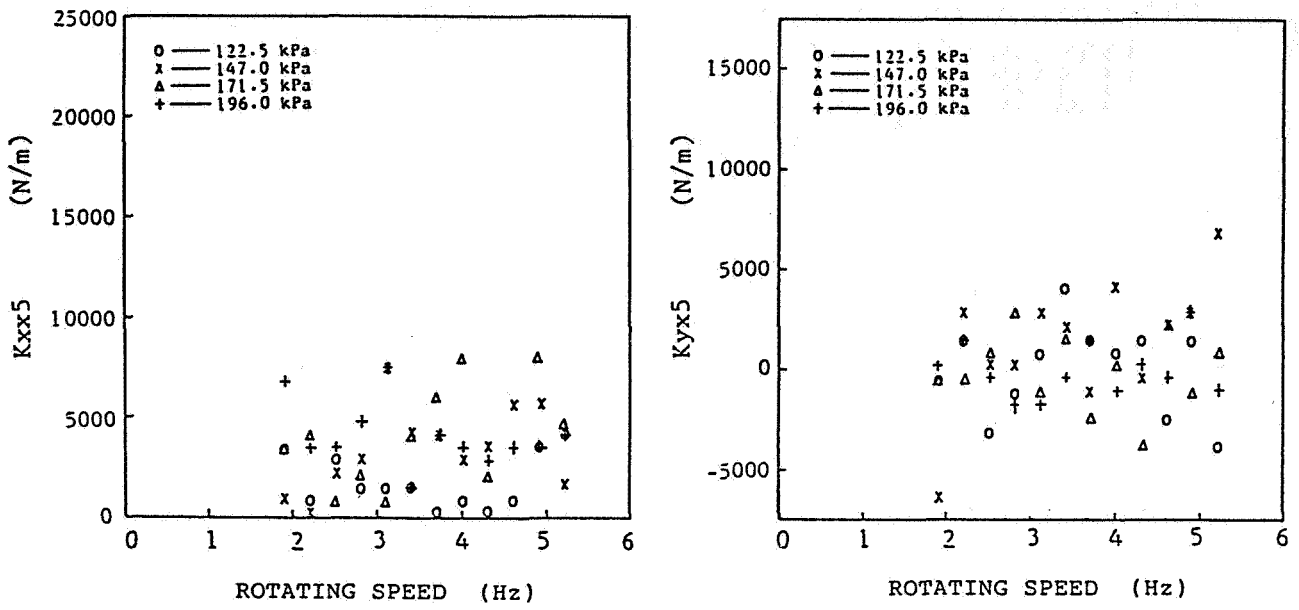

Figure 28. - Spring coefficients in the 5th chamber

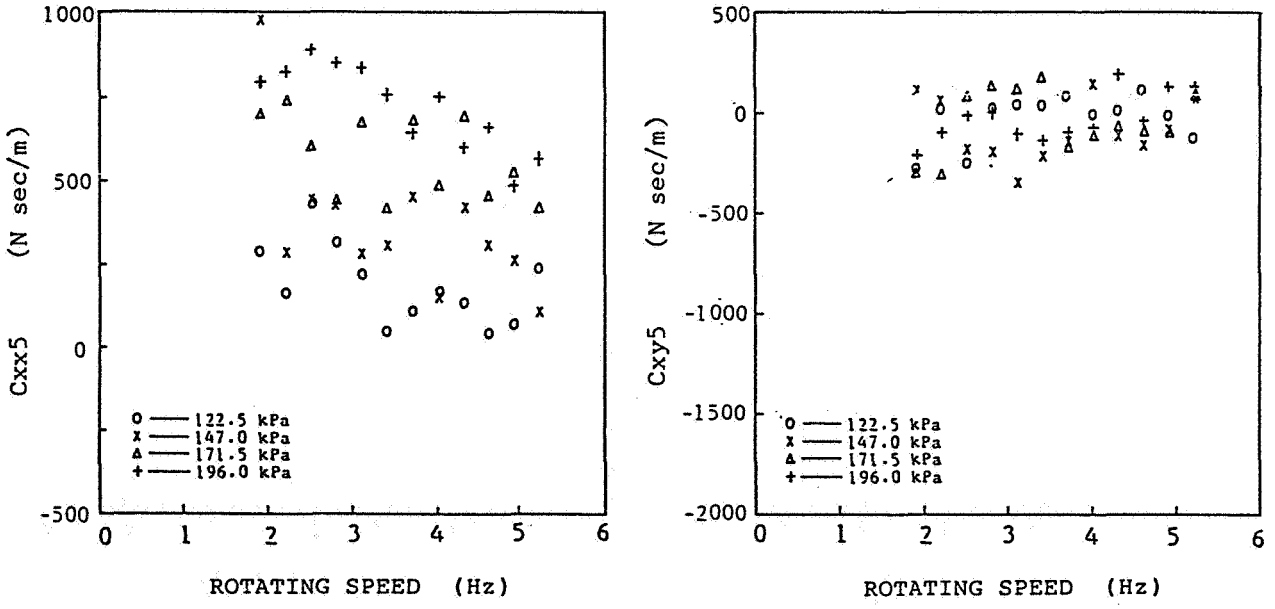

Figure 29. - Damping coefficients in the 5th chamber

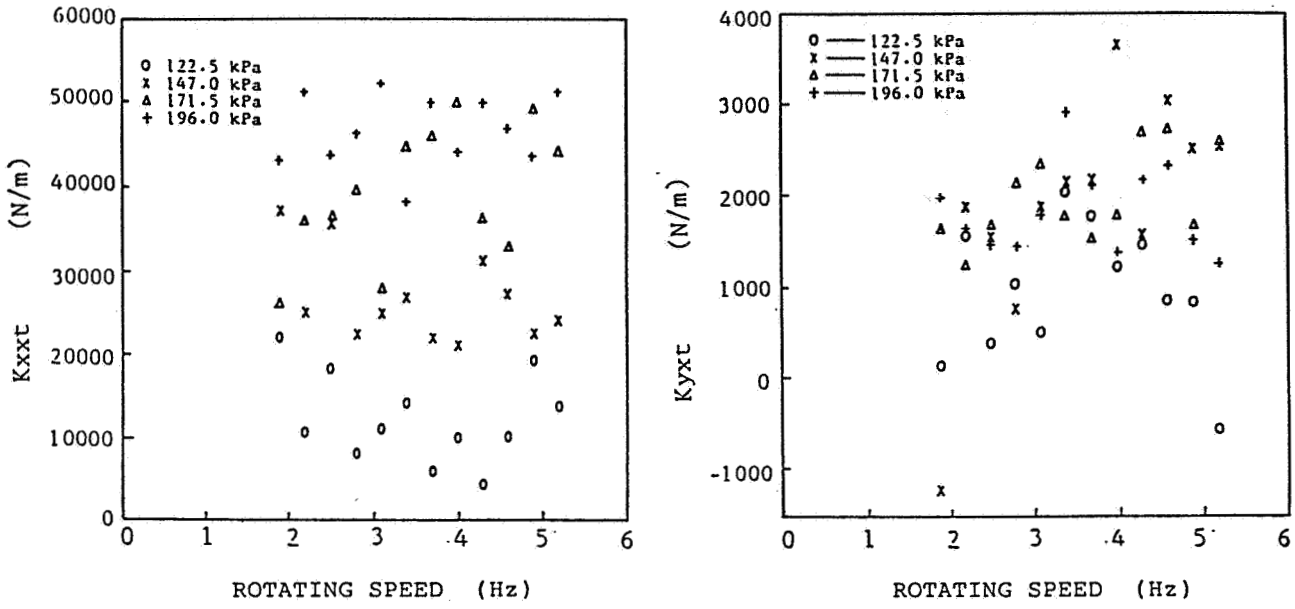

Figure 30. - Spring coefficients in the whole labyrinth seal.

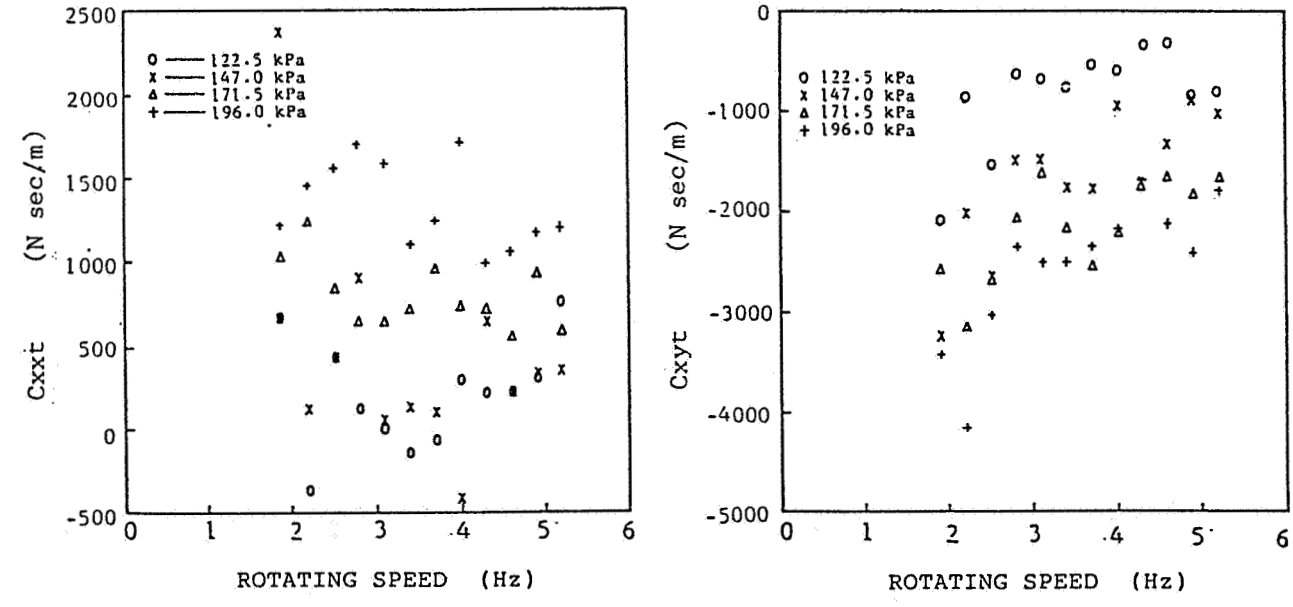

Figure 31. - Damping coefficients in the whole labyrinth seal.

PREDICTION OF FORCE COEFFICIENTS FOR LABYRINTH SEALS

Otto W. K. Lee, M. Martinez-Sanchez, and Eva Czajkowski
Massachusetts Institute of Technology
Cambridge, Massachusetts 02139

1. Introduction

Fluid-dynamic forces arising from nonuniform pressure patterns in labyrinth seal glands are known to be potentially destabilizing in high power turbomachinery. A well documented case in point is that of the space Shuttle Main Engine turbopumps (ref. 1), and other examples can be found in the literature, as for instance in the recent review of Ehrich (ref. 2) and Childs and Ehrich (ref. 3). Seal forces are also an important factor for the stability of shrouded turbines, acting in that case in conjunction with the effects of blade-tip clearance variations (refs. 4,5).

The basic mechanisms which produce the uneven pressure distribution in a labyrinth have been qualitatively or semi-qualitatively discussed in many references (refs. 6,7). In most instances, the basic agent is found to be flow swirl in the glands, either from pre-swirl (as in the case of turbine shrouds) or from frictional interaction with the rotating shaft (as in multichamber jet engine seals). Quantitative modeling of these forces has also been reported by a number of authors (refs. 8, 9,10), using lumped-parameter models for each gland. These models yield in general predictions of the direct and cross-wise stiffnesses and damping coefficients for small shaft displacements, and are useful for linear stability analyses. Non-linear predictions for fully developed unstable operation are less advanced.

Fairly extensive data also exist on the stiffness factors of seals of various geometries (refs. 4,5,11,12,13). These have been generally obtained in rotary rigs with adjustable shaft eccentricity. Much less satisfactory is the situation with respect to data on damping coefficients due to labyrinth seals, since these require dynamic measurements on either vibrating shafts, or shafts fitted with adjustable whirl mechanisms. Yet these data are almost as essential as those on stiffnesses, since the corresponding induced forces are of the same order. Ref.(13) reports damping data for non-rotating shafts.

In this paper we report on the development of a linear model for the prediction of labyrinth seal forces and on its comparison to available stiffness data. We also present a discussion of the relevance of fluid damping forces and report on the preliminary stages of a program to obtain data on these forces.

2. Model Formulation

The model is very similar in its main outline to those of Kostyuk (ref. 8) and Iwatsubo (ref. 9). It describes the flow of an ideal gas through the seal chambers, assuming largely constant temperature, but allowing for isentropic acceleration towards the narrow gaps and also for isentropic azimuthal flow redistribution in each chamber. Each chamber is assigned a pressure P_i and azimuthal velocity c_i, and these quantities are governed by equations of mass and azimuthal momentum conservation, written in integral form.

The axial flow rate q through each seal throttling is approximated by a commonly

used expression, which basically derives from Bernoulli's equation with a density halfway between those of the two adjacent chambers. Per unit length in the azimuthal direction, this gives

$$q_i = \mu_i \delta_i \sqrt{\frac{p_{i-1}^2 - p_i^2}{R_g T}} \tag{1}$$

where δ_i is the width of the narrow gap (see fig. 1) and $\mu_i = c_c \beta_i$ is the product of the usual contraction coefficient c_c times a carryover factor β_i to account for nonzero upstream axial velocity and nonzero pressure recovery in the downstream chamber. Eq. (1) is assumed to apply locally at each time t and azimuth ϕ. This semi-incompressible approximation is known to be reasonable up to gap Mach numbers of about 0.5; however, the last gap or two of a labyrinth with a high overall pressure ratio may be above that Mach number, and, in particular, the last chamber may choke. We have partially accommodated this effect by retaining Eq. (1) throughout, but replacing it by a choked-flow expression in the last chamber only if the first approximation indicates sonic or supersonic conditions there.

With reference to the geometry of fig. 1, the governing equations within each chamber are

$$\frac{\partial}{\partial t}(\rho_i f_i) + \frac{\partial}{\partial w}(\rho_i f_i c_i) + q_{i+1} - q_i = 0 \tag{2}$$

$$\frac{\partial}{\partial t}(\rho_i f_i c_i) + \frac{\partial}{\partial w}(\rho_i f_i c_i^2) + q_{i+1}\, c_i - q_i c_{i-1} + \tau_i' U' - \tau_i'' U'' + f_i \frac{\partial P_i}{\partial w} = 0 \tag{3}$$

These equations are first linearized about a condition of zero eccentricity. The zero'th order approximation provides a basic flow rate q^* and pressure and azimuthal velocity distributions P_i^*, c_i^*, (Appendix 1). The first approximation then provides linear equations for the perturbations, defined by

$$p_i = p_i^* (1 + \xi_i) \quad ; \quad q_i = q_i^* (1 + \zeta_i) \quad ; \quad c_i = c_i^* (1 + \eta_i) \tag{4}$$

where ξ_i, ζ_i, η_i are functions of t and $w = R_s \phi$. The right hand sides of these equations are determined by an assumed eccentric motion of the shaft, whose center follows an elliptic path

$$x_c = r_1 \cos \Omega t \quad ; \quad y_c = r_2 \sin \Omega t \tag{5}$$

where Ω is the shaft vibration frequency, closely identified with one of its natural frequencies.

The details of the analysis are given in references 14 and 15. For convenient solution, the perturbations (for a stationary oscillation) are expressed in the form

$$\xi = R_e \left[e^{i\Omega t} (\hat{\xi}_s \sin \phi + \hat{\xi}_c \cos \phi) \right] , \text{ etc.} \tag{6}$$

where R_e indicates the real part, and $\hat{\xi}_s$, $\hat{\xi}_c$ are in general complex numbers. After elimination of ζ_i, the following system of perturbation equations is obtained:

$$\begin{bmatrix} -F_i & 0 & 0 & 0 \\ 0 & -F_i & 0 & 0 \\ -Q_i & 0 & -S_i & 0 \\ 0 & -Q_i & 0 & -S_i \end{bmatrix} \begin{Bmatrix} \hat{\xi}_{s_{i-1}} \\ \hat{\xi}_{c_{i-1}} \\ \hat{\eta}_{s_{i-1}} \\ \hat{\eta}_{c_{i-1}} \end{Bmatrix} + \begin{bmatrix} E_i + i\Omega A_i & -B_i & 0 & -C_i \\ B_i & E_i + i\Omega A_i & C_i & 0 \\ P_i + i\Omega K_i & -M_i & R_i + i\Omega L_i & -N_i \\ M_i & P_i + i\Omega K_i & N_i & R_i + i\Omega L_i \end{bmatrix} \begin{Bmatrix} \hat{\xi}_{s_i} \\ \hat{\xi}_{c_i} \\ \hat{\eta}_{s_i} \\ \hat{\eta}_{c_i} \end{Bmatrix} +$$

$$+ \begin{bmatrix} -D_i & 0 & 0 & 0 \\ 0 & -D_i & 0 & 0 \\ -O_i & 0 & 0 & 0 \\ 0 & -O_i & 0 & 0 \end{bmatrix} \begin{Bmatrix} \hat{\xi}_{s_{i+1}} \\ \hat{\xi}_{c_{i+1}} \\ \hat{\eta}_{s_{i+1}} \\ \hat{\eta}_{c_{i+1}} \end{Bmatrix} = \begin{Bmatrix} -Z_i r_1 + \Omega J_i r_2 \\ i\Omega J_i r_1 - iZ_i r_2 \\ -Y_i r_1 + (-iW_i + \Omega X_i) r_2 \\ (W_i + i\Omega X_i) r_1 - iY_i r_2 \end{Bmatrix} \tag{7}$$

The expressions for the coefficients A_i, B_i, ... , Z_i are given in Appendix 2. For a seal with K chambers, i would range from $i = 1$ to K. The calculations reported here have assumed uniform inlet and exit conditions.

The forces are then obtained by integration of the perturbation pressures $P_i^* \xi_i(\phi)$ around the periphery of each chamber, followed by summation for all chambers. Since our attention will be restricted to the practical case of circular whirl ($r_1 = r_2 = r$), it is advantageous to project the forces in the directions towards the instantaneous minimum gap (F_d) and 90° ahead of it in the whirl direction (F_q), as shown in fig. 2. We obtain

$$F_{d_i} = -R_s \ell_i \int_0^{2\pi} P_i^* \xi_i \cos(\phi - \Omega t)\, d\phi \tag{8a}$$

$$F_{q_i} = -R_s \ell_i \int_0^{2\pi} P_i^* \xi_i \sin(\phi - \Omega t)\, d\phi \tag{8b}$$

These components can be expected to be time-invariant for a symmetric shaft in circular whirl. For this case, the form of the system of equations (7) indicates that we must have

$$\hat{\xi}_{c_i} = i\,\hat{\xi}_{s_i} \quad ; \quad \hat{\eta}_{c_i} = i\,\hat{\eta}_{s_i} \tag{9a,b}$$

and the system (7) reduces to

$$\begin{bmatrix} -F_i & 0 \\ -Q_i & -S_i \end{bmatrix} \begin{Bmatrix} \hat{\xi}_{s_{i-1}} \\ \hat{\eta}_{s_{i-1}} \end{Bmatrix} + \begin{bmatrix} E_i + i\,(-B_i + \Omega A_i) & -iC_i \\ P_i + i\,(-M_i + \Omega K_i) & R_i + i(-N_i + \Omega L_i) \end{bmatrix} \begin{Bmatrix} \hat{\xi}_{s_i} \\ \hat{\eta}_{s_i} \end{Bmatrix} +$$

$$+ \begin{bmatrix} -D_i & 0 \\ -0_i & 0 \end{bmatrix} \begin{Bmatrix} \hat{\xi}_{s_{i+1}} \\ \hat{\eta}_{s_{i+1}} \end{Bmatrix} = \begin{Bmatrix} -Z_i + \Omega J_i \\ -Y_i + \Omega X_i - iW_i \end{Bmatrix} r \qquad (10)$$

Also, the complex force vector $F_{d_i} + i\,F_{q_i}$ is found to be given simply by

$$F_{d_i} + i\,F_{q_i} = \pi\,R_s\,P_i^*\,(-i\,\hat{\xi}_{s_i})\,\ell_i \qquad (11)$$

whereas, if the forces F_x and F_y along fixed directions Ox, Oy are desired, they are given by

$$F_{x_i} + i\,F_{y_i} = (F_{d_i} + i\,F_{q_i})\,e^{i\Omega t} \qquad (12)$$

3. The stiffness and damping coefficients

Most data reported to date on seal forces refer to situations with a static offset, i.e., with $\Omega = 0$. Within a linear approximation, it is then unambiguous to define the direct and crosswise stiffness K_{xx}, K_{xy}, as $-F_d/r$ and $-F_q/r$, respectively. In practice, however, unstable whirl is observed to occur at or near (one of) the shaft natural frequencies, usually at the first one, Ω_o (and it first shows up at rotational frequencies ω of the order of twice this natural frequency). For purposes of dynamic modeling, then, it is of interest to calculate or measure the forces for $\Omega \simeq \Omega_o$, since the fluid disturbances are expected to translate into relatively small real and imaginary departures of Ω from its basic resonance value. A common expression for the disturbance forces in terms of the x_c, y_c deviations of the shaft center is

$$\begin{cases} F_x = -K_{xx}x_C + K_{xy}y_C - C_{xx}\dot{x}_C + C_{xy}\dot{y}_C \\ F_y = -K_{xy}x_C - K_{xx}y_C - C_{xy}\dot{x}_C - C_{xx}\dot{y}_C \end{cases} \qquad (13)$$

where the stiffnesses K_{ij} and damping factors C_{ij} are taken to be constant. This amounts to an approximation in which terms proportional to $\ddot{x}_c$, $\dddot{x}_c$, etc., are all neglected. It is easy to show that the corresponding approximation in terms of Ω is

one where the actual functions $F_d(\Omega)$, $F_q(\Omega)$ are replaced by their tangents at the frequency of interest:

$$\begin{cases} F_d(\Omega) \simeq F_{d_o} + F_{d_1}(\Omega - \Omega_o) \\ F_q(\Omega) \simeq F_{q_o} + F_{q_1}(\Omega - \Omega_o) \end{cases} \tag{14}$$

and then the K and C coefficients are given by

$$K_{xx} = -\frac{F_{d_o} - \Omega_o F_{d_1}}{r} \qquad C_{xx} = -\frac{F_{q_1}}{r}$$

$$K_{xy} = -\frac{F_{q_o} - \Omega_o F_{q_1}}{r} \qquad C_{xy} = +\frac{F_{d_1}}{r} \tag{15}$$

Thus, determination (either analytical or experimental) of F_d, F_q at two whirling frequencies near Ω_o is sufficient to extract the K and C coefficients in this formulation.

An alternative formulation is often found in the literature (refs. 8,9,15) and is, in fact, the basis for the results presented here. Analytically, it consists of solving the system of equations (7) for $r_2 = 0$, i.e., for a linear vibratory shaft motion, and adscribing to $-K_{xx}x_c$, $K_{xy}x_c$ those forces F_d, F_q in time phase with x_c, while attributing to $-C_{xx}\dot{x}_c$, $-C_{xy}\dot{x}_c$ those in quadrature with x_c. It can be shown that this leads to the definitions

$$K_{xx} = -\frac{F_d(\Omega) + F_d(-\Omega)}{2r} \qquad C_{xx} = -\frac{F_q(\Omega) - F_q(-\Omega)}{2\Omega r}$$

$$K_{xy} = -\frac{F_q(\Omega) + F_q(-\Omega)}{2r} \qquad C_{xy} = -\frac{F_d(\Omega) - F_d(-\Omega)}{2\Omega r} \tag{16}$$

A geometrical interpretation of the difference between equations (15) and (16) is shown in fig. 3. Experimental or analytical determination of the set (16) of coefficients requires data on F_d and F_q at both Ω and $-\Omega$.

The K's and C's given by (15) and (16) coincide only if F_d and F_q are linear functions of Ω. Since either definition may be used in the literature with little elaboration, it would be of interest to study the extent to which this leads to numerical differences; pending this, we will in this study adopt the definitions (16). An example for a single-chamber seal is shown in Appendix 3. From this limited evidence, it appears that the important coefficients K_{xy}, C_{xx} are about the same in both definitions.

4. Comparison to Literature Data

4.1 Data Used

Benckert and Wachter have published an extensive set of data (refs. 11,16) for multichamber labyrinth seals of simple "straight" or "full" types (fig. 4). The data were taken in a static-offset rig operating on pressurized air, and induced forces were obtained by integration of measured azimuthal pressure variations on a number of seal cavities. Labyrinths with up to 23 chambers were used. The experiments allowed variation of shaft speed, ω, overall pressure ratio P_{atm}/P_o, rotor eccentricity r, seal geometry (δ_i, ℓ_i, h_i, Fig. 1), number of chambers and entry swirl c_o^*. The seal flow rate q was measured and an averaged carry-over factor μ was deduced from these data and reported in a number of instances. In our calculations we used these "measured" factors when available directly; in other cases, we adopted values measured for chambers of the same geometry, or, for the "full" type of seal, where little carryover is expected we used $\mu = 1$. The contraction coefficient c_c was taken as a function of Reynolds number and strip geometry as given by Vermes (ref. 17) (fig. 5).

Data of Brown and Leong (ref. 18) were also used for validation of the undisturbed flow predictions.

4.2 Undisturbed Flow Parameters

Figure 6 compares Brown and Leong's data on the axial pressure distribution in an 11-chamber test seal with our calculated undisturbed pressure distribution. There is good agreement except for the sharp pressure drop shown by the data between the inlet and the first chamber. This is probably a reflection of a reduced carry-over factor on the first strip; the calculation used a constant μ (the value used is irrelevant to the comparison).

Benckert and Wachter reported for one particular case the axial variation of azimuthal velocities c_i^*. This was for a 23-chamber seal with $c_o^* = 40$ m/sec, $P_a/P_o = .66$, $R_s = 0.15$ m, $\omega = 1000$ rad/sec, $r_1 = 0.25$ mm, $r_2 = 0$, $\delta^* = 0.5$ mm, $\ell_i = 4$ mm and $h_i = 6$ mm. The data are shown in figure 7, together with the code predictions. The good agreement shown is important for the prediction of disturbance side forces, which depend critically on swirl velocities. These results appear to validate the formulation used for the friction factors between the fluid and the stator and rotor surfaces (turbulent pipe flow formulae with a standard correction for "pipe" curvature).

4.3 Stiffness Coefficients Without Shaft Rotation

The cross-spring coefficients $K_{yx} = -K_{xy}$ for a number of cases from Benckert and Wachter's tests with a non-rotating shaft were calculated and the results are summarized in Table 2 and figure 8. The key in Table 2 describing the test parameters is explained in Table 1.

The eccentricity r_1 used in the tests was 0.15 mm, except for Run 17, which had $r_1 = 0.25$ mm.

Table 1. Key for Table 2 (2nd column)

(Type, h, δ, ℓ)

Type	h: chamber height	δ: clearance	ℓ: pitch
S = Straight-through	0 = 2.75 mm	0 = 0.25 mm	0 = 5 mm
F = Full-interlocking	1 = 6.25 mm	2 = 0.5 mm	1 = 8 mm
	3 = 6 mm		2 = 4 mm

As figure 8 illustrates, the calculated values are somewhat lower than the data (about 19% for series (s,0,0,0), 5% only for series (s,1,0,0)). The trends of the calculation are in agreement with those observed in the tests. In particular, K_{yx} is seen in figure 9 to be approximately proportional to inlet swirl and to overall pressure ratio, both in the tests and in the calculations (although, as mentioned, with a somewhat lower proportionality factor in the latter case).

4.4 Stiffness Coefficients with Shaft Rotation

Results similar to those in the previous section, but including various shaft speeds are given in Table 3 and figure 10. The eccentricity is still static (no whirl, $\Omega = 0$), and is 0.25 mm in all cases. The parameter E_o^* was used in Ref. 11 to correlate entry swirl, and is

$$E_o^* = \frac{\frac{1}{2}\rho_o \, (c_o^*)^2}{p_o + \frac{1}{2}\rho_o \, V_{ax,o}^2 - p_a} \; ; \; V_{ax,o} = \frac{q^*}{\rho_o \delta_1^*} \qquad (17)$$

The comparison of data and theory shown in figure 10 indicates more scatter, but less systematic deviation than in the cases without shaft rotation (figures 8 and 9). The agreement is best for all the cases with 17 chambers (solid symbols in figure 10), which show an average error of 8.5% and little scatter.

4.5 Discussion

The two principal sources of uncertainty in our calculations are the friction factors (λ', λ'') and the carry-over coefficient β. The friction factor could in principle be substantially increased by the relative rotation of shaft and casing, since the fluid in each chamber is strongly sheared and develops marked secondary flow patterns, leading to enhanced mixing. Examination of data[19] for the somewhat related case of turbulent pipe flow with swirl does indeed show friction increases of up to a factor of four at high swirl. An accurate prediction of wall friction under the complex flow conditions of a labyrinth gland is not possible at this time, and this is an area requiring more experimental and analytical work.

The impact of friction factor inaccuracies on calculated cross-spring coefficients could be important, although not easily generalizable. In general, the cross-forces increase with the deviation between the swirl velocity and its frictional equilibrium value. An increase in wall friction in a non-rotating seal will accelerate the approach to this ultimate swirl, thus reducing the number of chambers where the excess or defect swirl is strong and thereby reducing the magnitude of K_{yx}

(whether positive or negative). This trend is always apparent at large enough friction coefficients, and especially for long multichamber seals. However, for short seals and weak frictional coupling a different effect dominates, namely the cross-stiffness tends to a limiting value independent of shaft rotation and in the direction of the inlet swirl. An example of this behavior for a one-chamber seal is presented in Appendix 3, figure A2, where it can be seen that for this particular case, increasing friction would lead to increases in $|K_{yx}|$. The behavior typical of long seals and large friction is illustrated in figure 11, corresponding to case 1 of Table 2; here, an increase of the friction factor above the nominal value leads to a reduced K_{yx}, although a reduction by more than about 0.6 would lead to the same effect.

The carry-over coefficient β is clearly another source of uncertainty in the model. The sensitivity of calculated cross-stiffness to β (or $\mu = \beta c_c$) is illustrated in figure 12, corresponding to parametric variations on Run 11 of Table 2, and figure 13 (from Run 7 of Table 3). The opposite trend in these two cases is due to the fact that in figure 12 the entry swirl is greater than its asymptotic value (reached after an infinite number of chambers), while the opposite is true in figure 13. In both cases, an increase of μ increases the flow rate q, which has the effect of delaying the transition towards the asymptotic c^* ; in figure 12 this means higher c_i^* in the first 10-12 chambers, with correspondingly larger cross-forces; in figure 13, the same delaying effect at higher μ implies lower c_i^* values in the first 6-8 chambers, and, consequently, lower cross-forces.

Unfortunately, the state of the art in *a priori* predictions of β is not satisfactory. A fuller discussion of this point is given in reference 15. Basically, the best-known models (Vermes (ref. 17), Egli (ref. 20), Komotori (ref. 21)), indicate substantially different variations of the carry-over factor with number of chambers, with Vermes' model taking no account of this number at all. The best hope here lies with the numerical methods which are now beginning to be applied to internal flow problems in seals, although the somewhat primitive state of affairs with respect to calculations of fully separated turbulent flows still indicates a need for improvements. Thus Wadia and Booth (ref. 22) analyzed seal flows with no rotation and observed discrepancies of up to 13% in calculated flow coefficients when compared to data. For dynamics studies in seals, these 2-D or 3-D methods may, in any case, be too laborious; their proper role should probably be in furnishing improved semi-empirical results for integration into a simple multi-chamber lumped-parameter model, of the type considered here.

5. Parametric Studies

Reference 15 includes a variety of calculations that illustrate the trends of the force coefficients versus variations of seal parameters. Only some of the salient results will be mentioned here.

(a) K_{yx} increases linearly (but not proportionally) with entry swirl velocity. For conditions where the entry swirl exceeds the asymptotic azimuthal velocity, K_{yx} is generally positive, leading to excitation of forward whirl (with respect to the swirl direction). The reverse may be true at lower entry swirls. There is in some cases a value of entry swirl at which K_{yx} is zero.

(b) For multichamber seals with low entry swirl, the first few chambers contribute negative K_{yx} values, while those towards the end of the seal contribute positive values. Thus as the seal is made longer, the sign of K_{yx} may at some point

reverse. For seals where the entry swirl exceeds the ultimate azimuthal velocity, no such reversal occurs.

(c) The damping coefficient C_{xx}, which, together with K_{yx} controls the side force F_q, is positive in all cases studied, leading to stabilizing forces of the same order as those due to K_{yx}. This point will be more fully discussed in what follows.

6. Considerations on Fluid Damping

An example of calculated damping coefficients is shown in figure 14 (corresponding to the seal configuration of Run 1 in Table 3). A whirl (critical) frequency of 739 rad/sec was assumed; at the commonly found ratio $\omega/\Omega = 2$ for instability onset, C_{xx} = 220 N sec/m , giving $\Omega C_{xx} = 1.626 \times 10^5$ N/m. This is several times larger than K_{yx}, and indicates that seal C_{xx} damping forces are in this case sufficient to ensure stability. Another example of this behavior is shown by the single-cavity seal of Appendix 3; here + ΩC_{xx} is roughly comparable to K_{yx} (but smaller).

A very simplified dynamic model will help to put in perspective the roles of the different coefficients in stability analysis. Assuming a shaft with mass M and structural stiffness K_o, the equations of motion for small side displacements x,y can be combined into

$$M \ddot{z} + \hat{C} \dot{z} + \hat{K} z = 0 \qquad (18)$$

where $\hat{C} = C_{xx} + i\, C_{xy}$, $\hat{K} = K_o + K_{xx} + i\, K_{xy}$ and $z = x + iy$.

Assuming K_{xx}, K_{xy}, $C_{xx}^2/4M$ and $C_{xy}^2/4M$ are all small compared to K_o, as is likely to be the case in practice, we can define the (small) nondimensional parameters

$$k_{ij} = \frac{K_{ij}}{K_o} \quad ; \quad \zeta_{kj} = \frac{C_{ij}}{2\sqrt{K_o M}} \qquad (19)$$

Then a simple analysis shows that, to the first approximation, the shaft complex displacement $\bar{z}$ will vary as $e^{\Omega_s t}$, where

$$\frac{\Omega_s}{\sqrt{K_o/M}} \simeq \left(- \zeta_{xx} \pm \frac{1}{2} k_{xy} \right) + i \left(\pm 1 \pm \frac{1}{2} k_{xx} - \zeta_{xy} \right). \qquad (20)$$

Thus any nonzero k_{xy} will be destabilizing (in one or the other whirl direction), while a negative ζ_{xx} will be always destabilizing; k_{xx} and ζ_{xy} will simply modify the shaft natural frequency. Also, the effects of equal values of $|K_{xy}|$ and $- \Omega\, C_{xx}$ are seen to be equivalent.

This discussion has served to indicate that knowledge of the damping factor C_{xx} is at least as essential to studies of fluid-induced destabilizing forces as is the side force factor K_{xy}. Yet, due to the more difficult experimental conditions, much fewer data are available on C_{xx} than on K_{xy}.

We are now in the design stage of a test rig intended to address this problem. The general size and flow parameters will be similar to those used by Benckert and Wachter, but the sealed shaft will be made to execute forced whirling motion at speeds controlled separately from the spinning motion. Pressure distributions will be dynamically measured and integrated to produce values of the direct and transverse forces F_d , F_q for a range of whirl speeds Ω. Both K and C coefficients can then be extracted by the methods described in this paper. These features are similar to those of a rig described in reference 23 for tests in water.

7. Conclusions

A linear analytical model for the prediction of fluid forces in labyrinth seals has been presented and discussed. Comparison to literature test data shows reasonable agreement for the important cross-stiffness K_{yx}. The importance of the damping factor C_{xx} has been highlighted and the need for $_{yx}$ damping data made clear.

References

1. Ek, M.C., "Solution of Subsynchronous Whirl Problem in the High Pressure Hydrogen Turbomachinery of the Space Shuttle Main Engine." SAE 14th Joint Propulsion Conference, 78-1002, July 25-27, 1978.

2. Ehrich, F.F., "Identification and Avoidance of Instabilities and Self-Excited Vibrations in Rotating Machinery," ASME Paper 72-DE-21, Oct. 1979.

3. Ehrich, F.F. and Childs, D., to appear in the ASME Journal.

4. Wohlrab, R., "Experimental Determination of Gap Flow-Conditioned Forces at Turbine Stages and Their Effect on the Running Stability of Simple Rotors." NASA TM-77293, Oct. 1983 (Translated from Doctoral Thesis at the Muenchen Tech. Univ., 1975).

5. Urlichs, K., "Clearance Flow-Generated Transverse Forces at the Rotors of Turbomachines." NASA TM-77292, Oct. 1983. (Translated from Doctoral Thesis at the Muenchen Tech. Univ., 1975).

6. Pollman, E., Schwerdtfeger, H., Termuehlen, H., "Flow Excited Vibrations in High-Pressure Turbines (Steam Whirl)."

7. Alford, J.S., "Protecting Turbomachinery from Self-Excited Rotor Whirl." Journal of Engineering for Power, October 1965.

8. Kostyuk, A.G., "A Theoretical Analysis of the Aerodynamic Forces in the Labyrinth Glands of Turbomachines." Teploenergetica, 1972, 19 (11), pp 29-33.

9. Iwatsubo, T., "Evaluation of Instability Forces of Labyrinth Seals in Turbines or Compressors." NASA CP 2133, May 1980.

10. Childs, D.W., "Dynamic Analysis of Turbulent Annular Seals Based on Hirs' Lubrication Equation." ASME Tr., Journal of Lubrication Technology, Vol. 105, pp 429-436. Also, "Finite Length Solutions for Rotordynamic Coefficients of Turbulent Annular Seals." Ibid., pp 437-445.

11. Benckert, H. and Wachter, J., "Flow-Induced Spring Coefficients of Labyrinth Seals for Application in Rotor Dynamics." NASA CP 2133, May 1980.

12. Wright, D.V., "Air Model Tests of Labyrinth Seal Forces on a Whirling Rotor." Journal of Engineering for Power, Trans. ASME, Vol. 100, p 533, 1978.

13. Childs, D.W. and Dessman, J.B., "Testing of Turbulent Seals for Rotordynamic Coefficients." NASA CF 2250, pp 157-171, May 1982.

14. Celorio-Villaseñor, A., "Analysis of Disturbing Aerodynamic Forces in Labyrinth Seals." MS Thesis, Dept. of Aeronautics and Astronautics, MIT, September 1982.

15. Lee. O.W.K., "Prediction of Aerodynamic Force Coefficients in Labyrinth Seals." MS Thesis, Dept. of Aeronautics and Astronautics, MIT, February 1984.

16. Benckert, H., "Stromungsbedingte Fedeskennwerte in Labyrinthdichtungen." Doctoral Thesis, Univ. of Stuttgart, October 1980.

17. Vermes, G., "A Fluid-Mechanics Approach to the Labyrinth Seal Leakage Problem," Journal of Basic Engineering, Tr. ASME, Series D, Vol. 82, No. 2, June 1960, pp 265-275.

18. Leong, Y.M.M.S. and Brown, R.D., "Circumferential Press Use Distribution in a Model Labyrinth Seal, NASA CP 2250, May 1982.

19. Nissan, A.H. and Bresan, V.P., "Swirling Flow in Cylinders," A.I. Ch. E. Journal, Vol. 7, No. 4, Dec. 1961, pp 543-547.

20. Egli, A., "The Leakage of Steam Through Labyrinth Seals," Trans. ASME, Vol. 57, 1935, pp 115-122.

21. Komotori, K., "A Consideration on the Labyrinth Packing of Straight-Through Type Seals," Nihon Kikai Gakkai, Trans. J.S.M.E., Vol. 23, No. 133, 1957, pp 617-623.

22. Wadia, A.R. and Booth, T.C., "Rotor Tip Leakage: Part II - Design Optimization Through Viscous Analysis and Experiment." ASME Paper 81-GT-72.

23. Adams, M.L., Mackay, E., and Diaz-Tous, I.A., "Measurement of Interstage Fluid-Annulus Dynamical Properties." NASA CP 2250, pp 147-156, May 1982.

Appendix 1. The Unperturbed Solution

Squaring Eq. (1) and adding for all chambers yields for the nominal flow rate

$$q^* = \left[\frac{P_o^2 - p_a^2}{R_g T \sum_{i=1}^{K} \left(\frac{1}{\mu_i^2 \delta_i^{*2}} \right)} \right]^{1/2} \qquad \text{(A-1)}$$

Also, adding for the first n chambers only gives

$$P_n^{*2} = P_o^{*2} - \frac{\sum_{i=1}^{n} \left(\frac{1}{\mu_i^2\ \delta_i^{*2}}\right)}{\sum_{i=1}^{K} \left(\frac{1}{\mu_i^2\ \delta_i^{*2}}\right)} (P_o^2 - P_a^2) \qquad \text{(A-2)}$$

The momentum equation (Eq. (3)) becomes in the steady state

$$q^*(c_i^* - c_{i-1}^*) + \tau_i' U' - \tau_i'' U'' = 0 \qquad \text{(A-3)}$$

with

$$\tau_i' = \frac{1}{8} \rho_i^* \lambda' c_i^{*2} \qquad \text{(A-4)}$$

$$\tau'' = \frac{1}{8} \rho_i^* \lambda'' (\omega R_s - c_i^*)^2 \qquad \text{(A-5)}$$

and λ (the Darcy friction factor) given by a modified pipe-flow expression

$$\lambda = \frac{0.3164}{R_e^{0.25}} \left[1 + 0.075\ R_e^{0.25} \left(\frac{D_h}{2R_s}\right)^{1/2}\right] \times \text{sign}\ (v_{REL}) \qquad \text{(A-6)}$$

Here R_e is the Reynolds number based on chamber height and the corresponding relative flow velocity for fixed or rotating surfaces. The factor sign (v_{REL}) is needed to give the forces τ_i', τ_i'' their proper direction. Thus, we append the factor sign (c_i^*) to λ' and the factor sign $(\omega R_s - c_i^*)$ to λ'', both here and in the first order calculations of Appendix 2. D_h is the gland hydraulic diameter. Eqs. (A-3) through (A-6) can be solved for the distribution c_i^* of azimuthal velocities. In particular, the asymptotic velocity (c_∞^*) follows from (A-3) when $c_i^* = c_{i-1}^*$ is assumed.

Appendix 2. Coefficients for the Perturbation Equations

Let the transverse area of a gland (fig. 1) be $f_i^* = (h_i + \delta_i^*)\ell_i^*$ in the centered position. An asterisk on any variable denotes the undisturbed (centered) condition. We obtain for Eq. (7) the following coefficients.

$$A_i = \frac{f_i^*}{\gamma} \qquad B_i = \frac{c_i^* f_i^*}{R_s \gamma} \qquad C_i = \frac{c_i^* f_i^*}{R_s}$$

$$D_i = \frac{P_{i+1}^* \mu_i^2 \delta_{i+1}^{*2}}{P_i^* q^*} \qquad E_i = P_i^* \frac{\delta_{i+1}^{*2} \mu_{i+1}^2 + \delta_i^{*2} \mu_i^2}{q^*}$$

$$F_i = \frac{P^{*2}_{i-1}\ \mu^{*2}_i\ \delta^{*2}_i}{P^*_i\ q^*} \qquad J_i = \ell_i \qquad Z_i = \frac{c^*_i\ \ell_i}{R_s}$$

$$K_i = \frac{f^*_i}{\gamma} \qquad L_i = f^*_i \qquad M_i = \frac{f^*_i}{R_s}\left(\frac{c^*_i}{\gamma} + \frac{R_g T}{c^{*2}_i}\right)$$

$$N_i = \frac{2c^*_i\ f_i}{R_s} \qquad O_i = \frac{P^{*2}_{i+1}\ \mu^2_{i+1}\ \delta^{*2}_{i+1}}{P^*_i\ q^*}$$

$$P_i = \frac{P^*_i\ \mu^2_{i+1}\ \delta^{*2}_{i+1}}{q^*} + \frac{P^*_i\ c^*_{i-1}\ \mu^2_i\ \delta^{*2}_i}{c^*_i\ q^*} + \frac{U'\ \lambda'\ c^*_i}{8\ \gamma} - \frac{U''\ \lambda''}{8c^*_i\gamma}(\omega R_s - c^*_i)^2$$

$$Q_i = \frac{P^{*2}_{i-1}\ c^*_{i-1}\ \mu^2_i\ \delta^{*2}_i}{P^*_i\ c^*_i\ q^*} \qquad R_i = \frac{q^*}{\rho^*_i} + \frac{\lambda'U'}{4}\ c^*_i + \frac{\lambda''\ U''}{4}(\omega R_s - c^*_i)$$

$$S_i = \frac{c^*_{i-1}}{c^*_i}\ \frac{q^*}{\rho^*_i} \qquad W_i = \frac{q^*}{\rho^*_i}\left(\frac{1}{\delta^*_{i+1}} - \frac{c^*_{i-1}}{c^*_i}\ \frac{1}{\delta^*_i}\right.$$

$$X_i = \ell_i \qquad Y_i = \frac{c^*_i\ \ell_i}{R_s}$$

Here γ is the ratio of specific heats and R_g the gas constant.

Appendix 3. "Local" vs. "Global" Coefficients

Sample calculations were made for a single-chamber straight-through seal with δ = 0.25 mm., ℓ = 8 mm., h = 3 mm., R_s = 15 cm., ω = 1000 rad/sec, c_o = 100 m/sec, P_o = 1.5 atm, P_a = 1 atm . For a range of whirl frequencies from $\Omega \cong 0$ to Ω = 750 rad/sec, the resulting direct and quadrature forces are shown in figure A1. The quadrature force F_q, which is the one of importance for stability considerations, is seen to be very nearly linear with Ω, indicating no difference between the local and the global definitions of the coefficients (Eqs. (15) and (16), respectively).

There is, on the other hand, a slight curvature in the F_d line. The values calculated for Ω = 500 rad/sec are as follows:

	K_{xx}(N/m)	K_{yx}(N/m)	C_{xx}(N sec/m)	C_{yx}(N sec/m)
Local (Eqs. (15))	610	11350	+ 13.7	- 0.95
Global (Eqs. (16))	652	11480	13.98	- 1.02

For the same seal, with Ω = 0 throughout, figure A2 shows the effect of parametric variations of the friction coefficients (λ' and λ'' varied simultaneously) at various shaft rotation speeds.

Table 2. K_{yx} Calculated vs. Experimental (ω_{rot} = 0)

Run #	Seal Type	K	P_a/P_o	C_{*o} (m/s)	μ	K_{yx} Exper. (x 10^5 N/m)	K_{yx} Calcula. (x 10^5 N/m)
1	S,0,0,0	17	.66	38.4	.92	.75	.611
2	S,0,0,0	17	.32	52.9	.92	2.57	2.091
3	S,1,0,0	17	.32	68.3	1.02	1.57	1.45
4	S,1,0,0	17	.66	33.4	1.02	.27	0.274
5	S,1,0,0	17	.66	48.5	1.02	.423	0.411
6	S,1,0,0	17	.56	39.0	1.02	.457	0.410
7	S,1,0,0	17	.79	38.2	1.02	.218	0.224
8	S,0,0,0	17	.49	63.5	.92	1.89	1.586
9	S,0,0,0	17	.39	54.3	.92	2.22	1.747
10	S,0,0,0	17	.79	15.6	.92	.184	0.160
11	S,0,0,0	17	.49	64.2	.92	1.75	1.605
12	S,0,0,0	17	.49	34.5	.92	1.05	0.807
13	S,1,0,0	17	.49	82.68	1.02	.98	1.098
14	S,1,0,0	17	.49	40.78	1.02	.57	0.509
15	S,0,0,0	17	.32	38.2	.92	1.9	1.431
16	S,0,0,0	17	.32	27.6	.92	1.2	0.937
17	F,3,2,1	9	.49	144.7	.665	1.47	1.606
18	S,0,0,0	17	.32	45.5	.92	2.39	1.757

Average error (in absolute value) = 18.3%

(4.5% for (S,1,0,0) , 18.6% for (S,0,0,0)).

Table 3. K_{yx} Calculated vs. Experimental ($\omega_{rot} \neq 0$)

Run #	Seal Type	K	P_a/P_o	C_{*o} (m/s)	ω_{rot} (rad/s)	μ	K_{yx} Exper. (x 10^5 N/m)	K_{yx} Calcula. (x 10^5 N/m)
1	F,3,2,2	17	.66	43.2	1000	.66	.189	0.177
2	F,3,2,2	23	.66	47.1	1000	.66	.44	0.349
3	F,3,2,2	23	.66	40.	1000	.66	.38	0.315
4	F,3,2,2	23	.79	---	993.3	.66	.307	---
5	F,3,2,2	23	.793	66.2	993.3	.66	.323	0.398
6	F,3,2,2	23	.793	49.8	746.67	.66	.189	0.228
7	F,3,2,2	17	.793	50.7	993.3	.66	.248	0.230
8	F,3,2,2	23	.657	86.74	993.3	.553[1]	.442	0.398
9	F,3,2,2	23	.657	83.64	746.67	.606[1]	.290	0.340
10	F,3,2,2	17	.66	27.9	1000	.66	.112	0.088
11[2]	F,3,2,2	17	.66	43.2	1000	.66	.20	0.187
12[2]	F,3,2,2	17	.66	27.9	746.67	.66	.12	0.0849
13[2]	F,3,2,2	17	.66	15.5	500.	.66	.044	0.0178
14[3]	F,3,2,2	23	.66	47.1	1000	.66	.40	0.328
15[3]	F,3,2,2	23	.66	30.	746.67	.66	.23	0.170
16[3]	F,3,2,2	23	.66	54.7	500	.66	.09	0.123

1 -- μ calculated from measured mass flow rate: friction factor for a channel used.
2 -- resultant forces from chambers 7 - 17 only.
3 -- resultant forces from chambers 7 - 23 only.

Average error (in absolute value) = 23.0%

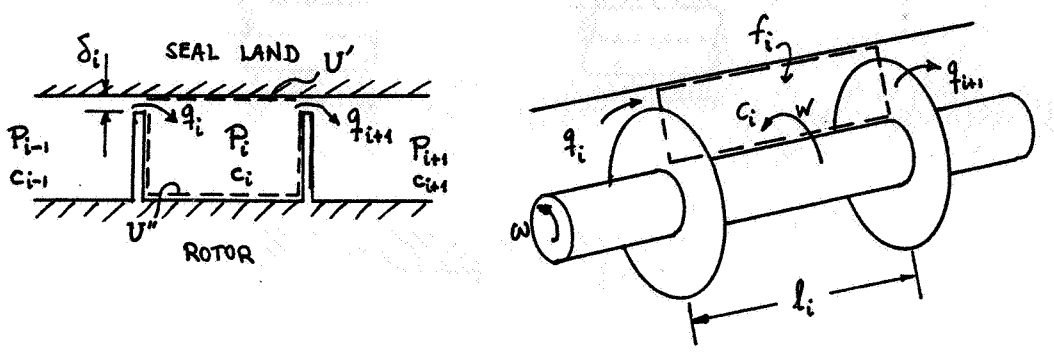

Figure 1. - Geometry for labyrinth seal analysis.

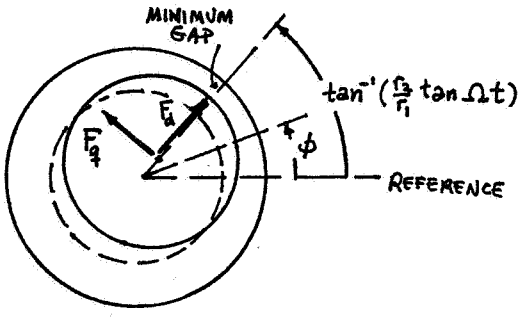

Figure 2. - Direct (F_p) and quadrature (F_q) forces due to rotor eccentricity.

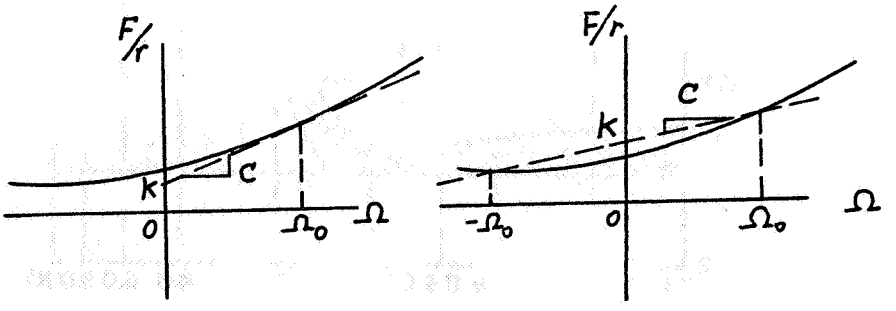

(a) Local (eqs. (15)). (b) Global (eqs. (16)).

Figure 3. - Two definitions of spring and damping coefficients.

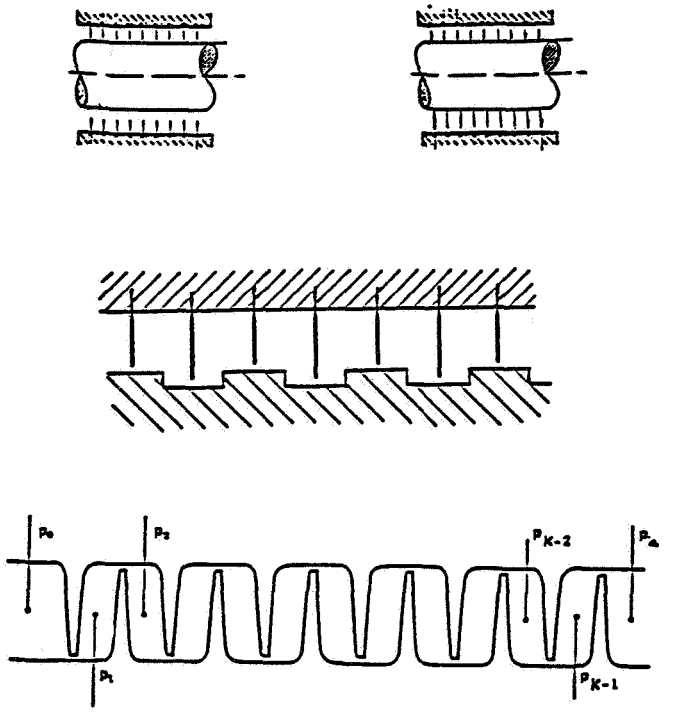

Figure 4. - Straight-through stepped and full labyrinth seals.

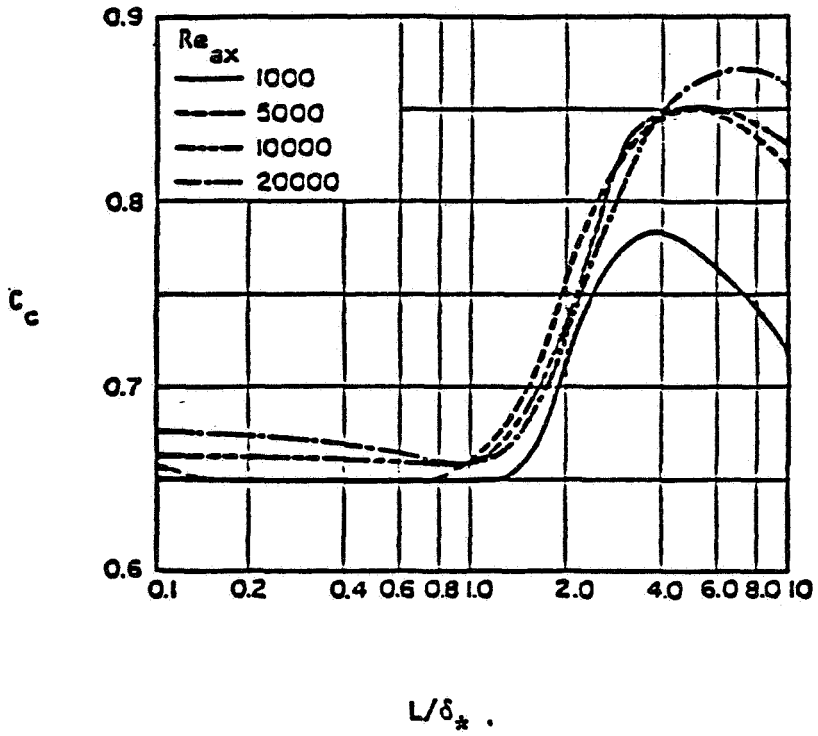

Figure 5. - Coefficient of contraction C_c.

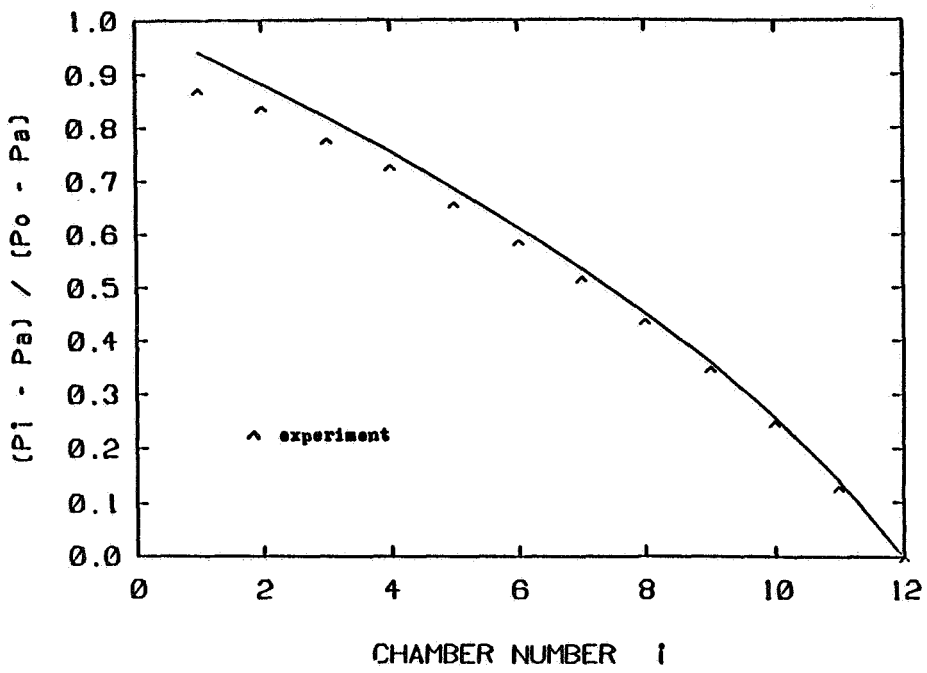

Figure 6. - Calculated versus experimental axial pressure distribution.

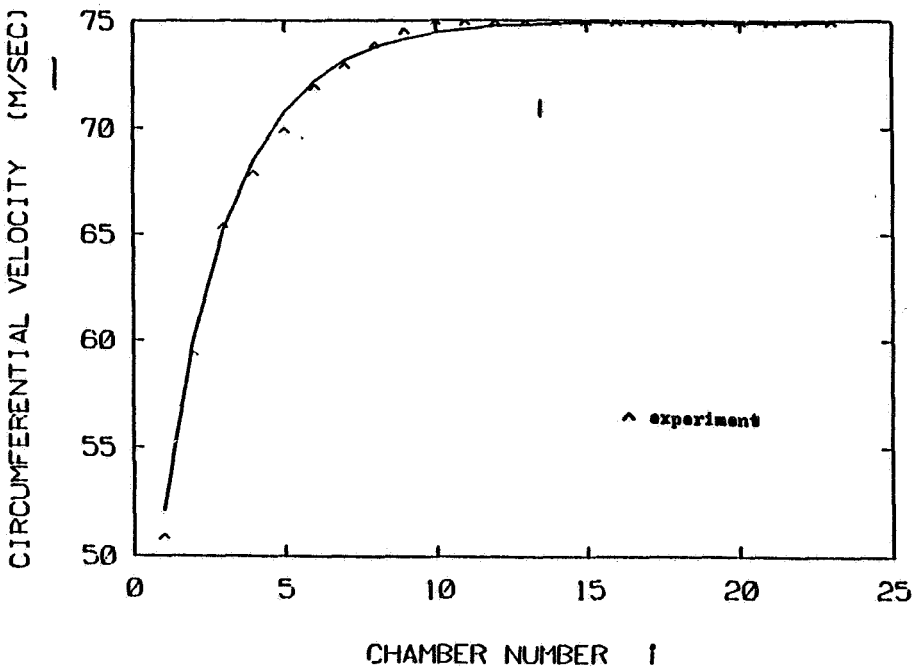

Figure 7. - Calculated versus experimental circumferential velocity distribution.

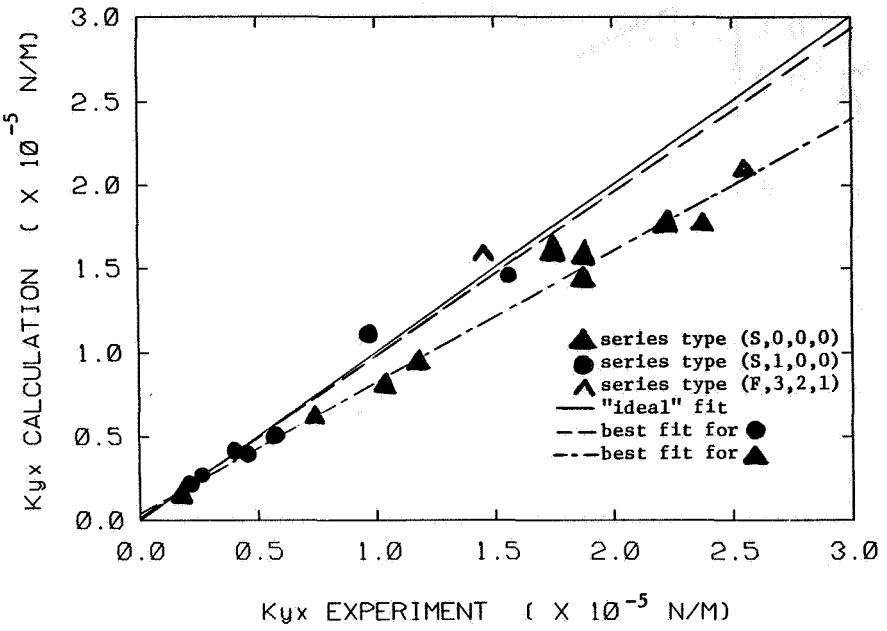

Figure 8. - Calculated versus experimental cross spring coefficient Kyx ($\omega_{rot} = 0$).

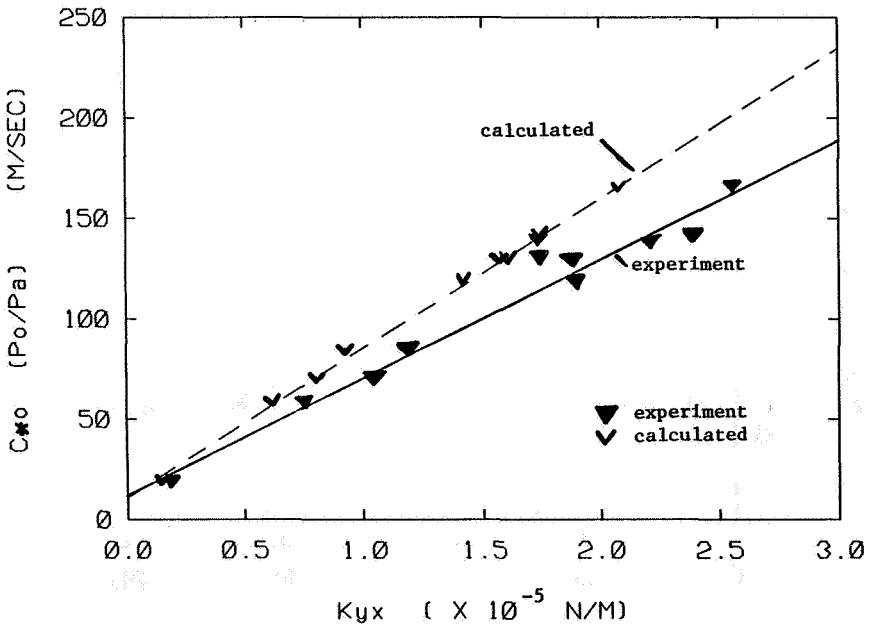

Figure 9. - Entry swirl parameter and calculated and experimental cross spring coefficient Kyx.

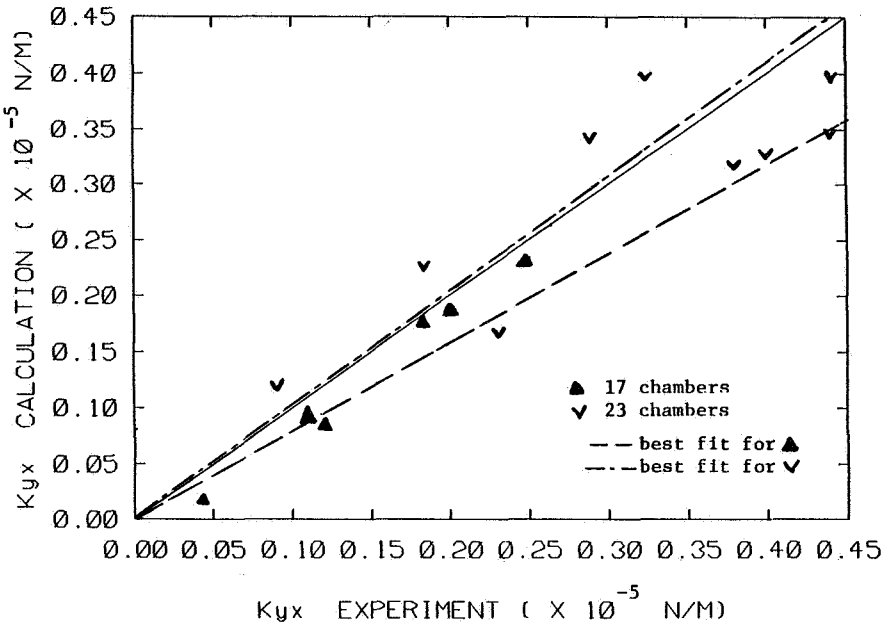

Figure 10. - Calculated versus experimental cross spring coefficient Kyx (ω_{rot} = 0).

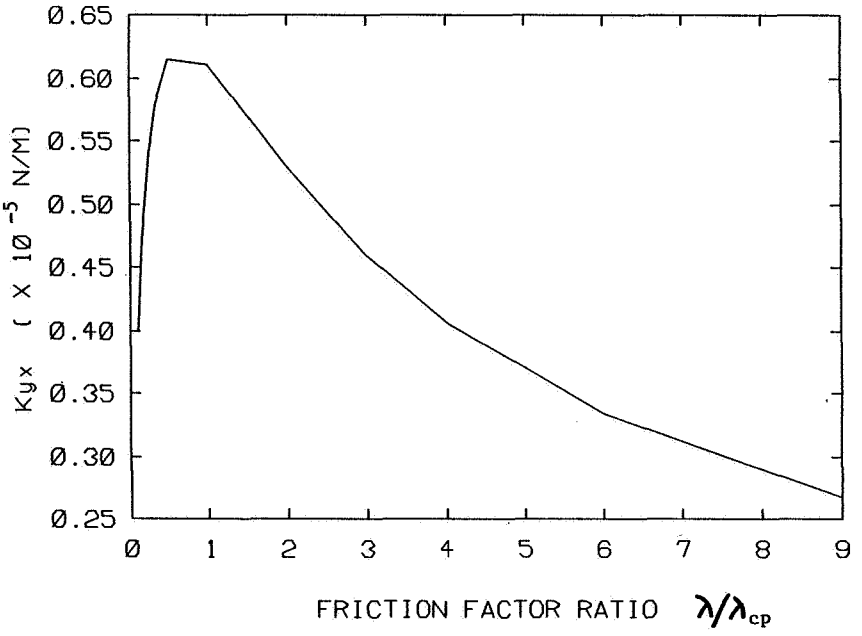

Figure 11. - Effect of friction factor on cross spring coefficient Kyx.

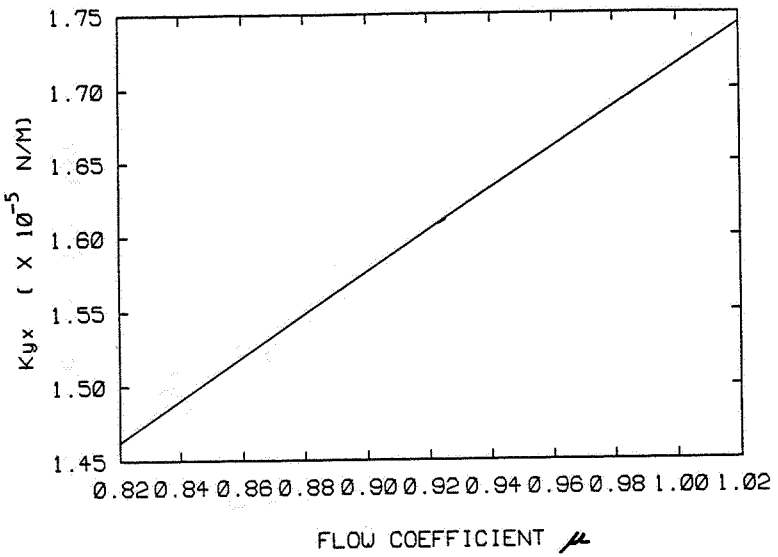

Figure 12. - Variation of cross spring coefficient with flow coefficient ($\omega_{rot} = 0$).

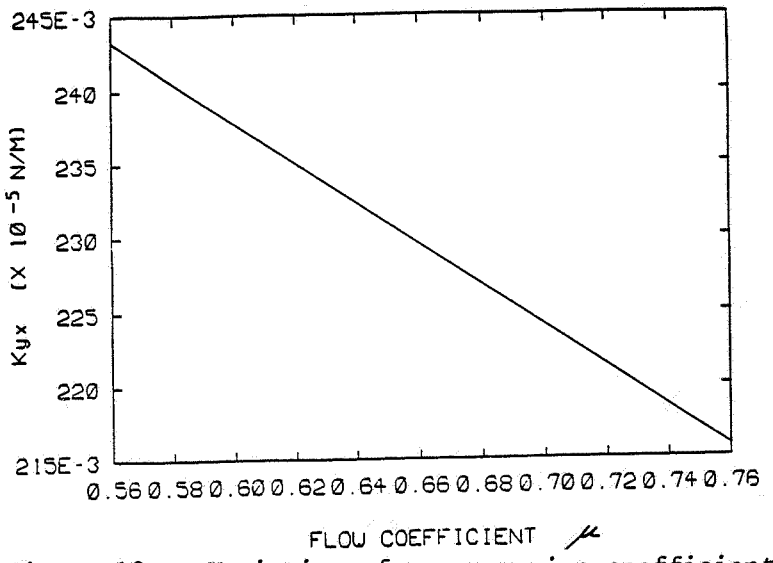

Figure 13. - Variation of cross spring coefficient with flow coefficient ($\omega_{rot} \neq 0$, $C^*_o < C^*_m$).

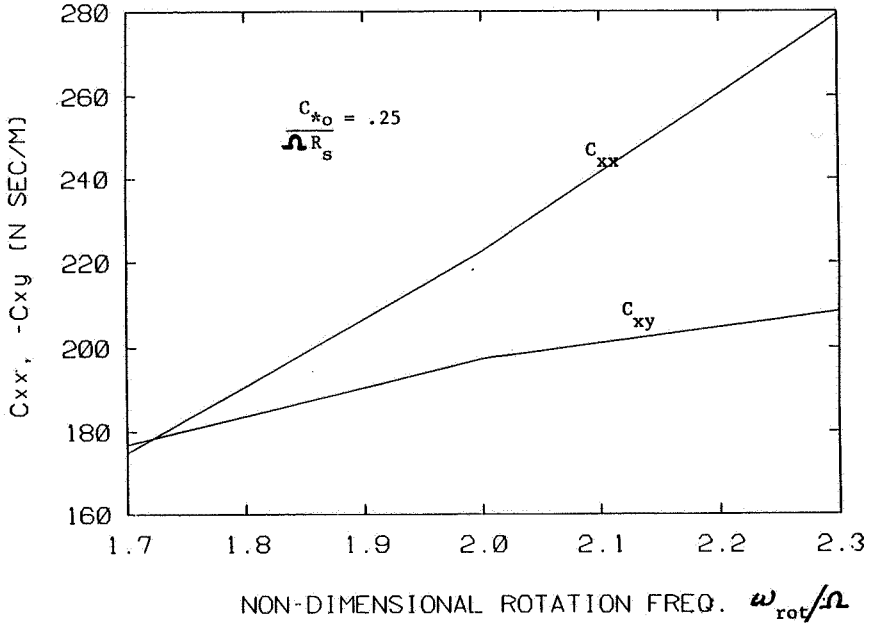

Figure 14. - Damping coefficients versus nondimensional rotation frequency, ω_{rot}/Ω.

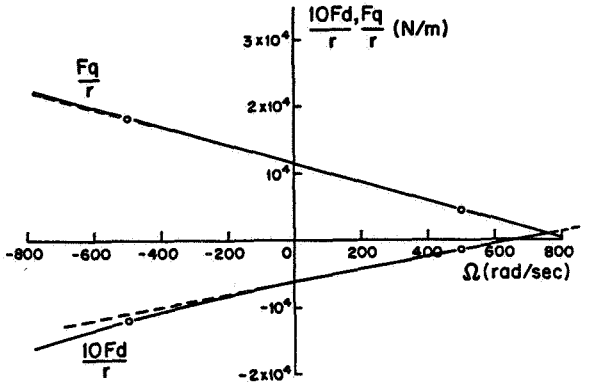

Figure A1. - Direct and quadrature forces in a short seal.

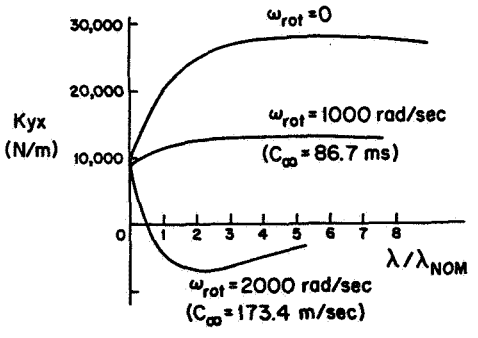

Figure A2. - Effect of friction factor variation on cross-stiffness in a short seal. Inlet swirl velocity, C_o, 100 m/sec.

AN IWATSUBO-BASED SOLUTION FOR LABYRINTH SEALS - COMPARISON WITH EXPERIMENTAL RESULTS

Dara W. Childs and Joseph K. Scharrer
Texas A & M University
College Station, Texas 77843

The basic equations are derived for compressible flow in a labyrinth seal. The flow is assumed to be completely turbulent in the circumferential direction where the friction factor is determined by the Blasius relation. Linearized zeroth and first-order perturbation equations are developed for small motion about a centered position by an expansion in the eccentricity ratio. The zeroth-order pressure distribution is found by satisfying the leakage equation while the circumferential velocity distribution is determined by satisfying the momentum equation. The first-order equations are solved by a separation of variables solution. Integration of the resultant pressure distribution along and around the seal defines the reaction force developed by the seal and the corresponding dynamic coefficients. The results of this analysis are compared to published test results.

INTRODUCTION

The problem of self excited vibration in turbomachinery due to labyrinth seals has led to the development of many analyses which attempt to model the physical phenomenon so that the problem can be better understood and therefore solved. The shortcoming with the analyses which have been presented to date is that they are difficult to understand and require limiting assumptions such as ignoring the area derivative in the circumferential direction, assuming that the friction factor is the same for all surfaces, and assuming that the flow coefficient is constant along the seal. These assumptions may be of some use mathematically, but do very little for the understanding of the physical occurrence. The first steps toward analysis of this problem were taken by Alford [1] , who neglected circumferential flow and Spurk et al [2] who neglected rotation of the shaft. Vance and Murphy [3] extended the Alford analysis by introducing a more realistic assumption of choked flow. Kostyuk [4] performed the first comprehensive analysis, but failed to include the change in area due to eccentricity which is responsible for the relationship between cross-coupled forces and parallel rotor displacements. Iwatsubo [5,6] refined the Kostyuk model to show this relationship by including the time dependency of area change, but he neglected the area derivative in the circumferential direction. Kurohashi [7] incorporated dependency

of the flow coefficient on eccentricity into his analysis, but assumed that the circumferential velocity in each cavity was the same.

The analysis presented here includes the variation of the area in the circumferential direction due to eccentricity and incorporates as many of the physical phenomena in the flow field as was thought necessary to produce an adequate result. The main purpose of this paper is to present a unified and comprehensive derivation of a reduced set of equations and a new solution format for those equations. The results of this analysis are compared to the published test results of Wachter and Benckert [8,9,10].

NOMENCLATURE

A- Cross sectional area of the cavity (L**2);defined in text
B- Height of labyrinth seal strip (L);defined in fig.(1)
C- Direct damping coefficient (Ft/L)
Cr- Nominal radial clearance (L);defined in fig.(1)
D- Hydraulic diameter of cavity (L);introduced in Eq.(3)
H- Radial clearance (L)
K- Direct stiffness coefficient (F/L)
L- Pitch of seal strips (L);defined in fig.(1)
NT- Number of seal strips
P- Pressure (F/L**2)
R- Gas constant
Rs- Radius of seal (L);Defined in fig.(1)
T- Temperature (T)
Rω- Surface velocity of rotor (L/t)
V- Average velocity of flow in circumferential direction (L/t)
a,b- Radial seal displacement components due to elliptical whirl (L);defined in Eq.(13)
ar- Dimensionless length upon which shear stress acts on rotor
as- Dimensionless length upon which shear stress acts on stator
c- Cross coupled damping coefficient (Ft/L);in Eq.(18)
k- Cross coupled stiffness coefficient (F/L);in Eq.(18)
m- Leakage mass flow rate per circumferential length (M/Lt)
mr,nr,ms,ns- Coefficients for Blasius relation for friction factor;defined in Eq.(3)
t- Time (t)
ω- Shaft angular velocity (1/t)
ρ- Density of fluid (M/L**3)
ν- Kinematic viscosity (L**2/t)
ϵ= e/Cr
γ- Ratio of specific heats
K_Q^* - Dimensionless cross-coupled stiffness parameter;defined in Eqs.(27)
E_O^*- Dimensionless entry-swirl parameter;defined in Eqs.(27)

Subscripts

o- Zeroth-order component

i- i-th chamber value
1- First-order component
x- X-direction
y- Y-directin
r- Reservoir value
s- Sump value

PROCEDURE

The analysis presented here is based on the see-through type of labyrinth seal shown in figure 1. The continuity and momentum equations will be derived for a single cavity control volume as shown in figures 2,3,4, and 5. A leakage model will be employed to account for the axial leakage. The governing equations will be linearized using perturbation analysis for small motion about a centered position. The zeroth-order continuity and momentum equations will be satisfied to yield the steady state pressure and velocity for each cavity. The first-order continuity and momentum equations will be reduced to linearly independent, algebraic equations by assuming an elliptical orbit of the shaft and a resulting harmonic response for the pressure and velocity fluctuations. The force on the shaft will be found by integration of the pressure fluctuations along and around the shaft. Using the equations for forced motion of the shaft, the stiffness and damping coefficients will be found.

ASSUMPTIONS

1) Fluid is considered to be an ideal gas.
2) Pressure variations within a chamber are small compared to the pressure difference across a seal strip.
3) The frequency of acoustic resonance in the cavity is much higher than that of the rotor speed.
4) Added mass terms are neglected.
5) The eccentricity of the rotor is small compared to the radial seal clearance.
6) In the determination of the shear stresses in the circumferential direction, the axial component of velocity is neglected.
7) The contribution of shear stress to the stiffness and damping coefficients is neglected.

GOVERNING EQUATIONS

Continuity Equation

Referring to the control volume in figures 2 and 3, the continuity equation for the control volume shown is:

$$\rho_i \frac{\partial A_i}{\partial t} + A_i \frac{\partial \rho}{\partial t} + \frac{\rho_i V_i}{R_s} \frac{\partial A_i}{\partial \theta} + \frac{\rho_i A_i}{R_s} \frac{\partial V_i}{\partial \theta} + \frac{A_i V_i}{R_s} \frac{\partial \rho_i}{\partial \theta} + \dot{m}_{i+1} - \dot{m}_i = 0 \qquad (1)$$

where the transverse surface area Ai is defined by;

$$A_i = [B_i + (Cr+\epsilon H_1)_i + B_{i+1} + (Cr+\epsilon H_1)_{i+1}]L_i/2$$

Momentum Equation

The momentum equation (2) is derived using figures 4 and 5 which show the pressure forces and shear stresses acting on the control volume. This equation includes the area derivative in the circumferential direction, which was neglected by Iwatsubo [5,6].

$$\frac{\partial \rho V_i A_i}{\partial t} + \frac{2\rho V_i A_i}{Rs}\frac{\partial V_i}{\partial \theta} + \frac{\rho V_i^2}{Rs}\frac{\partial A_i}{\partial \theta} + \frac{V_i A_i}{Rs}\frac{\partial \rho}{\partial \theta}$$
$$+ \dot{m}_{i+1}V_i - \dot{m}_i V_{i-1} = -\frac{A_i}{Rs}\frac{\partial P_i}{\partial \theta} + \tau_r arL_i - \tau_s asL_i \qquad (2)$$

where ar and as are the dimensionless length upon which the shear stresses act and are defined as;

$$as = L_i/L_i \qquad ar = (2B+L_i)/L_i$$

for teeth on the rotor and as;

$$as = (2B+L_i)/L_i \qquad ar = L_i/L_i$$

for teeth on the stator. Blasius [11] determined that the shear stresses for turbulent flow in a smooth pipe could be written as;

$$\tau = \frac{1}{2}\rho_i U_m^2 \, no \left(\frac{UmD}{\nu}\right)^{mo} \qquad (3)$$

This relationship is applied to the labyrinth surface for the hydraulic diameter;

$$D = \frac{2(Cri+B)Li}{(Cri+B+Li)}$$

and where Um is the mean flow velocity relative to the surface upon which the shear stress is acting. The constants mo and no can be empirically determined for a given surface from pressure flow experiments. However, for smooth surfaces the coefficients given by Yamada [12] for turbulent flow between annular surfaces are:

$$mo = -0.25 \qquad no = 0.079$$

For the control volume shown in figure 4, ns and ms represent tne constants for the stator surface and nr and mr represent those for the rotor surface. This feature allows one to tailor this analysis to a particular surface such as honeycomb or an abradable one.

Substituting the mean flow velocity relative to each surface and referring to figure 5, which accounts for the pressure on the sides of the control volume due to the eccentricity of the seal, the circumferential momentum equation for the seal is:

$$\frac{\partial \rho_i V_i A_i}{\partial t} + \frac{2\rho_i V_i A_i}{R_s}\frac{\partial Vi}{\partial \theta} + \frac{Vi^2 Ai}{Rs}\frac{\partial \rho i}{\partial \theta} + \frac{\rho_i V_i^2}{Rs}\frac{\partial A_i}{\partial \theta} + \dot{m}_{i+1}V_i - \dot{m}_i V_{i-1}$$

$$= \frac{A_i}{R_s}\frac{\partial Pi}{\partial \theta} + \frac{1}{2}\rho i(R\omega - Vi)^2 nr\left(\frac{(R\omega - V_i)D}{\nu}\right)^{mr} arL - \frac{1}{2}\rho_i V_i^2 ns\left(\frac{V_i D}{V}\right)^{ms} asL \quad (4)$$

If Eq.(1) times the circumferential velocity is now subtracted from Eq.(4), the following reduced form of the momentum equation is obtained:

$$\rho_i A_i \frac{\partial V_i}{\partial t} + \rho_i V_i A_i \frac{\partial V_i}{Rs\partial \theta} + \dot{m}_i (V_i - V_{i-1}) = \frac{-A_i}{Rs}\frac{\partial P_i}{\partial \theta}$$
$$- \frac{1}{2}\rho_i V_i^2 ns\left(\frac{V_i D}{\nu}\right)^{ms} asL_i + \frac{1}{2}\rho_1 (R\omega - V_i)^2 nr\left(\frac{(R\omega - V_i)D}{\nu}\right)^{mr} arL_i \quad (5)$$

In order to reduce the number of variables, all of the density terms are replaced with pressure terms using the ideal gas law (6).

$$P_i = \rho RT \quad (6)$$

Furthermore, in order to make the perturbation analysis easier, the following substitution is made in the continuity equation:

$$\dot{m}_{i+1} - \dot{m}_i = \frac{\dot{m}_{i+1}^2 - \dot{m}_i^2}{2\dot{m}_o}$$

Leakage Equation

To account for the leakage mass flow rate in the continuity and momentum equations, the leakage model of Neumann [13] was chosen. This model predicts leakage and pressures fairly accurately and has a term to account for kinetic energy carryover. However, the empirical flow coefficient relations given by Neumann were discarded in favor of the equations of Chaplygin [14] for flow through an orifice. This was done to produce a different flow coefficient for succeeding contractions along the seal as has been shown to be the case by Egli [15]. The form of the model is:

$$\dot{m}_o = \mu_1 \mu_2 RsC_{ri}\sqrt{\frac{P_{i-1}^2 - P_i^2}{RT}} \quad (7)$$

where the kinetic energy carryover coefficient μ_2 is defined for straight through seals as;

$$\mu_2=\sqrt{\frac{NT}{(1+j)NT + j}}$$

where

$$j= 1 - (1 + 16.6\ C_r/L)^{-2}$$

and is unity, by definition, for interlocking and combination groove seals. The flow coefficient is defined as;

$$\mu_1= \frac{\pi}{\pi+2-5s+2s^2} \qquad \text{where} \qquad s= \left(\frac{P_{i-1}}{P_i}\right)^{\frac{\gamma-1}{\gamma}} - 1$$

For choked flow, Fliegner's formula will be used for the last seal strip. It is of the form;

$$\dot{m}= \frac{0.6847\mu_1 P_{i-1} C_{ri}}{\sqrt{RT}} \tag{8}$$

where

$$\mu_1= 0.745$$

LINEARIZATION

Since an analytical solution to the governing equations is not available, the continuity and momentum equations will be expanded in the following perturbation variables:

$$P_i = P_{oi} + \epsilon P_1 \qquad H_i = (C_{ri} + \epsilon H_i)$$

$$V_i = V_{oi} + \epsilon V_1 \qquad A_i = A_{oi} + \epsilon L_i H_1$$

where $\epsilon = e/Cr$ is the eccentricity ratio. The zeroth-order equations define the leakage mass flow rate and the velocity distribution for a centered position. The first-order equations define the perturbations in pressure and circumferential velocity due to a radial position perturbation of the rotor. Strictly speaking, the results are only valid for small motion about a centered position.

Zeroth-Order Solution

Eq.(9) is used to determine the pressure distribution along the shaft in the following manner. The leakage is solved using Eq.(7) or Eq.(8), depending on the operating conditions. To determine if the flow is choked or not, assume that the pressure in the last cavity is equal to the critical pressure for choking. Using this pressure, find the leakage from Eq.(8) and then use Eq.(7) to determine the reservoir pressure necessary to produce

this condition. Based on this pressure, a determination can be made whether the flow is choked or not. The associated pressure distribution is determined by employing the correct leakage, along with a known boundary pressure, and solving Eq.(7) one cavity at a time.

$$\dot{m}_{i+1} = \dot{m}_i = \dot{m}_o \tag{9}$$

For cavity i, the zeroth-order circumferential momentum equation is:

$$\dot{m}_o(V_{oi}-V_{oi-1}) = \frac{1}{2}\frac{P_{oi}(R\omega-V_{oi})^2}{RT} nr \left(\frac{(R\omega-V_{oi})D}{\nu}\right)^{mr} arL$$
$$- \frac{1}{2}\frac{P_{oi}V_{oi}^2}{RT} ns\left(\frac{V_{oi}D}{\nu}\right)^{ms} asL \quad ; \; i=1,2,3,.....,NT-1 \tag{10}$$

With the pressure determined, the only variables remaining in the momentum equation for the cavities are the velocities. Given an inlet tangential velocity, a Newton root finding approach can be taken whereby Eq.(10) is solved for the i-th velocity, one cavity at a time. This is done starting at the first cavity and working down stream.

First-Order Solution

The governing first-order equations (11,12), define the pressure and velocity fluctuations resulting from the seal clearance function. The continuity equation (11) and momentum equation (12) follow:

$$G_1\frac{\partial P_{1i}}{\partial t} + G_1\frac{V_{oi}}{R_s}\frac{\partial P_{1i}}{\partial \theta} + G_1\frac{P_{oi}}{R_s}\frac{\partial V_{1i}}{\partial \theta} + G_3 P_{1i} + G_4 P_{1i-1} + G_5 P_{1i+1} \tag{11}$$
$$= -G_6 H_1 - G_2\frac{\partial H_1}{\partial t} - G_2\frac{V_{oi}}{R_s}\frac{\partial H_i}{\partial \theta}$$

$$X_1\frac{\partial V_{1i}}{\partial t} + \frac{X_1 V_{oi}}{R_s}\frac{\partial V_{1i}}{\partial \theta}\frac{A_{oi}}{R_s} + \frac{\partial P_{1i}}{\partial \theta} + X_2 V_{1i} - \dot{m}_i V_{1i-1} + X_3 P_{1i} \tag{12}$$
$$+ X_4 P_{1i-1} = X_5 H_1$$

where the X's and G's are defined in Appendix A. If the shaft center moves in an elliptical orbit, then the seal clearance function can be defined as:

$$\varepsilon H_1 = -a\cos\omega t\cos\theta - b\sin\omega t\sin\theta \tag{13}$$

The pressure and velocity fluctuations can now be stated in the associated solution format:

$$P_{1i} = P^{+}_{ci}\cos(\theta+\omega t) + P^{+}_{si}\sin(\theta+\omega t) + P^{-}_{ci}\cos(\theta-\omega t) + P^{-}_{si}\sin(\theta-\omega t) \quad (14)$$

$$V_{1i} = V^{+}_{ci}\cos(\theta+\omega t) + V^{+}_{si}\sin(\theta+\omega t) + V^{-}_{ci}\cos(\theta-\omega t) + V^{-}_{si}\sin(\theta-\omega t) \quad (15)$$

Substituting Eqs.(13),(14), and (15) into Eqs.(11) and (12) and grouping like terms of sines and cosines (as shown in Appendix B) eliminates the time and angular dependency and yields eight linear algebraic equations per cavity. The resulting system of equations for the i-th cavity is of the form;

$$[A_{i-1}]\,(X_{i-1}) + [A_i]\,(X_i) + [A_{i+1}]\,(X_{i+1}) = \frac{a}{\varepsilon}(B_i) + \frac{b}{\varepsilon}(C_i) \quad (16)$$

where

$$(X_{i-1}) = (P^{+}_{si-1},\ P^{+}_{ci-1},\ P^{-}_{si-1},\ P^{-}_{ci-1},\ V^{+}_{si-1},\ V^{+}_{ci-1},\ V^{-}_{si-1},\ V^{-}_{ci-1})^T$$

$$(X_i) = (P^{+}_{si},\ P^{+}_{ci},\ P^{-}_{si},\ P^{-}_{ci},\ V^{+}_{si},\ V^{+}_{ci},\ V^{-}_{si},\ V^{-}_{ci})^T$$

$$(X_{i+1}) = (P^{+}_{si+1},\ P^{+}_{ci+1},\ P^{-}_{si+1},\ P^{-}_{ci+1},\ V^{+}_{si+1},\ V^{+}_{ci+1},\ V^{-}_{si+1},\ V^{-}_{ci+1})^T$$

The A matrices and column vectors B and C are given in Appendix B. To use Eq.(16) for the entire seal solution, a system matrix must be formed which is block tridiagonal in the A matrices. The size of this resultant matrix is (8(NT-1)) x (8(NT-1)) since pressure and velocity perturbations at the inlet and the exit are assumed to be zero. This system is easily solved by various linear equation algorithms, and yields a solution of the form:

$$\begin{aligned} P^{+}_{si} &= \frac{a}{\varepsilon}F^{+}_{asi} + \frac{b}{\varepsilon}F^{+}_{bsi} \\ P^{-}_{si} &= \frac{a}{\varepsilon}F^{-}_{asi} + \frac{b}{\varepsilon}F^{-}_{bsi} \\ P^{+}_{ci} &= \frac{a}{\varepsilon}F^{+}_{aci} + \frac{b}{\varepsilon}F^{+}_{bci} \\ P^{-}_{Ci} &= \frac{a}{\varepsilon}F^{-}_{aci} + \frac{b}{\varepsilon}F^{-}_{bci} \end{aligned} \quad (17)$$

DETERMINATION OF DYNAMIC COEFFICIENTS

The force-motion equations for a labyrinth seal are assumed to be of the form:

$$-\begin{pmatrix} F_x \\ F_y \end{pmatrix} = \begin{bmatrix} K & k \\ -k & K \end{bmatrix} \begin{pmatrix} X \\ Y \end{pmatrix} + \begin{bmatrix} C & c \\ -c & C \end{bmatrix} \begin{pmatrix} \dot{X} \\ \dot{Y} \end{pmatrix} \tag{18}$$

The solution of Eq.(18) for the stiffness and damping coefficients is the objective of the current analysis. For the assumed elliptical orbit of Eq.(13), the X and Y components of displacement and velocity are defined as:

$$X = a\cos\omega t \qquad \dot{X} = -a\omega \sin\omega t$$
$$Y = b\sin\omega t \qquad \dot{Y} = b\omega \cos\omega t$$

Substituting these relations into (18) yields:

$$\begin{aligned} -F_x &= -Ka\cos\omega t - kb\sin\omega t + Ca\omega\sin\omega t - cb\omega\cos\omega t \\ -F_y &= -ka\cos\omega t - Kb\sin\omega t - ca\omega\sin\omega t - Cb\omega\cos\omega t \end{aligned} \tag{19}$$

Redefining the forces, Fx and Fy, as the following;

$$\begin{aligned} F_x &= F_{xc}\cos\omega t + F_{xs}\sin\omega t \\ F_y &= F_{yc}\cos\omega t + F_{ys}\sin\omega t \end{aligned} \tag{20}$$

and substituting back into (19) yields the following relations:

$$-Fxc = Ka + cb\omega \qquad -Fxs = -Ca\omega + kb$$
$$-Fyc = -ka + Cb\omega \qquad -Fys = Kb + ca\omega \tag{21}$$

The X and Y components of force can be found by integrating the pressure around the seal as follows:

$$Fx = -Rs \sum_{i=1}^{NT-1} \int_0^{2\pi} P_{1_i} L_i \cos\theta \, d\theta \tag{22}$$

$$Fy = -Rs \sum_{i=1}^{NT-1} \int_0^{2\pi} P_{1_i} L_i \sin\theta \, d\theta \tag{23}$$

Only one of these components needs to be expanded in order to determine the dynamic coefficients. For this analysis, the X component was chosen. Substituting Eq.(14) into (22) and integrating yields:

$$Fx = -\varepsilon\pi Rs \sum_{i=1}^{NT-1} L_i \left[(P^+_{si} - P^-_{si})\sin\omega t + (P^+_{ci} + P^-_{ci})\cos\omega t\right] \tag{24}$$

Substituting from Eq.(17) and (19) into Eq.(24) and equating coefficients of $\sin\omega t$ and $\cos\omega t$ yields:

$$F_{xs} = -\pi Rs \sum_{i=1}^{NT-1} L_i[a(F^+_{asi} - F^-_{asi}) + b\,(F^+_{bsi} - F^-_{bsi})]$$

$$F_{xc} = -\pi Rs \sum_{i=1}^{NT-1} L_i[a(F^+_{aci} + F^-_{aci}) + b\,(F^+_{bci} + F^-_{bci})] \qquad (25)$$

Equating the definitions for Fxs and Fxc provided by Eqs.(21) and (25) and grouping like terms of the linearly independent coefficients a and b yields the final solutions to the stiffness and damping coefficients:

$$K = \pi R \sum_{i=1}^{NT-1} (F^+_{aci} + F^-_{aci})\, L_i$$

$$k = \pi R \sum_{i=1}^{NT-1} (F^+_{bsi} - F^-_{bsi})\, L_i \qquad (26)$$

$$C = \frac{-\pi Rs}{\omega} \sum_{i=1}^{NT-1} (F^+_{asi} - F^-_{asi})\, L_i$$

$$c = \frac{\pi Rs}{\omega} \sum_{i=1}^{NT-1} (F^+_{bci} + F^-_{bci})\, L_i$$

SOLUTION PROCEDURE SUMMARY

In review, the solution procedure uses the following sequential steps;

a) Leakage is determined from Eq.(7) or (8).
b) Pressure distribution is found using Eq.(7).
c) Velocity distribution is determined using Eq.(10).
d) A system equation is formed and solved using the cavity Eq.(16).
e) Results of this solution as defined in Eqs.(17), are inserted into Eq.(26)

RESULTS

To compare the present analytic solution with the experimental results of Wachter and Benckert [8,9,10], the following dimensionless parameters are introduced. The dimensionless cross-coupled stiffness and entry-swirl parameters are defined by Wachter and Benckert as:

$$K_Q^* = \frac{Cr\ Kxy}{RsLNT(Pr-Ps)} \qquad E_o^* = \frac{0.5\rho_o V_o^2}{(Pr-Ps) + 0.5\rho_o V_x^2} \tag{27}$$

All of the results presented for comparison in this paper are for a seal with teeth on the stator, with entry swirl and no shaft rotation. Although Wachter and Benkert published results for shaft rotation, the data for the operating conditions and seal geometry were insufficient for use in this study. The results in figures 7,8,and 9 are from [8] and show the relationship between cross coupled stiffness and the entry swirl, for a seal with strips on the stator and the geometry shown in figure 6. The line shown is the experimental result and the symbols are the results from this analytical model. These figures show that the model compares favorably to the experimental results in magnitude and the overall trend for various operating conditions. The figures also show that the model does not yield a consistently high or low result. Instead, the model tends to over predict the value of the stiffness for a large number of strips and under predict stiffness for a small number of seals. This trend is probably due to errors in calculating the zeroth-order pressure distribution using the leakage model.

The results in table (1) are from [9,10] for a seal with strips on the stator. The results show the effect of change in seal parameters such as pitch, number of teeth, radius, strip height, and clearance on the cross coupled stiffness. The model accurately shows the increase in cross-coupled stiffness due to decrease in clearance and decrease in strip height, but it fails to remain constant for change of pitch and consistantly over estimates the cross-coupled stiffness for the larger radius cases by about 26%.

CONCLUSION

A clear and understandable analysis utilizing reduced equations has been presented for the problem of calculating rotordynamic coefficients for labyrinth seals. This paper was developed to provide a less restrictive analysis and a better explanation of the current analyses. The model developed gives results that were within 25% of the experimental results available. However, this error must be balanced against the known uncertainties in the experimental data. This is especially important since all of the data used are for a nonrotating shaft and the only influence on the cross coupled stiffness was the entry swirl. Although Wachter and Benckert published data for a rotating shaft, the data were not sufficient to calculate a result. Also, the only data available for see-through labyrinths is for the type with strips on the stator. For a more rigorous test of this and other models, more complete data are required over a wider range of parameters for different seal geometries. Finally, this analysis is only considered valid for the see-

through type of labyrinth seal since the model fared very poorly in comparison with interlocking and grooved seal data.

REFERENCES

[1] ALFORD, J.S.: Protecting Turbomachinery from Self-Excited Rotor Whirl. Transactions ASME, J. of Eng. f. Power, Oct. 1965, pp. 333-344.

[2] Spürk, J.H. and Keiper, R.: Selbsterregte Schwingungen bei Turbomaschinen infolge der Labyrinthstromung. Ingerieur-Archive 43, 1974, pp. 127-135.

[3] Vance, J.M and Murphy, B.T.: Labyrinth Seal Effects on Rotor Whirl Stability. Inst. of Mech. Eng.,1980 pp. 369-373.

[4] Kostyuk, A.G.: A Theoretical Analysis of the Aerodynamic Forces in the Labyrinth Glands of Turbomachines. Teploenergetica, 19(11), 1972, pp. 39-44.

[5] Iwatsubo, T.: Evaluation of Instability Forces of Labyrinth Seals in Turbines or Compressors. NASA CP 2133 Proceedings of a workshop at Texas A&M University 12-14 May 1980, Entitled Rotordynamic Instability Problems in High Performance Turbomachinery, pp. 139-167.

[6] Iwatsubo, T., Matooka, N., and Kawai, R.: Flow Induced Force and Flow Pattern of Labyrinth Seal, NASA CP 2250 Proceeding of a workshop at Texas A&M University 10-12 May 1982, Entitled Rotordynamic Instability Problems in High Performance Turbomachinery, pp. 205-222.

[7] Kurohashi, M., Inoue, Y., Abe, T., and Fujikawa, T.: Spring and Damping Coefficients of the Labyrinth Seal. Paper No. C283/80 delivered at the Second International Conference on Vibrations in Rotating Machinery, The Inst. of Mech. Eng.

[8] Wachter, J., and Benckert, H.: Querkrafte aus Spaltdichtungen -Eine mogliche Ursache fur die Laufunruhe von Turbomaschinen. Atomkernenergie Bd. 32, 1978, Lfg. 4, pp. 239-246.

[9] Wachter, J., and Benckert, H.: Flow Induced Spring Coefficients of Labyrinth Seals for Applications in Rotordynamics. NASA CP 2133 Proceedings of a workshop held at Texas A&M University 12-14 May 1980, Entitled Rotordynamic Instability Problems of High Performance Turbomachinery, pp. 189-212.

[10] Benckert, H.: Stromungsbedingte Federkennwerte in Labyrinthdichtungen. Doctoral dissertation at University of Stuttgart, 1980

[11] Blasius, H.: Forschungoarb. Ing.-Wes., No.131, 1913

[12] Yamada, Y.: Trans. Japan Soc. Mech. Engrs., Vol.27, No.180, 1961, pp.1267

[13] Neumann, K.: Zur Frage der Verwendung von Durchblickdichtungen im Dampfturbinenbau. Maschinentechnik, Vol. 13, 1964, No. 4.

[14] Gurevich, M.I.,The Theory Of Jets In An Ideal Fluid,Pergamon Press, 1966, pp.319-323

TABLE I. - COMPARISON OF DATA FOR VARIOUS GEOMETRIES AND OPERATING CONDITIONS FOR SEAL WITH TEETH ON STATOR AND NO SHAFT ROTATION [9,10]

E_o^*	U	NT	C(m)	L(m)	B(m)	R_s(m)	P_r(bar)	P_s(bar)	EXP. K_{xy}(N/mm)	CALC. K_{xy}(N/mm)	% Error
0.023	0.0	18	.00025	.005	.0025	0.15	2.947	0.943	257	325	+26
0.024	0.0	18	.00025	.005	.0025	0.15	1.43	0.943	75	90	+20
0.038	0.0	18	.00025	.005	.006	0.15	2.947	0.943	157	198	+26
0.018	0.0	18	.00025	.005	.006	0.15	1.43	0.943	27	36	+33
0.04	0.0	18	.00058	.005	.006	0.075	1.925	0.943	29	29	0
0.04	0.0	18	.00058	.005	.006	0.075	2.418	0,943	41	41	0
0.04	0.0	9	.00058	.010	.006	0.075	1.925	0.943	29	22	-24
0.04	0.0	9	.00058	.010	.006	0.075	2.418	0.943	41	32	-22

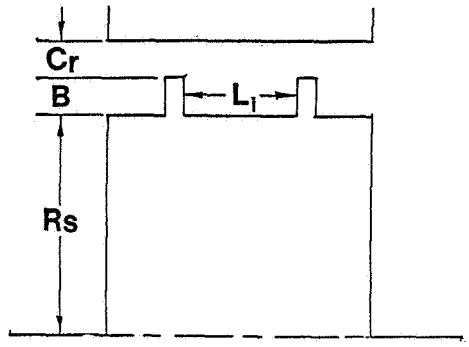

Figure 1. - Typical cavity.

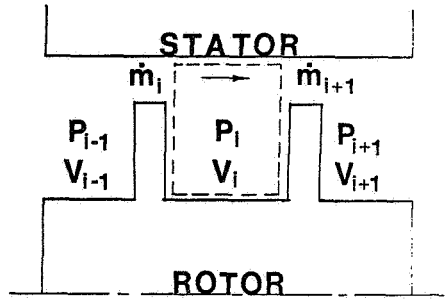

Figure 2. - Cavity control volume.

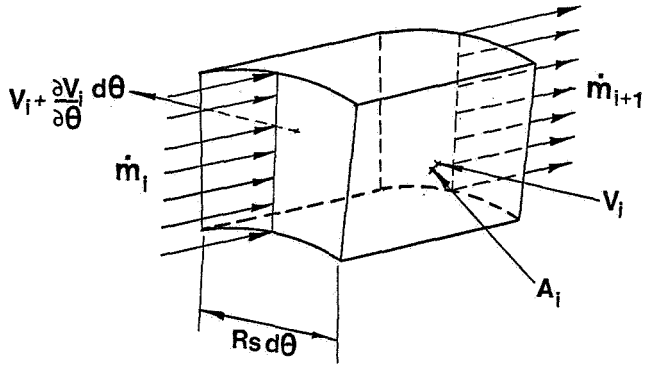

Figure 3. - Cavity control volume.

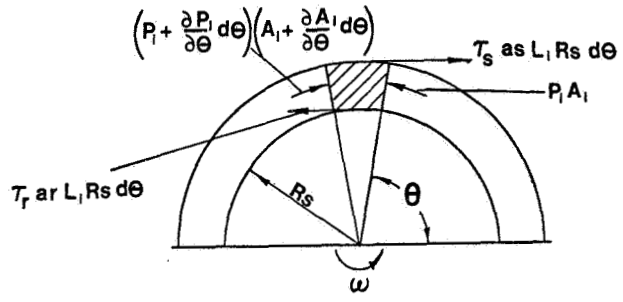

Figure 4. - Forces on control volume.

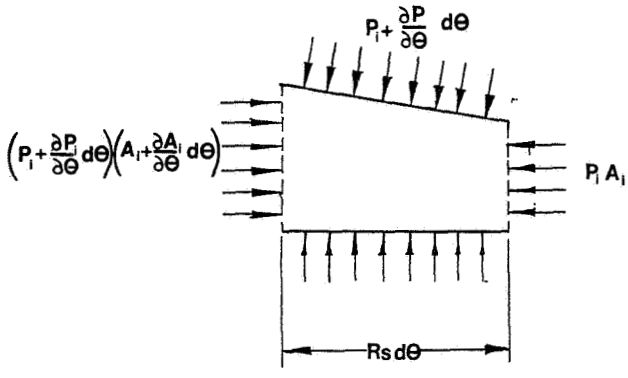

Figure 5. - Forces on control volume.

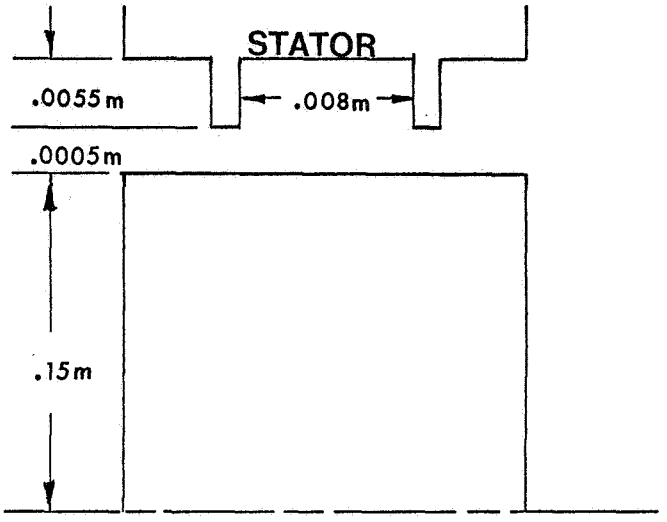

Figure 6. - Configuration used for experiment.

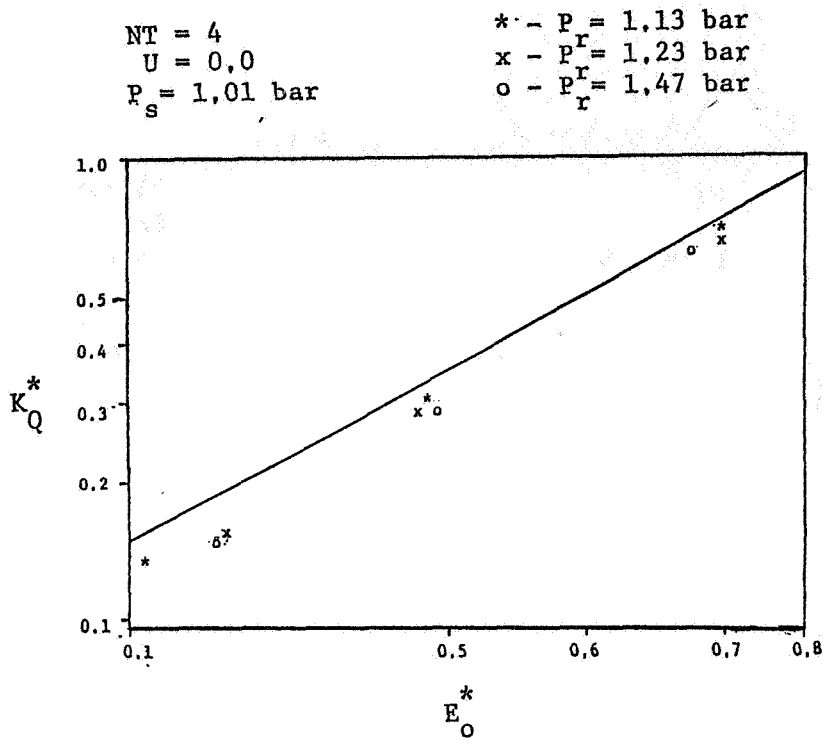

Figure 7. - Comparison with data of [8] for seal in figure 6.

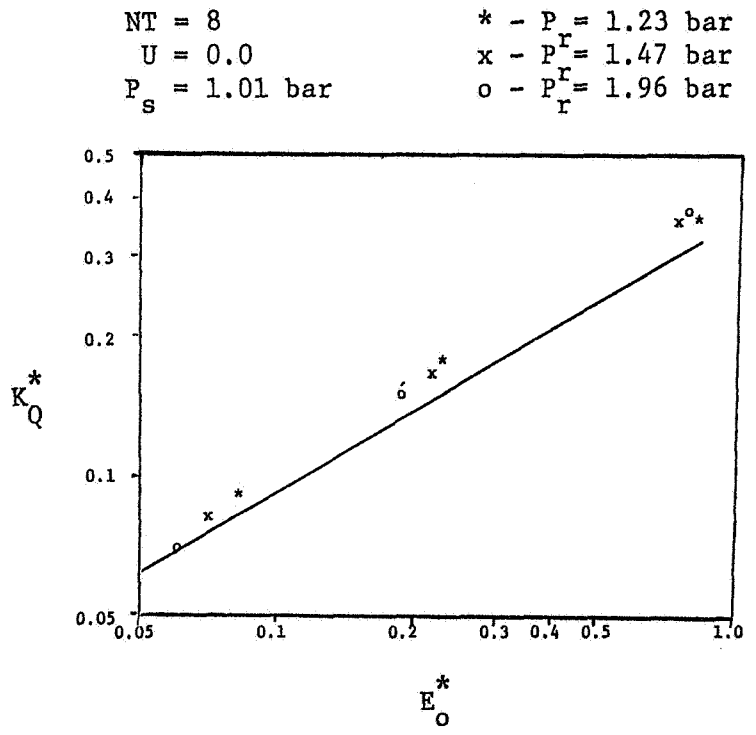

Figure 8. - Comparison with data of [8] for seal in figure 6.

NT = 13
U = 0.0
P_s = 1.01 bar

* - P_r = 1.23 bar
x - P_r = 1.96 bar
o - P_r = 3.43 bar

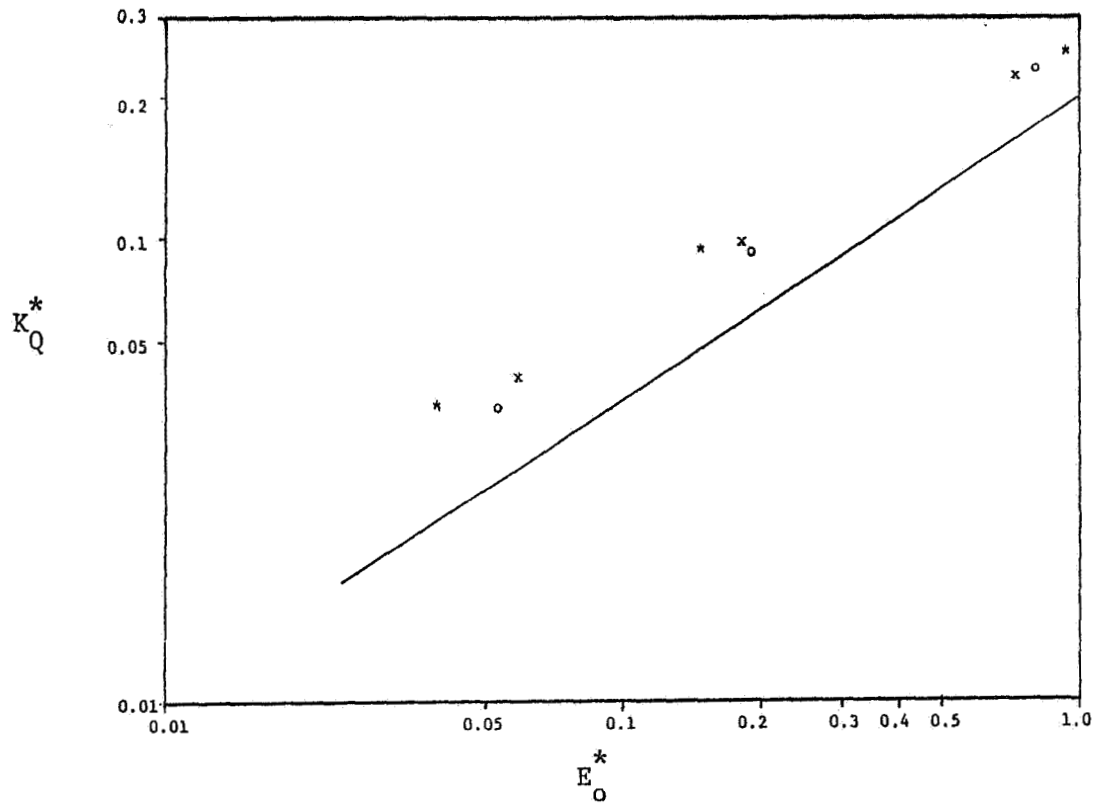

Figure 9. - Comparison with data of [8] for seal in figure 6.

APPENDIX A

DEFINITION OF FIRST-ORDER CONTINUITY AND MOMENTUM EQUATION COEFFICIENTS

$$G_1 = \frac{A_{oi}}{RT} \qquad G_2 = \frac{P_{oi} L}{RT}$$

$$G_3 = \frac{\mu_1^2 \ \mu_2^2}{\dot{m}_o RT} P_{oi} \left(C_{i+1}^2 + C_i^2\right) - \frac{\dot{m}o}{\pi} \frac{\mu_1 (4s - 5)}{P_{oi}} \left(\frac{\gamma - 1}{\gamma}\right)$$

$$\left[\left(\frac{P_{oi}}{P_{oi+1}}\right)^{-\frac{1}{\gamma}} + \left(\frac{P_{oi} - 1}{P_{oi}}\right)^{\frac{\gamma - 1}{\gamma}}\right]$$

$$G_4 = \frac{-\mu_1^2 \mu_2^2}{\dot{m}_o RT} C_i^2 P_{oi-1} + \frac{\dot{m}o}{\pi} \mu_1 (4s-5) \left[\frac{1}{P_{oi}} \left(\frac{\gamma-1}{\gamma}\right) \left(\frac{P_{oi-1}}{P_{oi}}\right)^{-\frac{1}{\gamma}}\right]$$

$$G_5 = \frac{-\mu_1^2 \mu_2^2}{\dot{m}_o RT} C_{i+1}^2 P_{oi+1} + \frac{\dot{m}o}{\pi} \mu_1 (4s-5) \left[\frac{1}{P_{oi+1}} \left(\frac{\gamma - 1}{\gamma}\right) \left(\frac{P_{oi}}{P_{oi+1}}\right)^{\frac{\gamma - 1}{\gamma}}\right]$$

$$G_6 = m_o \left(\frac{C_i - C_{i+1}}{C_{i+1} C_i}\right)$$

$$X_1 = \frac{P_{oi} A_{oi}}{RT} \qquad X_2 = \dot{m}_o + \frac{\tau_s asL(2+ms)}{Voi} + \frac{\tau_r arL(2+mr)}{(R\omega - Voi)}$$

$$X_3 = \frac{\tau_s asL}{P_{oi}} + \frac{\tau_R arL}{P_{oi}} \frac{\mu_1^2 \mu_2^2 C_i^2}{RT\dot{m}o} (V_{oi} - V_{oi-1}) P_{oi} + \frac{\dot{m}o}{\pi} \mu_1 (4s-5) \left[\frac{1}{P_{oi}} \left(\frac{\gamma - 1}{\gamma}\right)\right.$$

$$\left.\left(\frac{P_{oi-1}}{P_{oi}}\right)^{\frac{\gamma - 1}{\gamma}}\right] (V_{oi} - V_{oi-1})$$

$$X_5 = \frac{\dot{m}o}{c_i}(V_{oi} - V_{oi-1}) - \frac{mst_s asLD}{2(c+B)^2} + \frac{\tau_r armrLD}{2(C_i+B)^2}$$
$$+ \frac{\dot{m}_o(V_{oi} - V_{oi-1})}{2\mu_2^2}\left(\frac{2NT(NT-1)\ (16.6\ Cr/L)\ (1+16.6\ Cr/L)}{[(NT+1)^2 + (1 + 16.6\ Cr/L)]^2}\right)$$

$$X_4 = \frac{\mu_1^2\mu_2^2C_i^2}{RT\dot{m}o}\ (V_{oi} - V_{oi-1}\qquad P_{oi-1} - \frac{\dot{m}o}{\pi}(V_{oi} - V_{oi-1})\ \mu_1 \quad (4s-5)$$

$$\left[\frac{1}{P_{oi}}\left(\frac{\gamma - 1}{\gamma}\right)\left(\frac{P_{oi-1}}{P_{oi}}\right)^{-\frac{1}{\gamma}}\right]$$

APPENDIX B

SEPARATION OF CONTINUITY AND MOMENTUM EQUATIONS
AND DEFINITION OF SYSTEM MATRIX ELEMENTS

CONTINUITY:

$$\cos(\theta+\omega t): \quad G_1 P^+_{si}\left(\omega+\frac{Voi}{Rs}\right)+G_1\frac{Poi}{Rs}V^+_{si}+G_3 P^+_{ci}+G_4 P^+_{ci-1}=\frac{G_6}{2}(a-b)$$

$$\sin(\theta+\omega t): -G_1 P^+_{ci}\left(\frac{Voi}{Rs}+\omega\right)-G_1\frac{Poi}{Rs}V^+_{ci}+G_3 P^+_{si}+G_4 P^+_{si-1}+G_5 P^+_{si+1}=\frac{G_6}{2}\left(\frac{V_{oi}}{R_s}+\omega\right)\quad(b-a)$$

$$\cos(\theta-\omega t): \quad G_1\left(\frac{Voi}{Rs}-\omega\right)P^-_{si}+G_1\frac{Poi}{Rs}V^-_{si}+G_3 P^-_{ci}+G_4 P^-_{ci-1}+G_5 P^-_{ci+1}=\frac{G_6}{2}(a+b)$$

$$\sin(\theta-\omega t): \quad G_1\left(\omega-\frac{Voi}{Rs}\right)P^-_{ci}-\frac{G_1 P_{oi}}{Rs}V^-_{ci}+G_3 P^-_{si}+G_3 P^-_{si}+G_4 P^-_{si-1}+G_5 P^-_{si+1}=\frac{G_6}{2}\left(\omega\frac{-Voi}{Rs}\right)(a+b)$$

MOMENTUM:

$$\cos(\theta+\omega t): \quad X_1\left(\omega+\frac{Voi}{Rs}\right)V^+_{si}+\frac{A_{oi}}{Rs}P^+_{si}+X_2 V^+_{ci}-\dot{m}o\,V^+_{ci-1}+X_3 P^+_{ci}+X_4 P_{ci-1}=\frac{X_5}{2}\quad(b-a)$$

$$\sin(\theta+\omega t): \quad -X_1\left(\omega+\frac{Voi}{Rs}\right)V^+_{ci}-\frac{A_{oi}}{Rs}P^+_{ci}+X_2 V_{si}-\dot{m}o\,V^+_{si-1}+X_3 P^+_{si}+X_4 P^+_{si-1}=0$$

$$\cos(\theta+\omega t): \quad X_1\left(\frac{Voi}{Rs}-\omega\right)V^-_{si}+\frac{A_{oi}}{Rs}P^-_{si}+X_2 V^-_{ci}-\dot{m}o\,V^-_{ci-1}+X_3 P^-_{ci-1}=\frac{-X_5}{2}\quad(a+b)$$

$$\sin(\theta-\omega t): \quad X_1\left(\omega-\frac{Voi}{Rs}\right)P^-_{ci}-\frac{A_{oi}}{Rs}P^-_{ci}+X_2 V^-_{si}-\dot{m}o\,V^-_{si-1}+X_3 P^-_{si}+X_4 P^-_{si-1}=0$$

A_{i-1} MATRIX

$$a_{1,2} = a_{2,1} = a_{3,4} = a_{4,3} = G_4$$

$$a_{5,2} = a_{6,1} = a_{7,4} = a_{8,3} = X_4$$

$$a_{5,6} = a_{6,5} = a_{7,8} = a_{8,7} = -\dot{m}_o$$

The remaining elements are zero

A_i MATRIX

$$a_{1,1} = G_1 \left(\omega + \frac{V_{oi}}{Rs}\right) \qquad a_{2,2} = -G_1 \left(\omega + \frac{V_{oi}}{Rs}\right)$$

$$a_{3,3} = G_1 \left(\frac{V_{oi}}{Rs} - \omega\right) \qquad A_{4,4} = -G_1 \left(\frac{V_{oi}}{Rs} - \omega\right)$$

$$a_{1,2} = a_{2,1} = a_{3,4} = a_{4,3} = G_3$$

$$a_{5,2} = a_{6.1} = a_{7,4} = a_{8.3} = X_3$$

$$a_{5,1} = a_{7,3} = \frac{A_{oi}}{Rs} \qquad a_{6,2} = a_{8,4} = \frac{-A_{oi}}{Rs}$$

$$a_{5,5} = X_1 \left(\omega + \frac{V_{oi}}{Rs}\right) \qquad a_{6,6} = -X_1 \left(\omega + \frac{V_{oi}}{Rs}\right)$$

$$a_{7,7} = X_1 \left(\frac{V_{oi}}{Rs} - \omega\right) \qquad a_{8,8} = X_1 \left(\omega - \frac{V_{oi}}{Rs}\right)$$

$$a_{5,6} = a_{6,5} = a_{7,8} = a_{8,7} = X_2$$

$$a_{1,5} = a_{3,7} = G_1 \frac{p_{oi}}{Rs}$$

$$a_{2,6} = a_{4,8} = -G_1 \frac{P_{oi}}{Rs}$$

The remaining elements are zero

A_{i+1} MATRIX

$$a_{1,2} = a_{2,1} = a_{3,4} = a_{4,3} = G_5$$

THE REMAINING ELEMENTS ARE ZERO

B and C column Vectors

$$B = \begin{bmatrix} \frac{G_6}{2} \\ \frac{-G_2}{2}\left(\frac{V_{oi}}{Rs} + \omega\right) \\ \frac{G_6}{2} \\ \frac{G_2}{2}\left(\omega - \frac{V_{oi}}{Rs}\right) \\ \frac{-X_5}{2} \\ 0 \\ \frac{-X_5}{2} \\ 0 \end{bmatrix} \qquad C = \begin{bmatrix} \frac{-G_6}{2} \\ \frac{G_2}{2}\left(\frac{V_{oi}}{Rs} + \omega\right) \\ \frac{G_6}{2} \\ \frac{G_2}{2}\left(\omega - \frac{V_{oi}}{Rs}\right) \\ \frac{X_5}{2} \\ 0 \\ \frac{-X_5}{2} \\ 0 \end{bmatrix}$$

PRELIMINARY INVESTIGATION OF LABYRINTH PACKING PRESSURE DROPS AT ONSET OF SWIRL-INDUCED ROTOR INSTABILITY

E. H. Miller and J. H. Vohr
General Electric Company
Schenectady, New York 12345

Backward and forward subsynchronous instability has been observed in a flexible model test rotor under the influence of swirl flow in a straight-through labyrinth packing. The packing pressure drop at the onset of instability was then measured for a range of operating speeds, clearances and inlet swirl conditions.

The trend in these measurements for forward swirl and forward instability is generally consistent with the short packing rotor force formulations of Benchert and Wachter[1].

Diverging clearances were also destabilizing and had a forward orbit with forward swirl and a backward orbit with reverse swirl.

A larger, stiff rotor model system is now being assembled which will permit testing steam turbine-type straight-through and hi-lo labyrinth packings. With calibrated and adjustable bearings in this new apparatus, we expect to be able to directly measure the net destabilizing force generated by the packings.

INTRODUCTION

Destabilizing packing force measurement obtained by integrating circumferential and axial pressure distributions have been reported by several investigators[1,2,3,4] and serve to calibrate various analytical packing force prediction methods[5,6,7,8]. One investigator[9] Wright has reported success in making direct force measurements on a rotor system and in separating the destabilizing cross coupled direct force from the viscous damping forces.

To demonstrate the importance of inlet swirl in the generation of destabilizing packing forces, a rotor packing model with very simple instrumentation was built and tested in our laboratory. With inlet swirl velocities greater than packing surface speed and in the same direction, the rotor became unstable at its first critical speed. Shaft rotation was reversed and the rotor again became unstable with about the same pressure drop across the packing. In this case, however, the subsynchronous orbit continued rotating in the direction of inlet swirl opposing the direction of shaft rotation.

We then modified the packing model and with additional instrumentation, carried out a limited test program to measure the pressure and flow conditions which would cause instability with

alternate packing designs. These tests have the virtue that both direct and damping forces are physically integrated by the rotor. They have the disadvantage that, with the bearings and instrumentation used in this program, we could not quantify the level of the destabilizing force nor could we separate the direct from the damping forces to make comparisons with published data.

Discussion of Initial Test Results

Figure 1 shows the assembled rotor/labyrinth facility. The two flexible air hoses are independently valved to permit either forward or backward swirl without changing shaft rotation. By opening both valves together the inlet velocities are essentially cancelled and a test condition of negligible swirl exists. While the preliminary tests had used a single admission with reversed motor rotation to get backward swirl, the two admission modification greatly simplified the test procedure and analysis.

Figures 2 and 3 show the rotor and labyrinth components of this facility. Air is admitted to the central plenum through the tangential inlets. Pitot tubes installed in the plenum measured the swirl velocity. Two static pressure taps are also located in the inlet plenum.

The first series of tests were to determine if there was a strong rotational speed dependency. As shown by Figure 4, we did not find any. In future test programs we will measure the bearing dynamic characteristics over the speed range so that we can learn if the apparent larger packing forces at low speed is a real effect.

A typical vibration spectrum at the onset of instability is displayed on Figure 5 for a backward swirl. Filtered synchronous and subsynchronous orbits were simultaneously displayed and forward and backward orbits were easily distinguished. Figure 6 shows this display for the typical backward swirl condition.

Figure 7 shows some particularly interesting data. Both forward and reverse admission valves were fully opened to the shop air supply. The plenum chamber built up to 15 psia and the rotor remained "stable" by previous criteria. When the instrument gain was increased by 10X, a non-synchronous orbit was observed at about 15 Hertz, sometimes rotating in the synchronous direction sometimes against.

The initial tests were run at .010 radial clearance on all the teeth. The packing casing was then disassembled without disturbing the rotor and bearings, and the clearances were enlarged in a diverging geometry from .010" at the packing inlet to .020 mils at the exit. The third and last test of the clearance series was with the clearances further enlarged to a cylindrical .020" clearance. The data for the six test conditions are show on Figure 8. Since there has been much conjecture about the "stabilizing" effect of diverging clearance, special attention was given to the diverging test condition. In addition to the usual visual examination of orbits on the CRT, analysis of the signal confirmed that the

subsynchronous orbit with diverging clearance packings was in the same direction as inlet swirl and, in all respects, the diverging 10/20 mil clearance case behaved like an intermediate clearance between 10 and 20 mils.

The raw data is misleading in indicating a lower critical pressure, hence, a higher level of instability- as clearances are increased. This effect is related to our test model, since as clearances are increased the inlet velocity also increases and this increases inlet swirl. Benchert and Wachter's[1] short packing formula shows packing force increasing proportionally with inlet pressure and inlet swirl energy. Using average tangential velocities from our pitot data and the referenced force formulation, we have corrected the raw trend line of Figure 7 to a constant inlet swirl condition.

A further test was carried out to assess the effect of swirl, independent of clearance. The labyrinth packing casing was modified with temporary nozzle liners in the inlets and tests were repeated at the .010 mil clearance but now with higher nozzle inlet velocities. The results of these tests are shown on Figure 9 and confirm the strong correlation between destabilizing force and inlet swirl velocity.

PROPOSED TEST PROGRAM

As noted earlier, it was not possible to obtain a quantitative determination of destabilizing forces contributed by the packings because the flexible shaft and the unknown and asymmetrical cross coupling stiffness forces of the cylindrical bearings. In a future series of tests, this problem will be remedied by using a stiff test rotor supported on tilting pad bearings with adjustable, isotropic calibrated stiffness and damping characteristics. A picture of the test facility is shown in Figure 10.

This facility was originally designed for dynamic testing of bearings but is being modified by replacing the midspan test bearing with an appropriate labyrinth test seal and by installing the special isotropic support bearings. A schematic of the test rig is shown in Figure 11. Air is introduced into a central plenum, passes through the labyrinth and exhausts to atmosphere at either end. Various seal configurations and clearances will be tested. The air in the plenum will be introduced with controlled and measured swirl.

The tilting pad support bearings are mounted on springs having a stiffness value of approximately 2.3×10^4 lb/in. Two pads at each end of the rotor are oriented at 45° from vertical, resulting in isotropic stiffness and damping characteristics; i.e., vertical and horizontal stiffness are the same. Use of tilting pads eliminates any destabilizing cross coupling stiffness coefficients from the bearings.

For such an isotropic system, the force balance at the threshold of instability is:

$$K_S = (B_b + B_s)\gamma$$

where K_S is the destabilizing cross coupling stiffness force generated by the test seal, B_b is the isotropic damping coefficient of the spring mounted support bearings, B_S is the damping coefficient of the seal and γ is the natural frequency of the rotor on its support bearings. Because the tilting pad bearings are mounted on springs whose stiffness is relatively low compared with the stiffness of the oil film between the pad and the rotor, the effective damping B_b of the oil film and support spring in series is quite low and may be varied by changing the vertical load imposed on the shaft as shown in Figure 12. Test procedures would establish a desired level of damping B_b in the test rig by imposing the appropriate load, bring the rotor up to the desired test speed, and then slowly increase the plenum pressure in the test seal up to the onset of whirl. The net destabilizing force from the seal, $(K_S - B_S)\gamma$, will then be determined from the equation above. Damping of the support bearings, B_b, can be determined either by measuring the exponential decay of shaft vibration induced by striking the test rotor or by measuring the response of the rotor to a known unbalance.

A recognized deficiency of the proposed testing is that it will not yield separate determination of K_S and B_S, but only a measurement of the net destabilizing effect of the seal. However, the tests will suffice to check the ability of various analyses to predict this overall destabilizing force permitting one to evaluate the usefulness of these analyses as design tools.

ACKNOWLEDGMENT

The authors acknowledge the substantial assistance of L. L. Bethel and S. K. Tung in all phases of this rotor stability investigation.

REFERENCES

1. Benchert, H.; and Wachter, J.: Flow Induced Spring Constants of Labyrinth Seals, I. Mech. E., Sept. 1980.

2. Leong, Y.; and Brown, R.: Circumferential Pressure Distribution in a Model Labyrinth Seal, NASA CP-2250, 1982, pp. 223-241.

3. Childs, D.; and Dressman, J.: Testing of Turbulent Seals for Rotordynamic Coefficients, NASA CP-2250, 1982, pp. 157-171.

4. Greathead, S.; and Slocombe, M.: Further Investigations into Load Dependent Low Frequency Vibration of the High Pressure Rotor on Large Turbo-Generators, I. Mech. E., Sept. 1980.

5. Iwatsubo, T.; et al.: Flow Induced Force of Labyrinth Seal, NASA CP-2250, 1982, pp. 205-222.

6. Murphy, B; and Vance, J.: Labyrinth Seal Effects on Rotor Whirl Instability, Proceedings I. Mech. E., 1980.

7. Kurohashi, M.; et al.: Spring and Damping Coefficients of Labyrinth Seals, Proceedings I. Mech. E., 1980.

8. Kostyuk, A.: Theoretical Analysis of Aerodynamic Forces in Labyrinth Glands of Turbomachines, Teploenergetika, 1972.

9. Wright, D. V.: Air Model Tests of Labyrinth Seal Forces on a Whirling Rotor, Eng. Power, Oct. 1978.

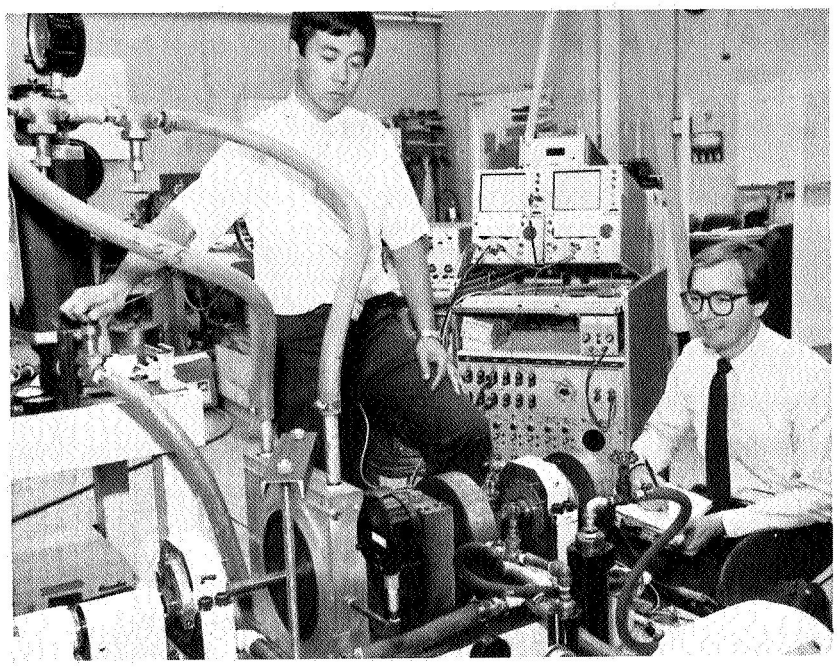

Figure 1. - Assembled rotor and labyrinth packing facility.

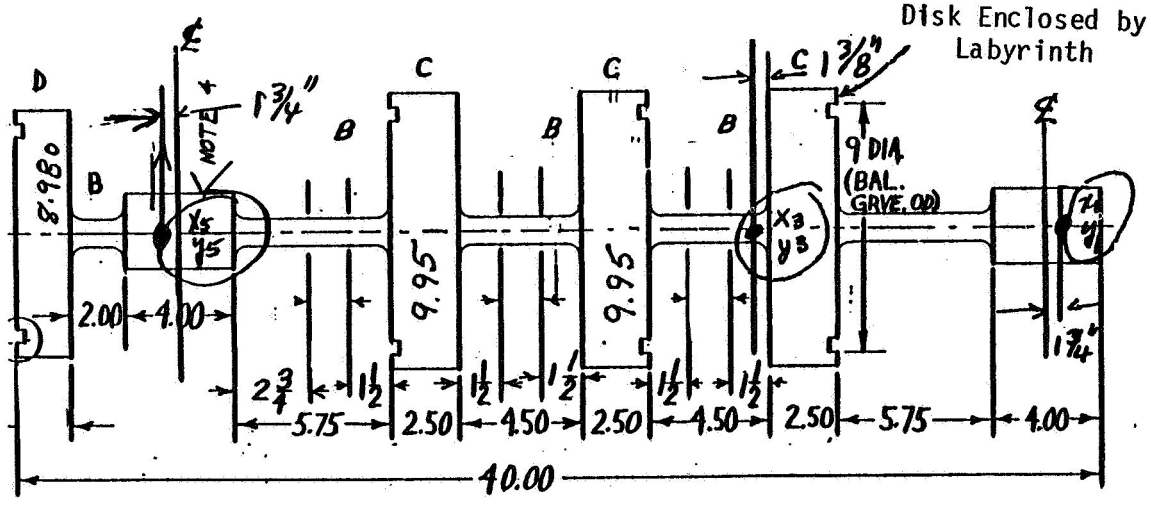

Figure 2. - Schematic of rotor for packing stability test.

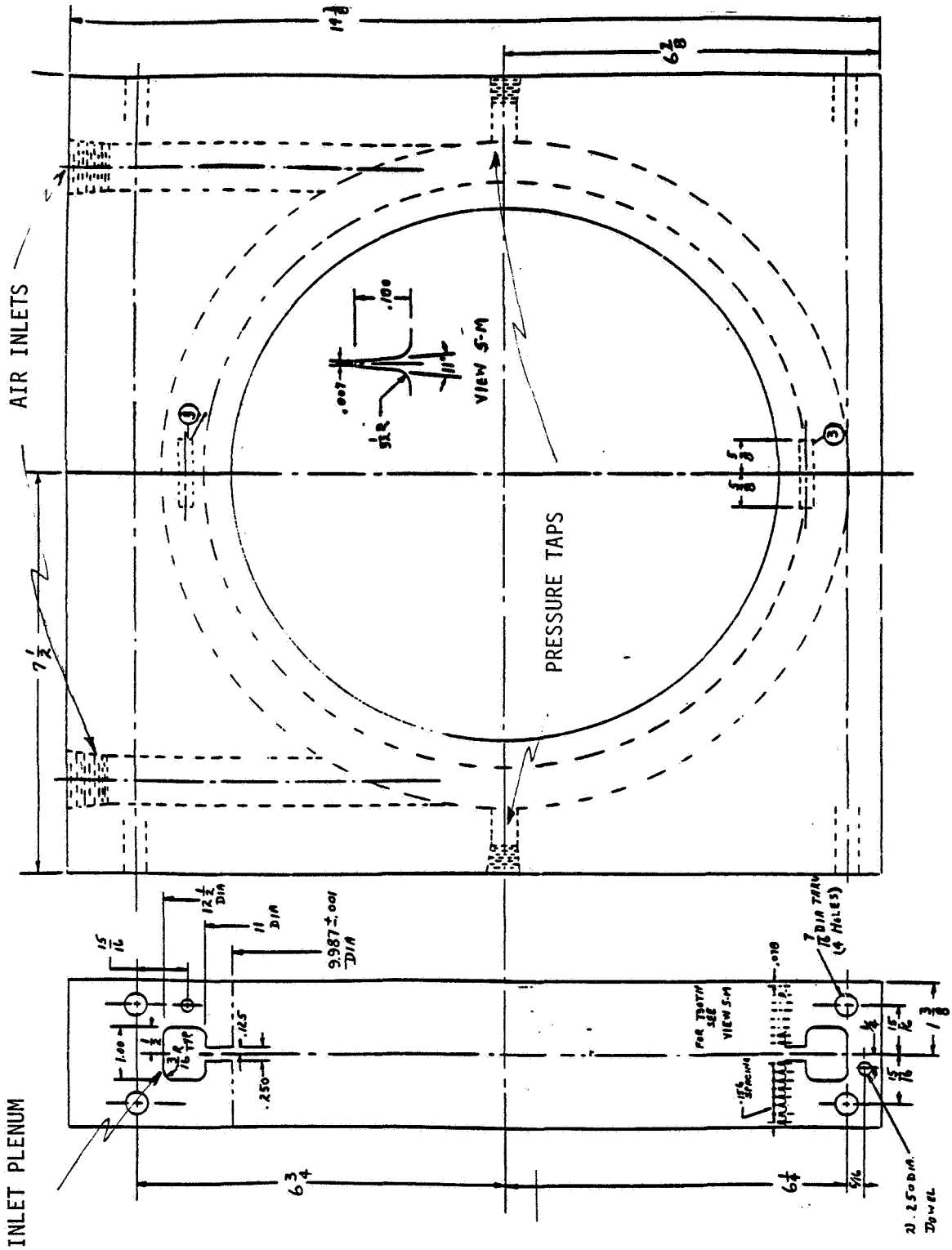

Figure 3. - Schematic of labyrinth for packing stability test.

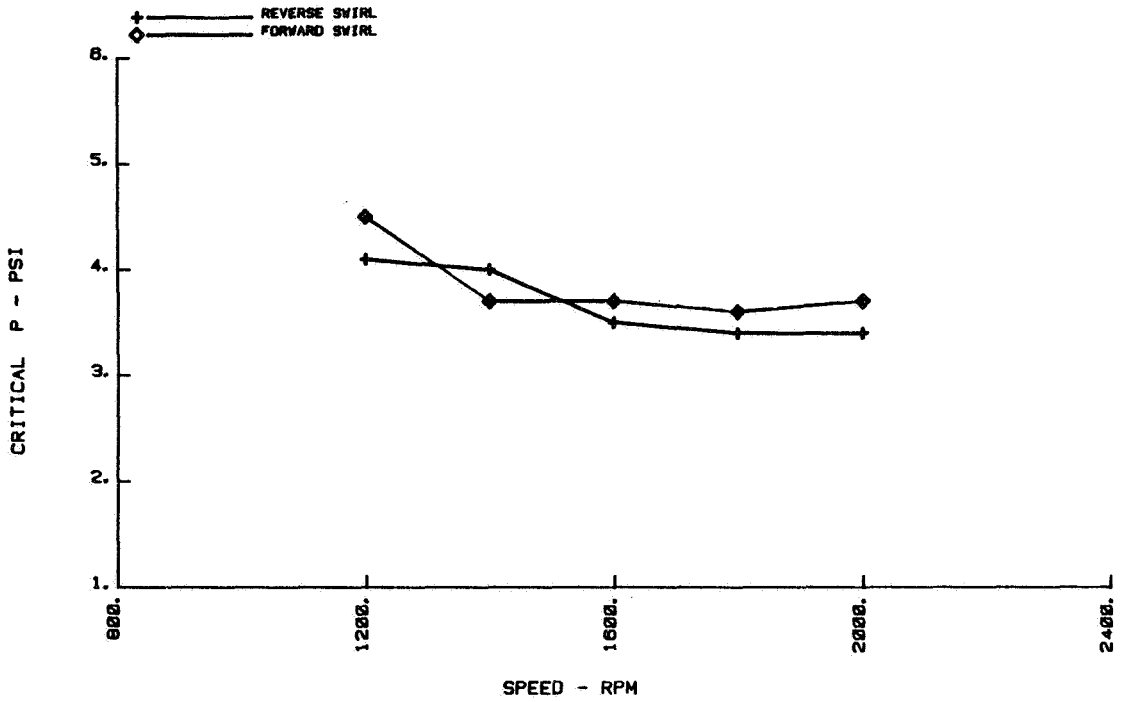

Figure 4. - Threshold pressure drop at various rotational speeds.

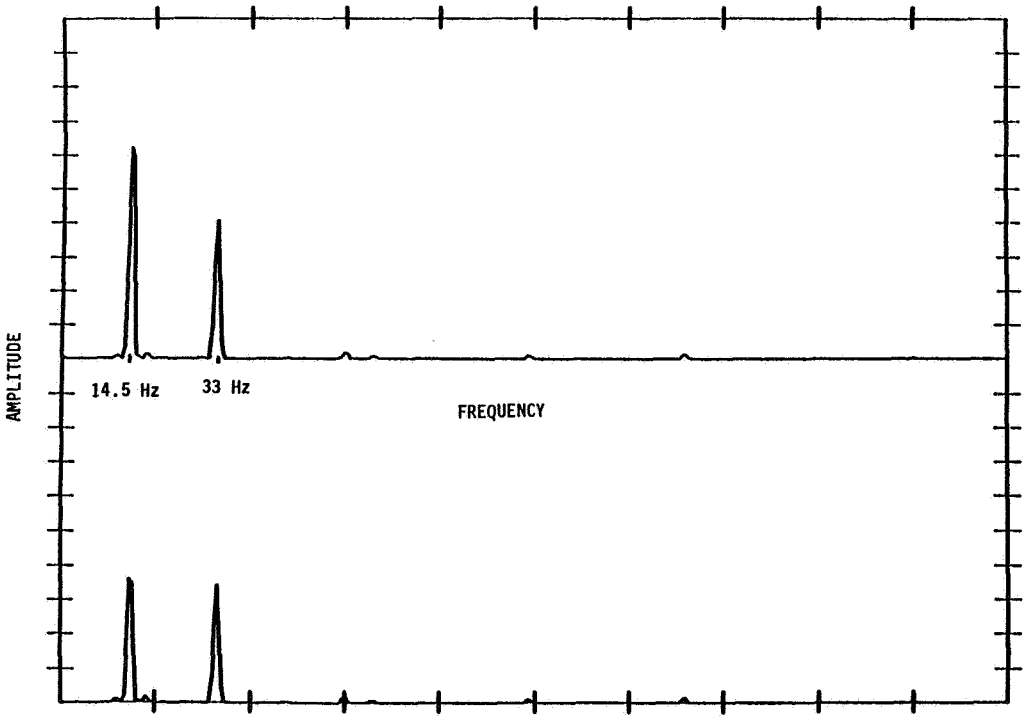

Figure 5. - Typical CCW admission vibration spectrum for packing stability test; CW rotation, 2000 rpm; 4 psi; CCW inlet.

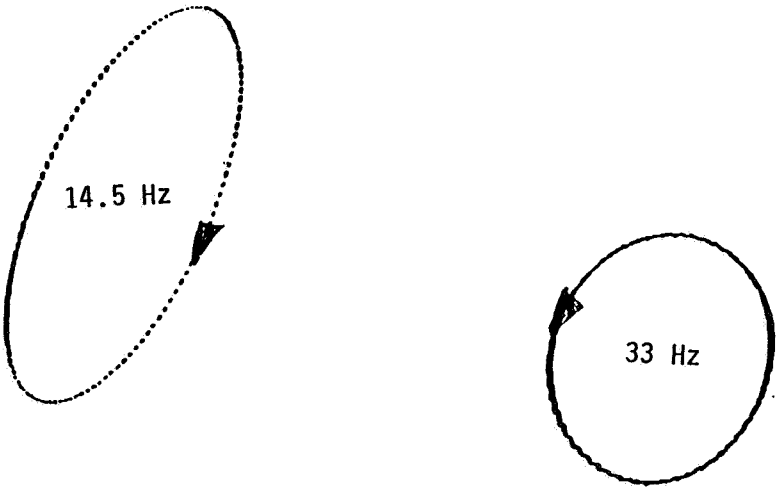

Figure 6. - Typical CCW admission orbits for packing stability test; CW rotation; 2000 rpm; 4 psi; CCW inlet.

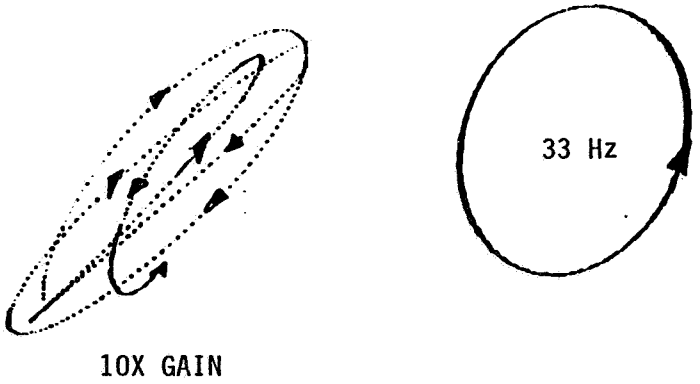

Figure 7. - CW and CCW admission orbits for packing stability test; CW rotation; 2000 rpm; 15 psi; both inlets fully open.

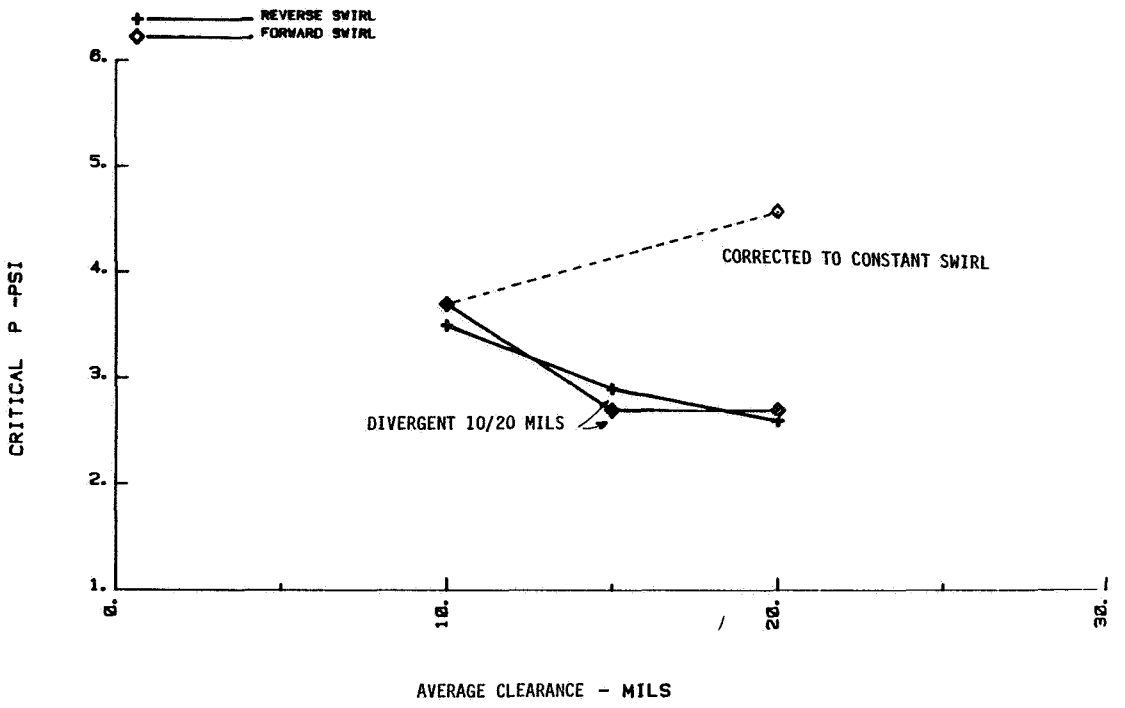

Figure 8. - Threshold pressure drop at various clearances. 1600 rpm.

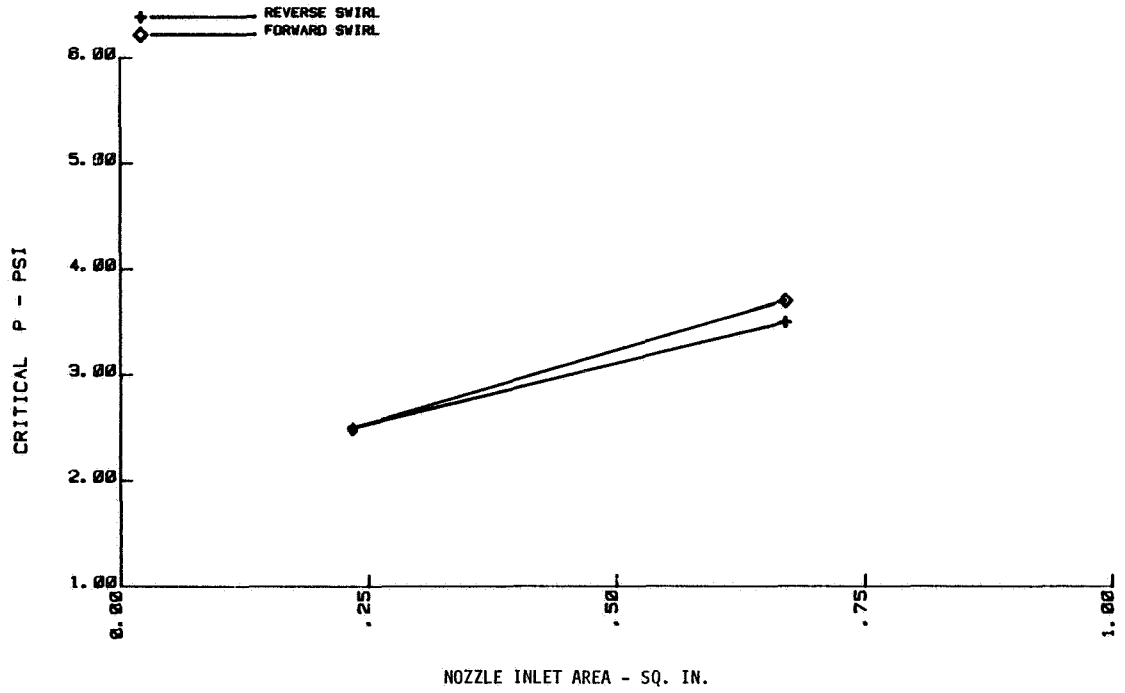

Figure 9. - Threshold pressure drop at alternate inlet areas. 1600 rpm.

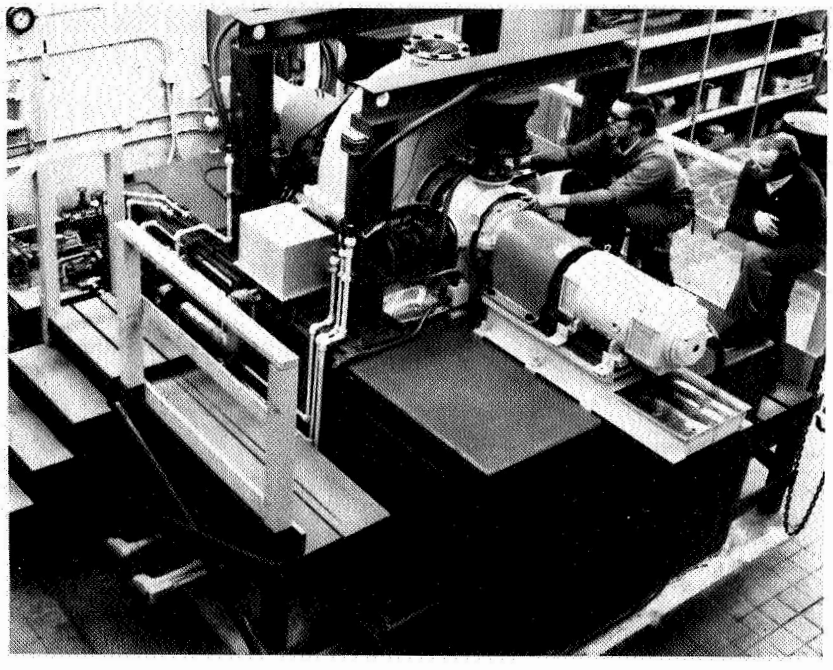

Figure 10. - Large-stiff-rotor labyrinth packing facility.

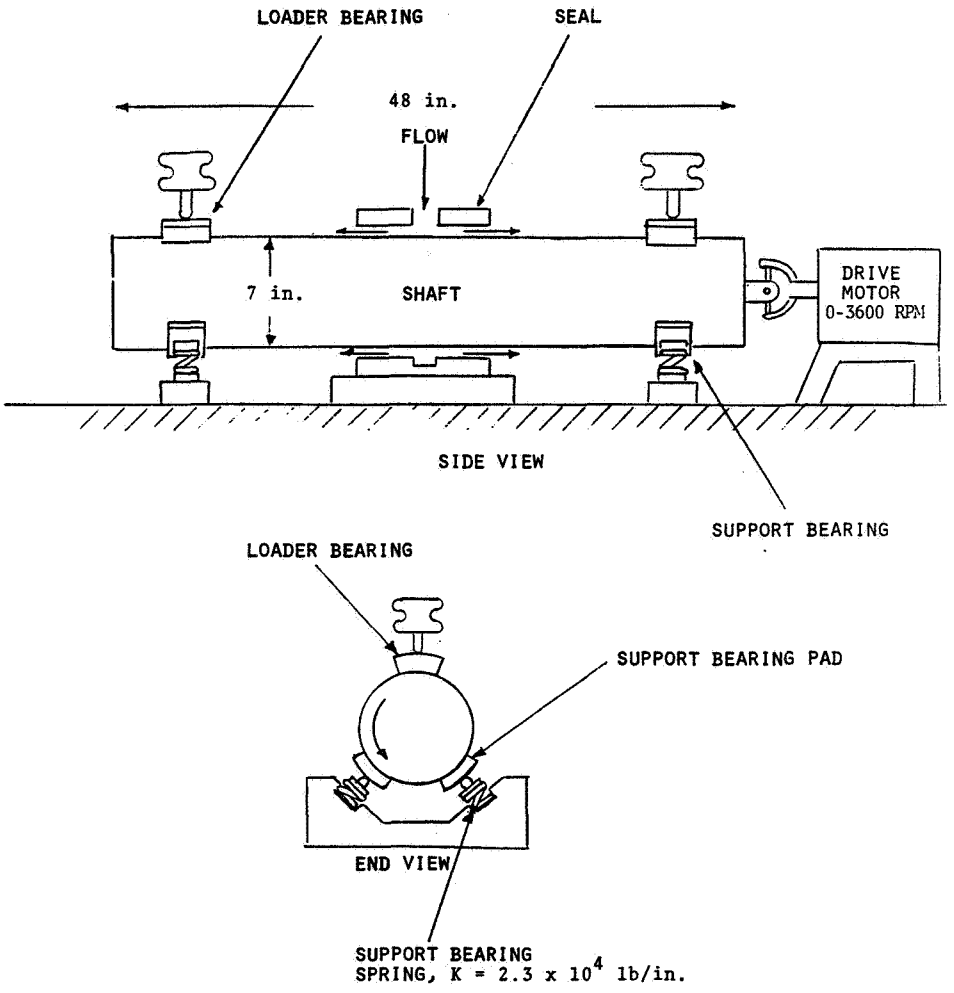

Figure 11. - Schematic of seal force test rig.

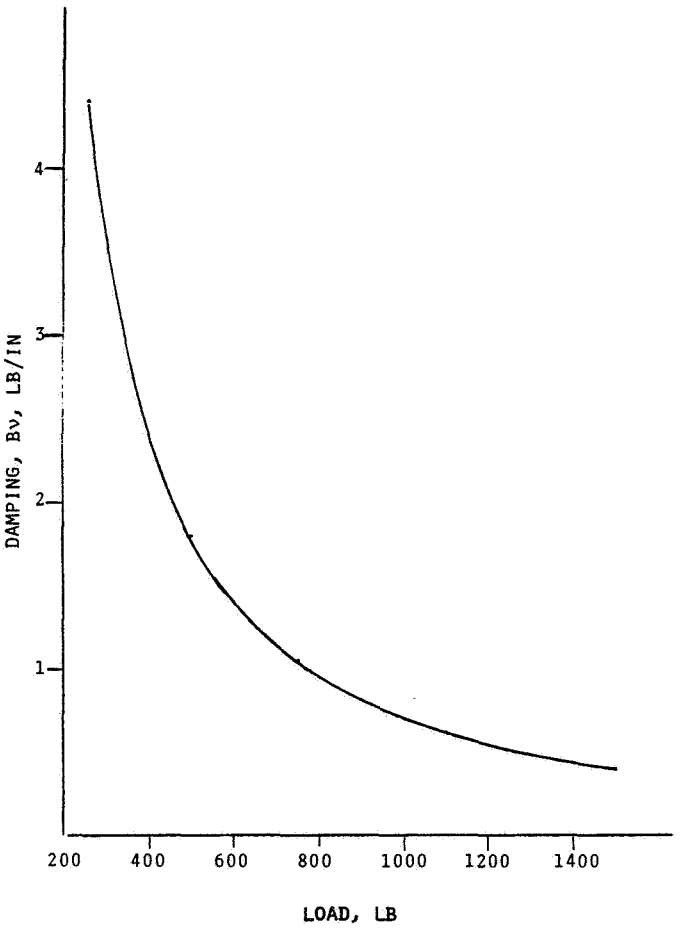

Figure 12. - Test rig damping at various bearing loads.

IDENTIFICATION OF DYNAMIC COEFFICIENTS OF ANNULAR TURBULENT SEALS

Rainer Nordmann and Harald Massmann
University of Kaiserslautern
Federal Republic of Germany

This paper presents an identification procedure to determine dynamic coefficients of annular turbulent seals in turbopumps. Measurements were carried out at a built test rig with two symmetrical arranged seals. A rigid rotating shaft is surrounded by an elastically supported housing, which is excited by impact forces. The relative radial motion between the rotating parts and the housing, respectively between the seal surfaces, is measured by displacement pick-ups and from the time signals complex frequency response functions can be calculated. Finally an analytical model, depending on the seal parameters, is fitted to the measured data, to find the dynamic coefficients.

INTRODUCTION

It is well known, that forces in annular pressure seals have a large influence on the vibrations of turbopump rotors. Therefore the knowledge about this forces is very important. In order to describe the real behavior of the seals, hydrostatic as well as hydrodynamic effects have to be considered (Ref. 1,2,3,4). Caused by this seal forces unstable bending vibrations may occur.

In the design stage a machine designer wants to know, whether a turbopump rotor will run stable during operation and what size the stability threshold speed will have. Precalculations should be carried out to evaluate the stability behavior. For this task in many cases a linear rotor model with inertia-, damping- and stiffness coefficients can be employed. It is no problem to find stiffness and inertia input data for the shaft. In contrary there is a uncertainty concerning the input data of seals.

Theoretical models exist to determine the required dynamic seal characteristics (Ref. 1,2,3,4), but there is a necessity to have more measured data to compare them with theoretical results and to modify existing seal models. In the case of turbulent seals in pumps only few experimental data are available today (Ref. 2,5,6,7). Childs and Dressman (Ref. 5) have developed a test facility for dynamic testing of straight and convergent tapered seals. Radial and tangential force components, resulting from a circular centered orbit, could be measured and the result were compared with various theoretical predictions. The circumferential forces are in a good correlation with the predictions of a finite length theory derived by Childs (Ref. 4). On the other hand the radial forces are underpredicted by this theory. Childs et al (Ref. 6) have designed another test rig for testing the leakage and rotordynamic characteristics of the interstage seal configurations for the High Pressure Fuel Turbopump (HPFTP) of the Space Shuttle Main Engine. In this test program the seals are geometrically similar to the HPFTP seals and are operating at the original high Reynolds numbers. Again in this test program it is planned to measure the seal forces directly.

In our paper an identification procedure is presented to determine the inertia-, damping- and stiffness coefficients of straight annular turbulent seals. A preliminary test facility has been developed consisting of a very stiff rotating shaft, which is surrounded by an elastically supported housing. Two symmetrical seals are arranged between the shaft and the housing and water flows axially across these two seals. The housing is excited by impact forces, resulting in a relative radial motion between rotor and housing, respectively between the seal surfaces. The measured input and output time signals are transformed to the frequency domain and complex frequency response functions are obtained, expressing the dynamic behavior of the seals including the mass of the housing. To find the dynamic seal coefficients an analytical model, depending on the seal parameters, is fitted to the measured data.

First measurement results are reported in this paper, pointing out the dependence of the seal dynamic coefficients on the rotational frequency and the axial velocity of the fluid in the seals.

DYNAMIC COEFFICIENTS OF ANNULAR TURBULENT SEALS

Black (Ref. 1) was the first, who has developed a dynamic model for short annular pressure seals. In this model he considers

- a turbulent leakage flow in axial direction caused by a pressure drop
- a circumferential fluid flow as a consequence of the shaft rotation
- and small radial motions of the rotor about a centered position (fig. 1)

With the basic equation of continuity, the momentum equation and the friction law for the fluid Black obtains the following linear force-motion relationship, expressed by inertia-, damping- and stiffness coefficients

$$-\begin{bmatrix} F_y \\ F_z \end{bmatrix} = \begin{bmatrix} m_{yy} & 0 \\ 0 & m_{zz} \end{bmatrix} \cdot \begin{bmatrix} \ddot{y} \\ \ddot{z} \end{bmatrix} + \begin{bmatrix} c_{yy} & c_{yz} \\ c_{zy} & c_{zz} \end{bmatrix} \cdot \begin{bmatrix} \dot{y} \\ \dot{z} \end{bmatrix} + \begin{bmatrix} k_{yy} & k_{yz} \\ k_{zy} & k_{zz} \end{bmatrix} \cdot \begin{bmatrix} y \\ z \end{bmatrix} \tag{1}$$

The equations are based on the leakage relation from Yamada (Ref. 8) for flow between concentric rotating cylinders

$$\Delta p = (1 + \xi + 2\sigma) \cdot \frac{\rho V^2}{2} \tag{2}$$

with

Δp	pressure difference across the seal
ξ	entry loss coefficient; $\xi = 0.5$ in the whole text
ρ	fluid density
V	average fluid velocity in axial direction

The friction loss coefficient σ is defined as

$$\sigma = \lambda \frac{L}{\Delta R} \tag{3}$$

with the seal length L, the radial clearance ΔR and the friction factor

$$\lambda = 0{,}079 \cdot Ra^{-1/4} \left[1 + \left(\frac{7R_r}{8R_a}\right)^2\right]^{3/8} \tag{4}$$

This factor depends on the radial as well as the axial Reynolds numbers

$$R_a = \frac{2V\Delta R}{\nu} \qquad R_r = \frac{R\Omega\Delta R}{\nu} \tag{5}$$

R	seal radius
Ω	rotational speed of the rotor
ν	kinematic viscosity of the fluid

It is shown in Black's analysis that the dynamic coefficients of equation (1) can be represented in the following form

Inertia coefficients:

$$m_{yy} = m_{zz} = \pi \, R \, \Delta \, p \cdot \mu_2 T^2/\lambda \tag{6}$$

Damping coefficients:

$$\begin{aligned} c_{yy} &= c_{zz} = \pi \, R \, \Delta \, p \cdot \mu_1 T/\lambda \\ c_{yz} &= -c_{zy} = \pi \, R \, \Delta \, p \cdot \mu_2 \Omega T^2/\lambda \end{aligned} \tag{7}$$

Stiffness coefficients:

$$\begin{aligned} k_{yy} &= k_{zz} = \pi \, R \, \Delta \, p \cdot (\mu_o - \mu_2 \Omega^2 T^2/4)/\lambda \\ k_{yz} &= -k_{ty} = \pi \, R \, \Delta \, p \cdot \mu_1 \Omega T/2\lambda \end{aligned} \tag{8}$$

They are dependent on the pressure difference Δp, the seal radius R, the friction factor λ, the rotational speed Ω, the average flow time T = L/V and finally on the quantities μ_o, μ_1, μ_2, which depend on the friction loss coefficient σ and the entry loss coefficient ξ (Ref. 2). Black's classical formulas correspond to short seals. An extension to finite length seals is possible by using correction terms, which had been determined by measurements (Ref. 2). Changes of λ for the circumferential direction as a fact of the radial shaft displacements are corrected by another factor.

Child (Ref. 3,4) has derived expressions for the dynamic coefficients of high pressure annular seals. In his analysis he assumes completely developed turbulent flow in both the circumferential and axial directions. His model is based on Hirs turbulent lubrication equations (Ref. 9). The short seal dynamic coefficients, derived by Childs (Ref. 3) are similar to the previous mentioned solutions from Black. In addition to Black's formulas the influence of an inlet swirl can be calculated. Childs (Ref. 4) has continued his analysis by deriving expressions for finite length seals. For use in the rotordynamic analysis of pumps the Hirs based models from Childs are the best currently available models.

IDENTIFICATION OF THE DYNAMIC SEAL COEFFICIENTS

The test rig, used for the experimental determination of the dynamic seal coefficients, consists of a very stiff rotating shaft and an elastically mounted rigid housing with two symmetric seals between rotor and housing (fig. 2). The housing is excited by test forces (input signal) and the system response is a relative motion between housing and shaft (output signal). From measured input and output signals mobility frequency response functions can be calculated. Finally an identification method, working in the frequency domain, is applied to the measurement data. It is possible to model a linear mechanical system corresponding to the real test rig. It consists of a rigid mass (housing) and the stiffness and damping coefficients of the seals. We assume that the equations of the model are known, but that the unknown parameters (seal coefficients) have to be determined. This can be done by a procedure requiring a good correlation between measured frequency response functions and analytical frequency response functions (fig. 3).

Mechanical and Mathematical Model

Fig. 4 shows the mechanical model with a rigidly supported very stiff shaft, the rigid mass m of the housing and the stiffness and damping elements corresponding to the seals, respectively to the flexible spring supporting the casing. Other forces acting on the housing, e.g. forces of the pipes, forces of the additional seals etc. are considered to be small. Applying test forces in the middle of the housing, the system responds only with translatory motion in the two directions y and z. The displacements can be described by the movements of the centre of gravity. The equations of motion for the model are

$$\begin{aligned} m\cdot\ddot{y} + 2(m_{yy}\cdot\ddot{y} + c_{yy}\cdot\dot{y} + c_{yz}\cdot\dot{z} + k_{yy}\cdot y + k_{yz}\cdot z) &= F_y \\ m\cdot\ddot{z} + 2(m_{zz}\cdot\ddot{z} + c_{zy}\cdot\dot{y} + c_{zz}\cdot\dot{z} + k_{zy}\cdot y + k_{zz}\cdot z) &= F_z \end{aligned} \tag{9}$$

With harmonic test forces, acting in both directions, four stiffness frequency functions as well as four mobility frequency functions can be calculated.
If the exciter forces are

$$\begin{aligned} F_y &= \hat{F}_y\cdot\sin\omega t = \hat{F}_y\cdot\mathrm{Im}(e^{i\omega t}) \\ F_z &= \hat{F}_z\cdot\sin\omega t = \hat{F}_z\cdot\mathrm{Im}(e^{i\omega t}) \end{aligned} \tag{10}$$

the system response has the form

$$\begin{aligned} &y = \mathrm{Im}(\hat{y}\cdot e^{i\omega t}), \quad z = \mathrm{Im}(\hat{z}\cdot e^{i\omega t}) \\ &\hat{y},\ \hat{z} \text{ complex amplitudes} \end{aligned} \tag{11}$$

and we obtain the force-displacement relation

$$2 \cdot \begin{bmatrix} k_{yy} - (\frac{m}{2} + m_{yy})\omega^2 + i\omega c_{yy} & k_{yz} + i\omega c_{yz} \\ k_{zy} + i\omega c_{zy} & k_{zz} - (\frac{m}{2} + m_{zz})\omega^2 + i\omega c_{zz} \end{bmatrix} \cdot \begin{bmatrix} \hat{y} \\ \hat{z} \end{bmatrix} = \begin{bmatrix} \hat{F}_y \\ \hat{F}_z \end{bmatrix} \qquad (12)$$

The inverse functions of (12) are the complex mobilities

$$\frac{1}{4\Delta} \cdot \begin{bmatrix} k_{zz} - (\frac{m}{2} + m_{zz})\omega^2 + i\omega c_{zz} & -(k_{yz} + i\omega c_{yz}) \\ -(k_{zy} + i\omega c_{zy}) & k_{yy} - (\frac{m}{2} + m_{yy})\omega^2 + i\omega c_{yy} \end{bmatrix} \cdot \begin{bmatrix} \hat{F}_y \\ \hat{F}_z \end{bmatrix} = \begin{bmatrix} \hat{y} \\ \hat{z} \end{bmatrix} \qquad (13)$$

$$\Delta = \{k_{yy} - (\frac{m}{2} + m_{yy})\omega^2 + i\omega c_{yy}\} \cdot \{k_{zz} - (\frac{m}{2} + m_{zz})\omega^2 + i\omega c_{zz}\}$$

$$- \{k_{yz} + i\omega c_{yz}\} \cdot \{k_{zy} + i\omega c_{zy}\}$$

Measurements of the Mobility Frequency Response Functions

Contrary to the complex stiffness functions (12) the mobility functions (13) are easy to measure. For the determination of these functions from measured input and output time data, we take advantage of the fact, that the ratios of the Fourier transformed signals are equal to the frequency responses. The force and response signals are measured in the time domain, transformed to the frequency domain by means of Fast Fourier Transformation and the quotient is calculated. This procedure is executed by efficient two-channel Fourier Analyzers. Fig. 5 Shows in principle the measuring equipments. The system is excited by a hammer impact, which is equal to an impuls force acting on the housing as a broadband excitation. Pulse duration, frequency content and force amplitude can be influenced by the variation of the hammer mass, the flexibility of the impact cap and the impact velocity. The relative displacements between housing and shaft are measured with inductive pick-ups. The time signals are amplified, digitized by the Fourier Analyzer and the frequency response functions are calculated. A bus system transfers the measured data to a digital computer, where an identification procedure calculates the unknown seal coefficients.

Estimation of the Dynamic Seal Coefficients

Different possibilities exist to determine the dynamic seal coefficients from the measured mobility response functions. The first idea is to fit analytical response functions to the measured ones. This can be done either directly with the flexibility functions or after the inversion of the measured curves, with the stiffness functions.

Another method will be presented in this paper. From a theoretical point of view the product of the complex mobility matrix $\underline{H}_{kin}$ (eq. 13) and the complex stiffness matrix $\underline{K}_{kin}$ (eq. 12) should be the unity matrix $\underline{E}$. By combining the measured matrix $\underline{H}_{kin}$ with the analytical Matrix $\underline{K}_{kin}$ the result will be $\underline{E}$ and an additional error matrix $\underline{S}$ because of measurement errors (noise, etc).

$$\underline{K}_{kin} \cdot \underline{H}_{kin} = \underline{E} + \underline{S} \tag{14}$$

or, with

$$\underline{K}_{kin} = \underline{K} - \omega^2 \underline{M} + i\omega \underline{C} \tag{15}$$

$$[\underline{K} - \omega^2 M + i\omega \underline{C}] \cdot \underline{H}_{kin} = \underline{E} + \underline{S} \tag{16}$$

The last formula can be rearranged to

$$\begin{aligned} &\text{real part:} && \underline{K}\,\underline{H}^{r}_{kin} - \omega^2 \underline{M}\,\underline{H}^{r}_{kin} - \omega\,\underline{C}\,\underline{H}^{i}_{kin} = \underline{E} + \underline{S}^{r} \\ &\text{imaginary part:} && \underline{K}\,\underline{H}^{i}_{kin} - \omega^2 \underline{M}\,\underline{H}^{i}_{kin} + \omega\,\underline{C}\,\underline{H}^{r}_{kin} = \underline{0} + \underline{S}^{i} \end{aligned} \tag{17}$$

respectively

$$\underline{A}\,\underline{X} = \underline{E}' + \underline{S}' \tag{18}$$

where $\underline{A}$ consists of the measured frequency response functions and of the related frequencies ω_i, $\underline{X}$ represents the unknown coefficients $\underline{M}$, $\underline{C}$ and $\underline{K}$, and $\underline{E}'$is a modified unity matrix with some zero elements because of the seperation of the complex values into two real values. Applying the Euclidean norm to this equation $\underline{S}'$shall become minimal. In practice there will be carried out a matrix multiplication from the left with the transpose matrix of $\underline{A}$.
By this we find the so-called normal equations, a determined system of equations for the unknown seal coefficients.

$$\underline{A}^{T} \underline{A}\,\underline{X} = \underline{A}^{T} \underline{E}' \tag{19}$$

In our case, measuring four frequency functions, the product $\underline{A}^{T}\underline{A}$ is a 6 x 6 matrix and $\underline{X}$ and $\underline{A}^{T}\underline{E}'$ are 6 x 2 matrixes. No assumptions are made in the procedure concerning the special structure of the matrices (skewsymmetry etc.). The advantages of the described algorithm are the fast calculation of the seal coefficients and the minimal requirement of storage space. Preliminary simulations have shown the practicability of this method.

DESCRIPTION OF THE TEST RIG

Mechanical and Hydraulic Design

Two annular sealing surfaces, integrated symmetrically in a stiff housing are the core parts of our testing plant (fig. 2). A shaft, rotating without contact inside the housing, is the second component of the seals. The fluid, in our case water, streams trough these radial clearances in an axial direction primarly. There is one central water supply for both seals and two drains, one for each. With this arrangement the housing cannot be displaced axially and we will measure only a translatorial, no rotational, movement of the casing in the radial direction if the geometries of the seals are identical. The shaft itself is resistant to bending and supported by rigid bearings. Shaft, motor and bottom-plate form the reference system for measuring the motion of the housing (mass m = 14.5 kg) which is fastened with soft springs to the fixed system. The necessary connections between both parts of the test rig are dimensioned in such a way that their influences are small compared with the seal behaviour.

Beside the mechanical component of the test stand we have the hydraulic part. A centrifugal pump (maximal throughput: q_{max} = 4.5 m^3/h) feeds water out of a reservoir into the system. Filter and slide values regulate the flow and the temperature of the water to make sure a steady state system. Through flexible hose pipes the water runs into and out of the housing.
With the geometrical values:

length of the seal:	L =	35 mm,
radius of the shaft:	R_s =	21.o mm,
radius of the housing:	R_h =	21.35 mm,
clearance of the seal:	ΔR =	$R_h - R_s$ = 350 µm,

the range for the number of revolutions U = 0...6000 1/min and the range for the fluid velocity in the seal V = 0...13.5 m/sec, the characteristical Reynolds numbers, R_a and R_r can be varied

R_a = 0....11 800 $\qquad$ R_r = 0....5 800

if the fluid temperature is 30°C (this temperature is used in every measurement). These ranges are restricted to

R_a = 7000....11 800 $\qquad$ (V = 9.o...13.5 m/sec)
R_r = 2400.... 5 800 $\qquad$ (U = 2500...6000 1/min)

in order to guarantee the turbulent region of flow in the seals. By changing the water temperature there will be available a different working range because of the temperature sensitivity of the kinematical viscosity ν.

Measured Quantities and Instrumentation

Three different groups of measuring values can be distinguished

- data of the fluid
- data of the exciter
- response data of the housing.

Pressure, temperature, density and viscosity characterize the fluid state. If working with an incompressible medium it is sufficient to measure pressure and temperature as the only variables of state and calculate the others.
Therefore several pressure - and temperature pick-ups are distributed over the test plant. Furthermore the fluid velocity is measured in the supply-line and the shaft speed is displayed by the motor control. With this, all necessary data in order to calculate the seal coefficients, are available. The excitation force of the hammer blow is measured with a piezoelectric accelerometer mounted in the hammer hed and a charge amplifier. The greatest forces obtainable are 120 N to 150 N. The third group of data belongs to the motion of the housing relative to the shaft. Inductive pick-ups with a carrier wave amplifier registrate the distance between shaft and housing contactlessly. Two working planes with two orthogonal measurement directions permit the control of the housing's displacements (translatorial, rotatorial).

The present data of the force and displacement as a function of the time are transformed to the frequency domain by a digital spectrum analyzer which calculates the transfer functions (ratio of displacement to force in the frequency domain) and stores them on tape. The identification of the system parameters $\underline{M},\underline{C},\underline{K}$ itself is carried out by a desktop computer with the stored data.

Previous Tests

In order to get to know the behaviour of the test rig itself without any "seal effects" several static tests had been performed: a constant load had been applied to the housing and the related movement had been measured, some kind of stiffness determination. When doing this without shaft rotation and fluid velocity (no seal effect), the stiffness of the system, that are the stiffness of the bolt springs, of the inlet and outlet pipes, of the instrument leads and so on, is measurable (fig. 6). We found a linear force-displacement relation, which differs for the four directions ($\pm$ y, $\pm$ z) but in general we found a stiffness of the set-up of about $5 \cdot 10^4$ N/m for the y and the z directions. This is an additional term similar to the mass of the housing which has to be taken into consideration while calculating the diagonal elements of the stiffness matrix.

Increasing the axial flow while the shaft speed is still zero, caused an increase of the system's stiffness which coincided quite well with the pre-calculated values from the models of Black (Ref. 1,2) and Childs (Ref. 3) (table 1). The constant error of those measurements could be a systematical one and consequently it could cause some problems in identifying the stiffness coefficients out of a dynamic measurement.

MEASUREMENTS OF THE DYNAMIC COEFFICIENTS

Measurement Procedure

Every measurement set consists of four frequency response functions H_{ik} (input direction k = y, z; response direction i = y, z). As described above our input data result from multiple successive impact signals (in order to reach a high energy level) of an optimized hammer which renders possible an excitation only for a linear seal behaviour. Force and response (distance between shaft and housing as a function of time) signals are measured simultaneously and later on processed in a digital fourier analyzer. The data set, obtained in this way, describes a single working condition of the test system, i.e. fluid velocity, fluid temperature and shaft speed are constant. To get the following results and dependences, only one parameter will be varied during one series of measurements. The temperature and with this the viscosity will be constant for all measurements and equal to $30^{o}C$.

By the way, at the moment we are measuring four frequency response functions in order to confirm the skew-symmetrical character of the frequency response matrix, but later on the expenditure of measurements could be probably reduced to two functions.

A desktop computer with a medium storage capacity takes over the subsequent treatment of the stored data. A program which contains the identification procedure itself ($\underline{H} \cdot \underline{K} = \underline{E}$) and an in-core solver for this determinante equation with respect to the unknown coefficients of the seal, calculates the parameters and, with the help of these, the fitted frequency response functions. Both functions, measurement and curve fit, can be displayed and plotted so we can estimate the quality of our curve fit algorithm visually. Furthermore the parameters $\underline{M}$, $\underline{C}$, $\underline{K}$ as functions of fluid velocity and shaft speed are reproduced by approximate equations which are polynominal equations whose order had been found in comparison with theoretical curves calculated with the above mentioned models and a least square method's optimization.

Presentation and Discussion of some Results

The described process is demonstrated for one working condition: V = 12.0 m/sec, U = 3000 min^{-1}, T = $30^{o}C$, in order to understand the results discussed later. Figure 7 shows the measured H_{ik}, plotted as magnitude and phase of the complex values, and the analytical frequency response functions too. The correlation of measured and analytical data is more or less good. Especially the additional peak in H_{yy} surprise. Furthermore the signal to noise ratio was expected to be better.

The resultant matrices of the seal coefficients can be read in fig. 8. As mentioned before the values for the complete system with two seals and all additional terms (mass of the housing, soft springs etc.) are presented. It can be seen, that the main diagonal elements are not equal, furthermore the expected skewsymmetry could not be found in the measured results. This is one result of a series of measurements, which point out the influence of the shaft rotation while the axial velocity is constant. The values of the whole series for constand axial fluid velocity V = 12 m/sec are drawn in fig. 9. The coefficients which should be equal in magnitude, when following the theory, are shown in one diagram and treated as two values for the same operating condition. Besides the measured coefficients fig. 9 points out the

corresponding values of the above mentioned theoretical models (Ref. 1,3). There is partly a good correlation, especially for the inertia and damping values. Even the traces of curves of the stiffnesses are similar to the theory, but here the values for k_{yy}, k_{zz} are found out 30 % to 40 % too small. The worst case we find for the cross-coupled stiffnesses k_{yz}, k_{zy}. Differences are possible up to 90 % of the theoretical values.

How can we explain and then correct this problem?
Suppose there is an inlet swirl of the water streaming through the inlet chamber, i.e. the fluid has an axial and, that's important, a circumferential velocity at the beginning of the seal. Applying the theory of Childs (Ref. 3) to our test system with a negative inlet swirl (the senses of rotation of the shaft and of the fluid are different), so the stiffness terms could reduce remarkably. On the other hand the cross-coupled dampings are influenced also very clearly. The problem at the moment is how to determine this inlet swirl and to decide whether or not it is constant with the shaft speed. Some experiments done with the contrary sense of rotation for the shaft, in that case an inlet swirl should change its sign and should effect the coefficients in some different manner, we got stiffness-values slightly different to the first results, but not as much influenced as expected!
We suppose: our test rig doesn't agree with the two-degree-of-freedom model which was described earlier in the paper. When looking at fig. 7 the two transfer functions H_{yy} and H_{zy} show a particularity, a break-down in magnitude at about 12 to 14 Hz only by exciting in the y direction. Also the coherences arent't good at all at this frequencies. That characteristic can be found in almost every measurement. In order to eliminate its reason we looked at the whole system and measured a vibration belonging to a motion of the complete test rig at that critical frequency. It's a vibration of the system on the flexible connections between itself and the environment in the y-direction. This causes a motion of the "fixed" reference system during our measurements. An expanded mathematical model for the test set-up (three degrees of freedom) points out a reduction of the stiffness elements. This may be an explanation for the small stiffness values in the measurements. To avoid this problem, a modification of the test rig supports will be carried out.

Fig. 10 points out the influence of the axial velocity V. At first some remarks to the theoretical values. If we increase the axial velocity the seal coefficients will increase too, except the inertia term. Two cases appear: the increasement of velocity results in a parallel shift of the k_{yy}, k_{zz}, c_{yy}, c_{zz} curves or the gradient rises for k_{yz}, k_{zy}.
Now let's look at the measurements. The statements form above are transferable very well. Even the absolute shift values of k_{yy}, k_{zz} and c_{yy}, c_{zz} are agreeing. The difference of the main stiffness element between V = 10.5 m/sec and V = 12.5 m/sec calculated for the measurements is $7 \cdot 10^4$N/m and for the theory $6 \cdot 10^4$N/m.
The main damping values aren't as constant as predicted but the difference between them of about 250 N/msec is comparable with theoretical results.

The cross-coupled stiffness element is very small but we find, that the main aspect, greater gradients for higher velocities, is right. The cross-coupled damping is approximately a linear function of the shaft speed but there is hardly an influence of the velocity. This fact and the numerical values confirm the annular seal models.
Finally no influence of the axial velocity can be seen for the inertia term, which is also in good correlation with the theory.
After a modification of our test rig further examinations will follow and we hope to obtain new results for the dynamic seal coefficients.

REFERENCES

1. Black, H.F., "Effects of Hydraulic Forces in Annular Pressure Seals on the Vibrations of Centrifugal Pump Rotors", I.M. Eng. Sci., Vol. 11, No. 2, pp. 206-213, 1969

2. Black, H.F. and Jensen, D.N., "Dynamic Hybrid Properties of Annular Pressure Seals", Proc. J. Mech. Engin., Vol. 184, pp. 92-100, 1970

3. Childs, D.W., "Dynamic Analysis of Turbulent Annular Seals Based on Hirs' Lubrication Equation", Journal of Lubrication Technology, ASME-Paper No. 82-Lub 41, 1982

4. Childs, D.W., "Finite Length Solutions for Rotordynamic Coefficients of Turbulent Annular Seals", Journal of Lubrication Technology, ASME-Paper No. 82-Lub 42, 1982

5. Childs, D.W. and Dressman, J.B., "Testing of Turbulent seals for Rotordynamic Coefficients", NASA Conference Publication 2250, Rotordynamic Instability Problems of High Performance Turbomachinery, Proceedings of a workshop held at Texas A&M University, 10-12 May 1982, pp. 157-171, 1982

6. Childs, D.W. et al, "A High Reynolds Number seal Test Facility: Facility Description and Preliminary Test Data", NASA Conference Publication 2250, Rotordynamic Instability Problems of High Performance Turbomachinery, Proceedings of a workshop held at Texas A&M University, 10-12 May 1982, pp. 172-186

7. Iino, T. and Kaneko, H., "Hydraulic Forces by Annular Pressure Seals in Centrifugal Pumps", NASA Conference Publication 2133, Rotordynamic Instability Problems of High Performance Turbomachinery, Proceedings of a workshop held at Texas A&M University, 12-14 May 1980, pp. 213-225, 1980

8. Yamada, Y., "Resistance of Flow through an Annulas with an Inner Rotating Cylinder", Bull. J. S.M.E., Vol. 5, No. 18, 1962, pp. 302-310

9. Hirs, G.G., "Fundamentals of a Balk-Flow Theory for Turbulent Lubrication Films", Ph. D. dissertation, Delft Technical University, The Netherlands, July 1970.

TABLE I. - STATIC STIFFNESS VALUES FOR U = 0 1/min

shaft speed [1/min]	axial velocity [m/sec]	measured K [N/m]	theoretical K [N/m]	Error [%]
0.0	7.5	132 500	164 000	-19.8
	9.0	171 800	208 000	-17.4
	10.5	216 000	270 000	-19.8
	12.0	266 600	330 000	-19.4
	13.5	308 100	390 000	-21.0

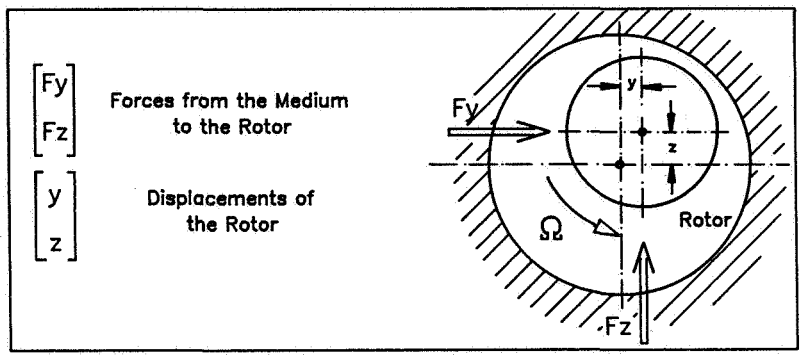

Figure 1. - Black's annular seal model.

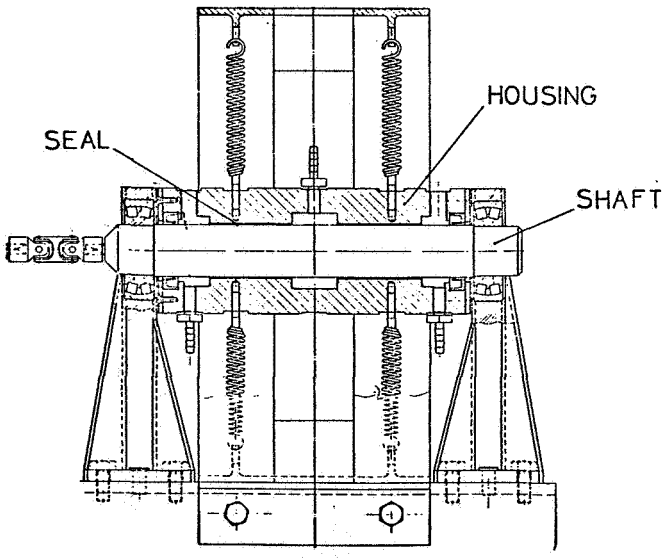

Figure 2. - Test rig.

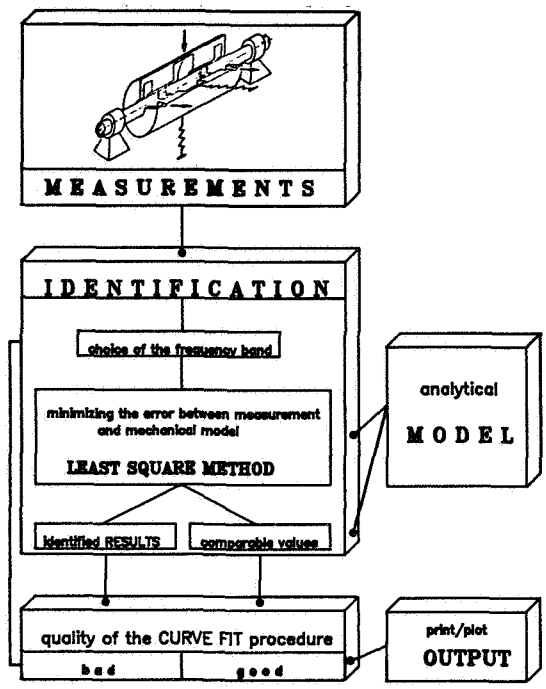

Figure 3. - Identification procedure.

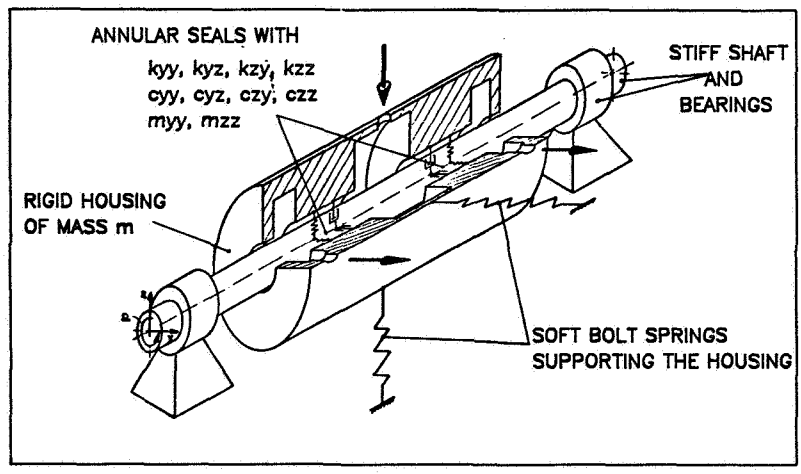

Figure 4. - Mechanical model of test rig.

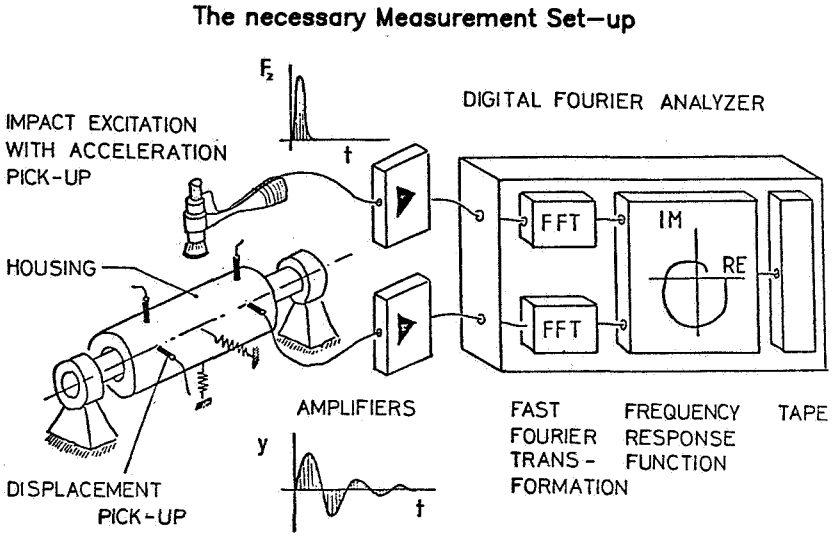

Figure 5. - Necessary measurement set-up.

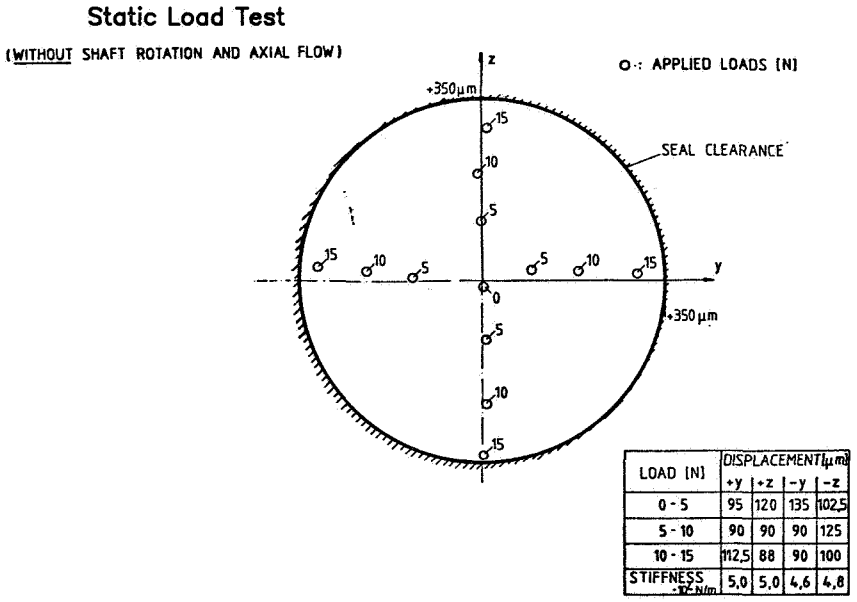

Figure 6. - Static load test (without shaft rotation and axial flow).

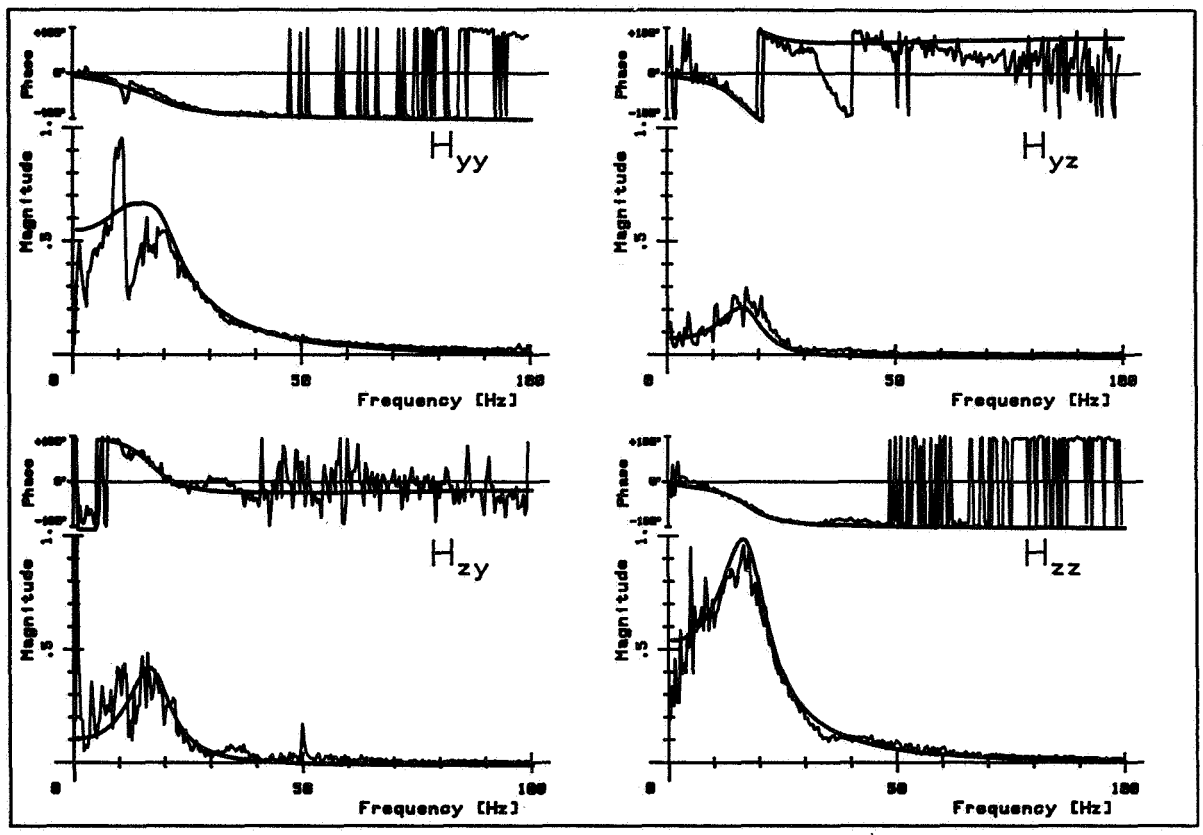

Figure 7. - Complete set of frequency response functions for U = 3000 1/min, V = 12.0 m/sec, and T = 30° C.

Fluidal and geometrical values:

Length of the Seal: 35 mm
Radius of the Seal: 21 mm
Radial Clearance: 0.35 mm

Pressure drop: 2.23 bar
Fluid Velocity: 12.03 m/sec
Rev. of the shaft: 3000 1/min

Temperature: 30.0°C
Density: 995 kg/m^3
Viscosity: 8.0E-7 m^2/sec

Reynolds-radial: 2 887
Reynolds-axial : 10 530

Representation of the identified SEAL-PARAMETERS

Inertia matrix [kg]

$$\begin{bmatrix} +16.40 & -0.70 \\ +1.82 & +19.40 \end{bmatrix}$$

Damping matrix [N/msec]

$$\begin{bmatrix} +1\,560 & -240 \\ +854 & +1\,100 \end{bmatrix}$$

Stiffness matrix [N/m]

$$\begin{bmatrix} +197\,000 & -33\,300 \\ +47\,200 & +210\,000 \end{bmatrix}$$

Figure 8. - Numerical results for example in figure 7.

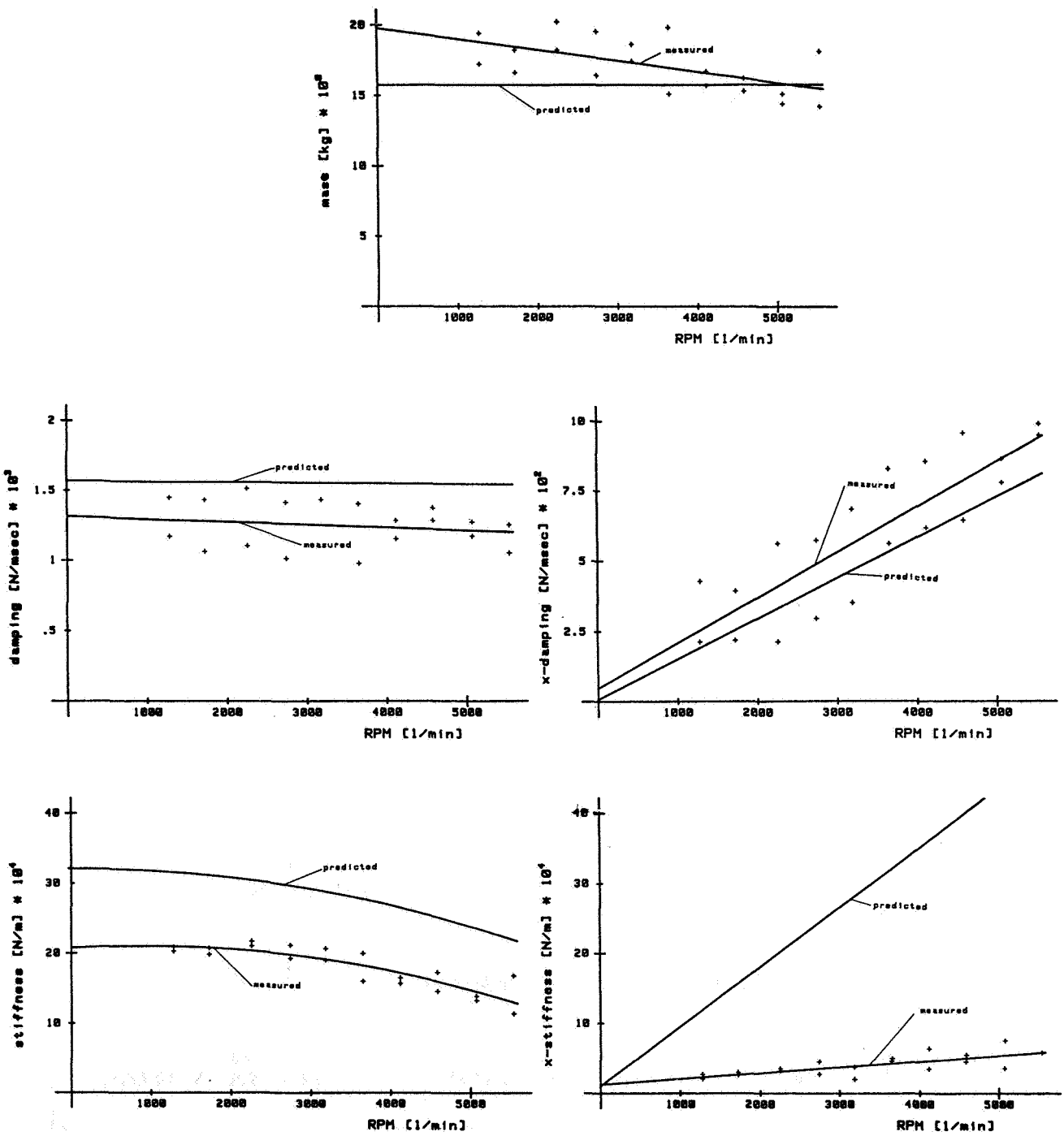

Figure 9. - Theoretical and experimental results for V = 12.0 m/sec and T = 30° C.

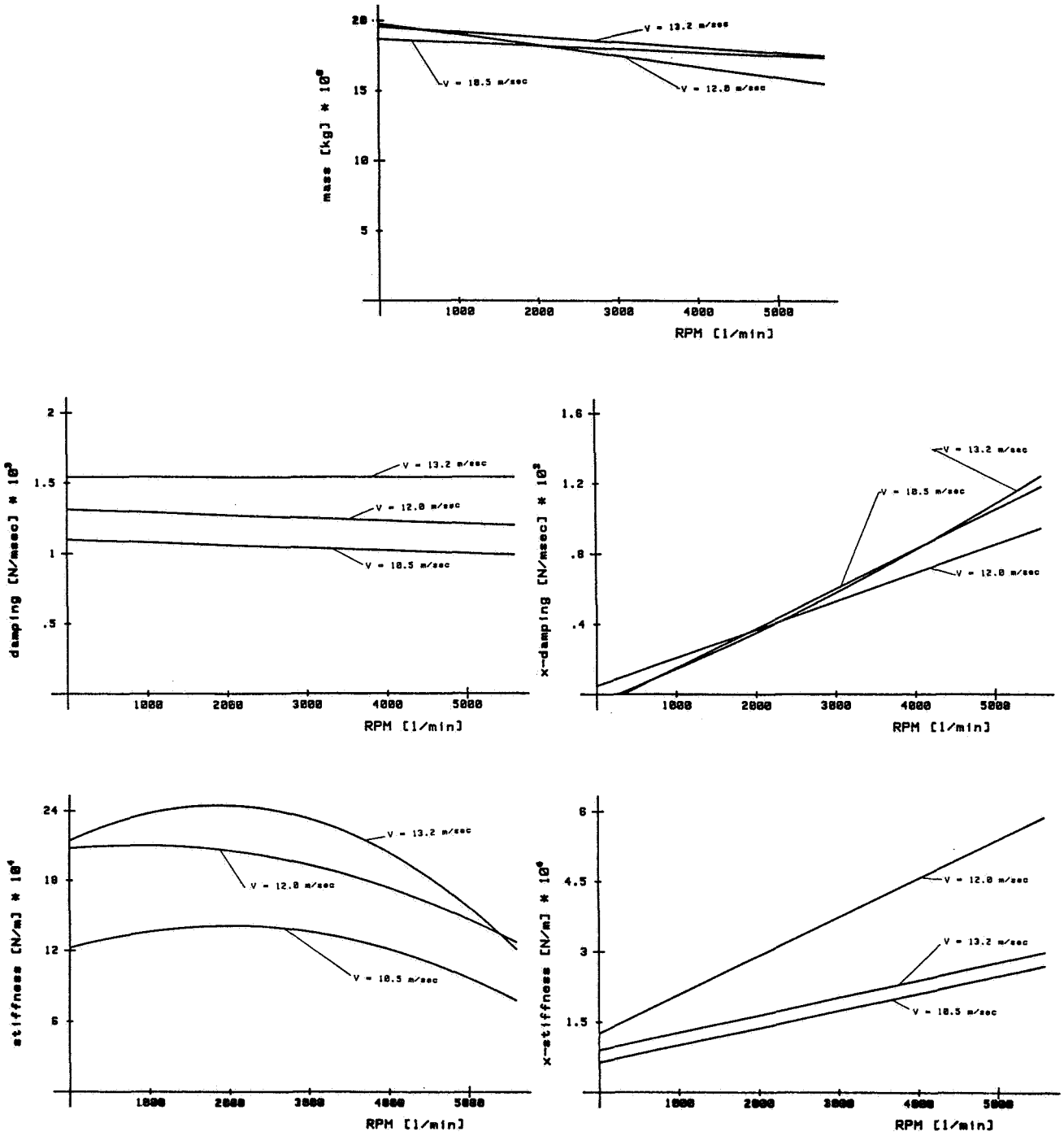

Figure 10. - Fitting curves of identified coefficients for V = 10.5, 12.0 and 13.2 m/sec.

ANALYSIS AND TESTING FOR ROTORDYNAMIC COEFFICIENTS OF TURBULENT ANNULAR SEALS WITH DIFFERENT, DIRECTIONALLY HOMOGENEOUS SURFACE-ROUGHNESS TREATMENT FOR ROTOR AND STATOR ELEMENTS*

D. W. Childs and Chang-Ho Kim
Texas A&M University
College Station, Texas 77843

A combined analytical-computational method is developed to calculate the transient pressure field and dynamic coefficients for high-pressure annular seal configurations which may be used in interstage and neck-ring seals of multistage centrifugal pumps. The solution procedure applies to constant-clearance or convergent-tapered geometries which may have different (but directionally-homogeneous) surface-roughness treatments on the stator or rotor seal elements. It applies in particular to so-called "damper-seals" which employ smooth rotors and deliberately-roughened stator elements to enhance rotor stability.

Hirs' turbulent lubrication equations are modified slightly to account for different surface-roughness conditions on the rotor and stator. A perturbation analysis is employed in the eccentricity ratio to develop zeroth and first order perturbation equations. The zeroth-order equations define both the leakage and the development of circumferential flow due to shear forces at the rotor and stator surfaces. The first-order equations define perturbations in the pressure and axial and circumferential velocity fields due to small relative motion between the seal rotor and stator. The solution applies for small motion about a centered position and does not employ linearization with respect to either the taper angle or the degree of swirl, i.e., the difference between the circumferential velocity at the given axial position and the asymptotic circumferential-velocity solution.

Test results for four different surface-roughness confirm the predicted net damping increase for "damper seals". A round-hole-pattern stator yielded the highest net damping and lowest leakage of all seals tested. The seals are substantially stiffer than predicted, but the theory does an adequate job of predicting net damping.

NOMENCLATURE

a_i	Dimensionless coefficients defined in Appendix A
$\tilde{c}$, $\tilde{C}$	Dimensionless damping coefficients defined by Eq. (34)
$f(z)$	Dimensionless clearance function defined by Eq. (9)

*The results reported herein were partially supported by NASA Contract NAS8-33716 from the George C. Marshall Space Flight Center; Contract Monitor Frank Garcia.

$h(z) = H/\overline{C}$	Dimensionless clearance function
h_1	First-order perturbation clearance function defined by Eqs. (11) and (18)
$\widetilde{k}$, $\widetilde{K}$	Dimensionless seal stiffness coefficients defined by Eq. (34)
$\widetilde{m}$, $\widetilde{M}$	Dimensionless mass coefficients defined by Eq. (34)
ms, ns mr, nr	Dimensionless empirical turbulence coefficients for stator and rotor
p	Fluid pressure (F/L^2)
$\widetilde{p} = p/\rho\overline{V}^2$	Dimensionless fluid-pressure introduced in Eq. (7)
$\widetilde{p}_o$, $\widetilde{p}_1$	Dimensionless fluid-pressure perturbations introduced in Eq. (11)
q	Taper-angle parameter defined in Eq. (10)
t	Independent variable time (T)
$u_Z = U_Z/\overline{V}$ $u_\theta = U_\theta/R\omega$	Dimensionless axial and circumferential velocity components introduced in Eq. (7)
$u_{\theta 0}$, $u_{\theta 1}$	Zeroth and first-order perturbations in u_θ
u_{Z0}, u_{Z1}	Zeroth and first-order perturbations in u_Z
$z = Z/L$	Dimensionless axial coordinate
A	Test orbit amplitude (L)
A_i	Dimensionless coefficients defined in Appendix A
$\overline{C}$	Nominal seal radial clearance, (L)
C_d	Seal discharge coefficients defined by Eq. (16)
C_0, C_1	Entrance and exit clearances, respectively, (L)
$H(z,\theta,t)$	Clearance function, illustrated in figure 2, and defined in Eq. (17), (L)
$H_o(z)$	Centered-clearance function defined by Eq. (9), (L)
L	Seal length (L)
P_s	Seal supply pressure (F/L^2)
ΔP	Nominal pressure-drop across seal (F/L^2)

R	Seal radius (L)
$R_a = 2\rho VH/\mu$	Axial Reynolds number
$R_{ao} = 2\rho\overline{VC}/\mu$	Centered-position, axial Reynolds number
$T = L/\overline{V}$	Transit time for a fluid element to traverse the seal
U_Z, U_θ	Axial and tangential bulk-flow fluid velocity components (L/T)
$V(z)$	Centered-position axial fluid velocity (L/T)
X, Y	Radial seal displacements (L)
Z, $R\theta$	Spatial coordinates illustrated in Figure 2
α	Seal taper angle illustrated in Figure 3
$\varepsilon = e/\overline{C}$	Seal eccentricity ratio introduced in Eq. (11)
$\hat{\varepsilon} = \hat{e}/2\overline{C}$	Relative roughness
ξ	Inlet pressure-loss coefficient
λ_s, λ_r	Dimensionless stator and rotor friction-factors defined in Eq. (15)
$\tau = t/T$	Dimensionless time
ω	Shaft angular velocity (T^{-1})
Ω	Shaft precessional velocity (T^{-1}), introduced in Eq. (22)

INTRODUCTION

Figure 1 illustrates the two seal types which have the potential for developing significant rotor forces. The neck or wear-ring seals are provided to reduce the leakage flow back along the front surface of the impeller face, while the interstage seal reduces the leakage from an impeller inlet back along the shaft to the back-side of the preceding impeller. Pump seals may be geometrically similar to plain journal bearings, but typically have clearance to radius ratios on the order of 0.005 as compared to 0.001 for bearings. Because of the clearances, and normally-experienced pressure differentials, fully-developed turbulent flow normally exists in pump seals.

As related to rotordynamics, analysis of seals has the objective of defining the reaction force acting on a rotor as a consequence of shaft motion. For small motion about a centered position, the relation between the reaction-force components and shaft motion may be expressed by

$$-\begin{Bmatrix} F_x \\ F_y \end{Bmatrix} = \begin{bmatrix} K & k \\ -k & K \end{bmatrix} \begin{Bmatrix} x \\ y \end{Bmatrix} + \begin{bmatrix} C & c \\ -c & C \end{bmatrix} \begin{Bmatrix} \dot{x} \\ \dot{y} \end{Bmatrix} + \begin{bmatrix} M & m \\ -m & M \end{bmatrix} \begin{Bmatrix} \ddot{x} \\ \ddot{y} \end{Bmatrix} \tag{1}$$

The off-diagonal coefficients in Eq. (1) are referred to as "cross-coupled" and arise due to fluid rotation within the seal. Seals, unlike plain journal bearings, develop significant direct stiffness values K in the centered, zero-eccentricity position due to the distribution between (a) inlet losses, and (b) the axial pressure gradient due to wall-friction losses. Lomakin [1] initially pointed out the phenomenon. Both analysis [2] and experiments [3] have shown the Eq. (1) holds for fairly large eccentricies on the order of 0.5; i.e., the dynamic coefficients tend to be relatively insensitive to changes in the static-eccentricity ratio.

Prior analytical and experimental developments have generally examined "smooth" seals where both stator and rotor elements of the seal are assumed to have the same nominally smooth surfaces. A review of the analytical and experimental developments for this type of seal is provided in references [4] and [5] and will not be repeated here. The subject of this investigation is the so-called "damper-seal" configuration recently proposed by von Pragenau [6], which employs a smooth rotor and a deliberately surface-roughened stator element. For the same surface roughness on the rotor and stator, the asymptotic, circumferential, bulk-flow velocity is $R\omega/2$ in the centered position because (a) the radial velocity distribution is assumed to be symmetrical about the midplane, and (b) the circumferential velocity is zero at the stator wall and $R\omega$ at the rotor wall. Von Pragenau's analysis demonstrates that the damper seal yields a lower asymptotic circumferential velocity which implies a reduction in the destabilizing cross-coupled stiffness coefficient k and a consequential improvement in rotordynamic stability.

Von Pragenau employs an approximate "short-seal" analysis to develop analytical expressions for the rotordynamic coefficients of constant clearance seals. The development of these analytical expressions is lengthy and difficult. The combined analytical-computational approach used in this development yields an exact numerical solution to the governing equations for both constant-clearance and convergent-tapered seals with significantly less labor. Following a slight modification to Hirs' [7] governing equation to account for different surface-roughness conditions on the rotor and stator, the analysis procedure is basically that of reference [4] and [5].

GOVERNING EQUATIONS

Figure 2 illustrates a differential element of fluid having dimensions $Rd\theta$, dz, and H (Z, θ, t). The upper and lower surfaces of the element correspond to the rotor and stator seal elements and have velocities of $R\omega$ and zero, respectively. The bulk velocity components of the fluid are U_θ and U_z; i.e., these are the averages across the fluid film height H of the circumferential and axial fluid velocities. The essence of Hirs' formulation is the definition of the wall shear stress τ_w as the following empirical function of the bulk flow velocity V_w relative to the wall

$$\tau_w = \rho \frac{V_w^2}{2} \text{ no } \left(\frac{2\rho V_w H}{\mu}\right)^{\text{mo}} = \rho \frac{V_w^2}{2} \text{ no } R_a^{\text{mo}} \tag{2}$$

The bulk flow velocities relative to the rotor and stator are, respectively

$$\underline{V}_r = (U_\theta - R\omega)\, \underline{\varepsilon}_\theta + U_z\, \underline{\varepsilon}_z$$

$$\underline{V}_s = U_\theta \underline{\varepsilon}_\theta + U_z\, \underline{\varepsilon}_z \tag{3}$$

Hence, the shear stress at the rotor and stator are

$$\tau_r = \rho \frac{V_r^2}{2} nr \left(\frac{2\rho V_r H}{\mu}\right)^{mr}$$
$$\tau_s = \rho \frac{V_s^2}{2} ns \left(\frac{2\rho V_s H}{\mu}\right)^{ms} \tag{4}$$

Hirs' formulation assumes that the surface roughness is the same on the stator and rotor; hence, the same empirical constants mo, no apply to both surfaces. The formulation of Eq. (4) accounts for different surface roughnesses in the seal elements via the empirical constants (mr, nr), (ms, ns) for the rotor and stator surfaces.

The components of wall shear surface stress in the Z and Rθ directions are

$$\tau_{r\theta} = \tau_r \ (U_\theta - R\omega) \ / V_r; \ \tau_{rZ} = \tau_r \ U_Z / V_r$$
$$V_r = [(U_\theta - R\omega)^2 + U_Z{}^2]^{\frac{1}{2}}$$
$$\tau_{s\theta} = \tau_s \ U_\theta / V_s, \ \tau_{sZ} = \tau_s \ U_Z / V_s \tag{5}$$
$$V_s = (U_\theta{}^2 + U_Z{}^2)^{\frac{1}{2}}$$

Summing forces in the Z and Rθ directions for the free-body diagram of figure 2 (b) yields the following momentum equations*:

$$-H \ \frac{\partial p}{\partial Z} = \frac{ns}{2} \rho \ U_Z{}^2 \ R_a{}^{ms} \left[1 + (U_\theta / U_Z)^2\right]^{\frac{ms+1}{2}}$$
$$+ \frac{nr}{2} \rho \ U_Z{}^2 \ R_a{}^{mr} \left\{1 + [(U_\theta - R\omega)/U_Z]^2\right\}^{\frac{mr+1}{2}} \tag{6a}$$
$$+ \rho \ H \left[\frac{\partial U_Z}{\partial t} + \frac{U_\theta}{R} \frac{\partial U_Z}{\partial \theta} + U_Z \frac{\partial U_Z}{\partial Z}\right]$$

$$-\frac{H}{R} \frac{\partial p}{\partial \theta} = \frac{ns}{2} \rho \ U_Z U_\theta \ R_a{}^{ms} \left[1 + (U_\theta / U_Z)^2\right]^{\frac{ms+1}{2}}$$
$$+ \frac{nr}{2} \rho \ U_Z (U_\theta - R\omega) \ R_a{}^{mr} \left\{1 + [(U_\theta - R\omega)/U_Z]^2\right\}^{\frac{mr+1}{2}} \tag{6b}$$
$$+ \rho \ H \left[\frac{\partial U_\theta}{\partial t} + \frac{U_\theta \partial U_\theta}{R \partial \theta} + U_Z \frac{\partial U_\theta}{\partial Z}\right]$$

The bulk-flow continuity equation is

$$\frac{\partial H}{\partial t} + \frac{1}{R} \frac{\partial (HU_\theta)}{\partial \theta} + \frac{\partial (HU_Z)}{\partial Z} = 0 \tag{6c}$$

*The continuity Eq. (6.c) has been used to simplify these momentum equations.

These equations may be nondimensionalized by introducing the following variables:

$$u_Z = U_Z/\overline{V},\ u_\theta = U_\theta/R\omega,\ \tilde{p} = p/\rho\overline{V}^2$$

$$h = H/\overline{C},\ \tau = t/T,\ z = Z/L \tag{7}$$

$$T = L/\overline{V},\ b = \overline{V}/R\omega$$

where $\overline{C}$ and $\overline{V}$ are the average clearance and axial velocity, respectively. The resultant equations are

$$-h\frac{\partial\tilde{p}}{\partial z} = \frac{ns}{2}\left(\frac{L}{\overline{C}}\right) R_a^{ms}\left[1+\left(\frac{u_\theta}{bu_z}\right)^2\right]^{\frac{ms+1}{2}} u_z^2 + \frac{nr}{2}\left(\frac{L}{\overline{C}}\right) R_a^{mr}\left[1+\left(\frac{u_\theta-1}{bu_z}\right)^2\right]^{\frac{mr+1}{2}} u_z^2 + h\left[\frac{\partial u_z}{\partial\tau} + u_\theta(\omega T)\frac{\partial u_z}{\partial\theta} + u_z\frac{\partial u_z}{\partial z}\right] \tag{8}$$

$$-b\left(\frac{L}{\overline{C}}\right) h\frac{\partial\tilde{p}}{\partial\theta} = \frac{ns}{2}\left(\frac{L}{\overline{C}}\right) R_a^{ms}\left[1+\left(\frac{u_\theta}{bu_z}\right)^2\right]^{\frac{ms+1}{2}} u_z u_\theta + \frac{nr}{2}\left(\frac{L}{\overline{C}}\right) R_a^{mr}\left[1+\left(\frac{u_\theta-1}{bu_z}\right)^2\right]^{\frac{mr+1}{2}} u_z(u_\theta-1) + h\left[\frac{\partial u_\theta}{\partial\tau} + u_\theta(\omega T)\frac{\partial u_\theta}{\partial\theta} + u_z\frac{\partial u_\theta}{\partial z}\right]$$

$$\frac{\partial h}{\partial\tau} + (\omega T)\frac{\partial(hu_\theta)}{\partial\theta} + \frac{\partial(hu_z)}{\partial z} = 0$$

PERTURBATION EQUATIONS

Seal Geometry

Figure 3 illustrates the geometry for a tapered seal. At the centered position, the clearance function is defined by

$$H_0(z) = \left(\overline{C} + \frac{\alpha L}{2}\right) - \alpha Z = [1 + q\ (1 - 2z)]\ \overline{C} = f\ \overline{C} \tag{9}$$

where α is the taper angle, and

$$\bar{C} = (C_0 + C_1)/2, \quad q = \frac{\alpha L}{2\bar{C}} = \frac{C_0 - C_1}{C_0 + C_1} \tag{10}$$

The parameter q is a measure of the degree of taper in a seal and varies from zero, for a constant-clearance configuration, to approximately 0.4 for a maximum-stiffness seal design [8].

Perturbation Analysis

The governing Eqs. (6) define the bulk-flow velocity components (u_θ, u_z) and the pressure, p, as a function of the spatial variables (Rθ, z) and time, t. An expansion of these equations in the perturbation variables

$$u_z = u_{z0} + \varepsilon\, u_{z1}, \quad h = h_0 + \varepsilon\, h_1$$

$$u_\theta = u_{\theta 0} + \varepsilon\, u_{\theta 1}, \quad \tilde{p} = \tilde{p}_0 + \varepsilon\, \tilde{p}_1 \tag{11}$$

where $\varepsilon = e/\bar{C}$ is the eccentricity ratio yields the following equations:

Zeroth-Order Equations:

(a) Axial-Momentum Equation

$$\frac{d\tilde{p}_0}{dz} = -\left[(a_{0s}\sigma_s + a_{0r}\,\sigma_r) + 4q\right]/2f^3 \tag{12a}$$

(b) Circumferential-Momentum Equation

$$\frac{du_{\theta 0}}{dz} = -\left[a_{0r}\,\sigma_r(u_{\theta 0} - 1) + a_{0s}\,\sigma_s\,u_{\theta o}\right]/2f \tag{12b}$$

(c) Continuity Equation

$$u_{z0} = 1/f \tag{12c}$$

First-Order Equations

(a) Axial-Momentum Equation

$$\frac{\partial \tilde{p}_1}{\partial z} = h_1 A_{1z} - u_{\theta 1} A_{2z} - u_{z1} A_{3z} - \left\{\frac{\partial u_{z1}}{\partial \tau} + (\omega T)\, u_{\theta 0}\frac{\partial u_{z1}}{\partial \theta} + \frac{1}{f}\frac{\partial u_{z1}}{\partial z}\right\} \tag{13a}$$

(b) Circumferential-Momentum Equation

$$b\left(\frac{L}{R}\right)\frac{\partial \tilde{P}_1}{\partial \theta} = h_1 A_{1\theta} - u_{\theta 1} A_{2\theta} - u_{z1} A_{3\theta} - \left\{ \frac{\partial u_{\theta 1}}{\partial \tau} + (\omega T)\, u_{\theta 0} \frac{\partial u_{\theta 1}}{\partial \theta} + \frac{1}{f}\frac{\partial u_{\theta 1}}{\partial z} \right\} \tag{13b}$$

(c) Continuity Equation

$$\frac{\partial u_{z1}}{\partial z} + (\omega T)\frac{\partial u_{\theta 1}}{\partial \theta} - \frac{2q}{f} u_{z1} = -\frac{1}{f}\left[\frac{2qh_1}{f^2} + (\omega T)\, u_{\theta 0}\frac{\partial h_1}{\partial \theta} + \frac{\partial h_1}{\partial \tau}\right] \tag{13c}$$

Most of the parameters of these equations are defined in Appendix A. The quanities σ_s, σ_r are defined by

$$\sigma_s = \left(\frac{L}{\bar{C}}\right)\lambda_s, \quad \sigma_r = \left(\frac{L}{\bar{C}}\right)\lambda_r \tag{14}$$

where the wall friction factors are defined by

$$\lambda_s = ns R_{a0}^{ms}\left(1 + \frac{1}{4b^2}\right)^{\frac{1+ms}{2}}, \quad \lambda_r = nr R_{a0}^{mr}\left(1 + \frac{1}{4b^2}\right)^{\frac{1+mr}{2}} \tag{15}$$

These expressions correspond to Yamada's [9] test correlation for flow between rotating annulli.

SOLUTION PROCEDURES

Zeroth-Order Equations

The zeroth-order equations define the steady-state leakage and the circumferential velocity development $u_{\theta 0}$ (z) due to wall shear. The governing equations, Eqs. (12), are coupled and nonlinear through the dependency of the coefficients a_{0r}, a_{0s}, $u_{\theta 0}$ and $\bar{V}$. The equations must be solved iteratively to determine the average leakage velocity $\bar{V}$ corresponding to a specified pressure drop ΔP and the circumferential velocity distribution $u_{\theta 0}$ (z). The resultant solution defines the leakage coefficient C_d of the leakage ΔP relationship

$$\Delta P = C_d \frac{\rho \bar{V}^2}{2} \tag{16}$$

The pressure drop at the entrance is defined by

$$\Delta P_0 = \frac{\rho \bar{V}^2}{2}\frac{(1+\xi)}{(1+q)^2}$$

where ξ is an entrance-loss coefficient which is generally on the order of 0.1 to 0.5.

First-Order Equations

The governing first-order equations define $p_1(z, \theta, \tau)$, $u_{z1}(z, \theta, \tau)$, and $u_{\theta 1}(z, \theta, \tau)$ resulting from the seal clearance functions $h_1(\theta, \tau)$. The clearance H is defined in terms of the components of the seal-journal displacement vector (X, Y) by

$$H = H_0 - X\cos\theta - Y\sin\theta \tag{17}$$

Hence, by comparison to Eq. (11),

$$\varepsilon h_1 = -x\cos\theta - y\sin\theta \tag{18}$$

where

$$x = X/\overline{C},\quad y = Y/\overline{C}$$

Note that h_1 is not a function of z, and its time dependency arises from the displacement variables x (t), y (t).

To satisfy circumferential continuity conditions, the following solution format is assumed:

$$\begin{aligned} u_{z1}(z, \theta, \tau) &= u_{z1C}(z, \tau)\cos\theta + u_{z1s}(z, \tau)\sin\theta \\ u_{\theta 1}(z, \tau, \theta) &= u_{\theta 1C}(z, \tau)\cos\theta + u_{\theta 1s}(z, \tau)\sin\theta \\ \tilde{p}_1(z, \theta, \tau) &= \tilde{p}_{1C}(z, \tau)\cos\theta + \tilde{p}_{1s}(z, \tau)\sin\theta \end{aligned} \tag{19}$$

Substituting from Eq. (19) into Eq. (13) eliminates θ as an independent variable, and yields six real equations. By introducing the complex variables

$$\begin{aligned} \hat{u}_{z1} &= u_{z1C} + j u_{z1s} \\ \hat{u}_{\theta 1} &= u_{\theta 1C} + j u_{\theta 1s} \\ \tilde{p}_1 &= \tilde{p}_{1C} + j\tilde{p}_{1s} \\ \frac{\hat{h}_1}{\varepsilon} &= \frac{x}{\varepsilon} + j\,\frac{y}{\varepsilon} \end{aligned} \tag{20}$$

into these equations, the following complex equations are obtained

$$\begin{aligned} -\frac{\partial \hat{p}_1}{\partial z} &= A_{1z}\left(\frac{\hat{h}_1}{\varepsilon}\right) + A_{2z}\,\hat{u}_{\theta 1} + A_{3z}\,\hat{u}_{z1} \\ &\quad + \frac{\partial \hat{u}_{z1}}{\partial \tau} - j\,(\omega T)\,u_{\theta 0}\,\hat{u}_{z1} + \frac{1}{f}\frac{\partial \hat{u}_{z1}}{\partial z} \\ j\,b\left(\frac{L}{R}\right)\hat{p}_1 &= A_{1\theta}\left(\frac{\hat{h}_1}{\varepsilon}\right) + A_{2\theta}\,\hat{u}_{\theta 1} + A_{3\theta}\,\hat{u}_{z1} \\ &\quad + \frac{\partial \hat{u}_{\theta 1}}{\partial \tau} - j\,(\omega T)\,u_{\theta 0}\,\hat{u}_{\theta 1} + \frac{1}{f}\frac{\partial \hat{u}_{\theta 1}}{\partial z} \end{aligned} \tag{21}$$

$$\frac{\partial \hat{u}_{z1}}{\partial z} - j\,(\omega T)\,\hat{u}_{\theta 1} - \frac{2q}{f}\,\hat{u}_{z1} = \frac{2q}{f^3}\left(\frac{\hat{h}_1}{\varepsilon}\right) - j\,\frac{(\omega T)}{f}\,u_{\theta o}\left(\frac{\hat{h}_1}{\varepsilon}\right) + \frac{1}{f}\,\frac{\partial}{\partial \tau}\left(\frac{\hat{h}_1}{\varepsilon}\right)$$

with the A_j coefficients defined in Appendix A. The time dependency in these equations is eliminated by assuming a harmonic seal motion of the form

$$\hat{h}_1 = \frac{R_o}{\bar{C}}\; e^{\,j\Omega t} = r_o e^{j\Omega T \tau} \tag{22}$$

where r_o is a <u>real</u> constant. The associated harmonic solution can then be stated

$$\begin{aligned} \hat{u}_{z1}\,(z,\,\tau) &= \bar{u}_{z1}\,(z)\; e^{j\Omega T\tau} \\ \hat{u}_{\theta 1}\,(z,\,\tau) &= \bar{u}_{\theta 1}\,(z)\; e^{j\Omega T\tau} \\ \hat{p}_1\,(z,\,\tau) &= \bar{p}_1\,(z)\; e^{j\Omega T\tau} \end{aligned} \tag{23}$$

Substitution from Eqs. (22) and (23) into Eq. (21) yields

$$\frac{d}{dz}\begin{Bmatrix} \bar{u}_{z1} \\ \bar{u}_{\theta 1} \\ \bar{p}_1 \end{Bmatrix} + [A]\begin{Bmatrix} \bar{u}_{z1} \\ \bar{u}_{\theta 1} \\ \bar{p}_1 \end{Bmatrix} = \left(\frac{r_o}{\varepsilon}\right)\begin{Bmatrix} g_1 \\ g_2 \\ g_3 \end{Bmatrix} \tag{24}$$

where

$$[A] = \begin{bmatrix} -2q/f & -j(\omega T) & 0 \\ fA_{3\theta} & f(A_{2\theta}+j\Gamma T) & -jfb(L/R) \\ (A_{3z}+2q/f^2+j\Gamma T) & A_{2z}+j(\omega T)/f & 0 \end{bmatrix} \tag{25a}$$

$$\begin{Bmatrix} g_1 \\ g_2 \\ g_3 \end{Bmatrix} = \begin{Bmatrix} (2q/f^3+j\Gamma T/f) \\ -fA_{1\theta} \\ -(A_{1z}+2q/f^4+j\Gamma T/f^2) \end{Bmatrix} \tag{25b}$$

and

$$\Gamma = \Omega - \omega u_{\theta 0}(z) \tag{26}$$

The following three boundary conditions are specified for the solution of Eq. (24):

(a) The exit pressure perturbation is zero; i.e.,

$$\bar{p}_1(L) = 0 \tag{27}$$

(b) The entrance circumferential velocity perturbation is zero; i.e.,

$$\bar{u}_{\theta 1}(0) = 0 \tag{28}$$

(c) The pressure loss at the seal entrance is defined by

$$p_s - p(0, \theta, \tau) = \frac{\rho}{2} u_z^2(0, \theta, \tau)\ (1 + \xi)$$

which yields the following boundary condition:

$$\bar{p}_1(0) = -\ (1 + \xi)\ u_{z1}(0)/(1+q) \tag{29}$$

Solution of the differential Eqs. (24) in terms of the boundary conditions is relatively straightforward, yielding a solution for the velocity and pressure fields of the form

$$\begin{Bmatrix} \bar{u}_{z1} \\ \bar{u}_{\theta 1} \\ \bar{p}_1 \end{Bmatrix} = \left(\frac{r_o}{\varepsilon}\right) \begin{Bmatrix} f_{1C}+jf_{1s} \\ f_{2C}+jf_{2s} \\ f_{3C}+jf_{3s} \end{Bmatrix} \tag{30}$$

Dynamic Coefficient Definitions

Having obtained the pressure-field solution of Eq. (30), solution for the dynamic coefficients will now be undertaken. The reaction-force components acting on the rotor due to shaft motion are defined by

$$F_X(t) = -\varepsilon RL \int_o^1 \int_o^{2\pi} p_1 \cos\theta d\theta dz = -\varepsilon RL\rho\bar{V}^2 \int_o^1 \int_o^{2\pi} \tilde{p}_1 \cos\theta d\theta dz$$

$$F_Y(t) = -\varepsilon RL \int_o^1 \int_o^{2\pi} p_1 \sin\theta d\theta dz = -\varepsilon RL\rho\bar{V}^2 \int_o^1 \int_o^{2\pi} \tilde{p}_1 \sin\theta d\theta dz$$

From the last of Eq. (19), these integrals further reduce to

$$F_X(t) = -\varepsilon RL\pi\rho\bar{V}^2 \int_o^1 \tilde{p}_{1C} dz;\quad F_Y(t) = -\varepsilon RL\pi\rho\bar{V}^2 \int_o^1 \tilde{p}_{1s} dz \tag{31}$$

The motion defined by Eq. (22) is orbital at the precessional frequency Ω and radius R_o. This statement may be confirmed by comparing Eq. (18) with Eq. (22) to obtain

$$X = \bar{C} r_o \cos\Omega t, \qquad Y = \bar{C} r_o \sin\Omega t \tag{32}$$

Definition of the reaction forces is simplified by performing the integration at a time when the rotating displacement vector is pointing along the X axis, i.e., when $\Omega t = 0$. Eq. (23) shows that $\hat{p}_1$ and $\bar{p}_1$ coincide for this time and location. Hence, Eq. (31) yields the following component force definitions parallel and normal to the displacement vector

$$F_r(\Omega T) = -r_o(\pi RL\rho\bar{V}^2) \int_o^1 f_{3C}(z) dz$$

$$F_\theta(\Omega T) = -r_o(\pi RL\rho\bar{V}^2) \int_o^1 f_{3s}(z)dz$$

The useful nondimensional version of these equations is

$$\frac{F_r(\Omega T)}{\pi R\Delta P r_o} = -\frac{2}{C_d}\quad \frac{L}{\bar{C}} \int_o^1 f_{3c}(z)dz$$

$$\frac{F_\theta(\Omega T)}{\pi R\Delta P r_o} = -\frac{2}{C_d}\quad \frac{L}{\bar{C}} \int_o^1 f_{3s}(z)dz \tag{33}$$

where $R_o = \bar{C}r_o$ is the amplitude of seal motion. The components are expressed as function of ΩT, because, for a given seal geometry (L, R, C) and set of operating conditions (ΔP, ω), the excitation frequency ΩT is the only independent variable. Stated-differently, Eq. (33) provides a frequency-response solution for the reaction force components.

To calculate seal coefficients, a comparable statement of reaction-force components is developed from the following nondimensional statement of Eq. (1)

$$-\frac{1}{\pi R\Delta P}\begin{Bmatrix} F_X \\ F_Y \end{Bmatrix} = \begin{bmatrix} \tilde{K} & \tilde{k} \\ -\tilde{k} & \tilde{K} \end{bmatrix}\begin{Bmatrix} X \\ Y \end{Bmatrix} + T\begin{bmatrix} \tilde{C} & \tilde{c} \\ -\tilde{c} & \tilde{C} \end{bmatrix}\begin{Bmatrix} \dot{X} \\ \dot{Y} \end{Bmatrix} + T^2\begin{bmatrix} \tilde{M} & \tilde{m} \\ -\tilde{m} & \tilde{M} \end{bmatrix}\begin{Bmatrix} \ddot{X} \\ \ddot{Y} \end{Bmatrix} \tag{34}$$

Substitution from Eq. (32) yields

$$-\frac{F_r(\Omega T)}{\pi R\Delta P r_o} = \tilde{K} + \tilde{c}(\Omega T) - \tilde{M}(\Omega T) = \frac{+2}{C_d}\left(\frac{L}{\bar{C}}\right) \int_o^1 f_{3c}(z)dz$$

$$\frac{F_\theta(\Omega T)}{\pi R\Delta P r_o} = \tilde{k} - \tilde{C}(\Omega T) - \tilde{m}(\Omega T) = \frac{-2}{C_d}\left(\frac{L}{\bar{C}}\right) \int_o^1 f_{3s}(z)dz \tag{35}$$

Hence, the dynamic seal coefficients (K, k, C, c, M, m) may be obtained by comparing the solution obtained by Eq. (33) with Eq. (35). More specifically, they are obtained by a least-square curve-fit of the solutions stated on the right-hand side of Eq. (35).

TANGENTIAL VELOCITY DEVELOPMENT

The frames of figure 4 illustrate the circumferential velocity development $u_{\theta o}(z)$ which is predicted by Eq. (12b) for the same and different rotor and stator surface roughnesses. Roughness is characterized by the empirical coefficients (mr, nr), (ms, ns). For the figures illustrated, the roughness of a smooth surface is defined by Yamada's [9] coefficients

$$mo = -0.25, \qquad no = 0.079$$

while the parameters

$$mo = -.0024, \qquad no = 0.0262,$$

corresponding to a theoretical relative roughness $\hat{\varepsilon} = \hat{e}/2\overline{C} = 0.1$ are used for the rough surface. Observe that the solution converges towards one half irrespective of whether both surfaces are smooth or rough. However, in figure 4 (b) the asymptotic solution is less or greater than one half depending on whether one uses a smooth-rotor/rough-stator or a rough-rotor/smooth-stator combination. The results of figure 4 substantially support von Pragenau's [6] central conclusion concerning the desirability of a rough-stator/smooth-rotor combination.

EXPERIMENTAL RESULTS

Introduction

The test results reported here were developed as part of an extended, NASA-funded, high-Reynolds-number test program of pump seal configurations in support of the SSME (Space Shuttle Main Engine) development program. High-Reynolds numbers, which are comparable to those achieved in the cryogenic turbopumps of the SSME, are achieved by using $CBrF_3$ as a test fluid. This is a DuPont-manufactured refrigerent and fire extinguisher fluid (Halon) which combines a high density and low absolute viscosity to achieve very low kinematic viscosity, actually less than liquid hydrogen [10]. Details of the flow loop are provided in [11].

Figure 5 illustrates the test apparatus. The test fluid enters the center and discharges axially across the two test seals. Seal inserts are pressed into cylindrical seats in the housing. The rotor segments of the seal are mounted eccentrically in the rotor with an eccentricity A. Hence, rotor rotation generates a synchronously-precessing pressure field. Axially-spaced, strain-gauge, pressure transducers are provided to measure the transient pressure field. Capacitance-type proximity probes are provided to simultaneously measure the rotor motion X(t), Y(t) relatives to the housing. The transient pressure measurements are integrated to define F_r/A and F_θ/A, the force coefficients parallel and normal to the seal eccentricity vector. In any test, five to ten cycles of data, containing on the order of 2,000 data points, are analyzed, yielding a calculated average and standard deviation for F_r/A and F_θ/A. The test results reported here were carried out to provide answers for the following questions:

(a) How do predictions from the current theory compare to test results?

(b) For damper seal configurations, (rough-stator/smooth-rotor) how do various roughness treatments compare in terms of leakage, stiffness, and damping?

Stator Configurations

Tests were carried out on the following stator configurations:

(a) smooth finish,

(b) knurled-indentation roughness,

(c) diamond-grid post pattern,

(d) round-hole pattern.

All seals use the same radial clearance, C_r = .527 mm. Seals b through d are illustrated in figures 6. The knurled-indentation roughness pattern is the same as that used in current test versions of the HPOTP (High Pressure Oxygen Turbopump), and the seal insert was supplied by Rocketdyne division of Rockwell International, the manufacturer of the SSME. The diamond-grid post pattern was manufactured by a milling operation which produced grooves which left the square post pattern. The round-hole pattern was also produced by a right-hand milling operation.

Empirical Turbulence Coefficients

With reference to the adequacy of current analysis, the stator and rotor roughness is characterized in terms of empirical coefficients. These coefficients must be calculated from the static test data before a theoretical prediction can be made for F_r/A and F_θ/A, and calculation of these coefficients is the subject of this subsection.

In the apparatus of figure 5, a smooth-seal insert is used in the left-hand side, while the damper-seal stators were inserted in the right hand side of the housing. To the extent possible, the same "very-smooth" finish was provided for both the smooth-seal insert and the rotor. Leakage rates and pressure gradients were measured for both the smooth and damper seals for all dynamic tests.

The steady-state axial pressure gradient equation has the form

$$-\frac{\partial p}{\partial z} = \sigma \left(\frac{\rho \bar{V}^2}{2}\right)$$

Hence, with a measured pressure gradient and a known density ρ and axial velocity $\bar{V}$, the parameter σ can be calculated. σ is related to the friction-factor coefficient λ by

$$\sigma = \lambda \left(\frac{L}{\bar{C}}\right)$$

The smooth-rotor/smooth-stator data were used to calculate σ_r and λ_r values which were assumed to apply for both the rotor and smooth stator. From the λ_r versus ω and R_{ao} data, the empirical coefficients mr, nr of the following friction-factor formula are calculated

$$\lambda_r = nr\, R_{ao}^{mr} \left[1 + (R\omega/\bar{V})^2\right]^{\frac{mr+1}{2}} \qquad (36)$$

on a least-square basis, yielding

$$nr = 0.0674, \qquad mr = -0.217$$

For the smooth-rotor/rough-stator combinations, a combined σ_c is measured, which is related to the corresponding rotor σ_r and (rough) stator σ_s by

$$\sigma_c = \frac{\sigma_r + \sigma_s}{2} \Rightarrow \sigma_s = 2\sigma_c - \sigma_r \qquad (37)$$

This formula was used to calculate σ_s for the rough stators by using measured values for σ_c and calculating a value for σ_r from Eq. (36) with the parameters of Eq. (37). The empirical coefficients obtained for the stator inserts are provided in table 1, together with an estimate of the relative-roughness parameter corresponding to pipe-friction data. The results are generally consistent with expectations,

except for the positive value for ms obtained for the hole-pattern stator; however, over the Reynolds-number range tested, the combined friction-factor λ_c actually increased (slightly) with increasing R_{ao} for this stator insert.

Dynamic Test Data

For a given seal configuration, a test matrix is obtained by varying the axial Reynolds number and running speed. The R_{ao} range varies between the maximum flow capacity of the supply pump and the minimum ΔP sufficient to generate reasonable transient pressure signal amplitudes. For a given R_{ao} value, the running speed is varied sequentially over the running-speed capacity of the drive motors. Figures 7 through 10 illustrate theoretical and experimental results for the four stators tested. An inspection of these results demonstrates "reasonable" agreement between theory and experiment for F_θ/A but much larger F_r/A magnitudes at lower speeds than predicted. Further, the magnitude of F_r/A decreases more rapidly with increasing running speed than predicted.

DISCUSSION OF EXPERIMENTAL RESULTS

Comparison to Theory

If a circular orbit of the form

$$X = A\cos\omega t \qquad Y = A\sin\omega t$$

is assumed, Eq. (1) yields the following definition of force coefficients

$$F_r/A = -K - c\omega + M\omega^2$$

$$F_\theta/A = k - C\omega$$

where the cross-coupled mass coefficient m has been dropped as being negligible in comparison to the influence of k and C. At first glance, these equations suggest that sufficient independent equations could be obtained, in the present apparatus, to independently calculate all the rotordynamic coefficients by holding the flowrate constant and running at three different speeds. However, the fact that the coefficients depend on ω precludes this approach. While K, C, and M are weak functions of ω through their dependence on σ, the "cross-coupled" coefficients k and c are linear functions of ω. In fact, if the fluid is prerotated prior to entering the seal such that the inlet tangential velocity is $U_{\theta o}(o) = R\omega/2$, then theory predicts that $k = C\omega/2$, $c = M\omega$, and

$$F_r/A = -K, \quad F_\theta/A = -C\omega/2$$

The present test apparatus provides no intentional prerotation, and the expected result is of the form

$$k = b_1 C\omega/2, \quad b_1 < 1$$

$$c = b_2 M\omega, \quad b_2 < 1$$

$$F_\theta/A \cong -C_{ef}\omega = -C(1-b_1/2)\omega$$

$$F_r/A \cong -K_{ef} + M_{ef}\omega^2 = -K + M(1-b_2)\omega^2$$

The term C_{ef} denotes the "net damping coefficient" resulting from the drag force $C\omega A$ and the forward whirl excitation force kA. A direct comparison between theory and experiment is obtained by curvefitting the theoretical and experimental results for the F_r/A and F_θ/A to obtain predictions for K_{ef}, C_{ef}, and M_{ef}. Note that the procedure of curvefitting the data with respect to ω eliminates the running-speed dependency. Further, K_{ef} is the zero-running speed intercept of the F_r/A versus ω curve, and C_{ef} is the slope of the F_θ/A versus ω curve.

A comparison of measured and experimentally-derived values for K_{ef}, C_{ef}, and M_{ef} are given in table 2 for the stators tested, and support the following general conclusions:

(a) Direct stiffness values are substantially underpredicted by theory. This result is consistent with earlier water test results [5, 12]. Improved correlation generally results at larger $\overline{C}/R$ ratios.

(b) Net damping coefficients are overestimated by theory, but the agreement is reasonable and generally improves with increasing R_{a_o}.

(c) The added-mass coefficient is substantially underpredicted by theory. However, this result is at variance with earlier water-test results [12] which show an overestimation of the added-mass coefficient.

Relative Performance of Stators

Dynamic Coefficients

Figures 11 and 12 illustrate K_{ef} and C_{ef} for the stators tested versus ΔP, and can be used for direct comparison of the stiffness and effective damping of the roughness designs. The results support the following conclusions.

(a) The knurled-indentation and the diamond-grid stators are, respectively, the most and least stiff. The hole-pattern and smooth stators have comparable stiffness.

(b) The hole-pattern and diamond-grid stators provide, respectively, the most and least net damping. The smooth and knurled-indentation stators have comparable net damping coefficients.

The disappointing performance of the diamond-grid stator is related to its larger average clearance. The relieving operation which yields the posts yields an average clearance of 0.889 mm as compared to the 0.527 mm minimum clearances of the remaining configurations.

Leakage Performance

To evaluate leakage performance, C_L is defined using the conventional discharge coefficient C_d definition

$$\Delta P = C_d \frac{\rho \overline{V}^2}{2}$$

which yields

$$\dot{Q} = 2\,R\overline{CV} = \left(\frac{\overline{C}}{R}\right) C_d^{-\frac{1}{2}} \cdot 2\pi R^2 \sqrt{\frac{2\Delta P}{\rho}} = C_L \cdot 2\pi R^2 \sqrt{\frac{2\Delta P}{\rho}}$$

Hence,

$$C_L = \left(\frac{\overline{C}}{R}\right) C_d^{-\frac{1}{2}} = \dot{Q} \Big/ \left(2\pi R^2 \sqrt{\frac{2\Delta P}{\rho}}\right)$$

The coefficient C_L is a nondimensional relative measure of the leakage to be expected through seals having the same radius. Figure 13 illustrates C_L versus ΔP for the seal stators and demonstrates that the round-hole pattern and smooth stators have, respectively, the best and worst performance. The knurled-indentation pattern has a slightly better leakage performance than the diamond-grid pattern.

CLOSURE

A theory is presented, based on a simple modification of Hirs' turbulent lubrication equations, to account for different but directionally-homogeneous surface roughness treatments for the rotor and stator of annular seals. The theoretical results agree with von Pragenau's predictions that a "damper seal" which uses a smooth rotor and a rough stator yields more net damping than a conventional seal which has the same roughness for both the rotor and stator.

Experimental results for four stators confirm that properly-designed roughened stators can yield higher net damping values and substantially less leakage than seals with smooth surfaces. The best seal from both damping and leakage viewpoints uses a round-hole-pattern stator. Initial results for this stator suggest that, within limits, seals can be designed to yield specified ratios of stiffness to damping. Additional testing for this type of seal is scheduled for 1984-1985 to examine the influence of hole depth, hole shape, and the ratio of hole-relieved area to total surface area.

APPENDIX A: PERTURBATION COEFFICIENTS

$$B_s a_{0s} = \left[1 + (u_{\theta 0}/bu_{Z0})^2\right]^{\frac{ms+1}{2}}, \quad B_s = \left(1 + \frac{1}{4b^2}\right)^{\frac{ms+1}{2}}$$

$$B_r a_{0r} = \left\{1 + \left[(u_{\theta 0}-1)/bu_{Z0}\right]^2\right\}^{\frac{mr+1}{2}}, \quad B_r = \left(1 + \frac{1}{4b^2}\right)^{\frac{mr+1}{2}}$$

$$B_s a_{1s} = \left[1 + (u_{\theta 0}/bu_{Z0})^2\right]^{\frac{ms-1}{2}}$$

$$B_r a_{1r} = \left\{1 + \left[(u_{\theta 0}-1)/bu_{Z0}\right]^2\right\}^{\frac{mr-1}{2}}$$

$$A_{1z} = \left[a_{0s}\sigma_s(1-ms) + a_{0r}\sigma_r(1-mr)\right] /2f^4$$

$$A_{2z} = \left[(ms+1)\sigma_s a_{1s} u_{\theta 0} + (mr+1)\sigma_r a_{1r}(u_{\theta 0}-1)\right] /2b^2 f$$

$$A_{3z} = \left[a_{0s}\sigma_s(2+ms) + a_{0r}\sigma_r(2+mr)\right] /2f^2 + 2q/f^2$$

$$- \left[a_{1s}\sigma_s(1+ms)u_{\theta 0}^2 + a_{1r}\sigma_r(1+mr)(u_{\theta 0}-1)^2\right] /2b^2$$

$$A_{1\theta} = \left[\sigma_s a_{0s} u_{\theta 0}(1-ms) + \sigma_r a_{0r}(u_{\theta 0}-1)(1-mr)\right] /2f^3$$

$$A_{2\theta} = (\sigma_s a_{0s} + \sigma_r a_{0r})/2f^2$$

$$+ \left[\sigma_s(1+ms)a_{1s}u_{\theta 0}^2 + \sigma_r(1+mr)a_{1r}(u_{\theta 0}-1)^2\right] /2b^2$$

$$A_{3\theta} = \left[\sigma_s ms\, a_{os} u_{\theta 0} + \sigma_r mr a_{0r}(u_{\theta 0}-1)\right] /2f$$

$$-f\left[\sigma_s a_{1s}(1+ms)u_{\theta 0}^3 + \sigma_r a_{1r}(1+mr)(u_{\theta 0}-1)^3\right] /2b^2$$

REFERENCES

1. Lomakin, A., "Calculation of Critical Speed and Securing of the Dynamic Stability of the Rotor of Hydraulic High Pressure Machines with Reference to Forces Arising in Seal Gaps," Energomashinostroenie, Vol. 4, 1958.

2. Allaire, P. E., Gunter, E. J., Lee, C.P., and Barrett, L. E., "The Dynamic Analysis of the Space Shuttle Main Engine High Pressure Fuel Turbopump Final Report, Part II, Load Capacity and Hybrid Coefficients for Turbulent Interstage Seals," University of Virginia Report UVA/528140/ME76/103, September 1976.

3. Black, H. F., and Jenssen, D. N., "Dynamic Hybrid Properties of Annular Pressure Seals," Proc. J. Mechanical Engineering, Vol. 184. pp. 92-100, 1970.

4. Childs, D. W., "Finite-Length Solutions for Rotordynamic Coefficients of Turbulent Annular Seals," ASME Trans. J. of Lubrication Technology, Vol. 105, pp. 437-444, July 1983.

5. Childs, D. W., "Finite-Length Solutions for the Rotordynamic Coefficients of Constant-Clearance and Convergent-Tapered Annular Seals," submitted for Third International Conference on Vibrations in Rotating Machinery, York, England, September 1984.

6. Von Pragenau, G. L., "Damping Seals for Turbomachinery," NASA Technical Paper 1987, 1982.

7. Hirs, G. G., "A Bulk-Flow Theory for Turbulence in Lubricant Films," ASME Trans. J. of Lubrication Technology. pp. 137-146, April 1973.

8. Fleming, D. P., "High Stiffness Seals for Rotor Critical Speed Control," ASME Paper 77-DET-10, Design Engineering Technical Conference, Chicago, Ill, 26-30 September 1977.

9. Yamada, Y., "Resistance of Flow through an Annulus with an Inner Rotating Cylinder," Bull. J.S.M.E., Vol. 5, No. 18, pp. 302-310, 1962.

10. Stephen, H. and Lucus, K., Viscosity of Dense Fluids, Plenum Press, New York - London, p. 59.

11. Childs, D., Nelson, C., Noyes, T., and Dressman, J. B., "A High-Reynolds-Number Test Facility: Facility Description and Preliminary Data," NASA Conference Publication 2250, Proceedings Workshop on Rotordynamic Instability Problems in High-Performance Turbomachinery - 1982, held at Texas A&M University, 10-12 May 1982.

12. Childs, D., and Dressman, J., "Convergent-Tapered Annular Seals: analysis and Testing for Rotordynamic Coefficients," accepted for publication ASME Trans. J. of Lubrication Technology.

TABLE I. - EMPIRICAL TURBULENCE COEFFICIENTS MS, NS, AND ESTIMATES FOR RELATIVE ROUGHNESS

	ms	ns	$\hat{\varepsilon} = \hat{e}/2\bar{C}$
Smooth	-.240	.0989	.00069
Knurled-Indentation	-.136	.0697	.022
Diamond-Grid	-.0350	.118	.460
Hole Pattern	.0190	.0150	.058

TABLE II. - A COMPARISON OF THEORETICAL AND MEASURED VALUES FOR EFFECTIVE STIFFNESS, DAMPING AND ADDED-MASS COEFFICIENTS

SEAL	R_{ao}	$\frac{KEF_{ex}}{KEF_{th}}$	$\frac{CEF_{ex}}{CEF_{th}}$	$\frac{MEF_{ex}}{MEF_{th}}$
Smooth	120,100	2.182	0.6636	1.38
	170,600	2.216	0.6900	1.38
	270,500	1.297	0.7567	4.45
	385,200	1.142	0.9350	6.88
	495,700	1.261	0.9964	9.35
	500,900	1.478	0.9401	0.986
Knurled-Indentation	115,700	1.630	0.5613	4.24
	160,200	1.598	0.8166	3.82
	335,600	1.678	0.9836	18.6
	350,500	1.664	1.027	11.2
	368,200	1.706	1.041	4.23
Diamond Grid	115,100	1.745	0.4265	1.88
	159,800	1.310	0.4795	2.61
	335,600	1.065	0.9954	7.58
	349,900	0.8026	0.9583	11.9
	384,000	1.128	1.012	4.83
Hole Pattern	89,410	1.573	0.4506	1.94
	130,400	1.768	0.6997	2.25
	159,700	1.876	0.7867	2.58
	328,400	2.175	1.205	1.88

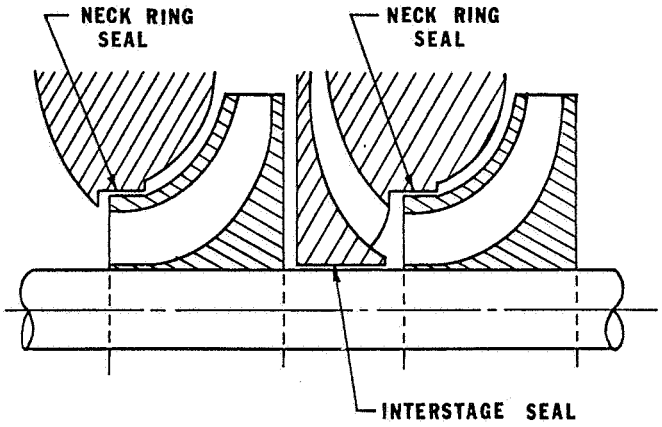

Figure 1. Neck-ring and interstage seals.

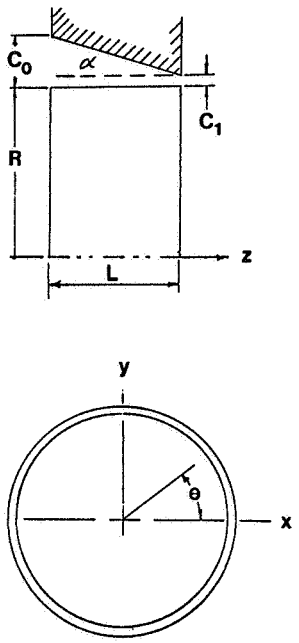

Figure 3. Tapered seal geometry.

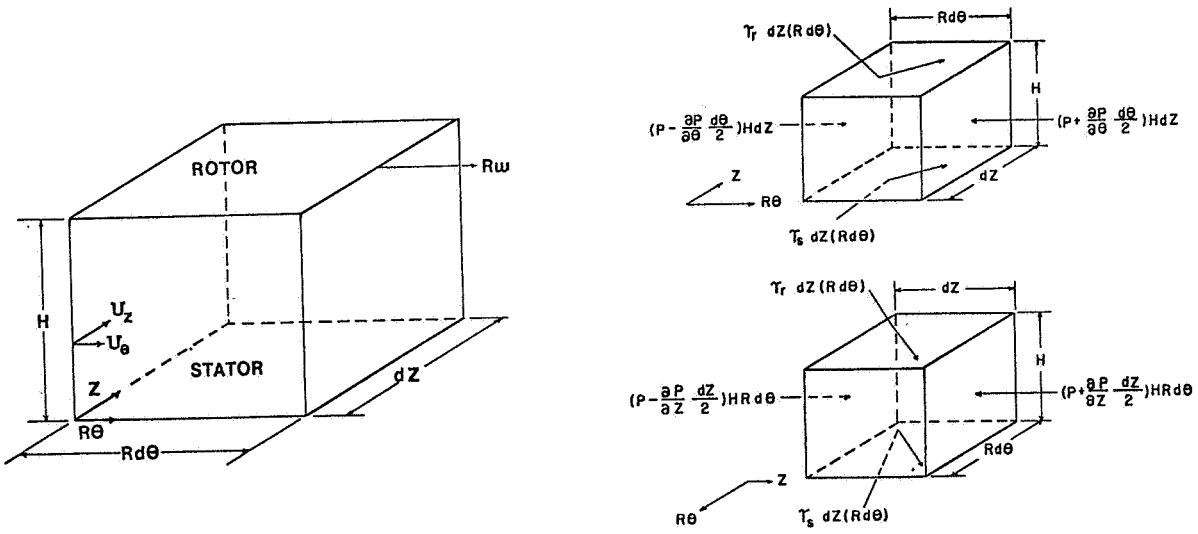

Figure 2. Seal differential element.

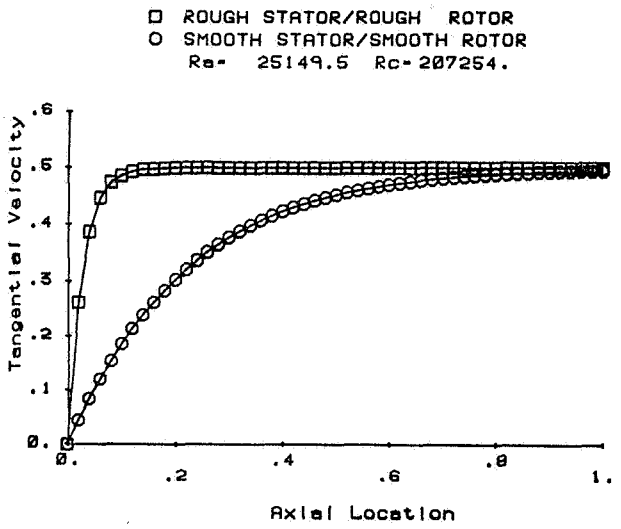

Figure 4(a). Predicted circumferential velocity development for the same rotor and stator roughnesses.

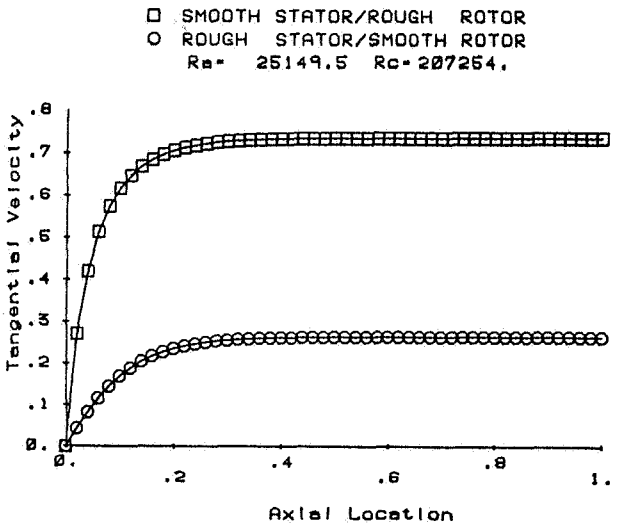

Figure 4(b). Predicted circumferential velocity development for different rotor and stator roughnesses.

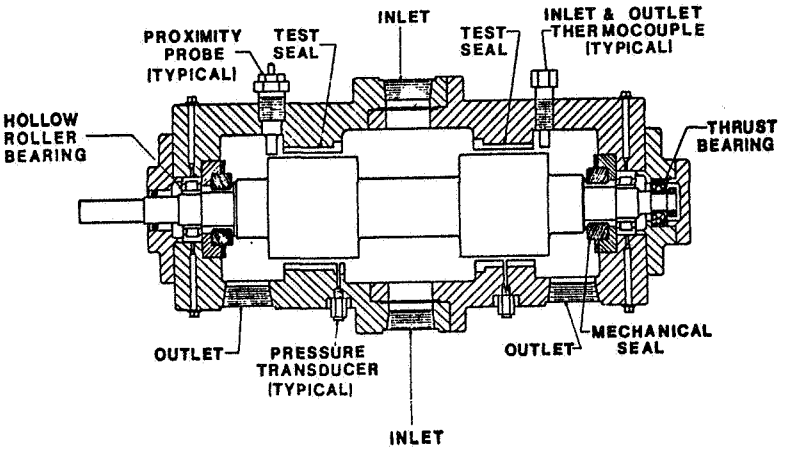

Figure 5. Test apparatus.

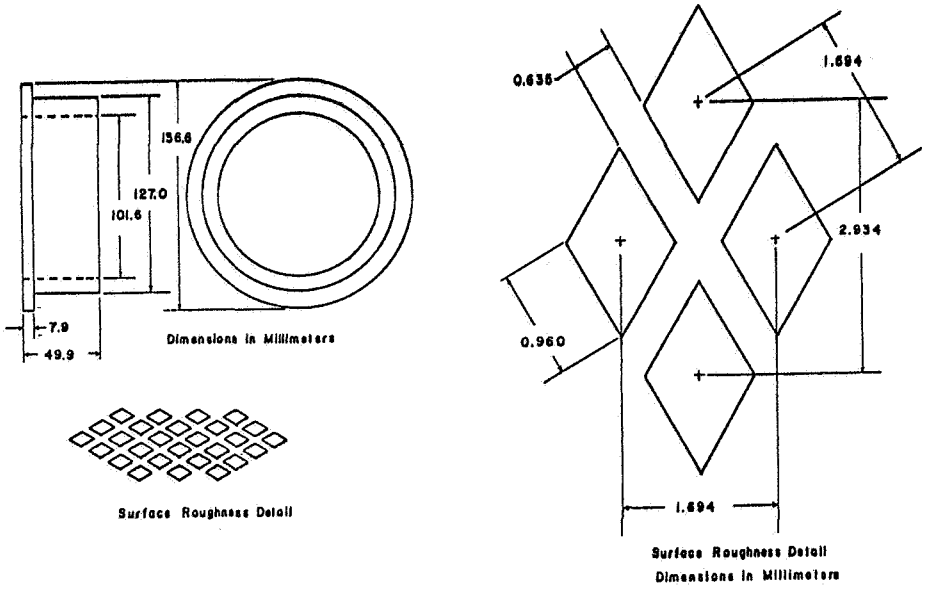

Figure 6(a). Rocketdyne-manufactured, knurled-indentation stator insert.

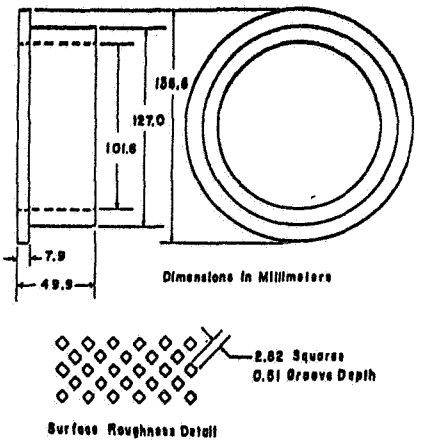

Figure 6(b). Diamond grid, post-roughness stator insert.

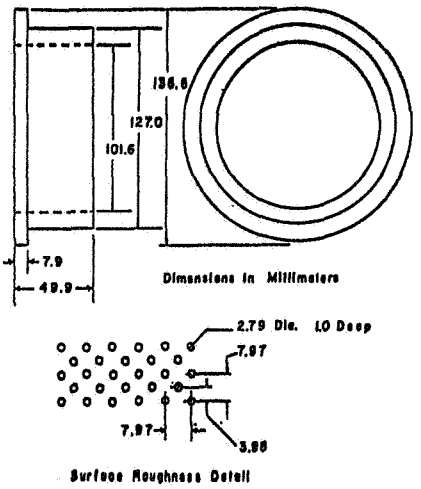

Figure 6(c). Round-hole pattern stator insert.

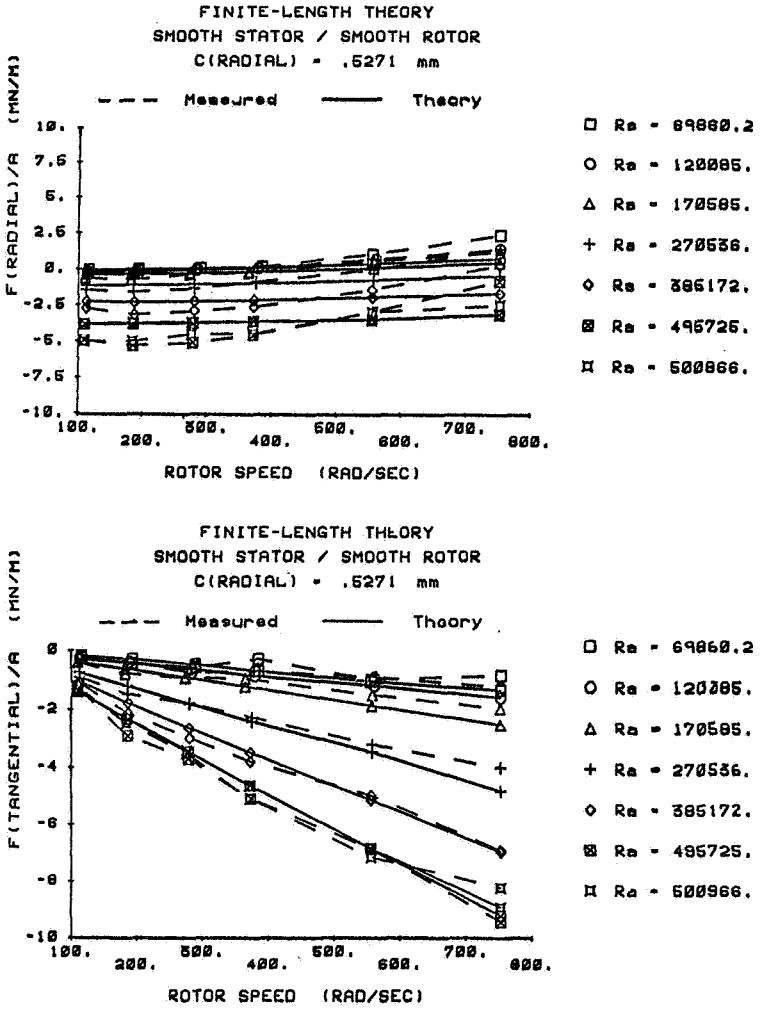

Figure 7.
Measured and theoretical results for F_r/A and F_θ/A; smooth stator.

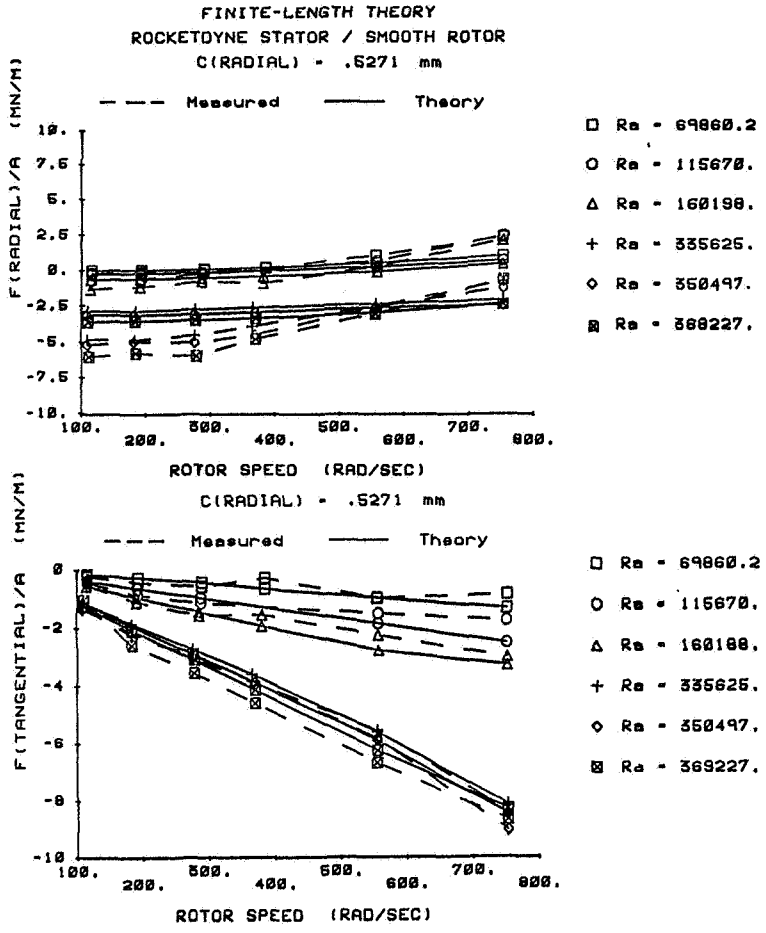

Figure 8.
Measured and theoretical results for F_r/A and F_θ/A; knurled-indentation stator.

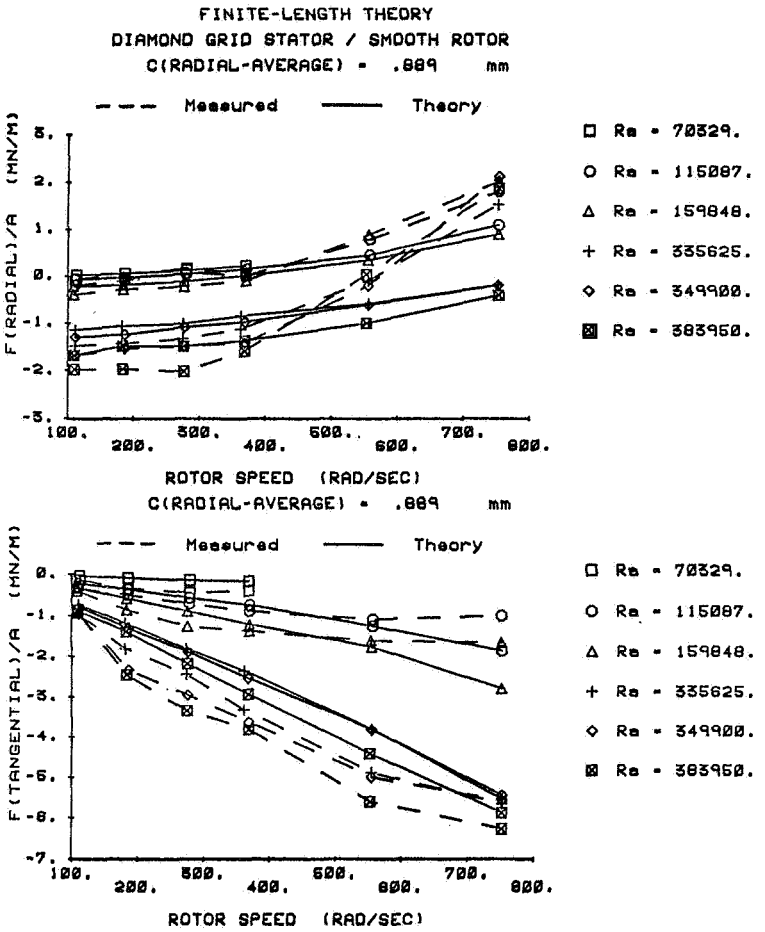

Figure 9.
Measured and theoretical results for F_r/A and F_θ/A; diamond-grid stator.

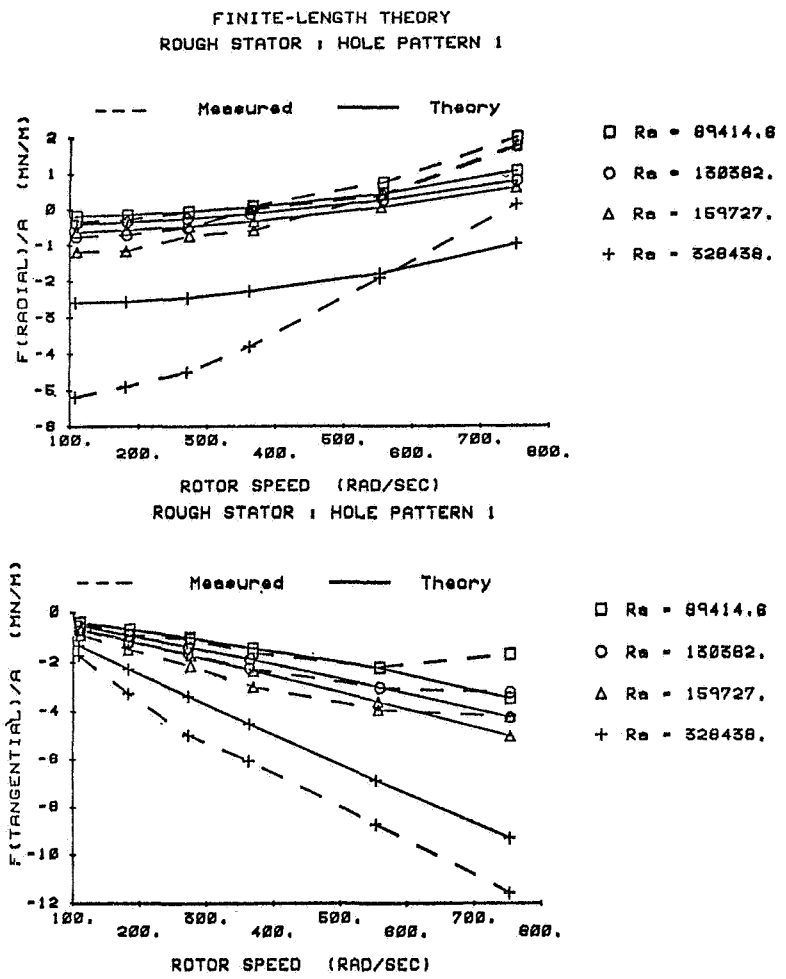

Figure 10.
Measured and theoretical results for F_r/A and F_θ/A; round-hole pattern.

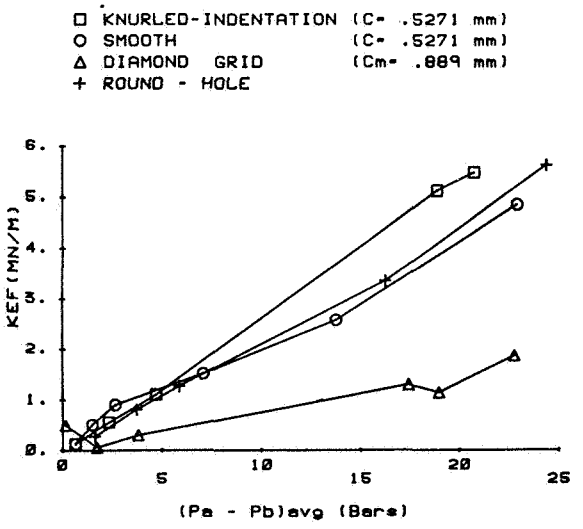

Figure 11. K_{ef} versus ΔP for stator inserts.

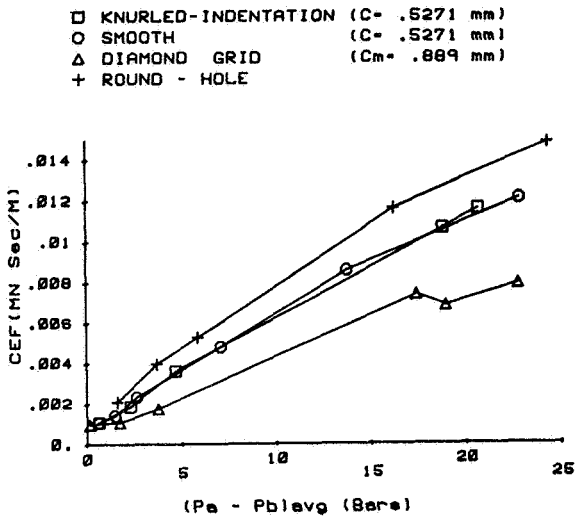

Figure 12. C_{ef} versus ΔP for stator inserts.

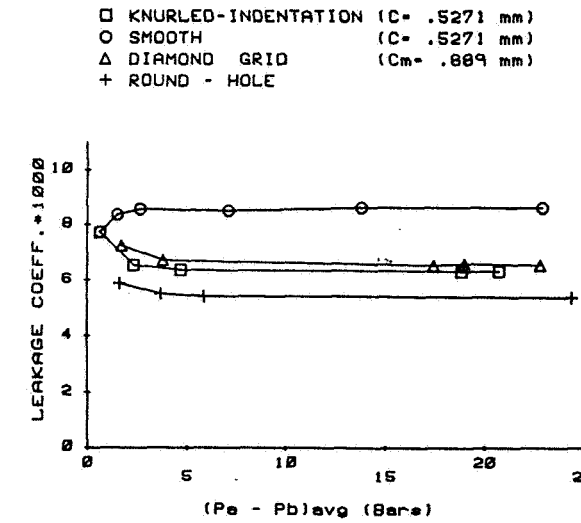

Figure 13. C_L versus ΔP for stator inserts.

ANALYSIS FOR LEAKAGE AND ROTORDYNAMIC COEFFICIENTS OF SURFACE ROUGHENED TAPERED ANNULAR GAS SEALS*

C. C. Nelson
Texas A&M University
College Station, Texas 77843

ABSTRACT

In order to soften the effects of rub, the smooth stators of turbine gas seals are sometimes replaced by a honeycomb surface. This deliberately roughened stator and smooth rotor combination retards the seal leakage and may lead to enhanced rotor stability. However, many factors determine the rotordynamic coefficients and little is known as to the effectiveness of these "honeycomb seals" under various changes in the independent seal parameters. This analysis develops an analytical-computational method to solve for the rotordynamic coefficients of this type of compressible-flow seal.

The governing equations for surface roughened tapered annular gas seals are based on a modified Hirs' turbulent bulk flow model. A perturbation analysis is employed to develop zeroth and first-order perturbation equations. These equations are numerically integrated to solve for the leakage, pressure, density, and velocity for small motion of the shaft about the centered position. The resulting pressure distribution is then integrated to find the corresponding rotordynamic coefficients. Finally, an example case is used to demonstrate the effect of changing from a smooth to a rough stator while varying the seal length, taper, preswirl, and clearance ratio.

NOMENCLATURE

$C(Z)$ = Centered position seal clearance

$\overline{C} = (C_e+C_x)/2$ = Nominal seal clearance

$\overline{c} = \overline{C}/R$ = Dimensionless nominal seal clearance

c_v = Specific heat at constant volume

C, c = Direct and cross-coupled damping coefficients of Eq. (1)

$\tilde{C}, \tilde{c}$ = Dimensionless direct and cross-coupled damping coefficients defined by Eq. (26)

D = Shaft diameter

$H(Z,\theta,t)$ = Local seal clearance

$h = H/\overline{C}$ = Dimensionless clearance

k = Entrance loss coefficient

K, k = Direct and cross-coupled stiffness coefficients of Eq. (1)

$\tilde{K}, \tilde{k}$ = Dimensionless direct and cross-coupled stiffness coefficients defined by Eq. (25)

L = Seal length

$\ell = L/R$ = Dimensionless seal length

$M = U_z\sqrt{\frac{\rho}{\gamma p}}$ = Mach number

m_s, m_r = Coefficients for Hirs' turbulent

n_s, n_r lubrication equations

$p_c = \frac{p_a}{(R\omega)^2\rho_a}$ = Pressure coefficient

p = Pressure

$\tilde{p} = p/p_a$ = Dimensionless pressure

R = Shaft radius

$R_{ao} = \frac{2\rho U_z C}{\mu}$ = Centered position, axial Reynolds number

$R_c = \rho(R\omega)\overline{H}/\mu$ = Circumferential Reynolds Number

$R_{co} = \rho(R\omega)\overline{C}/\mu$ = Centered position, nominal circumferential Reynolds number

R_g = Perfect gas constant

T = Temperature

t = Time

*This work is being supported by NASA Grant NAG3-181 from the Lewis Research Center.

$U = R\omega$ = Velocity of rotor surface

U_z, U_θ = Fluid velocity in the z and θ directions

$u_\theta = U_\theta/(R\omega)$, $u_z = U_z/(R\omega)$ = Dimensionless tangential and axial velocities

Z, $R\theta$ = Axial and circumferential seal coordinates illustrated in Fig. (1)

$z = Z/L$, θ = Dimensionless seal coordinates

$\gamma = c_p/c_v$ = Specific heat ratio

ε = Dimensionless seal eccentricity ratio

$e/2\bar{C}$ = Relative surface roughness

μ = Viscosity

ρ = Density

$\tilde{\rho} = \rho/\rho_a$ = Dimensionless density

τ_s, τ_r = Shear stress illustrated in Fig. (2)

$\tau = \tau\omega$ = Dimensionless time

Ω = Shaft orbital velocity

$\tilde{\Omega} = \Omega/\omega$ = Shaft whirl ratio

ω = Shaft angular velocity

Subscripts:

a, e, x, b = Reservoir, entrance, exit, and sump conditions, respectively

0, 1 = Zeroth and first-order perturbations in the dependent variables

s, r = Stator surface and rotor surface, respectively

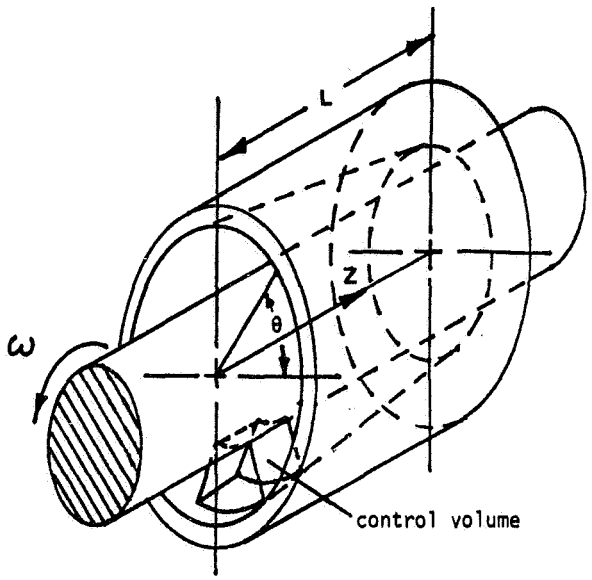

Figure 1. Smooth Tapered Annular Seal.

INTRODUCTION

Figure 1 illustrates the basic geometry of the convergent tapered annular turbine gas seal. In this figure both the rotor and the stator elements of the seal are shown to have the same nominally smooth surfaces. In practice, however, the smooth stator is sometimes replaced by a honey comb or other deliberately roughened surface. The purpose of this roughened surface is to soften the effects of rub from the rotor and to retard leakage. But in addition, the smooth rotor and rough stator combination may have significant influence on the seal's rotordynamic coefficients. In fact, von Pragenau [1] suggests just such a concept for an incompressible-flow "damper seal" which he believes will enhance rotor stability.

As related to rotordynamics, seal analysis has the objective of determining the reaction force acting on the rotor as a result of the shaft motion. For small motion about a centered position, the relation between the reaction-force components and the shaft motion can be written

$$-\begin{Bmatrix} F_X \\ F_Y \end{Bmatrix} = \begin{bmatrix} K & k \\ -k & K \end{bmatrix} \begin{Bmatrix} X \\ Y \end{Bmatrix} + \begin{bmatrix} C & c \\ -c & C \end{bmatrix} \begin{Bmatrix} \dot{X} \\ \dot{Y} \end{Bmatrix} + \begin{bmatrix} M & m \\ -m & M \end{bmatrix} \begin{Bmatrix} \ddot{X} \\ \ddot{Y} \end{Bmatrix} \quad (1)$$

The off-diagonal coefficients (k, c, m) are referred to as the cross-coupled stiffness, damping, and added-mass terms, respectively. These cross-coupled terms arise from the fluid's circumferential velocity component. This phenomenon is usually referred to as the effects of swirl. The circumferential velocity component is in part a function of the stator and rotor surface roughness. A rough stator and smooth rotor will tend to reduce the circumferential velocity, leading to a reduction in the destabilizing cross-coupled terms.

Fleming [2,3] made a separate analysis for the direct stiffness K, and for the direct damping C of smooth tapered annular gas seals. However, he did not include the effects of swirl and thus could not obtain the cross-coupled terms. Childs [4] developed an analysis for both direct and cross-coupled terms of incompressible-flow by using Hirs' [5] turbulent bulk-flow model and a perturbation technique. Nelson [6] used a similar approach to develop a numerical solution for the direct and cross-coupled stiffness and damping of smooth compressible-flow seals. The present analysis modifies the solution of reference [6] to include the effects of different stator and rotor surface conditions and then demonstrates the analysis on a specific seal example.

GOVERNING EQUATIONS

The control volume element shown in Fig. 1 has been enlarged and redrawn in Fig. 2. Note that the smooth stator surface has been replaced by a roughened honeycomb surface. The shear stresses τ_s and τ_r are the net wall shear stresses resulting from both the pressure induced flow and the drag induced flow. Hirs' turbulent bulk-flow model assumes that these stresses can be written as

$$\tau = \tfrac{1}{2}\rho U_m^2 n_o \left(\frac{2\,U_m H}{\mu}\right)^{m_o} \quad (2)$$

where U_m is the mean flow velocity relative to the surface upon which the shear stress is acting. Hirs' constants n_o and m_o are generally empirically determined from pressure flow experiments. For the control

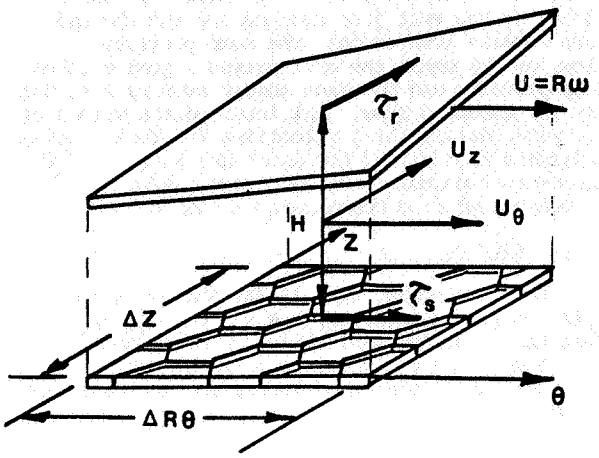

Figure 2. Control Volume for a Seal with a Honeycomb Stator.

volume in Fig. 2, n_s and m_s represent Hirs' constants relative to the stator surface and n_r and m_r represent those relative to the rotor surface. Substituting the mean flow velocity relative to each surface into Eq. (2) and then taking the appropriate component of the shear stress in the Z and θ-direction, the axial and circumferential momentum equations are

$$-H\frac{\partial p}{\partial Z} = p\left\{\frac{n_s}{2}\left(\frac{2\rho H}{\mu}\right)^{m_s} U_z\left(U_\theta^2+U_z^2\right)^{\frac{m_2+1}{2}} + \frac{n_r}{2}\left(\frac{2\rho H}{\mu}\right)^{m_r} U_z\left[(U_\theta-U)^2+U_z^2\right]^{\frac{m_r+1}{2}}\right\} + \frac{\partial(\rho U_\theta H)}{\partial t} + \frac{1}{R}\frac{\partial(\rho U_\theta U_z H)}{\partial\theta} + \frac{\partial(\rho U_z^2 H)}{\partial Z} \quad (3a)$$

$$-\frac{H}{R}\frac{\partial p}{\partial\theta} = \rho\left\{\frac{n_s}{2}\left(\frac{2\rho H}{\mu}\right)^{m_s} U_\theta\left(U_\theta^2+U_z^2\right)^{\frac{m_s+1}{2}} + \frac{n_r}{2}\left(\frac{2\rho H}{\mu}\right)^{m_r}(U_\theta-U)\left[(U_\theta-U)^2+U_z^2\right]^{\frac{m_r+1}{2}}\right\} + \frac{\partial(\rho U_\theta H)}{\partial t} + \frac{1}{R}\frac{\partial(\rho U_\theta^2 H)}{\partial\theta} + \frac{\partial(\rho U_\theta U_z H)}{\partial Z} \quad (3b)$$

The bulk-flow continuity equation is

$$0 = \frac{\partial(\rho H)}{\partial t} + \frac{1}{R}\frac{\partial(\rho U_\theta H)}{\partial\theta} + \frac{\partial(\rho U_z H)}{\partial Z} \quad (3c)$$

And for adiabatic flow the energy equation is

$$0 = \frac{\partial}{\partial t}\left[\left(c_v T + \frac{U_\theta^2}{2}+\frac{U_z^2}{2}\right)\rho H\right] + \frac{1}{R}\frac{\partial}{\partial\theta}\left[\left(c_v T+\frac{U_\theta^2}{2}+\frac{U_z^2}{2}+\frac{p}{\rho}\right)U_\theta\rho H\right] + \frac{\partial}{\partial Z}\left[\left(c_v T+\frac{U_\theta^2}{2}+\frac{U_z^2}{2}+\frac{p}{\rho}\right)U_z\rho H\right] + U(U_\theta-U)\frac{\rho n_r}{2}\left(\frac{2\rho H}{\mu}\right)^{m_r}\left[(U_\theta-U)^2+U_z\right]^{\frac{m_r+1}{2}} \quad (3d)$$

Assuming a perfect gas ($c_v T = p/\rho(\gamma-1)$) and using the dimensionless parameters defined in the Nomenclature, the above governing equations take the following dimensionless working form.

Momentum:

$$\frac{-P_c}{\tilde\rho\ell}\frac{\partial\tilde p}{\partial z} = \frac{u_z}{\bar{ch}}\left[f_s+f_r\right] + \frac{Du_z}{D\tau} \quad (4a)$$

$$\frac{-P_c}{\tilde\rho}\frac{\partial\tilde p}{\partial\theta} = \frac{1}{\bar{ch}}\left[u_\theta f_s + (u_\theta-1)\,f_r\right] + \frac{Du_\theta}{D\tau} \quad (4b)$$

Continuity:

$$0 = \frac{\partial(\tilde\rho h)}{\partial\tau} + \frac{\partial(\tilde\rho u_\theta h)}{\partial\theta} + \frac{1}{\ell}\frac{\partial(\tilde\rho u_z h)}{\partial z} \quad (4c)$$

Energy:

$$\frac{\tilde p}{h}\frac{\partial h}{\partial\tau} = u_\theta\left(\frac{\partial\tilde p}{\partial\theta}+\frac{\tilde\rho}{P_c}\frac{Du_\theta}{D\tau}\right) + u_z\left(\frac{1}{\ell}\frac{\partial\tilde p}{\partial z}+\frac{\tilde\rho}{P_c}\frac{Du_z}{D\tau}\right) + \frac{1}{\gamma-1}\left(\frac{D\tilde p}{D\tau}-\frac{\gamma\tilde p}{\tilde\rho}\frac{D\tilde\rho}{D\tau}\right) + \frac{\tilde\rho}{\bar{ch}P_c}(u_\theta-1)\,f_r \quad (4d)$$

where

$$f_s = \frac{n_s}{2}\left(u_\theta^2+u_z^2\right)^{\frac{m_s+1}{2}}(2R_c)^{m_s}$$

$$f_r = \frac{n_r}{2}\left[(u_\theta-1)^2+u_z^2\right]^{\frac{m_r+1}{2}}(2Rc)^{m_r} \quad (4e)$$

$$\frac{D}{D\tau} = \frac{\partial}{\partial\tau} + u_\theta\frac{\partial}{\partial\theta} + \frac{u_z}{\ell}\frac{\partial}{\partial z}$$

PERTURBATION ANALYSIS

The governing Eqs. (4a) through (4d) define the relationship between the dimensionless clearance, pressure, density, axial velocity, and circumferential velocity ($h, \tilde p, \tilde\rho, u_z, u_\theta$) as functions of the independent dimensionless spatial variables (θ, z) and the dimensionless time τ. Expansion of these equations in the perturbation variables

$$h = h_o + \varepsilon h_1 \quad \tilde\rho = \tilde\rho_o + \varepsilon\tilde\rho_1 \quad u_\theta = u_{\theta o} + \varepsilon u_{\theta 1}$$

$$\tilde p = \tilde p_o + \varepsilon\tilde p_1 \quad u_z = u_{zo} + \varepsilon u_{z1} \quad (5)$$

yields the zeroth and first-order equations as shown

in Appendix A.

Zeroth-Order Solution

The zeroth-order equations describe the steady flow resulting from a centered position rotating shaft. Before these equations can be integrated, values for Hirs' constants m_s, n_s, m_r, and n_r must be established. Lacking experimental data for these constants, values can be approximated by the use of Colebrook's formula [7].

$$\frac{1}{\sqrt{4n_o R_a^{m_o}}} = -2\log\left(\frac{e/2\bar{C}}{3.7} + \frac{2.51}{R_a\sqrt{4n_o R_a^{m_o}}}\right) \tag{6}$$

For a given relative roughness a least-squares fit is used to determine n_o and m_o over a range of R_a (say $5000<R_a<1000000$).

Integration begins by guessing an entrance zeroth-order Mach number $M_o(0)$. Defining an entrance loss coefficient k in a manner similar to Zuk [8], the following equations give the initial zeroth-order pressure and density.

$$\tilde{p}_o(0) = \frac{1}{\left[1 + \frac{(\gamma-1)(1+k)M_o^2(0)}{2}\right]^{\gamma/(\gamma-1)}} \tag{7}$$

$$\tilde{\rho}_o(0) = \frac{1 + \left[\frac{(\gamma-1)M_o^2(0)}{2}\right]}{\left[1 + \frac{(\gamma-1)(1+k)M_o^2(0)}{2}\right]^{\gamma/(\gamma-1)}} \tag{8}$$

In the first application, k is assumed to be 0.1. Expanding the Mach number as defined in the nomenclature in terms of the perturbation variables gives the following zeroth-order entrance equation

$$M_o^2(0) = \frac{u_{zo}^2(0)\tilde{\rho}_o(0)}{\gamma\tilde{p}_o(0)P_c} \tag{9}$$

From this equation, the initial zeroth-order axial velocity $u_{zo}(0)$ can be found. Having now $\tilde{p}_o(0)$, $\tilde{\rho}_o(0)$, and $u_{zo}(0)$, the centered position axial Reynolds number R_{ao} is determined and used to approximate a new loss coefficient from the data of Deissler [9] as

$$k = \sqrt{5.3/\log_{10}R_{ao}} - 1.0 \tag{10}$$

For $R_{ao}>200{,}000$, k is set equal to zero. This new loss coefficient is then used to determine new entrance conditions and the procedure repeated until a consistent result for k is found. Finally, the initial zeroth-order circumferential velocity, $u_\theta(0)$, is a given independent variable which indicates the amount of prerotation given to the entering fluid.

Having now the zeroth-order initial conditions, Eqs. (A.1a) through (A.1d) are numerically integrated along the seal length. The guess for the entrance Mach number is continually adjusted until: (a) the Mach number at the exit just reaches one and the exit pressure remains greater than the sump pressure for choked flow, or (b) until the exit pressure just matches the sump pressure and the Mach number remains less than one for unchoked flow. All intermediate values of the pressure, density, and velocities and their derivatives are then stored for later use in solving the first-order perturbation equations. Also, the leakage is determined from these zeroth-order values.

First-Order Solution

The first-order Eqs. (A.2a) through (A.2d) define $\tilde{p}_1(z,\theta,\tau)$, $\tilde{\rho}_1(z,\theta,\tau)$, $u_{z1}(z,\theta,\tau)$, and $u_{\theta 1}(z,\theta,\tau)$ resulting from the seal clearance function $h_1(z,\theta,\tau)$. If the shaft center moves in an elliptical orbit, then the rotation displacement vector to the shaft center has coordinates

$$X = Cx_o\cos\Omega t \quad , \quad Y = Cy_o\sin\Omega t \tag{11}$$

and the clearance function is

$$h_1 = -x_o\cos\tilde{\Omega}\tau\cos\theta - y_o\sin\tilde{\Omega}\tau\sin\theta \tag{12}$$

The assumed harmonic response is

$$\begin{aligned}
\tilde{p}_1 &= (\tilde{p}_x^c\cos\tilde{\Omega}\tau+\tilde{p}_x^s\sin\tilde{\Omega}\tau)\cos\theta+(\tilde{p}_y^c\cos\tilde{\Omega}\tau+\tilde{p}_y^s\sin\tilde{\Omega}\tau)\sin\theta\\
\tilde{\rho}_1 &= \tilde{\rho}_x^c\cos\tilde{\Omega}\tau+\tilde{\rho}_x^s\sin\tilde{\Omega}\tau)\cos\theta+(\tilde{\rho}_y^c\cos\tilde{\Omega}\tau+\tilde{\rho}_y^s\sin\tilde{\Omega}\tau)\sin\theta\\
u_{z1} &= (u_x^c\cos\tilde{\Omega}\tau+u_x^s\sin\tilde{\Omega}\tau)\cos\theta+(u_y^c\cos\tilde{\Omega}\tau+u_y^s\sin\tilde{\Omega}\tau)\sin\theta\\
u_{\theta 1} &= (v_x^c\cos\Omega\tau+v_x^s\sin\Omega\tau)\cos\theta+(v_y^c\cos\Omega\tau+v_y^s\sin\Omega\tau)\sin\theta
\end{aligned} \tag{13}$$

Substitution of Eqs. (12) and (13) into the first-order Eqs. (A.2a) through (A.2d) yields sixteen first-order ordinary differential equations which can be written in the form

$$[A(z)]\frac{d\underline{X}}{dz} + [B(z)]\underline{X} = x_o\underline{C}(z) + y_o\underline{D}(z) \tag{14}$$

where

$$\underline{X}=(\tilde{p}_x^c,\tilde{p}_x^s,\tilde{p}_y^c,\tilde{p}_y^s,\tilde{\rho}_x^c,\tilde{\rho}_x^s,\tilde{\rho}_y^c,\tilde{\rho}_y^s,u_x^c,u_x^s,u_y^c,u_y^s,v_x^c,v_x^s,v_y^c,v_y^s).$$

The coefficients of [A], [B], $\underline{C}$, and $\underline{D}$ are given in Appendix B. These coefficients are completely determined from the values obtained in the zeroth-order solution.

The necessary sixteen boundary conditions for Eq. (14) are now written by examining the perturbation conditions that must exist at the entrance and exit for choked or unchoked flow. For ease in writing these conditions, the following definitions are made:

$$\underline{p}_1 = \begin{Bmatrix}\tilde{p}_x^c\\ \tilde{p}_x^s\\ \tilde{p}_y^c\\ \tilde{p}_y^s\end{Bmatrix}, \quad \underline{\rho}_1 = \begin{Bmatrix}\tilde{\rho}_x^c\\ \tilde{\rho}_x^s\\ \tilde{\rho}_y^c\\ \tilde{\rho}_y^s\end{Bmatrix}, \quad \underline{u}_{z1} = \begin{Bmatrix}u_x^c\\ u_x^s\\ u_y^c\\ u_y^s\end{Bmatrix}, \quad \underline{u}_{\theta 1} = \begin{Bmatrix}v_x^c\\ v_x^s\\ v_y^c\\ v_y^s\end{Bmatrix} \tag{15}$$

(a.1) For choked flow, the first-order perturbation in in the exit Mach number is set equal to zero. Using the definition of the Mach number, the first-order perturbation is

$$M_1 = M_o\left(\frac{\tilde{\rho}_1}{2\tilde{\rho}_o} + \frac{u_{z1}}{u_{zo}} - \frac{\tilde{p}_1}{2\tilde{p}_o}\right) \tag{16}$$

This yields

$$\frac{\tilde{p}_1(1)}{2\tilde{\rho}_o(1)} + \frac{u_{z1}(1)}{u_{zo}(1)} - \frac{\tilde{p}_1(1)}{2\tilde{p}_o(1)} = 0 \tag{17}$$

(a.2) For unchoked flow, the first-order perturbation in the exit pressure is zero giving

$$\tilde{p}_1(1) = 0 \tag{18}$$

(b) At the entrance, the circumferential velocity perturbation is zero, i.e.

$$u_{\theta 1}(0) = 0 \tag{19}$$

(c) Expansion of the pressure loss Eq. (7) in terms of the perturbation pressure and the perturbation Mach number from Eq. (16) yields the following first-order pressure loss equation which must be satisfied at the entrance:

$$\tilde{p}_1(0) + \frac{r\tilde{p}_o(0)}{2\tilde{p}_o(0)-r}\left(\frac{\tilde{p}_1(0)}{\tilde{p}_o(0)} + \frac{2u_{z1}(0)}{u_{zo}(0)}\right) = 0 \tag{20}$$

where

$$r = \frac{\gamma(k+1)\tilde{p}_o(0)M_o^2(0)}{1+(\gamma-1)(k+1)\dfrac{M_o^2(0)}{2}} \tag{21}$$

(d) A similar expansion for the density change at the entrance defined by Eq. (8) gives

$$\tilde{\rho}_1(0) + \frac{rs\tilde{\rho}_o(0)}{2\tilde{\rho}_o(0)+rs}\left(\frac{2u_{z1}(0)}{u_{zo}(0)} - \frac{\tilde{p}_1(0)}{\tilde{p}_o(0)}\right) = 0 \tag{22}$$

where

$$s = 1+(\gamma-1)\frac{[M_o^2(0)(k+1)-2]}{2\gamma(k+1)} \tag{23}$$

Solution of the differential Eq. (14) in terms of the above sixteen boundary conditions can be found by numerical integration techniques. The solution will take the form

$$\underline{X} = x_o\underline{f}(z) + y_o\underline{g}(z) \tag{24}$$

Dynamic Coefficient Definitions

As shown in reference [6] if the added mass terms are neglected, the dynamic seal coefficients can be obtained by numerically integrating the appropriate solution component of Eq. (24), i.e.,

$$\tilde{K} = \frac{K\bar{C}}{p_a RL} = \pi\int_0^1 f_1(z)dz \qquad \tilde{k} = \frac{k\bar{C}}{p_a RL} = -\pi\int_0^1 f_3(z)dz \tag{25}$$

$$\tilde{C} = \frac{C\bar{c}\,\Omega}{p_a RL} = \pi\int_0^1 g_3(z)dz \qquad \tilde{c} = \frac{c\bar{C}\Omega}{p_a RL} = \pi\int_0^1 g_1(z)dz \tag{26}$$

NUMERICAL EXAMPLE

For the compressible flow seal with different stator-rotor surface roughness treatments, there are fourteen independent geometric and fluid dynamic seal variables. Assuming a perfect gas, these variables can be reduced to ten dimensionless parameters. One possible set is $P_c = p_a/(\rho_a\omega^2R^2)$, $R_{coa} = \rho_a\bar{C}\omega R/\mu$, p_a/p_b, γ, L/D, C_e/C_x, $\bar{C}/R$, $e_s/2\bar{C}$, $e_r/2\bar{C}$ and $u_\theta(0) = U_\theta(0)/(\omega R)$. Due to this large number of independent parameters, it is unreasonable to attempt to describe the leakage and dynamic coefficient's dependence in the form of a complete set of design charts. Thus, a specific seal geometry and flow condition was chosen, and only the length, taper, fluid prerotation, and clearance ratio (L/D, C_e/C_x, $u_{\theta o}(0)$, and $\bar{C}/R$) were independently varied. The particular seal selected is equivalent to the turbine interstage seal of the High Pressure Oxidizer Turbopump (HPOTP) of the Space Shuttle Main Engine operating at Rated Power Level. The rotor is smooth and the stator is a honeycomb surface, resulting in the following seal parameters as supplied by Jackson [10]:

p_a = 34.05 MPa (4938 psia)

p_b = 26.41 MPa (3830 psia)

T_a = 773°K (1391°R)

R = 7.282 cm (2.867 in)

C_e = 0.381 mm (0.015 in)

C_x = 0.254 mm (0.010 in)

L = 2.527 cm (0.995 in)

γ = 1.4

R_g = 2480 m·N/kg°K (461 ft·lb/lbm°R)

$\mu = 2.05 \times 10^{-5}$ Pa·s (1.38×10^{-5} lb_m/ft·s)

$U_{\theta o}(0)$ = 0.25

ω = 28352 rpm

$e_s/2\bar{C} = 1.54 \times 10^{-2} \Rightarrow m_s = -0.0251$, $n_s = 0.01534$

$e_r/2\bar{C} = 3.08 \times 10^{-4} \Rightarrow m_r = -0.1691$, $n_r = 0.03976$

Results obtained for this seal are shown in Table 1. The first row of data represents the seal with the given smooth rotor and rough stator. The second row represents the results if both the stator and rotor are smooth. As expected, the rough stator decreases the leakage and cross-coupled stiffness. However, it also has the effect of significantly reducing the direct stiffness and slightly decreasing the direct damping.

	$\dot{\rho}$ (kg/s)	$K\times10^{-7}$ (N/m)	$k\times10^{-7}$ (N/m)	C (N·s/m)	c (N·s/m)
rough	1.23	3.07	0.147	1770	13.0
smooth	1.35	3.40	0.160	1800	-0.9

Table 1. Leakage and Rotordynamic Coefficients for the HPOTP Turbine Interstage Seal

Results obtained by varying the seal geometry are plotted in Figs. 3 through 6. In these graphs, the broken lines represent the given rough stator and the continuous lines represent a smooth stator. The

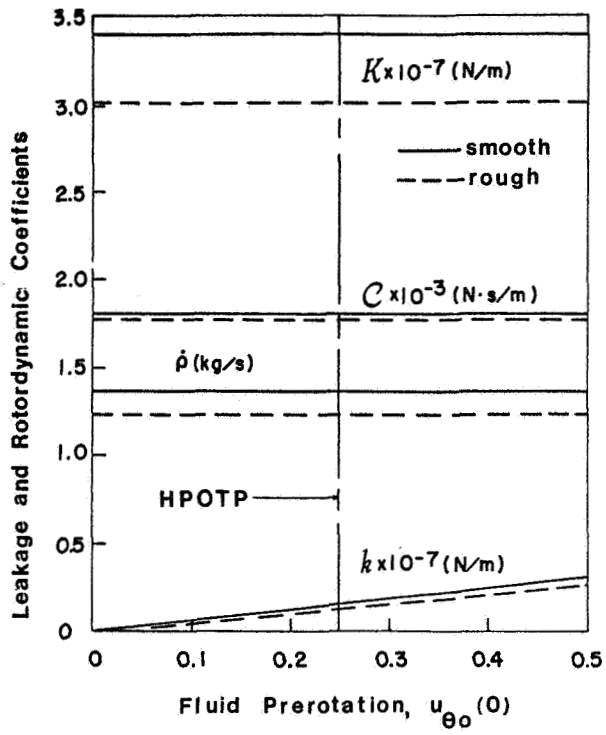

Figure 3. Leakage and rotordynamic coefficients vs. fluid prerotation (unchoked flow)

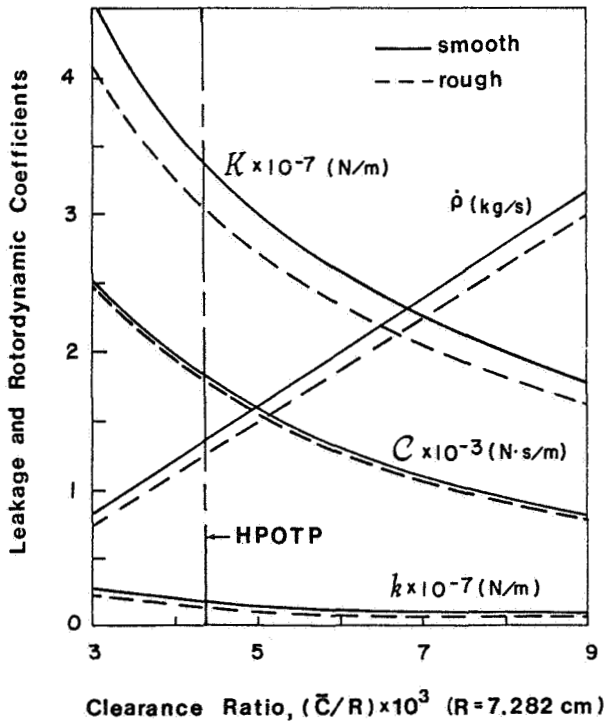

Figure 4. Leakage and Rotordynamic Coefficients vs. Clearance Ratio. (unchoked flow)

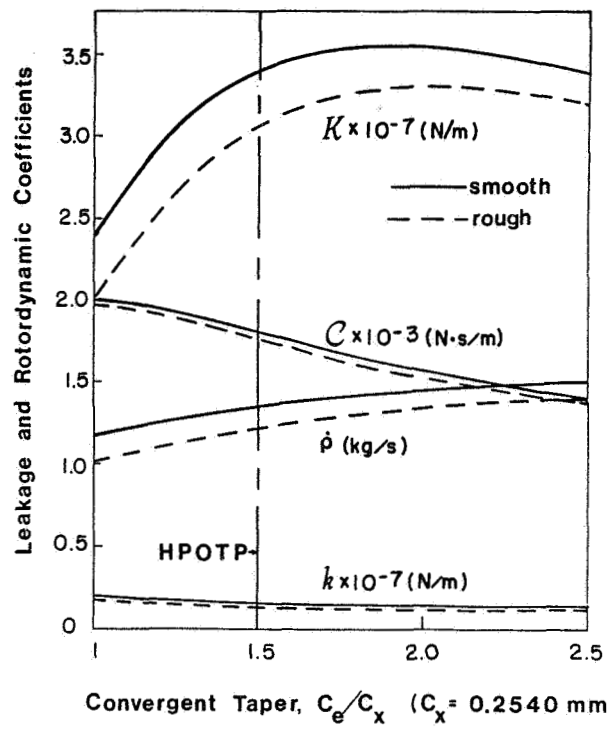

Figure 5. Leakage and Rotordynamic Coefficients vs. Convergent Taper (unchoked flow)

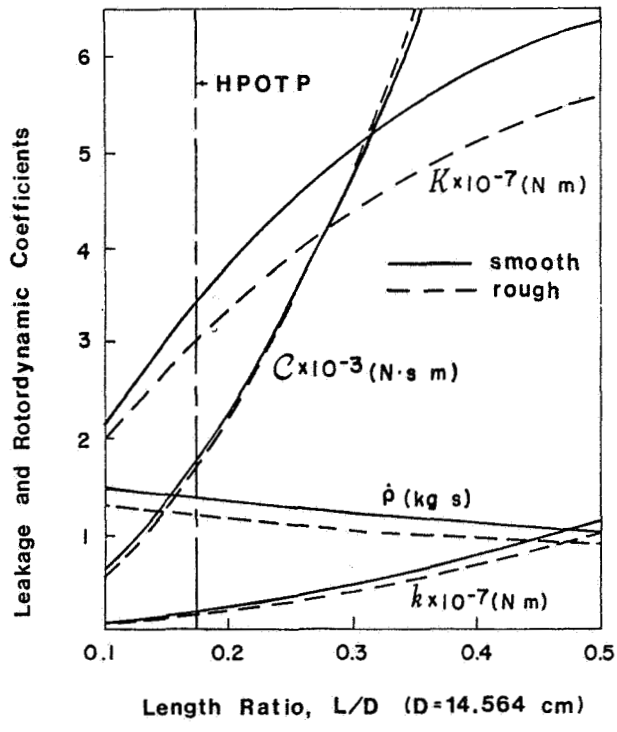

Figure 6. Leakage and rotordynamic coefficients vs. length ratio (unchoked flow)

vertical broken line represents the actual value of the independent variable for the HPOTP seal. Cross-coupled damping is not shown since it was found to be relatively insignificant.

Figure 3 shows the effect of fluid prerotation (preswirl). Clearly, prerotation has no effect on ρ, K, or C. However, there is a direct linear relationship for k.

Figure 4 shows the effect of changing the nominal clearance $\bar{C}$ (convengent taper was held constant). Within the range shown, decreasing the clearance results in an exponential increase in all coefficients and a linear decrease in leakage.

Figure 5 shows the effect of convergent taper, C_e/C_x. For these results, the exit clearance was held constant and the entrance clearance increased. It should be noted that this also has the effect of increasing the nominal clearance. Thus $1.0 \leq C_e/C_x \leq 2.5$ results in $0.0035 \leq C/R \leq 0.0061$. As might be expected from Fig. 4, increasing the taper in this manner increases ρ and decreases k and C. However, K shows roughly a 50% increase when the seal is changed from straight to having a convergent taper ratio of $C_e/C_x=2$.

Finally, Fig. 6 shows the effect of seal length. Generally, as L/D increases, the coefficients increase and the leakage decreases. However, for a very long seal (i.e., L/D =0.8), K does reach a maximum and thereafter decreases.

CONCLUDING REMARKS

An analysis has been presented which calculates the leakage and rotordynamic coefficients for tapered annular gas seals in which the rotor and stator have different surface roughness treatments. To demonstrate this analysis, the effect of changes in seal length, taper, clearance and fluid prerotation was shown for the HPOTP turbine interstage seal. Generally, changes in the abovementioned seal parameters resulted in major changes in the leakage and rotordynamic coefficients.

In terms of the honey comb stator enhancing rotor stability, the results appear mixed. There is a favorable 9% reduction in cross-coupled stiffness and leakage. But at the same time, direct damping decreases almost 2% and direct stiffness decreases 10%. Thus, general statements concerning the problems of instability and critical speeds can only be addressed by considering the entire rotordynamic system - clearly a problem outside the scope of this analysis. It should also be kept in mind that the selection of Hirs' constants may not accurately reflect the actual shear stresses developed over the honey comb surface. Experimental tests need yet to be performed to determine the correct values for these constants.

REFERENCES

1. von Pragenau, G. L., "Damping Seals for Turbomachinery," NASA Technical Paper-1987, George C. Marshall Space Flight Center, Alabama 35812.
2. Fleming, D. P., "Stiffness of Straight and Tapered Annular Gas Path Seals," J. Lubr. Technol., Vol. 101, No. 3, pp. 349-355, July 1979.
3. Fleming, D. P., "Damping in Ring Seals for Compressible Fluids," NASA CP-2133, 1980.
4. Childs, D. W., "Finite Length Solutions for the Rotordynamic Coefficients of Convergent-Turbulent Annular Seals," Mechanical Engineering, Texas A&M University, 1982.
5. Hirs, G. G., "Fundamentals of a Bulk-Flow Theory for Turbulent Lubrication Films," Ph.D. Dissertation, Delft Technical University, The Netherlands, July 1970.
6. Nelson, C. C., "Rotordynamic Coefficients for Compressible Flow in Tapered Annular Seals," Mechanical Engineering, Texas A&M University, 1983.
7. White, F. M., Fluid Mechanics, McGraw-Hill, 1979.
8. Zuk, J., Ludwig, L. P., and Johnson, R. L., "Quasi-One-Dimensional Compressible Flow Across Face Seals and Narrow Slots," NASA Technical Note D-6668, May 1972.
9. Deissler, R. G., "Analysis of Turbulent Heat Transfer and Flow in the Entrance Regions of Smooth Passages," NACA TN 3016, 1953.
10. Jackson, E. D., Manager, Rotating Machinery Analysis, Rockwell International, Rocketdyne Division, personal correspondence, 1983.

APPENDIX A: PERTURBATION EQUATIONS

Zeroth-Order Equations

$$\frac{-P_c}{\tilde{\rho}}\frac{\partial \tilde{p}_o}{\ell \partial z} = \frac{u_{zo}}{\bar{c}h_o}\left[f_{so}+f_{ro}\right] + \frac{u_{zo}}{\ell}\frac{\partial u_{zo}}{\partial z} \tag{A.1a}$$

$$0 = \frac{1}{\bar{c}h_o}\left[u_{\theta o}f_{so}+(u_{\theta o}-1)f_{ro}\right] + \frac{u_{zo}}{\ell}\frac{\partial u_{\theta o}}{\partial z} \tag{A.1b}$$

$$0 = \tilde{\rho}_o u_{zo}\frac{\partial h_o}{\partial z} + \tilde{\rho}_o h_o \frac{\partial u_{zo}}{\partial z} + u_{zo}h_o\frac{\partial \tilde{\rho}_o}{\partial z} \tag{A.1c}$$

$$0 = u_{\theta o}\frac{\partial u_{\theta o}}{\partial z} + u_{zo}\frac{\partial u_{zo}}{\partial z} + \frac{P_c\gamma}{\tilde{\rho}_o(\gamma-1)}\left(\frac{\partial p_o}{\partial z} - \frac{p_o}{\tilde{\rho}_o}\frac{\partial \rho_o}{\partial z}\right) + \frac{\ell(u_{\theta o}-1)f_{ro}}{\bar{c}h_o u_{zo}} \tag{A.1d}$$

where

$$f_{so} = \frac{n_s}{2}\left(u_o^2 + u_{zo}^2\right)^{\frac{m_s+1}{2}}(2R_{co})^{m_s}$$

$$f_{ro} = \frac{n_r}{2}\left[(u_o-1)^2 + u_{zo}^2\right]^{\frac{m_r+1}{2}}(2R_{co})^{m_r}$$

First-Order Equations

$$\frac{-P_c}{\tilde{\rho}_o\ell}\frac{\partial \tilde{p}_1}{\partial z} = \frac{-P_c\tilde{\rho}_1}{\tilde{\rho}_o^2\ell}\frac{\partial p_o}{\partial z} + \frac{1}{\bar{c}h_o}\left[u_{zo}(f_{s1}+f_{r1}) + \left(u_{z1}-u_{zo}\frac{h_1}{h_o}\right)(f_{s1}+f_{r1})\right] + \frac{\partial u_{z1}}{\partial \tau} + u_{\theta o}\frac{\partial u_{z1}}{\partial \theta} + \frac{u_{zo}}{\ell}\frac{\partial u_{z1}}{\partial z} + \frac{u_{z1}}{\ell}\frac{\partial u_{zo}}{\partial z} \tag{A.2a}$$

$$\frac{-P_c}{\tilde{\rho}_o}\frac{\partial \tilde{p}_1}{\partial \theta} = \frac{1}{\bar{c}h_o}\left[u_{\theta o}\left(f_{s1} - \frac{h_1}{h_o} f_{so}\right)\right.$$

$$+ (u_{\theta o}-1)\left(f_{r1} - \frac{h_1}{h_o} f_{ro}\right) + u_{\theta 1}(f_{so}+f_{ro})$$

$$\left. + \frac{\partial u_{\theta 1}}{\partial \tau} + u_{\theta o}\frac{\partial u_{\theta 1}}{\partial \tau} + \frac{u_{z0}}{\ell}\frac{\partial u_{\theta 1}}{\partial z} + \frac{u_{z1}}{\ell}\frac{\partial u_{\theta o}}{\partial z}\right]$$

(A.2b)

$$0 = \frac{\tilde{\rho}_o}{h_o}\frac{\partial h_1}{\partial \tau} + \frac{\partial \tilde{\rho}_1}{\partial \tau} + \frac{\tilde{\rho}_o u_{\theta o}}{h_o}\frac{\partial h_1}{\partial \theta} + \tilde{\rho}_o\frac{\partial u_{\theta 1}}{\partial \theta} + u_{\theta o}\frac{\partial \tilde{\rho}_1}{\partial \theta}$$

$$+ \frac{1}{\ell h_o}\left[h_1\frac{\partial(\tilde{\rho}_o u_{zo})}{\partial z} + \frac{\partial(\tilde{\rho}_o u_{z1} h_o)}{\partial z} + \frac{\partial(\tilde{\rho}_1 u_{zo} h_o)}{\partial z}\right]$$

(A.2c)

$$\frac{P_c \tilde{\rho}_o}{\tilde{\rho}_o h_o}\frac{h_1}{\partial \tau} = u_{zo}\left[\frac{\partial u_{z1}}{\partial \tau} + u_{\theta o}\frac{\partial u_{z1}}{\partial \theta} + \frac{1}{\ell}\left(u_{zo}\frac{\partial u_{z1}}{\partial z}\right.\right.$$

$$\left. + 2u_{z1}\frac{\partial u_{zo}}{\partial z} + u_{\theta 1}\frac{\partial u_{\theta o}}{\partial z}\right) + u_{\theta o}\left[\frac{\partial u_{\theta 1}}{\partial \tau}\right.$$

$$\left. + u_{\theta o}\frac{\partial u_{\theta 1}}{\partial \theta} + \frac{1}{\ell}\left(u_{zo}\frac{\partial u_{\theta 1}}{\partial z} + u_{z1}\frac{\partial u_{\theta o}}{\partial z}\right)\right]$$

$$+ \frac{\gamma P_c}{\tilde{\rho}_o(\gamma-1)}\left\{\frac{1}{\gamma}\frac{\partial \tilde{p}_1}{\partial \tau} + u_{\theta o}\frac{\partial \tilde{p}_1}{\partial \theta} + \frac{u_{\theta o}}{\ell}\frac{\partial \tilde{p}_1}{\partial z}\right.$$

$$+ \frac{1}{\ell}\frac{\partial \tilde{p}_o}{\partial z}\left(u_{z1} - u_{zo}\frac{\tilde{\rho}_1}{\rho_o}\right) - \frac{\tilde{p}_o}{\rho_o}\left[\frac{\partial \tilde{\rho}_1}{\partial \tau}\right.$$

$$+ u_{\theta o}\frac{\partial \tilde{\rho}_1}{\partial \theta} + \frac{u_{zo}}{\ell}\frac{\partial \tilde{\rho}_1}{\partial z} + \frac{1}{\ell}\frac{\partial \tilde{\rho}_o}{\partial z}\left(u_{z1}\right.$$

$$\left.\left.\left. + u_{zo}\left(\frac{\tilde{\rho}_1}{\tilde{p}_o} - \frac{2\tilde{\rho}_1}{\tilde{\rho}_o}\right)\right)\right]\right\}$$

$$+ \frac{\tilde{\rho}_o(u_{\theta o}-1) f_{ro}}{\bar{c}h_o P_c}\left[\frac{\tilde{\rho}_1}{\tilde{\rho}} + \frac{u_{\theta 1}}{(u_{\theta o}-1)} + \frac{f_{r1}}{f_{ro}} - \frac{h_1}{h_o}\right]$$

(A.2d)

where

$$f_{s1} = f_{so}\left[m_s\left(\frac{\tilde{\rho}_1}{\tilde{\rho}_o} + \frac{h_1}{h_o}\right) + a(u_{\theta o}u_{\theta 1} + u_{zo}u_{z1})\right.$$

$$f_{r1} = f_{ro}\left[m_r\left(\frac{\tilde{\rho}_1}{\tilde{\rho}_o} + \frac{h_1}{h_o}\right) + b((u_{\theta o}-1)u_{\theta 1} + u_{zo}u_{z1})\right]$$

$$a = (m_s+1)/(u_{\theta o}^2 + u_{zo}^2)$$

$$b = (m_r+1)/[(u_{\theta o}-1)^2 + u_{zo}^2]$$

APPENDIX B: MATRIX COEFFICIENTS

All coefficients are zero except those defined below. Also, $\gamma=\gamma P_c/[\tilde{\rho}_o(\gamma-1)]$ and $q=\tilde{\rho}_o(u_{\theta o}-1)f_{bo}/(\bar{c}h_o P_c)$

Matrix [A]

$a_{i,i+4} = u_{zo}/\ell$ i=1,2,3...12

$a_{i,i+8} = \tilde{\rho}_o/\ell$ i=1,2,3,4

$a_{i+4,i} = \frac{P_c}{\tilde{\rho}_o \ell}$ i=1,2,3,4

$a_{i+12,i} = \gamma' u_{zo}/\ell$ i=1,2,3,4

$a_{i+8,i} = \frac{-\gamma'\tilde{p}_o u_{zo}}{\tilde{\rho}_o \ell}$ i=5,6,7,8

$a_{i+r,i} = \frac{u_{zo}^2}{\ell}$ i=9,10,11,12

$a_{i,i} = \frac{u_{zo}u_{\theta o}}{\ell}$ i=13,14,15,16

Matrix [B]

$b_{i,i+4} = \frac{1}{\ell h_o}\frac{d(u_{zo}h_o)}{dz}$ i=1,2,3,4

$b_{i,i+5} = -b_{i+1,i+4} = \tilde{\Omega}$ i=1,3,5...11

$b_{i,i+6} = -b_{i+2,i+4} = u_{\theta o}$ i=1,2,5,6,9,10

$b_{i,i+8} = \frac{1}{\ell h_o}\frac{d(\tilde{\rho}_o h_o)}{dz}$ i=1,2,3,4

$b_{i,i+14} = -b_{i+2,i+12} = \tilde{\rho}_o$ i=1,2

$b_{i,i} = \frac{u_{zo}}{\bar{c}h_o\tilde{\rho}_o}(m_s f_{so}+m_r f_{ro}) - \frac{P_c}{\tilde{\rho}_o^2 \ell}\frac{d\tilde{p}_o}{dz}$ i=5,6,7,8

$b_{i,i+4} = \frac{1}{\bar{c}h_o}\left\{f_{so}[1+u_{zo}^2 a] + f_{ro}(1+u_{zo}^2 b)\right\} + \frac{1}{\ell}\frac{du_{zo}}{dz}$ i=5,6,7,8

$b_{i,i+8} = \frac{u_{zo}}{\bar{c}h_o}[u_{\theta o}f_{so}a + (u_{\theta o}-1)f_{so}b]$ i=5,6,7,8

$b_{i+6,i} = -b_{i+8,i-2} = P_c/\tilde{\rho}_o$ i=3,4

$b_{i+4,i} = \frac{1}{\bar{c}h_o\tilde{\rho}_o}[u_{\theta o}m_s f_{so} + (u_{\theta o}-1)m_r f_{ro}]$ i=5,6,7,8

$b_{i,i} = \frac{u_{zo}}{\bar{c}h_o}[u_{\theta o}f_{so}a + (u_{\theta o}-1)f_{ro}b] + \frac{1}{\ell}\frac{du_{\theta o}}{dz}$ i=9,10,11,12

$$b_{i,i+4} = \frac{1}{\bar{c}h_o}[f_{so}(1+u_{\theta o}^2 a)+f_{ro}(1+(u_{\theta o}-1)^2 b_1] \qquad i=9,10,11,12$$

$$b_{i+12,i} = \frac{-\gamma u_{zo}}{\tilde{\rho}_o \ell}\frac{d\tilde{\rho}_o}{dz} \qquad i=1,2,3,4$$

$$b_{i+11,i} = -b_{i+12,i-1} = \frac{\gamma'\Omega}{\gamma} \qquad i=2,4$$

$$b_{i+10,i} = -b_{i+13,i-1} = \gamma' u_{\theta o} \qquad i=3,4$$

$$b_{i+8,i} = \frac{\gamma' u_{zo}}{\ell\tilde{\rho}_o}\left(\frac{2\tilde{p}_o}{\tilde{\rho}_o}\frac{d\tilde{\rho}_o}{dz} - \frac{d\tilde{p}_o}{dz}\right) + \frac{q(1+m_r)}{\tilde{\rho}_o} \qquad i=5,6,7,8$$

$$b_{i+7,i} = -b_{i+8,i-1} = -\gamma'\frac{\tilde{p}_o\tilde{\Omega}}{\tilde{\rho}_o} \qquad i=6,8$$

$$b_{i+6,i} = -b_{i+9,i-1} = -\gamma'\frac{\tilde{p}_o u_{\theta o}}{\tilde{\rho}_o} \qquad i=7,8$$

$$b_{i+4,i} = \frac{\gamma'}{\ell}\left(\frac{d\tilde{p}_o}{dz} - \frac{\tilde{p}_o}{\tilde{\rho}_o}\frac{d\tilde{\rho}_o}{dz}\right) + \frac{2u_{zo}}{\ell}\frac{du_{zo}}{dz} + \frac{u_{\theta o}}{\ell}\frac{du_{\theta o}}{dz} + qf_{ro}u_{zo} \qquad i=9,10,11,12$$

$$b_{i+3,i} = -b_{i+4,i-1} = u_{zo}\tilde{\Omega} \qquad i=10,12$$

$$b_{i+2,i} = -b_{i+5,i-1} = u_{zo}u_{\theta o} \qquad i=11,12$$

$$b_{i,i+1} = -b_{i+1,i} = u_{\theta o}\tilde{\Omega} \qquad i=13,15$$

$$b_{i,i+2} = -b_{i+2,i} = u_{\theta o}^2 \qquad i=13,14$$

Vectors $\underline{C}$ and $\underline{D}$

$$c_1 = d_4 = \frac{1}{\ell h_o}\frac{d(\tilde{\rho}_o u_{zo})}{dz}$$

$$c_2 = -d_3 = -\tilde{\rho}_o\tilde{\Omega}/h_o$$

$$c_3 = -d_2 = -\tilde{\rho}_o u_{zo}/h_o$$

$$c_5 = d_7 = \frac{u_{zo}}{\bar{c}h_o^2}[(m_s-1)f_{so}+(m_r-1)f_{ro}]$$

$$c_9 = d_{12} = \frac{1}{\bar{c}h_o^2}[u_{\theta o}(m_s-1)f_{so}+(u_{\theta o}-1)(m_r-1)f_{ro}]$$

$$c_{13} = d_{13} = \frac{q(m_r-1)}{h_o}$$

$$c_{14} = -d_{15} = \frac{P_c\tilde{p}_o\tilde{\Omega}}{\tilde{\rho}_o h_o}$$

DESIGN OF ELECTROMAGNETIC BEARING FOR VIBRATION CONTROL OF FLEXIBLE TRANSMISSION SHAFT*

V. Gondhalekar
E.T.H. Zürich, Switzerland

R. Holmes
Department of Mechanical Engineering
University of Southampton, U.K.

Recently magnetic bearings have been proposed by several researchers and shown to be viable on a variety of rotor assemblies. This paper is concerned with the design and construction of such a bearing, which employs features hitherto not used by other workers. These include an original approach to the design of the electromagnets and their amplifiers, and to software in a digital control system, to condition the control signals so as to make the magnets appear to be linear and uncoupled. The resulting system is used to control a rotor-bearing assembly, whose speed range covers two flexural-critical speeds.

INTRODUCTION

The feasibility of using magnet forces to control shaft vibrations has recently been a subject of attention from a number of researchers and successful application of bearings and dampers in rotating assemblies has been reported [1,2,3]. A flexible transmission shaft is a special case of a rotating assembly which needs some form of control to maintain its vibration amplitudes within reasonable limits when passing through its critical speeds. Squeeze-film bearings have been shown to be capable of reducing vibration amplitudes but these can normally only react to the rotor displacement at the bearing locations. A controlled electromagnet (CEM) located at a point along the length of a transmission shaft has also been shown to be effective in reducing vibration amplitudes [2]. The CEM offers the possibility of applying a force which is a function of displacement and/or velocity at the CEM location or at a location remote from it. This offers the possibility of implementing a control strategy which responds to one signal or to the weighted average of more than one signal measurement remote from the CEM location.

Some magnetic bearing configurations proposed by past workers are shown in Fig.1. The static member of that shown in Fig.1a is the simplest to construct but in an attempt to combat eddy current effects the rotating sleeve must be made from

*The authors gratefully acknowledge the Science & Engineering Research Council, U.K., for their financial support.

rectangular laminations. Any lamination completing the flux path only does so for a short time increment and other laminations sequentially perform this function as the shaft rotates. A relatively long axial length is needed to provide a given magnetic force. The radial flux configuration of Fig.1b makes lamination of both the static and rotating members easy, the latter now being constructed from flat discs. A disadvantage, however, is inefficient radial space utilization. Also the long narrow limbs lead to high magnetic saturation, that is high flux concentration at the magnet bases.

Magnetic bearings are best designed to operate in an attraction rather than a repulsion mode, but in either case the basic inverse square-law relationship between magnetic force and gap has to be overcome since this can lead to instability. Schweitzer [1] describes a design similar to that of Fig. 1b in which stability is achieved, together with the linearity of the force-current characteristic by a differential circuit, in addition to a circuit ensuring premagnetisation with a constant current. Thus operation takes place about a non-zero steady-state condition. Easier analysis and controller design are assured by the improvement in linearity but bulky magnets are necessary to dissipate the consequent heat produced by the premagnetisation current.

A logical next step is to integrate all four magnets into a single structure as shown in Fig. 1c. However, there is here a high degree of interaction between the four poles, and consequently the magnet performance has to be improved by special techniques requiring bidirectional drive amplifiers to alter the direction of the flux as required [2]. This disadvantage can be overcome by using the four active/four passive pole configuration of Fig. 1d [3], in which four unidirectional amplifiers can be used.

Fig. 1e shows a 3 pole active/3 pole passive configuration as used in the present work, as it gives a better space utilization than does that of Fig. 1d, as well as reducing magnet interaction. However, since the magnets do not lie on mutually perpendicular axes, xy, cross-coupling is introduced between these axes. This is counteracted by suitable software using a microprocessor interface which in any case is essential for adaptive control purposes. Also it was decided to design for operation about a point of zero magnet excitation as this obviates the need for an extra coil to supply a constant magnetising current. Thus resistive heating of the magnet coils is reduced and consequently their weight and size. The whole device is required to exert dynamic rather than static force components and hence there is no need from that point of view for a non-zero quiescent operating point. One of the main objectives of the present work is to design software to condition the control signals so as to make the magnets appear linear (and uncoupled) in spite of using this zero-excitation

operating point.

The rotor system controlled by the electromagnets is shown in Fig.2, and the final electromagnet configuration in Fig.3. The overall system including the microprocessor and associated peripherals is shown in Fig.4. The electromagnets, their drive electronics and the computer system are described in some detail and some results obtained from the rig to date are presented.

THE ELECTROMAGNETS AND THEIR DRIVE ELECTRONICS

A block diagram of the electromagnet system designed for the present work is shown in Fig.5. Each power amplifier, A, which drives a magnet coil, C, is of the switching type, employing pulse-width modulation to reduce power losses. It is designed to operate at a maximum A.C. input of 220 v rms and as a result approximately 300 v D.C. is available to drive each coil, with a current limit of 10 amp, but with available capacity up to 15 amp.

The electromagnet configuration of Fig.3 consists of six radial poles - 3 active and 3 passive - the latter acting as return flux paths. The electromagnets and the rotor sleeve are constructed from 0.1 mm disc laminations to eliminate eddy currents up to approximately 300 Hz and the 3 active poles were suitably energised to generate forces along the x and y axes. This particular configuration was chosen because it utilizes the available radial space more efficiently in terms of force than a similar structure consisting of four active poles, and the number of drive amplifiers is reduced from 4 to 3. One disadvantage is the force interaction introduced between the orthogonal axes, but as mentioned above, software is employed to overcome this problem.

An electromagnet exerts a force approximately proportional to the square of the magnet flux present at the pole face. It is also unstable in an open loop mode since, as the deflection increases towards a magnet, so does the attractive force from that magnet. The system can, however, be made stable by feeding back a signal v_H produced by a Hall probe, which is proportional to the flux at the pole face (Fig.5).

Since the electromagnets can only operate effectively in an attraction mode, with no repulsion, then in order to overcome this unidirectional forcing feature in creating restoring forces to counteract displacements, X and Y, the excitation signals, S_1, S_2, S_3, to the three drive amplifiers A (Fig.5) would be constituted as follows:

$$S_1 = [Y]_{T/2}^{T} - 0.5[X]_{0}^{T/4} + 0.5[X]_{T/4}^{3T/4} - 0.5[X]_{3T/4}^{T}$$

$$S_2 = -[Y]_{0}^{T/2} - [X]_{0}^{T/4} - [X]_{3T/4}^{T} \qquad (1)$$

$$S_3 = -[Y]_{0}^{T/2} + [X]_{T/4}^{3T/4}$$

where T is the periodic time. For displacements X and Y as shown in Fig. 6a, the signals S thus appear as shown in that figure.

It will be noted that all three signals contain both X and Y components. This is because magnets 2 and 3 have to exert forces to counter X and Y displacements, but in the process introduce unwanted X-dependent forces in the Y direction. These are neutralised by additional X-component forces generated in magnet 1 by signal S_1. Assuming that a linear relationship exists between the signals and the attraction forces produced by the magnets, then, for some amplifier gain, C,

$$F_y = C[-S_1 + (S_2 + S_3)\cos 60^\circ]$$

$$F_x = (2C/\sqrt{3})[(S_2 - S_3)\cos 30^\circ].$$

In fact, the force produced at each pole face is proportional to the square of the flux at that face and hence to the square of the current supplied to each magnet coil. Thus, if there is a linear relation between any signal S and its coil current then each magnet force will be proportional to S^2 and not to S as assumed above. However, this can be partially accommodated by replacing the multiplier 0.5 in the first of equations (1) by 0.5, the other two equations remaining unaltered. This is followed by writing F_y and F_x as

$$F_y = [-(S_1)^2 + [(S_2)^2 + (S_3)^2]\cos 60^\circ]C$$

$$F_x = \{[(S_2)^2 - (S_3)^2]\cos 30^\circ\}(2C/\sqrt{3})$$

As a result, the forms of the forces produced in the x,y directions are shown in Fig. 6b. When combined to produce a

polar force diagram a signficant 3rd Harmonic is revealed (Fig.6c).

Linearisation of each magnet device can, however, be achieved by using the square root of the control signal input, S, to each magnet amplifier. This input signal then produces a proportional flux, the approximate square of which is proportional to the force exerted on the rotor. The control signal S, vs force output thus follows an approximately linear relationship and allows the signal and hence force contributions of the three magnets to be added linearly.

The square root of a number can be found using software by computing a finite number of terms of a series expansion, but this can be time-consuming in a real-time application. A piece-wise linear approximation to the function $y = K/S$ was therefore used, where S is the control signal, and K is a constant. The above function is divided into 32 segments of progressively greater length, since a square root function varies rapidly around zero, and the software computes the square root in 96 μsec on a Z8002 cpu. The square-rooting procedure, when applied to the control signals of all 3 magnets results in the polar force diagram shown in Fig. 6d, indicating considerable improvement over that shown in Fig. 6c. The software can be adapted, if required,to compensate for the saturation of the magnet core material also.

As well as being influenced by the square-law non-linearity, the magnet forces are also subject to current-rate saturation in the drive amplifiers. This occurs if more than the maximum drive voltage of the amplifier is demanded. Fortunately, in practice, the current rates demanded are low enough to be unaffected by any limitations in V, particularly when the restoring forces provided by the magnets are kept within reasonable limits.

CONTROL STRATEGY

Assuming negligible internal damping, the rotor vibration can be represented by the following set of equations:

$$y_i = \sum_{j=1}^{j=3} \alpha_{ij}(P_j + m_j\omega^2 y_j) - \alpha_{i4}K_d y_4, \quad i = 1 \text{ to } 4$$

where α_{ij} are the influence coefficients (m/N) relating to the mass stations 1, 2 and 3, ω is the rotor speed in rad/s, P_j are the forces due to mass unbalance, y_j are displacement amplitudes at the mass stations and K_d is the stiffness introduced by the CEM at station 4. The negative dynamic stiffness curve at station 4 for this rotor is shown in Fig.7. Dynamic stiffness is the rotor dynamic force at station 4

divided by dynamic displacement, and the frequencies at which the negative stiffness equals the dynamic stiffness of the support at station 4 are the natural frequencies of the complete system. Thus the intersections with a horizontal line K_d parallel to the ω-axis give the natural frequencies ω_n (that is critical speeds) of the rotor system. A speed-dependent controller can ensure that the natural frequencies of the rotor system are sufficiently removed from the mass-unbalance disturbance frequency (that is the rotational speed) by automatically adjusting the stiffness K_d.

It is also possible to introduce both stiffness and damping at station 4. Fig. 8 shows some typical response curves taken from the rotating assembly of Fig.2, sample values of stiffness and damping provided by the controlled electromagnets being indicated. These serve to indicate how the critical speeds can be altered and the peak responses brought down to acceptable levels.

CONCLUSIONS

The results of this research indicate that efficient and compact electromagnets have been designed to effectively control the vibrations of a supercritical rotating assembly. By the use of a microprocessor, software has been designed to overcome any problems of cross-coupling between orthogonal axes and of inherent non-linear force-deflection characteristics in the magnets. By the same microprocessor a considerable degree of control can also be achieved, as indicated in Fig. 8.

REFERENCES

1. Schweitzer, G. and Ulbrich, H. 'Magnetic Bearings - a novel type of suspension'. I.Mech.E. Conference on Vibrations in Rotating Machinery, Cambridge, Sept. 1980.

2. Nikolajsen, J.N., Holmes, R. and Gondhalekar, V. 'Investigation of an electromagnetic damper for vibration control of a transmission shaft'. Proc. I.Mech.E. Vol. 193, No.31, 1979.

3. Habermann, H. 'Le Palier magnetique actif "ACTIDYNE"'. AGARD Conference Proceedings, No. 323, 'Problems in Bearings and Lubrication', Ottawa, Canada, May 1982.

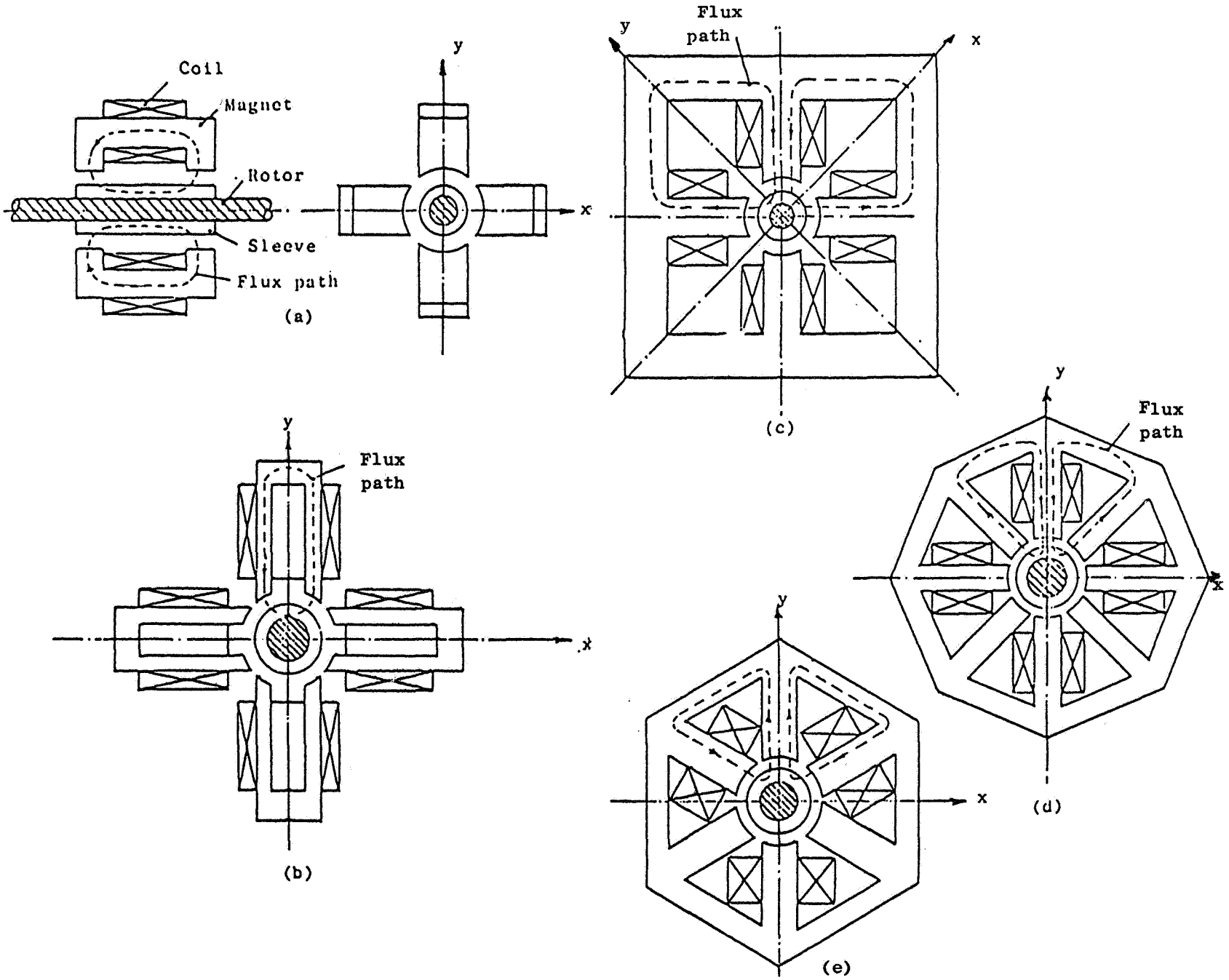

Figure 1. - Viable magnetic bearing configurations.

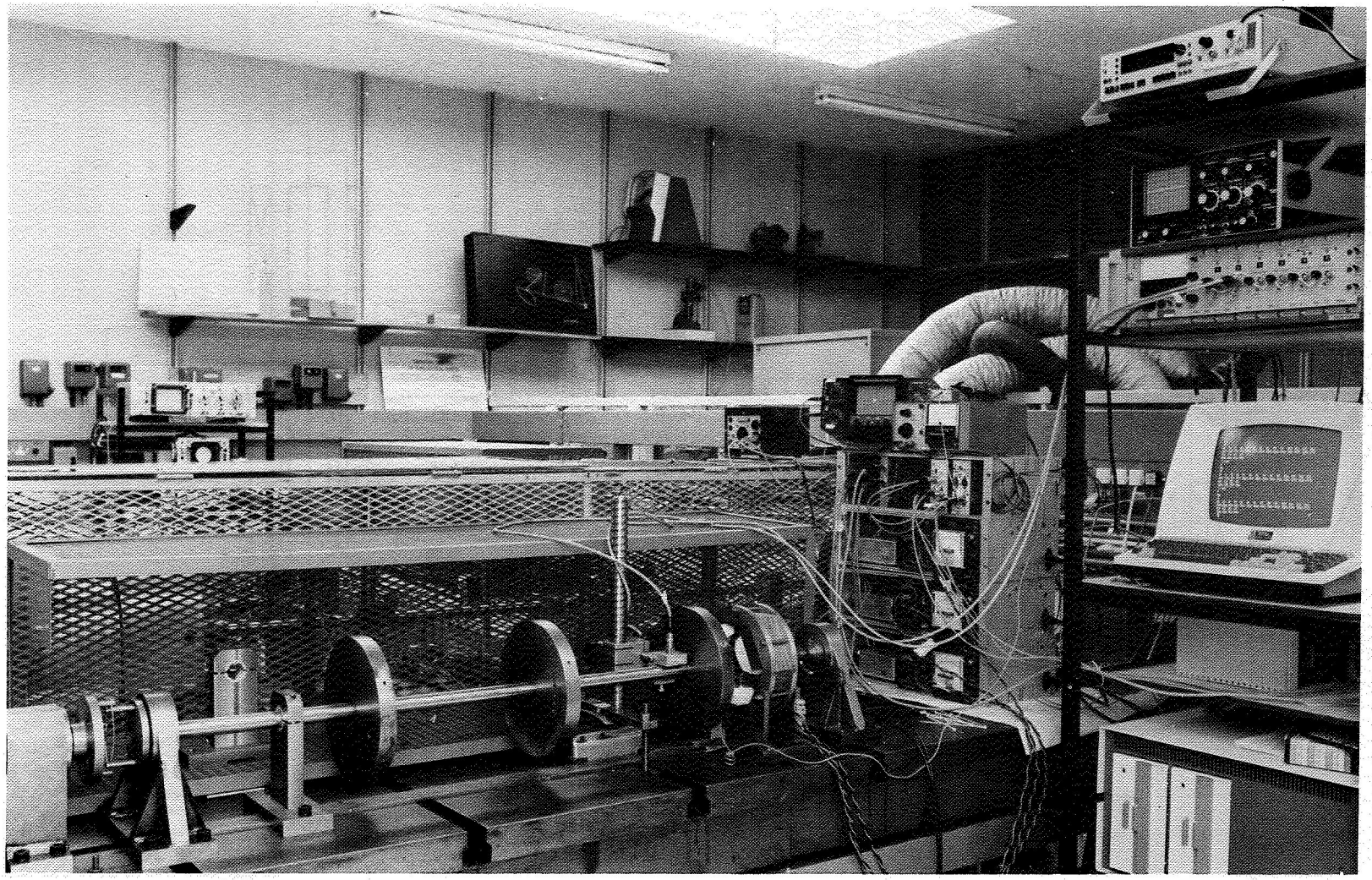

Figure 2. - Rotor and electromagnetic device. Span, 1.265 m; total mass, 30 kg.

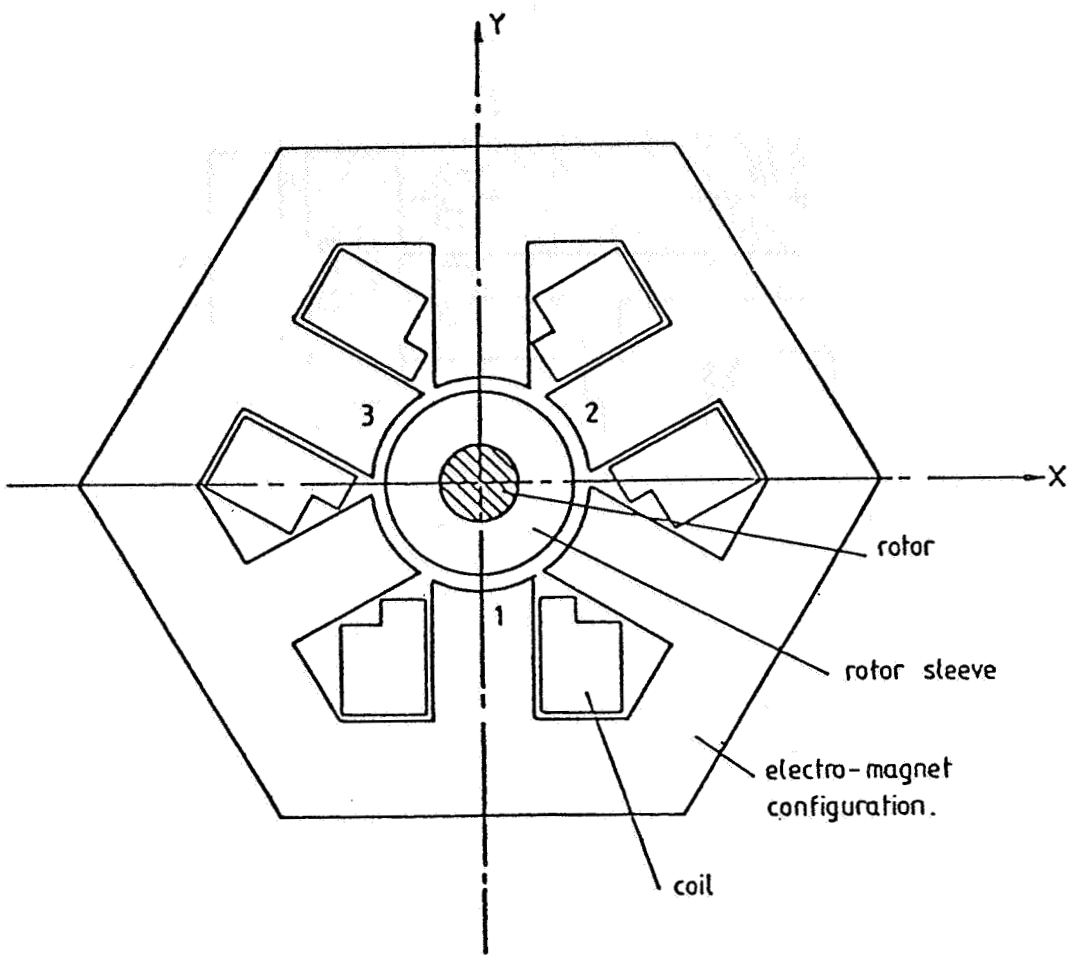

Figure 3. - Active-pole electromagnet configuration. Radial air gap, 2 mm; radial stiffness, 1×10^5 to 10×10^5 N/m; peak power requirement, 200 W.

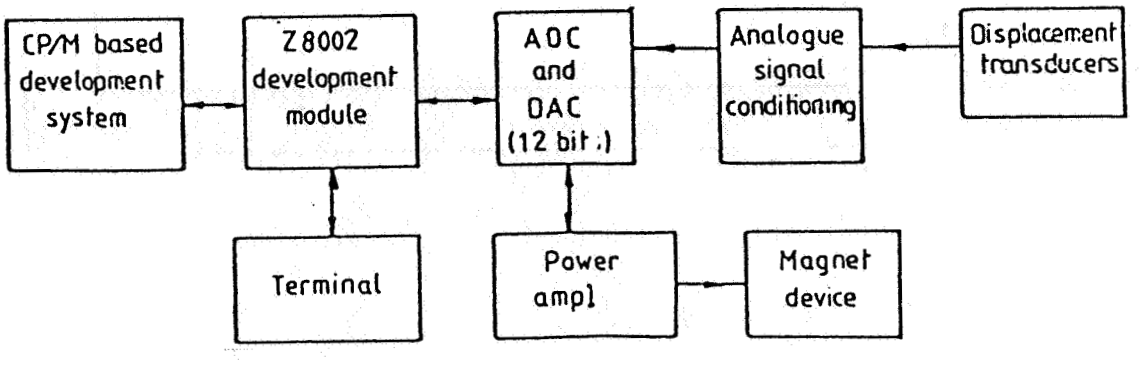

Figure 4. - Computer and electromagnet system.

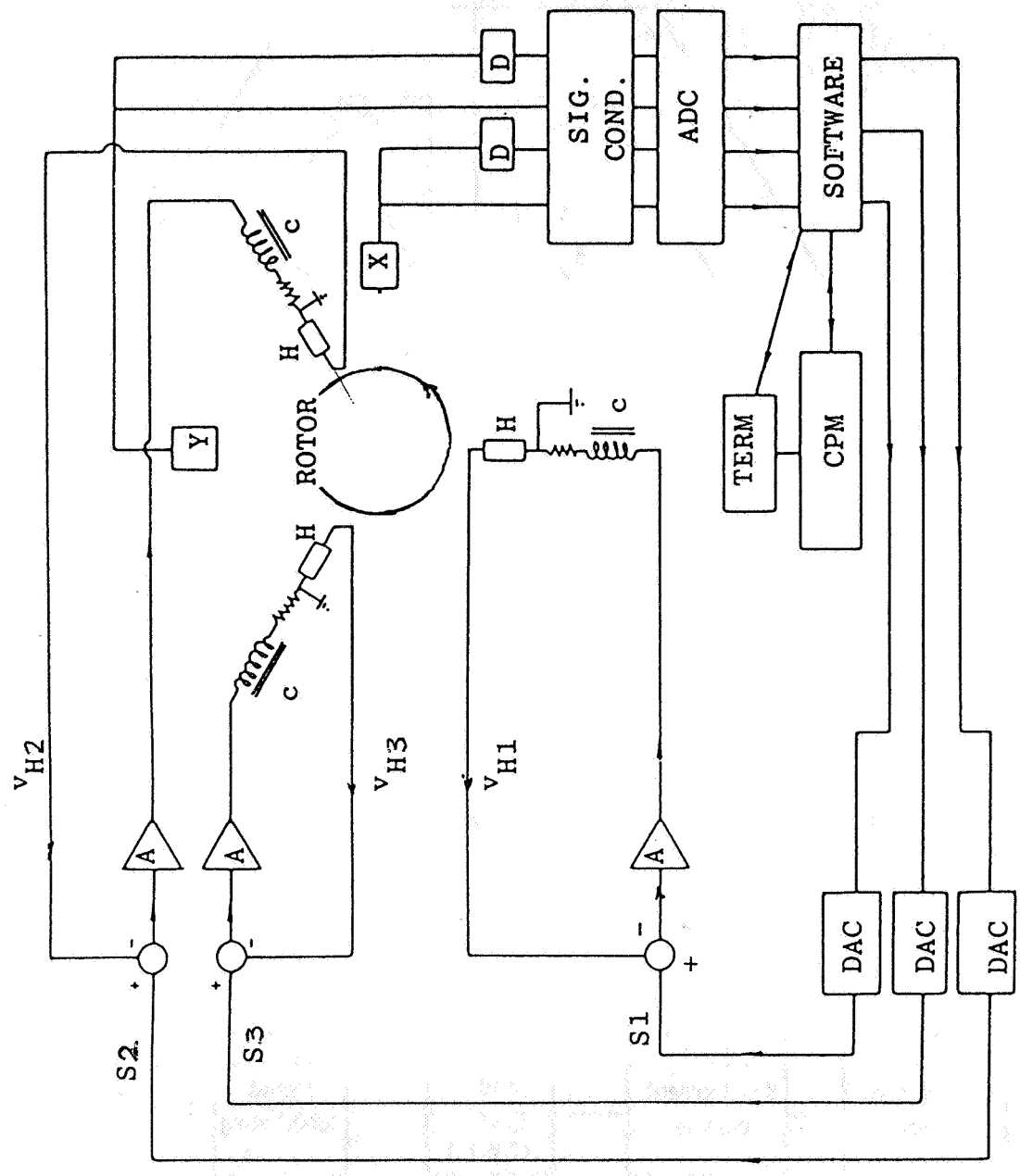

Figure 5. - Electromagnet system.

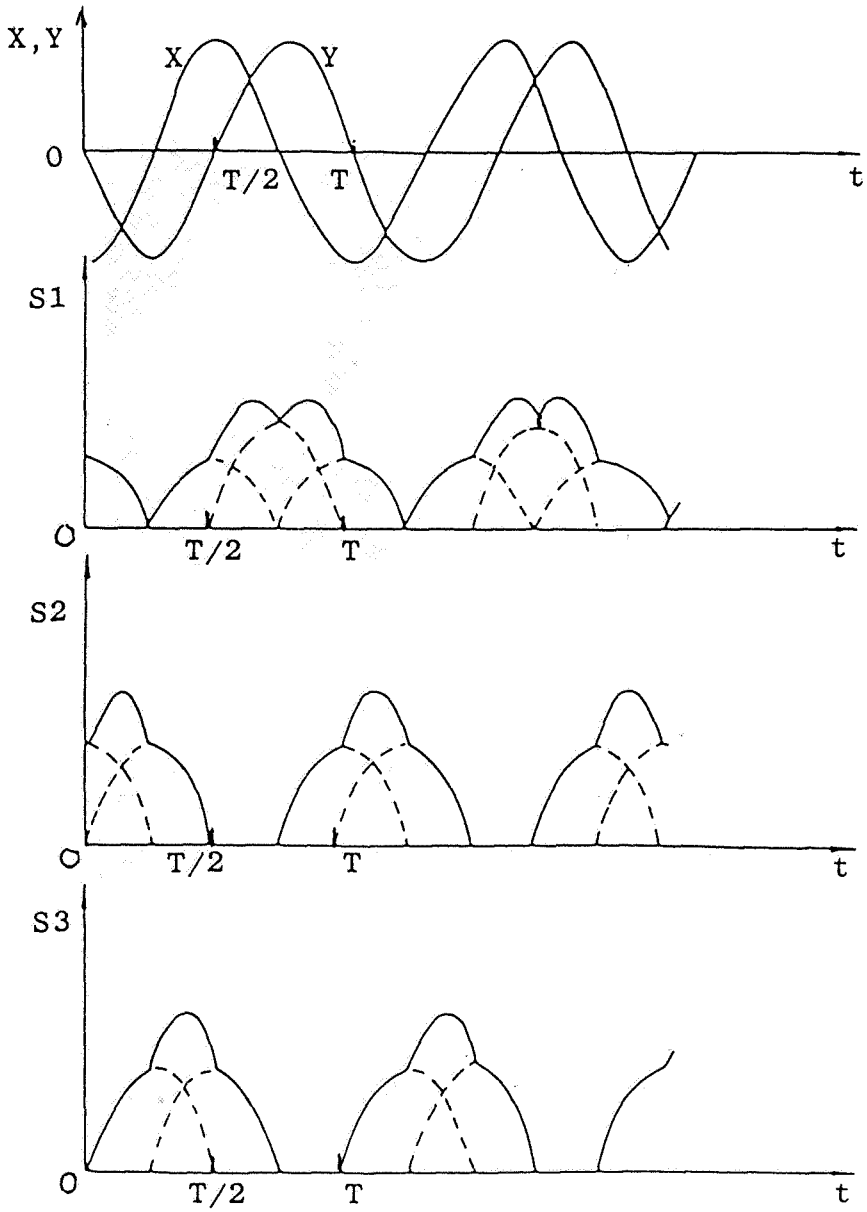

Figure 6a. - Excitation signals.

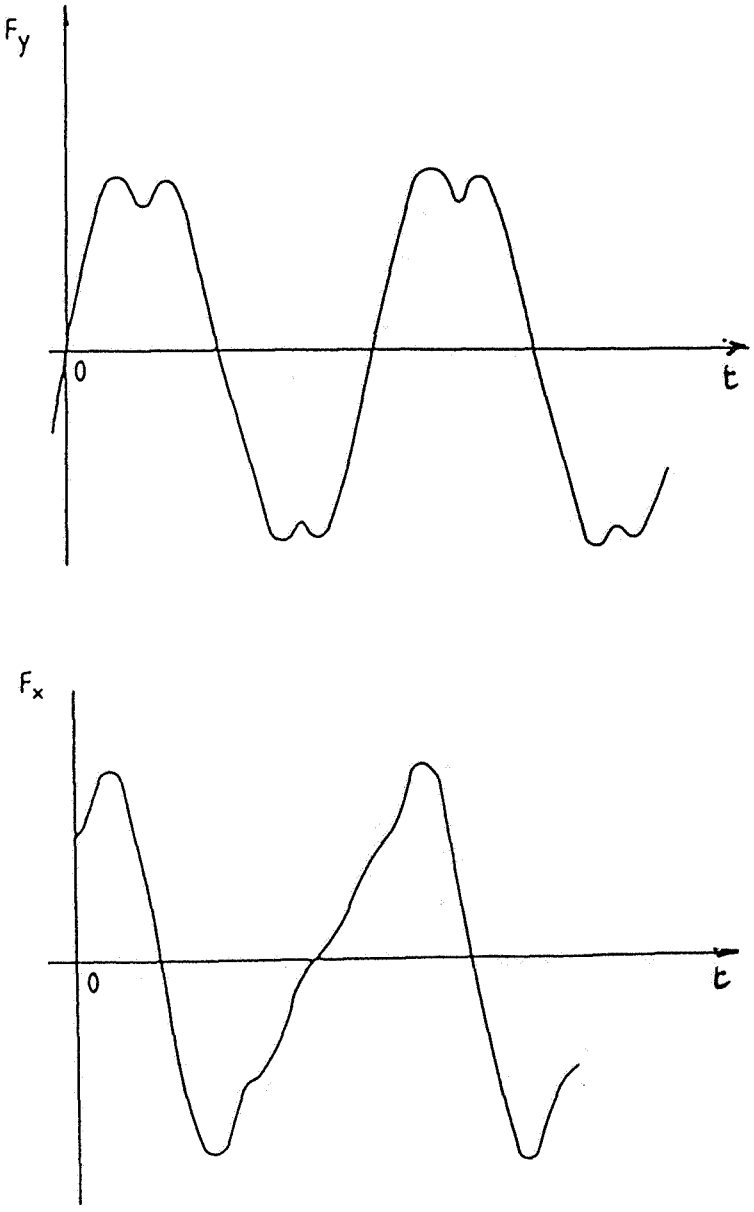

Figure 6b. - Forces in orthogonal directions.

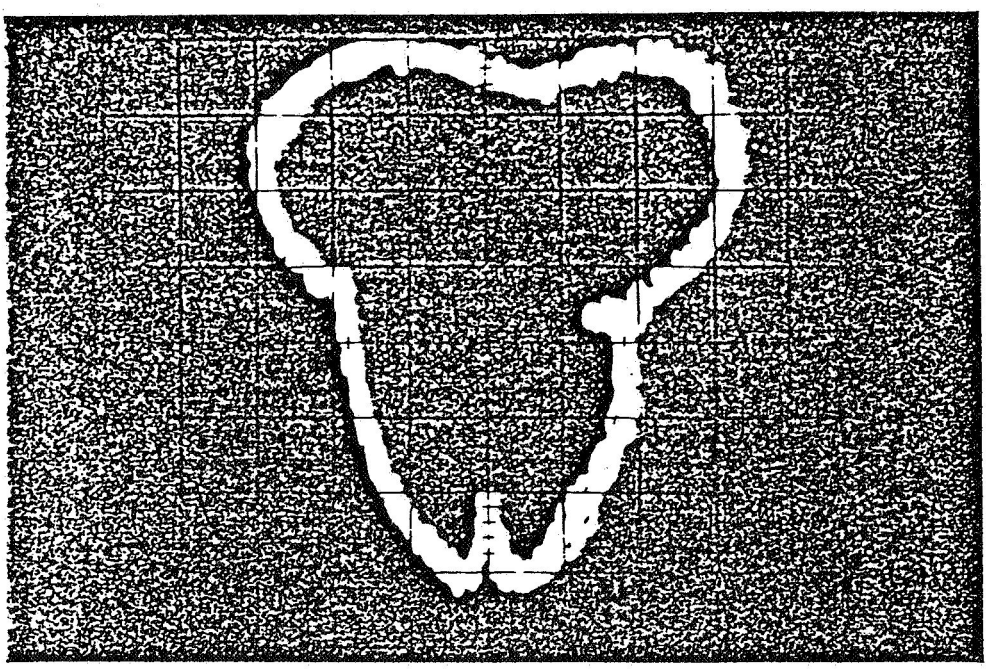

Figure 6c. - Polar force diagram.

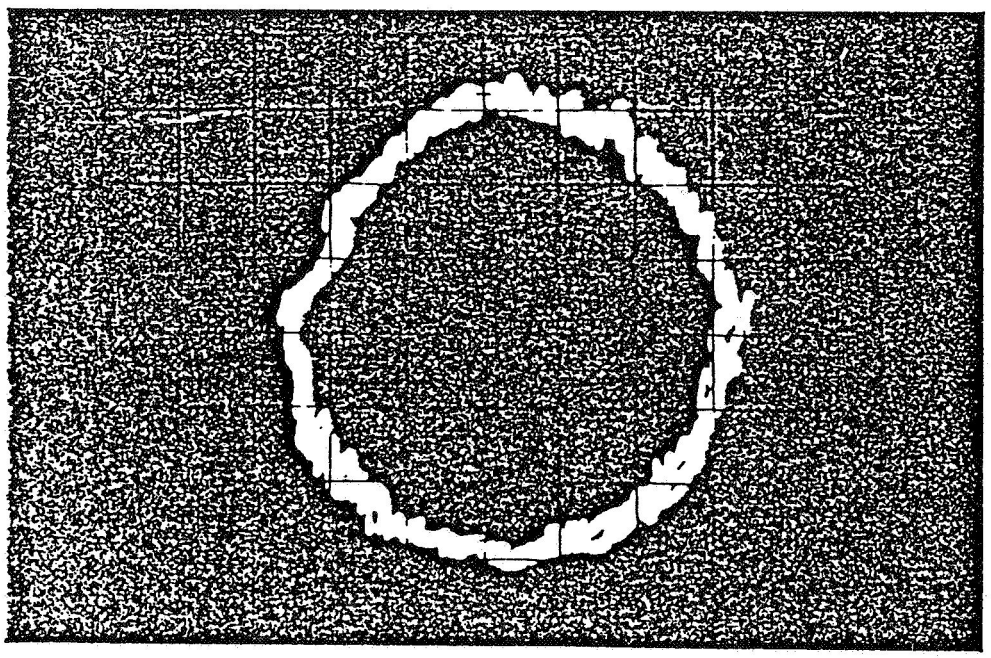

Figure 6d. - Improved polar force diagram.

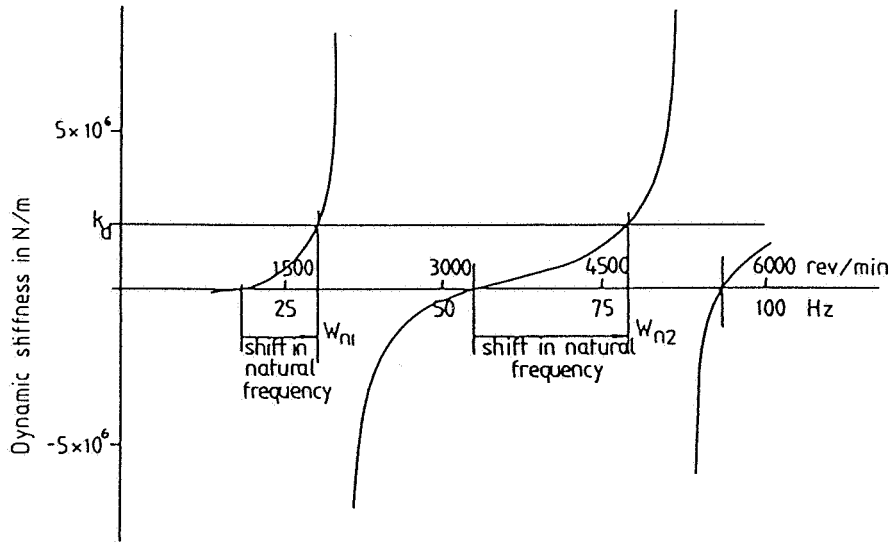

Figure 7. - Negative dynamic stiffness curve and shifts in natural frequency due to k_d.

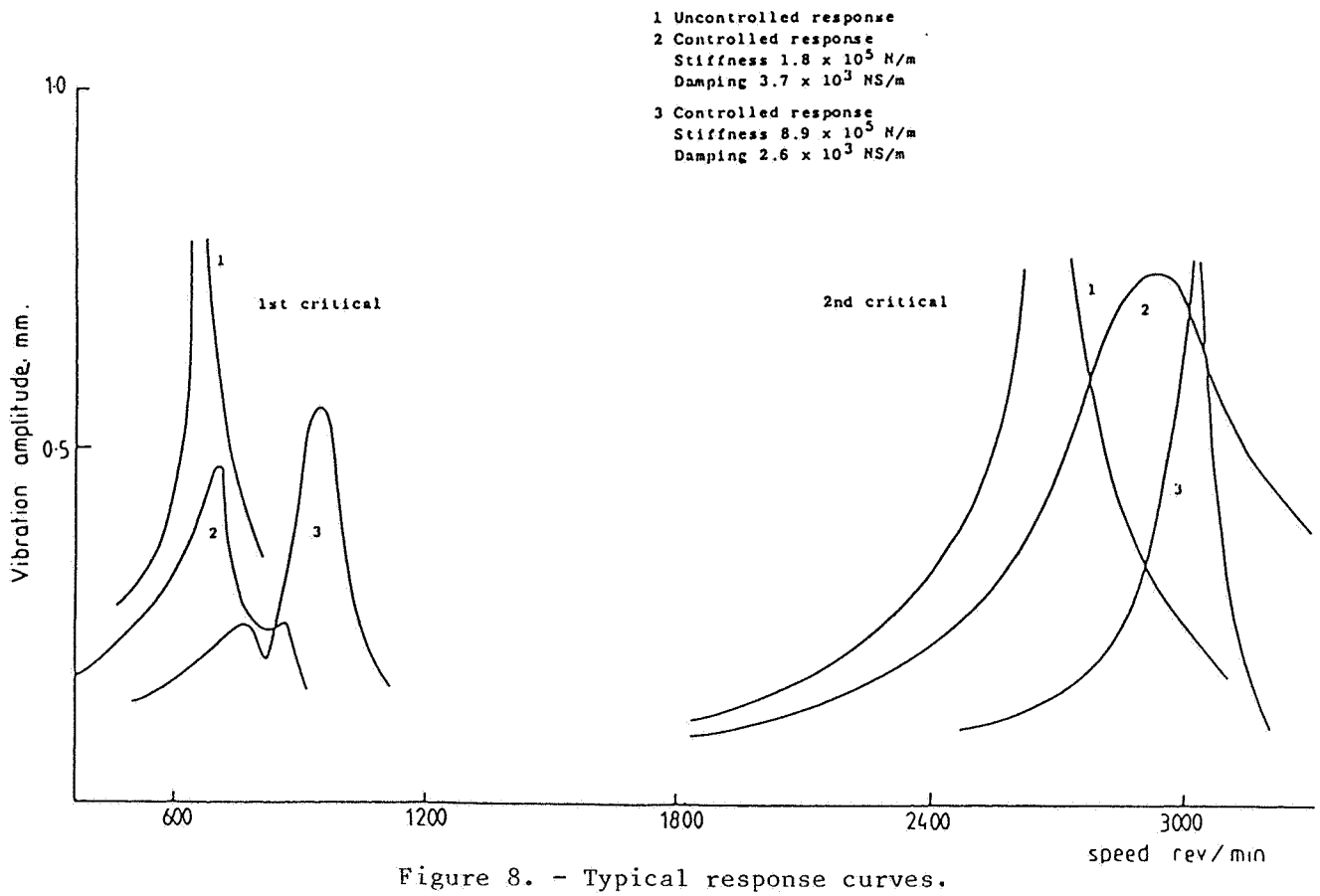

Figure 8. - Typical response curves.

EFFECTS OF FLUID INERTIA AND TURBULENCE ON FORCE COEFFICIENTS FOR SQUEEZE FILM DAMPERS*

Luis San Andrés and John M. Vance
Texas A&M University
College Station, Texas 77843

The effects of fluid inertia and turbulence on the force coefficients of squeeze film dampers are investigated analytically. Both the convective and the temporal terms are included in the analysis of inertia effects. The analysis of turbulence is based on friction coefficients currently found in the literature for Poiseuille flow.

The effect of fluid inertia on the magnitude of the radial direct inertia coefficient (i.e. to produce an apparent "added mass" at small eccentricity ratios, due to the temporal terms) is found to be completely reversed at large eccentricity ratios. The reversal is due entirely to the inclusion of the convective inertia terms in the analysis.

Turbulence is found to produce a large effect on the direct damping coefficient at high eccentricity ratios. For the long or sealed squeeze film damper at high eccentricity ratios, the damping prediction with turbulence included is an order of magnitude higher than the laminar solution.

NOMENCLATURE

a = inner cylinder radius

$\overline{a_r} = -\varepsilon$ = dimensionless journal center radial acceleration

b = outer cylinder radius

$\overline{C_{rt}}$, $\overline{C_{tt}}$ = dimensionless damping coefficients in (r,t) directions due to tangential velocity $\overline{V}_t$

C_{rt}, C_{tt} = damping coefficients = $(\overline{C_{rt}}, \overline{C_{tt}}) * \mu kL/\delta^3$

$\overline{D_{rr}}$, $\overline{D_{tr}}$ = dimensionless inertia coefficients in (r,t) direction due to normal acceleration $\overline{a}_r$

D_{rr}, D_{tr} = inertia coefficients = $(\overline{D_{rr}}, \overline{D_{tr}}) * \mu kL/\delta^3\omega$

e = circular centered orbit radius

f_r, f_t = dimensionless fluid film force in (r,t) direction

*This research was supported by the Turbomachinery Research Consortium at Texas A&M University.

f_θ, f_ξ = inertial wall shear stress functions

$H = 1 + \varepsilon c\theta$: dimensionless film thickness

$h = b\delta H$ = film thickness

$I_{\theta\theta}$, $I_{\theta\xi}$, $I_{\xi\xi}$ = momentum integrals over the film thickness

k = geometry parameter = $(L/b)^2$ for short SFD assumption, 1 for others

k_θ, k_ξ = parameters depending on the nature of the flow

L = squeeze film damper length

p = pressure

$\bar{p} = p\delta^2/(k\omega\mu)$ = dimensionless pressure

q_θ, q_ξ = dimensionless local flow rates in (θ,ξ) direction

$Re = \omega\delta^2 b^2/\nu$ = squeeze Reynolds number

$Rep = \frac{Re}{\delta}\left[(q_\theta+H)^2 + (L/b\ q_\xi)^2\right]^{\frac{1}{2}}$ = Poiseuille flow Reynolds number

u = fluid relative velocity along lubricant film

u* = absolute fluid velocity along lubricant film = $u+b\omega$

$\bar{u}$ = $u/b\omega$: dimensionless fluid velocity

$\bar{u}_m = \int_0^1 \bar{u}d\eta$ = mean fluid velocity along lubricant film

v = fluid velocity across lubricant film

$\bar{v}$ = $v/b\delta\omega$ = dimensionless fluid velocity

$\bar{V}_t$ = ε = dimensionless journal center tangential velocity

w = fluid velocity in the axial direction

$\bar{w}$ = $w/L\omega$ = dimensionless axial velocity

$\bar{w}_m = \int_0^1 \bar{w}d\eta$ = mean fluid velocity in axial direction

ω = frequency of damper motion

t = time

(x,y,z) = moving coordinate system

(x,y,z)* = fixed coordinate system

$\alpha_1, \alpha_2, \alpha_3$ = coefficients eventually depending on Re for turbulent motion

γ = $\partial H/\partial\theta$ = film thickness gradient along circumferential direction

Γ = $\Gamma(\overline{um}^2)$ = dimensionless inertia function for long SFD assumption

δ = $(b-a)/b$ = clearance ratio

ϵ = $e/b\delta$ = dimensionless circular orbit radius, eccentricity radius

(θ,η,ξ) = dimensionless coordinates = $(x/b, y/h, z/L)$

$\Delta\tau_{\theta\eta}$, $\Delta\tau_{\xi\eta}$ = wall shear stress difference in (θ,ξ) direction

ρ = fluid density

μ = fluid viscosity

ν = μ/ρ = kinematic viscosity

τ = $t\omega$ = dimensionless time

Subscripts:

o = inertialess or purely viscous

i = inertial

INTRODUCTION

Squeeze film dampers (SFD) are designed to have a stabilizing effect on the rotordynamics of turbomachinery. This has generally been accomplished by using the Reynolds effect in a thin oil film around a bearing to produce a predictable damping coefficient. The increase in size and speed of modern turbomachinery using light viscosity oils has brought the need to include fluid inertia effects in the design analysis. Sparked by the recent pioneering work of Tichy [1-4], researchers are now extending the lubrication theory into the range where the Reynolds (slow flow) assumption is no longer applicable.

At least for some simple geometries and motions, the fluid inertia effects have been shown to be quite significant.

To the rotordynamicist fluid film forces and dynamic coefficients are more important than velocity or pressure fields. Analytical [2,7] and numerical [5,6] approaches have been developed for calculating the damping and inertia coefficients, assuming motions of small amplitude α about an equilibrium point. In this case, it can be shown that the convective inertial terms may be neglected in the equations of motion, since they are of order α^2 while the temporal terms are of order α. In all these analyses, the trend of the damping and inertia coefficients is to increase as the static eccentricity ratio increases, a fact that has been shown to be true in practice.

However, for large excursions of the journal center about its centered position the full inertial term should be retained in the momentum equations. The temptation to neglect convective terms in order to simplify and linearize the problem is no longer justifiable even for very simple cases such as the long or short bearing solutions. For example, reference [9] recently presented numerical calculations for the dynamic coefficients of an SFD performing circular orbits (CCO) about the center of the bearing housing. Using the same approach as in [5], the convective inertia effects were neglected, so the coefficients have the characteristic form described above. This behavior of the fluid film forces will be shown to be in error even for moderate eccentricities and totally incorrect at large orbit amplitudes. Furthermore, in reference [9] the direct damping and inertia coefficients for the cavitated SFD were found to be one half the value of the full film case and independent of the inertia parameters of the fluid. This appears unreasonable since if cavitation is allowed, the extent of the region where the film is broken will be influenced by the magnitude of the inertial forces. Our purpose in the present analysis will be to determine the dynamic coefficients taking into account the full inertial terms for simple geometries in order to understand better the action of viscous and inertial forces in an SFD.

The inclusion of inertia complicates the problem in a SFD, and turbulence effects make the problem even more involved. Unlike the journal bearing case where a considerable amount of analytical and experimental work has been done, turbulence in squeeze film dampers remains rather obscure due to the lack of experimental data or a good understanding of the mechanics of squeezing flows. Nelson [11] used the empirical friction coefficient for pure Poiseuille flows in an attempt to include turbulent effects for the long SFD case. No satisfactory results were obtained since the fluid apparent viscocity was used to calculate the empirical friction factor for the flow.

Tichy [4] suggests that turbulent flow in SFD's will occur at higher Reynolds numbers than for Poiseuille flows, i.e. Rep > 2000. This assertion seems reasonable since the velocity field in a SFD is constantly changing and adjusts itself to the normal motion of the boundary, thus making the flow more stable. It also seems reasonable that transition from laminar to turbulent regions should be smooth in order to satisfy continuity of the flow. All these considerations make the problem more untractable and point out the urgent need of experimental data. In the meantime, it will prove helpful to use the empirical correlations currently found in the literature and thus obtain upper bounds for the forces and dynamic coefficients when turbulence is present in the flow.

STATEMENT OF THE PROBLEM

Figure 1 shows the geometry of the SFD system. The equations of motion for the flow in the annular region between a whirling nonrotating inner cylinder and its bearing housing are stated in a moving coordinate frame. Appendix A contains the details of the integration of the motion equations across the lubricant film, to finally obtain in dimensionless form:

$$\mathrm{Re}\left\{\frac{\partial}{\partial\theta} I_{\theta\theta} + \frac{\partial}{\partial\xi} I_{\theta\xi}\right\} = -\mathrm{Hk}\,\frac{\partial\bar{p}}{\partial\theta} + \Delta\tau_{\theta\eta} \qquad (1)$$

$$\mathrm{Re}\left\{\frac{\partial}{\partial\theta} I_{\theta\xi} + \frac{\partial}{\partial\xi} I_{\xi\xi}\right\} = -Hk\ (b/L)^2 \frac{\partial \bar{p}}{\partial\xi} + \Delta\tau_{\xi\eta} \tag{2}$$

$$\frac{\partial}{\partial\theta} q_\theta + \frac{\partial}{\partial\xi} q_\xi = 0 \tag{3}$$

This system of equations must be solved with appropriate boundary conditions for the flow rates (q_θ, q_ξ) and the pressure $\bar{p}$. Analytical solutions to the problem are extremely difficult since the exact form of the wall shear stress difference ($\Delta\tau_{\theta\eta}$, $\Delta\tau_{\xi\eta}$) is unknown and some assumption regarding their functional form becomes necessary. Presumably, the problem may be solved numerically on a computer with its full tridimensional complexity, but such an effort may prove to be unnecessarily costly or even impractical.

As a first approximation to a practical solution of the problem, we assume that for the laminar region, and even in the presence of turbulent effects, the shear stresses at the walls may be written as:

$$\Delta\tau_{\theta\eta} \doteq -k_\theta \frac{(q_\theta+H)}{H^2} + \mathrm{Re}\ f_\theta \tag{4a}$$

$$\Delta\tau_{\xi\eta} = -k_\xi \frac{q_\xi}{H^2} + \mathrm{Re}\ f_\xi \tag{4b}$$

The approximate form of the functions k_θ, k_ξ, f_θ and f_ξ will be discussed later in the analysis. Note also that in equations (4) we have included an explicit contribution of inertia to the wall shear stress difference.

Once a solution to the system of equations (1) to (3) has been obtained the fluid film forces acting on the inner cylinder are calculated by integration of the pressure distribution over the flow region. For rotordynamics applications, the forces are expressed in terms of damping and inertia coefficients. Let (f_r, f_t) be the radial (along the centerline of both cylinders) and tangential dimensionless fluid film forces, and given by:

$$f_r = \int_R \bar{p} \cos\theta\, dR = -\bar{C}_{rt}\,\bar{V}_t - \bar{D}_{rr}\,\bar{a}_r \tag{5a}$$

$$f_t = \int_R p \sin\theta\, dR = -\bar{C}_{tt}\,\bar{V}_t - \bar{D}_{tr}\,\bar{a}_r \tag{5b}$$

$$R = \{0\le\theta\le 2\pi,\ 0\le\xi\le 1\}$$

In equations (5), $\bar{V}_t$, $\bar{a}_r$ are the dimensionless journal center tangential velocity and radial acceleration, respectively; and ($\bar{C}_{rt}$, $\bar{C}_{tt}$), ($\bar{D}_{rr}$, $\bar{D}_{tr}$) are the dimensionless damping and inertia coefficients. The dimensional counterparts of these coefficients are given by the relations:

$$C_{ij} = \frac{\mu k L}{\delta^3}\bar{C}_{ij}\ ,\quad D_{ij} = \frac{\mu k L}{\delta^3\omega}\bar{D}_{ij} \tag{6}$$

Our interest is to obtain approximate solutions to the uncavitated case, and present the dynamic coefficients with inertia and turbulence effects accounted for in the flow. This is a necessary step preliminary to any more refined analysis, since it will contribute to a better understanding of the problem. We will treat the laminar and turbulent solutions for the long and short SFD's separately. No cavitation is considered in the flow region. This last assumption is unrealistic for some cases, but permits us to do a first treatment of the fluid film forces with inertia and turbulence included, and will be accurate for high supply pressures. Furthermore, the direct effects of fluid inertia and turbulence will be isolated from the indirect effect caused by changes in the region of cavitation.

LAMINAR FLOW SOLUTIONS

Long Bearing Assumption

In this section we assume that the cylinders are infinite in extent, or that very tight end seals are placed at the ends of the SFD, or that the axial flow q_ξ is negligible. We are left with the equation:

$$q_\theta = \bar{u}_m H \tag{7}$$

$$\frac{\partial \bar{p}_o}{\partial \theta} = \frac{-k_\theta}{H^3}\,(q_\theta + H) \tag{8}$$

$$\frac{\partial \bar{p}_i}{\partial \theta} = \frac{\gamma}{35H}\,[-7 + 35\alpha_1\,\bar{u}_m^{\,2}] + \frac{f_\theta}{H} \tag{9a}$$

$$\bar{p} = \bar{p}_o + \mathrm{Re}\,\bar{p}_i$$

Here we have divided the pressure into two parts so that $\bar{p}_i$ contains explicitly the influence of inertia.

For small Reynolds numbers, $\mathrm{Re} \leq 1$, Brindley [7] and the first author [10] have found that $k_\theta = 12$ as in the usual lubrication approximation, and that the inertial pressure gradient is given by:

$$\frac{\partial \bar{p}_i}{\partial \theta} = \frac{\gamma}{35H}\,[-6 + 6\,\bar{u}_m + 54\,\bar{u}_m^{\,2}] \tag{9b}$$

For large Reynolds numbers, assuming that the flow remains stable and laminar, the inviscid pressure gradient is given as:

$$\frac{\partial \bar{p}_i}{\partial \theta} = \frac{\gamma}{H}\,\bar{u}_m^{\,2} \tag{9c}$$

Equation (9c) is different from the result presented by Tichy in [4], apparently due to an error in the boundary conditions used for the inviscid flow region.

For both extreme values of the inertial parameter Re, the dimensionless flow rate q_θ is unaffected by inertia and is equal to:

$$q_\theta = \frac{2(\varepsilon^2-1)}{(2+\varepsilon^2)} \tag{10}$$

In order to make a quantitative comparison of equations (9a-9c) we let:

$$\Gamma = \frac{H}{\gamma}\frac{\partial \bar{p}_i}{\partial \theta} = \Gamma(\bar{u}_m^2) \tag{11}$$

be a function that indicates the magnitude of the inertia term in the pressure equation.

Figure 2 shows equations (9a-9c); curve A represents (9a) with $f_\theta = 0$, α_1=1.2, curves B & C, equation (9b-c), respectively.

A brief look at figure 2 shows the surprisingly similar behavior of the flow for the large range of Re considered. The actual value of Γ for moderate Reynolds numbers will lie between curves A and B; curve F shows the best fitting line between the A and B curves from which we select the inertial contribution to the wall shear stress difference as:

$$f_\theta = \frac{4}{35}\gamma\frac{q_\theta^2}{H^2} \tag{12}$$

Thus, we assume that for moderate Reynolds numbers, the wall shear stress difference is approximately given by:

$$\Delta\tau_{\theta\eta} = -12\frac{(q_\theta+H)}{H^2} + \mathrm{Re}\,\frac{4}{35}\gamma\frac{q_\theta^2}{H^2} \tag{13}$$

With these considerations, the pressure field for the flow can be determined, and from this, the dynamic coefficients. As previously stated, only the uncavitated SFD is treated here so that the effect of inertia on the fluid film forces can be clearly isolated. Otherwise, the extent of the cavitated region is dependent on the Reynolds number and the dynamic coefficients must be determined numerically for each change in the inertia parameter.

Integration of equations (8) and (9), subject to the continuity condition for the pressure field, is relatively easy and is given in [8]. The dynamic coefficient for the long SFD with laminar flow come to be:

$$\bar{C}_{rt} = \bar{D}_{tr} = 0\ , \quad \bar{C}_{tt} = \frac{24\pi}{(2+\varepsilon^2)(1-\varepsilon^2)^{\frac{1}{2}}} \tag{14}$$

Note that the direct damping coefficient $\bar{C}_{tt}$ is the same as in the inertialess solution. Analytical expressions for the direct inertia coefficient $\bar{D}_{rr}$ are given in Table I. Figure 3 shows a comparison of this coefficient for the different cases considered. The behavior of the inertia coefficient $\bar{D}_{rr}$ divided by Re is surprisingly similar for the large range of Reynolds number considered. The largest

difference occurs at small and large eccentricities but is never more than 20%, (between Re=0 and Re=∞). The rapid decrease of the inertia coefficient as the eccentricity ratio grows larger appears to contradict the recent results presented in [9]. The reason for the discrepancy is that in the MTI study only temporal acceleration effects were accounted for in the equation of motion while here both the convective and temporal inertia terms are retained. The upper dashed curve in figure 3 shows the inertia coefficient when only the temporal effects are included. The coefficient grows rapidly and even goes to infinity as the orbit size approaches the radial clearance.

Short Bearing Assumption

In this section we assume that the SFD has small L/D ratios, the ends are open to the atmosphere, and for simplicity we also assume that no high externally induced axial flow is present in the damper. The reason for the latter assumption is to avoid pressure boundary conditions which would require the explicit presence of the inertial parameter Re. As is current practice for the short journal bearing analysis, the circumferential flow is assumed to be negligible. We set $k=(L/b)^2$ in eqs. (1) to (3) and get the following set of equations:

$$q_\theta = -H \tag{15}$$

$$\frac{\partial q_\xi}{\partial \xi} = \gamma \tag{16}$$

$$H \frac{\partial \bar{p}_o}{\partial \xi} = -12 \frac{q_\xi}{H^2} \tag{17}$$

$$H \frac{\partial \bar{p}_i}{\partial \xi} = f_\xi + \frac{\partial q_\xi}{\partial \theta} - \frac{\alpha_3}{H} \frac{\partial}{\partial \xi} (q_\xi^2) \tag{18a}$$

The axial inertial pressure gradient obtained for small Re using a regular perturbation solution in Re is given by Tichy (3) as:

$$H \frac{\partial \bar{p}_i}{\partial \xi} = 1.2 \frac{\partial q_\xi}{\partial \theta} - \frac{51}{35H} \frac{\partial}{\partial \xi} (q_\xi^2) \tag{18b}$$

Assuming the flow remains stable and laminar, for large Re the inviscid pressure gradient is given by:

$$H \frac{\partial \bar{p}_i}{\partial \xi} = \frac{\partial q_\xi}{\partial \theta} - \frac{1}{H} \frac{\partial}{\partial \xi} (q_\xi^2) \tag{18c}$$

From a quantitative comparison of equation (18a-c), for moderate Reynolds numbers we select the inertial contribution to the wall shear stress difference to be:

$$f_\xi = - \frac{2}{35H} \frac{\partial}{\partial \xi} (q_\xi^2) + \frac{1}{10} \frac{\partial q_\xi}{\partial \theta} \tag{19}$$

Thus, we assume that the wall shear stress difference for the short SFD approximation is given by:

$$\Delta\tau_{\xi\eta} = - k_{\xi} \frac{q_{\xi}}{H^2} - \frac{2}{35H} \frac{\partial}{\partial\xi} (q_{\xi}^2) + \frac{1}{10} \frac{\partial q_{\xi}}{\partial\theta} \tag{20}$$

With these considerations, equations (17) and (18a-c) are integrated to obtain the pressure field. For the full film assumption, the dynamic coefficients come to be:

$$\bar{C}_{rt} = \bar{D}_{tr} = 0 \ , \quad \bar{C}_{tt} = \frac{\pi}{(1-\varepsilon^2)^{3/2}} \tag{21}$$

Note that the direct damping coefficient $\bar{C}_{tt}$ is the same as in the inertialess solution. Analytical expressions for the direct inertia coefficient $\bar{D}_{rr}$ are given in Table II. For the different cases considered, figure 4 shows the inertia coefficient $\bar{D}_{rr}$ divided by Re as a function of the eccentricity. As in the long SFD case, the form of the inertia coefficient is surprisingly similar for the large range of squeeze Reynolds numbers considered. Note the tremendous influence that the convective inertial terms have on the coefficient when compared to the dashed curve which is based only in the inclusion of temporal effects on the equation of motion. Thus, analyses based on small perturbation about an equilibrium point are in large error compared to the exact solution, if the orbit is large.

TURBULENT FLOW SOLUTIONS

The inclusion of turbulence effects into the flow complicates the problem enormously. Although the mechanism of turbulence for fully developed Couette and Poiseuille flows has been studied extensively, both analytically and experimentally, and many contributions to the analysis of flow in narrow channels have been given in the past years; the mechanics of squeezing flows are far more complicated. The subject still remains obscure due to the complete absence of theoretical-empirical formulation and the lack of experimental results.

Undaunted, we assume that the coefficients k_{θ} & k_{ξ} to be used in turbulent flow in a SFD are given by:

$$k_{\xi} = k_{\theta} = 12 + 0.005 \ \mathrm{Rep} \tag{22}$$

where

$$\mathrm{Rep} = \frac{\mathrm{Re}}{\delta} \left[(q_{\theta}+H)^2 + (L/b)^2 \, q_{\xi}^2 \right]^{\frac{1}{2}} \tag{23}$$

is the Poiseuille Reynolds number currently found in the literature.

Relation (22) was obtained as the best fitting curve between the experimental correlation given by Hirs (12) and the analytical results based on the mixing length theory given by Elrod and Ng (13). Here we have assumed that the transition from the laminar to turbulent regions in a SFD must be smooth in order to insure continuity of the flow.

The assumed expressions may be far away from the actual expressions which should be obtained from experimental results. However, we have chosen them in the absence of better empirical formulations, and the results obtained will prove to be upper bounds of the actual forces and dynamic coefficients.

Long Journal-Bearing Assumption

As in section 3.a, the axial flow is neglected and the pressure gradient field is given by:

$$\frac{\partial \bar{p}}{\partial \theta} = -(12 + 0.005 \frac{Re}{\delta} 1H + q_\theta 1) \frac{(H+q_\theta)}{H^3} + \frac{Re}{35} \frac{\gamma}{H} [-7+46 \frac{q_\theta^2}{H^2}] \quad (24)$$

$$q_\theta = q_\theta (\varepsilon, Re, \delta) \quad (25)$$

Note that we have assumed that f_θ given in (12) prevails even in the turbulent regime. A very simple computer code was written to obtain the pressure field. Using numerical integration, the dynamic coefficients were calculated for an uncavitated SFD with a clearance ratio $\delta = 0.001$.

Figure 5 shows the direct damping coefficient $\bar{C}_{tt}$ as a function of the eccentricity ratio for different Re, and figure 6 depicts the same coefficient as a function of the Reynolds number for different orbit radius ε. From the figures it is evident that turbulence has a large effect on the damping coefficient, and consequently on the tangential force. This is due to the increase in the apparent viscocity of the fluid as the inertia parameter grows.

Figure 7 shows the direct inertia coefficient $\bar{D}_{rr}/Re$ for various orbit radius, the pattern of the curves is the same as in figure 3 for moderate Reynolds numbers. It is clearly seen that the effect of turbulence is to increase the coefficient, especially at large whirling orbits, this is due to the increase in flow rate q_θ as ε grows in order to satisfy continuity of the pressure field.

A comparison of the results given in figures 5 and 7 shows that the ratio $\bar{D}_{rr}/\bar{C}_{tt}$ is less than 1/10 for all eccentricities and Reynolds numbers considered, this may be an important result since it implies that the tangential force will be larger than the purely inertial radial force.

Short Journal Bearing Assumption

For the short SFD assumption, the axial pressure gradient equation comes to be:

$$\frac{\partial \bar{p}}{\partial \xi} = -(12+0.005\frac{Re}{\delta} (L/b)\ 1q\varepsilon 1) \frac{q_\xi}{H^3} + \frac{Re}{H} [\frac{11}{10} \frac{\partial q_\xi}{\partial \theta} - \frac{44}{35H} \frac{\partial}{\partial \xi} q_\xi^2] \quad (26)$$

$$\frac{\partial q_\xi}{\partial \xi} = -\gamma \quad (27)$$

Assuming that there is no high axial flow externally induced into the SFD, the flow q_ξ remains unchanged from the inertialess solution. Equations (26) and (27) are amenable of closed form integration, the details of the same are omitted for

brevity; it is found that the direct inertia coefficient $\overline{D}_{rr}$ is the same as given in equation (2) of Table 2.

Figure 8 shows the direct damping coefficient $\overline{C}_{tt}$ as a function of the eccentricity ratio for different values of the squeeze Reynolds number Re, and figure 9 shows the same coefficient as a function of Re for various values of the orbit radius ε. All calculations were made for an uncavitated SFD with a clearance ratio of δ=0.001, and a L/D ratio equal to 0.25. From the figures a significant influence of turbulence on the damping coefficient is seen. As expected, the larger the Reynolds number, the larger the dynamic coefficient and consequently the tangential force increases proportionally. Once again, this effect is due to the increase in the apparent viscocity of the fluid as the inertia parameter grows.

SUMMARY

The present paper has considered the influence of inertia and turbulence on the flow in the annular region between a whirling damper journal, describing circular centered orbits, and its bearing. After an analysis of the fluid-flow equation for the problem, the usual assumptions considering the length of the SFD are made to obtain the classical long and short journal bearing approximations.

The region of flow was assumed to be continuous, i.e. no cavitation was allowed in the fluid. This allowed a clear analysis of the effect of inertia and turbulence on the fluid film forces and the dynamic coefficients. The laminar solution showed the importance of the inclusion of convective inertia terms in the equations of motion. The resulting reversal of the "added mass effect" makes it clear that numerical or analytical approaches that calculate the dynamic coefficients for large motion amplitudes in base to small perturbations about an equilibrium point may be largely in error.

In the absence of empirical coefficients for the turbulent motion in squeezing flows, a friction coefficient based on the Poiseuille analysis of Hirs and Elrod and Ng was used. This may be modified by experimental results in the future, since the transition from laminar to turbulent motion may turn out to appear at larger Reynolds numbers than here considered. As suggested in reference (4), the values here presented should be considered as upper bounds for the actual dynamic coefficients and as qualitative indicators of the influence of turbulence on the flow. If these bounds are even approached by the real case, turbulence will be found to have a large effect on the direct damping coefficient for squeeze film dampers.

The present analysis should prove to be stepping stones for future developments that will consider SFD's of finite extent and also the influence of inertia in the boundary conditions of the flow.

REFERENCES

1. Modest, M. F., and J. A. Tichy, "Squeeze Film Flow in Arbitrarily Shaped Journal Bearings Subject to Oscillations," Journal of Lubrication Technology, July 1978, pp. 323-329.

2. J. A. Tichy, "Effects of Fluid Inertia and Viscoelasticity on Squeeze Film Bearing forces," ASLE Transactions, Vol. 25, January 1982, pp. 125-132.

3. J. A. Tichy, "A Simple Low Deborah Number Model for Unsteady Hydrodynamic Lubrication, Including Fluid Inertia," Journal of Rheology, Vol. 24, 1980, pp. 829-845.

4. J. A. Tichy, "The Effect of Fluid Inertia in Squeeze Film Damper Bearings: A Heuristic and Physical Description," ASME paper 83-GT-177.

5. Reinhardt, E. and Lund , J. W., "The Influence of Fluid Inertia on the Dynamic Properties of Journal Bearings," Journal of Lubrication Technology, April 1975, pp. 159-175.

6. Szeri, A. Z., A. A. Raimondi, A. Giron-Duarte, "Linear Force Coefficients for Squeeze Film Dampers," Journal of Lubrication Technology, July 1983, pp. 326-334.

7. Brindley, J., L. Elliott, J. T. McKay, "Flow in a Whirling Rotor Bearing," Journal of Applied Mechanics, December 1979, Vol. 46, pp. 767-771.

8. Szeri, A. Z., "Tribology: Friction, Lubrication and Wear," McGraw-Hill Co., N.Y., 1980, pp. 40.

9. Lund, J. W., A. J. Smalley, J. A. Tecza, J. F. Walton, "Squeeze Film Damper Technology: Part 1-Prediction of Finite Length Damper Performance," ASME Paper 83-GT-247.

10. San Andres, A., "Flow in a Journal Bearing Subject to Arbitrary Motions," Internal Report, Turbomachinery Labs, Mechanical Engineering Dept., Texas A&M University, December 1983.

11. Nelson, C., "The Effect of Turbulence and Fluid Inertia on a Squeeze Film Damper," AIAA/SAE/ASME, 16th Joint Propulsion Conference, June 30-July 2, 1980.

12. Hirs, G. G., "A Bulk Flow Theory for Turbulence in Lubricant Films," ASME Journal of Lubrication Technology, April 1973, pp. 137-146.

13. Elrod, H. G., C. W. Ng, "A Theory for Turbulent Fluid Films and its Applications to Bearings," ASME Journal of Lubrication Technology, July 1967, pp. 346-362.

TABLE I. Direct Inertia Coefficient $\overline{D}_{rr}$ for the Long Squeeze Film Damper

Re	$\overline{D}_{rr}/Re$	
small Re<<1	$\frac{12}{35}\pi\ [\Gamma_2(1+2\beta b) + 9\Gamma_1]$	(1.2)
large Re→→∞	$2\pi\Gamma_1$	(1.3)
moderate R_e f_θ=0	$\frac{14}{35}\pi\ [\Gamma_2 + 6\Gamma_1]$	(1.4)
moderate R_e f_θ from eqn. (12)	$\frac{14}{35}\pi\ [\Gamma_2 + 6.5714285\ \Gamma_1]$	(1.5)

Definitions:

$$\beta = (1-\varepsilon^2)^{\frac{1}{2}}\ ,\quad b = (2+\varepsilon^2)^{-1} \qquad (1.1)$$

$$\Gamma_1 = 2\beta b^2\ ,\quad \Gamma_2 = (\beta-1)/\varepsilon^2$$

For temporal effects only:

$$D_{rr}/Re = \frac{-24}{10}\pi\ \Gamma_2 \qquad (1.6)$$

TABLE II. Direct Inertia Coefficient $\overline{D}_{rr}$
for the Short Squeeze Film Damper

$$\overline{D}_{rr}/Re = -\Gamma\,[C_1 + C_2\,(\beta-1)] \qquad (2.1)$$

Re	C_1	C_2	
small Re<<1	1.2	102/35	(2.3)
large Re>>1	1.0	2.0	(2.4)
moderate R_e f_ξ=0	1.0	2.4	(2.5)
moderate R_e f_ξ from eqn. (19)	1.1	2(1+2/35)	(2.6)

Definitions:

(2.1) $$\beta = (1-\varepsilon^2)^{\frac{1}{2}}\,, \quad \Gamma = \frac{\pi(\beta-1)}{6\beta\varepsilon^2} \qquad (2.2)$$

Temporal Effects Only:

$$C_1 = 1.2\,, \quad C_2 = 0 \qquad (2.7)$$

APPENDIX A

Coordinate System and Equations of Motion

Consider two circular cylinders of radii a and b (>a) and assume that the center of the smaller cylinder rotates with constant angular velocity ω in a circle of radius e about the center of the larger one. The condition that the cylinders do not touch is

$$0 \leq \varepsilon < 1 \tag{A.1}$$

where $\delta = \frac{b-a}{a} << 1$, $\varepsilon = \frac{e}{(b-a)}$ (A.2)

Here δ and ε are the clearance and eccentricity ratios, respectively.

The first characteristic of the geometry of lubricant films that permits simplicication of the problem is that the thickness of the lubricant film, h, is very small compared to its length or to its radius of curvature. As consequences of this the following assumptions are made (8).

1) The effects of the curvature of the film are negligible.
2) The variation of the pressure across the film is small and may be neglected.
3) The rate of change of any velocity component along the film is small when compared to the rate of change of this same velocity component across the film and can be neglected.

In accordance with assumption (1), we can prescribe a fixed orthogonal cartesian coordinate frame $\{x_i^*\}_{i=1}^3$ in the plane of the lubricant film. See figure 1, where the y* axis is in the direction of the minimum film dimension. A moving orthogonal coordinate frame $\{x_i\}_{i=1}^3$ translating with velocity T=bω with respect to $\{x_i^*\}_{i=1}^3$ and its x axis perpendicular to the line joining the centers of both cylinders is introduced, and it can be shown that the flow will be steady to an observer moving with the $\{x_i\}_{i=1}^3$ frame.

The following dimensionless coordinates are introduced:

$$\theta = \frac{x}{b} , \quad \xi = \frac{z}{L} , \quad \eta = \frac{y}{h} , \quad \tau = t\omega \tag{A.3}$$

where $h = b\delta H(\theta)$, $H(\theta) = 1 + \varepsilon\cos\theta$ (A.4)

is the lubricant film thickness at location θ.

Dimensionless velocity components in the two coordinate frames are defined as

$$\bar{u}^* = \frac{u^*}{b\omega} , \ \bar{v}^* = \frac{v}{\delta b\omega} = \bar{v}, \ \bar{w}^* = \frac{w^*}{L\omega} = \bar{w}, \ \bar{u} = \frac{u}{b\omega} \tag{A.5}$$

$$\bar{u}^* = \bar{u} + 1$$

The pressure and the shear stresses are made dimensionless according to

$$\bar{p} = \frac{(p-pa)\delta^2}{\omega\nu/\rho} \quad k^{-1}, \quad \tau_{\theta\eta} = \frac{\tau_{xy}}{\omega\mu/\delta}, \quad \tau_{\xi\eta} = \frac{\tau_{zy}}{\omega\mu/\delta} \ (b/L) \tag{A.6}$$

and k=1 for long bearing assumption

$$k = (L/b)^2 \text{ for short bearing assumption} \tag{A.7}$$

With these considerations, the momentum and continuity equations for the tridimensional flow, expressed in the moving coordinate system are

$$\text{Re} \left\{ \frac{\partial \bar{u}^2}{\partial\theta} + \frac{1}{H}\frac{\partial}{\partial\eta}\left[\bar{u}\bar{v} - \eta\gamma\bar{u}^2\right] + \frac{\gamma\bar{u}^2}{H} + \frac{\partial}{\partial\xi}(\bar{u}\bar{w}) \right\} = -k\frac{\partial\bar{p}}{\partial\theta} + \frac{1}{H}\frac{\partial}{\partial\eta}\tau_{\theta\eta} \tag{A.8}$$

$$\text{Re} \left\{ \frac{\partial \bar{w}^2}{\partial\xi} + \frac{1}{H}\frac{\partial}{\partial\eta}\left[\bar{w}\bar{v} - \eta\gamma\bar{w}\bar{u}\right] + \frac{\gamma\bar{w}^2}{H} + \frac{\partial}{\partial\theta}(\bar{u}\bar{w}) \right\} = -k\left(\frac{b}{L}\right)^2\frac{\partial\bar{p}}{\partial\xi} + \frac{1}{H}\frac{\partial}{\partial\eta}\tau_{\xi\eta} \tag{A.9}$$

$$\frac{\partial\bar{u}}{\partial\theta} + \frac{1}{H}\frac{\partial}{\partial\eta}\left[\bar{v} - \eta\gamma\bar{u}\right] + \frac{\gamma\bar{u}}{H} + \frac{\partial\bar{w}}{\partial\xi} = 0 \tag{A.10}$$

where $\gamma = \partial H/\partial\theta$ and

$$\text{Re} = \frac{\omega\delta^2}{\nu} b^2 \tag{A.11}$$

is the squeeze Reynolds number.

The boundary conditions appropriate for the flow are

$$\begin{array}{lll} \text{at } \eta=0 & \bar{u}=-1, & \bar{v}=\bar{w}=0 \\ \eta=1 & \bar{u}=-1, & \bar{v}=-\gamma, \ \bar{w}=0 \end{array} \tag{A.12}$$

(Note that we have neglected the velocity component due to the motion of the surface $\eta=1$ in the θ-direction since it is of order δ).

The pressure must satisfy appropriate conditions at the ends of the SFD and must be single-valued and periodic in the circumferential direction, i.e.

$$\oint \frac{\partial\bar{p}}{\partial\theta}\, d\theta = 0 \tag{A.13}$$

Equations (A.8) to (A.10) are integrated across the film to obtain

$$\text{Re}\left\{\frac{\partial}{\partial\theta} I_{\theta\theta} + \frac{\partial}{\partial\xi} I_{\theta\xi}\right\} = -kH\frac{\partial\bar{p}}{\partial\theta} + \Delta\tau_{\theta\eta} \tag{A.14}$$

$$\text{Re}\left\{\frac{\partial}{\partial\theta} I_{\theta\xi} + \frac{\partial}{\partial\xi} I_{\xi\xi}\right\} = -kH\,(b/L)^2\frac{\partial\bar{p}}{\partial\xi} + \Delta\tau_{\xi\eta} \tag{A.15}$$

$$\frac{\partial}{\partial\theta} q_\theta + \frac{\partial}{\partial\xi} q_\xi = 0 \tag{A.16}$$

where q_θ and q_ξ are the dimensionless local flow rates in the θ and ξ directions,

$$q_\theta = H\int_0^1 \bar{u}d\eta = H\,\bar{u}_m \tag{A.17a}$$

$$q_\xi = H\int_0^1 \bar{w}d\eta = H\,\bar{w}_m \tag{A.17b}$$

and the Iij's are defined as:

$$Iij = H\int_0^1 \bar{u}_i\,\bar{u}_j\,d_\eta \tag{A.18}$$

To proceed, further assumptions about the velocity distribution should be made. To this end we assume that the shape of the velocity field is not greatly affected by inertia, and we let the velocity momentum integrals in (A.18) be given by

$$\begin{aligned} I_{\theta\theta} &= \alpha_1\, q_\theta^2/H + 0.4\, q_\theta + 0.2\, H \\ I_{\theta\xi} &= \alpha_2\, q_\theta q_\xi/H + 0.2\, q_\xi \\ I_{\xi\xi} &= \alpha_3\, q_\xi^2/H \end{aligned} \tag{A.19}$$

For the type of flow considered, the range of variation of the coefficients $\{\alpha_i\}_{i=1}^{3}$ is between 1.2 and 1.0 for small Reynolds numbers and large Reynolds numbers, respectively; thus it may be assumed that averaged values will suffice to obtain meaningful results.

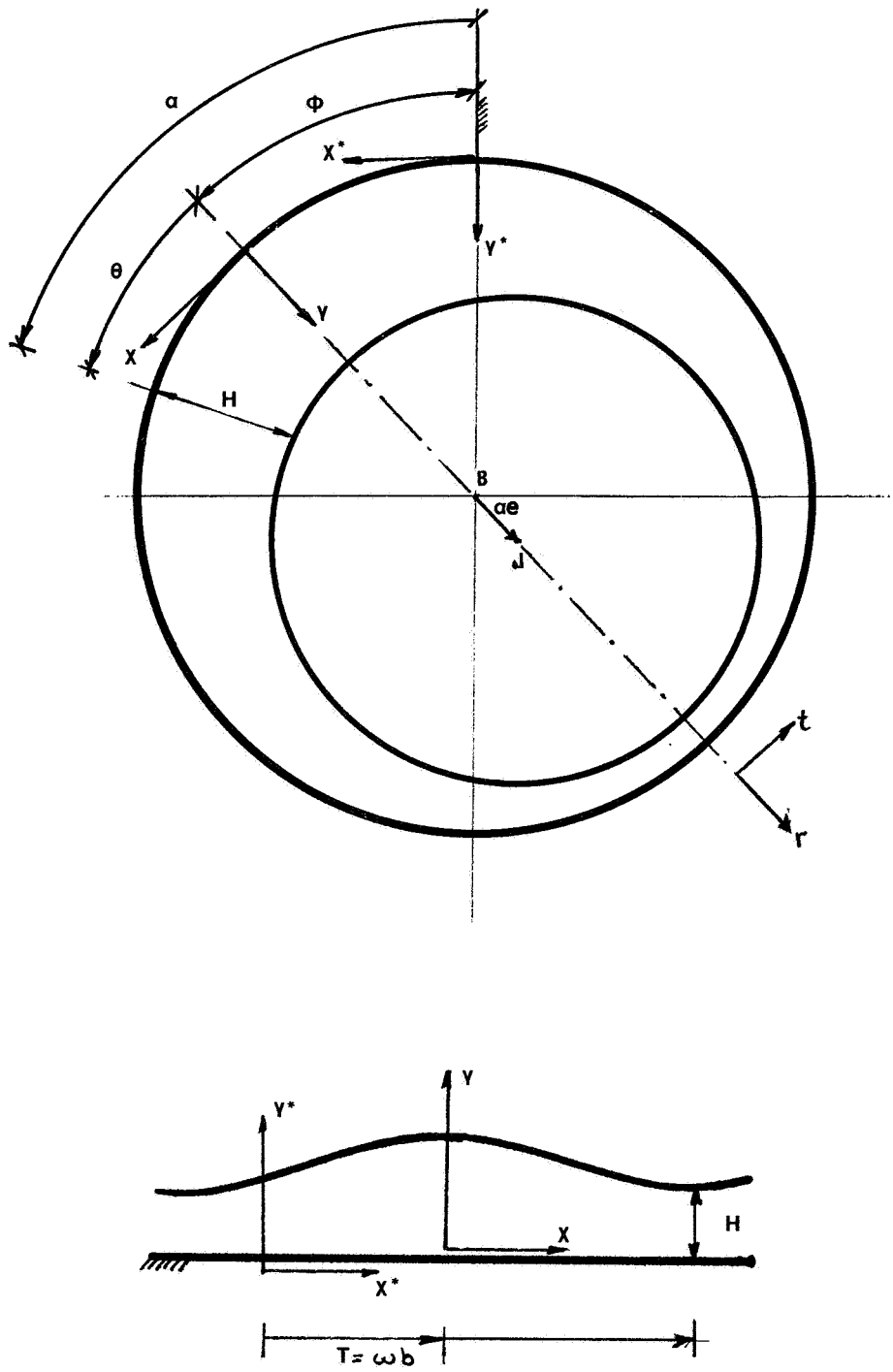

Figure 1. - Squeeze film damper geometry and coordinate systems.

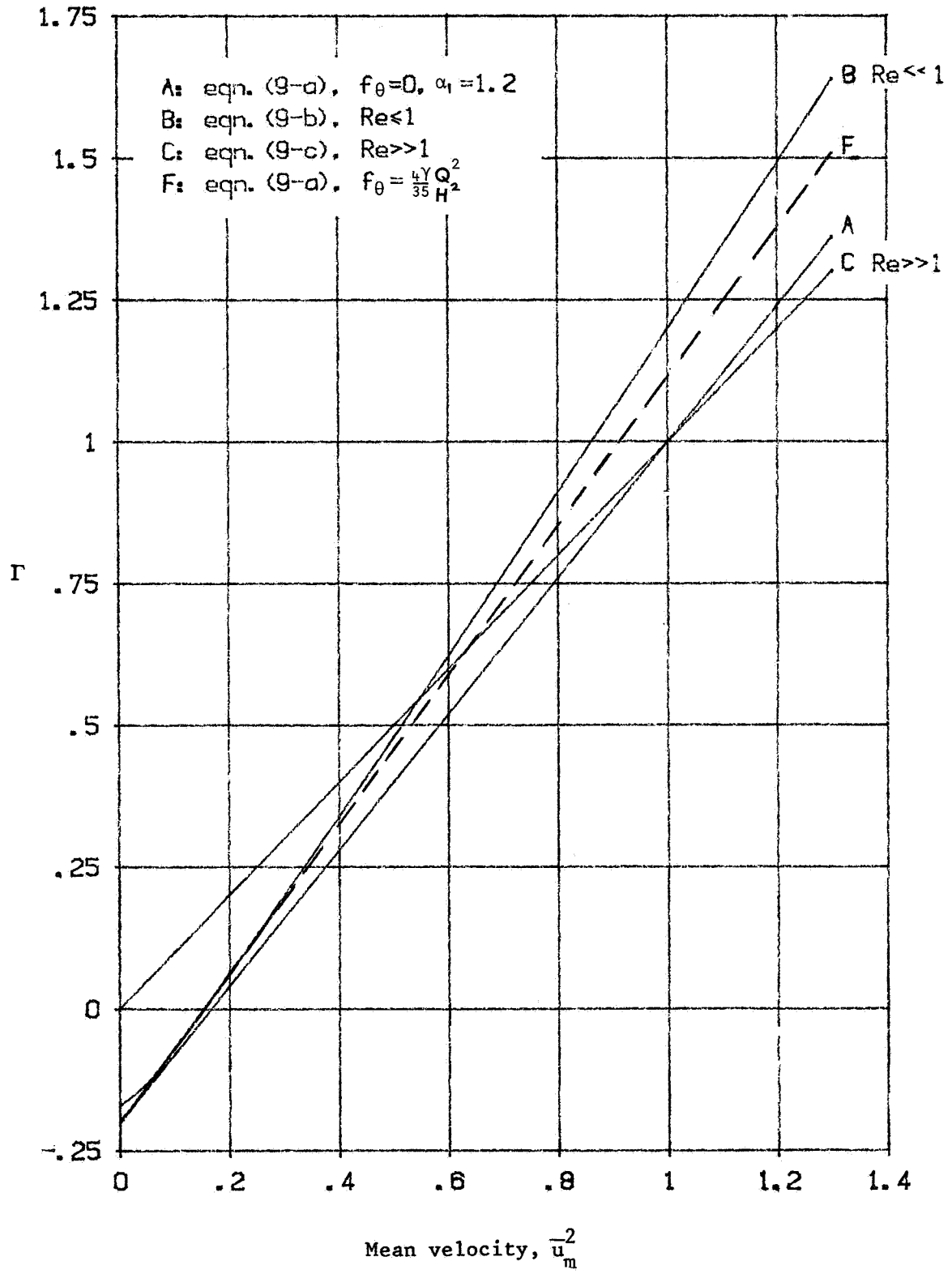

Figure 2. - Function $\Gamma(\bar{u}_m^2)$ indicating magnitude of inertia term in pressure equation for infinitely long squeeze film damper.

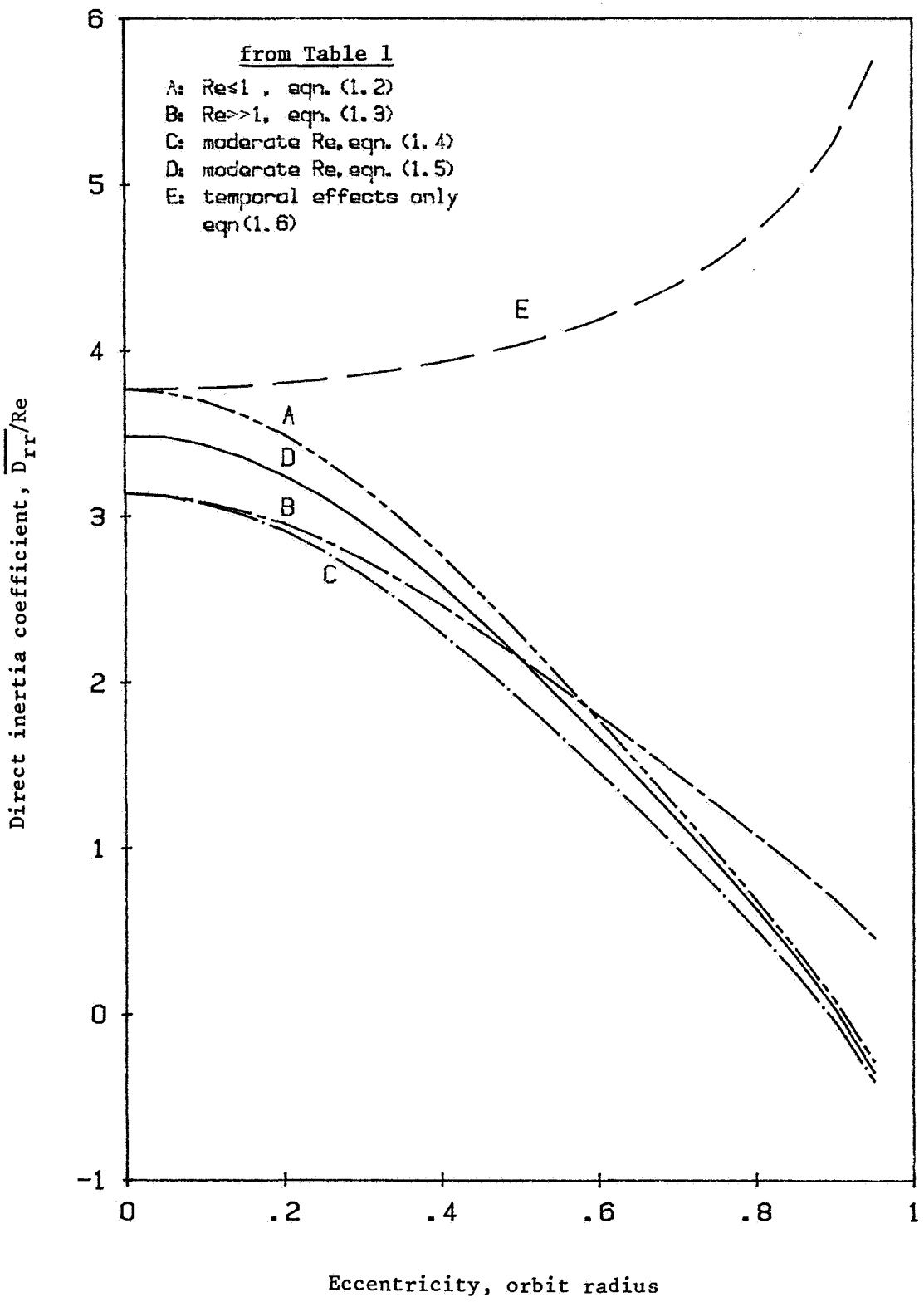

Figure 3. - Direct inertia coefficient $\overline{D_{rr}}/Re$ for circular centered orbits as function of eccentricity - long squeeze film damper assumption; laminar flow solution.

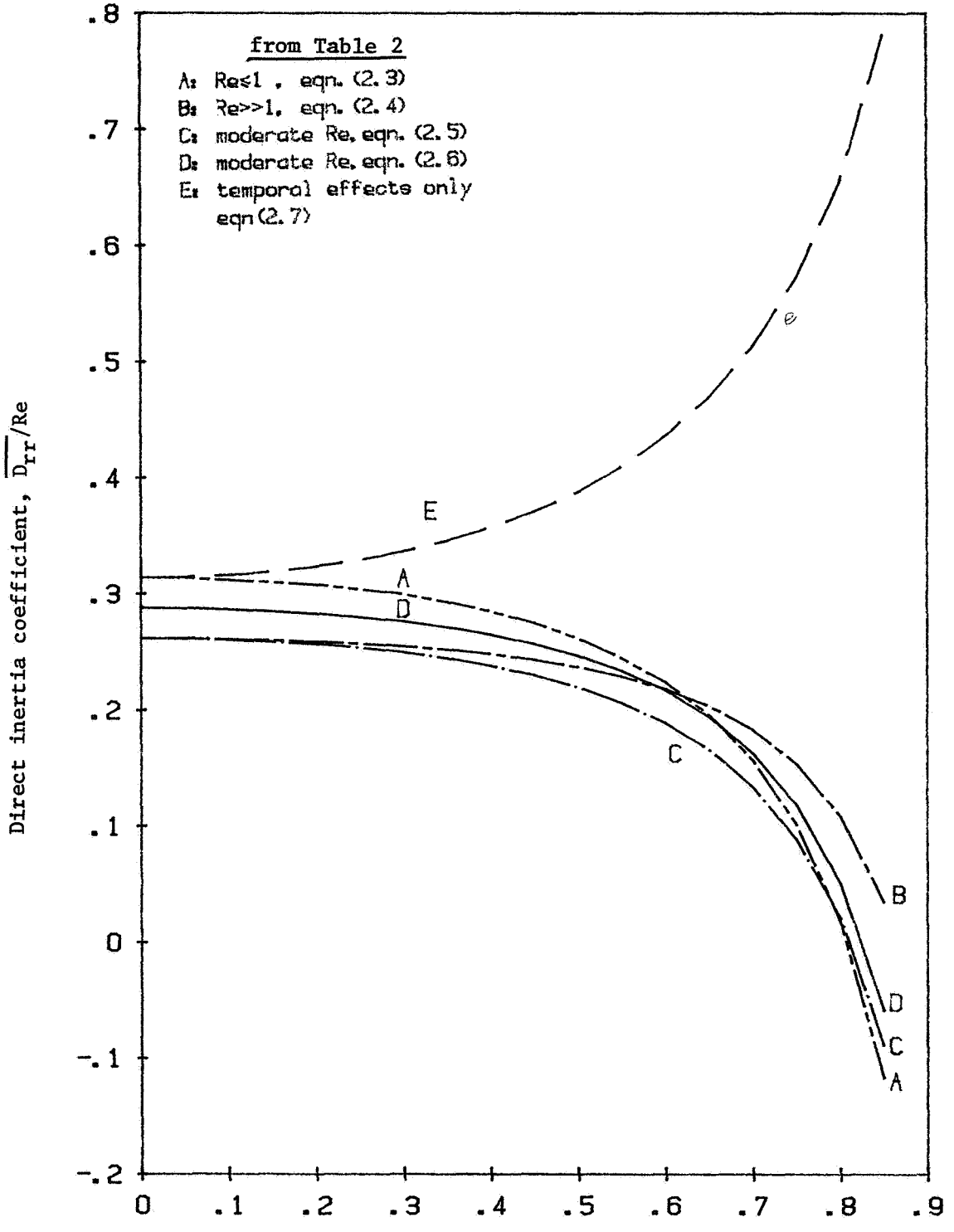

Figure 4. - Direct inertia coefficient $\overline{D_{rr}}/Re$ for circular centered orbits as function of eccentricity - short squeeze film damper assumption; laminar flow solution.

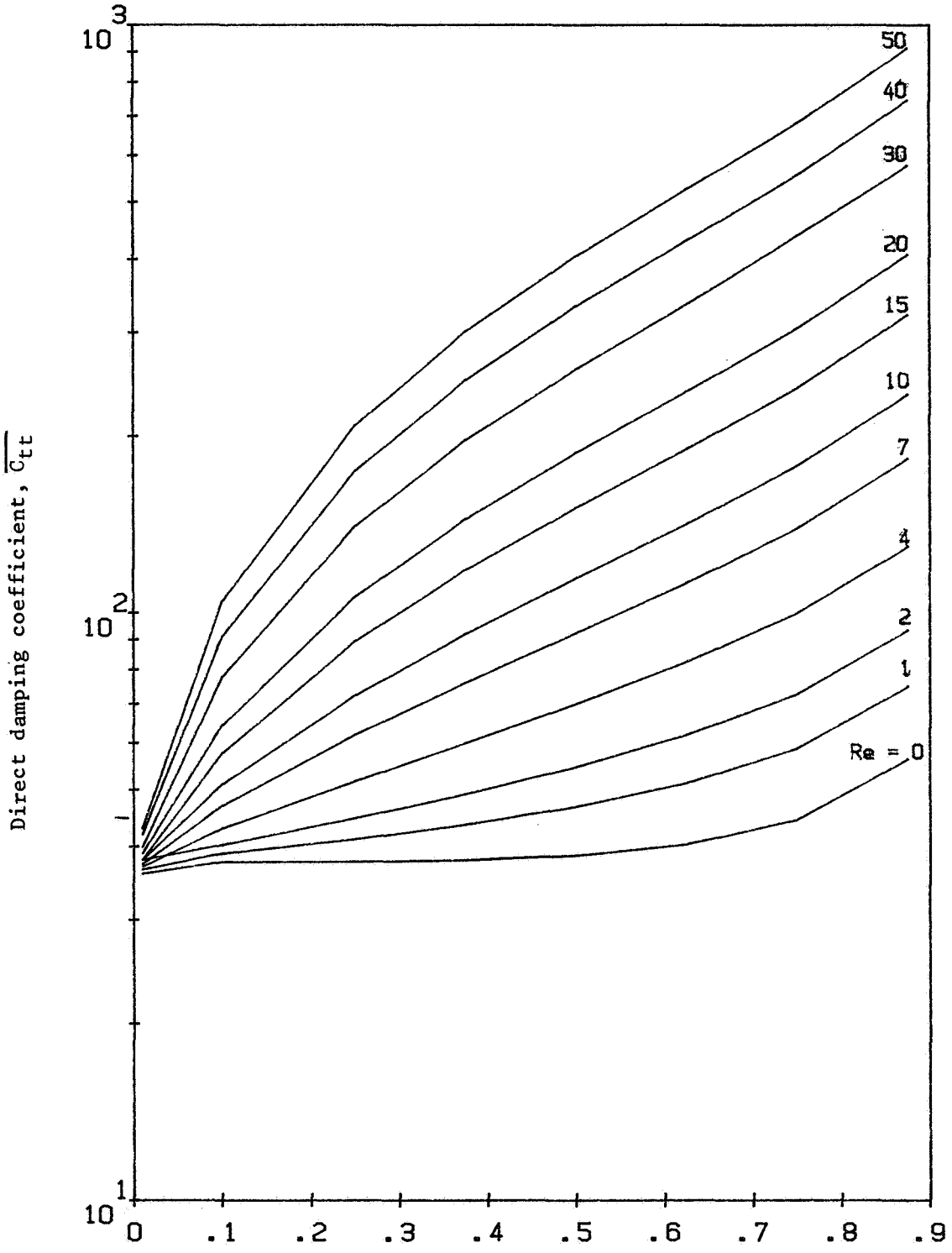

Figure 5. - Direct damping coefficient $\overline{D_{tt}}$ for circular centered orbits as function of eccentricity - long squeeze film damper assumption; turbulent motion solution.

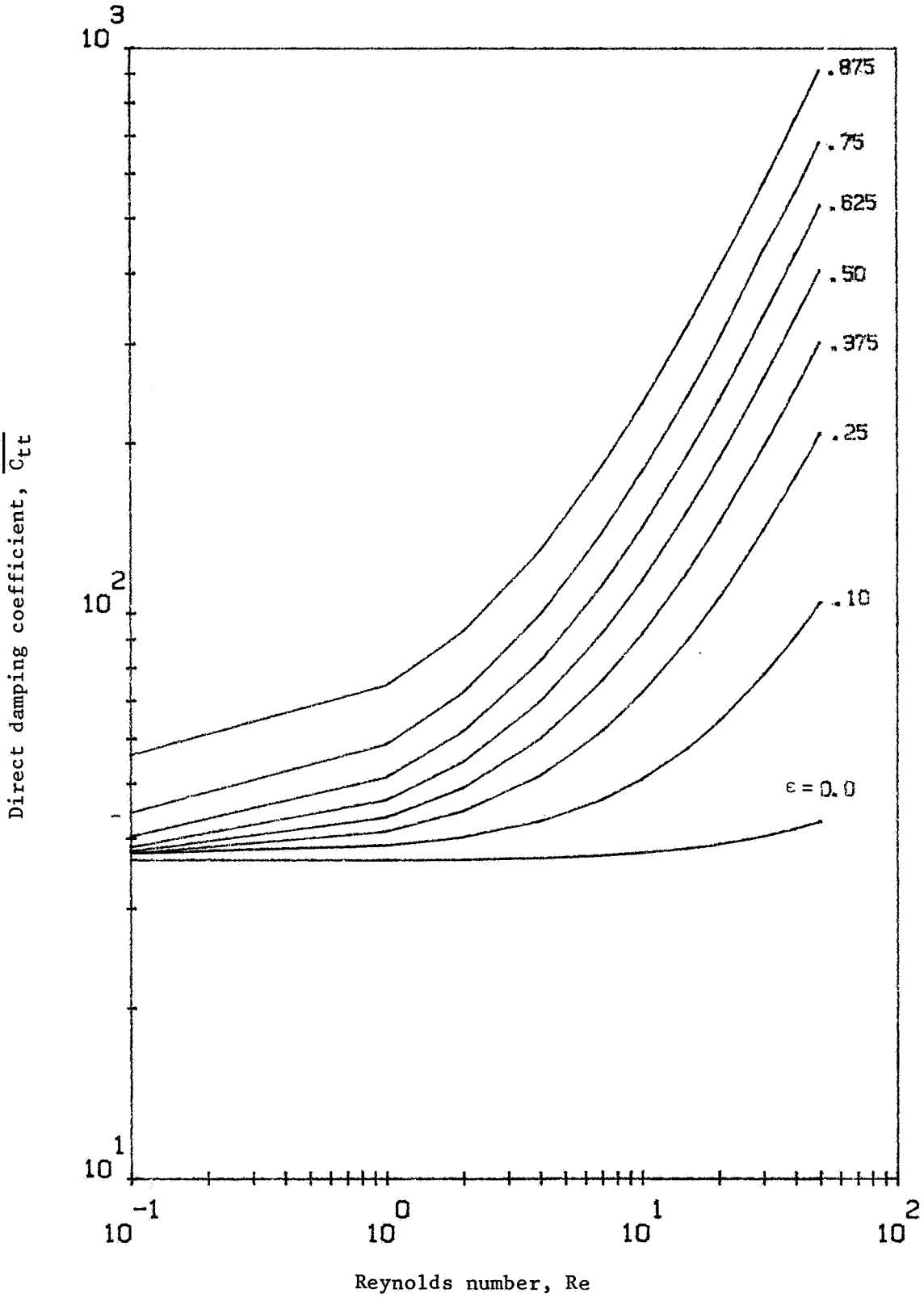

Figure 6. - Direct damping coefficient $\overline{C_{tt}}$ for circular centered orbit as function of Reynolds number - long squeeze film damper assumption; turbulent motion solution.

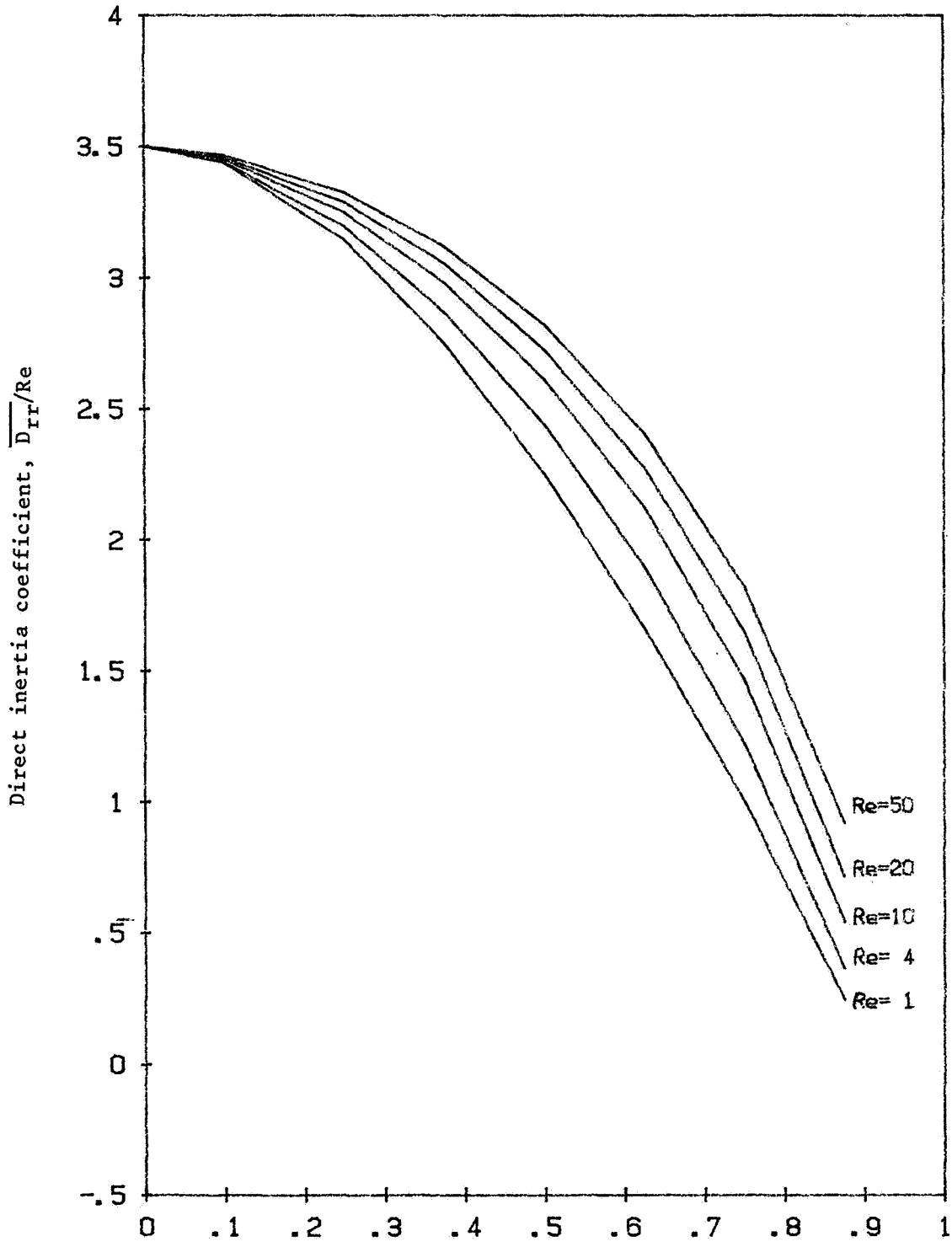

Figure 7. - Direct inertia coefficient $\overline{D_{rr}}/Re$ for circular centered orbits as function of eccentricity - long squeeze film damper assumption; turbulent flow solution.

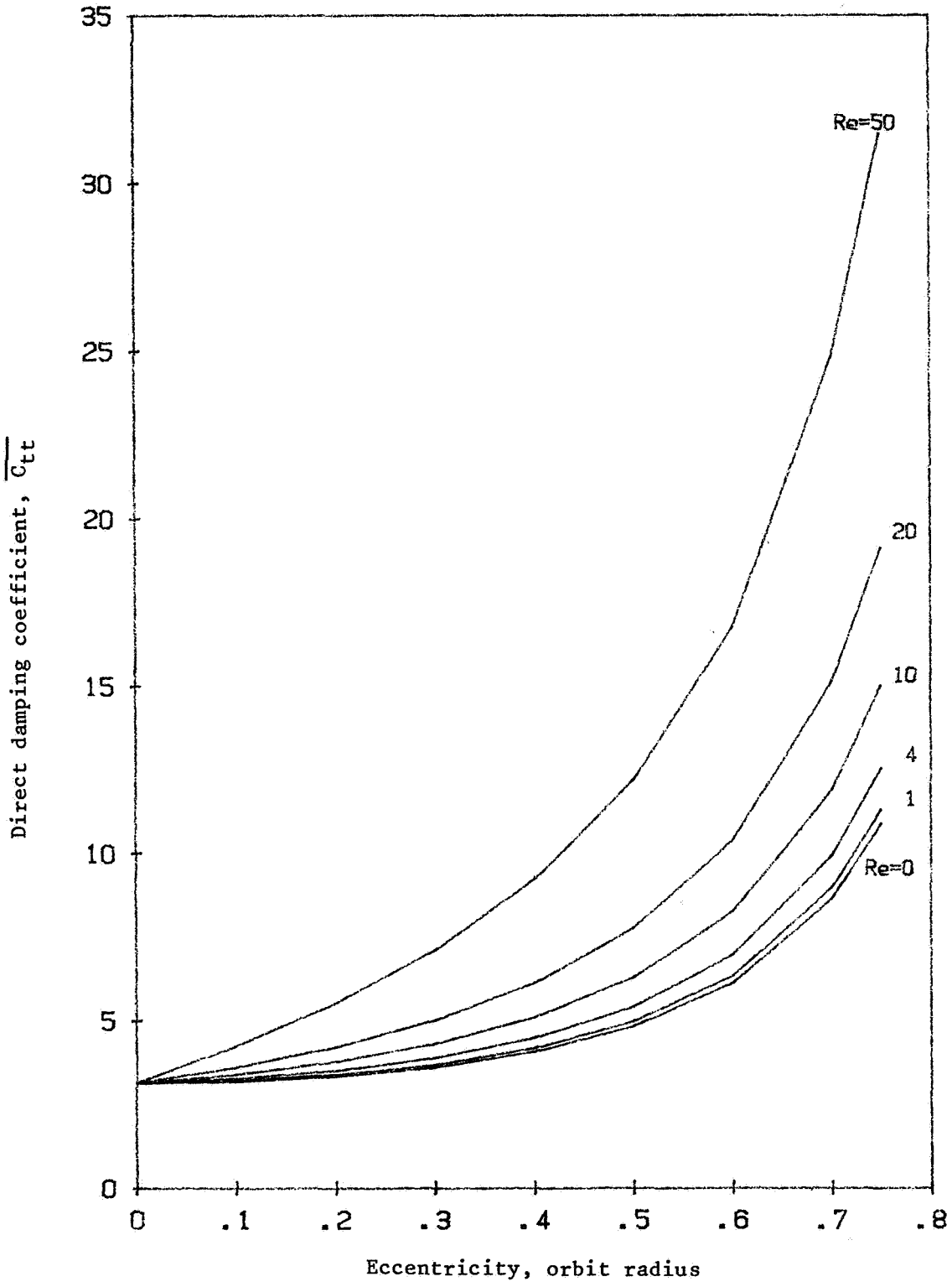

Figure 8. - Direct damping coefficient $\overline{C_{tt}}$ for circular centered orbits as function of eccentricity - short squeeze film damper assumption; L/D=0.25; turbulent motion solution.

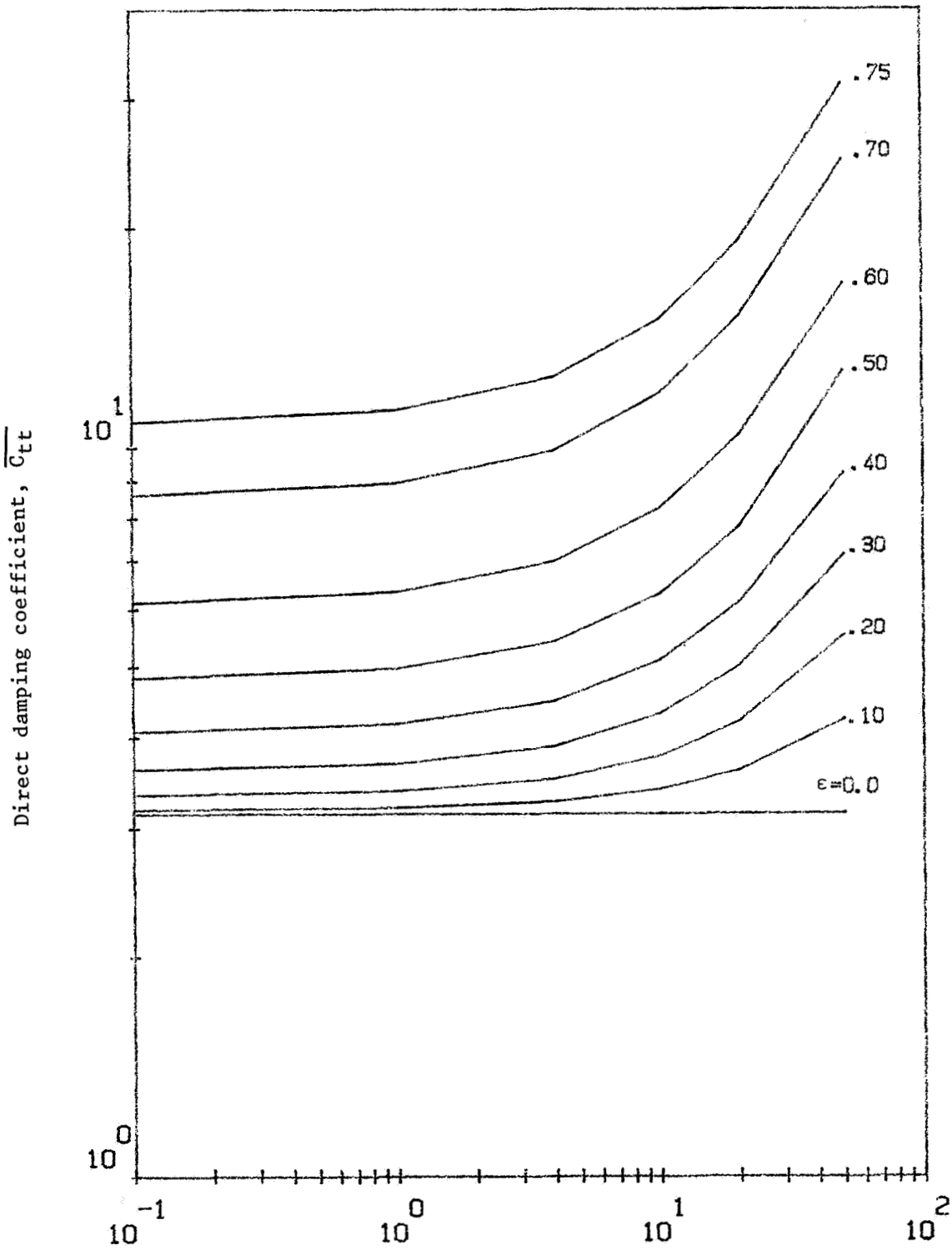

Figure 9. - Direct damping coefficient $\overline{C_{tt}}$ for circular centered orbits as function of Reynolds number - short squeeze film damper assumption; L/D=0.25; turbulent motion solution.

SQUEEZE-FILM DAMPERS FOR TURBOMACHINERY STABILIZATION

L. J. McLean and E. J. Hahn
University of New South Wales
Kensington, N.S.W., 2033, Australia

This paper presents a technique for investigating the stability and damping present in centrally preloaded radially symmetric multi-mass flexible rotor bearing systems. In general, one needs to find the eigenvalues of the linearized perturbation equations, though zero frequency stability maps may be found by solving as many simultaneous non-linear equations as there are dampers; and in the case of a single damper, such maps may be found directly, regardless of the number of degrees of freedom. The technique is illustrated for a simple symmetric four degree of freedom flexible rotor with an unpressurized damper. This example shows that whereas zero frequency stability maps are likely to prove to be a simple way to delineate multiple solution possibilities, they do not provide full stability information. Further, particularly for low bearing parameters, the introduction of an unpressurized squeeze film damper may promote instability in an otherwise stable system.

INTRODUCTION

The use of centrally preloaded squeeze film dampers for the attenuation of the unbalance response in turbomachinery has been well documented, and solution techniques which enable all equilibrium operation possibilities to be conveniently portrayed for general multi-degree of freedom rotor bearing systems are increasingly available (refs. 1, 2). However, the question as to which of these equilibrium solutions is stable has not been as fully addressed. Indeed, earlier stability investigations for simpler squeeze film damped flexible rotors (ref. 3) showed that instability (in the linear sense) was indeed possible with unpressurized dampers below and above the first pin pin critical speed, though no instability was noted for pressurized dampers with retainer springs. The utility of squeeze film dampers to accommodate the influence of gyroscopic effects, non-rigid bearing mounts and supercritical operation on stability needs to be better quantified. Hence, it is the purpose of this paper to present a straightforward but general technique for investigating the stability and degree of damping present in general multi-mass flexible rotor bearing systems incorporating one or more centrally preloaded squeeze film dampers. The technique will be illustrated for a simple symmetric four degree of freedom flexible rotor.

SYMBOLS

$\mathbf{A,B}$	square matrices defined by equations (27) and (28)	$\hat{\mathbf{C}}$	$= \mathbf{T}^{-1}\mathbf{C}\mathbf{T}^*$
		$\mathbf{C}^*$	matrix defined by equation (18)
C	radial clearance of damper	C_1	$= c_1/[(m_1+m_2)\omega]$
$\mathbf{C}$	matrix of viscous damping and gyroscopic coefficients	$2c_1$	viscous damping of disc in figure 3

C_{rs}, etc. = $Q_{R34}/[(m_1+m_2)\omega]$, etc.

e_i eccentricity of i^{th} damper; $i=1,\ldots,m$

$F_{1,2}$ unbalance excitation forces defined by equation (31)

$\underline{F}_S$, $\underline{F}_R$ Vectors of system excitation and hydrodynamic forces in stationary and rotating frames respectively

$\delta\underline{F}_S$, $\delta\underline{F}_R$ vectors of perturbated system excitation and hydrodynamic forces in stationary and rotating frames respectively

F_{S_i}, F_{R_i} elements of $\underline{F}_S$ and $\underline{F}_R$ respectively; $i=1,\ldots,n$

i subscript (omitted where meaning is clear)

j subscript or $\sqrt{-1}$ depending on context

$\mathbf{K}$ system stiffness matrix

$\mathbf{K}^*$ matrix defined by equation (19)

$K_{1,2}$ = $k_{1,2}/[(m_1+m_2)\omega^2]$

K_{rs}, etc. = $P_{R34}/[(m_1+m_2)\omega^2]$, etc.

k_1 rotor stiffness in figure 3

k_2 retainer spring stiffness in figure 3

L damper length

$\mathbf{M}$ system mass matrix

$\hat{\mathbf{M}}$ = $\mathbf{T}^{-1}\mathbf{M}\mathbf{T}^*$

$M_{1,2}$ = $m_{1,2}/[m_1+m_2]$

m number of hydrodynamic damper stations or some characteristic system mass

$\mathbf{m}$ matrix defined by equation (A11)

$\hat{\mathbf{m}}$ matrix defined by equation (A12)

$2m_1$ lumped mass of disc in figure 3

m_2 lumped mass at bearing stations in figure 3

n number of system degrees of freedom (necessarily even)

$\mathbf{P}_S$, $\mathbf{P}_R$ matrix of damper stiffness coefficients in stationary and rotating frames respectively

$P_{S_{ij}}$, $P_{R_{ij}}$ elements of $\mathbf{P}_S$ and $\mathbf{P}_R$ defined by equations (7) and (20) respectively

$\mathbf{Q}_S$, $\mathbf{Q}_R$ matrix of damper damping coefficients in stationary and rotating frames respectively

$Q_{S_{ij}}$, $Q_{R_{ij}}$ elements of $\mathbf{Q}_S$ and $\mathbf{Q}_R$ defined by equations (8) and (21) respectively

R radius of damper journal

S, R subscripts denoting stationary (XYZ) and rotating (xyZ) frames respectively

r, s subscripts denoting damper degrees of freedom x_3 and x_4 respectively

$\mathbf{T}$ transformation matrix defined by equation (11)

$\mathbf{T}^*$ matrix defined by equations (A4) to (A6)

t real time

U unbalance parameter = $\rho_1 m_1/[(m_1+m_2)C]$

$\underline{u}$ state vector defined by equation (26)

XYZ, xyZ stationary and rotating cartesian reference frames respectively

$\underline{X}$, $\underline{x}$ system displacement vector in stationary and rotating frames respectively

$\underline{X}_o$, $\underline{x}_o$ system steady state displacement vector in stationary and rotating frames respectively

$\delta\underline{X}$, $\delta\underline{x}$ perturbed system displacement vector in the stationary and rotating frames respectively

X_i, x_i elements of $\underline{X}$ or $\underline{x}$

$\bar{x}_1$, etc. = x_1/C, etc.

γ_i phase difference between i^{th} lumped mass and the stationary frame as defined in figure 2

ε	damper eccentricity ratio = e/C		system as defined by equation (22)
ζ	damping ratio at rotor mid-span in figure 3 = $c_1/(2m_1\omega_c)$	ψ	Phase difference between rotating and stationary frames as defined in figure 2
$\underline{\eta}$	eigenvector of the perturbed system as defined by equation (29)	Ω	natural frequency at stability threshold
$\mathbf{A}$	transformation matrix as defined by equation (12)	ω	rotor speed
$\mathbf{A}^*$	matrix defined by equation (A5)	ω_c	a characteristic system frequency = $\sqrt{k_1/m_1}$ in figure 3
λ	system eigenvalue	ω_b	a bearing parameter = $\mu RL^3/[(m_1+m_2)C^3]$ in figure 3
μ	lubricant viscosity	ω_r	= $\sqrt{k_2/(m_1+m_2)}$
ρ_1	disc mass eccentricity in figure 3	$\cdot$	denotes differentiation with respect to time t
τ	non-dimensional time = ωt	$'$	denotes differentiation with respect to time τ
ϕ	angle between axes 0X and 0x as defined in figure 2		
$\underline{\chi}$	eigenvector of the perturbed		

THEORY

Figure 1 depicts a general n degree of freedom rotor bearing system incorporating one or more squeeze film dampers. For the system, the equations of motion, in fixed cartesian co-ordinates, may be written as:

$$\mathbf{M}\ddot{\underline{X}} + \mathbf{C}\dot{\underline{X}} + \mathbf{K}\underline{X} = \underline{F}_S(\underline{X},\dot{\underline{X}}) \ . \tag{1}$$

Assuming (i) axially symmetric rotor and foundation stiffnesses, (ii) viscous damping, (iii) central preloading of the hydrodynamic dampers, (iv) synchronous unbalance excitation, (v) negligible torsional and axial vibration, one can obtain circular synchronous solutions $\underline{X}_o$ to equation (1) as explained in reference 2, i.e.

$$\mathbf{M}\ddot{\underline{X}}_o + \mathbf{C}\dot{\underline{X}}_o + \mathbf{K}\underline{X}_o = \underline{F}_S(\underline{X}_o,\dot{\underline{X}}_o) \ . \tag{2}$$

Note that $\underline{X}_o$ is a function of time. It is the degree of stability of these steady state solutions $\underline{X}_o$ that is of interest.

If the steady state solution $\underline{X}_o$ is perturbed by $\delta\underline{X}$ to $\underline{X}$, whereupon $\underline{F}_S(\underline{X}_o,\dot{\underline{X}}_o)$ changes to $\underline{F}_S(\underline{X},\dot{\underline{X}})$, i.e. if:

$$\underline{X} = \underline{X}_o + \delta\underline{X} \ , \tag{3}$$

then substitution of equation (3) in equation (1) and utilizing equation (2) yields:

$$\mathbf{M}\delta\ddot{\underline{X}} + \mathbf{C}\delta\dot{\underline{X}} + \mathbf{K}\delta\underline{X} = \delta\underline{F}_S \ , \tag{4}$$

where

$$\delta\underline{F}_S = \underline{F}_S(\underline{X},\dot{\underline{X}}) - \underline{F}_S(\underline{X}_o,\dot{\underline{X}}_o) \tag{5}$$

$$= \mathbf{P}_S\delta\underline{X} + \mathbf{Q}_S\delta\dot{\underline{X}} + \text{higher order terms} \ , \tag{6}$$

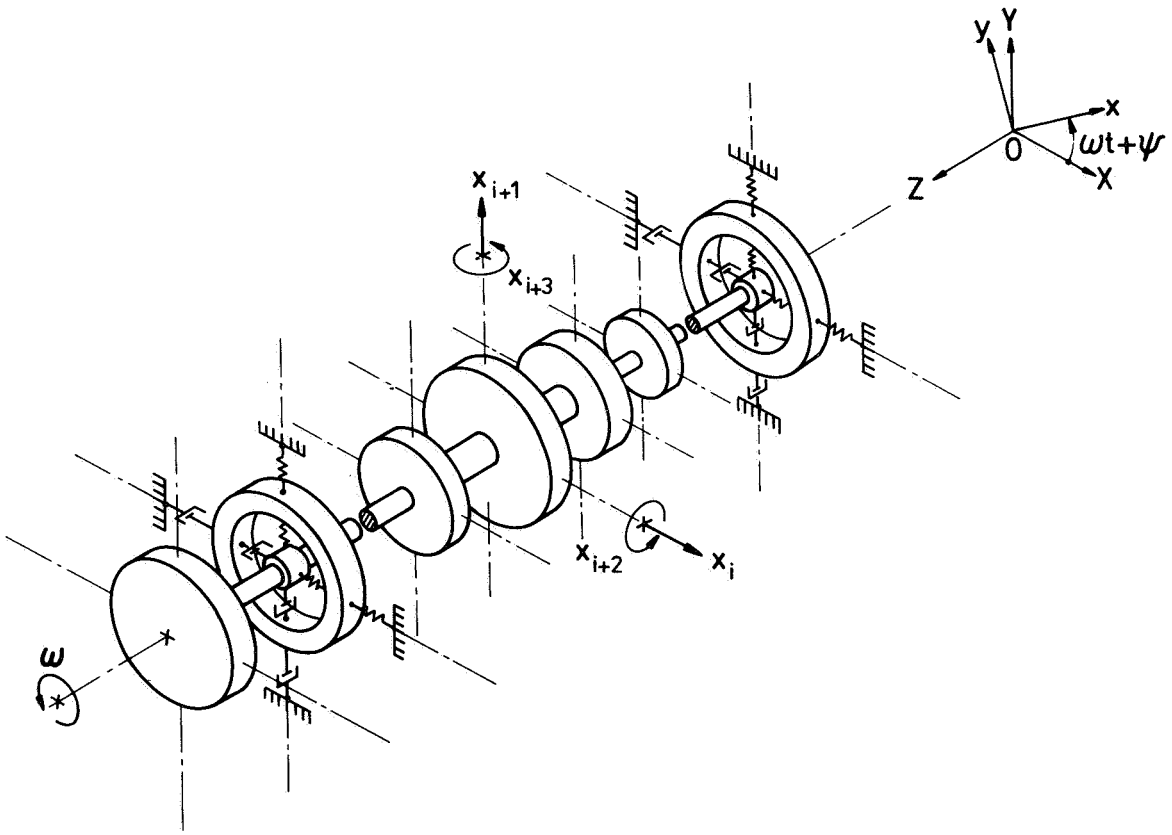

Figure 1 Typical multimass flexible rotor running in damped flexible supports

and where $$P_{S_{ij}} = \frac{\partial F_{S_i}}{\partial X_j} , \tag{7}$$

and $$Q_{S_{ij}} = \frac{\partial F_{S_i}}{\partial \dot{X}_j} . \tag{8}$$

Thus, neglecting higher order terms, equation (4) may also be written as:

$$\mathbf{M}\delta\ddot{\underline{X}} + (\mathbf{C} - \mathbf{Q}_S)\delta\dot{\underline{X}} + (\mathbf{K} - \mathbf{P}_S)\delta\underline{X} = \underline{0} . \tag{9}$$

The existence of the partial derivatives is assumed and they are evaluated at $\underline{X}_o, \dot{\underline{X}}_o$.

Unfortunately, the elements of $\mathbf{Q}_S$ and $\mathbf{P}_S$, involving derivatives of damper forces, are in general time dependent, so that equations (9) do not reduce to an eigenvalue problem. To overcome this difficulty, one may choose a rotating cartesian reference frame (x,y,Z) wherein the cartesian axis pair (x,y) rotates with angular velocity ω about the Z axis as shown in figure 1. If $\underline{x}$ be the vector of displacements in the rotating frame, then:

$$\underline{X} = \mathbf{T}\underline{x} , \tag{10}$$

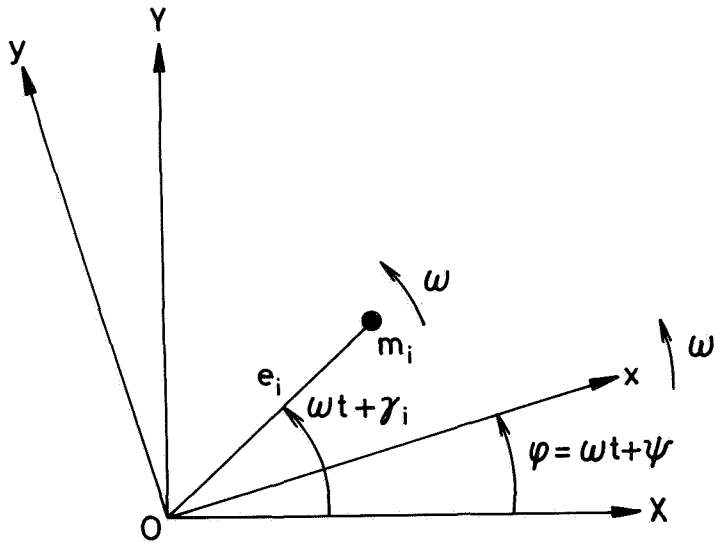

Figure 2 Location of damper mass m_i in fixed and rotating reference frames

where for an n degree of freedom system (n even), the transformation matrix $\mathbf{T}$ is given by:

$$\mathbf{T} = \begin{bmatrix} \mathbf{\Lambda} & & \mathbf{0} \\ & \ddots & \\ \mathbf{0} & & \mathbf{\Lambda} \end{bmatrix}, \tag{11}$$

with equal 2×2 diagonal submatrices $\mathbf{\Lambda}$, where:

$$\mathbf{\Lambda} = \begin{bmatrix} \cos\phi & -\sin\phi \\ \sin\phi & \cos\phi \end{bmatrix}, \tag{12}$$

and

$$\phi = \omega t + \psi \quad . \tag{13}$$

Note that ψ, the angular displacement of the xy axes from the XY axis at time t=0 is arbitrary. Premultiplying equation (1) by $\mathbf{T}^{-1}$ gives forces in the rotating frame, i.e.:

$$\mathbf{T}^{-1}(\mathbf{M}\ddot{\underline{X}} + \mathbf{C}\dot{\underline{X}} + \mathbf{K}\underline{X}) = \mathbf{T}^{-1}\underline{F}_S = \underline{F}_R \quad . \tag{14}$$

Hence, as shown in the Appendix, substitution of equation (10) into equation (14) yields:

$$\mathbf{M}\ddot{\underline{x}} + (\mathbf{C} + 2\omega\hat{\mathbf{M}})\dot{\underline{x}} + (-\omega^2\mathbf{M} + \omega\hat{\mathbf{C}} + \mathbf{K})\underline{x} = \underline{F}_R \quad . \tag{15}$$

If $\underline{x}_o$ be the steady state solutions of equation (15), then following the same arguments as above for the stationary frame, the equations of motion consequent upon system perturbation $\delta\underline{x}$, become:

$$\mathbf{M}\delta\ddot{\underline{x}} + (\mathbf{C} + 2\omega\hat{\mathbf{M}} - \mathbf{Q}_R)\delta\dot{\underline{x}} + (-\omega^2\mathbf{M} + \omega\hat{\mathbf{C}} + \mathbf{K} - \mathbf{P}_R)\delta\underline{x} = \underline{0} , \tag{16}$$

or

$$\mathbf{M}\delta\ddot{\underline{x}} + \mathbf{C}^*\delta\dot{\underline{x}} + \mathbf{K}^*\delta\underline{x} = \underline{0} , \tag{17}$$

where

$$\mathbf{C}^* = \mathbf{C} + 2\omega\hat{\mathbf{M}} - \mathbf{Q}_R , \tag{18}$$

$$\mathbf{K}^* = \mathbf{K} + \omega\hat{\mathbf{C}} - \omega^2\mathbf{M} - \mathbf{P}_R , \tag{19}$$

$$P_{R_{ij}} = \frac{\partial F_{R_i}}{\partial x_j} , \tag{20}$$

and

$$Q_{R_{ij}} = \frac{\partial F_{R_i}}{\partial \dot{x}_j} . \tag{21}$$

Again, the $P_{R_{ij}}$ and the $Q_{R_{ij}}$ are assumed to exist and are evaluated at $\underline{x}_o$. (Note that $\dot{\underline{x}}_o = \underline{0}$.)

In general, the steady state damper eccentricities e_i will have constant phase angles $(\gamma_i - \psi)$ with respect to the x axis, as shown in figure 2. Hence, the elements of $\mathbf{P}_R$ and $\mathbf{Q}_R$ will be functions of e_i and $(\gamma_i - \psi)$, where ψ is arbitrary. By selecting ψ equal to one of the γ_i's (say γ_1), $\mathbf{P}_R$ and $\mathbf{Q}_R$ will, in the general case of m dampers, be functions of $(2m-1)$ quantities $e_1, e_2, \ldots, e_m, \gamma_2-\gamma_1, \gamma_3-\gamma_1, \ldots, \gamma_m-\gamma_1$.

Note that the coefficients of $\delta\ddot{\underline{x}}$, $\delta\dot{\underline{x}}$ and $\delta\underline{x}$ in equation (17) are constants, i.e. independent of time, so one is immediately in a position to investigate the stability and the damping pertaining to the equilibrium solutions $\underline{x}_o$ by examining the solutions of equation (17), a set of n homogeneous second order linear differential equations with constant coefficients. Thus, by assuming solutions of the form:

$$\delta\underline{x} = \underline{\chi}e^{\lambda t} , \tag{22}$$

where the $\underline{\chi}$ and λ may be complex, non-trivial solutions of equation (17) exist, if, and only if:

$$\det[\lambda^2\mathbf{M} + \lambda\mathbf{C}^* + \mathbf{K}^*] = 0 . \tag{23}$$

Equation (23), the characteristic equation of the perturbed system, is a polynomial of degree 2n in λ. The stability of, and the damping pertaining to the equilibrium solutions $\underline{x}_o$ depend on the real parts of the roots of equation (23) with the stability threshold being determined by that combination of system parameters which result in any pair of roots, $\lambda_{1,2} = \pm j\Omega$, where Ω is the natural frequency at the stability threshold. Note that one such possible stability threshold corresponding to $\Omega=0$ (i.e. $\lambda_{1,2} = \pm j0$) will occur whenever:

$$\det[\mathbf{K}^*] = 0 . \tag{24}$$

If stability threshold determinations were the sole requirement, one could dispense with the need to find the roots $\lambda_1, \ldots, \lambda_{2n}$ and apply a linear systems theory technique, e.g. Routh's Criterion, to the coefficients of equation (23). Such was

the procedure adopted in reference 3. If the degree of damping is of interest, one needs to resort in general to some numerical procedure for finding the roots.

An alternative and numerically far more simply approach, in so far as programming effort is concerned, is to utilize generally available eigenvalue solution procedures, by recasting equations (17) into a recognizable eigenvalue problem. The normal procedure is to transform these n second order differential equations into the 2n first order equations (see for example reference 4):

$$\mathbf{A}\dot{\underline{u}} + \mathbf{B}\underline{u} = \underline{0} , \tag{25}$$

where

$$\underline{u} = \begin{bmatrix} \delta\dot{\underline{x}} \\ \delta\underline{x} \end{bmatrix} , \tag{26}$$

$$\mathbf{A} = \begin{bmatrix} \mathbf{0} & \mathbf{M} \\ \mathbf{M} & \mathbf{C}^* \end{bmatrix} , \tag{27}$$

and

$$\mathbf{B} = \begin{bmatrix} -\mathbf{M} & \mathbf{0} \\ \mathbf{0} & \mathbf{K}^* \end{bmatrix} . \tag{28}$$

By assuming solutions of the form:

$$\underline{u} = \underline{\eta} e^{\lambda t} , \tag{29}$$

where the $\underline{\eta}$ and λ may be complex, non-trivial solutions of equation (23) exist if, and only if:

$$\det[\lambda\mathbf{A} + \mathbf{B}] = 0 . \tag{30}$$

Equation (30) is a polynomial of degree 2n in λ. It is equivalent to the characteristic equation (23). The 2n values of λ, the roots of the characteristic equation, are in this formulation more commonly referred to as eigenvalues. Once the 2n eigenvalues have been located for a given choice of system parameters, both the stability and the degree of damping present can be quantified.

SYSTEM WITH ONE DAMPER

So far the problem formulation has been quite general. If one restricts attention to a single damper, an important simplification occurs if ψ is set equal to γ_1, whereupon the elements of $\mathbf{P}_R$ and $\mathbf{Q}_R$ in equations (16) are functions of e_1 only. Thus, the need to evaluate γ_1 is avoided, thereby simplifying stability evaluation and design data portrayal.

For design study purposes, it is convenient to non-dimensionalize equations (16) by dividing the force equations by $mC\omega^2$ and the moment equations by $mC^2\omega^2$ and introducing the non-dimensional time $\tau = \omega t$. The above theory is otherwise unchanged, except all quantities are now non-dimensional. In particular, one can utilize equation (24) immediately to find those stability thresholds which pertain to zero

natural frequency. Note that the non-zero elements of $\mathbf{P}_R$ are located in a 2×2 submatrix, the elements of which are products of ω_b/ω and functions of ε, where ω_b is a bearing parameter involving the bearing dimensions and lubricant viscosity. Thus, whereas equation (24) is a non-linear equation in ε, and for a given ω_b, could be solved iteratively by some appropriate technique such as the search procedure, one may note that for some assumed ε but unspecified ω_b, this equation is a quartic in ω_b when the damper is flexibly supported, and a quadratic in ω_b when the damper is rigidly supported. Hence one can determine directly from equation (24) the physically meaningful values of ω_b (if any) which satisfy it. A repetition of this for other values of ω would enable the stability thresholds corresponding to zero natural frequency and various values of ε to be drawn on a design map with ω_b as ordinate and ω as abscissa.

Note that such a map is possible regardless of the number of degrees of freedom, or of the unbalance distribution. If drawn to the same scale, it can be directly superimposed on the corresponding equilibrium orbit eccentricity design maps in reference 2, thereby indicating at a glance, the likelihood of operation in the vicinity of, or within, this particular type of unstable region. Note that the absence of other stability thresholds (at some non-zero natural frequency) has not been proven, and to be sure that all stability regions have been located, one would need to apply a more general technique, e.g. Routh's Criterion, to equation (23) over the range of $0 < \varepsilon < 1$, for the range of values of ω_b and ω of interest, a rather daunting task even for systems with only four degrees of freedom.

ILLUSTRATIVE EXAMPLE

The utility of the above approach will be illustrated for the single disc symmetric flexible rotor, previously investigated for stability in reference 3 and for which equilibrium solutions are available in reference 2.

Figure 3 is a diagram of this system with node 1 being taken at the central disc of mass $2m_1$, and nodes 2 and 3 at the ends of the rotor which are supported by identical squeeze film dampers. The lumped mass at the bearing ends is m_2, the retainer spring for central preloading has stiffness k_2 and the rotor stiffness between the central and either end node is k_1. All unbalance is assumed to be at the disc, resulting in a disc mass eccentricity ρ_1. Viscous damping at the disc is $2c_1$. Since the rotor is symmetric about the disc, it will suffice to consider one half of the system only. The equations of motion, appropriately ordered, for this system at a rotor speed ω are given by:

$$\left.\begin{aligned} m_1\ddot{X}_1 + c_1\dot{X}_1 + k_1(X_1 - X_2) &= \rho_1 m_1\omega^2\cos(\omega t) = F_1 \\ m_1\ddot{X}_2 + c_1\dot{X}_2 + k_1(X_2 - X_4) &= \rho_1 m_1\omega^2\sin(\omega t) = F_2 \\ m_2\ddot{X}_3 + k_1(X_3 - X_1) + k_2X_3 &= F_3 \\ m_2\ddot{X}_4 + k_1(X_4 - X_2) + k_2X_4 &= F_4 \end{aligned}\right\} \quad (31)$$

The equations of motion for the perturbed system are given by equations (16), which, in nondimensional form, upon dividing each equation by $(m_1+m_2)C\omega^2$ and letting $\tau = \omega t$, become:

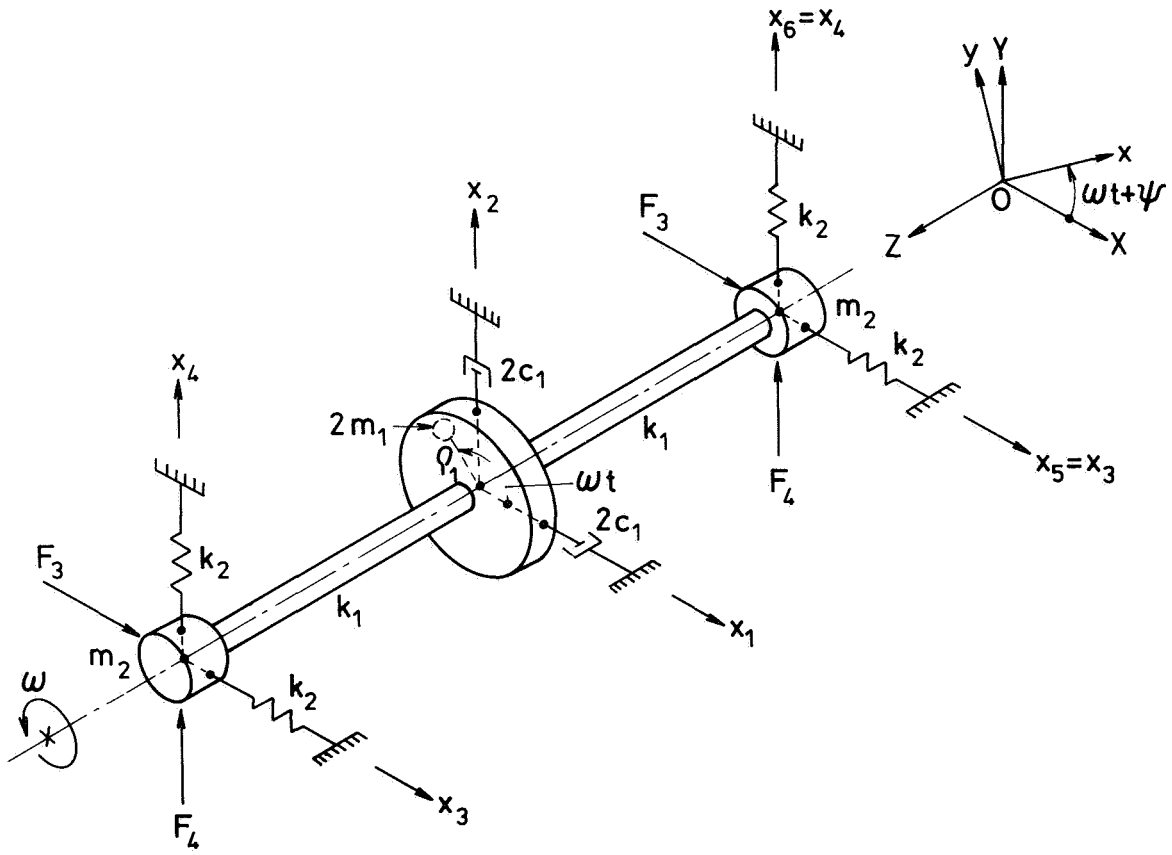

Figure 3 Flexible, symmetric unbalanced rotor supported on identical squeeze film dampers and retainer springs

$$\begin{bmatrix} M_1 & 0 & 0 & 0 \\ 0 & M_1 & 0 & 0 \\ 0 & 0 & M_2 & 0 \\ 0 & 0 & 0 & M_2 \end{bmatrix} \begin{bmatrix} \bar{x}_1'' \\ \bar{x}_2'' \\ \bar{r}'' \\ \bar{s}'' \end{bmatrix} + \begin{bmatrix} C_1 & -2M_1 & 0 & 0 \\ 2M_1 & C_1 & 0 & 0 \\ 0 & 0 & -\omega_b C_{rr}/\omega & -\omega_b C_{rs}/\omega - 2M_2 \\ 0 & 0 & -\omega_b C_{sr}/\omega + 2M_2 & -\omega_b C_{ss}/\omega \end{bmatrix} \begin{bmatrix} \bar{x}_1' \\ \bar{x}_2' \\ \bar{r}' \\ \bar{s}' \end{bmatrix}$$

$$+ \begin{bmatrix} K_1 - M_1 & -C_1 & -K_1 & 0 \\ C_1 & K_1 - M_1 & 0 & -K_1 \\ -K_1 & 0 & K_1 + K_2 - M_2 - \omega_b K_{rr}/\omega & -\omega_b K_{rs}/\omega \\ 0 & -K_1 & -\omega_b K_{sr}/\omega & K_1 + K_2 - M_2 - \omega_b K_{ss}/\omega \end{bmatrix} \begin{bmatrix} \bar{x}_1 \\ \bar{x}_2 \\ \bar{r} \\ \bar{s} \end{bmatrix} = \underline{0} \quad , \qquad (32)$$

where, to simplify the notation, the damper degrees of freedom x_3 and x_4 are denoted by r and s respectively. The coefficients K_{rr}, C_{rr}, ..., etc. are available in analytical form for unpressurized and fully pressurized (π and 2π film) dampers for both the short (Ocvirk) and finite width (Warner) bearing approximations (ref. 5). Thus, for the unpressurized or fully pressurized bearings respectively, and using the

short bearing approximation, one has:

$$K_{rr} = -\frac{4\varepsilon(1+\varepsilon^2)}{(1-\varepsilon^2)^3} \quad \text{or} \quad 0 \ , \tag{33}$$

$$K_{rs} = -C_{ss} = \frac{\pi}{2(1-\varepsilon^2)^{3/2}} \quad \text{or} \quad \frac{\pi}{(1-\varepsilon^2)^{3/2}} \ , \tag{34}$$

$$K_{sr} = C_{rr} = \frac{-\pi(1+2\varepsilon^2)}{2(1-\varepsilon^2)^{5/2}} \quad \text{or} \quad \frac{-\pi(1-2\varepsilon^2)}{(1-\varepsilon^2)^{5/2}} \ , \tag{35}$$

and

$$K_{ss} = C_{rs} = C_{sr} = \frac{-2\varepsilon}{(1-\varepsilon^2)^2} \quad \text{or} \quad 0 \ . \tag{36}$$

The equation obtained by setting the determinant of $\mathbf{K}^*$ in equation (32) equal to zero is a quadratic in ω_b, and may be solved for given values of ε and ω.

To present the data in terms of non-dimensional quantities, it is convenient to plot a non-dimensional bearing parameter ω_b/ω_c against the non-dimensional rotor speed ω/ω_c, where ω_c is some characteristic natural frequency of the system, say, the highest undamped natural frequency of the system which will fall below the desired operating speed. Equation (24) was then solved for ω_b/ω_c over a range of ω/ω_c and ε to obtain the zero natural frequency stability threshold maps if figure 4, using the following values of the non-dimensional system parameters:

$$M_2 = 0.25 \ ,$$

$$M_1 = 1 - M_2 = 0.75 \ ,$$

$$K_1 = (1 - M_2')/(\omega/\omega_c)^2 = 0.75(\omega/\omega_c)^2 \ ,$$

$$K_2 = (\omega_r/\omega_c)^2/(\omega/\omega_c)^2 = 0.25(\omega/\omega_c)^2 \ ,$$

$$C_1 = 2\zeta(1 - M_2)/(\omega/\omega_c) = 0.0075/(\omega/\omega_c) \ .$$

The quantities ω_r, ω_c and ζ are defined in the notation. (Using the notation in reference 3, the above choice of parameters would correspond to $\alpha = 0.25$, $f = 0.5$, $\zeta = 0.0005$, $a = \omega/\omega_c$ and $B = \omega_b/\omega_c$.) Here, ω_c is the first pin-pin critical speed of the rotor.

Note that provided the same scales are used for the axes ω_b/ω_c and ω/ω_c, one can overlay this stability threshold map not only over the equilibrium eccentricity orbit map given in figure 3 in reference 2 which is for an unbalance parameter $U = 0.3$, but also over any such map for the system, regardless of the unbalance distribution. These zero frequency stability thresholds were compared to the stability thresholds for $\omega_b/\omega_c = 0.1$, 0.3, 0.6 and 1.0 in figure 8 of reference 3, which were determined using Routh's Criterion. No stability thresholds were found for $\varepsilon \leqslant 0.61$. For $\omega/\omega_c \leqslant 1$ there is agreement. However, for $\omega/\omega_c > 1$, the predicted regions of instability in figure 8 of reference 3 exceed those of figure 4. Thus, figure 4 does <u>not</u> provide full stability threshold information; and for this, one would need to resort to an approach such as Routh's Criterion.

As an alternative or in addition to seeking stability thresholds, and to determine the degree of damping pertaining to the equilibrium solutions, one can find the eigenvalues λ_i for the system in figure 3 by forming equation (25) and using an

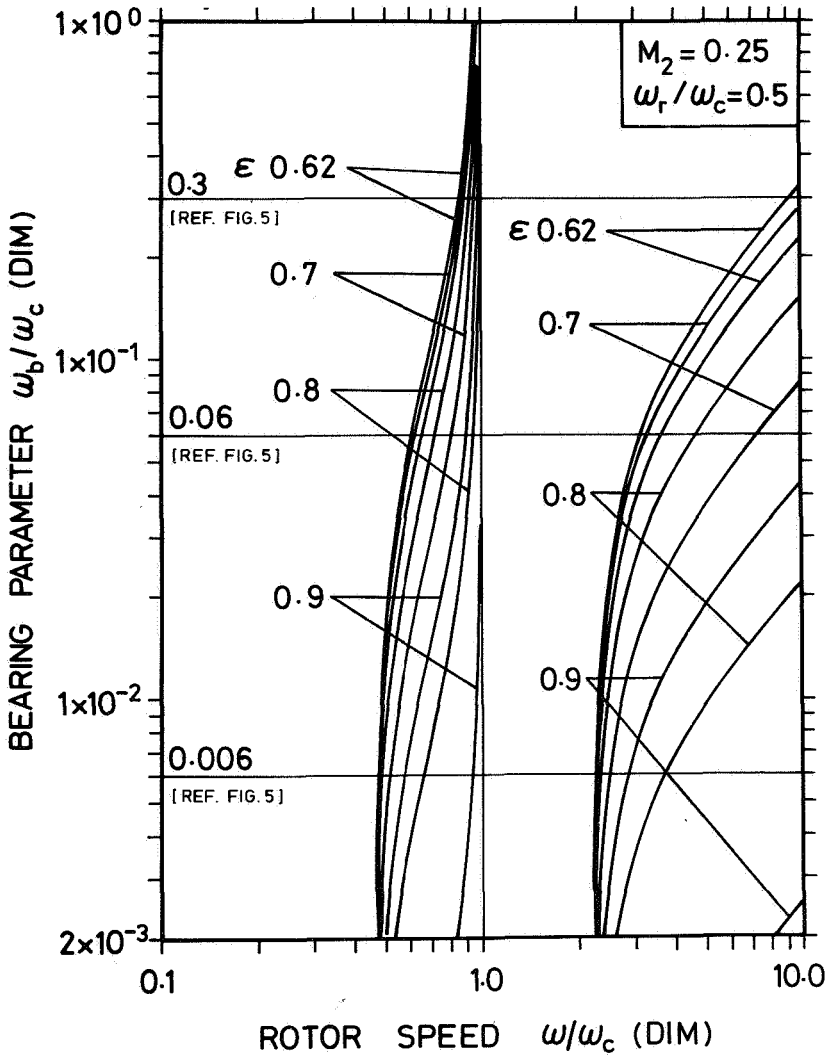

Figure 4 Zero natural frequency stability map for the system in figure 3

eigenvalue solver to determine the λ_i (i =1, 2, ..., 8). This was done for the particular equilibrium solutions indicated on figure 5 (corresponding to figure 4 in reference 2). If any of the λ_i have non-negative real parts, the solution is regarded as unstable. Where all the λ_i have negative real parts the solution is stable. Of particular interest is the degree of relative damping present in such stable solutions, particularly in the low orbit eccentricity solution when multiple solutions are possible, as this gives a qualitative indication of the likelihood of jumping to the undesirable and possibly unstable high orbit solution upon some system perturbation. Various means of determining this relative damping are available (ref.4) such as the smallest logarithmic decrement, $-2\pi Re(\lambda)/|Im(\lambda)|$, or the smallest damping ratio, $-Re(\lambda)/|\lambda|$. Either of these quantities requires the determination of the λ_i. The latter quantity is indicated for illustrative purposes in figure 5. For example, at ω/ω_c =0.3, the damping ratios corresponding to ω_b/ω_c =0.006, 0.06 and 0.3 are 0.0053, 0.047 and 0.23 respectively. The equilibrium solution for ω_b/ω_c =0.3 could

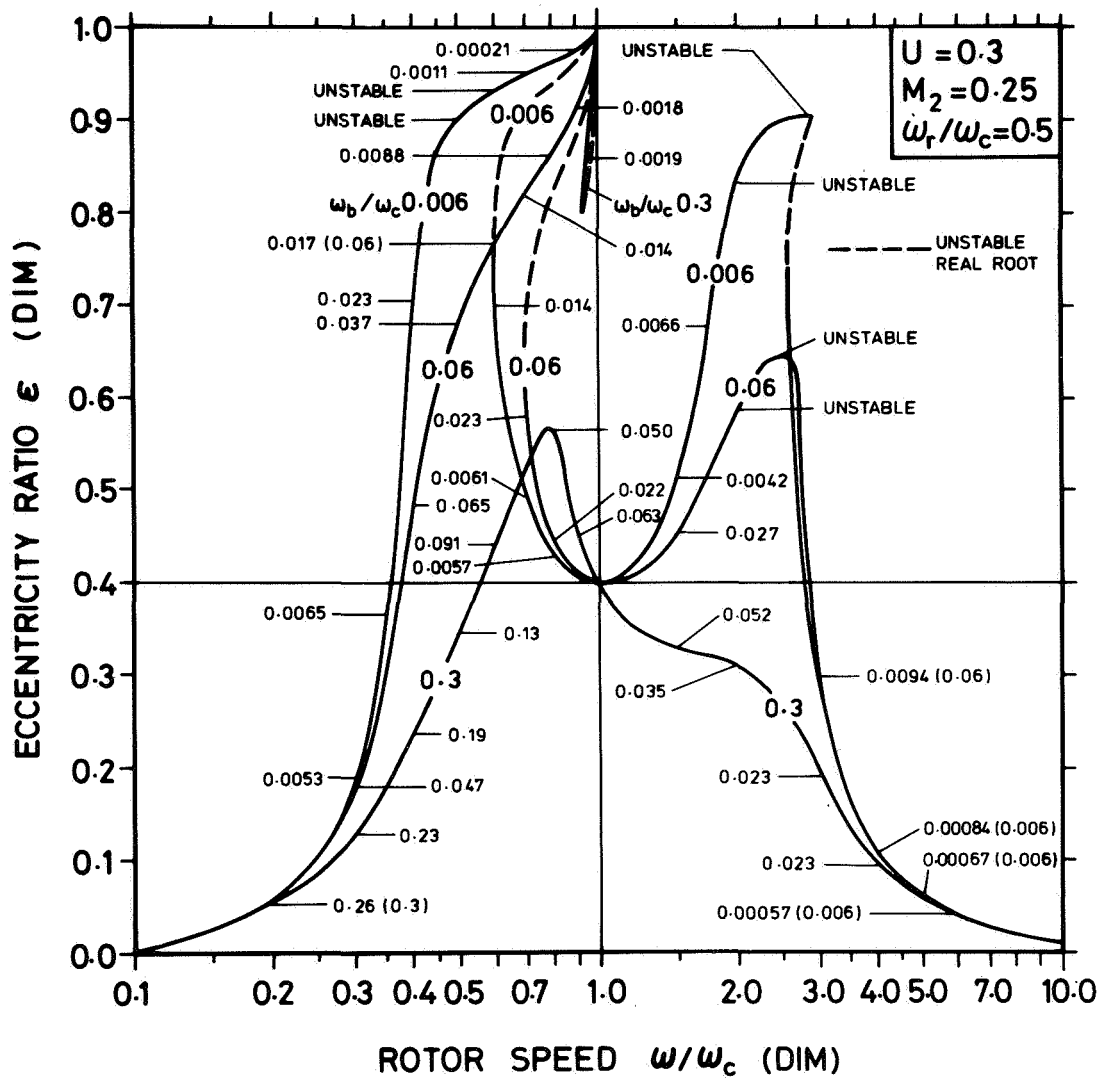

Figure 5 Damping ratios at selected points on the rotor response curves for various values of bearing parameter for the system in figure 3

be regarded as having a high degree of relative damping whereas that for $\omega_b/\omega_c = 0.006$ could be regarded as having a low degree of relative damping.

Wherever multiple solution possibilities exist, all intermediate solutions were unstable. In all such cases, the oscillation frequency was zero, and the instability was predicted by the stability map of figure 4. However, unstable single solutions are also indicated, as well as unstable higher eccentricity solutions in case of multiple solutions. In such cases the introduction of the damper has worsened system behaviour. Such unexpected unstable solutions occurred for ω_b/ω_c equal to 0.006 and 0.06 but not for 0.3. In all such cases, the oscillation frequency was always non-zero and was not predicted by the zero frequency stability map of figure 4.

This provides additional proof that figure 4 does not provide full stability threshold information. The number of equilibrium solutions investigated for instability proved insufficient to yield definitive trends in the variation of relative damping as one progresses along any particular frequency response curve in figure 5. To pick up such trends, a more thorough investigation of the λ_i would need to be undertaken. This is not warranted, for the purpose of this example was not to investigate in detail the particular system of figure 3, but rather to illustrate how simply the technique developed in the paper may be put to practical use.

Note that although figure 4 does not represent global stability thresholds, it does predict the instability of all the "intermediate" solutions and so, it serves as a locator of jump speeds, i.e. speeds at which there is a transition from a speed for which there is only one solution to one where there are at most two stable solutions or vice versa. Since the high orbit eccentricity solution, if stable, is still undesirable, generally resulting in unbalance force magnification, operation in the vicinity of such jump speed regions should be avoided. Though only proven for the model in figure 3, this equivalence between the zero frequency stability map and jump speed location is expected to be valid for general multi-degree of freedom systems. If so, a relatively simple way has been found for delineating multistable operation possibilities for any system with one damper.

CONCLUSIONS

1. A technique is developed for investigating the stability of and the degree of damping in the circular synchronous orbit solutions of n degree of freedom rotor bearing systems. In general, the technique requires finding the 2n eigenvalues of the linearized perturbation equations.

2. The perturbation equations of motion are not a function of the unbalance distribution, so for a given system a single global stability map suffices for all unbalance distributions of interest.

3. Zero-frequency stability thresholds may be found by solving as many simultaneous non-linear equations as there are dampers. If the system contains one damper only, all such stability thresholds may be found directly by solving at most a quartic equation.

4. Zero-frequency stability maps do not provide full stability information, but for the four degree of freedom system investigated in the illustrative example, and probably for more general higher degree of freedom systems as well, such maps provide a simple way to delineate multiple solution possibilities.

5. Depending on the system parameters, single equilibrium and, where multiple equilibrium solution possibilities exist, the high orbit eccentricity solution may also be unstable, with the likelihood of instability apparently increasing as the bearing parameter is reduced. Thus, the introduction of an unpressurized squeeze film damper may promote instability in an otherwise stable system.

REFERENCES

1. Greenhill, L.M. and Nelson, H.D.: Iterative Determination of Squeeze Film Damper Eccentricity for Flexible Rotor Systems. ASME Journal of Mechanical Design, vol. 104, no. 2, 1982, pp. 334-338.

2. McLean, L.J. and Hahn, E.J.: Unbalance Behaviour of Squeeze Film Damped Multi-Mass Flexible Rotor Bearing Systems. ASME Journal of Lubrication Technology, vol. 105, no. 1, 1983, pp. 22-28.

3. Rabinowitz, M.D. and Hahn, E.J.: Stability of Squeeze Film Damper Supported Flexible Rotors. ASME Journal of Engineering for Power, vol. 99, no. 4, 1977, pp. 545-551.

4. Tse, F.S., et al: Mechanical Vibrations, 2nd ed., Allyn and Bacon, Inc., Boston, 1978.

5. Hahn, E.J.: Stability and Unbalance Response of Centrally Preloaded Rotors Mounted in Journal and Squeeze Film Bearings. ASME Journal of Lubrication Technology, vol. 101, no. 2, 1979, pp. 120-128.

6. Nelson, H.D.: A Finite Rotating Shaft Element Using Timoshenko Beam Theory. ASME Journal of Mechanical Design, vol. 102, no. 4, 1980, pp. 793-803.

APPENDIX

Since

$$\underline{X} = \mathbf{T}\underline{x} \quad , \tag{A1}$$

$$\dot{\underline{X}} = \dot{\mathbf{T}}\underline{x} + \mathbf{T}\dot{\underline{x}} \quad , \tag{A2}$$

$$\ddot{\underline{X}} = \ddot{\mathbf{T}}\underline{x} + 2\dot{\mathbf{T}}\dot{\underline{x}} + \mathbf{T}\ddot{\underline{x}} \quad , \tag{A3}$$

where

$$\dot{\mathbf{T}} = \omega \begin{bmatrix} \mathbf{\Lambda}^* & & \mathbf{0} \\ & \ddots & \\ \mathbf{0} & & \mathbf{\Lambda}^* \end{bmatrix} \quad , \tag{A4}$$

and

$$\mathbf{\Lambda}^* = \begin{bmatrix} -\sin\phi & -\cos\phi \\ \cos\phi & -\sin\phi \end{bmatrix} \quad , \tag{A5}$$

it follows that

$$\dot{\mathbf{T}} = \omega \mathbf{T}^* \quad , \tag{A6}$$

and

$$\ddot{\mathbf{T}} = -\omega^2 \mathbf{T} \quad . \tag{A7}$$

Hence, substitution of equation (10) into equation (14) gives:

$$\mathbf{T}^{-1}\mathbf{M}\mathbf{T}\ddot{\underline{x}} + (2\omega\mathbf{T}^{-1}\mathbf{M}\mathbf{T}^{*} + \mathbf{T}^{-1}\mathbf{C}\mathbf{T})\dot{\underline{x}} + (\omega\mathbf{T}^{-1}\mathbf{C}\mathbf{T}^{*} + \mathbf{T}^{-1}\mathbf{K}\mathbf{T} - \omega^{2}\mathbf{T}^{-1}\mathbf{M}\mathbf{T})\underline{x} = \underline{F}_{R} \quad , \tag{A8}$$

where
$$\mathbf{T}^{-1} = \begin{bmatrix} \mathbf{\Lambda}^{-1} & \cdots & \mathbf{0} \\ \vdots & \ddots & \vdots \\ \mathbf{0} & \cdots & \mathbf{\Lambda}^{-1} \end{bmatrix} \quad , \tag{A9}$$

and
$$\mathbf{\Lambda}^{-1} = \begin{bmatrix} \cos\phi & \sin\phi \\ -\sin\phi & \cos\phi \end{bmatrix} \quad . \tag{A10}$$

To evaluate $\mathbf{T}^{-1}\mathbf{M}\mathbf{T}$, it is convenient to partition it into 2×2 submatrices. Any one of these submatrices will have the form $\mathbf{\Lambda}^{-1}\mathbf{m}\mathbf{\Lambda}$, where $\mathbf{m}$ is the corresponding submatrix of $\mathbf{M}$. Then it is easy to show that $\mathbf{\Lambda}^{-1}\mathbf{m}\mathbf{\Lambda}$ equals $\mathbf{m}$, if, and only if, the elements of $\mathbf{m}$ are of the form:

$$\mathbf{m} = \begin{bmatrix} m_1 & -m_2 \\ m_2 & m_1 \end{bmatrix} \quad . \tag{A11}$$

Hence, if equation (A11) is satisfied for all submatrices of $\mathbf{M}$, then $\mathbf{T}^{-1}\mathbf{M}\mathbf{T}$ equals $\mathbf{M}$. Conditions similar to equation (A11) are required for $\mathbf{T}^{-1}\mathbf{C}\mathbf{T}$ and $\mathbf{T}^{-1}\mathbf{K}\mathbf{T}$ to equal $\mathbf{C}$ and $\mathbf{K}$ respectively. As may be seen from reference 6, such conditions are satisfied for $\mathbf{M}$, $\mathbf{C}$ and $\mathbf{K}$ matrices in general, even when gyroscopic effects are present.

To evaluate $\mathbf{T}^{-1}\mathbf{M}\mathbf{T}^{*}$, it is again convenient to partition it into 2×2 submatrices. Any one of these submatrices will have the form $\mathbf{\Lambda}^{-1}\mathbf{m}\mathbf{\Lambda}^{*}$, where $\mathbf{m}$ is the corresponding submatrix of $\mathbf{M}$. Hence, noting that $\mathbf{m}$ will be of the form given by equation (A11), $\mathbf{\Lambda}^{-1}\mathbf{m}\mathbf{\Lambda}^{*}$ will equal $\hat{\mathbf{m}}$ where $\hat{\mathbf{m}}$ is given by:

$$\hat{\mathbf{m}} = \begin{bmatrix} -m_2 & -m_1 \\ m_1 & -m_2 \end{bmatrix} \tag{A12}$$

Thus $\mathbf{T}^{-1}\mathbf{M}\mathbf{T}^{*}$ equals $\hat{\mathbf{M}}$, where the 2×2 submatrices $\hat{\mathbf{m}}$ of $\hat{\mathbf{M}}$ are formed from the corresponding submatrices $\mathbf{m}$ of $\mathbf{M}$ according to equations (A11) and (A12). Similarly $\mathbf{T}^{-1}\mathbf{C}\mathbf{T}^{*}$ equals $\hat{\mathbf{C}}$. Hence, equation (A8) simplifies to:

$$\mathbf{M}\ddot{\underline{x}} + (2\omega\hat{\mathbf{M}} + \mathbf{C})\dot{\underline{x}} + (-\omega^{2}\mathbf{M} + \omega\hat{\mathbf{C}} + \mathbf{K})\underline{x} = \underline{F}_{R} \quad . \tag{A13}$$

Equation (A13) is the equation of motion in the rotating frame. Note that the coefficients of $\underline{x}$, $\dot{\underline{x}}$ and $\ddot{\underline{x}}$ are all constants.

DAMPING CAPACITY OF A SEALED SQUEEZE FILM BEARING*

M. M. Dede, M. Dogan, and R. Holmes
University of Southampton
Southampton, U. K.

In an earlier paper [1] the advantages of incorporating an open-ended or weakly-sealed squeeze-film bearing in a flexible support structure simulating an aero-engine assembly were examined. In the present paper attention is given to empirically modelling the hydrodynamics of the more usual tightly-sealed squeeze-film bearing, with a view to assessing its damping performance.

INTRODUCTION

A squeeze-film is an annulus of oil supplied between the outer race of a rolling-element bearing (or the bush of a sleeve bearing) and its housing. It is often used as a multi-directional damping element for the control of rotor vibrations.

In most aeroengine applications, the purpose of the squeeze film is to introduce damping so that the rotor can safely negotiate any critical speeds and operate smoothly at a higher speed. The amount of damping can be quite critical: If it is too little, excessive movement will take place within the squeeze-film annulus, if too great the damper will act like a rigid link, making its presence superfluous.

A squeeze-film damper is in effect a journal bearing in which the inner member does not rotate. Hence, it is not possible to assign to it any linear stiffness coefficients which might allow the oil film to take any gravity or other static load, since such coefficients are directly dependent on journal speed. Any lift emanates instead from non-linear effects. For certain operating conditions, such as in the regions of critical speeds, where any static load is small compared to the dynamic load, circular concentric orbits could possibly be assumed, with the result that quasi-linear amplitude-dependent coefficients could be used. Linear analyses could thus be carried out to obtain the vibration orbits in an interative fashion and transmitted forces could be

*The authors gratefully acknowledge Rolls Royce (UK) Limited for their financial support, and ASME for permission to publish.

computed. For cases where the static load is not small a non-linear analysis is called for. Any analysis requires a specification of the effect of cavitation, which has a profound influence on the dynamic load-carrying capacity. Indeed, an uncavitated film may be shown to lead to the complete elimination of load-carrying capacity.

In order to investigate closely the performance of the squeeze-film damper in this kind of application, an experimental rigid rotor [1] was designed and built to simulate an aeroengine gas turbine running at speeds up to 6000 rev/min in rolling-element bearings, one mounted into a housing with an annular gap constituting the squeeze-film damper. This damper was provided with a circumferential groove and supplied with oil at a prescribed pressure. Each land on either side of the groove was of diameter 130 mm and length 9 mm and the radial clearance of the squeeze-film was 0.216 mm. The purpose of the test rig is to study the orbits of vibration and dynamic squeeze-film pressures resulting from various degrees of mass unbalance.

Notation

c	radial clearance of squeeze film
d	seal gap
e	journal eccentricity
$f(\overline{z})$	function of $\overline{z}$
h	squeeze-film thickness
$\overline{h}$	nondimensional film thickness = $h/c = 1 + \varepsilon\cos\theta$
ℓ	radial width of seal
L	bearing-land length
m	effective rotor mass
p	oil film pressure
$p_c(\theta)$	pressure using the long-bearing approximation
p_o	pressure at maximum film thickness
p_s	supply pressure
p_{cav}	cavitation pressure
$\overline{p}$	nondimensional film pressure = $p/\eta\omega(R/c)^2$
$\overline{p_o}$	nondimensional pressure at maximum film thickness = $p_o/\eta\omega(R/c)^2$
$\overline{p_s}$	nondimensional supply pressure = $p_s/\eta\omega(R/c)^2$
$\overline{p_{cav}}$	$p_{cav}/\eta\omega(R/c)^2$
P	static load per land
P_c	dynamic load per land = $mu\omega^2$

P_1, P_2	squeeze-film forces in radial, transverse directions
Q	$P/mc\omega^2$
Q_c	$P_c/mc\omega^2 = u/c$
R	bearing radius
t	time
u	eccentricity of mass unbalance
z	axial coordinate
$\overline{z}$	z/L
α	attitude angle measured in direction of unbalance force rotation
β	nondimensional viscosity = $\eta R(L/c)^3/m\omega$
γ	end leakage flow coefficient
ε	eccentricity ratio = e/c
η	oil viscosity
θ	circumferential coordinate
θ_1, θ_2	oil film boundaries
λ	end-leakage factor = $(c/d)^3\, \ell/L$
ω	angular velocity of rotor.

THEORETICAL TREATMENT

The Reynolds equation, suitably adapted for a squeeze-film bearing in which the inner member does not rotate, may be written in a nondimensional form as

$$\frac{\partial}{\partial\theta}\left(\overline{h}^3 \frac{\partial\overline{p}}{\partial\theta}\right) + \left(\frac{R}{L}\right)^2 \frac{\partial}{\partial\overline{z}}\left(\overline{h}^3 \frac{\partial\overline{p}}{\partial\overline{z}}\right) = 12(\varepsilon'\cos\theta + \varepsilon\alpha'\sin\theta) , \quad (1)$$

where

$$\overline{p} = p/\eta\omega\left(\frac{R}{c}\right)^2 ,$$

$$\overline{h} = h/c = 1+\varepsilon\cos\theta ,$$

$$\overline{z} = z/L ,$$

and

$$(') = d/d(\omega t).$$

The variables are given in the notation.

A common type of squeeze-film damper configuration with a central circumferential oil groove and without end seals was investigated in ref [1]. For such a damper, it was assumed that the oil flow in the circumferential direction was negligible when compared with the flow in the axial direction. This is known as the short-bearing approximation. Hence the first term on the left-hand side of eqn (1) was dropped.

Integrating twice with respect to $\bar{z}$, and putting,

$$\bar{p} = \bar{p}_s \text{ at } \bar{z} = -1/2$$

and

$$\bar{p} = 0 \text{ at } \bar{z} = 1/2,$$

gave

$$\bar{p}(\theta,\bar{z}) = 6(\frac{L}{R})^2 \frac{(\varepsilon'\cos\theta + \varepsilon\alpha'\sin\theta)}{(1 + \varepsilon\cos\theta)^3} (\bar{z}^2 - \frac{1}{4}) + \bar{p}_s (\frac{1}{2} - \bar{z}) \quad (2)$$

This is the general expression for nondimensional pressure in a short squeeze-film with a circumferential oil supply groove and without end seals.

The sealed squeeze-film

It is not uncommon to use seals in squeeze-film dampers to reduce end-leakage and thus to increase the effective damping. This application, however, makes computations difficult to carry out since any mathematical model for predicting the squeeze-film pressure is dependent on the amount of oil leakage allowed by the seals. First, let us consider that the seals allow only small leakage from the ends of the damper. It is therefore assumed that the pressure gradient in the axial direction is negligible compared to that in the circumferential direction. This is known as the long-bearing approximation. Hence eqn.(1) becomes

$$\frac{\partial}{\partial\theta}(\bar{h}^3 \frac{\partial\bar{p}}{\partial\theta}) = 12(\varepsilon'\cos\theta + \varepsilon\alpha'\sin\theta) \quad (3)$$

The solution of eqn (3) for pressure, satisfying boundary conditions $\bar{p} = \bar{p}_o$ at $\theta = 0$, and 2π is readily available in the literature [2] and is quoted here as

$$\bar{p}_c(\theta) = -12\alpha'(\frac{\varepsilon}{2+\varepsilon}) \frac{(2 + \varepsilon\cos\theta)\sin\theta}{(1 + \varepsilon\cos\theta)^2} + 6\frac{\varepsilon'}{\varepsilon}[\frac{1}{(1 + \varepsilon\cos\theta)^2} - \frac{1}{(1 + \varepsilon^2)^2}] + \bar{p}_o \quad (4)$$

where $\bar{p}_o$ is the nondimensional pressure at the maximum film thickness. It could be taken as the supply pressure $\bar{p}_s$ but more reasonably can be obtained from the short-bearing pressure expression (eqn (2)) by setting the conditions $\bar{p}(\theta,\bar{z}) = \bar{p}_o$ at $\theta = 0$, and averaging over the land length. This gives

$$\bar{p}_o = -(\frac{L}{R})^2 \frac{\varepsilon'}{(1 + \varepsilon)^3} + \bar{p}_s,$$

and ensures that $\bar{p}_c(\theta)$ in eqn (4) is not a function of $\bar{z}$. $\bar{p}_s$ is used instead of $\bar{p}_s/2$ since with sealing there will be little attenuation of p_s. Eqn (4) is true only for squeeze-film bearings in which the pressure gradient in the axial direction is relatively small, or for bearings which have a large length to diameter ratio.

It appears that neither the short-film model nor the long-film model offers a suitable solution from which to calculate the pressure distribution in a centrally-grooved and sealed squeeze-film damper with a restricted but not necessarily small oil leakage. This is because the pressure gradients in both axial and circumferential directions should both be significant for such dampers. For this reason and for speed of computation using non-linear programs, an analytical pressure expression which includes the effect of axial oil flow as well as circumferential oil flow is essential in order to calculate the squeeze-film forces.

To construct such an analytical model, let us assume that the pressure distribution in the $\bar{z}$-direction in a centrally grooved and sealed squeeze-film damper is to be built up as illustrated in Fig.1. Now the boundary condition at $\bar{z} = -1/2$ is readily available as the oil supply pressure in the groove, but the boundary condition at the ends of the squeeze-film (at $\bar{z} = 1/2$) is dependent on the oil-leakage flow rate. For a given damper design this boundary condition may be specified by introducing an end-leakage factor, say λ, and writing the boundary condition as

$$\bar{p} = \lambda \, \bar{p}_c(\theta),$$

in which $\lambda = 0$ for full leakage and $\lambda = 1$ for zero leakage.

$\bar{p}_c(\theta)$ is readily given by eqn (4) as the nondimensional pressure in the θ-direction for the relatively simple case of the long-bearing approximation. It should be noted that this allows pressure to be variable in the circumferential direction at the ends of the damper, whereas often the short-bearing approximation is used in conjunction with the specification of a constant pressure at the ends of the damper.

Now using these boundary conditions as

$$\bar{p} = \bar{p}_s \text{ at } \bar{z} = -1/2$$

and

$$\bar{p} = \lambda \bar{p}_c(\theta) \text{ at } \bar{z} = 1/2,$$

we obtain the final form of the modified pressure expression

$$\bar{p}(\theta,\bar{z}) = 6\left(\frac{L}{R}\right)^2 \frac{(\varepsilon'\cos\theta + \varepsilon\alpha'\sin\theta)}{(1 + \varepsilon\cos\theta)^3} \left(\bar{z}^2 - \frac{1}{4}\right) + \lambda\bar{p}_c(\theta) \left(\bar{z} + \frac{1}{2}\right)$$

$$+ \bar{p}_s\left(\frac{1}{2} - \bar{z}\right) \qquad (5)$$

Fig. 2(a) shows a typical set of circumferential pressure distributions at the mid-land position for two different values of the factor λ, together with the theoretical predictions for the short-bearing and the long-bearing film assumptions. Fig. 2(b) shows a comparison of axial pressure distributions between the short-bearing and the modified film model for $\lambda = 0.09$. The indication is that the modified film model may provide a useful approximation to the experimental case when the value of λ is selected correctly.

Calculation of squeeze-film forces with curtailment of negative pressure

The squeeze-film forces P_1 and P_2 are obtained by integrating the squeeze-film pressure distribution in directions respectively along and normal to the line of centres of the journal and the bearing as follows:

$$P_{1,2} = -\eta\omega\left(\frac{R}{c}\right)^2 RL\int_{\theta_1}^{\theta_2}\int_{-\frac{1}{2}}^{\frac{1}{2}} \overline{p}(\theta,\overline{z}) \begin{pmatrix}\cos\theta \\ \sin\theta\end{pmatrix} d\overline{z}d\theta \qquad (6)$$

where θ_1 and θ_2 are the film boundaries in the circumferential direction.

In this work, with a view to obtaining adequate predictions of vibration orbits, each numerical hydrodynamic pressure distribution was curtailed at its experimentally-observed negative pressure limit before integration to obtain the squeeze-film forces as in ref [1].

Experimental tests

Tests were first carried out using oil of viscosity 6.15 cp, an end-plate clearance of 0.0635 mm and a supply pressure of 5 lbf/in^2 gauge (345 kN/m^2). Fig. 3(a) shows counter-clockwise orbits within the clearance circle of 0.216 mm radius,and dynamic pressure recordings at a mid land position at the base of the damper, at various rotor speeds for $Q_C = 0.459$, while Fig. 3(b) shows the corresponding numerical predictions, for which the value of the λ factor used was 0.09. The negative pressure limit noted in each experimental pressure recording was used as a limiting condition for the corresponding numerical computation of dynamic pressure. Similar comparisons for a higher value of Q_C of 1.055 are given in Figs.4(a) and (b) again using a λ factor of 0.09 for the numerical computations. These results show experimental vibration orbits and pressure waveforms in good agreement with their numerical counterparts. In all the experimental pressure waveforms the horizontal base line denotes atmospheric pressure.

Effect of supply pressure on the damper performance

Since the supply pressure is added linearly to the dynamic

variation in the λ factor appears to be relatively small, in particular for tight sealing, that is low values of d/c.

SOME FURTHER CONSIDERATIONS OF THE OUTLET BOUNDARY CONDITION

As already pointed out the outlet boundary condition for the sealed squeeze-film is dependent on the oil leakage flow rate allowed by the seals. A means of specifying this boundary condition was given by the introduction of an end leakage factor λ. Some further considerations relating to the introduction of this λ factor will now be given.

Assume a solution to the Reynolds equation (eqn 1) of the form

$$\overline{p}(\theta,\overline{z}) = f(\overline{z})\ \overline{p}_c(\theta), \tag{7}$$

where $f(\overline{z})$ and $\overline{p}_c(\theta)$ are functions for pressure in the axial and circumferential directions respectively, the latter being specified at the mid-land position. Substituting eqn (7) into eqn (1) and dividing by $\overline{p}_c(\theta)\overline{h}^3$, gives

$$\overline{b} + g^2\ f(\overline{z}) - \left(\frac{R}{L}\right)^2 \frac{d^2 f}{d\overline{z}^2} = 0 \tag{8}$$

where $\overline{b} = 12\ (\varepsilon' \cos\theta + \varepsilon\alpha' \sin\theta)/\overline{p}_c\ (\theta)\ \overline{h}^3$, and

$$g^2 = \frac{\partial}{\partial\theta}\left(\overline{h}^3 \frac{\partial \overline{p}_c(\theta)}{\partial\theta}\right)/\overline{p}_c(\theta)\ \overline{h}^3 .$$

The solution of eqn (8) for $f(\overline{z})$, with g^2 being treated as a parameter, is straight forward, and is of the form

$$f(\overline{z}) = C_1 e^{gL\overline{z}/R} + C_2 e^{-gL\overline{z}/R} - \frac{\overline{b}}{g^2} \tag{9}$$

where C_1 and C_2 are constants to be determined from the boundary conditions. For the damper under consideration these boundary conditions are:

$$\overline{p}(\theta,\overline{z}) = \overline{p}_s \text{ at } \overline{z} = -1/2,$$

and a boundary condition at $\overline{z} = 1/2$ which can be obtained by considering the axial flow balance across any unit circumferential area around the seal as

$$-\frac{h^3}{12\eta}\left(\frac{\partial p}{\partial z}\right) = \frac{d^3 p}{12\eta\ell},$$

where d is the end seal gap width,
ℓ is the effective length of the gap,

pressure, the effect on the vibration orbits of a higher supply pressure should theoretically be akin to the effect of a lower negative pressure. In fact, an increase in the supply pressure would result in a reduction in the orbit size, and sufficient increase would suppress the negative pressure region completely and thus eliminate the load carrying capability of the squeeze-film [3]. To show the effect of supply pressure on the vibration orbits and cavitation pressure, a set of experimental recordings is given in Fig. 5(a) for Q_c equal to 1.055. Fig. 5(b) shows the corresponding numerical predictions for $\lambda = 0.09$. For these tests supply pressures of 5, 25 and 45 psig (34.5, 172 and 310 kN/m^2) were used. From these figures, it can be seen that the reductions in the orbit size are substantial between 5 and 25 psig , whilst the reductions between 25 and 45 psig are relatively small. An accompanying feature is the development of negative pressure with increase in supply pressure, as can clearly be seen in the recordings of dynamic pressure. This may be due to the fact that for 5 psig, venting from atmosphere takes place, while for higher supply pressures this is prevented by continuous flushing. Such flushing would remove cavitation bubbles and allow the tension spikes to form as shown at the higher supply pressures. It is also interesting to note that no significant rise in the positive peak pressure level was observed or predicted with increase in supply pressure, probably due to the accompanying reduction in orbit size.

Effect of the sealing gap on damper performance

The next phase of the present work was to investigate the effect of end-plate sealing on damper performance and thus to give a graphical estimation for the value of the λ factor for a given end-plate clearance. For convenience testing was first carried out for a supply pressure of 5 psig.(345 kN/m^2). Three different end-plate clearances of 0.114 mm, 0.139 mm and 0.216 mm were used, being set by the insertion of spacing shims. The experimental recordings shown in Fig. 6(a) are for a Q_c value of 0.549, a speed of 3500 rev/min and for an oil vicosity of 6.15 cp. These compare with the display of Fig. 3(a) (3500 rev/min) for a sealing gap of 0.0635 mm. Fig. 6(b) shows the corresponding numerical predictions. For each sealing gap the value of the most appropriate λ factor is given in the figures. From these comparisons, it can be seen that the general size of the orbit increases with increase in the value of end-plate clearance. Good agreement can also be observed between the experimental recordings and the numerical predictions for both orbits and pressure waveforms. From a wide range of results, covering a variety of rotor speeds, supply pressures and unbalance ratios u/c,a plot of the λ factor against the end-clearance ratio (defined as the ratio of end-plate clearance to the damper radial clearance) is shown in Fig. 7. It indicates that for a given end-clearance the appropriate value of the λ factor is increased with increase in oil viscosity. However, given the viscosity range used, the

p and $\partial p/\partial z$ are the pressure and the pressure gradient at the end of the damper ($z = L/2$) respectively.

This boundary condition has been used by Marmol and Vance [5] with some success. Rearranging and writing in nondimensional form, we obtain,

$$\bar{p}(\theta,\bar{z}) = \bar{p} = -\gamma\bar{h}^3 \left(\frac{\partial\bar{p}}{\partial\bar{z}}\right) \text{ at } \bar{z} = 1/2,$$

where $\gamma = (c/d)^3\, \ell/L$, and is introduced as a flow coefficient.

Thus, in terms of the function $f(\bar{z})$, these boundary conditions are:

$$f(\bar{z}) = \bar{p}_s/\bar{p}_c(\theta) \text{ at } \bar{z} = -1/2, \text{ and}$$

$$f(\bar{z}) = -\gamma\bar{h}^3\, df/d\bar{z} \text{ at } \bar{z} = 1/2.$$

Inserting the above boundary conditions into eqn (9) and solving for C_1 and C_2, we obtain

$$C_1 = \left(\frac{\bar{p}_s}{\bar{p}_c(\theta)} + \frac{\bar{b}}{g^2}\right) e^{gL/2R} - C_2 e^{gL/2R}, \tag{10}$$

where

$$C_2 = \frac{\left(\frac{\bar{b}}{g^2}\right) e^{gL/2R} - \left(\frac{\bar{p}_s}{\bar{p}_c(\theta)} + \frac{\bar{b}}{g^2}\right)(1 + \gamma g\bar{h}^3 L/R)\, e^{3gL/2R}}{(1 - \gamma\bar{h}^3 L/R) - (1 + \gamma g\bar{h}^3 L/R)e^{2gL/R}}$$

Equation (9) for the $f(\bar{z})$ function also requires the functional form of g^2. Observing that as $L/R \to \infty$, $df/d\bar{z} \to 0$ and $f \to 1$, then from eqn (8) g^2 becomes

$$g^2 = -\bar{b} = -12\,(\varepsilon'\cos\theta + \varepsilon\alpha'\sin\theta)/\bar{p}_c(\theta)\bar{h}^3 \tag{11}$$

where $\bar{p}_c(\theta)$ is the nondimensional pressure from the long-bearing approximation of the Reynolds equation. Having obtained the required functions the pressure can then be found from eqn (7) as

$$\bar{p}(\theta,\bar{z}) = \bar{p}_c(\theta)\,(C_1\, e^{gL\bar{z}/R} + C_2\, e^{-gL\bar{z}/R} + 1) \tag{12}$$

where g, C_1 and C_2 are calculated from eqns (11) and (10), respectively. Equation (12) is a general pressure expression for any finite-length squeeze-film damper with central circumferential oil supply and end-seals. A similar approach was used by Barrett et al [6] but for an open-ended journal bearing. It was shown to give reliable results.

Some idea of the variation of the pressure distribution with sealing can be obtained from Figs. 8(a), (b), and (c). Fig.8(a) shows a typical set of circumferential pressure distributions at the mid-land position for two extreme values of the flow coefficient γ ($\gamma = 0$ and $\gamma \to \infty$), together with the theoretical predictions based on the short-bearing and the long-bearing film assumptions. In this comparison the modified film model is also included, using a value of the λ factor of 0.09. Fig. 8(b) shows a comparison of axial pressure distributions for these models, whilst Fig. 8(c) shows a comparison of circumferential pressure distributions at the ends of the damper for the finite-length and the modified film models. It should be noted that the value of γ of 27 corresponds to the case of tight sealing for which the value of λ of 0.09 was found by trial to give the best agreement in respect of orbit size and pressure wave form. From Fig. 8(a), it can be seen that even with the full sealing condition ($\gamma \to \infty$) the corresponding peak pressure is considerably smaller than that obtained from the long-bearing approximation. For full leakage ($\gamma = o$), the finite-length solution is nearly identical to the short-bearing solution, as is expected due to the small L/R ratio employed in the test bearing. As far as the specification of the end boundary condition is concerned, similarity (but not equality) can be observed in Fig. 8(c) between the pressure profiles obtained from the two different approaches of using the λ factor of 0.09 and the γ coefficient of 27.

To give a graphic view of the approach, two sets of numerical orbits and pressures are shown in Figs. 9(a) and (b), using respectively values of γ of 27 and ∞ (the full sealing condition). These results should be compared with the experimental recordings of Fig. 3(a) and the numerical predictions of Fig. 3(b). From these comparisons, it can be seen that, even with full-sealing ($\gamma = \infty$)the predicted orbits are considerably larger than the experimental ones and the ones predicted by using the λ factor of 0.09, in particular for the case of 5800 rev/min. A reversal in the position of the sharp "tail" between 3500 and 4000 rev/min was not observed when using the γ coefficient. The numerical pressure waveforms of Figs 9(a) and (b) also do not show good agreement with experiment. These comparisons are typical of the other experimental cases considered. A general observation was that, using the approach of this appendix, the numerical predictions were in poor agreement with the experimental results, in particular for high values of Q_c and at high rotor speeds, with tight sealing.

The λ factor discussed previously may be introduced into the specification of the outlet boundary condition by again considering the end pressure obtained from the flow balance as follows. This pressure has been shown to be,

$$\overline{p(\theta,\overline{z})} = \overline{p} = -\gamma\overline{h}^3 \left(\frac{\partial \overline{p}}{\partial z}\right) \quad \text{at } \overline{z} = 1/2$$

From eqn (7) the pressure gradient is

$$\frac{(\partial \overline{p})}{\partial z} = \overline{p_c}(\theta)(\frac{\partial f}{\partial z}).$$

Hence,

$$p = \overline{p_c}(\theta)(-\gamma \overline{h^3} \frac{\partial f}{\partial z}) \tag{13}$$

Comparing this with the equation,

$$\overline{p} = \lambda \overline{p_c}(\theta), \tag{14}$$

shows that λ replaces

$$(-\gamma \overline{h^3} \frac{\partial f}{\partial z}).$$

There are two possible reasons why equation (13) does not give satisfactory results. These may be enumerated as follows:

1) The leakage flow through the end seals may not be truly radial. However, even if a screw type of flow is assumed by increasing γ say, we have seen (Fig. 9(b)) that this still does not give adequate agreement with the experimental results, even when $\gamma = \infty$.

2) Equation (13) assumes reverse flow from the seals when the pressure p is negative. However, this does not seem likely since there is no oil reservoir behind the seals, and indeed in the experiments, ingress of air was the more likely occurrence.

Thus, while there is no obvious parametric link between λ and the dimensions of the end seals, the λ approach appears to be one to give adequate predictions of vibration orbit and dynamic squeeze-film pressure. Fig. 7 can then be used to establish an empirical link between parameters.

CONCLUSIONS

The work presented in this paper has dealt with the performance of the sealed squeeze-film damper when used in aero-engine applications. In such applications, the operation of the damper is governed by five nondimensional groups. These groups are the nondimensional static force Q, the nondimensional dynamic force Q_c, the nondimensional viscosity β, the nondimensional supply pressure $\overline{p_s}$ and the nondimensional cavitation pressure p_{cav}. Good agreement has been observed between experimental observations and numerical predictions using an empirical leakage factor, over a wide range of operating parameters. This work has also demonstrated experimentally that sustained lift of the rotor in the squeeze

film annulus can be obtained without the use of any parallel support stiffness, and the squeeze-film was shown to provide this lift by the assumption of a cavitated film model.

It has been shown that the use of an end-leakage factor λ has resulted in successful predictions of vibration orbits and dynamic pressures in the sealed squeeze-film. It has been demonstrated experimentally that the damping can be increased effectively by decreasing the sealing gap and a means of determining λ for a given gap has been given graphically. One indication was that this gap should be made less than half the damper radial clearance to achieve effective damping.

There remains the problem of needing to know in advance the value of negative pressure to adopt for curtailing the squeeze-film pressure during computation of the squeeze-film forces and orbits in any given application. Experimental recordings of dynamic pressure show that this negative pressure appears to take one of three approximate values:

(i) Approximately atmospheric, when the supply pressure is not great enough to prevent ingress of atmospheric air, which fills the cavitation zone;

(ii) Approximately absolute zero, when cavitation bubbles exist due to the liberation of dissolved gases and fluid vapour. The supply pressure here has to be somewhat higher to prevent ingress of air, but is still not high enough to flush the bubbles away;

(iii) Lower than absolute zero, when the oil temporarily supports tension, many cavitation bubbles in the previous cycles being flushed away by a fairly high supply pressure.

For the bearing assembly considered in this work, when used under most engine conditions, it could reasonably be expected that much of the performance could be such as to produce cavitation pressures in the third region when a value of about -40 psig seems a fair average. This is based on the assumption that the external oil pressure at the squeeze-film groove is likely to be around 40 - 50 psig. It is suggested that, given the highly complicated mechanism of negative pressure development in the squeeze-film, reliance can be placed on the use of fairly high supply pressures to ensure a measure of consistency in the negative pressure at which film rupture is assumed to occur.

REFERENCES

[1] Holmes,R. and Dogan, M. 'Investigation of squeeze film dampers in flexible support structures', NASA Conference Publication 2250 entitled 'Rotor dynamic instability problems in High Performance Turbomachinery - 1982'.

[2] Pinkus, O. and Sternlicht, B. 'Theory of hydrodynamic lubrication'. McGraw-Hill Inc., New York, 1961.

[3] Holmes, R. 'The non-linear performance of squeeze-film bearings'. Jnl Mech.Eng.Sci., Vol.14, no.1, 1972.

[4] Holmes, R. and Dede, M. 'Dynamic pressure determination in a squeeze-film damper'. Inst. Mech.Engrs. Second Int. Conf. on Vibrations in Rotating Machinery, Sept. 1980.

[5] Marmol, R.A. and Vance, J.M. 'Squeeze-film damper charactersitics for gas turbine engines'. ASME Paper No. 77-DET-18, Oct. 1977.

[6] Barrett, L,E,, Allaire, P.E. and Gunter, E.J. 'A finite length correction factor for short bearing theory'. Trans. ASME Jnl Lub. Tech. Vol.102, July 1980.

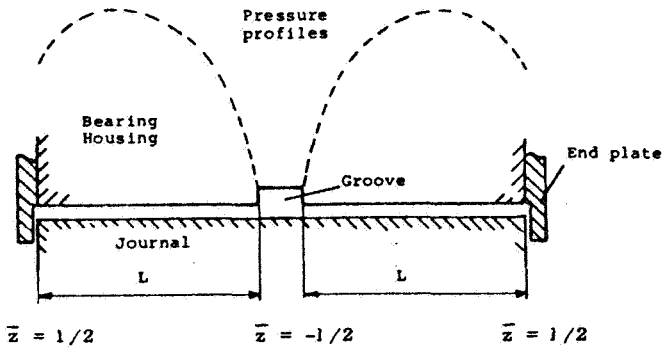

Fig. 1 Damper configuration with circumferential oil supply groove and end plates

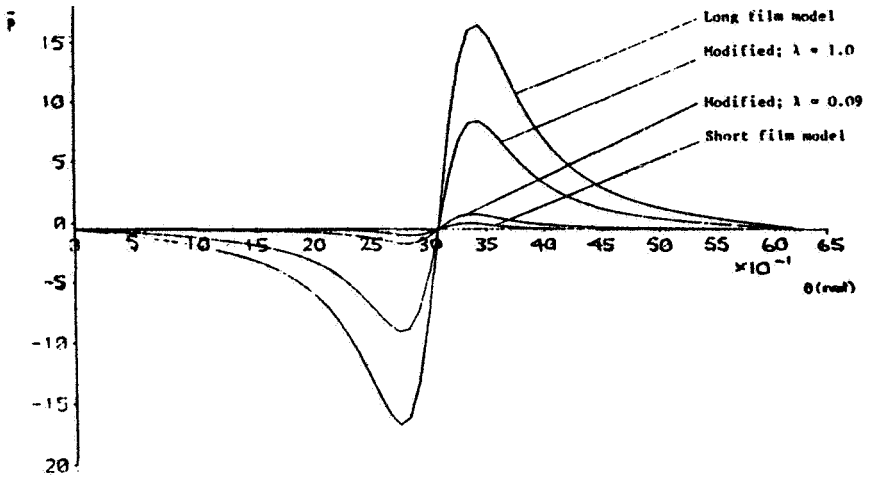

Fig. 2(a) Circumferential pressure distributions

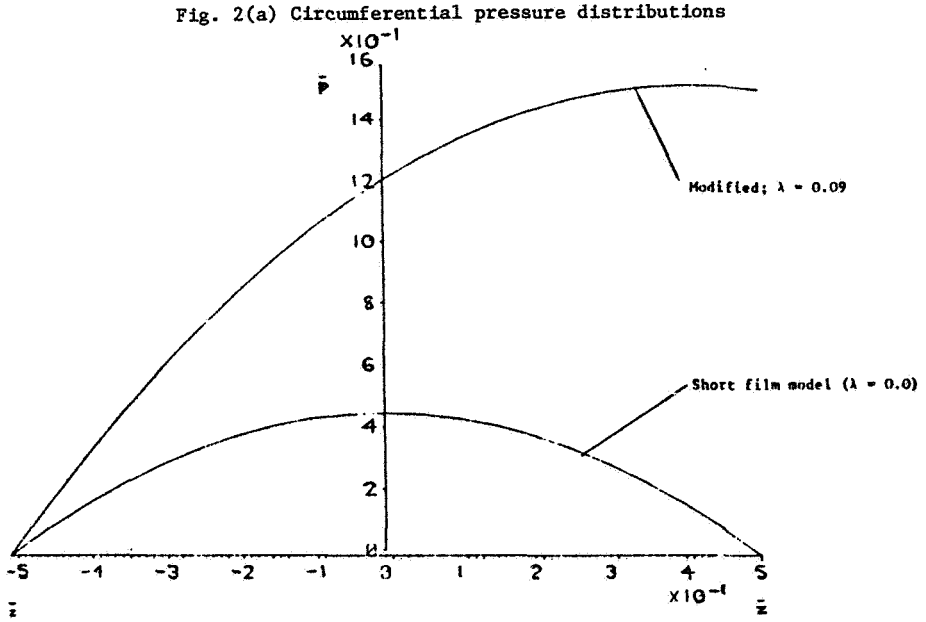

Fig. 2(b) Axial pressure distributions

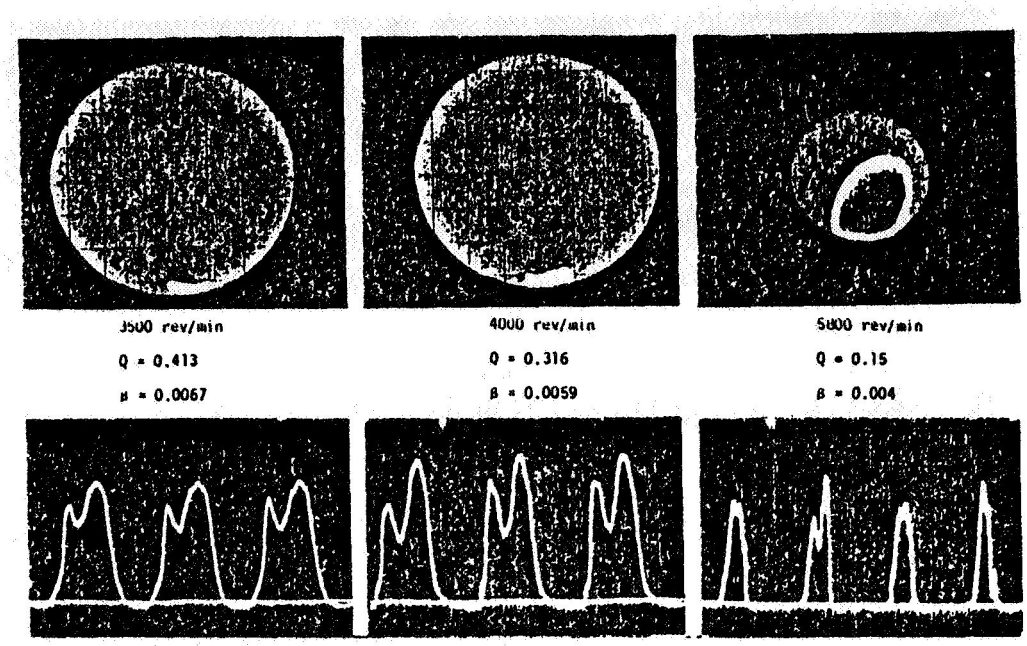

(a)

Vertical Scale

500 psi
3450 kN/m^2

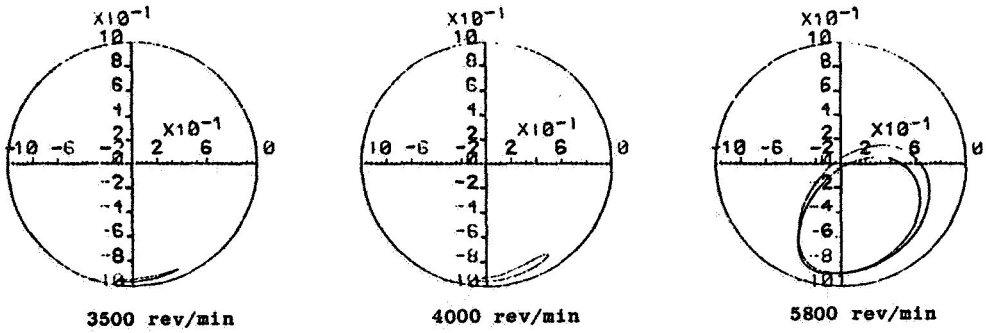

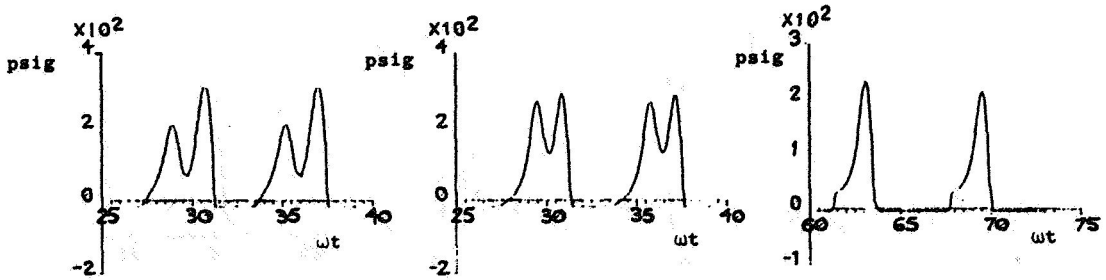

(b)

Fig.3. Q_c = 0.459; (a) experimental orbits and pressure recordings, (b) numerical orbits and pressures.

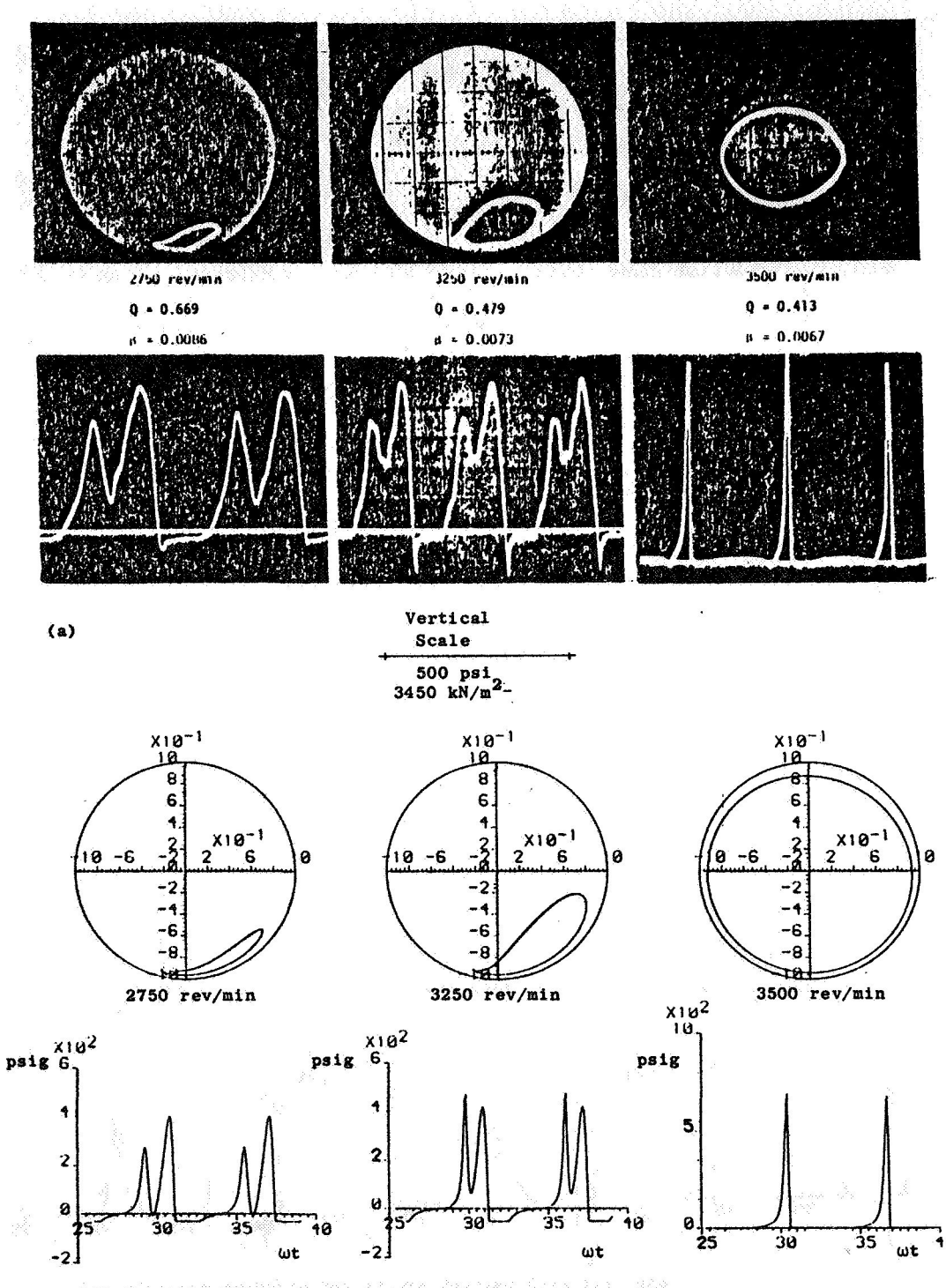

Fig.4 Q_c = 1.055; (a) experimental orbits and pressure recordings, (b) numerical orbits and pressures.

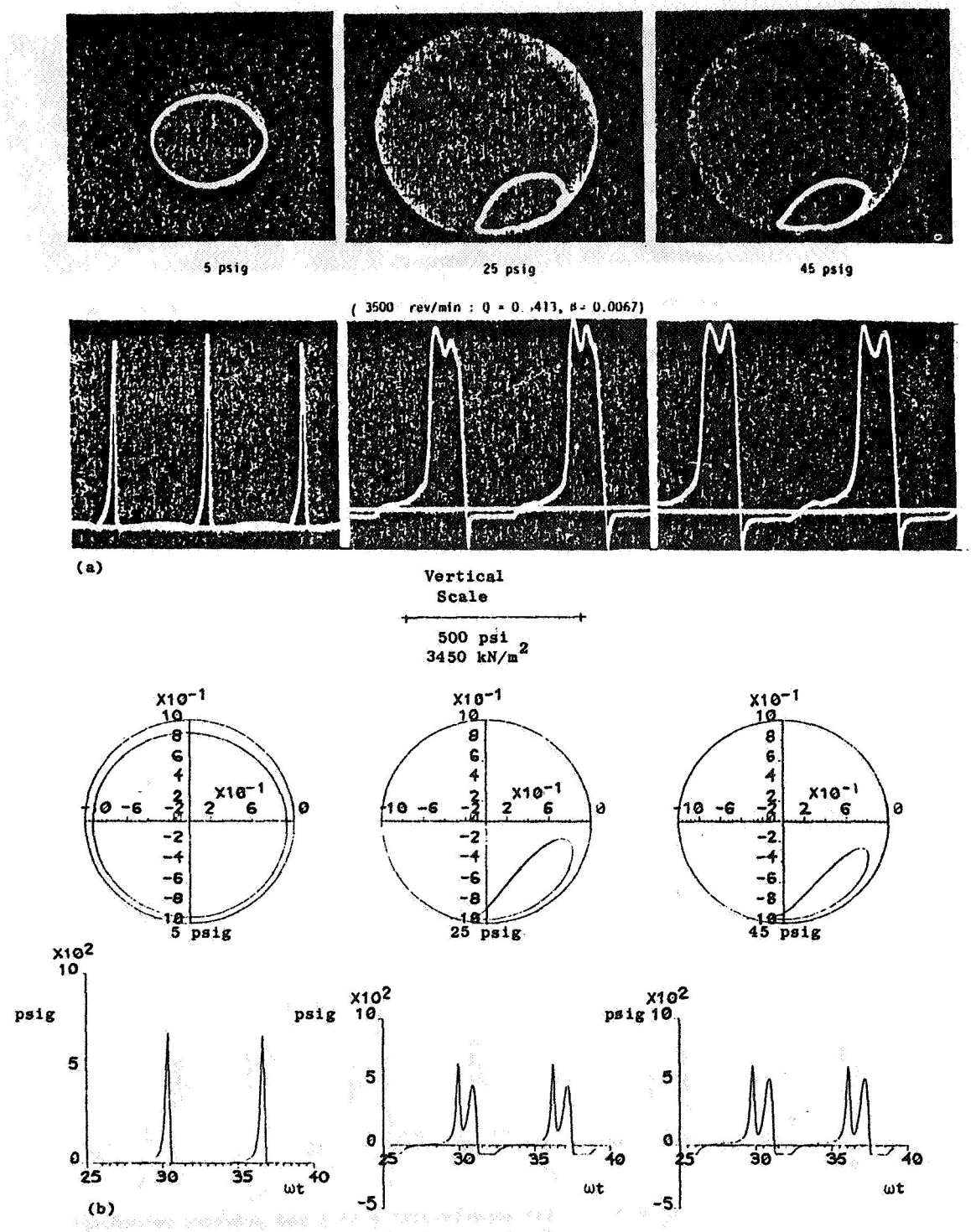

Fig. 5 Q_c = 1.055; (a) experimental orbits and pressure recordings
(b) numerical orbits and pressures

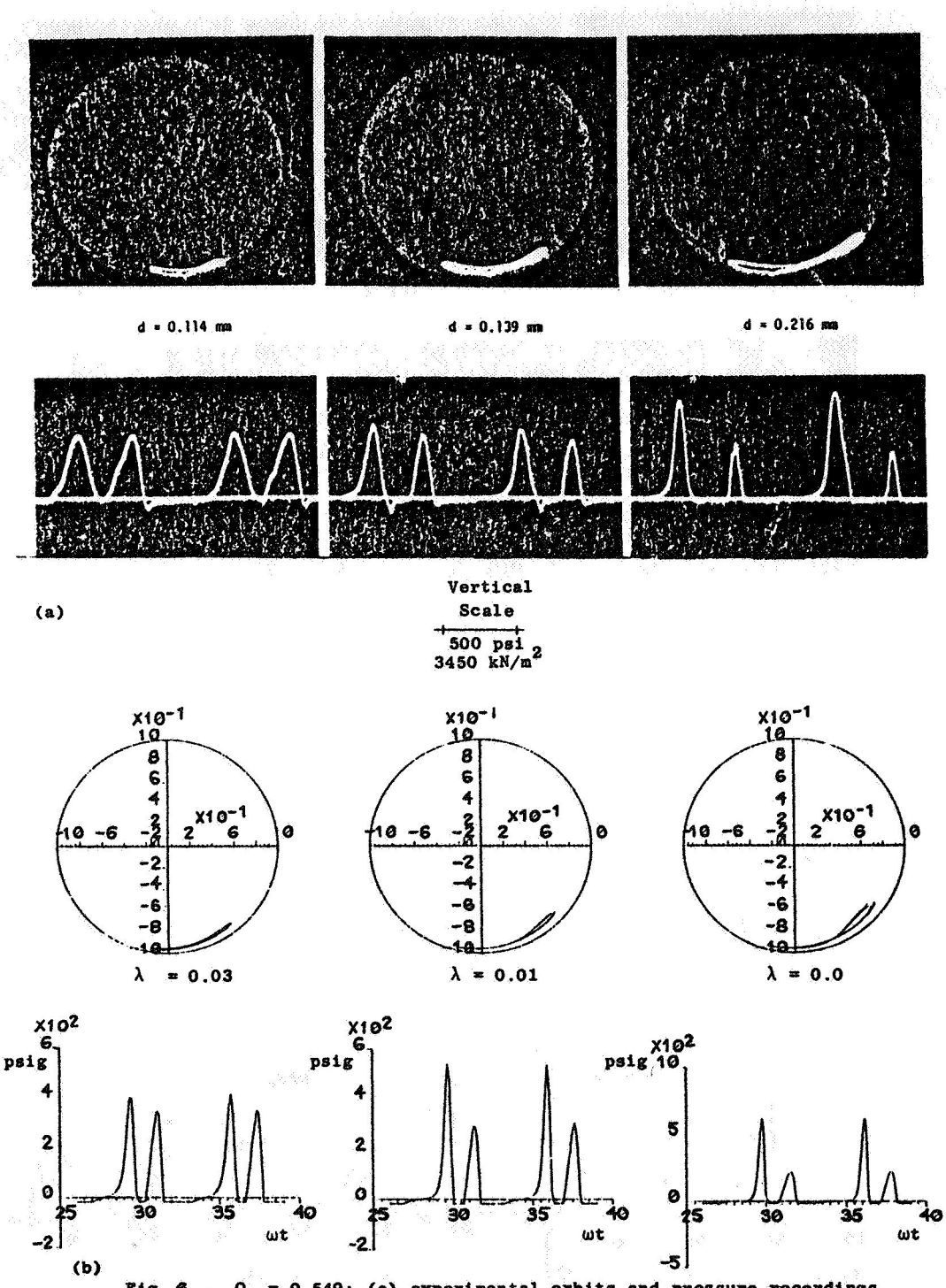

Fig. 6 . Q_c = 0.549; (a) experimental orbits and pressure recordings, (b) numerical orbits and pressures.

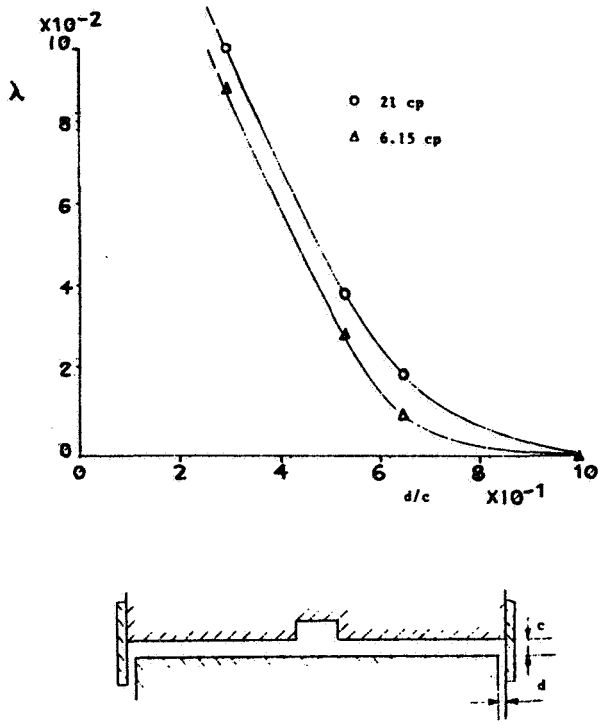

Fig. 7 End-plate seal factor λ vs end-clearance ratio d/c.

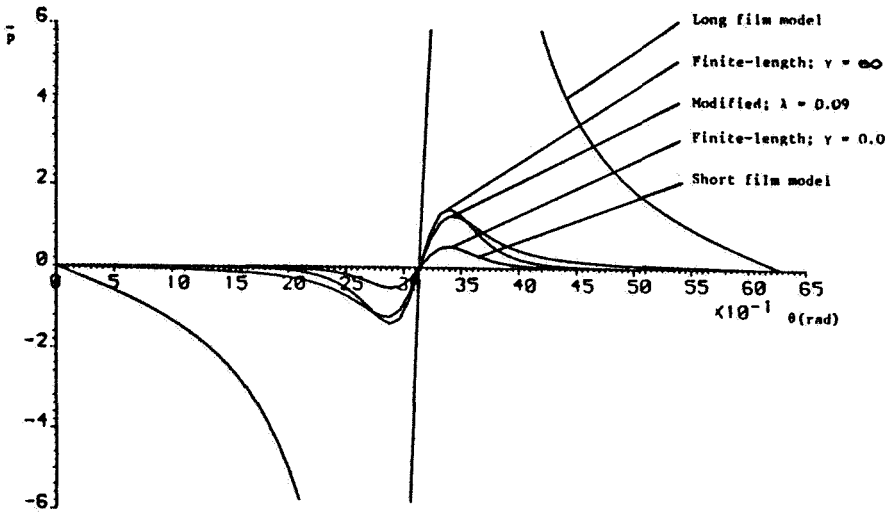

Fig. 8 (a) Circumferential pressure distributions

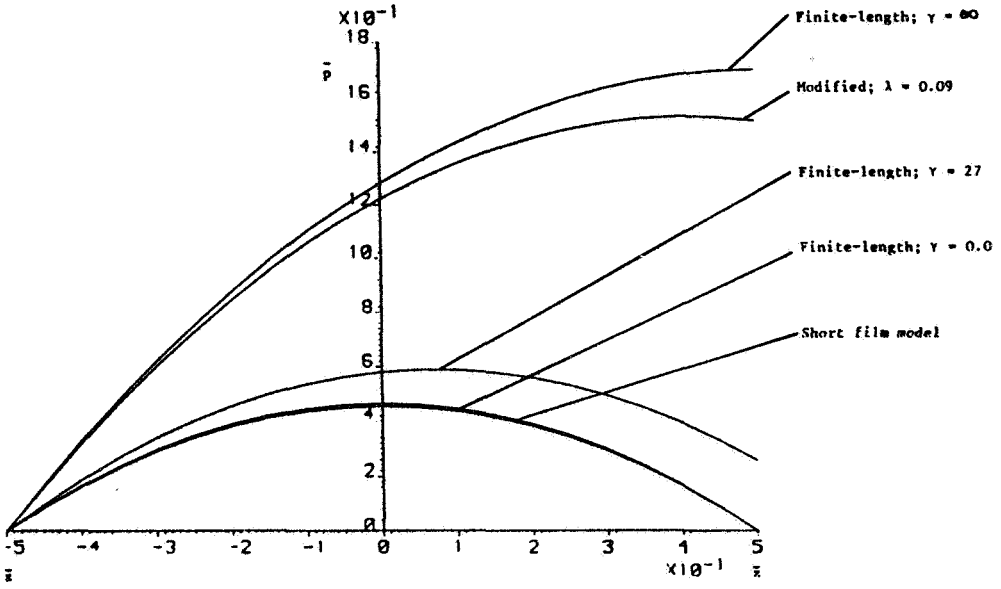

Fig. 8 (b) Axial pressure distributions.

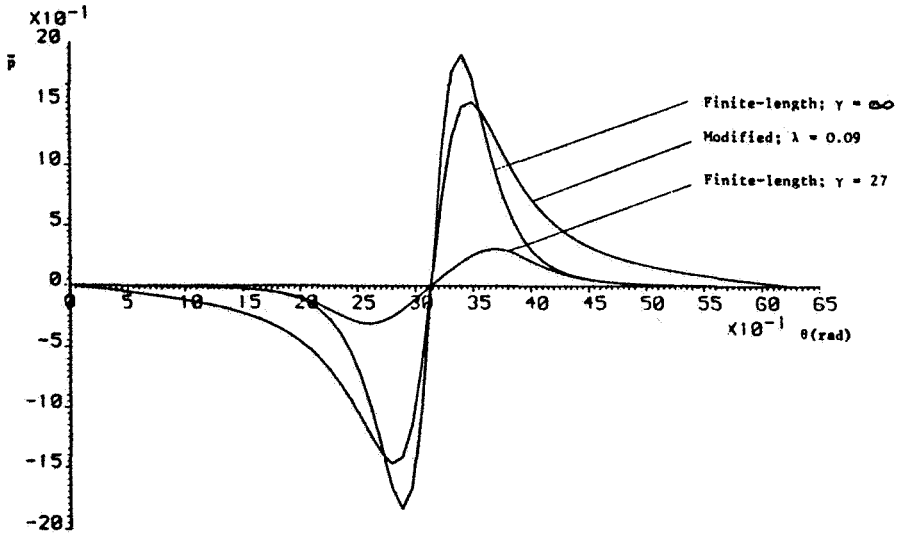

Fig. 8(c) A comparison of circumferential pressures around the seal (at $\bar{z} = 1/2$).

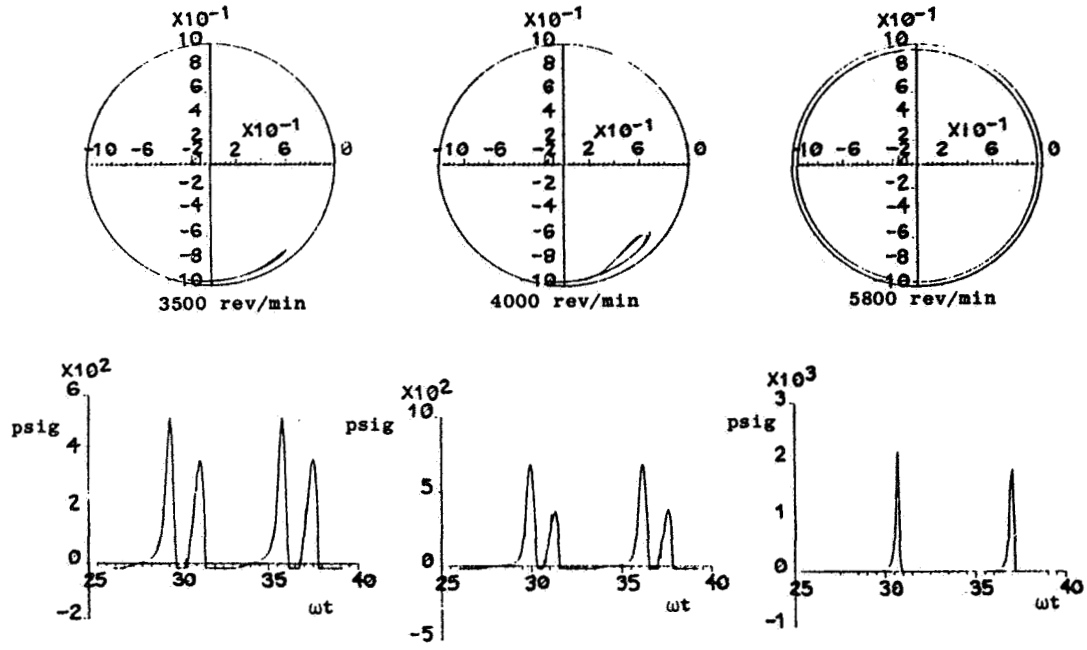

Fig. 9(a). Q_c = 0.459; numerical orbits and pressures using γ = 27

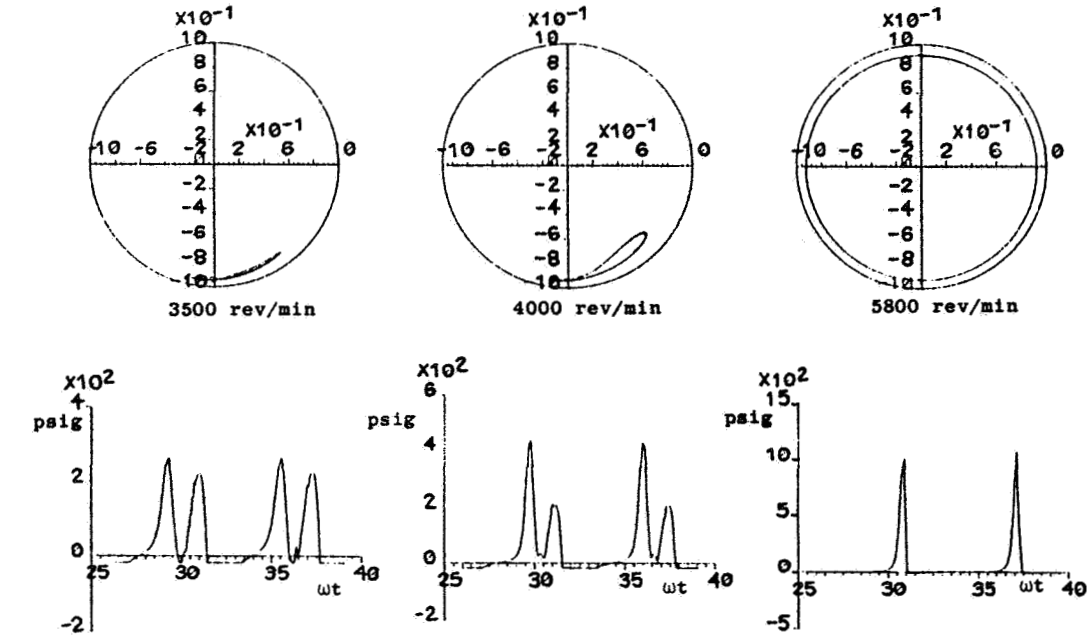

Fig. 9 (b). Q_c = 0.459; numerical orbits and pressures using $\gamma = \infty$.

INFLUENCE OF STATIONARY COMPONENTS ON UNSTEADY FLOW IN INDUSTRIAL CENTRIFUGAL COMPRESSORS

Luciano Bonciani and Luciano Terrinoni
Nuovo Pignone
Florence, Italy

An experimental investigation was performed to determine the characteristics of the onset and the growth of rotating nonuniform flow in a standard low specific speed stage, normally utilized in high pressure applications, in relation to change of stationary component geometry.
Four configurations, differing only in the return channel and crossover geometry were tested on an atmospheric pressure open loop test rig.
Experimental results make conspicuous the effect of return channel geometry and give the possibility of shifting the unstable zone onset varying such geometry.
An attempt was made to interpret the experimental results in the light of Emmons - Stenning's rotating stall theory.

1. INTRODUCTION.

Present experience with aeroinduced vibrations in turbomachines has emphasized two types of aerodynamic forces giving rise to completely different kinds of vibrational behavior:

- Forces depending on displacement and displacement velocity of the rotor

- Forces independent of rotor vibration caused by aerodynamic instability of the flow somewhere in the machine.

Although such forces are always present, usually they do not pose operational problems in low density applications. However, when the gas handled density increases, their intensity can grow till causing severe vibration problems.
Forces of the first type can completely destroy the damping present in the system, giving rise to high amplitude limit cycles at the first natural bending frequency of the rotor (often, unfortunately, the limit cycle amplitude is higher than the allowable clearances) (Ref. 1-8).
Forces of the second type are more benevolent in nature: their effect is limited to a strong low frequency vibration of the rotor.
In this case, the frequency, in a figurative sense, belongs to the force not to the rotor and the amplitude depends on the damping and stiffness characteristics of the rotor-bearing system (which are unaffected by the phenomenon).

Full load tests carried out on centrifugal compressors (Ref. 9, 10, 11) have put in evidence that forces of the second type always arise near the surge when reducing the flow at constant speed.
It is quite remarkable that the second type phenomenon can easily be studied even at atmospheric pressure (Ref. 21).
In order to provide a deeper understanding of the phenomenon, a research program was scheduled with the following main aims:

- Identifying the parameters ruling the unsteady flow condition onset.

- Finding, if possible, which of the stage components (impeller, diffuser, return channel) bears major responsibility.

- Defining the modifications necessary to displace the phenomenon onset (can it happen near an operating point? And if so, what should be done?).

This paper describes the results of such research, obtained studying a typical reinjection stage, tested in four configurations. Part of the results have already been presented (Ref. 21).

SYMBOLS

R Radius (m)

P Static pressure (kgf/m^2)

Po Total pressure (kgf/m^2)

q Dynamic pressure (kgf/m^2)

Ω Impeller angular speed (sec^{-1})

Cr Radial velocity (m/sec.)

C_ϑ Tangential velocity (m/sec.)

f_s Fundamental frequency of pressure oscillations (sec^{-1})

A Amplitude of pressure oscillations (kgf/m^2)

$\hat{C}r$ Nondimensional radial velocity ($\hat{C}r = Cr/\Omega R$)

$\hat{C}_\vartheta$ Nondimensional tangential velocity ($\hat{C}_\vartheta = C_\vartheta / \Omega R$)

$\hat{f}_s$ Fundamental frequency of pressure oscillations normalized to impeller speed ($\hat{f}_s = 2\pi f_s / \Omega$)

$\hat{A}$ Amplitude of pressure oscillations nondimensionalized with dynamic pressure ($\hat{A} = A/q$)

Mu Tip speed Mach number

φ Inlet flow coefficient

τ Total enthalpy rise coefficient

α Absolute flow angle (referring to tangential direction) (Deg.)

β_5 Inlet angle of return channel vanes (referring to tangential direction) (Deg.)

i_5 Incidence angle on return channel vanes ($i_5 = \alpha_5 - \beta_5$) (Deg.)

Cp Pressure recovery coefficient

Subscripts:

10 = Measured at section 10

10' = " " " 10'

20 = " " " 20

20' = " " " 20'

30 = " " " 30'

40 = " " " 40

40' = " " " 40'

50' = " " " 50'

60 = " " " 60

60' = " " " 60'

D = Diffuser

RC = Return channel

* = Onset of unsteady flow

2. TEST FACILITIES AND INSTRUMENTATION.

Tests were performed on an atmospheric pressure open loop test rig dedicated to the individual stage development (Ref. 12). A cross section of the test rig is shown in Fig. 1. The stage consisted of an impeller, a free-vortex diffuser, a crossover and a return channel.
Speed was adjusted by an hydraulic coupling torque converter while an electrically actuated discharge valve was operated to vary the flow.
Table 1 shows the conventional instrumentation usually used for industrial stage development testing.
Table 2 shows the instrumentation utilized to detect pressure oscillations connected with nonstationary flow conditions. Details of the conventional instrumentation are given below.

- The data acquisition system was based on a Solartron system 35 with a PDP 11/03 control unit.
- All pressure readings were connected, through a scannivalve, to a single pressure transducer. The transfer function of the measurement chain was experimentally tested to check that the output was the time average of the pressure within the frequency range of interest.

Regarding nonstationary readings we can note that:

- Static pressure probes were the Kulite XT-190-50 type
- Dynamic pressure probes were the Kulite XB-093-50G type
- Probe signals were recorded on an Ampex PR 2200 tape recorder and finally analyzed through an Ono-Sokki CF-500 real time spectrum analyzer. Data shown for each tested point are the RMS average of 256 spectra.

Four configurations (indicated in the following by the capital letters A, B, C, D) were tested, differing only in return channel and crossover geometry. The main geometrical dimensions are shown in Table 3.

3. DATA REDUCTION.

A brief note about data reduction may be in order here.

- At every measurement section, along the flow path in the stage, static pressure is assumed to be the average of the readings from the available pressure taps.
- The inlet and outlet stage values of the total pressure (sections 10 and 60) are the average of the readings from a four-Kiel type probe rack.
- Total pressure and flow angle traverse data at diffuser inlet and outlet (sections 20 and 40) were taken using a three-hole Cobra probe. Such readings were combined with the static pressure value and the total temperature readings, in order to calculate a mass-averaged total pressure.
- Total inlet temperature was assumed to be the average of the readings from eight circumferentially and radially spaced thermocouples.
- Total temperature traverse data at section 20 were taken with two thermocouples. Such values were combined with total and static pressure values in order to calculate a mass-averaged total temperature.

- Total temperature at section 40 was not measured: the mass-averaged value calculated from section 20 was assumed valid for section 40 too.
- Total outlet temperature (section 60) was practically coincident with the one measured at section 20 (except for efficiency calculation purposes), thus confirming the validity of the previous assumption.
- Flow angles were measured by Cobra probes at sections 10, 20, 40.

Measured angles at sections 20 and 40 showed a regular trend with the flow in the steady flow zone, but were found badly scattered in the unsteady one. On the contrary the angles calculated using

. Mass-flow
. Static pressure
. Mass-averaged total pressure
. Mass-averaged total temperature

showed a regular trend with flow under any condition (steady or unsteady). They were found to be strictly repetitive and were in good agreement, in the steady flow region, with the angles measured by the Cobras at the middle of the diffuser width.

At section 20 an additional check was performed calculating the angle by

. Mass-flow
. Static pressure
. Mass-averaged total temperature rise.

The agreement between the two procedures was satisfactory. As the latter method could be applied only to section 20, the former one was chosen for both sections.

Finally a very important parameter, the incidence angle on the return channel leading edge i_5, was calculated from the continuity equation assuming constant density and angular momentum conservation between station 40 and return channel inlet.

4. TEST PROCEDURE DESCRIPTION.

Each configuration was tested by varying the flow from the maximum allowed till surge and vice versa at constant speed. The procedure was then repeated at different speeds.
While testing configuration A the readings from the conventional instrumentation were not recorded simultaneously with the pressure oscillation readings (see Ref. 21); during other configuration tests, time-averaged and instantaneous measurements were recorded together.

5. TEST RESULTS.

5.1. Configuration A.

5.1.1. Unsteady flow behavior.

The test results (detailed in Ref. 21) will be, for the sake of completeness,

briefly summarized here.
Fig. 2 shows the observed frequencies normalized to the impeller angular speed versus the inlet flow coefficient. Reducing the flow at constant speed, the following behavior was observed:

. Pressure oscillations started simultaneously on all pressure transducers with very low amplitude and almost sinusoidal shape.
. A small flow reduction resulted in a slight increase in frequency and a considerable increase in amplitude, the signal shape remaining sinusoidal.
. Further flow reductions produced different results according to the test tip speed Mach number. It was found that the unsteady flow pattern could exhibit two distinct shapes:
  - A double frequency shape (DFS) so indicated because the frequency analysis showed the presence of two components at f_s and $f_s/2$ having practically the same amplitude.
  - A single frequency shape (SFS) characterized by a dominant component at f_s. Higher order harmonics, while present in both cases, had negligible amplitudes.

  The phase difference between static probes at the same radius was 90° for the DFS signal and 180° for the SFS one, thus indicating that DFS was associated with a single lobe pattern while SFS was associated with a two lobe one. It was found that at Mu = 0.45 and Mu = 0.60, the DFS was stable from the onset region till the region before surge, where a sudden shift to the SFS shape was always found. At higher test Mach numbers (Mu = 0.75 and Mu = 0.85) the switch from one shape to the other could happen in practically any point of the unsteady flow region, but the factors governing it were not understood: sometimes a spontaneous transition from the SFS to the DFS was observed several minutes after the latest valve positioning, sometimes (but not always) the introduction of the conventional probes into the diffuser was able to trigger such transition.
. Amplitudes at section 10' (impeller inlet) were always negligible till the surge.
. On opening the valve and exploring the phenomenon starting from the surge, the frequencies and amplitudes were generally repetitive related to flow; however, a slight hysteresis was noted in the onset region.

Since it was evident from the test results that two different unsteady patterns were fully compatible with the same flow and RPM (or better with the same φ - Mu values), an attempt to stabilize one of the two patterns was made. To attain this aim a small strip of sandpaper was glued on the leading edge (suction side) of five consecutive vanes of the return channel.

Testing such configuration, no difference was found in the onset zone, but the DFS was not found anymore at whatever test Mach number. In addition, the single frequency shape exhibited the same amplitude, frequency and phase lag than before for a given flow coefficient and tip speed Mach number (Fig. 3). After this result, no additional tests were carried out on configuration A.

5.1.2. Time-averaged results.

Fig. 4 shows the pressure ratios at section 60 (static-to-total and total-to-total) versus flow coefficient. A variation in the slope can be noted at the onset of the pressure oscillations followed by a region with a positive slope. At Mu = 0.75 and Mu = 0.85, two distinct branches clearly identify the regions relevant to the two shapes of the previously described signal (DFS and SFS). The inlet flow coefficient corresponding to the onset of the pressure oscillations continuously grows when the tip speed Mach number increases. However, if the inlet flow coefficient is plotted versus any of the impeller outlet variables, for example $\hat{C}_{r20}$ as shown on Fig. 5, it can be noted that the unsteady flow condition invariably appears for a practically constant value of such variables. In addition, as the more interesting parameters are surely the flow angles, we can note that the onset values are (see Fig. 6):

$$\alpha_{20*} \simeq 10°$$

$$\alpha_{40*} \simeq 13°$$

$$i_{5*} \simeq -6°$$

The behavior of the diffuser pressure recovery coefficient (Fig. 7) shows considerable scattering corresponding to the α_{20} onset value.
Quite remarkable is the sudden drop of the return channel pressure recovery coefficient C_{pRC} (Fig. 8) corresponding to the i_5 onset value. The figure clearly shows the two branches corresponding to the two signal shapes shown before.
Figs. 9, 10, 11, 12, 13 show the behavior of the configuration A with sandpaper on the return channel vanes. While the unsteady flow onset values (i_5 in particular) are unchanged, the return channel pressure recovery coefficient presents only the lower branch (SFS) to the left of the onset discontinuitv.
The following tendency in readings at sections 20 and 40 in the unsteady flow region is worth noting:

- While total temperature readings at section 20 did not show any trend to flatten after the onset (Fig. 14), total pressure readings, on the contrary, tended to flatten and even to decrease, so that dynamic pressure at section 20 tended to decrease too (Fig. 15).
  The agreement between the measured total pressure and the one calculated from total temperature rise, static pressure and mass flow got poorer and poorer. Even higher deviations from a regular trend are found at section 40 (Fig. 15). Measured flow angles began to be badly scattered, previous agreement with the calculated values being gradually lost.

This behavior of the readings was almost the same for every configuration tested.

5.2. Configuration B.

Configuration B differs from configuration A only in the return channel width and the crossover geometry as reported in Ref. 21. The width was increased to have, at the design point of the stage, an incidence angle on the R.C. leading edge, equal to - 6 degrees (the onset value for the configuration A).

5.2.1. Unsteady flow behavior.

This time only the single frequency shape was encountered all over the tested range of tip speed Mach numbers. The onset as well as the growth of the pressure oscillations was found to be quite similar to the one experienced when testing the configuration A when the SFS was present. Fig. 16 shows the observed frequencies, normalized to the impeller angular speed, versus the inlet flow coefficient.
The phase difference between static probes at the same radius was 180° as observed for the SFS signal in the previous configuration.

5.2.2. Time-averaged results.

The onset of the unsteady flow (Fig. 17) was now shifted to considerably higher flows. As before, the onset of the pressure oscillations started for a constant value of any impeller exit variable (Fig. 18). However, in this case, we found (see Fig. 19):

$$\alpha_{20*} \simeq 14°$$

$$\alpha_{40*} \simeq 18°$$

$$i_{5*} \simeq -6°$$

As the calculated R.C. incidence angle is practically coincident with the critical one found when testing configuration A, while vaneless diffuser inlet angles differ 4 degrees, it seems evident that the phenomenon tracks the return channel.
As before, the R.C. pressure recovery coefficient exhibited a sudden drop, coinciding with the start of the pressure oscillations, but only the lower branch to the left of the onset discontinuity was observed (Fig. 20).
Fig. 21 shows the diffuser pressure recovery coefficient versus α_{20}. Scattering is reduced and the onset drop is less evident.

5.3. Configuration C.

In order to obtain additional confirmation of the previous test results, a different channel was designed, having the same width of the B one but a lower vane inlet angle. The modified vane had a greater camberline curvature and a slightly different thickness distribution on the leading edge zone. The aim was to displace the onset back to the zone where it was found when testing the configuration A.

5.3.1. Unsteady flow behavior.

Only the test at Mu = 0.75 has been analyzed in detail, as behavior at different tip speed Much numbers was similar. Again, the onset and the growth of the pressure oscillations was found to be very similar to the ones previously shown. The signal corresponding to unsteady flow was once more a single frequency shape (Fig. 22) with 180° phase lag.

5.3.2. Time-averaged results.

As can be seen, the onset was now displaced to a slightly lower value, but higher than the expected one (Figs. 23 and 24). The diffuser inlet and exit flow angle at the onset were (see Fig. 25):

$$\alpha_{20*} \simeq 13°$$

$$\alpha_{40*} \simeq 16°$$

As before, the onset of pressure oscillations coincides with a sudden drop of the return channel pressure recovery coefficient (Fig. 26). The same figure suggests the reason for the apparent failure: the new return channel exhibits a lower critical incidence. The camberline modification seems to have lowered the critical incidence angle from - 6 to - 4 degrees. Therefore, the onset flow coefficient is about 20% higher than expected based on $i_5 = -6°$.

5.4. Configuration D.

At this point, an additional verification was of course necessary: the return channel width was reduced, keeping unchanged the camberline and the thickness distribution. The width was chosen equal to configuration A 's to facilitate the comparison.

5.4.1. Unsteady flow behavior.

The general behavior, from the point of view of the onset and the growth of the phenomenon, was essentially unchanged.
The present configuration resembled the configuration A: the double frequency shape was again encountered at both tested tip speed Mach numbers (Fig. 28).
In addition at Mu = 0.45 a certain sensitivity to the introduction of the pressure probes in the diffuser was found. In this case, however, the effect was not the shift from SFS to DFS signal but a slight frequency variation of SFS. Such sensitivity was not noted at Mu = 0.75.
The phase lag was 180° for SFS and again 90° for the DFS signal.

5.4.2. Time-averaged results.

Figs. 29, 30, 31 show that the unsteady region was displaced to a lower flow coefficient and the diffuser inlet and exit flow angle at the onset were

$\alpha_{20*} \simeq 9°$

$\alpha_{40*} \simeq 11°5$

Again the return channel pressure recovery coefficient (Fig. 32) shows a discontinuity corresponding to the pressure oscillation start.
The hypothesis of a lower critical incidence angle due to the camberline and thickness modification seems to be confirmed: the incidence angle at R.C. leading edge on the onset was again $i_{5*} \simeq -4°$.
Finally, Fig. 33 shows the behavior of the diffuser Cp_D.

6. NONDIMENSIONAL FREQUENCY AND AMPLITUDE OF THE PRESSURE OSCILLATIONS.

The analysis of the experimental results easily suggests that, for each configuration, the frequency-amplitude curves at different Mach numbers can be made to collapse, with a suitable choice of nondimensionalization factors, when plotted versus whatever outlet variable. The choice of the scale factors and of the outlet variable can be made in many ways, bringing in all cases to a single curve for the frequency and for the pressure amplitude. However, the four tested configurations differ only in the R.C. geometry and, in every case, the onset of the unsteady flow was found to correspond to a constant value of the incidence on the leading edge of the R.C. vanes. The phenomenon seems to be controlled by the R.C. to such a large extent that five strips of sandpaper were sufficient, when testing configuration A, to eliminate the double frequency shape. Such considerations suggest as the best nondimensionalization factor for the frequency the angular speed at section 40 ($C_{\vartheta 40}/R_{40}$).
As for the amplitudes, it was found that, using the local dynamic pressure as nondimensionalization factor, the same order of magnitude was obtained at every measurement section (with the exception of the impeller inlet). So in the following, the four configuration results will be compared on the basis of the so defined nondimensional frequency and amplitude (at section 40') versus R.C. vane incidence angle.

6.1. Comparison of the nondimensional frequency and amplitudes for the A, B, C, D, configurations.

The data reduction results are shown in Figs. 34, 35, 36 (configuration A), Figs. 37, 38 (configuration A with sandpaper), Figs. 39, 40 (configuration B), Figs. 41, 42 (configuration C) and finally in Figs. 43, 44, 45 (for configuration D). In any case the reduction to a single curve is very satisfactory.
Comparing all the nondimensional frequency plots we can note:

- The nondimensional frequency, $f_s/C_{\vartheta_{40}}$, is practically a linear function of the incidence and the slope is almost the same for each configuration.
- The onset values of the nondimensional frequency (both SFS and DFS when present) are the same for configurations having the same inlet width.
- Nondimensional amplitude curves (A_{40}/q_{40}) of configurations A and B are practically coincident. The corresponding curve of configuration C can be made to coincide with the preceding ones by an incidence shift of 2 degrees. Configuration D seems to be a case somewhat apart: the amplitudes are comparatively lower and very scattered.

So, the comparison seems to lead to the following conclusion:
- The frequency curves can be represented fairly accurately by

$$\hat{f}_s/\hat{C}_{\vartheta_{40}} = (\hat{f}_s/\hat{C}_{\vartheta_{40}})_* + K(i_5 - i_{5*})$$

but while the K value is the same for each configuration, $(\hat{f}_s/\hat{C}_{\vartheta_{40}})_*$ seems to depend on the relative width of the return channel.
For configurations A and D, we have:

$K \simeq 0.057$ (i_5 measured in degrees)

$(\hat{f}_s/\hat{C}_{\vartheta_{40}})_* \simeq 0.25\text{-}0.30$

Exactly half of such values is of course found for $f_s/2$ when the DFS is present.
For configurations B and C, we have:

$K \simeq 0.057$

$(\hat{f}_s/\hat{C}_{\vartheta_{40}})_* \simeq 0.18\text{-}0.22$

- The amplitude curves can be represented fairly well by a single relation of the kind

$$\hat{A} = f(i_5 - i_{5*})$$

for configurations A, B, C. No explanation can be suggested for the apparent deviation of configuration D.

It is a bit puzzling that the relative width of the return channel seems to influence only the onset values of nondimensional frequency, but not the slope of the frequency versus incidence curves, nor the amplitude relations (at least for configurations A, B, C).

7. AN APPLICATION OF ROTATING STALL THEORIES.

In the light of the previous discussion, it seems that the phenomenon can be explained on the basis of rotating stall on the R.C. vanes.

So an attempt can be made to utilize the existing theories on rotating stall. Due to the complexity of the problem, most of such theories (Ref. 22, 23, 24, 25) are based on an inviscid, linearized formulation of the motion equations. This approach is able to give information about the stall propagation speed as a function of some steady-state parameters (speed, inlet angle, pressure rise coefficient etc.). As natural consequence of the linearization, the pressure oscillation amplitudes and the spatial stall configuration are left indetermined. Even though the agreement with the experimental results is only fair, such methods are useful in providing qualitative understanding of the phenomena and in suggesting correlations among the relevant parameters.

7.1. Emmons - Stenning's theory.

Emmons - Stenning's theory is a typical flow stability calculation which can be extended without difficulties to cascades between revolution surfaces. Basic assumptions are:

- The flow upstream the cascade is potential and the fluctuating velocity components vanish at infinity.
- The cascade pressure rise coefficient derived from steady conditions is considered valid in unsteady conditions too.
- Pressure oscillations at the cascade outlet are negligible.

The calculated stall speed is then given by

$$\frac{Vp}{C_\vartheta} = \frac{1}{1+nJ} \cdot \frac{1 - Cp}{\cos^2\alpha}$$

where n is the number of lobes and J a geometrical nondimensional parameter (see appendix A). As a consequence, the (calculated) observed frequencies are given by

$$\frac{\omega_s R}{C_\vartheta} = \frac{n}{1+nJ} \cdot \frac{1-Cp}{\cos^2\alpha} = \frac{\hat{f}_s}{\hat{C}_\vartheta}$$

Some criticism can of course be made about the use of such relations in the present case:

- The pressure oscillations do not fade away with the distance from the leading edge of the R.C. vanes, showing that the coupling with the impeller-diffuser system cannot be neglected.
- Due to the influence of the impeller outlet fluctuating conditions, the flow in the diffuser can hardly be considered potential in nature.

A more complete analysis could be attempted which, while retaining the basic hypotheses of the previous theory, takes into account the interference between the return channel and the other components of the stage.
However, an attempt to find a correlation with the variables involved in the Emmons and Stenning's formula is justified by the strong influence of the R.C. geometry on the phenomenon.

To this end, the observed nondimensional frequencies were plotted versus $(1-C_{pRC})/\cos^2\alpha_5$ with the exclusion of configuration A (the lack of simultaneousness between conventional measurement and pressure oscillation readings hindered that).

Comparing all the nondimensional frequencies versus $(1-Cp_{RC})/\cos^2\alpha_5$ plots (Figs. 46, 47, 48, 49) we can note:

- For each configuration there exists a range of the abscissa values where the curve is practically linear. This range corresponds to the narrow range of flow where the Cp_{RC} suddenly drops, just after the onset. In this zone (the only zone where the theory can be expected to work), the agreement between theoretical and experimental results is fairly good. When the pressure oscillation amplitude increases, the linear relation is lost and the frequency becomes quite independent of the abscissa.
- Configurations having the same R.C. width exhibit almost identical curves. However, the slope of the linear zone is different for configurations A, D and configurations B, C. While the theory accounts for geometrical differences through the J factor, the slope difference is higher than predicted.
- The agreement between theoretical and experimental results is better for configurations A and D. Such condition is however limited to the upper frequency in case of DFS signal: the lower one is overestimated. It is worthy of note that in such case the ratio of the predicted frequencies is not integer, while during the configuration A, D tests such ratio was exactly 2.

In view of the limits of the present approach, expecting such details from the theory appears to be asking a bit much. On the whole, the results can be considered fairly satisfactory. It must be remarked that the Emmons-Stenning's theory provides a correlation rather than a prediction method: critical incidence, maximum Cp etc. cannot usually be predicted with the required accuracy.

8. CONCLUSIONS.

The main results of the present investigation are the following:

1. The four configurations clearly showed that the return channel bears major responsibility for the onset of the unsteady flow.
2. For every configuration, the unsteady flow onset was found to occur when a well defined incidence angle on the leading edge of the return channel vanes was reached. The critical incidence was found to be dependent on the vane skeleton, but independent of the crossover geometry.
3. The general behavior of the nondimensional frequencies and amplitudes is similar for the four configurations when plotted versus the difference between the actual incidence and the critical one. However, the narrower return channels exhibited higher onset frequencies and, in addition, could exhibit two distinct unsteady flow patterns (SFS and DFS). Within the tested Mu range, such behavior was never observed with the wider ones (configurations B and C).
4. The comparison with the Emmons-Stenning's theory can be considered fairly satisfactory and provides additional confirmation of the fact that the phenomenon is controlled by the return channel rotating stall.

Additional theoretical and experimental work would be required in order to complete and extend the present results.

REFERENCES

1. Fowlie D.W., Miles D.D., Vibration Problems with High Pressure Centrifugal Compressors, ASME Paper n. 75-Pet-28

2. Smith K.J., An Operation History of Fractional Frequency Whirl, Proc. 4th Turbomachinery Symposium, Gas Turbine Laboratories, Texas A & M University, Oct 1975.

3. Wachel J.C., Nonsynchronous Instability of Centrifugal Compressors, ASME Paper n. 75-Pet-22.

4. Criqui A.F., Wendt P.G., Design and Closed Loop Testing of High Pressure Centrifugal Gas Compressors for the Suppression of Subsynchronous Vibrations, ASME Paper n. 79-GT-86.

5. Fujikawa T., Ishiguaro N., Ito M., Asynchronous Vibration Problem of Centrifugal Compressor, NASA Conference Publication 2133, May 12-14, 1980.

6. Coletti N.J., Crane M.E., Centrifugal Compression of the Arun High Pressure Injection Project, I. Mech. E. 1981, C 54/81.

7. Wachel J.C., Rotordynamic Instability Field Problems, NASA Conference Publication 3250, May 10-12, 1982

8. EK. M.C., Solution of the Subsynchronous Whirl Problem in the High Pressure Hydrogen Turbomachinery of the Space Shuttle Main Engine, AIAA/SAE 14th Joint Propulsion Conference, Las Vegas, Nevada, July 25-27, 1978.

9. Ferrara P.L., Tesei A., High Pressure Centrifugal Compressors, Inst. Mech. Eng. Conference Publications 1978, March 3, 1978.

10. Bonciani L., Ferrara P.L., Timori A., Aero-Induced Vibrations in Centrifugal Compressors, NASA Conference Publication 2133, May 12-14, 1980.

11. Sabella D., Terrinoni L., Timori A., Full Load Testing of Centrifugal Natural Gas Injection Compressors, Inst. Mech. Eng. Conference Publication 1981, March 3, 1981.

12. Benvenuti E., Aerodynamic Development of Stages for Industrial Centrifugal Compressors, Part. 1 & 2, ASME Paper n. 8-GT 4 & 5.

13. Jansen W., Rotating Stall in a Radial Vaneless Diffuser, Transaction of the ASME Journal of Basic Engineering, Dec. 1964 pp. 750-758.

14. Abdelhamid A.N., Colwill W.H., Barrows J.F., Experimental Investigation of Unsteady Flow Phenomena in Vaneless Radial Diffusers, ASME Paper n. 78-GT-23.

15. Abdelhamid A.N., Bertrand J., Distinctions Between Two Types of Selfexcited Gas Oscillations in Vaneless Radial Diffusers, ASME Paper n. 79-GT-58.

16. Abdelhamid A.N., Analysis of Rotating Stall in Vaneless Diffusers of Centrifugal Compressors, ASME Paper n. 80-GT-184.

17. Abdelhamid A.N., Effects of Vaneless Diffuser Geometry on Flow Instability in Centrifugal Compression Systems, ASME Paper n. 81-GT-10.

18. Abdelhamid A.N., Control of Selfexited Flow Oscillations in Vaneless Diffuser of Centrifugal Compressor Systems, ASME Paper n. 82-GT-188.

19. Van Den Braembussche R., Frigne P., Roustan M., Rotating Nonuniform Flow in Radial Compressors, AGARD C.P. 282, May 1980.

20. Van Den Braembussche R., Frigne P. Comparative Study of Subsynchronous Rotating Flow Patterns in Centrifugal Compressors with Vaneless Diffusers, NASA Conference Publication 2250, May 10-12, 1982.

21. Bonciani L., Terrinoni L., Tesei A., Unsteady Flow Phenomena in Industrial Centrifugal Compressor Stage, NASA Conference Publication 2250, May 10-12, 1982.

22. Emmons H.W., Pearson C.E., Grant N.P., Compressors Surge and Stall Propagation, Trans. ASME Vol. 77, 1955.

23. Stenning A.H., Kriebel A.R., Stall Propagation in a Cascade of Aerofoils, ASME Paper n. 57-SA-29.

24. Leone M.J., A Study of Existing Information on Rotating Stall with New Observations Concerning Changes in Stall-cell Size and Number, Rensselaer Polytechnic Inst., TR. A.E. 6810, September 1968.

25. Ludwig G.R., Nenni J.P., Rice J.R.R.S., An Investigation of Rotating Stall Phenomena, Cornell Aeronautical Laboratory, Inc. Buffalo, N.Y. - TR AFAPT-TR-70-26, May 1970.

APPENDIX A

STABILITY OF THE FLOW THROUGH AN ISOLATED CASCADE.

A brief account of the Emmons-Stenning's theory will be given here.
Suppose we have an isolated annular cascade bounded by revolution surfaces extended, upstream and downstream at a great distance compared with the blade meridional length. The motion equations (with the assumptions below specified) are written for the upstream field and the flow between the blades (a major assumption of the theory makes calculations for the downstream field unnecessary) and a stability analysis is performed in a classical way.

1. Upstream field.
   Assuming incompressible nonviscous flow with uniform conditions at infinity, the energy equation in a system rotating with the cascade is written

$$\frac{\partial \phi}{\partial t} + \frac{p}{\rho} + \frac{\omega^2}{2} - \frac{U^2}{2} = \frac{p_0}{\rho}$$

   where ϕ, ω, U are the velocity potential, the relative flow velocity and the local blade velocity ($U = \Omega r$), while p_0 is the stagnation pressure.

2. Cascade.
   Assuming incompressible unidimensional flow, the motion equation is written

$$\frac{\partial w}{\partial t} + w\frac{\partial w}{\partial l} - U\frac{\partial U}{\partial l} = -\frac{1}{\rho}\frac{\partial p}{\partial l} - \frac{f}{\rho}$$

   where w, U have the usual meaning and f is the term due to the wall shear stresses.
   Integrating along the mean line of the channel from the inlet (1) to the outlet (2), we obtain

1. $$\int_0^L \frac{\partial w}{\partial t}\,dl + \frac{w_2^2 - w_1^2}{2} + \int_0^L \frac{f}{\rho}\,dl - \frac{U_2^2 - U_1^2}{2} + \frac{p_2 - p_1}{\rho} = 0$$

   The following procedure is now followed:
   - Each equation is linearized using as reference the steady conditions and retaining the first order terms only. Due to the assumed conditions, the upstream perturbation field is potential and the velocity is given by

$$w_m = W_m + \frac{\partial \phi}{\partial m}$$

$$w_\theta = W_\theta + \frac{\partial \phi}{r\partial \theta}$$

- Upstream perturbation velocity variation along the cascade pitch is negligible. This immediately allows expressing the velocity perturbation between the blades as

$$w = \frac{s\,b_1}{A}\,\frac{\partial \phi}{\partial m}$$

where s, b_1, A are the pitch, the inlet width and the normal section of the channel defined by two consecutive blades.

- When linearizing equation 1, it is assumed that the term

$$\frac{w_1^2 - w_2^2}{2} - \int_0^L \frac{f}{\rho}\,dl$$

can be represented, even in unsteady conditions, by

$$C_p\,(tg\beta_1)\,\frac{1}{2}\,(w_{m_1}^2 + w_{\theta_1}^2)$$

where β_1, w_{m_1}, w_{θ_1} are the flow angle and the velocity components at the cascade inlet.

- Lastly, outlet pressure variations are assumed to be zero all over the circumference. This assumption, suggested by the physical behavior of a cascade in incipient stall, allows a major simplification: we no longer have to calculate the downstream field which, never being potential in unsteady conditions, usually poses greater difficulties than the upstream. Eliminating the inlet pressure variations, we finally find

$$\frac{\partial \phi}{\partial t} + \left(b_1 s \int_0^L \frac{dl}{A}\right) \frac{\partial^2 \phi}{\partial m \partial t} +$$

$$\left\{(1 - C_p)\,W_{m_1} - \frac{\partial C_p}{\partial\, tg\beta_1}\, tg\beta_1 \frac{w_1^2}{2 W_{m_1}}\right\} \frac{\partial \phi}{\partial m} +$$

$$\left\{(1 - C_p)\,W_{\theta_1} + \frac{\partial C_p}{\partial\, tg\beta_1}\, tg\beta_1 \frac{w_1^2}{2 W_{\theta_1}}\right\} \frac{\partial \phi}{r\,\partial \theta} = 0$$

where the perturbation potential derivatives have to be calculated at the cascade inlet (m = 0).

The potential ϕ must satisfy the equation

$$\frac{\partial}{\partial m}\left(br\frac{\partial \phi}{\partial m}\right) + \frac{b}{r^2}\frac{\partial^2 \phi}{\partial \theta^2} = 0$$

with the condition

$$\lim_{m \to -\infty} \nabla \phi = 0$$

It is convenient to perform a change of variable by defining

$$\xi = \int_0^m \frac{dm}{r}$$

and to develop the potential in Fourier series

$$\phi = \Sigma A X_n(\xi) e^{in\theta}$$

where the functions X_n are the solutions of the boundary value problem

$$\frac{d^2 X_n}{d\xi^2} + \frac{1}{b}\frac{db}{d\xi}\frac{dX_n}{d\xi} - n^2 X_n = 0 \quad ; \quad X_n(0) = 1 \quad X_n(-\infty) = 0$$

The potential derivatives at the cascade inlet are

$$\frac{\partial \phi}{\partial t} = \Sigma \dot{A}_n e^{in\theta}$$

$$\frac{\partial \phi}{r \partial \theta} = \Sigma A_n \frac{in}{r_1} e^{in\theta}$$

$$\frac{\partial \phi}{\partial m} = \Sigma A_n \frac{n}{r_1}\left(\frac{1}{n}\frac{dX_n}{d\xi}\right)_{m=0} e^{in\theta} = \Sigma A_n \frac{n}{r_1} K_n e^{in\theta}$$

$$\frac{\partial^2 \phi}{\partial m \partial t} = \Sigma \dot{A}_n \frac{n}{r_1} K_n e^{in\theta}$$

With the position

$$J = \frac{b_1 s}{r_1}\int_0^L \frac{dl}{A}$$

we find

$$\dot{A}_n (1 + nK_n J) + \frac{nK_n}{r_1}\left\{(1 - C_p) W_{m_1} - \frac{\partial C_p}{\partial tg\beta_1} tg\beta_1 \frac{W_1^2}{2W_{m_1}}\right\} A_n +$$

$$i\frac{n}{r_1}\left\{(1 - C_p) W_{\theta_1} + \frac{\partial C_p}{\partial tg\beta_1} tg\beta_1 \frac{W_1^2}{2W_{\theta_1}}\right\} A_n = 0$$

Neutral stability conditions are predicted when

$$\frac{\partial C_p}{\partial tg\beta_1} = (1 - C_p) \sin 2\beta_1$$

The stall propagation speed is given by

$$\frac{V_p}{W_{\theta 1}} = \frac{1}{1 + n\kappa_n J} \frac{1 - C_p}{\cos^2 \beta_1}$$

and the corresponding nondimensional frequencies by

$$\frac{\omega_s r_1}{W_{\theta 1}} = \frac{n}{1 + n\kappa_n J} \frac{1 - C_p}{\cos^2 \beta_1}$$

The formulas are strictly valid at the instability onset, but it can be hoped that they maintain their validity even in the initial phase of the phenomenon. The κ_n values are dependent on the width distribution in front of the cascade and deriving general results is not so easy. However, if it is assumed that the width varies monotonically from some value b_1 at $\xi = 0$ to some value b_∞ at $\xi = -\infty$ it can be shown that

$$\frac{db}{d\xi} \gtrless 0$$

results

$$\kappa_n \lessgtr 1$$

So, when the width increases toward the cascade leading edge, a slight frequency increase should be expected. It is however doubtful that this approach could model the crossover geometry: as matter of fact, the experimental results show the opposite trend. For comparison with experimental results, $\kappa_n = 1$ was utilized for any configuration.

As a final remark the following can be noted:
in the case of rotating cascade, assuming zero inlet whirl, the observed non-dimensional frequency is given by

$$\frac{\omega_s}{\Omega} = n - \frac{n}{1 + n\kappa_n J} \frac{1 - C_p}{\cos^2 \beta_1}$$

In the case of stationary cascade, we have directly

$$\frac{\omega_s r_1}{c_{\theta 1}} = \frac{n}{1 + n\kappa_n J} \frac{1 - C_p}{\cos^2 \beta_1}$$

This means that impeller rotating stall must generate frequencies much higher than return channel rotating stall (order of magnitude 0.8 instead of 0.2). In addition, the frequency is expected to decrease when decreasing the flow. Such predictions are confirmed by the experimental results of Ref. 20.

TABLE I

Measuring sect.	Total pressure probes	Static pressure probes	Thermoelements
Sec. 10 (impeller inlet)	4 Kiel 1 Cobra	1	8 (circum. and radially spaced)
Sec. 20 (diffuser inlet)	1 Cobra	1	2 (circum. spaced)
Sec. 40 (diffuser exit)	1 Cobra	4	
Sec. 60 (return channel exit)	4 Kiel	8 (4+4 at inner and over radius)	8 (circum. and radially spaced)

TABLE II

Measuring sect.	Total pressure probes	Static pressure probes
Sec. 10' (impeller inlet)	1	1
Sec. 20' (diffuser inlet)	1	2 (90° spaced)
Sec. 30' (diffuser midspan)	1	2 (90° spaced)
Sec. 40' (diffuser exit)		2 (90° spaced)
Sec. 50' (return channel throat area)		2 (90° spaced. Throat area of two sections of the return channel)
Sec. 60' (return channel exit)		1 (at the exit of one of the two sections of sec. 50')

TABLE III

Impeller Outlet Width	:	0.050			
Diffuser Inlet Width	:	0.0311			
Diffuser Exit Width	:	0.0256			
			Configurations		
		A	B	C	D
Return Channel Inlet Width	:	0.0278	0.0400	0.0400	0.0278
Return Channel Outlet Width	:	0.0400	0.0522	0.0522	0.0400
Return Channel Inlet Angle	:	18°	18°	14°.5	14°.5

(All dimensions are referred to impeller external diameter)

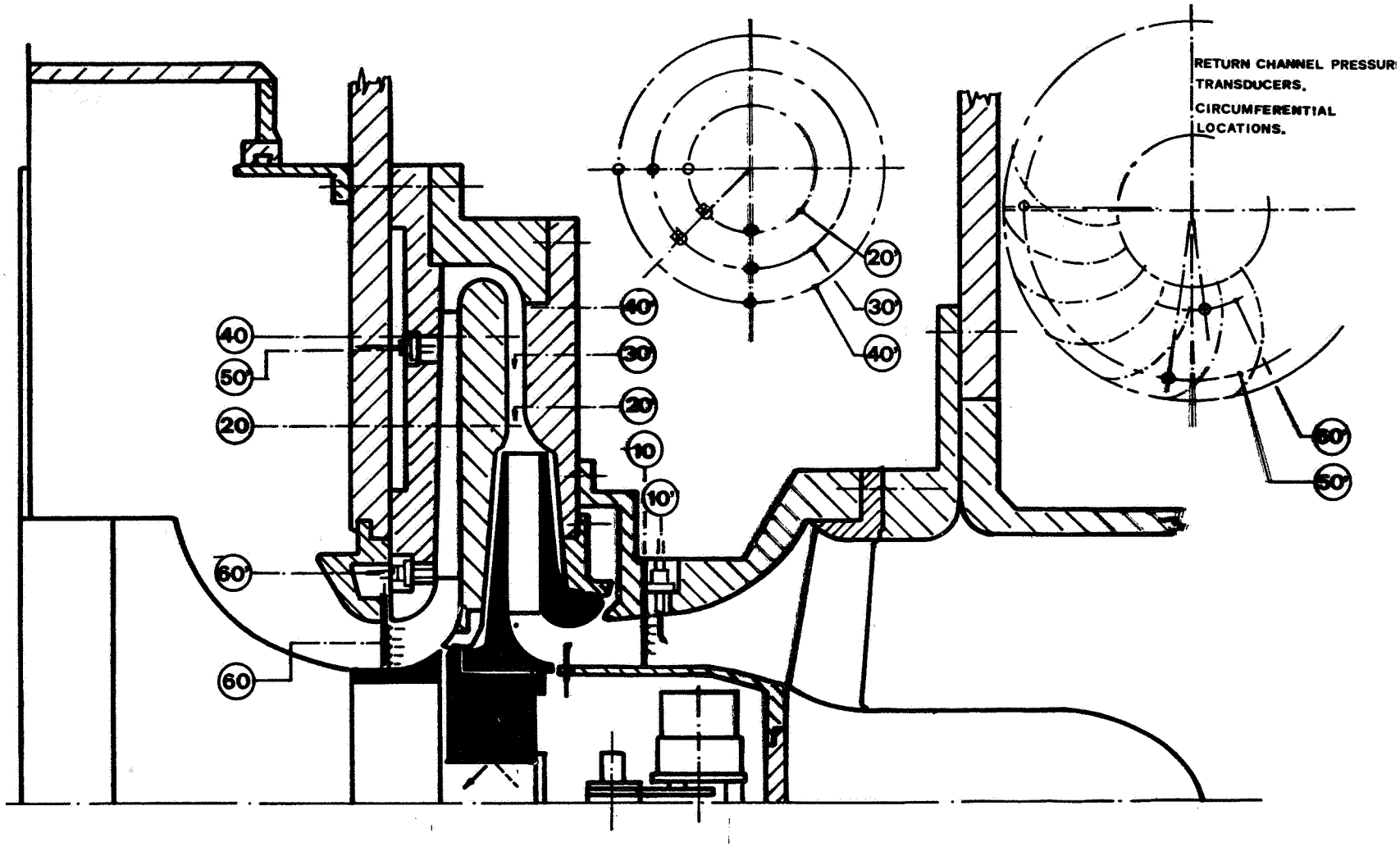

Figure 1. - Cross section of test rig.

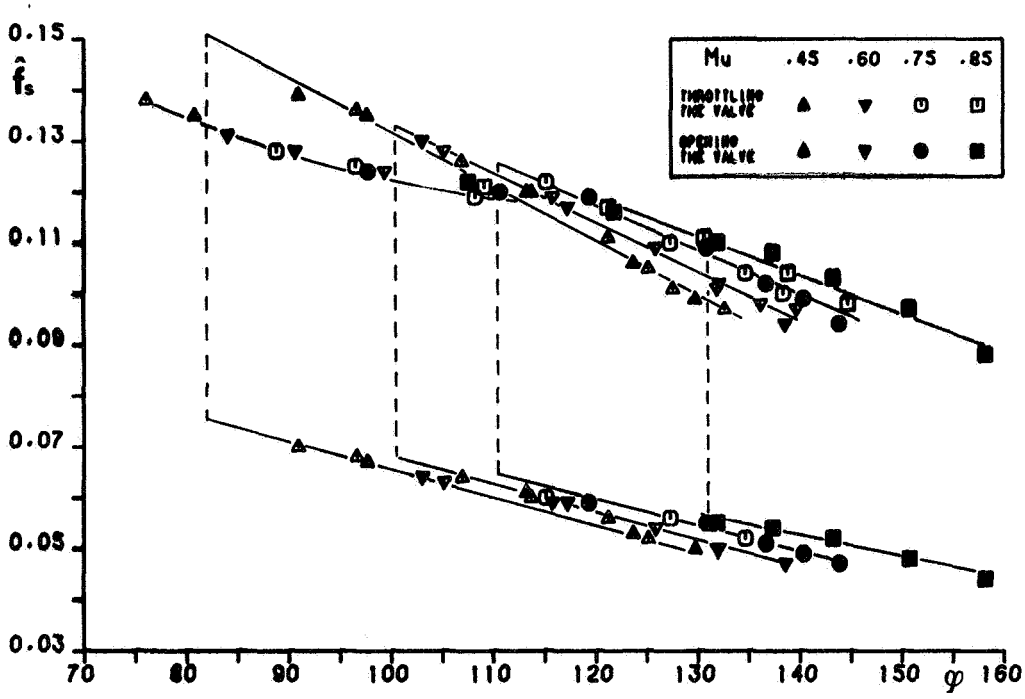

Figure 2. - Normalized observed frequency versus inlet flow coefficient. (Configuration A.)

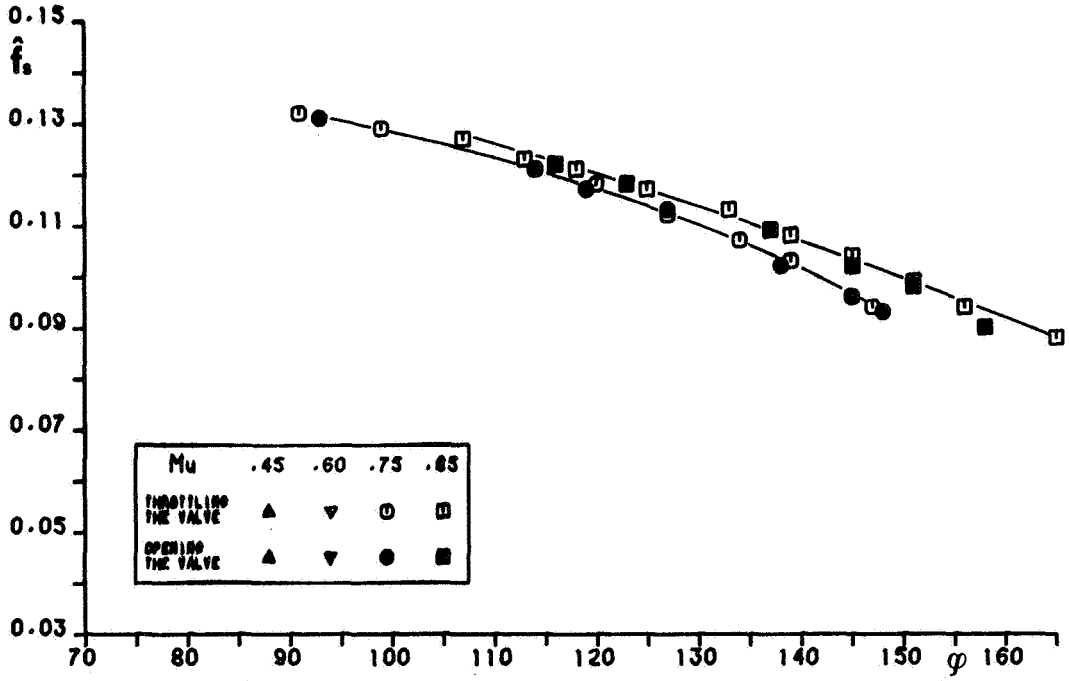

Figure 3. - Normalized observed frequency versus inlet flow coefficient. (Configuration A with sandpaper.)

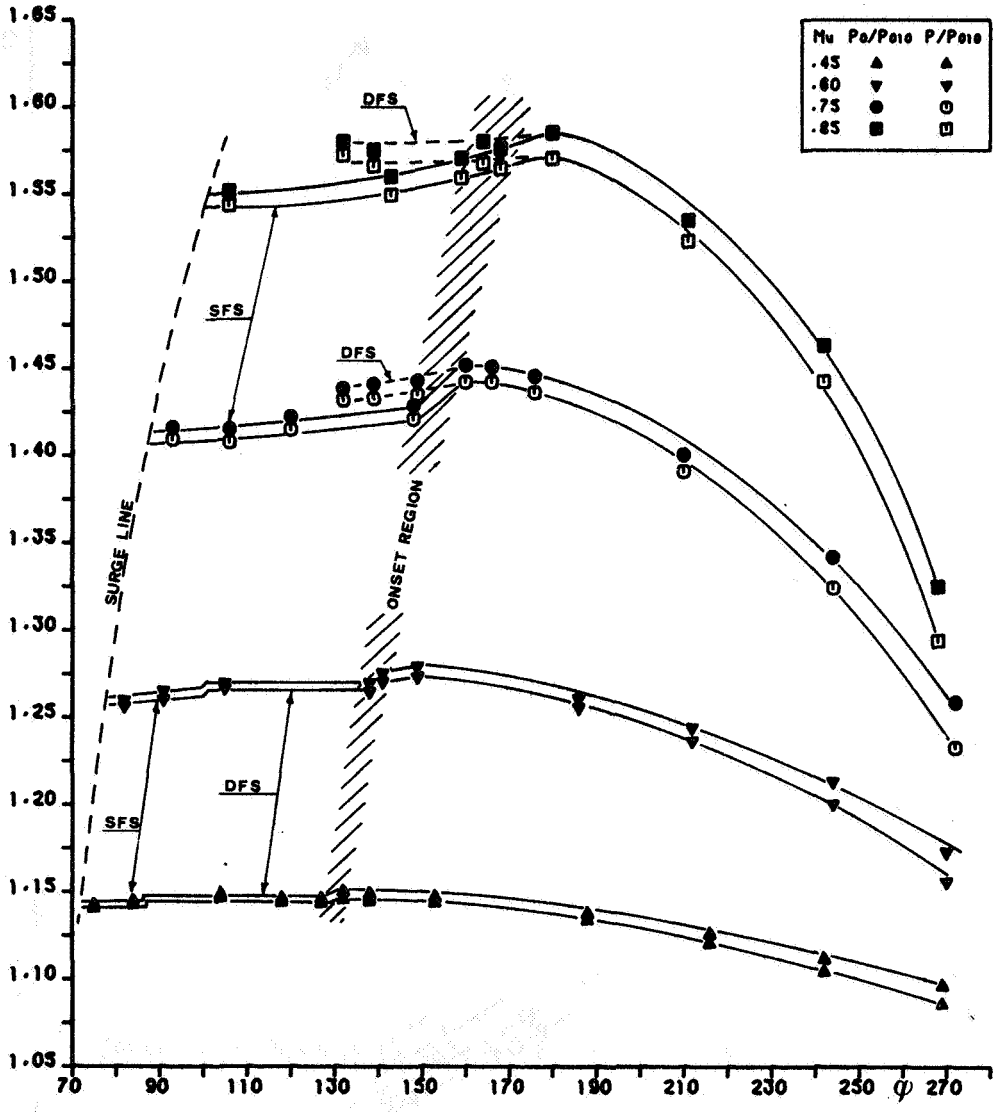

Figure 4. - Static-to-total and total-to-total pressure ratios at section 60 versus inlet flow coefficient. (Configuration A.)

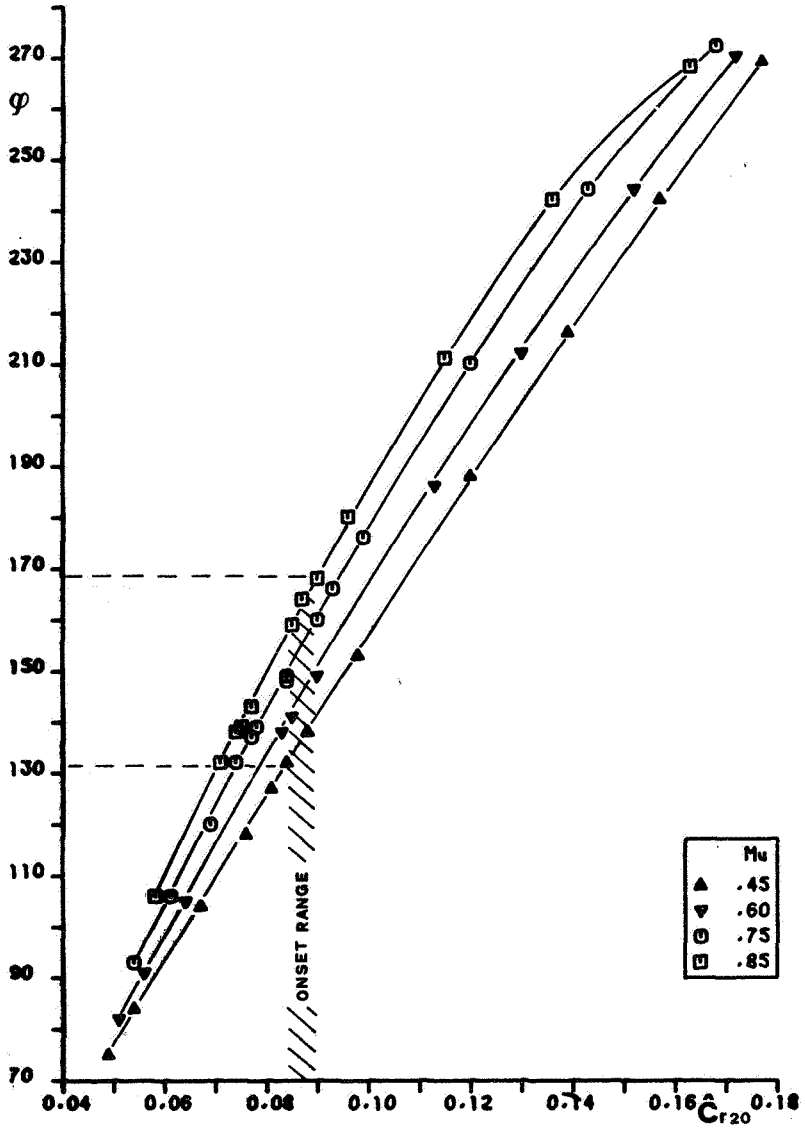

Figure 5. - Inlet flow coefficient versus nondimensional radial velocity at section 20. (Configuration A.)

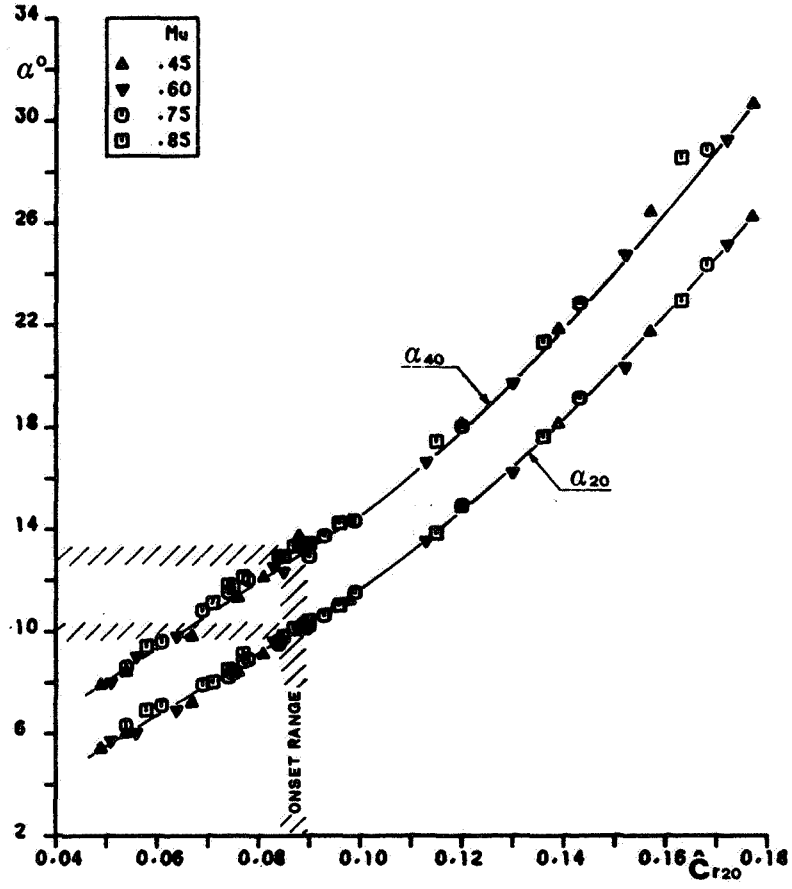

Figure 6. - Absolute flow angles at sections 20 and 40 versus nondimensional radial velocity at section 20. (Configuration A.)

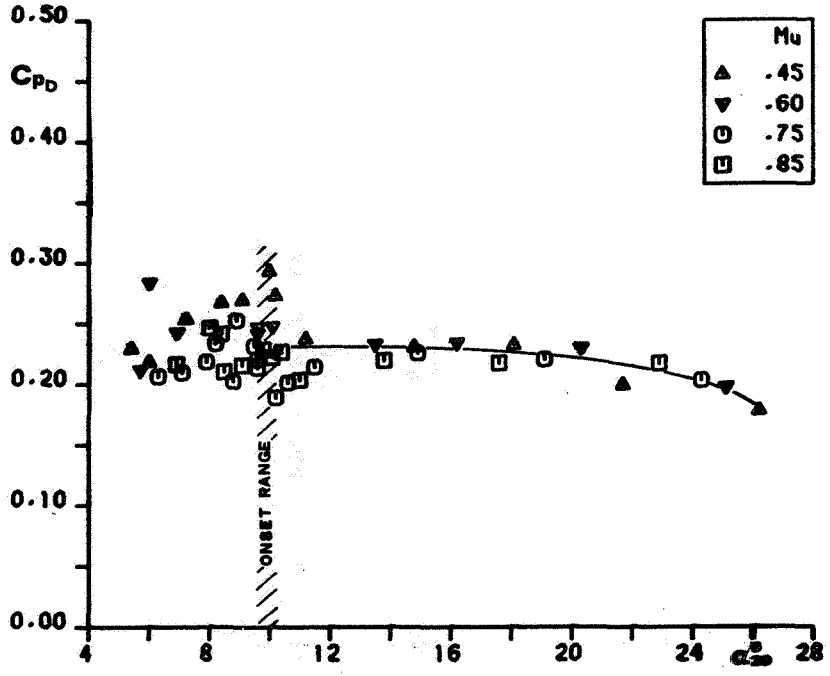

Figure 7. - Vaneless diffuser pressure recovery coefficient versus absolute flow angle at section 20. (Configuration A.)

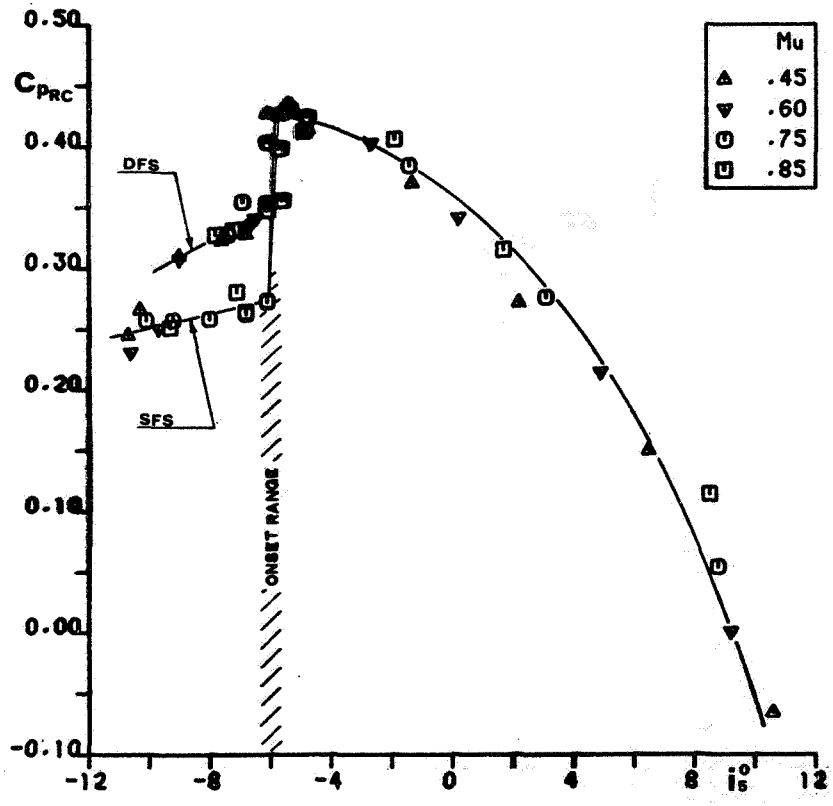

Figure 8. - Return channel pressure recovery coefficient versus incidence angle. (Configuration A.)

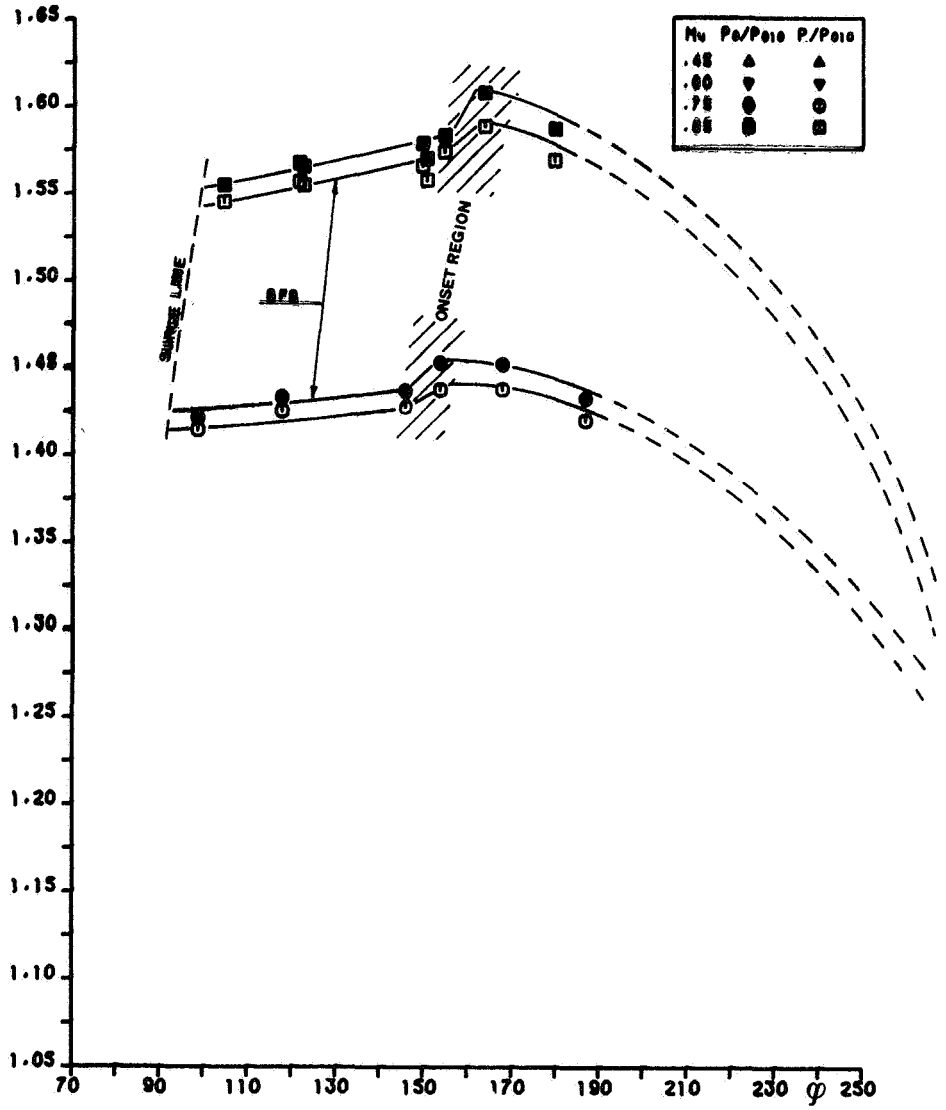

Figure 9. - Static-to-total and total-to-total pressure ratios at section 60 versus inlet flow coefficient. (Configuration A with sandpaper.)

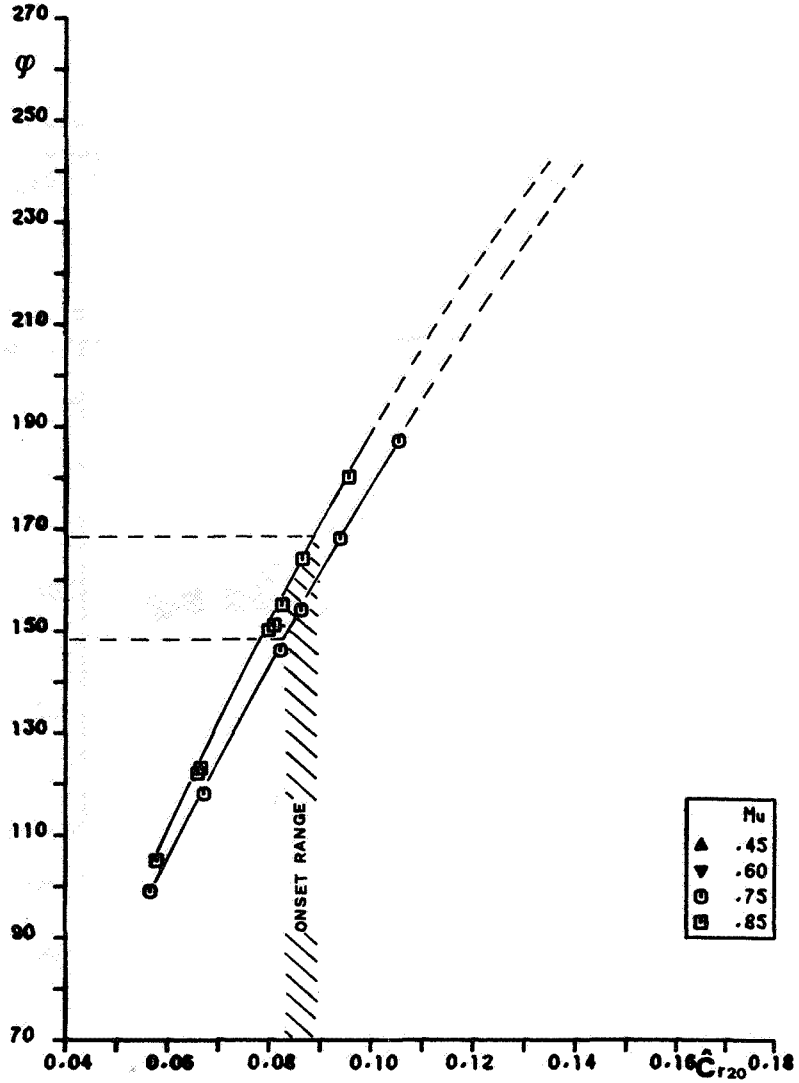

Figure 10. - Inlet flow coefficient versus nondimensional radial velocity at section 20. (Configuration A with sandpaper.)

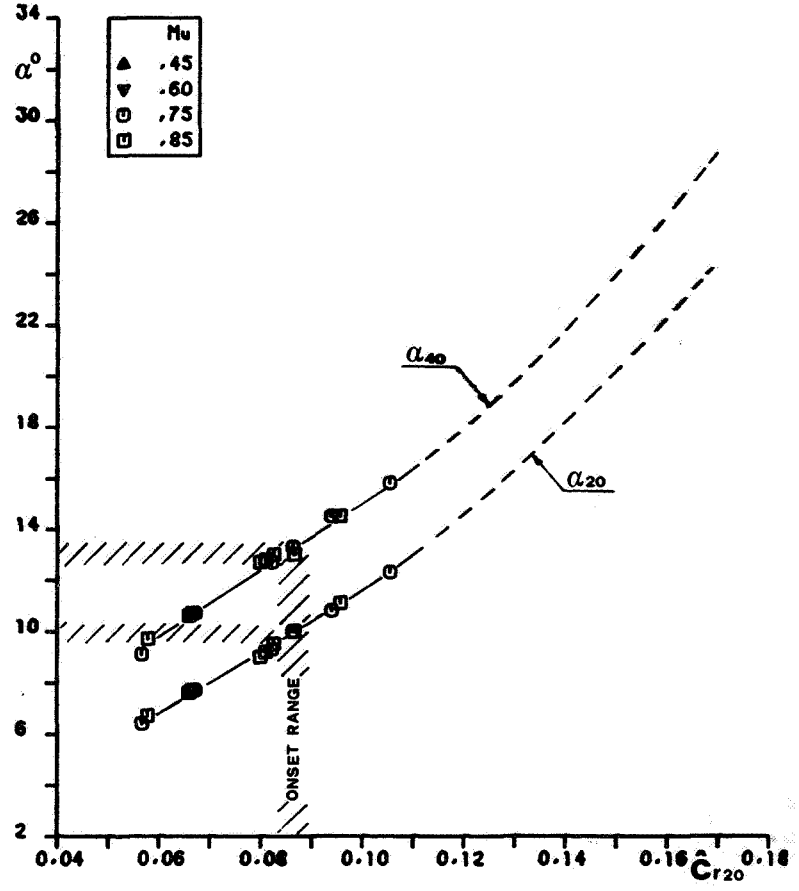

Figure 11. - Absolute flow angles at sections 20 and 40 versus nondimensional radial velocity at section 20. (Configuration A with sandpaper.)

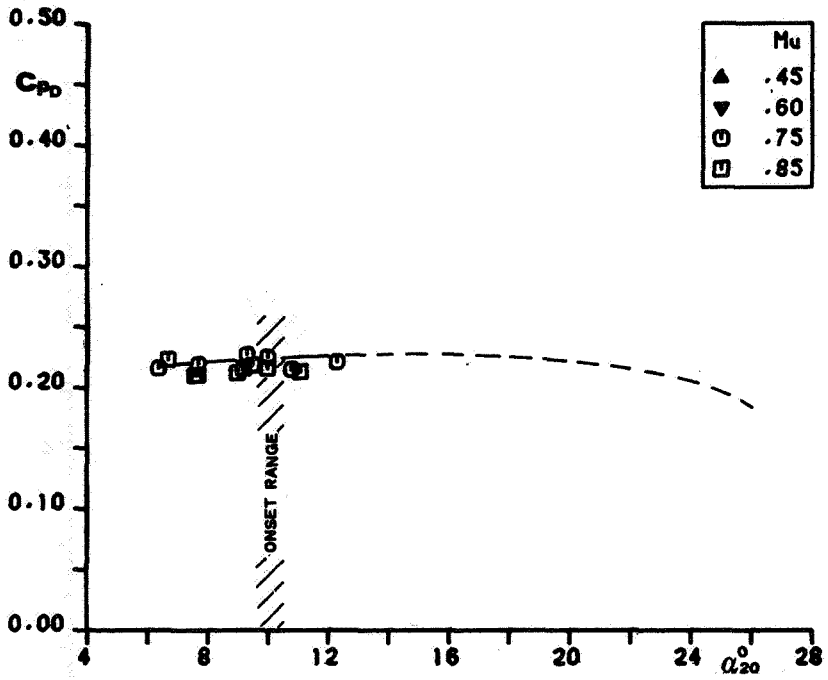

Figure 12. - Vaneless diffuser pressure recovery coefficient versus absolute flow angle at section 20. (Configuration A with sandpaper.)

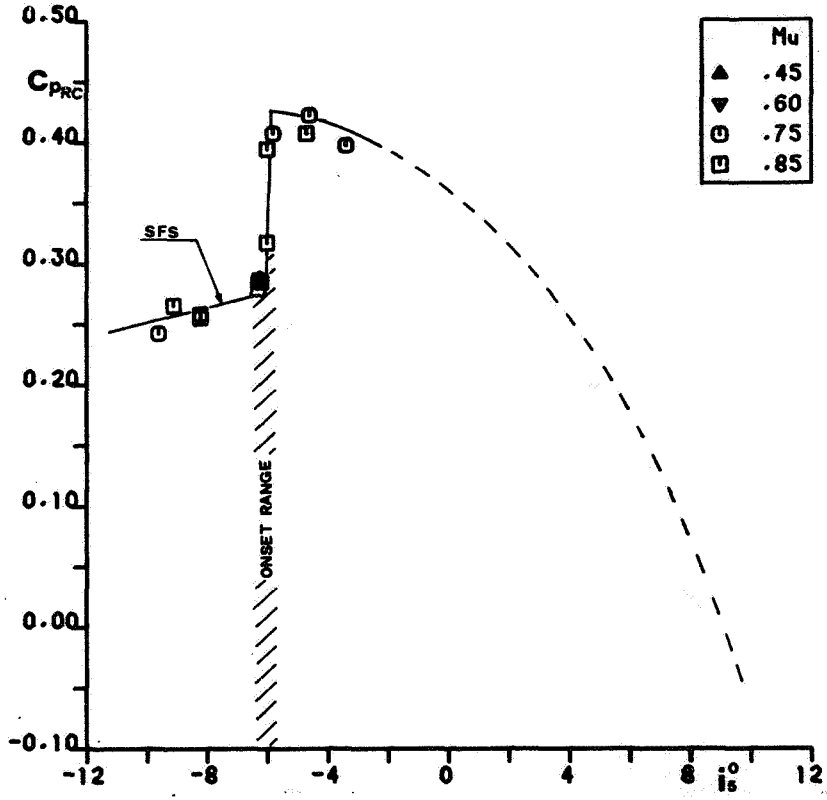

Figure 13. - Return channel pressure recovery coefficient versus incidence angle. (Configuration A with sandpaper.)

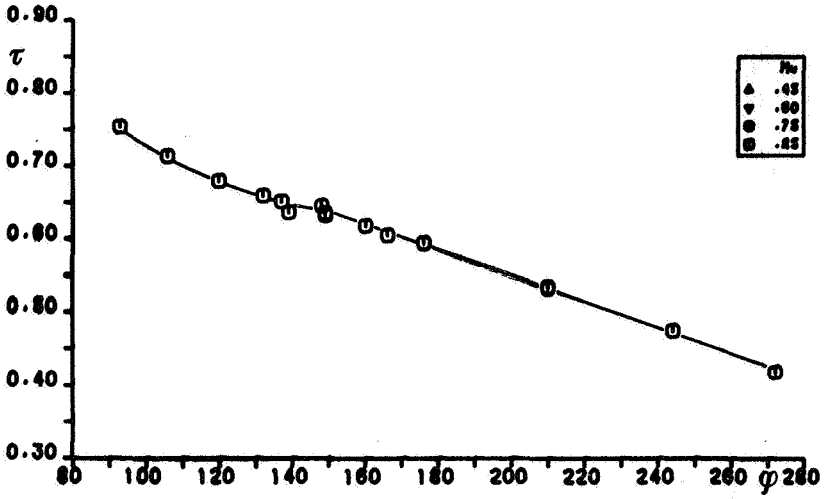

Figure 14. - Total enthalpy rise coefficient versus inlet flow coefficient. (Configuration A.)

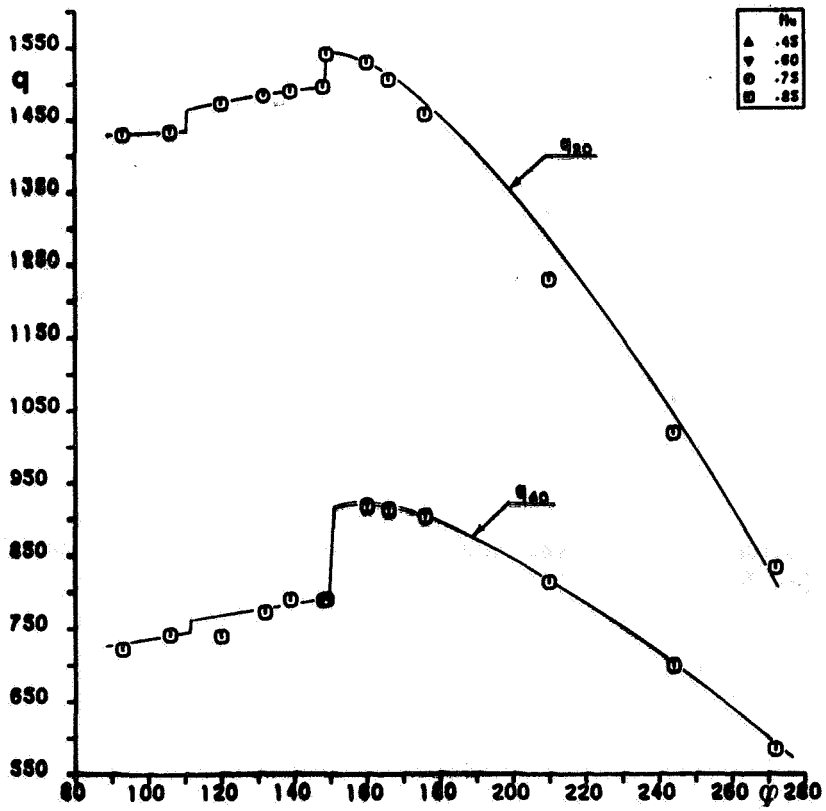

Figure 15. - Dynamic pressure at sections 20 and 40 versus inlet flow coefficient. (Configuration A.)

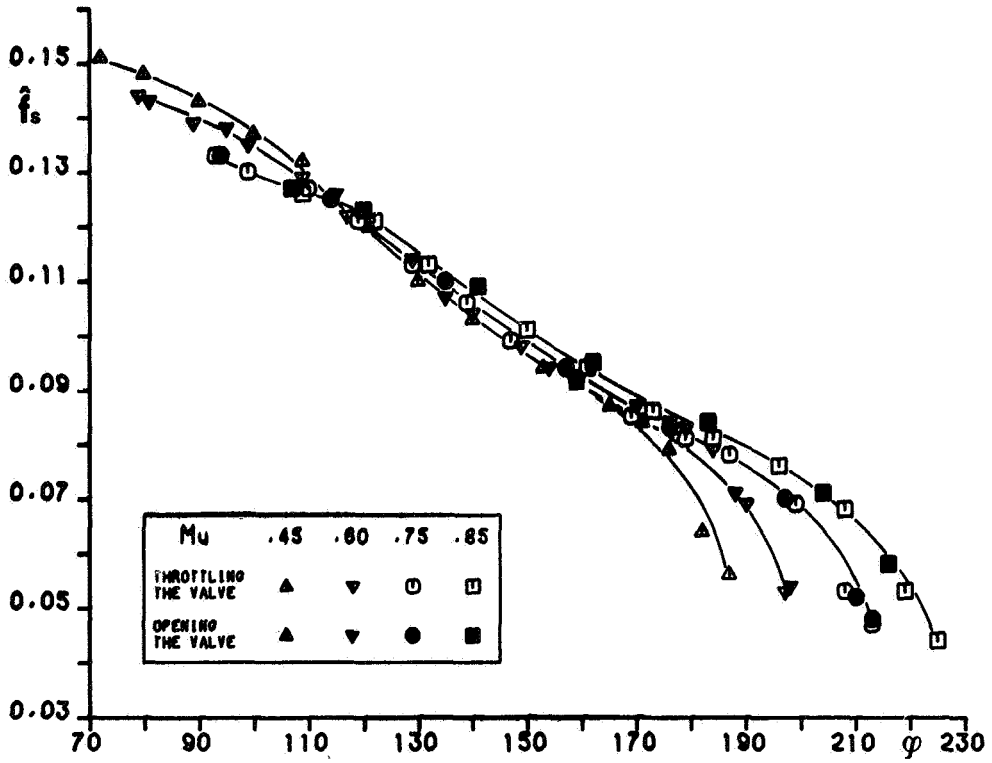

Figure 16. - Normalized observed frequency versus inlet flow coefficient. (Configuration B.)

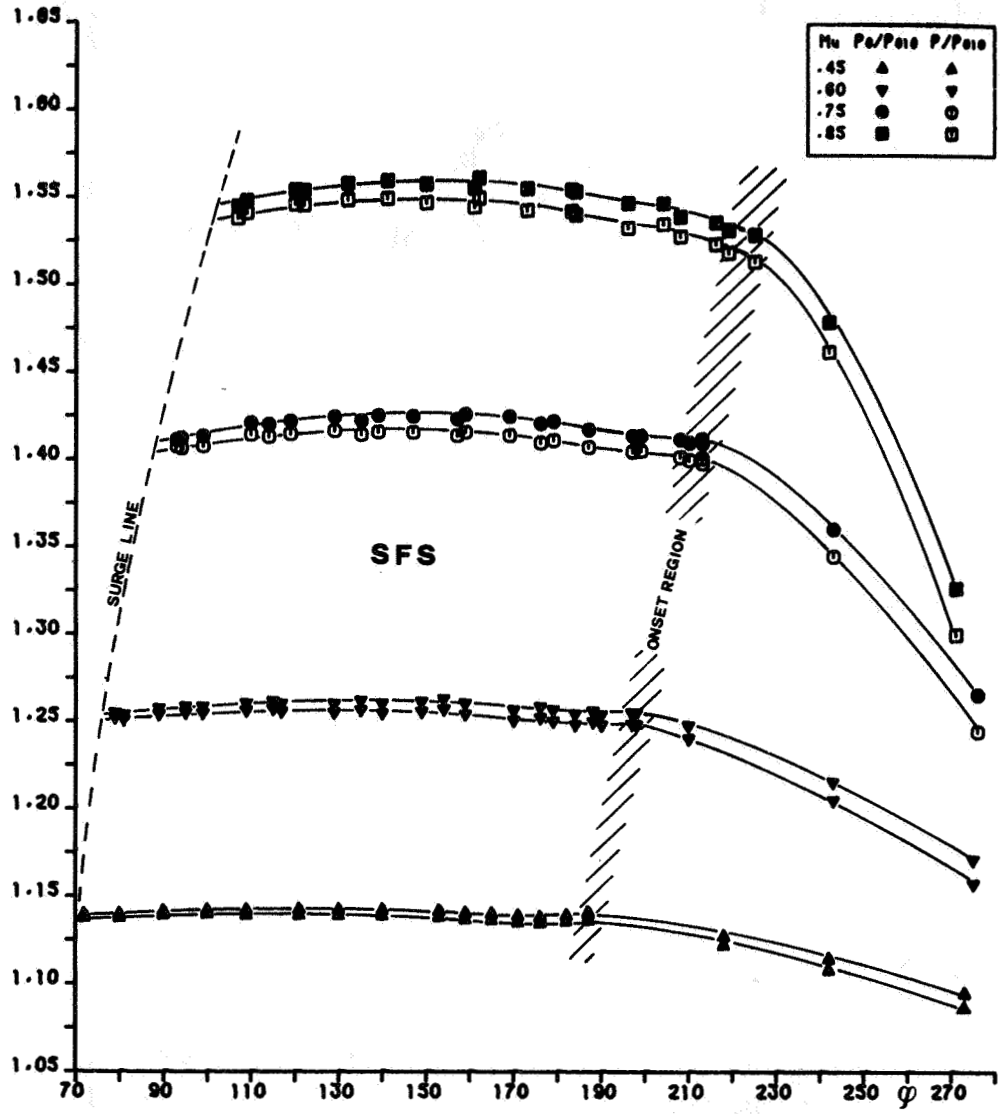

Figure 17. - Static-to-total and total-to-total pressure ratios at section 60 versus inlet flow coefficient. (Configuration B.)

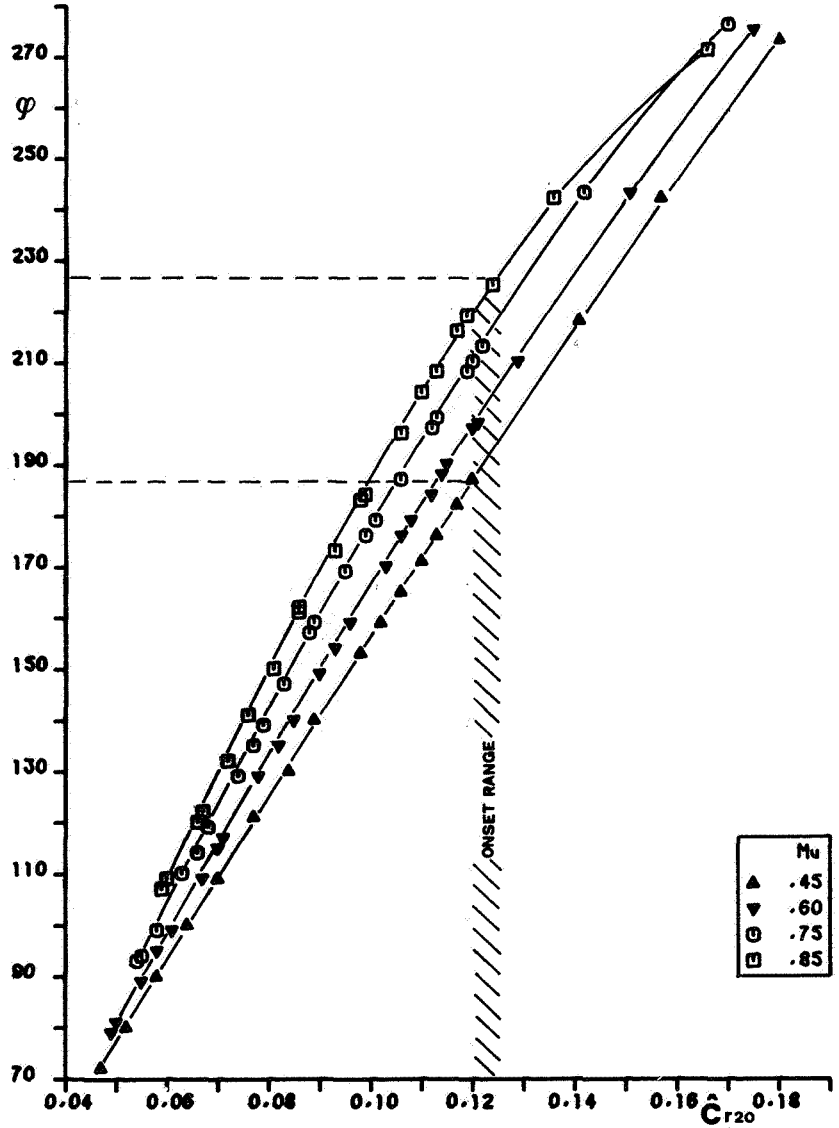

Figure 18. - Inlet flow coefficient versus nondimensional radial velocity at section 20. (Configuration B.)

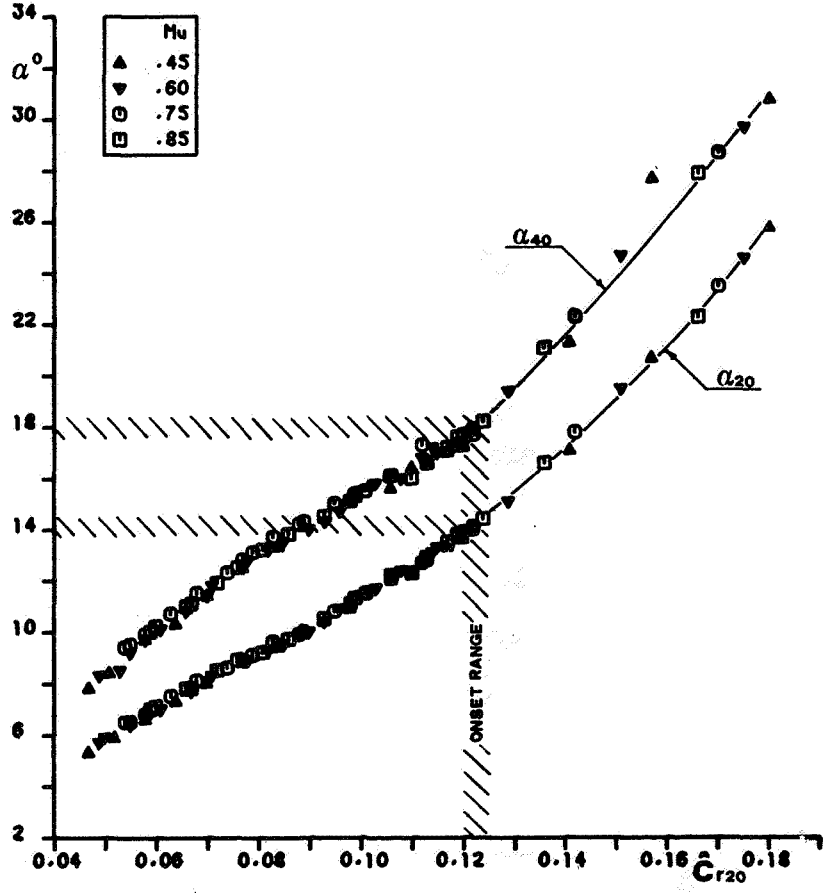

Figure 19. - Absolute flow angles at sections 20 and 40 versus nondimensional radial velocity at section 20. (Configuration B.)

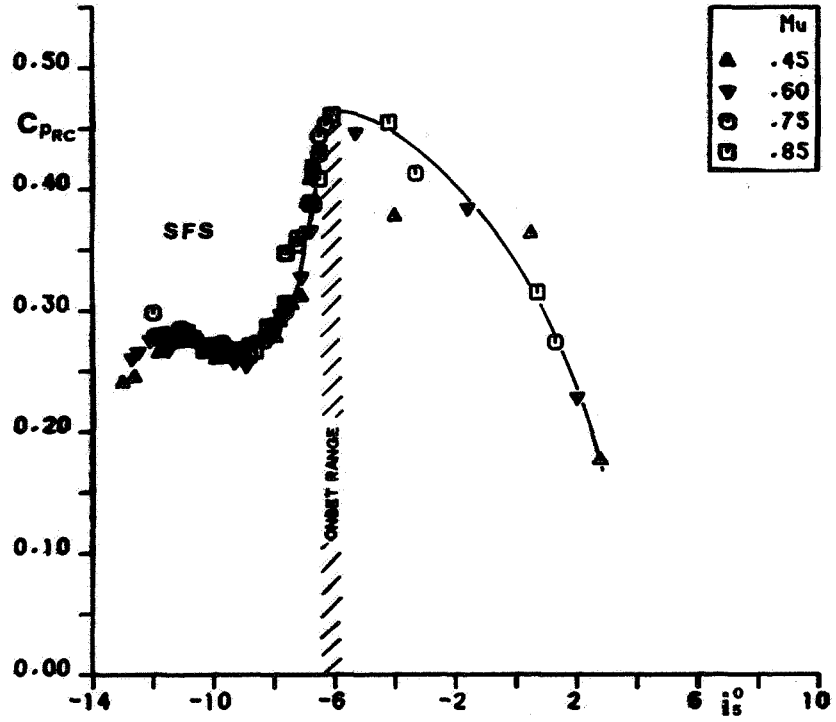

Figure 20. - Return channel pressure recovery coefficient versus incidence angle. (Configuration B.)

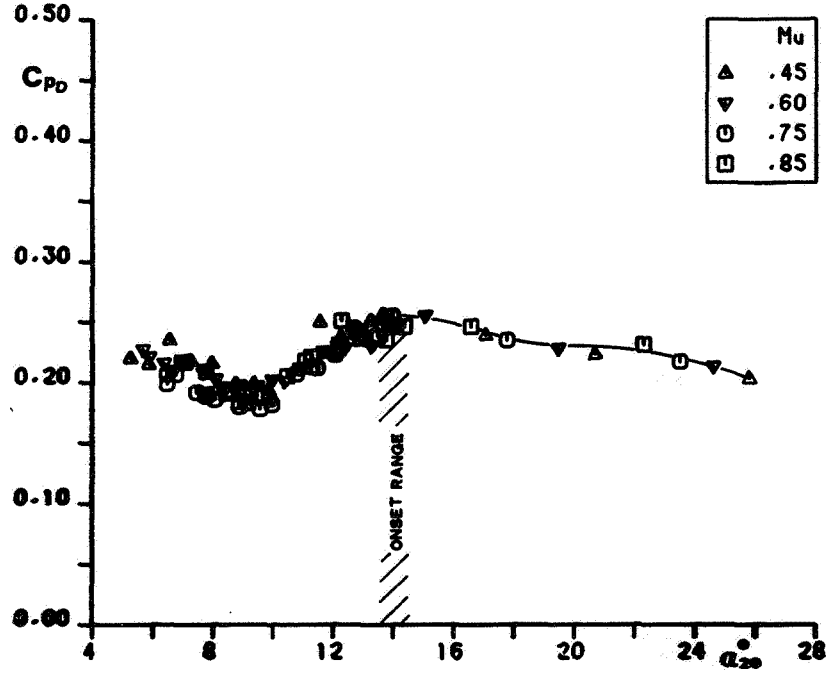

Figure 21. - Vaneless diffuser pressure recovery coefficient versus absolute flow angle at section 20. (Configuration B.)

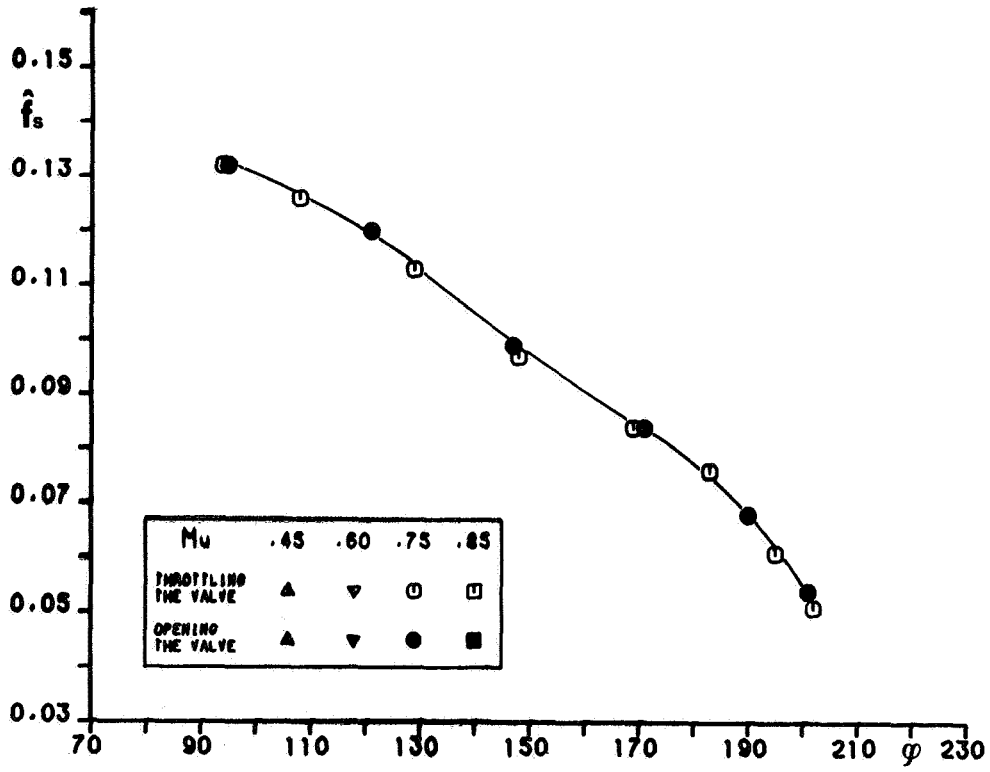

Figure 22. - Normalized observed frequency versus inlet flow coefficient. (Configuration C.)

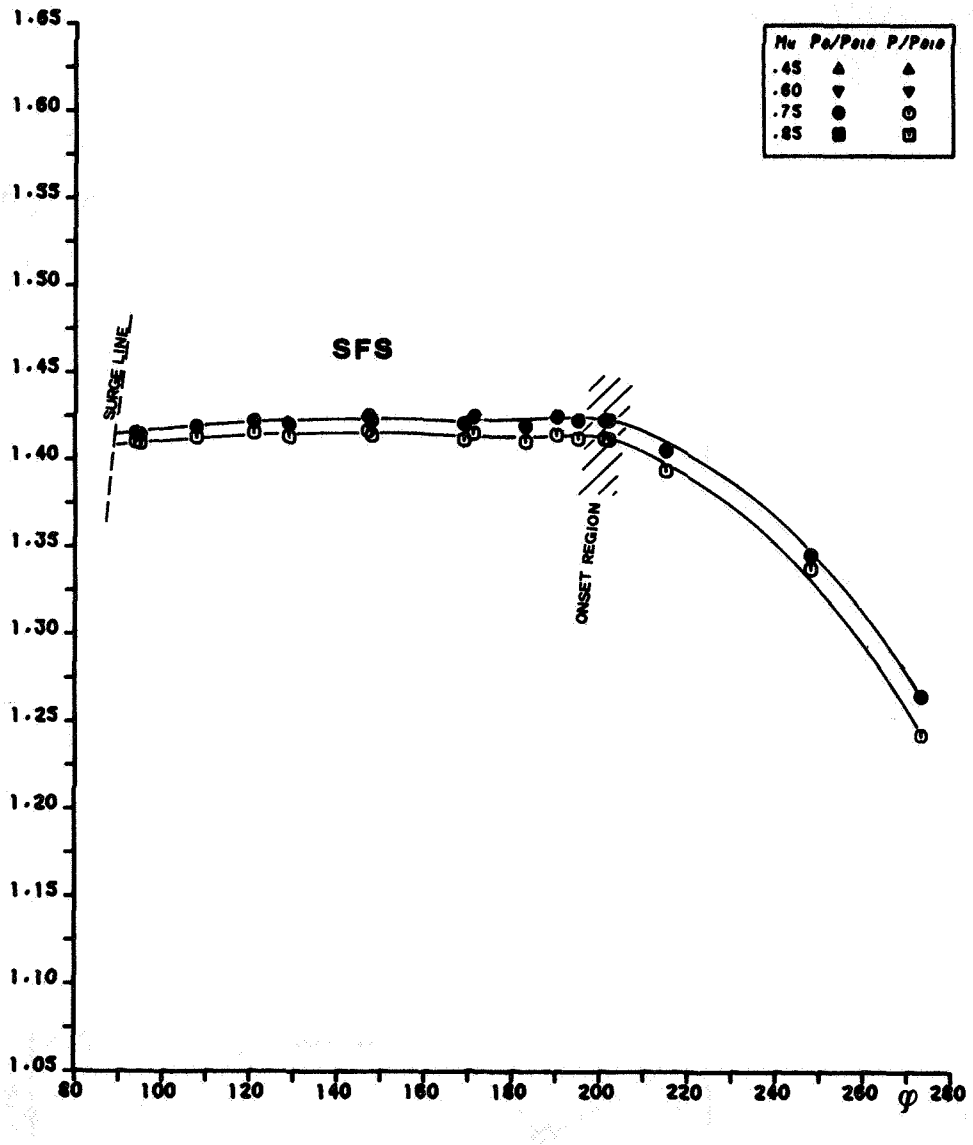

Figure 23. - Static-to-total and total-to-total pressure ratios at section 60 versus inlet flow coefficient. (Configuration C.)

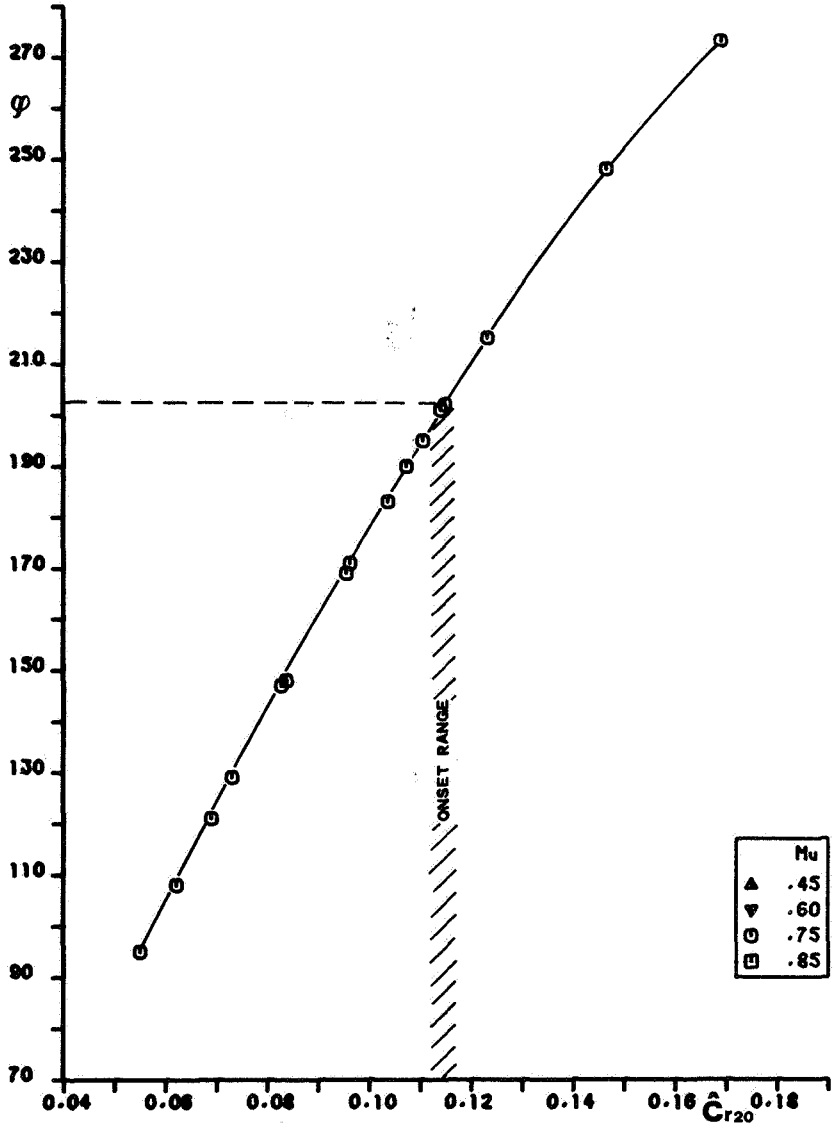

Figure 24. - Inlet flow coefficient versus nondimensional radial velocity at section 20. (Configuration C.)

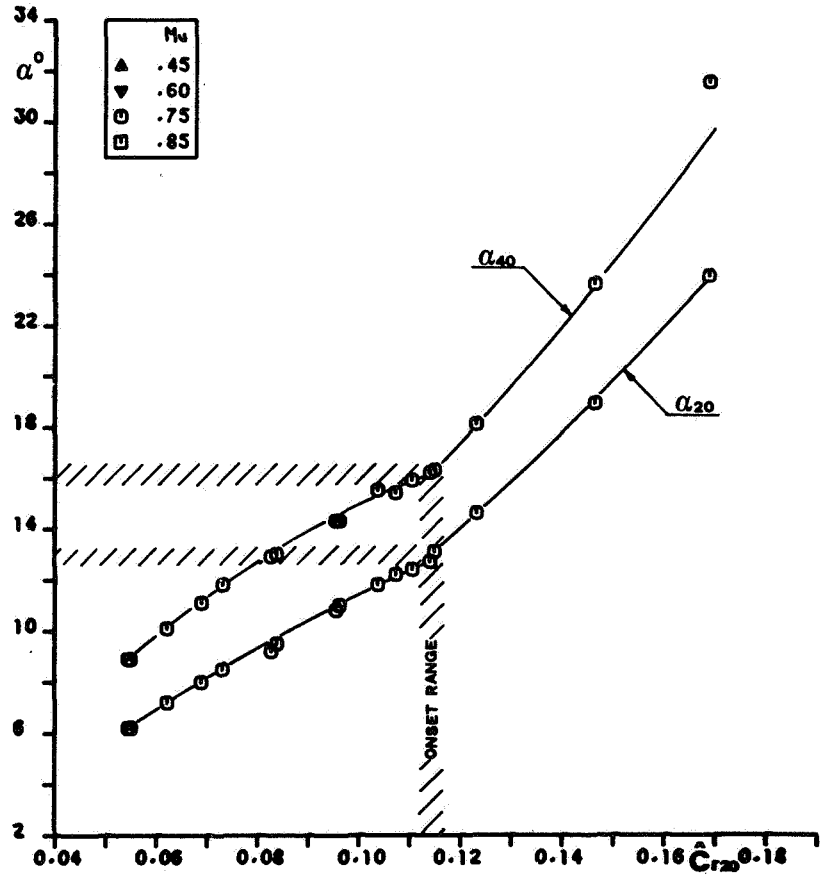

Figure 25. - Absolute flow angles at sections 20 and 40 versus nondimensional radial velocity at section 20. (Configuration C.)

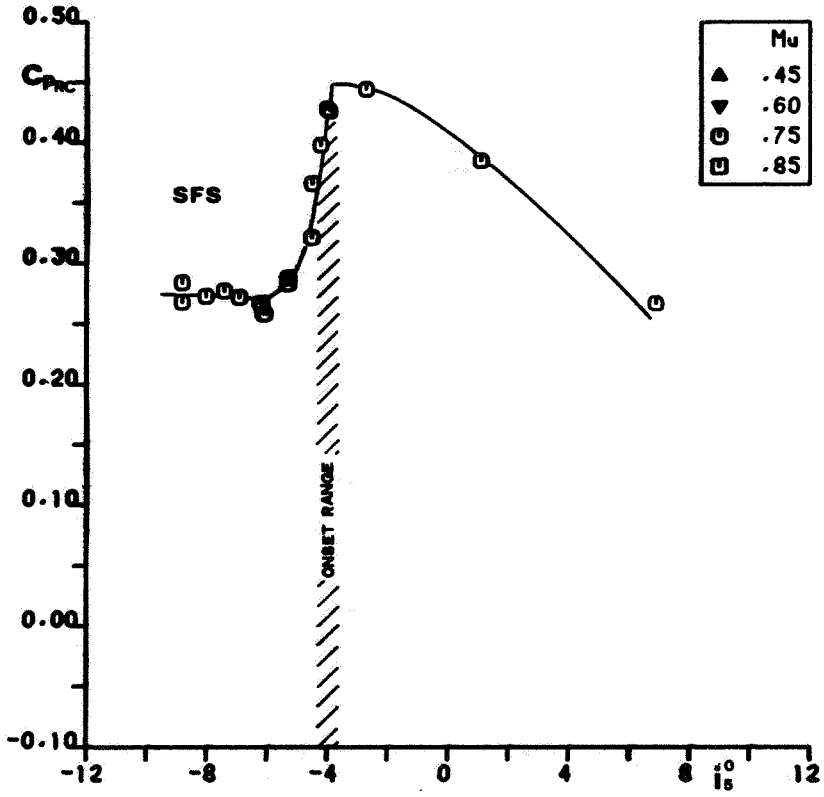

Figure 26. - Return channel pressure recovery coefficient versus incidence angle. (Configuration C.)

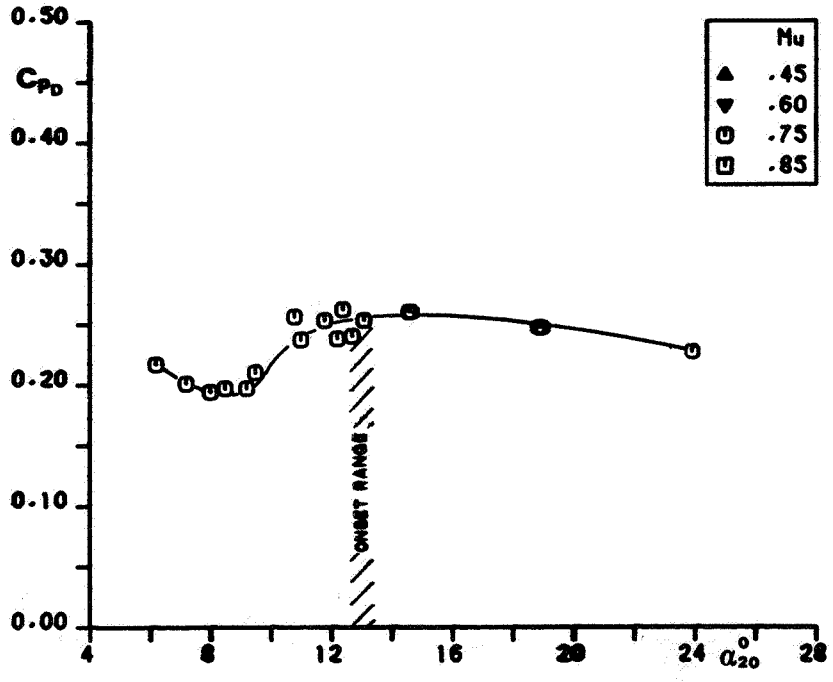

Figure 27. - Vaneless diffuser pressure recovery coefficient versus absolute flow angle at section 20. (Configuration C.)

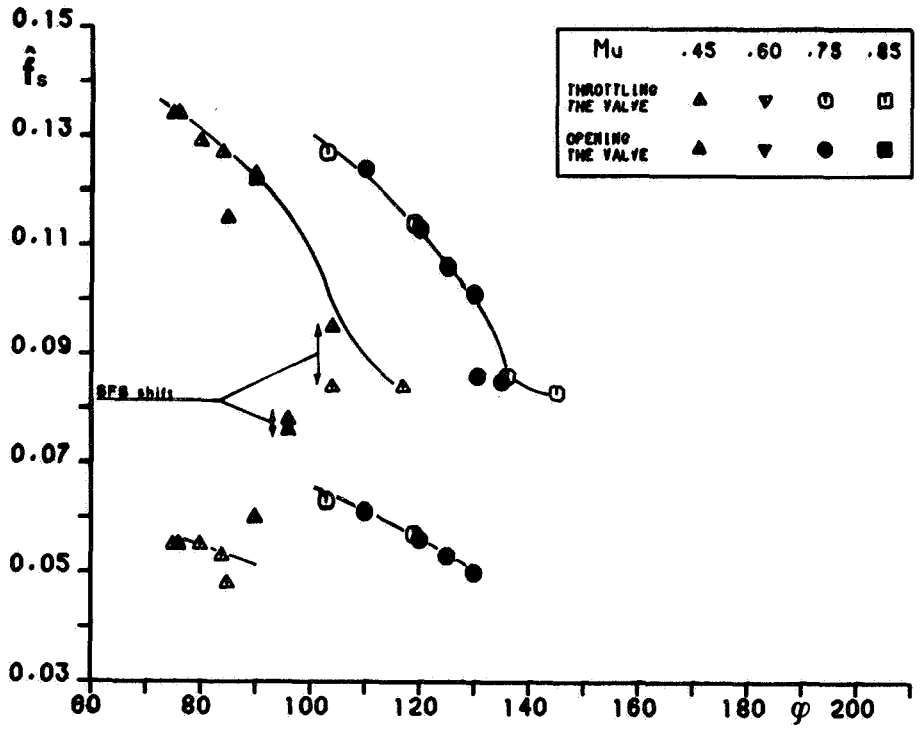

Figure 28. - Normalized observed frequency versus inlet flow coefficient. (Configuration D.)

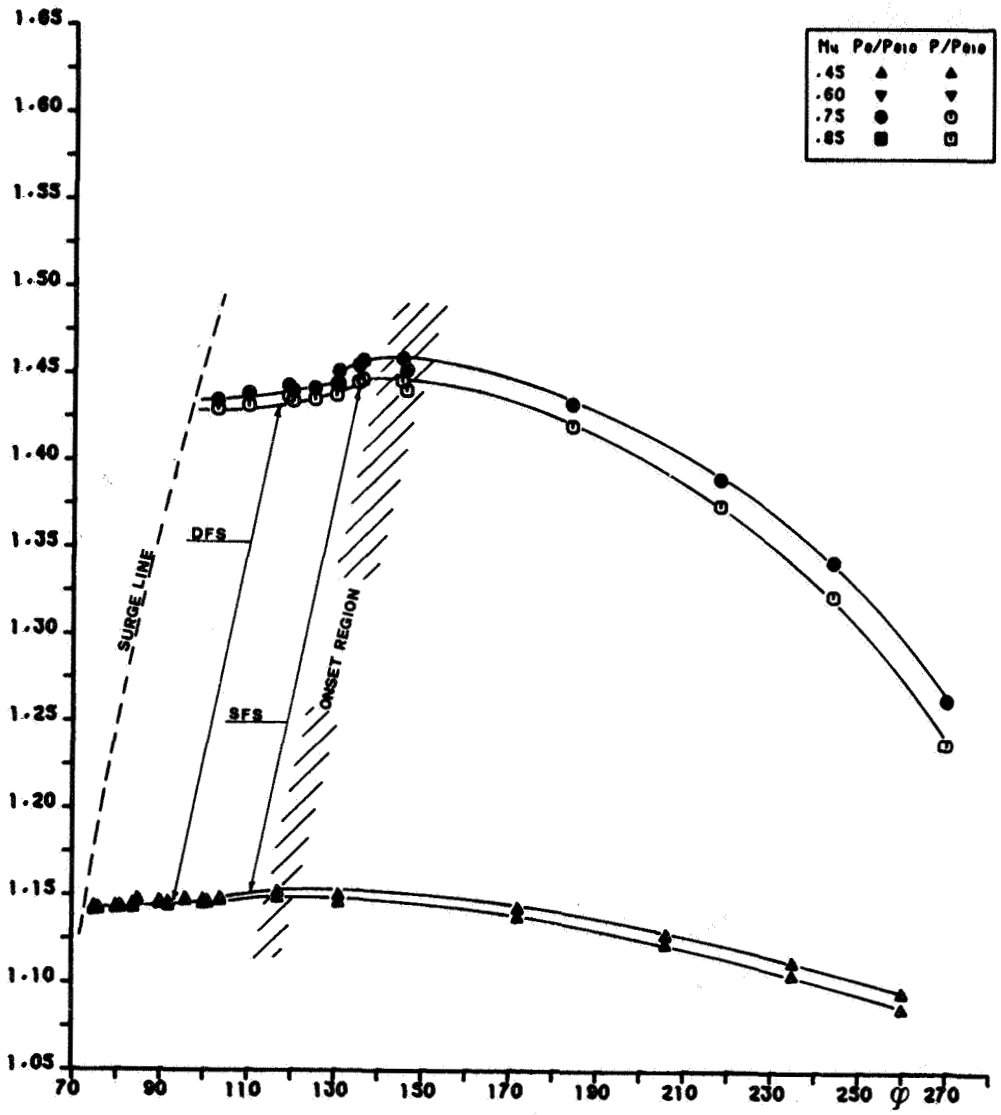

Figure 29. - Static-to-total and total-to-total pressure ratios at section 60 versus inlet flow coefficient. (Configuration D.)

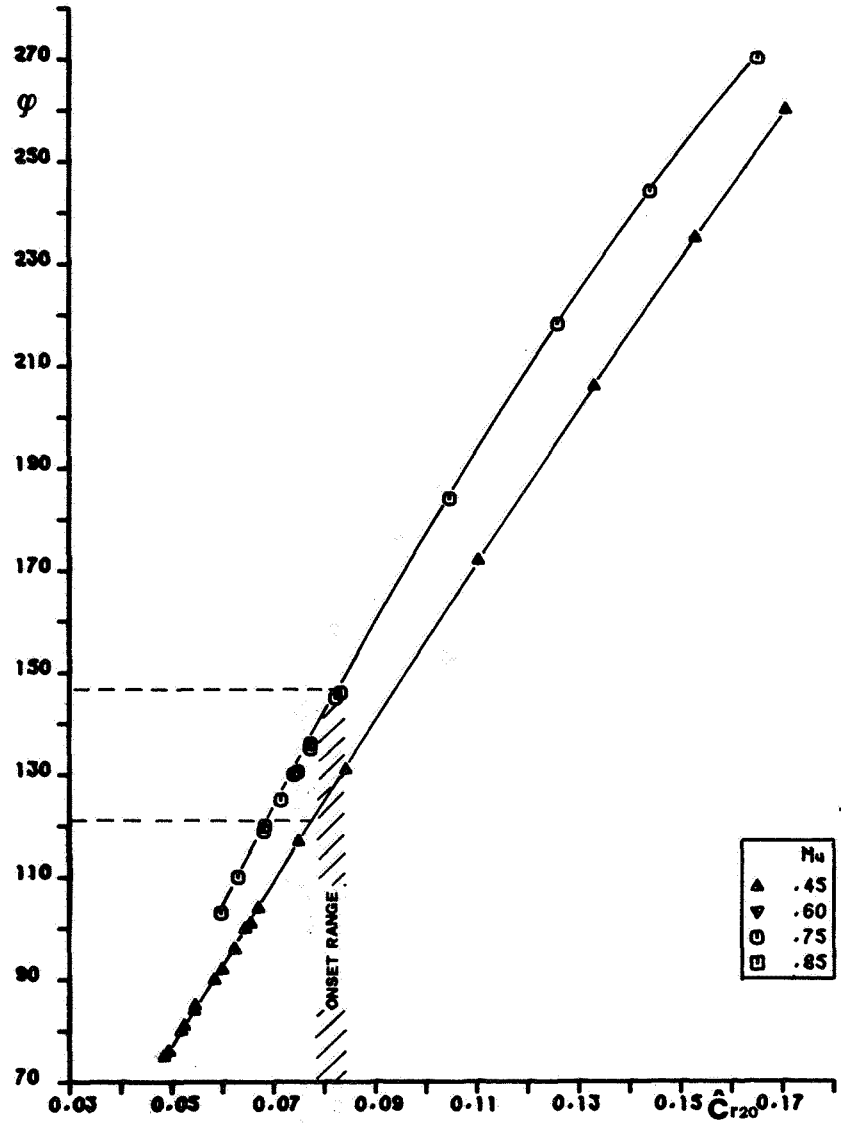

Figure 30. - Inlet flow coefficient versus nondimensional radial velocity at section 20. (Configuration D.)

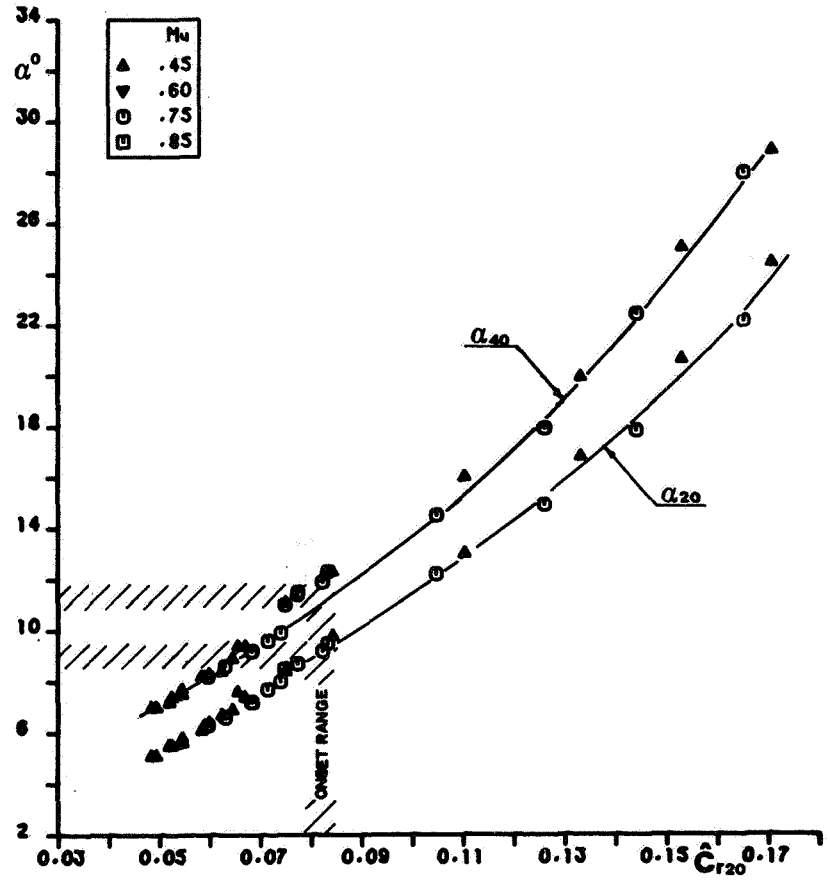

Figure 31. - Absolute flow angles at sections 20 and 40 versus nondimensional radial velocity at section 20. (Configuration D.)

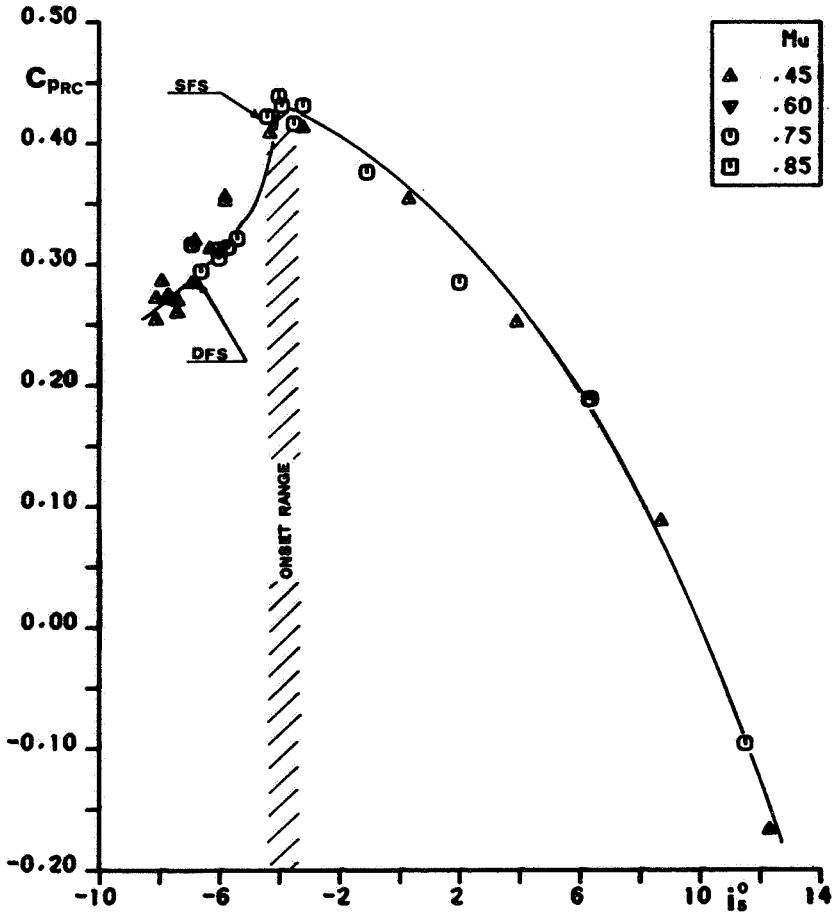

Figure 32. - Return channel pressure recovery coefficient versus incidence angle. (Configuration D.)

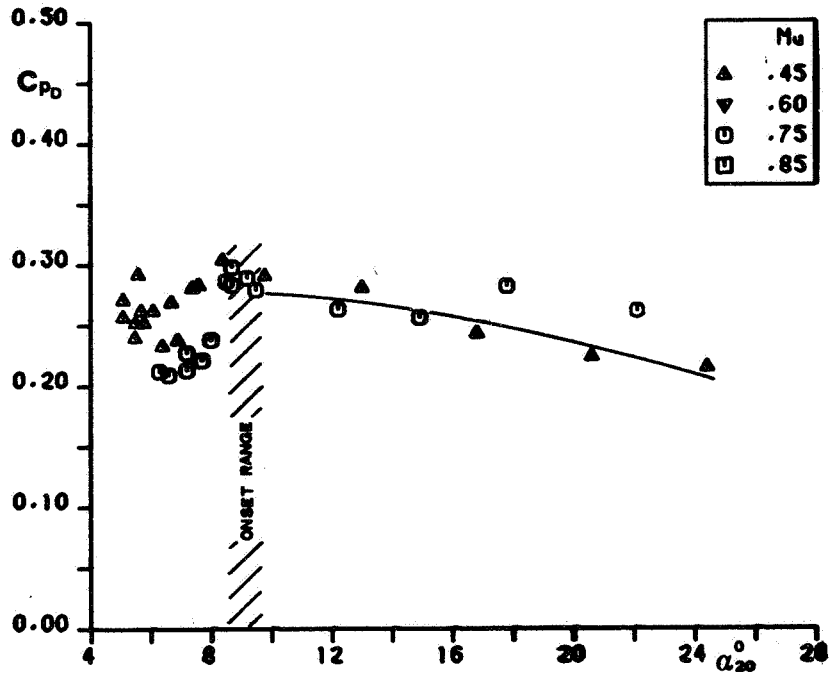

Figure 33. - Vaneless diffuser pressure recovery coefficient versus absolute flow angle at section 20. (Configuration D.)

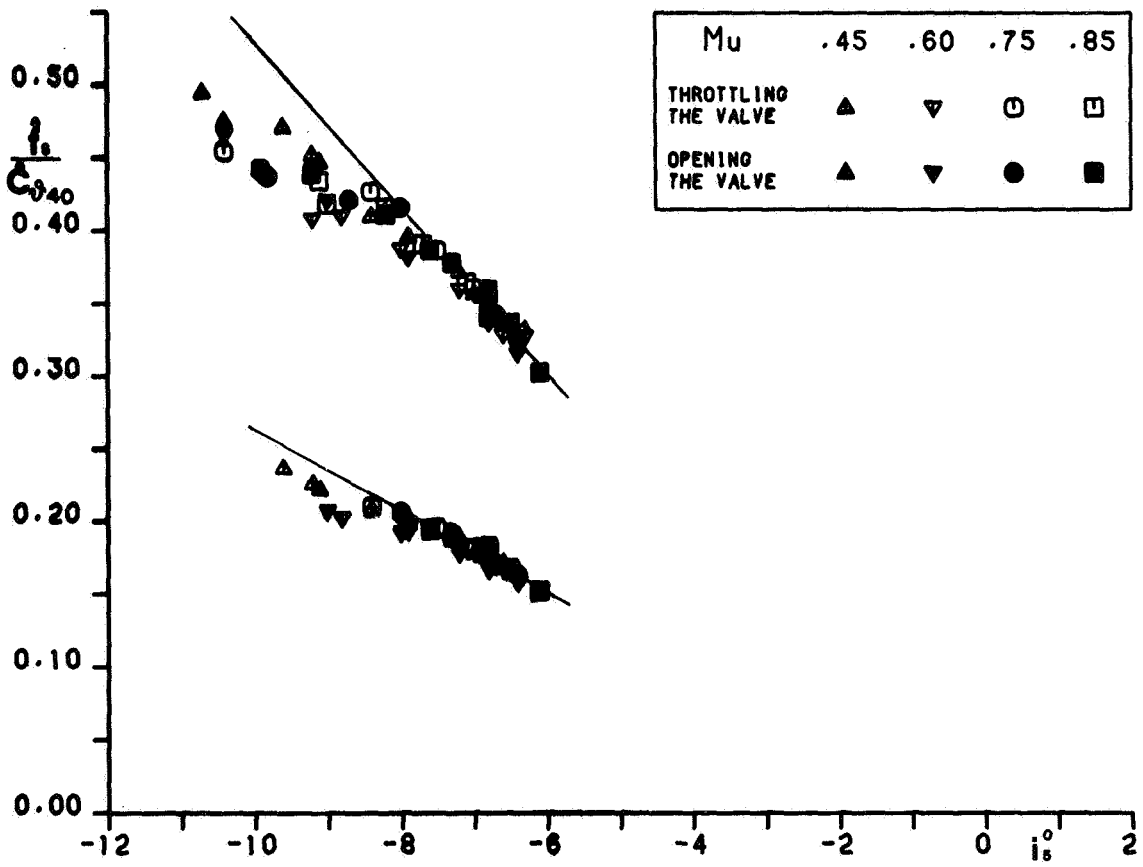

Figure 34. - Nondimensional frequency versus incidence angle. (Configuration A.)

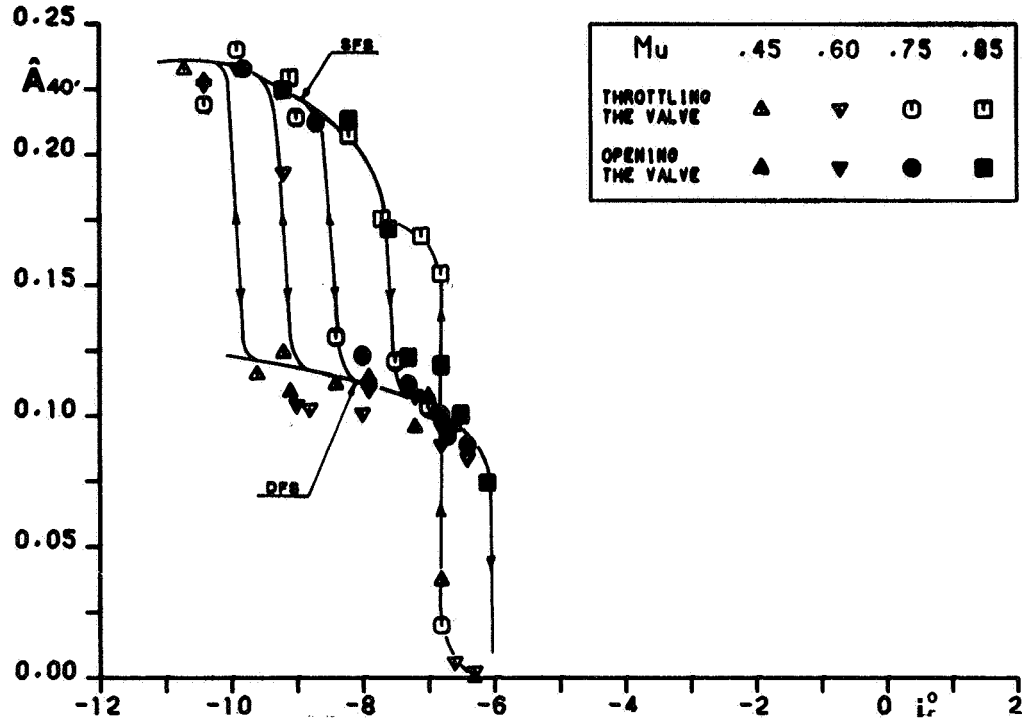

Figure 35. - Nondimensional amplitude (fs) at section 40' versus incidence angle. (Configuration A.)

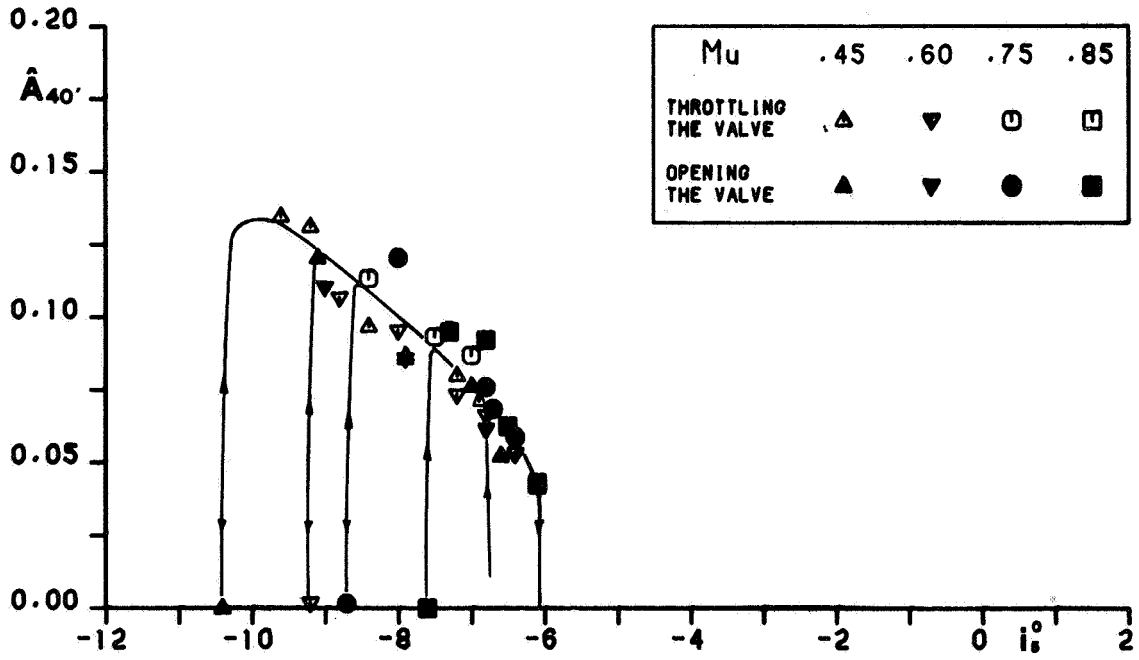

Figure 36. - Nondimensional amplitude (fs/2) at section 40' versus incidence angle. (Configuration A.)

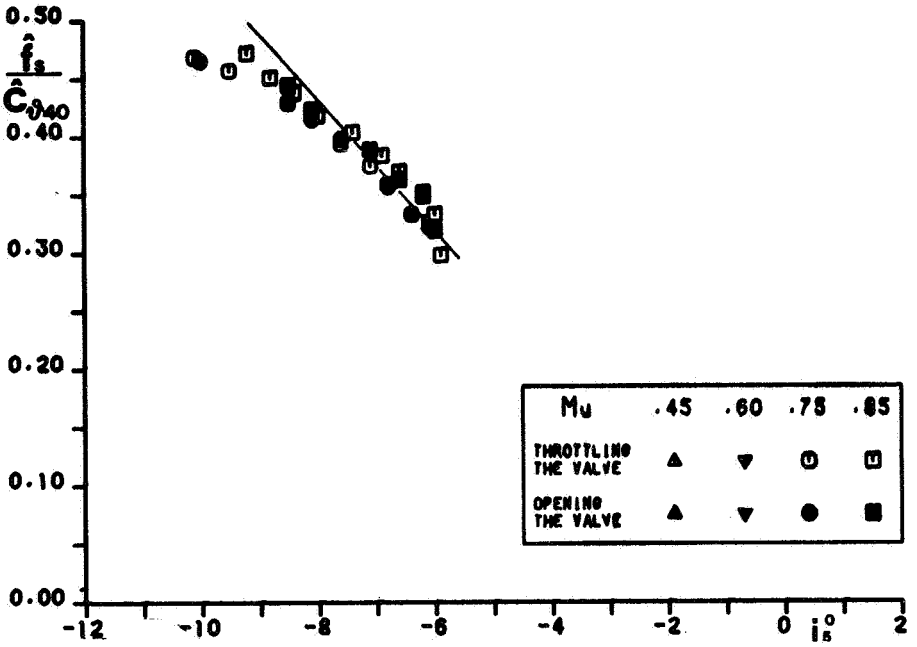

Figure 37. - Nondimensional frequency versus incidence angle. (Configuration A with sandpaper.)

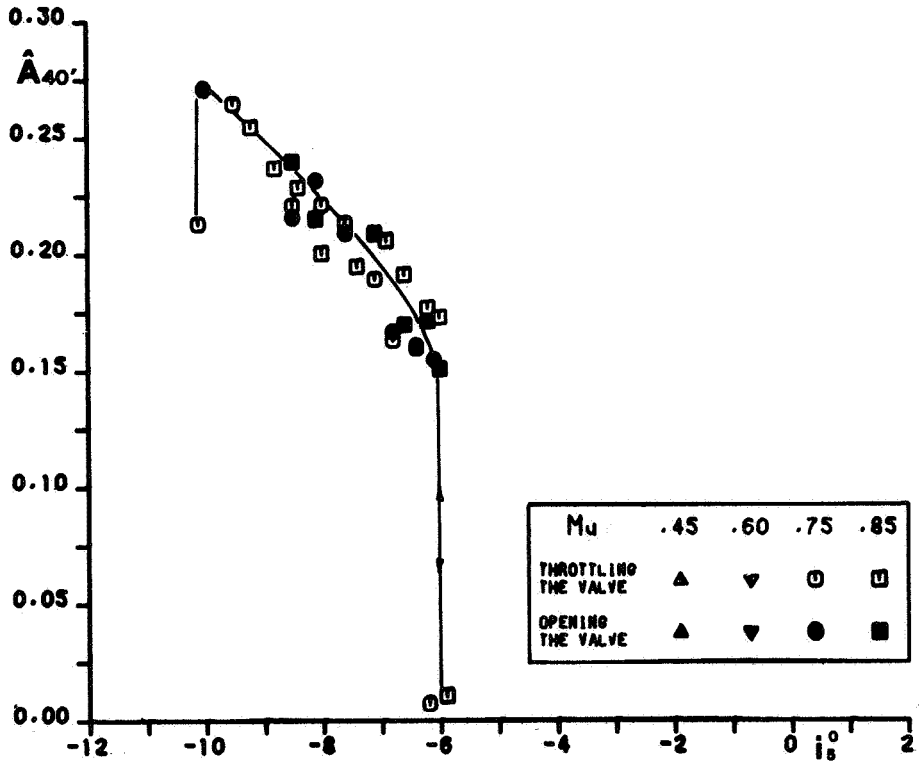

Figure 38. - Nondimensional amplitude at section 40' versus incidence angle. (Configuration A with sandpaper.)

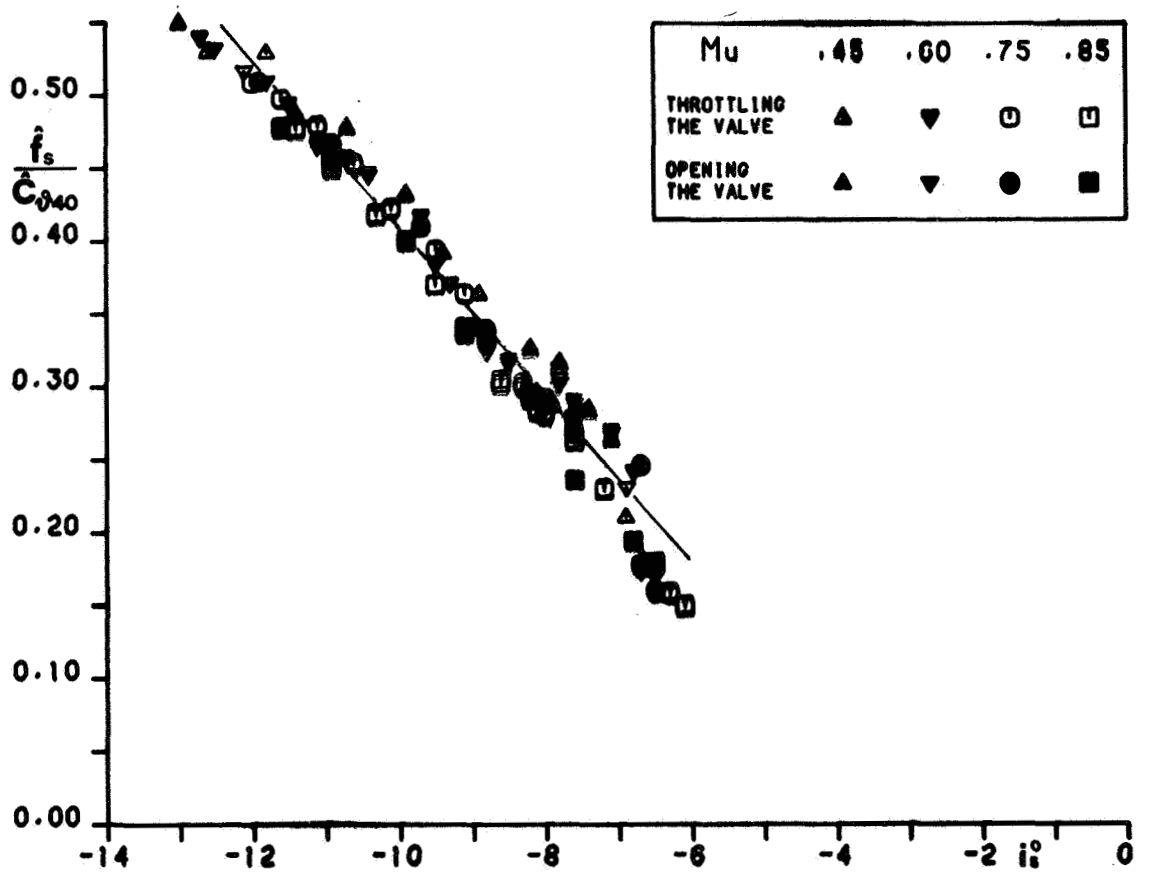

Figure 39. - Nondimensional frequency versus incidence angle. (Configuration B.)

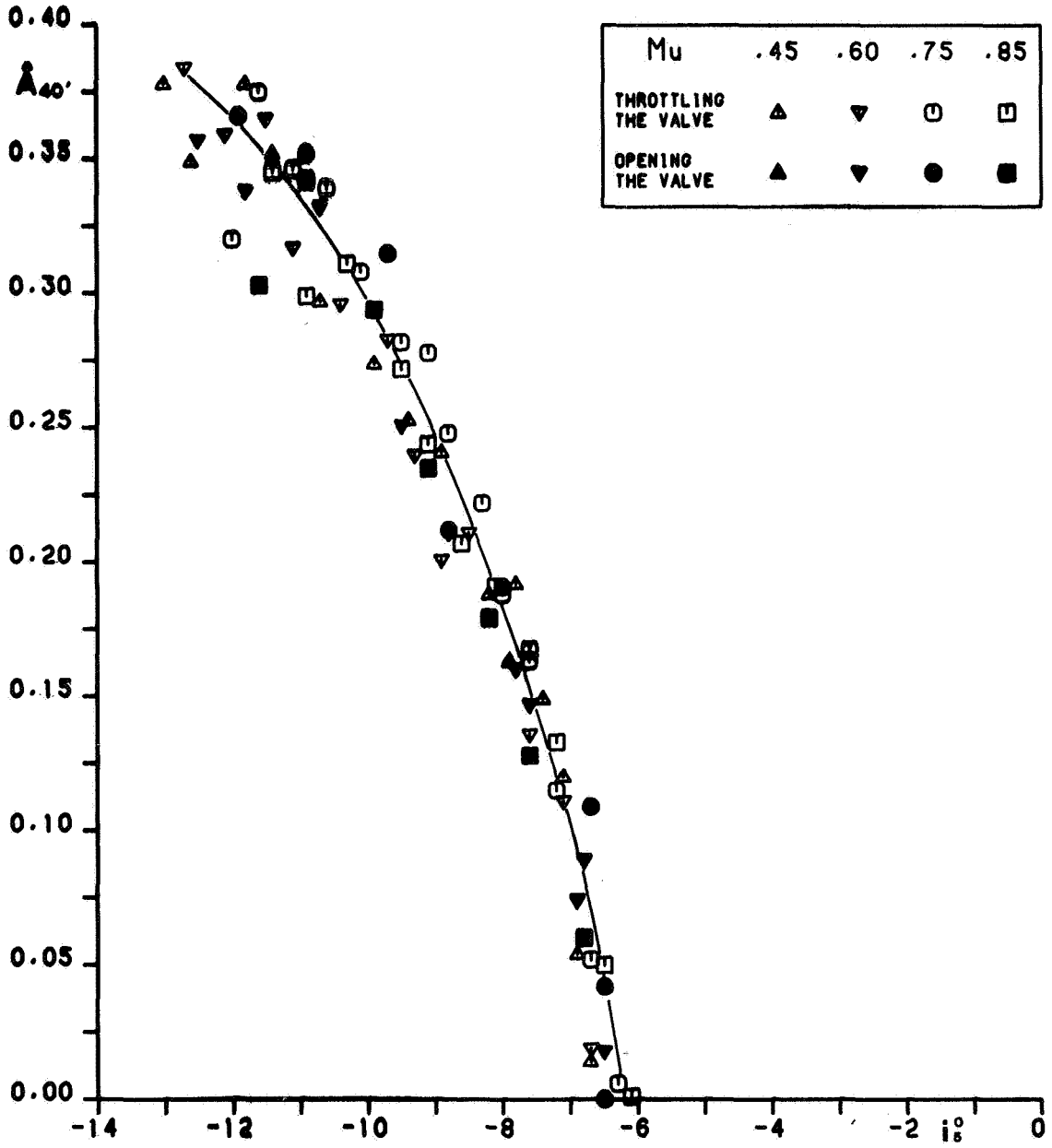

Figure 40. - Nondimensional amplitude at section 40' versus incidence angle. (Configuration B.)

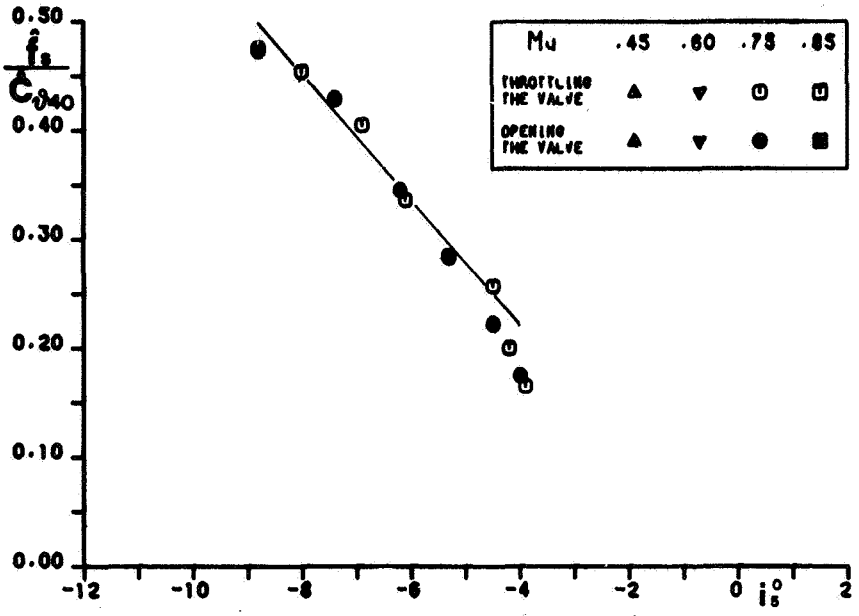

Figure 41. - Nondimensional frequency versus incidence angle. (Configuration C.)

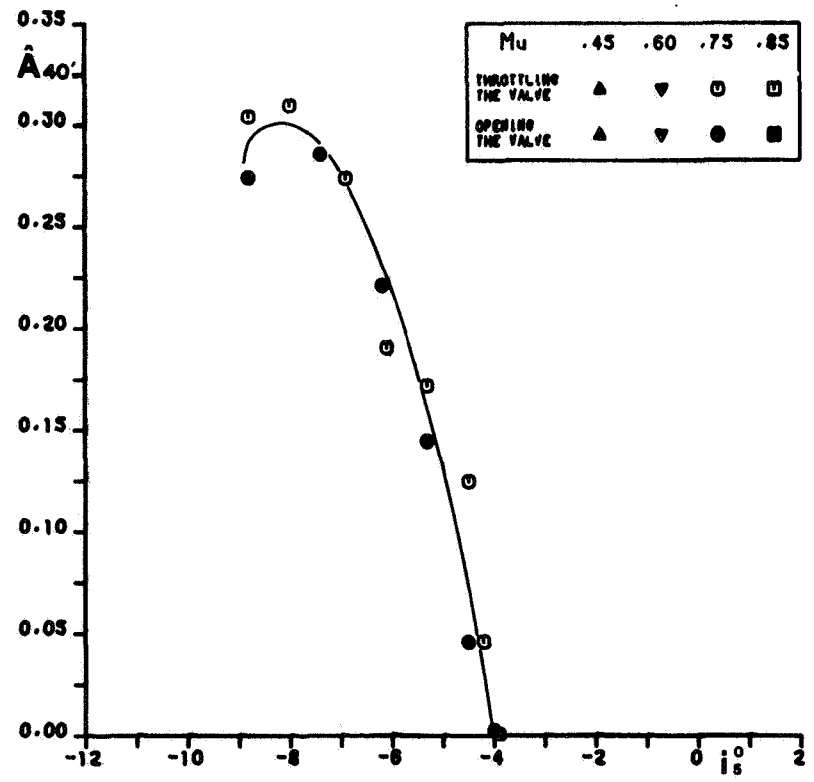

Figure 42. - Nondimensional amplitude at section 40' versus incidence angle. (Configuration C.)

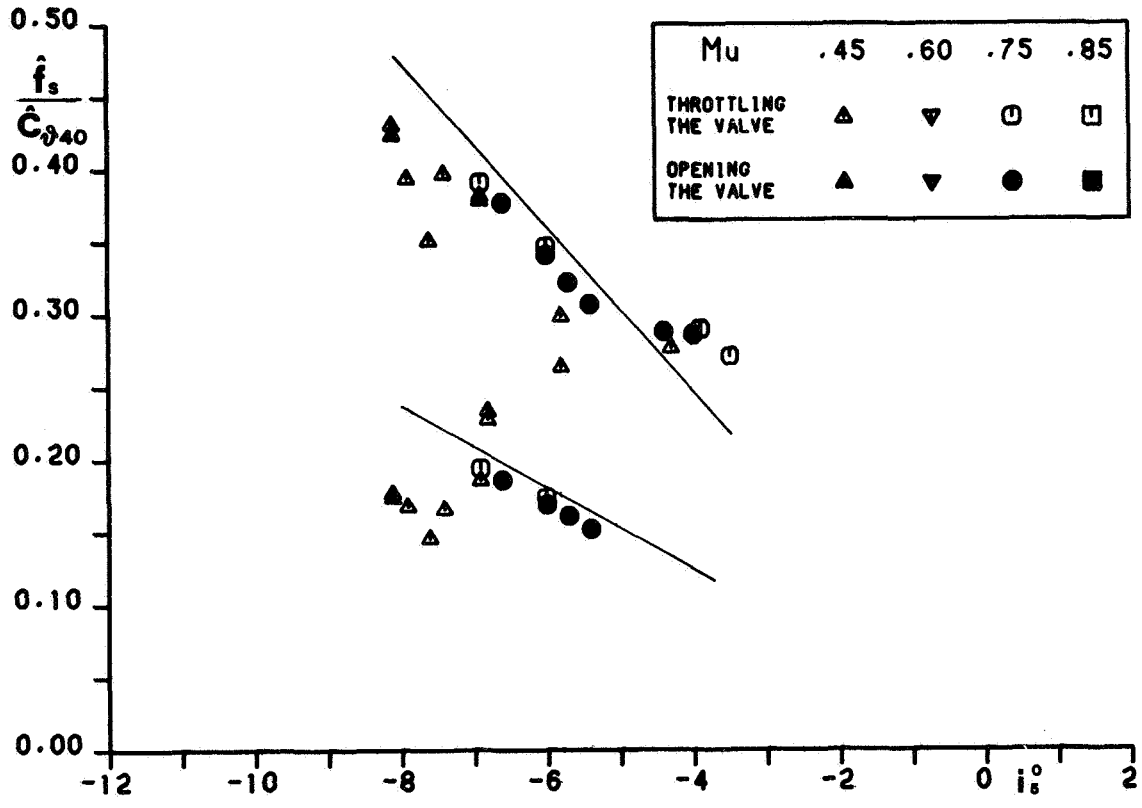

Figure 43. - Nondimensional frequency versus incidence angle. (Configuration D.)

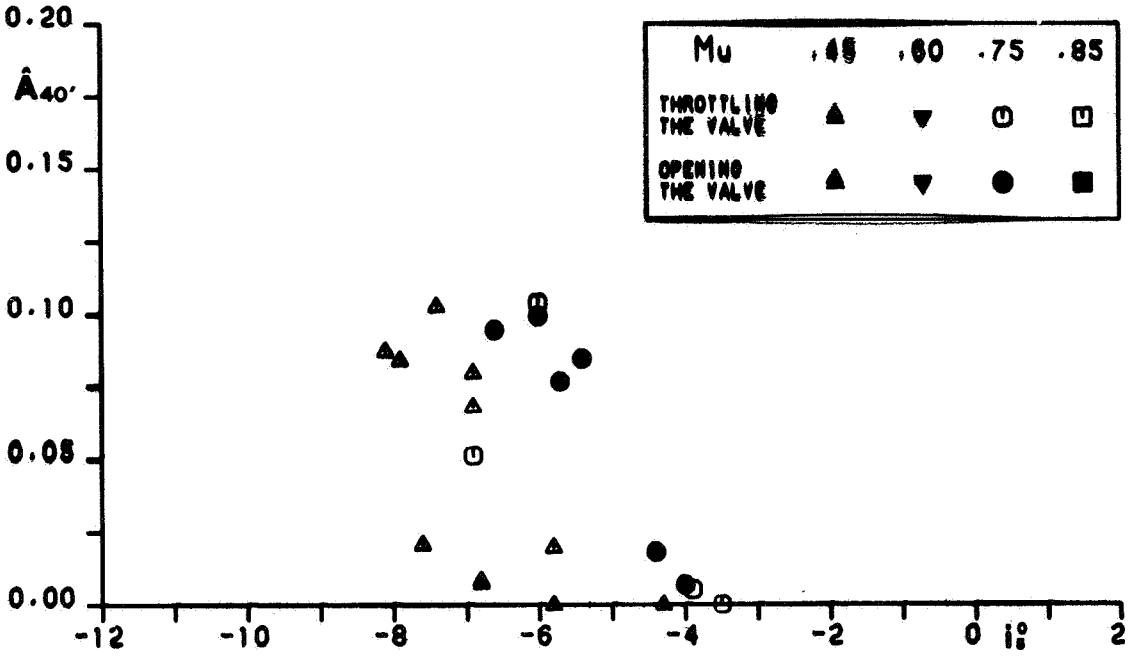

Figure 44. - Nondimensional amplitude (fs) at section 40' versus incidence angle. (Configuration D.)

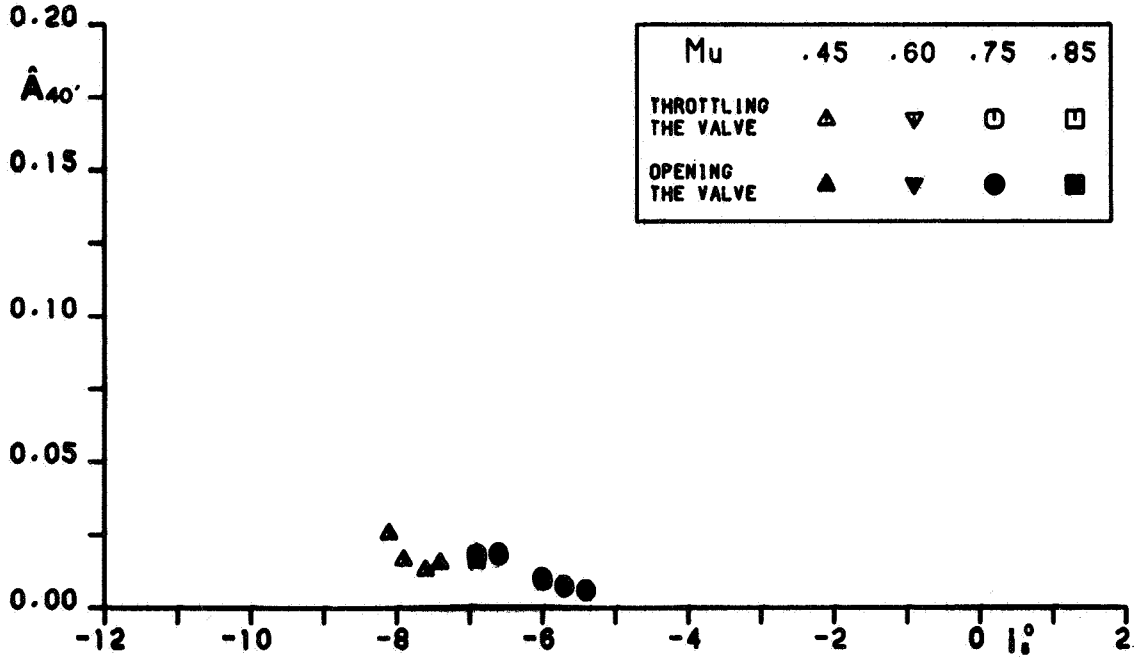

Figure 45. - Nondimensional amplitude (fs/2) at section 40' versus incidence angle. (Configuration D.)

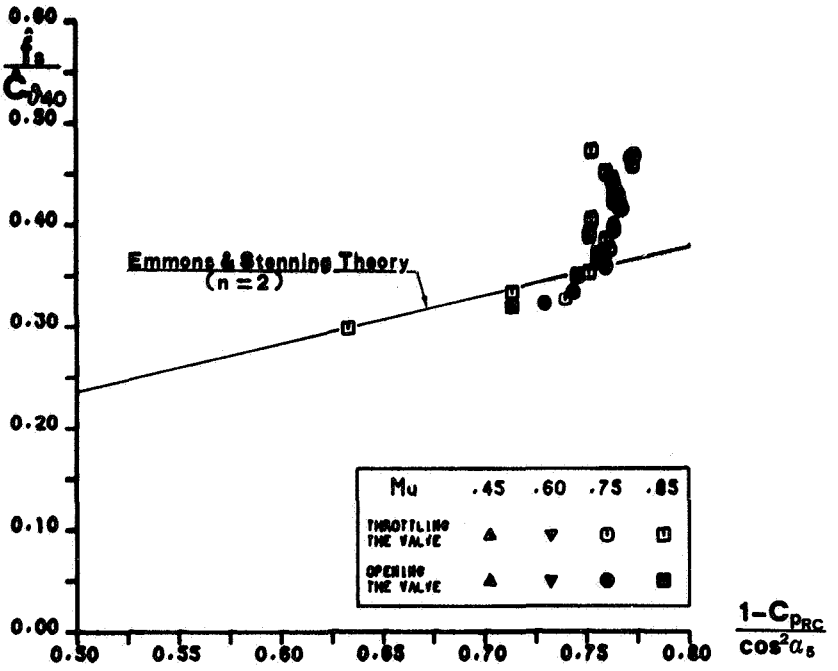

Figure 46. - Nondimensional observed frequency. (Configuration A with sandpaper.)

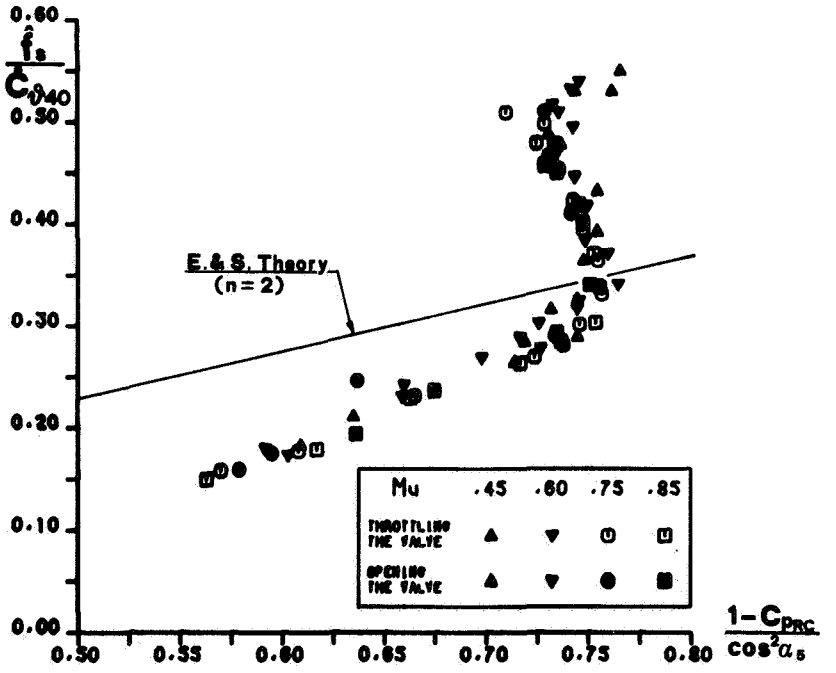

Figure 47. - Nondimensional observed frequency. (Configuration B.)

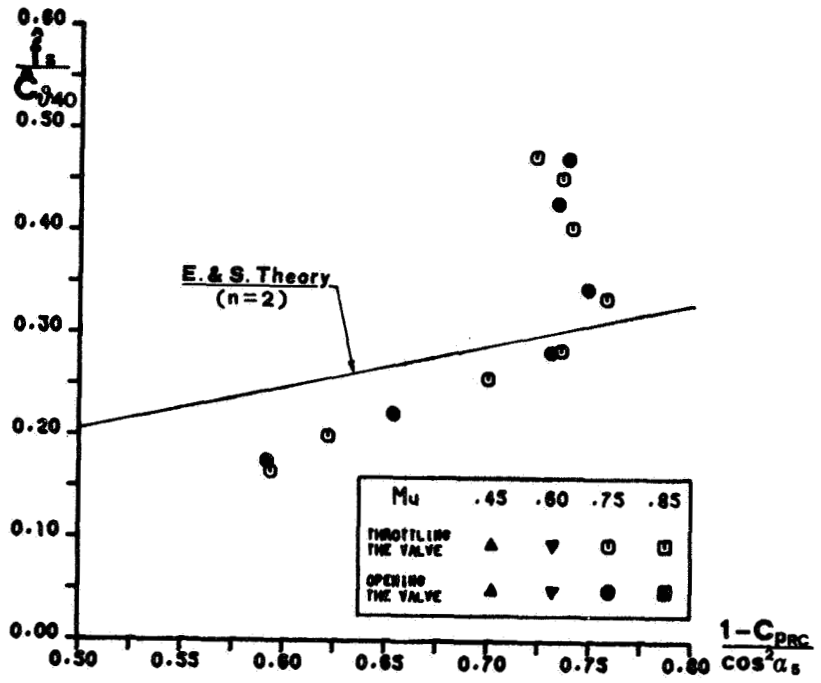

Figure 48. - Nondimensional observed frequency. (Configuration C.)

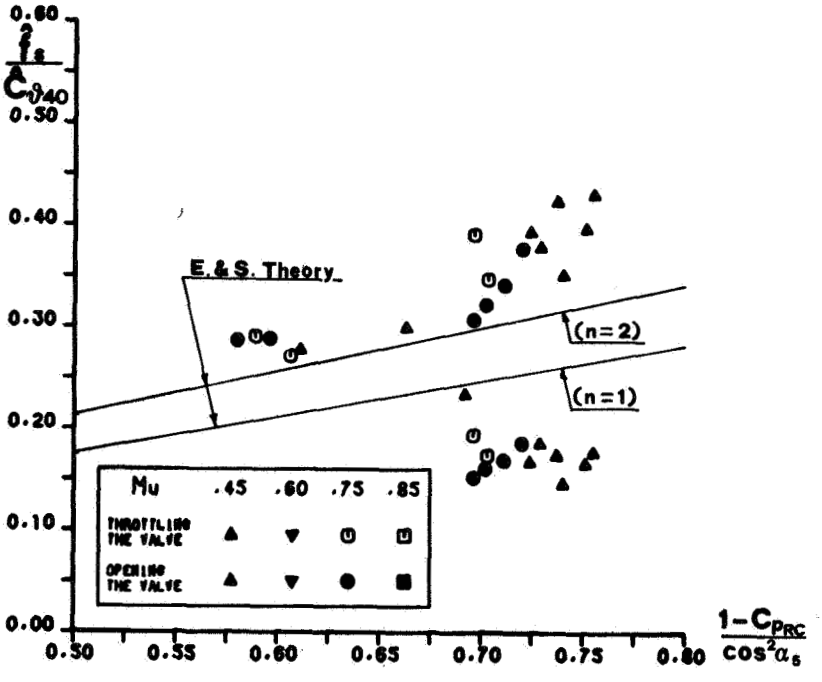

Figure 49. - Nondimensional observed frequency. (Configuration D.)

DYNAMIC STIFFNESS CHARACTERISTICS OF HIGH ECCENTRICITY RATIO BEARINGS AND SEALS BY PERTURBATION TESTING

Donald E. Bently and Agnes Muszynska
Bently Nevada Corporation
Minden, Nevada 89423

In prior work perturbation methodology was done to describe the behavior of lightly loaded bearings or seals. This work helped to clarify the stiffness algorithms and to show the algorithm of the fluid inertia effect.

This paper takes up the much more complex behavior of cylindrical bearings and seals that are statically loaded to eccentricities in excess of 0.7. The stiffness algorithms as a function of static load are developed from perturbation methodology by empirical modeling.

INTRODUCTION

In prior papers by the authors [1-3] perturbation methodology was employed to study the behavior of lightly loaded seals and bearings.

Most studies of rotor instability mechanisms caused by fluid (liquid, steam, or gas) forces, and studies of the behavior of squeeze film dampers have been to measure, by theory and/or by experiment, the bearing/seal dynamic stiffness characteristics. To this effect, most often the perturbation technique, either by imbalance at rotative speed or by static loading with the rotor at its operational speed has been applied. Such examination is perfectly valid, however, the data of the direct and cross stiffness terms are limited to those two data points, instead of across a wide range of perturbation speeds. Because of this, much needed data is not known.

Examination of the direct and quadrature dynamic stiffness characteristics of a rotor system when it is at its operating speed and conditions, is best accomplished by sinusoidal perturbation across the range of speeds where the dynamic stiffness terms are desired. Generally, these are in the range of (a) the average fluid precession rate (usually 40 to 50% of rotative speed in an uncontrolled seal or

bearing), or (b) in the region of the self balance resonances (usually the first one, and usually below operating speed).

In some studies of rotor systems, such as identifying a resonance above maximum operating speed, the perturbation method is easily employed to excite the rotor to obtain this data that is otherwise very difficult or uncertain, or available only from calculation.

For another example, the study of the frequency shift of the forward and reverse resonances due to gyroscopic effects of rotors as a function of rotative speed, the perturbation methodology produces excellent results. For such a study, the rotor is perturbed by circular perturbation, both forward (in direction of shaft rotation), and in reverse (in opposite direction of shaft rotation) for each rotative speed of the rotor system of interest.
Perturbation methodology is also of great assistance in the many faceted studies of full and partial rub mechanisms of a rotor system.

NOTATION

K_D	Direct dynamic stiffness (if symmetric)	lbs/inch
K_{DX}	Direct dynamic stiffness (X axis)	lbs/inch
K_{DY}	Direct dynamic stiffness (Y axis)	lbs/inch
K_Q	Quadrature dynamic stiffness (if symmetric)	lbs/inch
K_{QX}	Quadrature dynamic stiffness (X axis)	lbs/inch
K_{QY}	Quadrature dynamic stiffness (Y axis)	lbs/inch
$K_{ext\ x}$	External spring coefficient (X axis)	lbs/inch
$K_{ext\ y}$	External spring coefficient (Y axis)	lbs/inch
D	Bearing Damping coefficient (if symmetric)	lb sec/inch
D_x	Bearing Damping coefficient (X axis)	lb sec/inch
D_Y	Bearing Damping coefficient (Y axis)	lb sec/inch
M	Rotor effective mass	lb sec^2/inch
M_F	Bearing fluid inertia coefficient (if symmetric)	lb sec^2/inch
M_{FX}	Bearing fluid inertia coefficient (X axis)	lb sec^2/inch
M_{FY}	Bearing fluid inertia coefficient (Y axis)	lb sec^2/inch
ω_R	Rotor rotative speed	rad/sec
ω_P	Perturbation speed (+fwd, -rev)	rad/sec

λ	Ratio of average fluid swirling velocity divided by rotative speed	-----
η	Oil viscosity	centipoise
W_U	Perturbation imbalance	grams
M_U	Perturbation imbalance mass	lb sec^2/inch
R_U	Perturbation imbalance radius	inches
P	Static load on rotor	lbs
A	Angle of application of the static load P measured in direction of shaft rotation from vertical	degrees
$\bar{F}_x$	Force vector in X direction	lbs
$\bar{F}_y$	Force vector in y direction	lbs
t	Time	seconds
j	$\sqrt{-1}$	-----

HISTORY

For several years the authors believed that Ed Hull [4-6] did the first published (and some unpublished) experiments, of perturbing a rotor system across a frequency range (at other than synchronous or steady state) in 1955, but recently found a reference in Paul Trumpler's book [7], to Stone and Underwood [8], dating the methodology back to 1947, so it is possible that other earlier work exists.

Even though these researchers showed the resultant amplitude and phase of the perturbation correctly, neither took the next step of dividing the input force vectors by the motion vectors to obtain the direct and quadrature dynamic stiffnesses. However, both researchers did brilliant work in obtaining vector motion measurements considering the extremely crude electronics tools that were available to them at the time they did their work.

APPLICATION OF PERTURBATION METHODS IN ROTATING MACHINERY

To input a perturbation of either motion or force to a mechanical system, a wide variety of methods may be employed, such as impulse, step white noise, square waves and so forth.

However, when the direct and quadrature dynamic stiffness coefficients of a rotating machine are desired, then the perturbation forcing method becomes highly restricted. It is necessary to use continuous sinusoidal perturbation with high accuracy of phase and amplitude of both the force (perturbation by force) as well as the motion (perturbation by motion).

There is a free choice of driving the system with either a known motion vector and observing the resultant force vectors, or driving the system with a known force vector and observing the motion. However, it is extremely difficult to build a test system to drive a known input motion, and relatively easy to build a system with a known input perturbation force. Further it is much easier to measure response motion vectors than to measure response force vectors. As a result, the authors chose to input with a known amplitude and phase a sinusoidal perturbation force, and observe the response motion vectors. This methodology may be used to test a real rotor system as well as a laboratory experiment. The reduction of the data is equally difficult with either method.

There also appears to be a free choice of whether to apply the perturbation force to the rotor casing or directly on to the shaft. The authors chose to directly perturb the shaft as close as possible to the bearing or seal under test in order to eliminate or minimize the possible errors introduced by the complexities of any other method.

Since two degrees of freedom of the rotor motion are involved, there is one more vital consideration of the sinusoidal perturbation forcing input: (1) it may be in one radial axis, such as vertical (2) it may be circular forward, or circular reverse, or (3) it may be somewhere between these, specifically an ellipse with forward or reverse characteristics.

When gyroscopic effects are the subject of study, it is obvious that circular perturbation force must be employed, as any other force (elliptical or unidirectional), contains a mixture of forward and reverse components. Only forward circular perturbation yields the forward resonances clearly, and only reverse circular perturbation yields the backwards resonances clearly.

The ideal perturbation system when the dynamic stiffnesses are not symmetric is to maintain a resultant perturbation motion of circular nature. This may

be achieved using Adams' method [9] which is to introduce a circular perturbation motion or else to adjust the amplitude and phase of the input perturbation force to obtain a circular motion response. Both methods yield directly reducible dynamic stiffness terms, but both are very difficult to accomplish. As a result, the studies in this report were done with circular sinusoidal foward and reverse input perturbation force, as in previous studies [3].

LABORATORY STUDY OF STABILITY CHARACTERISTICS OF A 360° LUBRICATED CYLINDRICAL BEARING AS A FUNCTION OF STATIC LOAD, ROTATIVE SPEED, OIL SUPPLY PRESSURE, AND VISCOSITY

The experimental rotor set-up for the bearing/seal perturbation test is shown in Figures 1 and 2.

In previous experiments, the authors studied the direct and quadrature stiffness terms of the same bearing and same rotor configuration for light preloads. In the present study, the constant preload was varied from 0 to 32 lbs., (increasing by 4 lbs at each sequence of tests) in order to observe the behavior of the dynamic stiffness terms when the oil film is broken (or partially broken) in the negative pressure region of the bearing. Rotative speeds of 0, 100, 200, 300, 400, 500 and 600 rad/sec were employed with circular perturbation frequencies from - (reverse) 400 rad/sec to + (forward) 400 rad/sec. The bulk of these studies were with a constant perturbation imbalance weight of 28 grams, and with a constant oil supply pressure of 5 psi. At the end of the tests, the oil pressure was raised to 20 psi, with results shown in Figure 5. Temperature was held a oil outlet constant at 65°, 90°F, and 130°F. T-10 turbine oil was employed for all data.

For zero, or light loads and symmetric rotor, the vertical and horizontal force algorithms are:

Eq. (1) $\bar{F}y=[K_{ext}+j\omega_p D-(\lambda\omega_R-\omega_p)^2 M_F]y + j[\lambda\omega_R D]\bar{x}$

Eq. (2) $\bar{F}_X=[K_{ext}+j\omega_p D(-\lambda\omega_R-\omega_R)^2]\bar{x}-j[\lambda\omega_R D]\bar{y}$ and since

Eq. (3) $\bar{x}=j\bar{y}$ because the resultant orbit are circular, equations 1 and 2 reduce to:

Eq. (4) $\vec{F}_Y=\bar{y}[K_{ext}-(\lambda\omega_R-\omega_p)^2M_F-\omega_p{}^2M+j(\omega_pD-\lambda\omega_RD)]$

Eq. (5) $\vec{F}_X=\bar{x}[K_{ext}-(\lambda\omega_R-\omega_p)^2M_F-\omega_p{}^2M+j(\omega_pD-\lambda\omega_RD)]$

The dynamic stiffness vectors are:

Eq. (6) $\vec{K}_Y=K_D+jK_Q=\vec{F}_y/\bar{y}$

Eq. (7) $\vec{K}_X=K_D+jK_Q=\vec{F}_x/\bar{x}$

with the result that for a symmetrical, lightly loaded 360° lubricated bearing, or a lightly loaded seal it becomes:

Eq. (8) $K_D=K_{ext}-\omega_p{}^2M-(\lambda\omega_R-\omega_p)^2M_F$ Direct Dynamic Stiffness

Eq. (9) $K_Q=(\omega_p-\lambda\omega_R)D$ Quadrature Dynamic Stiffness

More detailed deviation of the above relationships can be found in the publications [1-3].

It may be noted that direct dynamic stiffness versus perturbation speed is parabola and offset from zero speed toward the average swirl speed of the oil ($\lambda\omega_R$), and that the quadrature term consists of a straight line with a value of zero at a perturbation speed of exactly $\omega_p=\lambda\omega_R$ (the traditional "½ speed" of oil whirl). The quadrature term at zero frequency perturbation represents the famous tangential term, otherwise known as "aerodynamic cross coupling" term, "cross coupled" spring coefficients "K_{XY}", "K_{YX}", etc. As a matter of fact, this is the oil wedge support term of a cylindrical bearing, from the single action that the shaft must move sideways (at quadrature) a sufficient distance to create a constriction of the oil in order to form a pressure wedge 90° behind this constriction in order to support the load. (As such, a cylindrical bearing or seal is an elementary servomechanism with very poor stability control.)

Static Load Study

Before running the forward and reverse perturbation tests, a complete series of static loading tests were run across the variations of static load, static load

angle, viscosity, and oil pressure while maintaining the rotor constant operational speed. A brief matrix summary of the results of the steady state deflection versus load tests are shown in Figures 3, 4 and 5.

Since ω_P is zero and K_{ext} is also zero for these sets of tests, equations (8) and (9) reduce to the following equations (10) and (11) for the lightly loaded condition. This extends from zero load to wherever the knee (an evident non-linearity) of the static displacement occurs.

(10) $K_D=-\lambda^2\omega_R{}^2M_F$ Static Direct Stiffness
(12) $K_Q=-\lambda\omega_R D$ Static Quadrature Stiffness

Clearly, the fluidic inertia term, $(-\lambda^2\omega_R{}^2M_F)$, controls the direct dynamic stiffness, and equally clearly, the "cross spring" term, (fluid wedge support term $-\lambda\omega_R D$), controls the quadrature stiffness in the lightly loaded bearings.

Since the wedge support term is formed by the shaft moving sideways to the static load to form a restriction to form the wedge support, the shaft deflection is ahead of the static load angle by 90 degrees in the direction of rotation. When the direct term Eq. (8) is net negative, as in the above situation of the negative direct spring effect of fluid inertia, then the shaft attitude angle is in excess of 90 degrees.

Figure 3 shows the curves of attitude angle and eccentricity ratio for various preload at temperatures 65°F, 90°F, and 130°F of T-10 oil. It may be observed that the attitude angle is highest for highest viscosity at light loads, but that this reverses at high static preload. This infers that fluid inertia is a function of viscosity, but it is the belief of the authors that this relationship is a secondary result of the continuity of the oil film in the negative pressure region. This graph (and other results shown later) indicate that if the fluid film in the negative pressure region collapses, or partially collapses, the fluid inertia term is drastically reduced. It is predominantly this effect that is shown in the graph. The variation of the eccentricity ratio and attitude angle as a function of rotative speed at constant oil temperature (90°F) and pressure (5 psi) is shown in Figure 4.

Somewhat similar to the previous picture, the effect reverses from low to high

static load, with ever increasing attitude angle as a function of rotative speed until the knee of the curve (following the fluid inertia term $-\lambda^2\omega_R{}^2M_F$), then reversing at the knee. Again, the authors believe that this loss of the fluid inertia term is primarily a function of the partial collapse of the film in the negative pressure region. Simply, when air moves in, to replace the oil in either the steady state or dynamic negative pressure region, there is no need to jet oil through the thin film region from the high pressure region to the low pressure region; therefore major decrease of the fluidic inertia term occurs.

Figure 5 shows the effect of the static deflection versus static load for oil supply pressure variations from 5 to 25 psi, at constant speed of 200 rad/sec and oil temperature of 90°F. Here a new type of inversion is observed.

Before the knee of the curve, the attitude angle increases with pressure from 5 to 20 psi, but at 25 psi it is clearly reversed. This shows a collapse of the fluid inertia term between 20 and 25 psi supply pressure. It is believed that the collapse of the fluid inertia term in this instance is because the new oil feed to the bearing supplies the negative pressure region, alleviating the need for the fluid inertia effect. Note that this is for a different reason than occurs in the other tests. It should be noted that these deflections versus load graphs also reverse beyond the knee of the curve.

The Perturbation Tests

Hundreds of runs were made to establish the direct and quadrature dynamic stiffness terms. These tests were predominantly run at 5 psi oil supply pressure (with a few at higher pressure), with rotative speeds from 100 rad/sec to 600 rad/sec, in steps of 100 rads/sec, with oil temperatures of 65, 90 and 130°F, (thus viscosities of 64.3, 35.6 and 15 centipoise), with perturbation speeds of 30 to 400 rad/sec, mostly forward, (and enough in reverse to show the typical stiffness behavior), and with a 28 gram perturbation weight at 1.1 inch radius. A very brief summary of these tests are shown in this report.

Figure 6 shows the direct and quadrature dynamic stiffness is at zero and light preloads at three viscosities, at 100 rad/sec, at 5 psi oil supply pressure, and for forward and reverse perturbation. The quadrature stiffness shows its regular performance. (1) zero crossover at 48% of rotative speed, which is the average

swirl ratio λ, (2) a slope, which is D lbs.sec/in of damping directly dependent on viscosity, and (3) the oil wedge support term (cross spring) a direct function of λ, ω_R rotative speed, and D damping.

The direct term shows its typical parabola behavior due primarily to the fluid inertia term. For very light dynamic perturbation loads, as previously studied, the fluid inertia term is independent of viscosity. However, with the heavy dynamic load employed for this test, and for the very low oil supply pressure, the fluid inertia term increases with increasing viscosity. The authors believe that this shift of the fluid inertia term is due to partial loss of the negative pressure region at the lower viscosities.

The figures 7 through 10 show the effects on the dynamic stiffness terms with static loading of 0 to 24 pounds in steps of 4 lbs. These runs are at an oil supply pressure of 5 psi, at an outlet oil temperature of 65°F (64.3 centipoise) and at constant rotative speed of 300 rad/sec.

It may be observed that the dynamic quadrature stiffness tends to increase in slope with higher static load, but that this is a small effect, with a 24 pound static load indicating an increase in damping of about 50 percent over the damping at zero static load.

However, the direct dynamic stiffness show much greater variations with static load, especially (1) at 24 pounds, where a large increase in the dynamic direct vertical spring term occurs, and (2) at perturbation rates from about -10% of rotative speed to about +30% of rotative speed. The horizontal direct dynamic stiffness term shows increase as a function of static loading more evenly for each increment of static load. These results should be related to the deflection versus static load shown in Figures 3 and 4.

CONCLUSIONS

First, it may be concluded that for a 360 degree lubricated bearing a simple algorithm to describe its dynamic behavior is virtually impossible when any condition exists which allows air to be pulled into the negative pressure region. This may be caused by many factors, including low oil supply pressure or broken flow, high static loading, high dynamic loading, low rotative speed, etc. It

follows that it is very difficult to establish a clear mathematic rule for stability for such a bearing. Cole and Hughes [10] stated essentially the same thing on their remarks of a Boeker and Sternlicht paper [11] 30 years ago with less evidence, and apparently no knowledge of the fluid inertia term or extreme possible variations of that term. "During the course of some film extent experiments on a transparent sleeve bearing (1 X 1 X 0.002 in.) with a single-hole oil entry, we have observed that whirl at frequency near to half shaft speed may occur over a wide speed range but only while the film remains complete. As soon as the film breaks, as a result of increased eccentricity ratio or changed oil-supply conditions, whirl ceases."

Second, it is concluded that a 360 degree lubricated bearing is not a good prototype model for work with liquid or gas seals. For liquid seals, the pressure of the supply is orders of magnitude higher than that of typical oil supply pressures, so that the fluid inertia term will be much greater and much more consistent in the speeds of interest. For the gas seal, there can be no occurrence of an incomplete or cavitated film in the negative pressure region, so that much higher similarity may be expected. However, the principle of feeding the test bearing from the center should be a very good method of studying seals, as a seal test rig may be center fed at high pressure, and the low pressure at the ends, which can be equivalent to two halves of a seal with high pressure at one end, and low pressure at the other end. With this configuration a test stand for seals is simple to construct and use, as there is no secondary high pressure seal area on the rotor system. If anti-swirling methods are being employed and tested. However, they would be in opposite directions on opposite ends of the test seal.

REFERENCES:

1. Bently, D.E., Muszynska, A., "Stability Evaluation of Rotor/Bearing System by Perturbation Tests," Rotordynamic Instability Problems in High Performance, Turbomachinery, NASA CP-2250, 1982, pp. 307-322.

2. Bently, D.E., Muszynska, A., "Oil Whirl Identification by Perturbation Test," Advances in Computer-Aided Bearing Design, ASME/ASLE Lubrication Conference, Washington, D.C., October 1982.

3. Bently, D.E., Muszynska, A., "Perturbation Tests of Bearing/Seal For Evaluation of Dynamic Coefficients," Symposium on Rotor Dynamical Instability, Summer Annual Conference of the ASME Applied Mechanics Division, Houston, Texas, June 1983.

4. Hull, E.H., "Journal Bearing Behavior Under Periodic Loading," G.I. Research Laboratory, Rep. No. 55-RL-1354, Schenectady, New York 1955.

5. Hull, E.H., "Oil Whip Resonance," Trans. ASME, October 1958

6. Hull, E.H., Darrow, K.A., "Hydrodynamic Oil Film Stiffness", G.I. Research Laboratory, Rep. No. 59-RL-2217, Schenectady, New York 1959.

7. Trumpler, Paul R., "Design of Film Bearings," Dept. of Mechanical Engineering, University of Pennsylvania, 1966.

8. Stone, J.M., Underwood, F.A., "Load Carrying Capacity of Journal Bearings," SAE Quart. Trans., 1 (1947), p. 56.

9. Adams, A.L., "Rotor Perturbation Test by Forced Motion," Private Communication.

10. Cole, J.A., and Hughes, C.J., "Visual Study of Film Extent in Dynamically Loaded Complete Journal Bearings," Conference on Lubrication and Wear, London, England, 1 October 1957.

11. Boeker, G.F., and Sternlicht,B., "Investigation of Translatory Fluid Whirl in Vertical Machines," ASME/ASLE Lubrication Conference, Baltimore, Marlyland, 18 October 1954.

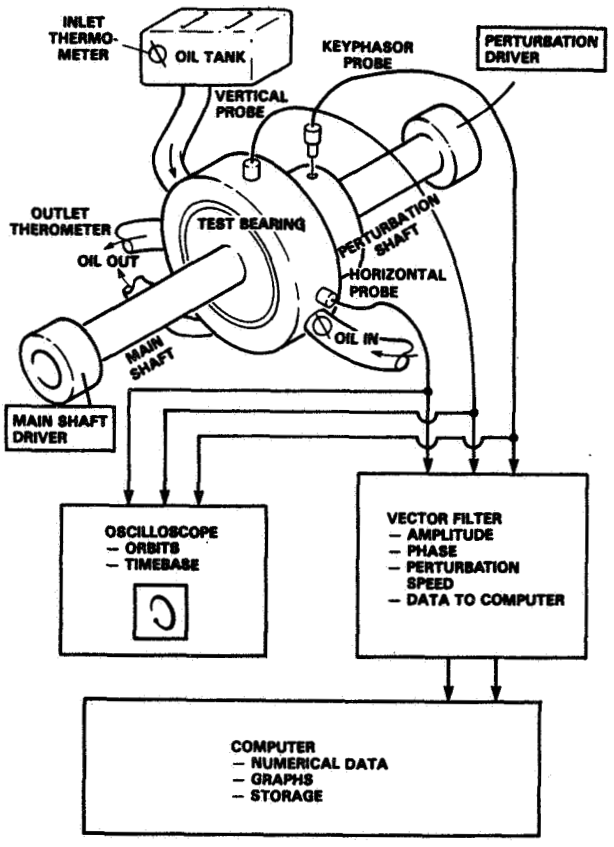

Figure 1. - Experiment setup.

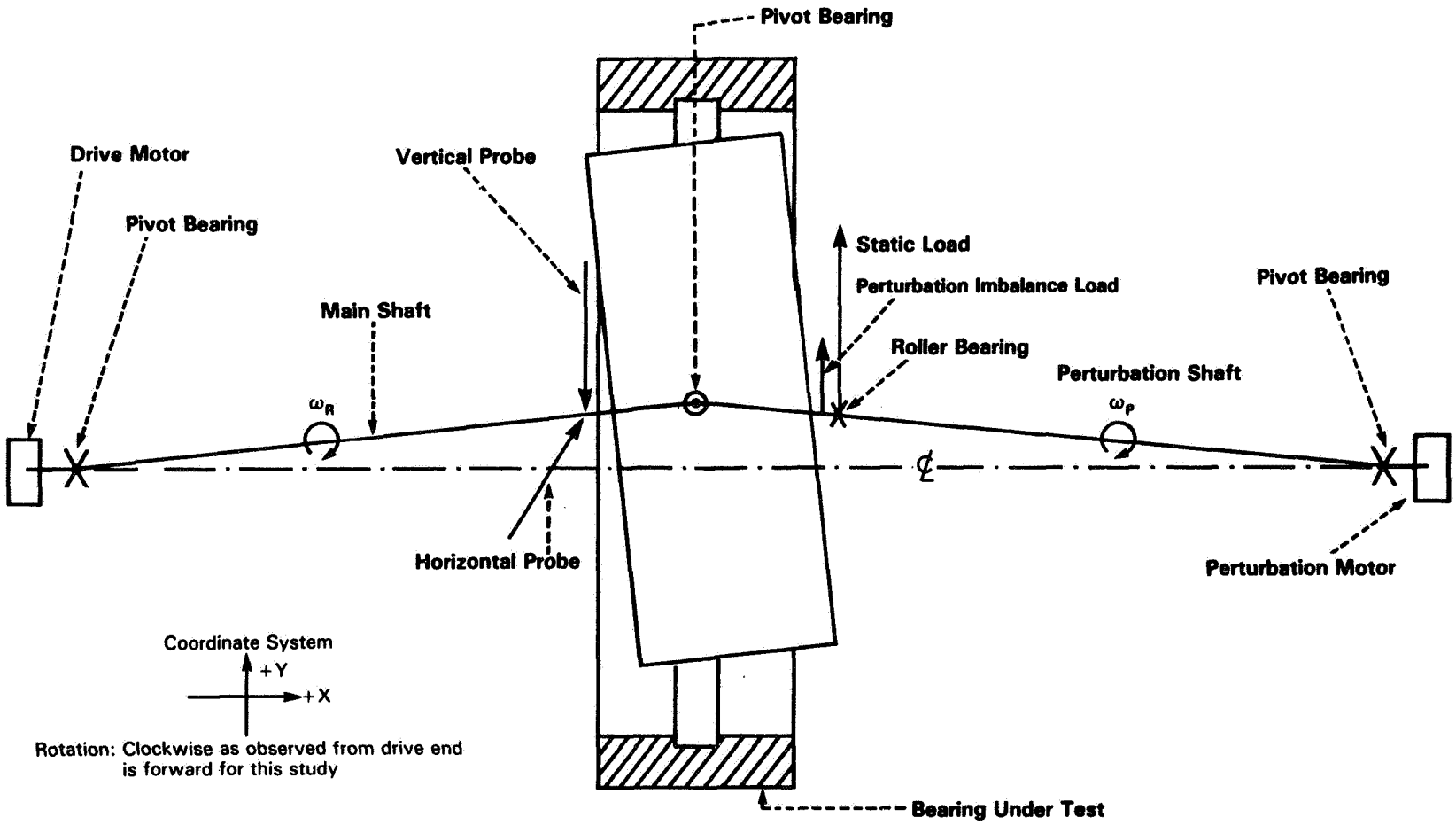

Figure 2. - Diagram of perturbation test system.

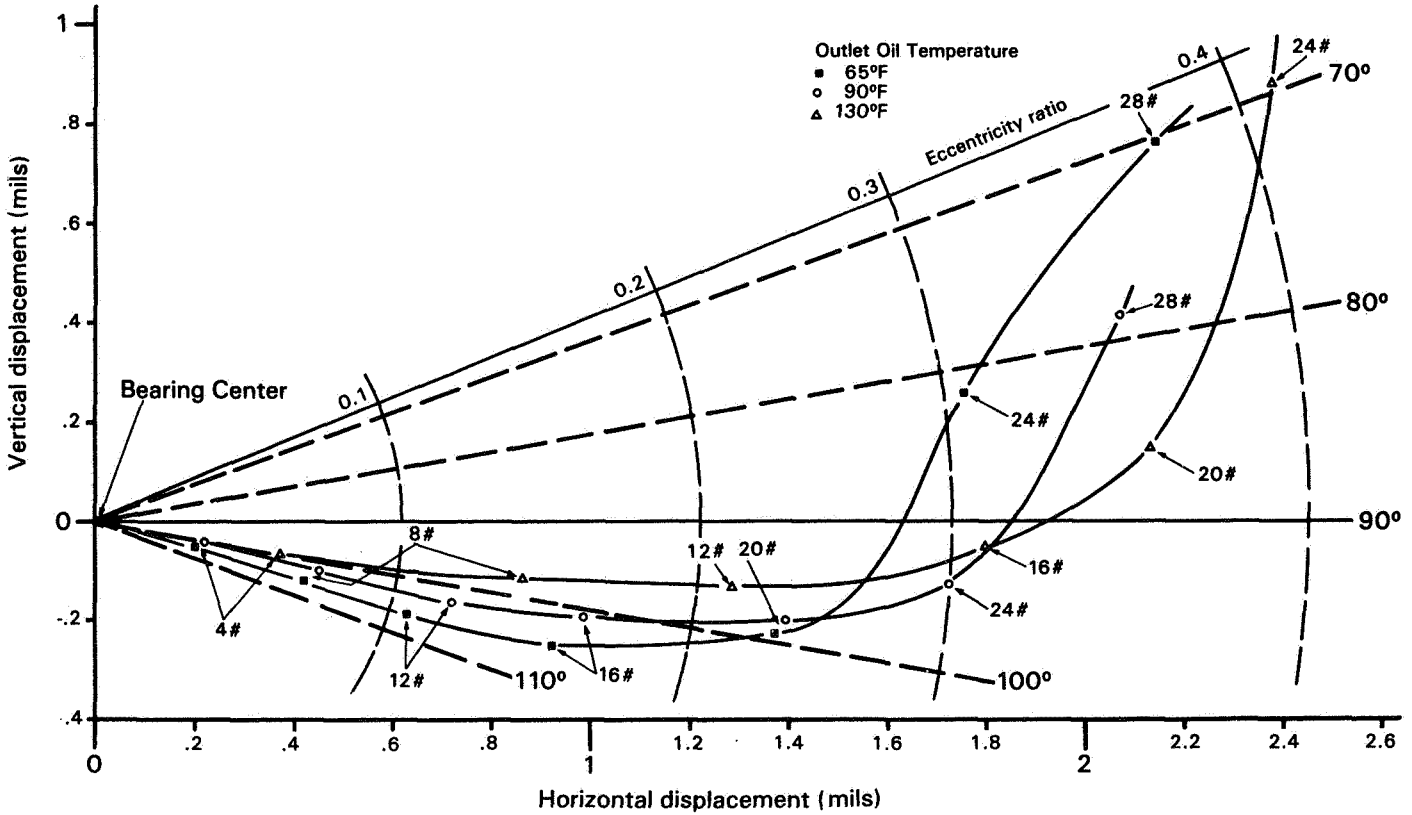

Figure 3. - Static deflection at oil outlet temperatures of 65°, 90°, and 130° F (64.3, 35.6, and 15.7 cP), rotative speed of 400 rad/sec, oil supply pressure of 5 psi, and static loads to 28 lb with clockwise rotation.

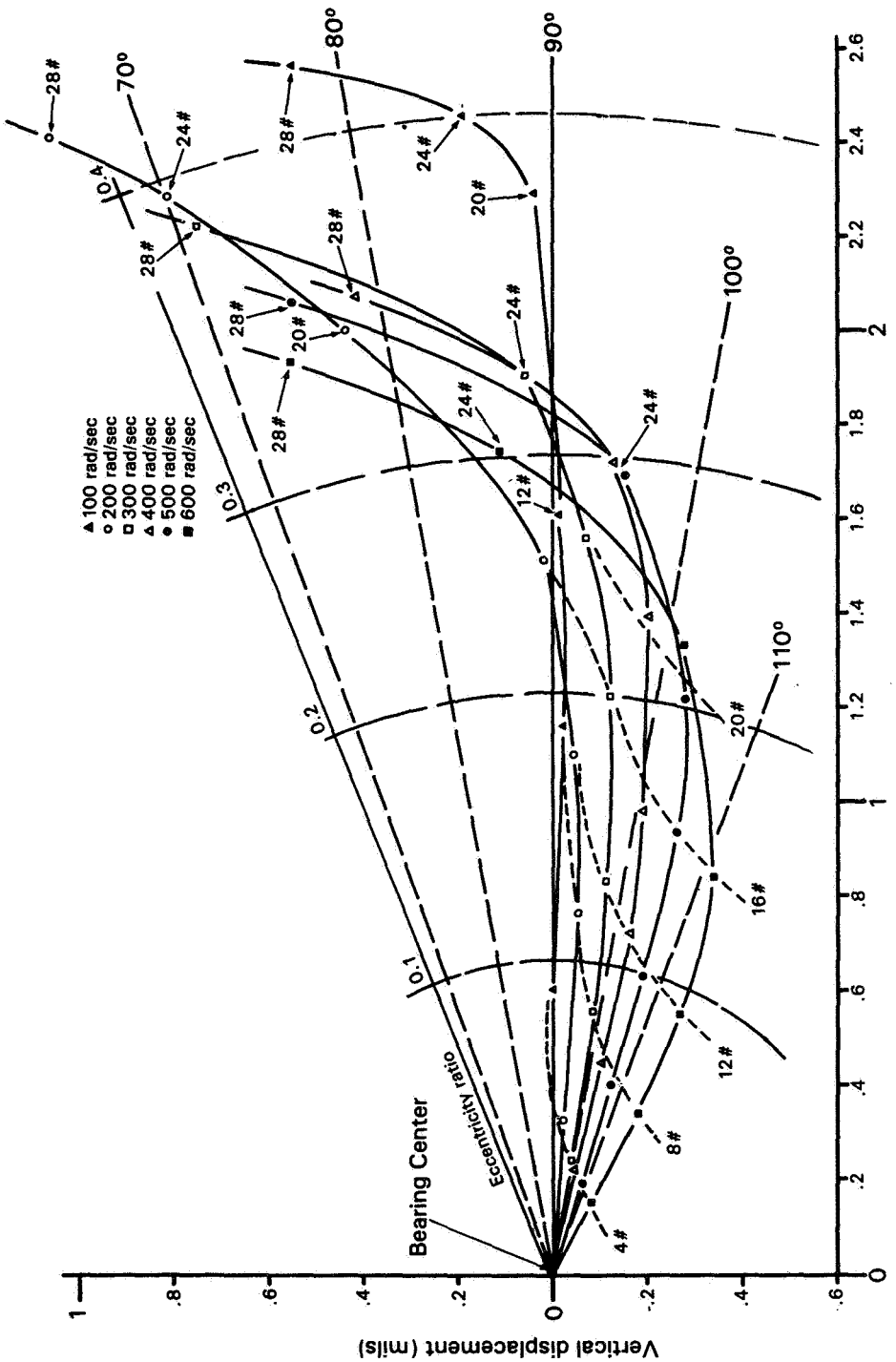

Figure 4. - Static deflection at rotative speeds of 100, 200, 300, 400, 500, and 600 rad/sec, oil outlet temperature of 98° F (35.6 cP), oil supply pressure of 5 psi, and static loads to 28 lb with clockwise rotation.

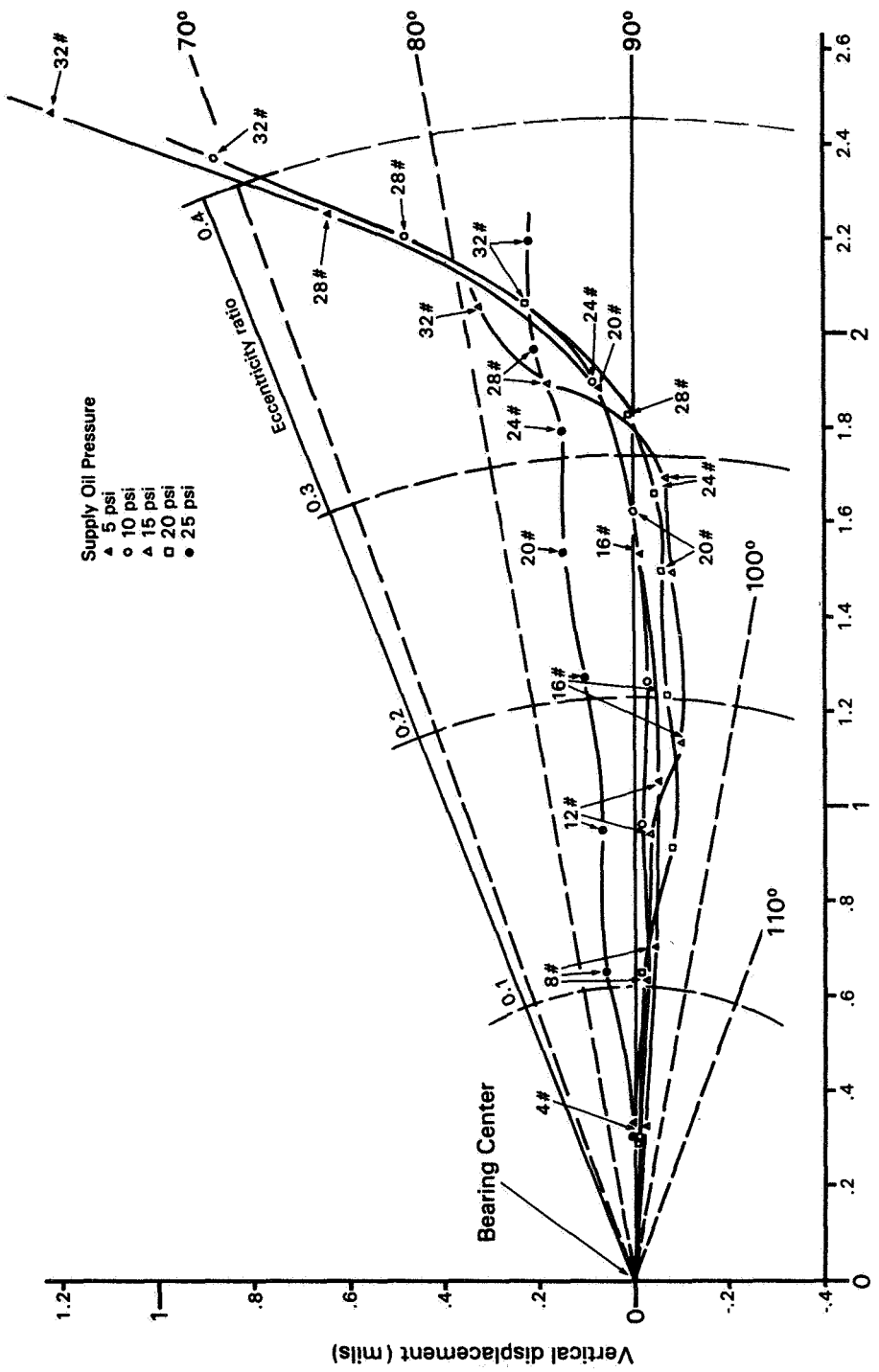

Figure 5. - Static deflection at oil supply pressures of 5, 10, 15, 20, and 25 psi, rotative speed of 200 rad/sec, oil outlet temperature of 90° F (35.6 cP), and static load to 32 lb with clockwise rotation.

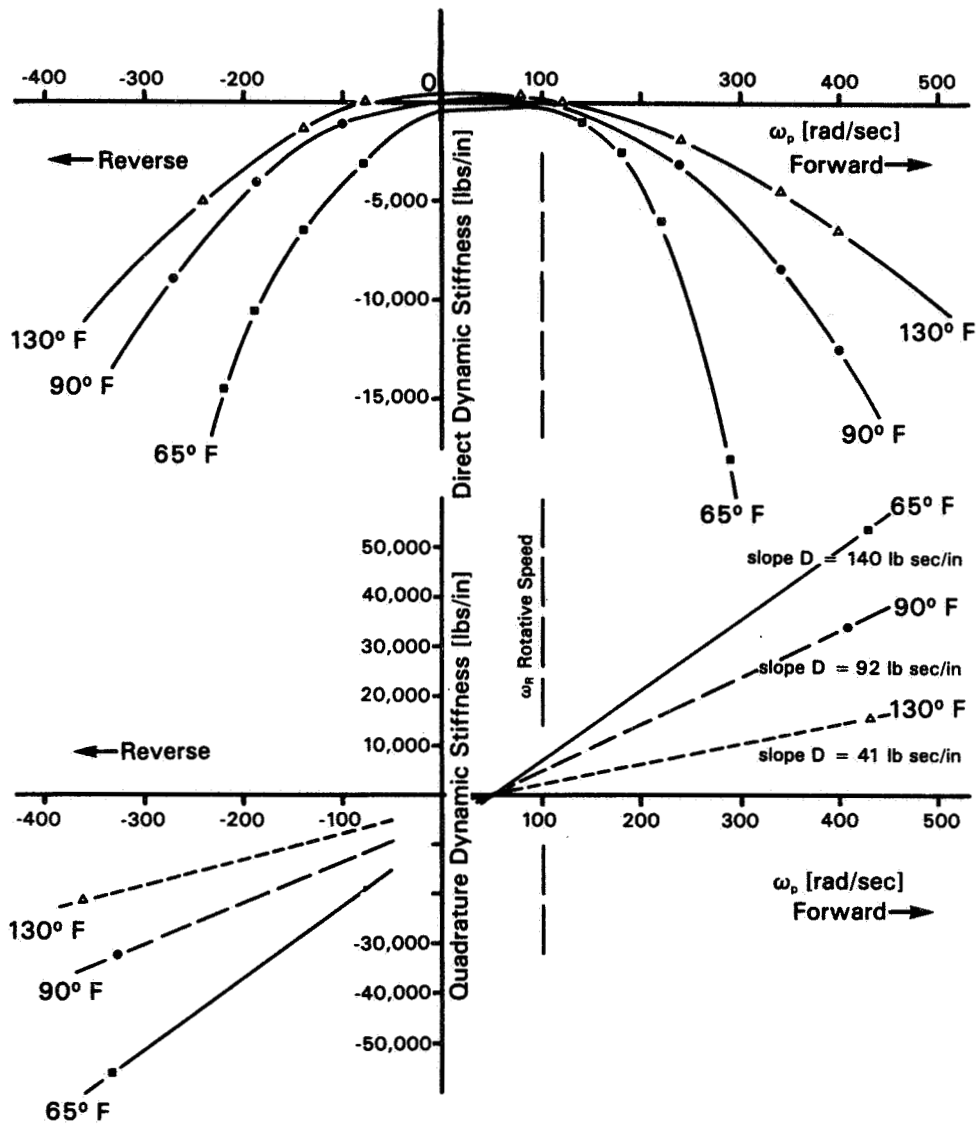

Figure 6. - Direct and quadrature dynamic stiffness at rotative speed of 100 rad/sec, oil outlet temperatures of 65°, 90°, and 130° F, oil supply pressure of 5 psi, and no static load.

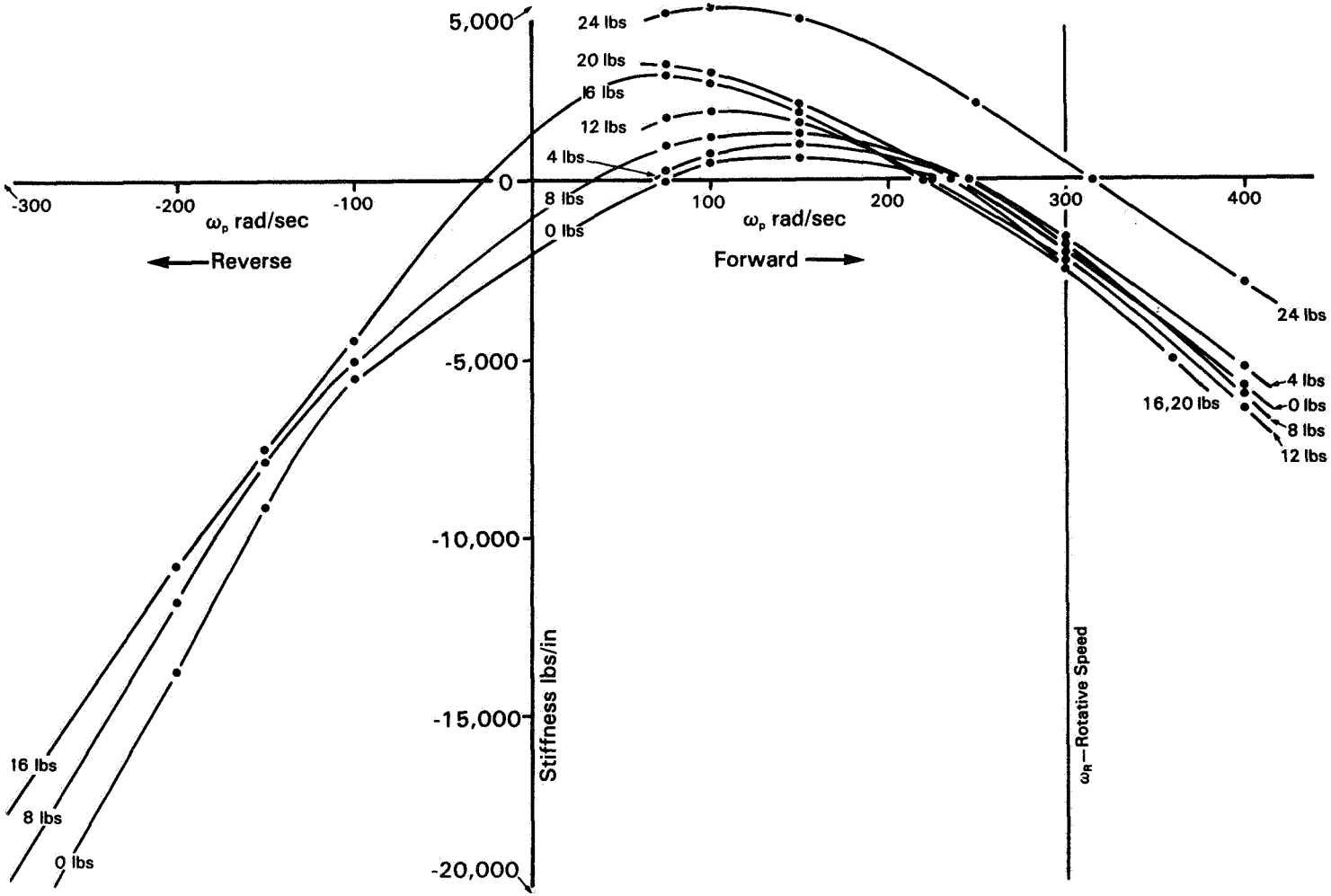

Figure 7. - Vertical direct dynamic stiffness at oil outlet temperature of 65° F (64.3 cP), rotative speed of 300 rad/sec, oil supply pressure of 5 psi, and static loads to 24 lb at

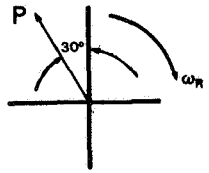

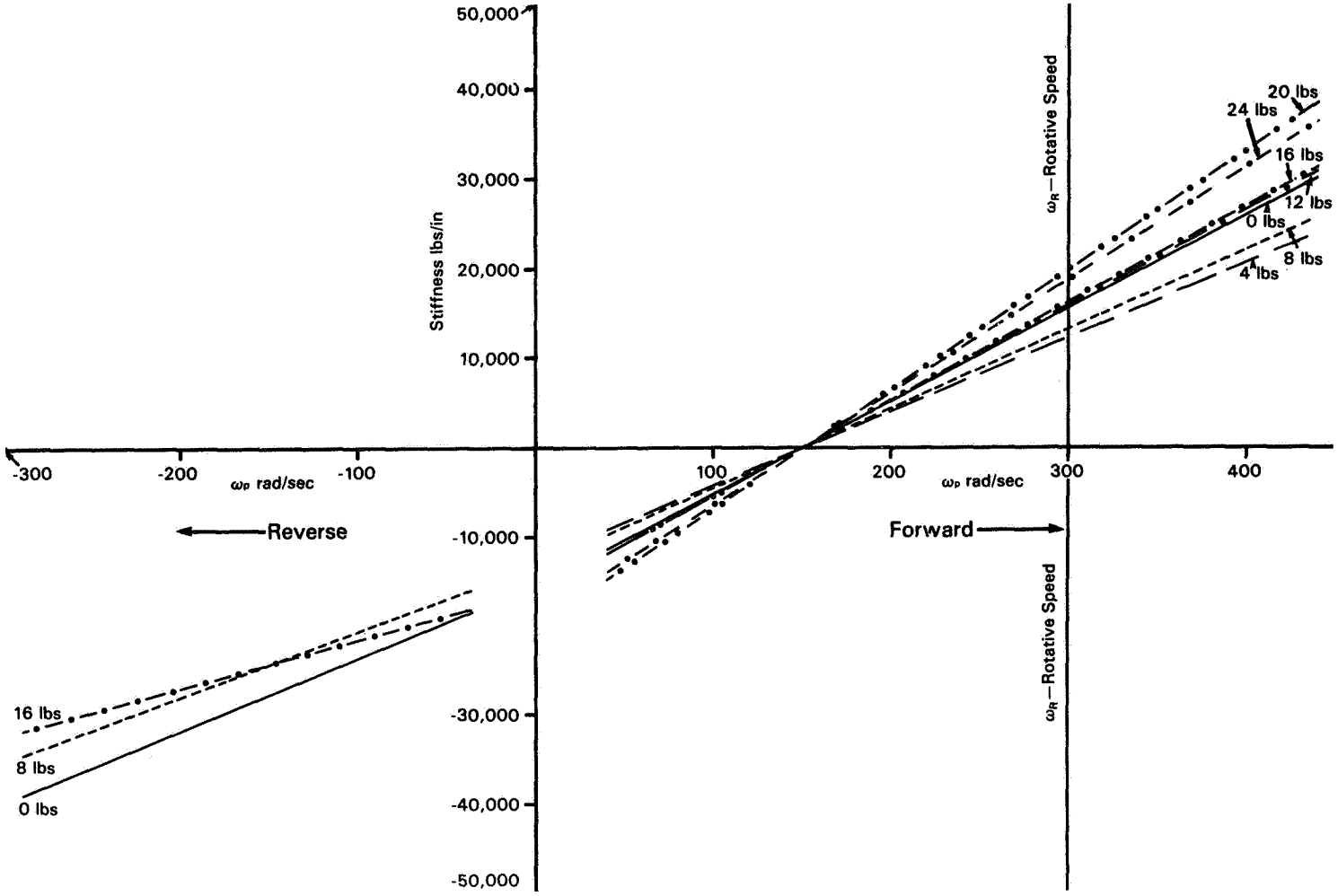

Figure 8. - Vertical quadrature dynamic stiffness at rotative speed of 300 rad/sec, oil outlet temperature of 65° F, oil supply pressure of 5 psi, and static loads to 24 lb.

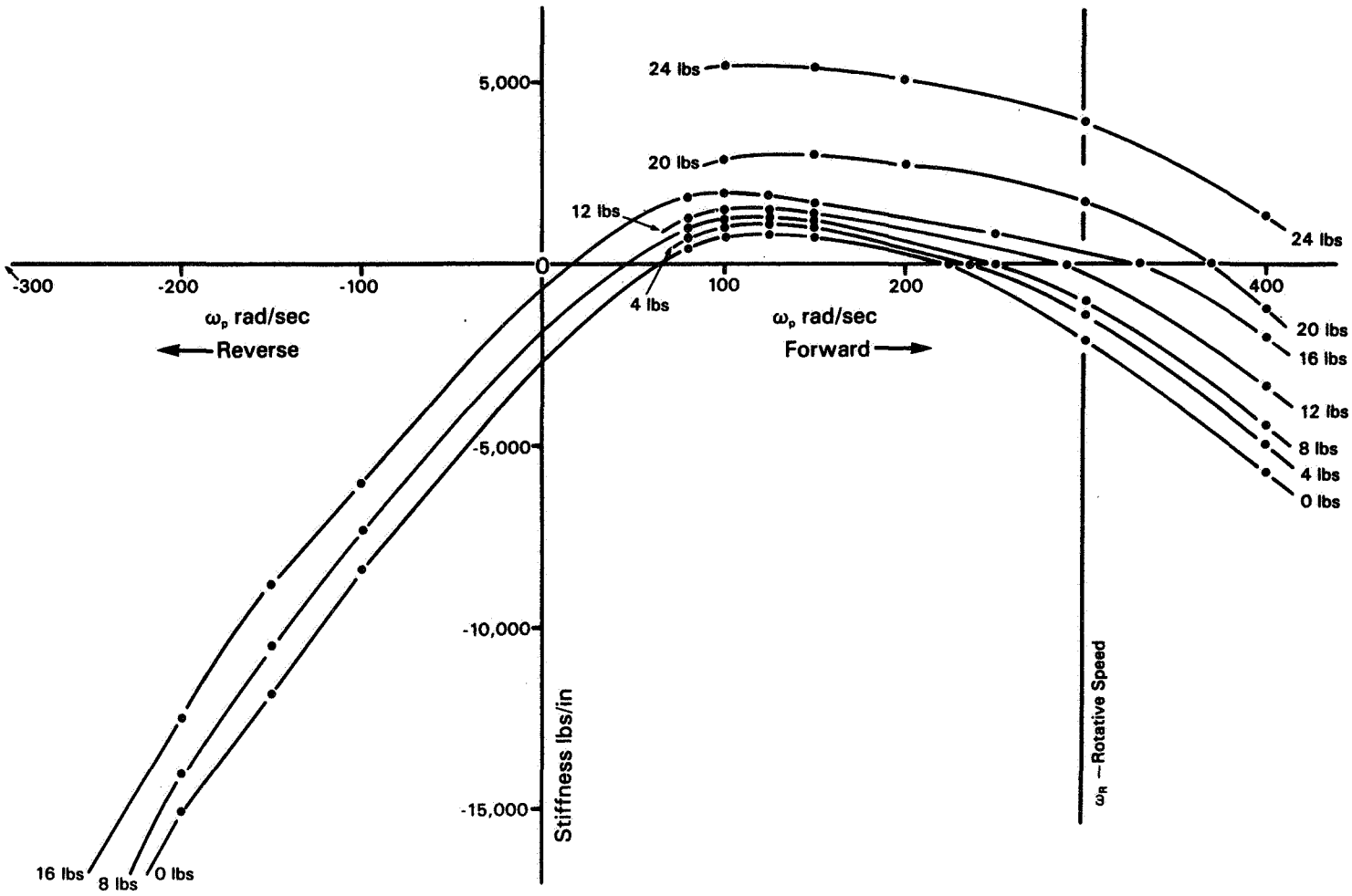

Figure 9. - Horizontal direct dynamic stiffness at oil outlet temperature of 65° F (64.3 cP), rotative speed of 300 rad/sec, oil supply pressure of 5 psi, and static loads to 24 lb at P

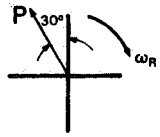

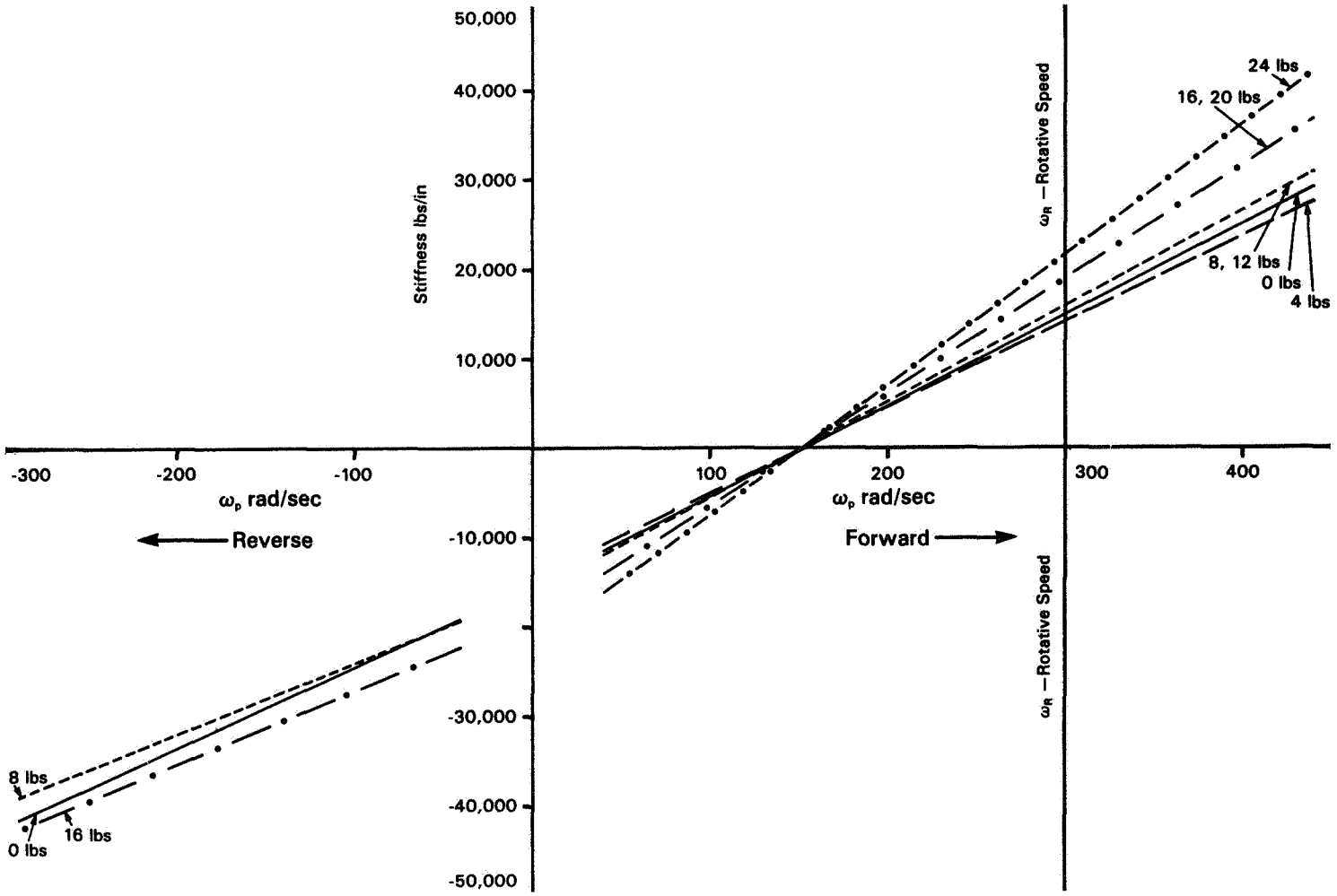

Figure 10. - Horizontal quadrature dynamic stiffness at rotative speed of 300 rad/sec, oil outlet temperature of 65° F, oil supply pressure of 5 psi, and static loads of 0, 4, 8, 12, 16, 20, and 24 lb.

1. Report No.	2. Government Accession No.	3. Recipient's Catalog No.
NASA CP-2338		

4. Title and Subtitle	5. Report Date
Rotordynamic Instability Problems in High-Performance Turbomachinery - 1984	December 1984
	6. Performing Organization Code 505-32-42
7. Author(s)	8. Performing Organization Report No. E-2214
	10. Work Unit No.
9. Performing Organization Name and Address National Aeronautics and Space Administration Lewis Research Center Cleveland, Ohio 44135	11. Contract or Grant No.
	13. Type of Report and Period Covered Conference Publication
12. Sponsoring Agency Name and Address National Aeronautics and Space Administration Washington, D.C. 20546	14. Sponsoring Agency Code

15. Supplementary Notes

The workshop was sponsored by Texas A&M University, College Station, Texas; the U.S. Army Research Office, Durham, North Carolina; and the Aeropropulsion Laboratory, Wright Patterson Air Force Base, Ohio, and held at Texas A&M University on May 28-30, 1984.

16. Abstract

The first rotordynamics workshop proceedings (NASA CP-2133, 1980) emphasized a feeling of uncertainty involved in predicting the stability of characteristics of high-performance turbomachinery. In the second workshop proceedings (NASA CP-2250, 1982) these uncertainties were reduced through programs established to systematically resolve problems with emphasis on experimental validation of the forces that influence rotordynamics. The present workshop proceedings illustrates that many of these programs for predicting or measuring forces and force coefficients in high-performance turbomachinery are producing results. The availability of these data for designing new machines with enhanced stability characteristics or upgrading existing machines, with researchers continuing their attempts to explain discrepancies and evolve new theories, is particularly encouraging.

17. Key Words (Suggested by Author(s))	18. Distribution Statement
Rotordynamics Turbomachinery Instability	Unclassified - unlimited STAR Category 37

19. Security Classif. (of this report)	20. Security Classif. (of this page)	21. No. of pages	22. Price*
Unclassified	Unclassified	507	A22

*For sale by the National Technical Information Service, Springfield, Virginia 22161